Vol. 20. No 1, 2018

ISSN 1507-2711
Cena: 25 zł (w tym 5% VAT)

EKSPLOATACJAINIEZAWODNOŚĆ
MAINTENANCEANDRELIABILITY

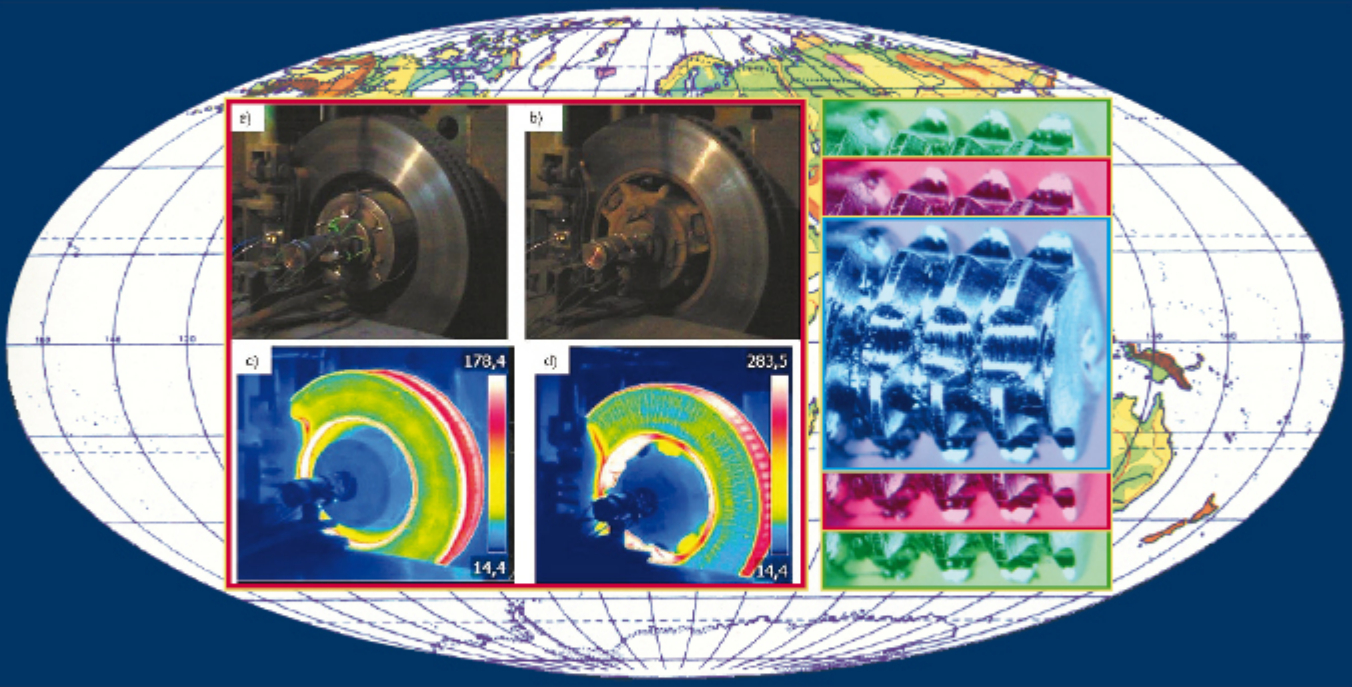

Polskie Naukowo Techniczne Towarzystwo Eksploatacyjne
Warszawa

Polish Maintenance Society
Warsaw

The Journal is indexed and abstracted in the Journal Citation Reports (JCR Science Edition), Scopus, Science Citation Index Expanded (SciSearch®) and Index Copernicus International.

The Quarterly appears on the list of journals credited with a high impact factor by the Polish Ministry of Science and Higher Education and is indexed in the Polish Technical Journal Contents database – BAZTECH and the database of the Digital Library Federation.

All the scientific articles have received two positive reviews from independent reviewers.

Our 2016 Impact Factor is 1.145

Editorial staff:	Dariusz Mazurkiewicz, PhD, DSc (Eng), Associate Professor (Editor-in-Chief, Secretary of the Editorial Board) Tomasz Klepka, PhD, DSc (Eng), Associate Professor (Deputy Editor-in-Chief) Teresa Błachnio-Krolopp, MSc (Eng) (Editorial secretary) Andrzej Koma (Typesetting and text makeup) Krzysztof Olszewski, PhD (Eng) (Webmaster)
Publisher:	Polish Maintenance Society, Warsaw
Scientific patronage:	Polish Academy of Sciences Branch in Lublin
Address for correspondence:	"Eksploatacja i Niezawodność" – Editorial Office ul. Nadbystrzycka 36, 20-618 Lublin, Poland e-mail: office@ein.org.pl http://www.ein.org.pl/
Circulation:	550 copies

KOWALSKI S. **The influence of selected PVD coatings on fretting wear in a clamped joint based on the example of a rail vehicle wheel set**. Eksploatacja i Niezawodnosc – Maintenance and Reliability 2018; 20 (1): 1–8, http://dx.doi.org/10.17531/ein.2018.1.1.

In this article, laboratory test results concerning the influence of selected PVD coatings on the initiation and development of fretting wear in clamped joints are presented. TiN and CrN+a-C:H:W coatings were applied to shafts, and the results of wear tests compared with those for uncoated shafts. Wear tests were conducted at a test bed which simulated the operation conditions of the wheel sets of rail vehicles moving along a straight track. The sample elements for testing were assembled by forcing the sleeve onto the shaft with the tolerance of 0.02 mm. To assess fretting at shaft top layers being tested, macroscopic observations, microscopic observations with the use of a scanning microscope, x-ray microanalysis of the chemical composition by means of the EDS method and the measurement of the top layer topography in the place of wear were performed. Test results presented concern the shaft top layer because it is that layer which mainly determines the life of a clamped joint. The results of the macroscopic observations of the sleeve hub top layer were presented, too, for comparison of the image of wear between mating surfaces.The results of the observations of the various shaft top layers indicate the mitigation of the development of fretting wear in the case of shafts with coatings; CrN+a-C:H:W coatings influence the mitigation of fretting wear better indeed. The main damage comprised by fretting in all the samples being tested is material build-up occurring as a result of adhesion. That build-up undergoes oxidation during operation. Micropits and microabrasion of the top layer are observed in places.

KOWALSKI S. **Wpływ wybranych powłok PVD na zużycie frettingowe w połączeniu wtłaczanym na przykładzie modelu zestawu kołowego pojazdu szynowego**. Eksploatacja i Niezawodnosc – Maintenance and Reliability 2018; 20 (1): 1–8, http://dx.doi.org/10.17531/ein.2018.1.1.

W artykule zaprezentowano wyniki badań laboratoryjnych dotyczące wpływu zastosowania wybranych powłok PVD na inicjację i rozwój zużycia frettingowego w połączeniach wtłaczanych. Na wały nałożono powłoki TiN a także CrN+a-C:H:W, wyniki badań zużyciowych porównano z wynikami badań wałów bez powłok. Badania zużyciowe wykonywano na stanowisku badawczym, które symulowało warunki pracy zestawów kołowych pojazdów szynowych poruszających się po torze prostym. Montaż elementów próbki przeznaczonej do badań wykonano przez wtłoczenie tulei na wał z wartością wcisku 0,02mm. W celu oceny zjawiska frettingu dla badanych warstw wierzchnich wałów wykonano obserwacje makroskopowe, mikroskopowe przy użyciu mikroskopu skaningowego, mikroanalizę rentgenowską składu chemicznego metodą EDS oraz pomiar topografii warstwy wierzchniej w miejscu zużycia. Zaprezentowane wyniki badań dotyczą warstwy wierzchniej wałów, ponieważ to ona w głównej mierze determinują trwałość połączenia wtłaczanego. Zaprezentowano również wyniki obserwacji makroskopowych warstwy wierzchniej piasty tulei, w celu porównania obrazu zużycia pomiędzy współpracującymi powierzchniami. Wyniki obserwacji poszczególnych warstw wierzchnich wałów wskazują na ograniczenie rozwoju zużycia frettingowego w przypadku wałów z zastosowanymi powłokami, przy czym powłoki CrN+a-C:H:W korzystniej wpływają na zmniejszenie zużycia frettingowego. Głównym uszkodzeniem składającym się na zjawisko frettingu we wszystkich badanych próbkach są nalepienia materiału, powstałe w wyniku zjawiska adhezji. W czasie eksploatacji nalepienia te ulegają utlenianiu. Lokalnie obserwuje się mikrowżery i mikrowytarcia warstwy wierzchniej.

SZUDROWICZ M. **Layered composite increasing the resistance of patrol and intervention vehicles to the impact of improvised explosive devices (IED) from below**. Eksploatacja i Niezawodnosc – Maintenance and Reliability 2018; 20 (1): 9–15, http://dx.doi.org/10.17531/ein.2018.1.2.

Model layered composites were made of polyester resin reinforced with layers of glass fibre and aramid fibre fabrics. The fabrics for the study were selected in a manner enabling the comparison of their ballistic resistance depending on the material type and density. Additionally, aluminium plates were used to produce the composites.The study examined the resistance of the model composites to 1.1 g fragment simulating projectile (FSP) penetration, their susceptibility to deformation caused by shock waves produced by pure TNT charges, and their resistance to the effects of detonation of model improvised explosive devices (IED) containing fragments in the form of bearing balls. The analysis and optimisation of the test results enabled the selection of a layer configuration combining the materials studied that has the lowest area density and that protects car bottom structures against perforation in the case of a detonation of a small improvised explosive device.

SZUDROWICZ M. **Kompozyt warstwowy zwiększający odporność samochodów patrolowych i interwencyjnych na atak improwizowanych ładunków wybuchowych (IED) od dołu**. Eksploatacja i Niezawodnosc – Maintenance and Reliability 2018; 20 (1): 9–15, http://dx.doi.org/10.17531/ein.2018.1.2.

Wykonano modelowe kompozyty warstwowe do budowy których wybrane zostały:ul. skro żywica poliestrowa zbrojona warstwami tkanin z włókien szklanych i aramidowych. Tkaniny do badań dobrano w sposób umożliwiający porównanie odporności balistycznej w zależności od rodzaju materiału i gęstości. Dodatkowo do konstrukcji kompozytów użyto blachy aluminiowej. Zbadano odporność wykonanych modeli kompozytów na przebicie pociskami symulującymi odłamek (FSP) o masie 1,1 g, ich podatność na deformację w wyniku oddziaływania fali uderzeniowej czystych ładunków trotylu, odporność na detonację modelowych improwizowanych urządzeń wybuchowych IED, zawierające odłamki w postaci kulek łożyskowych. Analiza i optymalizacja wyników badań eksperymentalnych pozwoliła dobrać układ warstwowy, będący kombinacją badanych materiałów, o najmniejszej gęstości powierzchniowej chroniący dno samochodów przed przebiciem w przypadku detonacji małego improwizowanego ładunku wybuchowego.

PIELECHA I, CIEŚLIK W, SZAŁEK A. **Operation of electric hybrid drive systems in varied driving conditions**. Eksploatacja i Niezawodnosc – Maintenance and Reliability 2018; 20 (1): 16–23, http://dx.doi.org/10.17531/ein.2018.1.3.

Hybrid vehicles allow an increase in the powertrain efficiency thanks to their design. One such factor is the use of increased voltage supplying electric motors to the voltage supplying the high voltage battery. The battery voltage is increased several times in the inverter (boost) system to increase the final electric power supplied to the electric motor. The article presents the possibilities of using such a voltage boost in urban and non-urban driving conditions. The tests were performed on the latest generations of parallel hybrid drive systems in Lexus NX 300h and Toyota RAV4 hybrid vehicles. It has been shown that the boost system is used in about 30–40% of the urban drive distance (up to 20% of the driving time). The power supply voltage boost of the electric motors of both vehicles is used throughout the entire engine speed range of these machines at high torque values. Research has shown that the maximum voltage gain – approximately three times (up to 650 V) – is within the maximum torque range of the electric motors and allows for doubling the torque generated by the drive.

PIELECHA I, CIEŚLIK W, SZAŁEK A. **Eksploatacja elektrycznych układów napędowych pojazdów hybrydowych w zróżnicowanych warunkach ruchu**. Eksploatacja i Niezawodnosc – Maintenance and Reliability 2018; 20 (1): 16–23, http://dx.doi.org/10.17531/ein.2018.1.3.

Pojazdy z napędem hybrydowym dzięki swojej konstrukcji, pozwalają na zwiększenie sprawności układu napędowego. Jednym z takich czynników jest stosowanie zwiększonego napięcia zasilającego silniki elektryczne w stosunku do napięcia zasilającego akumulator wysokonapięciowy. Napięcie akumulatora zostaje zwiększone kilkukrotnie w układzie inwertera (boost) w celu zwiększenia końcowej mocy elektrycznej doprowadzonej do silnika elektrycznego. W artykule przedstawiono możliwości wykorzystania takiego wzmocnienia napięcia w warunkach jazdy miejskiej i pozamiejskiej. W badaniach wykorzystano najnowsze generacje układów napędu hybrydowego równoległego w pojazdach Lexus NX 300h oraz Toyota RAV4 hybrid. Wykazano, że układ wzmocnienia napięcia w warunkach miejskich wykorzystany jest w około 30–40% dystansu (do 20% czasu jazdy). Wzmocnienie napięcia zasilającego maszyny elektryczne obu pojazdów wykorzystane jest w całym zakresie prędkości obrotowej tych maszyn przy dużych wartościach momentu obrotowego. Badania wykazały, że maksymalne wzmocnienie napięcia – około trzykrotne (do wartości 650 V) – występuje w zakresie maksymalnego momentu obrotowego silników elektrycznych i pozwala na ponad 2-krotne zwiększenie generowanego momentu obrotowego układu napędowego.

VAIČIŪNAS G, BUREIKA G, STEIŠŪNAS S. **Research on metal fatigue of rail vehicle wheel considering the wear intensity of rolling surface**. Eksploatacja i Niezawodnosc – Maintenance and Reliability 2018; 20 (1): 24–29, http://dx.doi.org/10.17531/ein.2018.1.4.

The article overviews scientific research studies that examine the interaction between railway vehicle wheel and rail, and the phenomena of wear on wheel rolling surface. Unique experimental research has been conducted, in which regularity of weariness on rolling surface of exploitable locomotive wheel and phenomena of metal fatigue on wheel were researched. A hypothesis is made, that according to the differences in weariness intensity of wheel rolling surface it is possible to determine the start of metal fatigue. The inequality of wear intensity of different locomotive wheels is assessed by the Sharpe ratio, adapting it to describe the wheel wear intensity criteria. Based on

VAIČIŪNAS G, BUREIKA G, STEIŠŪNAS S. **Badanie zmęczenia metalu koła pojazdu szynowego z uwzględnieniem intensywności zużycia powierzchni tocznej**. Eksploatacja i Niezawodnosc – Maintenance and Reliability 2018; 20 (1): 24–29, http://dx.doi.org/10.17531/ein.2018.1.4.

W artykule omówiono badania naukowe dotyczące wzajemnych oddziaływań między kołem pojazdu szynowego a szyną oraz zjawiska zużycia powierzchni tocznej kół. Przeprowadzono nowatorskie badania eksperymentalne, w których zbadano prawidłowości dotyczące zużywania się powierzchni tocznej eksploatowanego koła lokomotywy oraz zjawisko zmęczenia metalu koła. Założono hipotezę, że na podstawie różnic w intensywności zużycia powierzchni tocznej kół można określić początek procesu zmęczenia metalu. Różnice w intensywności zużycia różnych kół lokomotywy oceniano na podstawie współczynnika Sharpe'a, dostosowując go do opisu kryteriów intensywności zużycia kół.

the results of research, the authors propose a simplified and reliable methodology for determining metal fatigue on locomotive wheels at initial stages. The uneven wear on rolling surface of different wheels of wheelset inevitably changes the values of Sharpe ratio, which can accurately describe the conditions in which the critical metal fatigue on wheels begins to emerge.

Na podstawie wyników badań autorzy zaproponowali uproszczoną, rzetelną metodologię określania zmęczenia metalu kół lokomotywy na początkowym etapie tego procesu. Nierównomierne zużycie powierzchni tocznej różnych kół zestawu kołowego zmienia wartości współczynnika Sharpe'a, które można wykorzystać do precyzyjnego opisu warunków, w jakich dochodzi do krytycznego zmęczenia metalu kół.

KAJZER W, JAWORSKA J, JELONEK K, SZEWCZENKO J, KAJZER A, NOWIŃSKA K, HERCOG A, KACZMAREK M, KASPERCZYK J. **Corrosion resistance of Ti6Al4V alloy coated with caprolactone-based biodegradable polymeric coatings**. Eksploatacja i Niezawodnosc – Maintenance and Reliability 2018; 20 (1): 30–38, http://dx.doi.org/10.17531/ein.2018.1.5.

The aim of this study was to determine the influence of long-term exposure of Ringer's solution on degradation of the anodically oxidated Ti6Al4V alloy coated with a biodegradable polymer coating. Polymeric coatings made of poly(glycolide-ε-caprolactone) – G-Cap and poly(glycolide- ε-caprolactone-lactide) – G-Cap-L were applied by a dip-coating method. Degradation was assessed on the basis of the results of pitting corrosion resistance and density of metal ions infiltrating to the solution. Studies were conducted for samples after 3, 6, 8, 10 and 12 weeks of exposure to the corrosive environment. In addition, topography of the surface of the polymer coating was assessed. As a result of potentiodynamic studies, the value of the polarization resistance and corrosion potential for the G-Cap and G-Cap-L coated samples was significantly decreased while simultaneous reduction of the density of metal ions infiltrating to the solution throughout the whole study period. There was also observed a faster degradation of the G-Cap coating compared to G-Cap-L, which showed localized discontinuity after 12 weeks of exposure. The obtained results provide the basis for the development of polymeric coatings on surface of metal implants with predictable time / kinetics of degradation by selecting the composition of polymers while simultaneous limitation of metal ions infiltration into surrounding tissues.

KAJZER W, JAWORSKA J, JELONEK K, SZEWCZENKO J, KAJZER A, NOWIŃSKA K, HERCOG A, KACZMAREK M, KASPERCZYK J. **Odporność korozyjna stopu Ti6Al4V pokrytego biodegradowalnymi powłokami polimerowymi na bazie kaprolaktonu**. Eksploatacja i Niezawodnosc – Maintenance and Reliability 2018; 20 (1): 30–38, http://dx.doi.org/10.17531/ein.2018.1.5.

Celem pracy było określenie wpływu długotrwałego oddziaływania rozworu Ringera na proces degradacji utlenianego anodowo stopu Ti6Al4V pokrytego powłoką biodegradowalnego polimeru. Powłoki polimerowe wykonane z poli(glikolido- ε-kaprolaktonu) – G-Cap oraz poli(glikolido ε-kaprolaktono- laktydu) – G-Cap-L naniesiono metodą zanurzeniową (dip-coating). Proces degradacji w funkcji czasu oceniano na podstawie wyników badań odporności na korozję wżerową oraz gęstości masy jonów metalowych przenikających do roztworu. Badania przeprowadzono dla próbek po 3, 6, 8, 10 i 12 tygodniach ekspozycji na środowisko korozyjne. Ponadto oceniano topografię powierzchni powłoki polimerowej. W wyniku przeprowadzonych badań potencjodynamicznych stwierdzono wyraźne obniżenie wartości oporu polaryzacyjnego i potencjału korozyjnego dla próbek z naniesionymi powłokami G-Cap i G-Cap-L przy jednoczesnym wyraźnym ograniczeniu gęstości jonów metalowych przenikających do roztworu w całym okresie badawczym. Stwierdzono również szybszą degradację powłoki typu G-Cap w porównaniu do G-Cap-L, dla której po 12 tygodniu ekspozycji stwierdzono lokalnie występujące przerwania ciągłości. Uzyskane wyniki dają podstawę do opracowywania na powierzchni implantów metalowych powłok polimerowych o przewidywalnym czasie/określonej kinetyce degradacji, poprzez dobór składu polimerów z jednoczesnym ograniczeniem możliwości przenikania jonów metalowych do otaczających tkanek.

POSZWA P, SZOSTAK M. **Influence of scale deposition on maintenance of injection molds**. Eksploatacja i Niezawodnosc – Maintenance and Reliability 2018; 20 (1): 39–45, http://dx.doi.org/10.17531/ein.2018.1.6.

The cooling system of an injection mold serves a substantial role in the process of plastic injection. It is responsible for efficient dissipation of heat from the injection mold, generated by the plasticized material which during the injection phase is introduced into the mold. Apart from rapid heat dissipation, it is important to achieve uniform distribution of temperatures on the surface of the molding cavity. This study focuses on the phenomenon of lime scale deposition in injection mold cooling systems. Lime scale deposition results in reduction of the cooling canal's section diameter, as well as a clear reduction in cooling efficiency due to its lowered thermal conductivity. The study specifies the influence of many factors (geometry of the cooling system and molded piece, coolant temperature, type of plastic material) on the utilization of the injection mold as a result of the occurrence of lime scale in the cooling system. The conducted numerical simulations have allowed to account for the impact of the deposit layer's thickness on the distribution of temperatures on the molding cavity's surface, the average injection mold temperature, as well as the time required to solidify the plastic material products.

POSZWA P, SZOSTAK M. **Wpływ odkładania się kamienia na eksploatację form wtryskowych**. Eksploatacja i Niezawodnosc – Maintenance and Reliability 2018; 20 (1): 39–45, http://dx.doi.org/10.17531/ein.2018.1.6.

Układ chłodzenia formy wtryskowej odgrywa niebagatelną rolę w procesie wtryskiwania tworzyw sztucznych. Odpowiada on za sprawny odbiór ciepła z formy wtryskowej dostarczonego przez uplastycznione tworzywo, które w fazie wtrysku jest wprowadzone do formy. Oprócz szybkiego odbioru ciepła istotne jest, aby rozkład temperatury na powierzchni gniazda formującego był równomierny. W niniejszej pracy skupiono się na zjawisku osadzania się kamienia w układach chłodzących form wtryskowych. Kamień powoduje zarówno zwężenie przekroju kanału chłodzącego, jak i wyraźny spadek wydajności chłodzenia ze względu na jego niską przewodność cieplną. W pracy określono wpływ wielu czynników (geometria układu chłodzenia oraz wypraski, temperatura cieczy chłodzącej, rodzaj tworzywa) na eksploatację formy wtryskowej w wyniku pojawienia się kamienia w układzie chłodzącym. Przeprowadzone symulacje numeryczne pozwoliły uwzględnić wpływ grubości warstwy osadu na rozkład temperatury na powierzchni gniazda formującego, średnią temperaturę formy wtryskowej, a także czas potrzebny do zestalenia wyrobów produkowanych z tworzyw sztucznych.

ROMANIUK M. **Optimization of maintenance costs of a pipeline for a V-shaped hazard rate of malfunction intensities**. Eksploatacja i Niezawodnosc – Maintenance and Reliability 2018; 20 (1): 46–56, http://dx.doi.org/10.17531/ein.2018.1.7.

In this paper I focus on an evaluation of maintenance costs of a water distribution system (WDS), if a concept of a value of money in time is taken into account. Contrary to more classical approaches, instead of a constant yield, a strictly stochastic process (i.e., the one-factor Vasicek model) of an interest rate is assumed. Such an assumption presents uncertain, future behaviour of the yield in a more correct, realistic way. Moments of failures of connections in a WDS are generated using the Monte Carlo simulations via a new kind of a convex hazard rate function (HRF), which is proposed in this paper. Moreover, quality of a pipeline and a number of previous failures have direct influence on statistical properties of this introduced HRF. Apart from an analysis of the simulated output (like the maintenance costs), the Kiefer-Wolfowitz method is used for a better adjustment of one of parameters of a WDS – deterministic and unconditional replacement (i.e., planned replacement) time of each pipe. Algorithms, for both the simulations of the failure moments for the introduced HRF and the optimization step, are also provided. Additionally, some examples of a WDS for a crisp and a fuzzified settings are statistically analysed.

ROMANIUK M. **Optymalizacja kosztów eksploatacyjnych rurociągu dla V-kształtnej funkcji intensywności uszkodzeń**. Eksploatacja i Niezawodnosc – Maintenance and Reliability 2018; 20 (1): 46–56, http://dx.doi.org/10.17531/ein.2018.1.7.

W niniejszej publikacji skupiam się na obliczeniu kosztów eksploatacji wodociągu (water distribution system – WDS), jeśli pod uwagę zostanie wzięta wartość pieniądza w czasie. W przeciwieństwie do klasycznego podejścia, zamiast stałej wartości stopy procentowej, zakładam stochastyczny proces stopy procentowej (w postaci jednoczynnikowego modelu Vasicka). Założenie to przedstawia niepewne, przyszłe zachowanie stopy procentowej w bardziej dokładny i realistyczny sposób. Momenty awarii połączeń w WDS generowane są z wykorzystaniem metody Monte Carlo poprzez zastosowanie nowego typu funkcji intensywności uszkodzeń (hazard rate function – HRF), który zaproponowany został w niniejszej publikacji. Ponadto, jakość połączenia oraz ilość wcześniejszych uszkodzeń ma bezpośredni wpływ na statystyczne właściwości wprowadzonej HRF. Oprócz analizy wygenerowanych za pomocą symulacji wyników (takich jak koszty eksploatacji), użyta została metoda Kiefera-Wolfowitza w celu lepszego dopasowania jednego z parametrów WDS – deterministycznego i bezwarunkowego momentu wymiany każdego z połączeń (czyli wymiany planowanej). Zaprezentowane zostały również algorytmy zarówno dla symulowania momentów uszkodzeń przy użyciu zaproponowanej HRF, jak i dla kroku optymalizacyjnego. Ponadto, wykonana została analiza statystyczna kilku przykładów WDS dla dokładnych („crisp") i rozmytych („fuzzy") wartości parametrów.

SAWCZUK W. **Analytical model coefficient of friction (COF) of rail disc brake on the basis of multi-phase stationary tests**. Eksploatacja i Niezawodnosc – Maintenance and Reliability 2018; 20 (1): 57–67, http://dx.doi.org/10.17531/ein.2018.1.8.

SAWCZUK W. **Model analityczny zmienności współczynnika tarcia kolejowego hamulca tarczowego na podstawie wielofazowych badań stanowiskowych**. Eksploatacja i Niezawodnosc – Maintenance and Reliability 2018; 20 (1): 57–67, http://dx.doi.org/10.17531/ein.2018.1.8.

Similarly to road vehicles, a disc brake remains the main friction brake in rail vehicles. Due to the increasing train speeds, a disc brake has already replaced the traditional clasp brake that is however, still used in cargo trains. In the process of long-term operation of the brake pad-brake disc friction pair, the parameters of the braking process such as the curve of the coefficient of friction are changed, which extends the braking distance. The paper presents the results of several years of investigations on the railway disc brake in different wear conditions in the aspect of the requirements set by the UIC (International Union of Railways) related to the brake pads approval for use.

W pojazdach szynowych, podobnie jak w samochodowych, podstawowym hamulcem roboczym jest cierny hamulec tarczowy. Ze względu na coraz większe prędkości jazdy, hamulec tarczowy w wielu pojazdach kolejowych jak i tramwajowych wyparł już hamulec klockowy, który niezmiennie jeszcze jest stosowany w pociągach towarowych. W procesie dłuższej eksploatacji pary ciernej tarcza-okładzina główne parametry procesu hamowania jak przebieg współczynnika tarcia obniża się, co w konsekwencji wydłuża drogę hamowania. W artykule przedstawiono wyniki kilkuletnich badań kolejowego hamulca tarczowego w różnych stanach jego zużycia z uwzględnieniem między innymi wymagań stawianych przez Międzynarodowy Związek Kolei UIC w zakresie dopuszczenia okładzin hamulcowych do eksploatacji.

KONTREC N, PANIĆ S, PETROVIĆ M, MILOŠEVIĆ H. **A stochastic model for estimation of repair rate for system operating under performance based logistics**. Eksploatacja i Niezawodnosc – Maintenance and Reliability 2018; 20 (1): 68–72, http://dx.doi.org/10.17531/ein.2018.1.9.

Performance Based Logistics (PBL) concept has an aim to improve the system availability and it has been extensively researched in the recent years. These researches showed that inventory level does not impact system availability as much as component reliability and repair time in repairable system operating under PBL contract. Based on that, in this paper, we propose a new stochastic model for determination of annual repair rate for critical aircraft components in such system in order to achieve desired availability. The result obtained could be used for planning of base stock level and capacity of repair facilities.

KONTREC N, PANIĆ S, PETROVIĆ M, MILOŠEVIĆ H. **Stochastyczny model do szacowania intensywności naprawdla systemu działającego w warunkach logistyki wydajnościowej**. Eksploatacja i Niezawodnosc – Maintenance and Reliability 2018; 20 (1): 68–72, http://dx.doi.org/10.17531/ein.2018.1.9.

Koncepcja Logistyki Opartej na Wydajności (Performance Based Logistics, PBL), której celem jest poprawa gotowości systemów, została w ostatnich latach szeroko zbadana. Badania te wykazały, że w przypadku systemów działających w warunkach PBL, poziom zapasów nie wpływa na gotowość systemu w tak dużym stopniu jak niezawodność elementów składowych oraz czasy napraw. Opierając się na tej obserwacji, w niniejszym artykule proponujemy nowy model stochastyczny do określania rocznej intensywności napraw krytycznych elementów samolotu tworzących system tego typu. Model ten pozwala na osiągnięcie pożądanej gotowości. Uzyskany model może być wykorzystany do planowania bazowego poziomu zapasów oraz przepustowości zakładów remontowych.

TAHA R. **On system reliability of increasing multi-state linear k-within-(m,s)-of-(m,n):F lattice system**. Eksploatacja i Niezawodnosc – Maintenance and Reliability 2018; 20 (1): 73–82, http://dx.doi.org/10.17531/ein.2018.1.10.

A “multi-state linear k-within-(m,s)-of-(m,n):F lattice system” (MS L(k,m,s,n:F)) comprises of m×n components, which are ordered in m rows and n columns. The state of system and components may be one of the following states: 0, 1, 2, …, H. The state of MS L(k,m,s,n:F) is less than j whenever there is at least one sub-matrix of the size m×s which contains kl or more components that are in state less than l for all $j \leq l \leq H$. This system is a model for many applications, for example, tele communication, radar detection, oil pipeline, mobile communications, inspection procedures and series of microwave towers systems. In this paper, we propose new bounds of increasing MS L(k,m,s,n:F) reliability using second and third orders of Boole-Bonferroni bounds with i.i.d components. The new bounds are examined by previously published numerical examples for some special cases of increasing MS L(k,m,s,n:F). Also, illustration examples of modelling the system and numerical examples of new bounds are presented. Further, comparisons between the results of second and third orders of Boole-Bonferroni bounds are given.

TAHA R. **Zwiększanie niezawodności wielostanowych systemów liniowych typu k-w- (m,s) -z- (m,n):F o strukturze kratowej**. Eksploatacja i Niezawodnosc – Maintenance and Reliability 2018; 20 (1): 73–82, http://dx.doi.org/10.17531/ein.2018.1.10.

"Wielostanowy system liniowy k-w- (m, s) -z- (m, n):F o strukturze kratowej" (MS L(k, m, s, n:F)) składa się z m × n elementów, uporządkowanych w m wierszach i n kolumnach. Stan systemu i elementów może być jednym z następujących stanów: 0, 1, 2, ..., H. Stan MS L (k, m, s, n: F) jest mniejszy niż j, gdy istnieje co najmniej jedna pod-matryca o rozmiarze m × s, która zawiera kl lub więcej elementów, które znajdują się w stanie mniejszym niż l dla wszystkich $j \leq l \leq H$. System ten stanowi model dla wielu zastosowań, na przykład w telekomunikacji, detekcji radarowej, rurociągach naftowych, komunikacji mobilnej, procedurach przeglądu oraz systemach wież radiolinii. W niniejszym artykule proponujemy nowe granice zwiększania niezawodności MS L (k, m, s, n: F) z wykorzystaniem drugiego i trzeciego stopnia nierówności Boole'a–Bonferroniego z niezależnymi elementami o jednakowym rozkładzie. Nowe granice omówiono na podstawie poprzednio publikowanych przykładów numerycznych dla niektórych szczególnych przypadków zwiększania MS L (k, m, s, n: F). Przedstawiono także przykłady ilustrujące modelowanie systemu oraz numeryczne przykłady nowych granic. Ponadto porównano wyniki uzyskane dla drugiego i trzeciego stopnia nierówności Boole'a–Bonferroniego.

PIELECHA I, SKOWRON M, MAZANEK A. **Evaluation of the injectors operational wear process based on optical fuel spray analysis**. Eksploatacja i Niezawodnosc – Maintenance and Reliability 2018; 20 (1): 83–89 http://dx.doi.org/10.17531/ein.2018.1.11.

The diagnostics of combustion engine components currently requires the integration of many technical and scientific fields in order to quickly and accurately locate faults or pinpoint the causes of malfunction. This article analyzes the wear of injectors based on the geometric indicators of the fuel spray. Using a number of available parameter data, a selection has been made to best judge the wear of injectors in their operating conditions. Optical fuel spray tests were used to assess the injector wear. Various geometric indicators of the fuel stream have been presented, indicating their diagnostic utility and applicability. In conclusion, it was found that the current injection systems require the combination of mechanical injector diagnostics and advanced optical fuel spray diagnostics.

PIELECHA I, SKOWRON M, MAZANEK A. **Ocena eksploatacyjnego zużycia wtryskiwaczy na podstawie analizy optycznej rozpylenia paliwa**. Eksploatacja i Niezawodnosc – Maintenance and Reliability 2018; 20 (1): 83–89 http://dx.doi.org/10.17531/ein.2018.1.11.

Diagnostyka elementów silnika spalinowego wymaga obecnie integracji wielu dziedzin techniki i nauki w celu szybkiej i trafnej lokalizacji uszkodzenia lub poszukiwania przyczyn niesprawności. Artykuł dotyczy analizy zużycia wtryskiwaczy na podstawie wskaźników geometrycznych strugi rozpylanego paliwa. Na podstawie kilku dostępnych wielkości badawczych dokonano wyboru pozwalającego najlepiej ocenić zużycie wtryskiwaczy w warunkach ich eksploatacji. Do oceny diagnostycznej zużycia wtryskiwaczy wykorzystano badania optyczne rozpylenia paliwa. Przedstawiono różne wskaźniki geometryczne strugi paliwa, wskazując na ich użyteczność diagnostyczną oraz możliwość zastosowania. W podsumowaniu stwierdzono, że badania obecnych układów wtryskowych wymagają połączenia mechanicznych metod diagnostyki wtryskiwaczy oraz zaawansowanej diagnostyki optycznej rozpylenia paliwa.

ZELIĆ A, ZUBER N, ŠOSTAKOV R. **Experimental determination of lateral forces caused by bridge crane skewing during travelling**. Eksploatacja i Niezawodnosc – Maintenance and Reliability 2018; 20 (1): 90–99, http://dx.doi.org/10.17531/ein.2018.1.12.

Crane condition depends on the large number of variables randomly changing in time. Due to the large number of parameters, skewing forces have stochastic character. Though in standards treated as occasional loads, their dynamic action in certain cases can cause fatigue damage of the crane travelling mechanisms, structure and runway components. Current European Norms have left the question of skewing forces influence upon the fatigue damage occurrence unresolved. The paper presents an experimental determination of lateral forces acting on the vertical wheels of a bridge crane using two different solutions of transducers for the direct measurement on the wheels of the cranes in operation, without changing the way of lateral guiding. As an illustration, few records of the measured wheel lateral force vs. time are shown. Presentation of such records in the form of a loading spectrum (e.g. using the software nCode), obtained

ZELIĆ A, ZUBER N, ŠOSTAKOV R. **Eksperymentalne wyznaczanie sił poprzecznych wywołanych skrętem suwnicy podczas jazdy**. Eksploatacja i Niezawodnosc – Maintenance and Reliability 2018; 20 (1): 90–99, http://dx.doi.org/10.17531/ein.2018.1.12.

Stan suwnicy pomostowej zależy od dużej liczby zmiennych losowo zmieniających się w czasie. Ze względu na dużą liczbę parametrów, siły skośne mają charakter stochastyczny. Chociaż w normach traktowane są one jako obciążenia sporadyczne, ich dynamiczne oddziaływanie w niektórych przypadkach może powodować zmęczeniowe uszkodzenie mechanizmu jazdy suwnicy, jak również jego konstrukcji oraz elementów toru jezdnego. Obecnie obowiązujące normy europejskie pozostawiają bez rozwiązania kwestię wpływu sił skośnych na występowanie uszkodzeń zmęczeniowych. W pracy przedstawiono metodę eksperymentalnego wyznaczania sił poprzecznych działających na koła pionowe suwnicy pomostowej. Metoda ta polega na użyciu dwóch różnych rozwiązań przetworników do bezpośredniego pomiaru sił na kołach pracującej suwnicy, bez zmiany sposobu prowadzenia bocznego . Dla ilustracji pokazano kilka zapisów pomiarów siły poprzecznej

during long-lasting or continuous monitoring of cranes in operation, is the first step in finding the relevant answer to the previously unresolved question.

koła w funkcji czasu. Przedstawienie takich zapisów w postaci widma obciążenia (np. za pomocą oprogramowania nCode), uzyskanego podczas długotrwałego lub ciągłego monitorowania suwnicy w trakcie jej eksploatacji, stanowi pierwszy krok do znalezienia rozwiązania nierozwikłanego do tej pory problemu.

BUREK R, WYDRZYŃSKI D, SĘP J, WIĘCKOWSKI W. **The effect of tool wear on the quality of lap joints between 7075 T6 aluminum alloy sheet metal created with the FSW method**. Eksploatacja i Niezawodnosc – Maintenance and Reliability 2018; 20 (1): 100–106, http://dx.doi.org/10.17531/ein.2018.1.13.

The article concerns the issues of tool wear effect on the quality of a friction stir welding joint quality. The experiment used aluminum alloy 7075 T6 sheet metal, which is used primarily in the aerospace industry. 1.0mm and 0.8mm thick lap joints were tested. Tool wear was determined based on multiple readings on a multisensory machine. The tool wear evaluation was done on the basis of a static tensile strength test and metallographic sections of the joints. The pin of the tool works in more demanding conditions and is more exposed to friction. This results from tooling operations performed at full depth dive in the jointed material. When also considering the small dimensions of the pin such as the diameter and the great forces occurring in this process, it is easy to see why this element is most susceptible to tool wear. The welding process causes the tool to undergo friction wear, which is the cause of reduced tool dive depth in the jointed material. As a result, it is paramount to constantly control the tool extension to achieve the desired quality parameters of the joint. After creating 200m of joints, a decrease in the strength of joints was observed as well as the repeatability of the results connected to a change in the stirring conditions in the material. The change in joint strength and tool wear is also confirmed in the metallographic analysis, which states that the continued degradation of the tool makes it subject to a decrease in size of the characteristic sizes of the thermoplastic zone that is the main determining factor of the joint strength.

BUREK R, WYDRZYŃSKI D, SĘP J, WIĘCKOWSKI W. **Wpływ zużycia narzędzia na jakość połączeń zakładkowych blach ze stopu Aluminium 7075 T6 wykonanych metodą FSW**. Eksploatacja i Niezawodnosc – Maintenance and Reliability 2018; 20 (1): 100–106, http://dx.doi.org/10.17531/ein.2018.1.13.

Opracowanie podejmuje problematykę wpływu zużycia narzędzia na jakość zgrzeiny otrzymanej metodą zgrzewania tarciowego z przemieszaniem FSW. Do badań użyto stopu aluminium Al 7075 T6, stosowanego głównie w przemyśle lotniczym. Badano połączenia zakładkowe blach o grubości 1,0mm i 0,8mm. Zużycie narzędzia oceniano na podstawie pomiarów na maszynie multisensorycznej. Ocenę wpływu zużycia przeprowadzono w oparciu o statyczną próbę rozciągania oraz analizę zgładów metalograficznych wykonanych połączeń.Trzpień narzędzia pracuje w trudniejszych warunkach i jest bardziej narażony na ścieranie. Wynika to z pracy przy pełnym zagłębieniu w łączonym materiale. Zważywszy również na stosunkowo małe wymiary trzpienia tj. jego średnicę i duże siły występujące w procesie to ten element jest najbardziej narażony na zużycie. W procesie zgrzewania narzędzie ulega zużyciu ściernemu, co jest powodem zmniejszania zagłębienia narzędzia w materiale łączonym. W związku z powyższym konieczna jest ciągła kontrola wysunięcia narzędzia dla uzyskania pożądanych parametrów jakościowych zgrzeiny. Po wykonaniu 200m zgrzeiny zauważono zmniejszenie wytrzymałości zgrzeiny, jak również powtarzalności wyników związany ze zmianą warunków mieszania materiału. Zmiana wytrzymałości zgrzeiny oraz zużycia narzędzia ma również potwierdzenie w badaniach metalograficznych, z których wynika, iż w związku z postępującą degradacją narzędzia zmniejszeniu ulegają wymiary charakterystyczne strefy termo–plastycznej odpowiedzialnej w główniej mierze za wytrzymałość zgrzeiny.

NIKONIUK M, KOZŁOWSKI M. **Energy properties of a contactless power supply in PRT (Personal Rapid Transit) laboratory model**. Eksploatacja i Niezawodnosc – Maintenance and Reliability 2018; 20 (1): 107–114, http://dx.doi.org/10.17531/ein.2018.1.14.

The article presents the results of research on the operational properties of contactless power supply system used in the PRT vehicle demonstration model, made within the framework of the ECO Mobility project. The area of transport applications of the PRT automated rail transport system is presented. Elements of the ECO Mobility PRT Drive System have been described – an inductive linear motor, dynamic contactless power supply, and supercapacitor recuperation system. Electrical performance maps of the linear motor and contactless power system were presented. Also shown was the method of their use in calculation of traction energy consumption by means of theoretical journeys. The results of the simulation calculations for the trial track were presented. The results of design calculations of the power supply parameters for the planned line of the demonstrator with real dimensions are presented.

NIKONIUK M, KOZŁOWSKI M. **Własności energetyczne układu zasilania bezstykowego modelu laboratoryjnego pojazdu PRT (Personal Rapid Transit)**. Eksploatacja i Niezawodnosc – Maintenance and Reliability 2018; 20 (1): 107–114, http://dx.doi.org/10.17531/ein.2018.1.14.

Artykuł prezentuje wyniki badań własności eksploatacyjnych układu zasilania bezstykowego zastosowanego w modelu demonstracyjnym pojazdu PRT, wykonanym w ramach projektu ECO Mobilność. Przedstawiono obszar zastosowań transportowych systemu szynowego automatycznych środków transportu PRT. Opisano rozwiązanie układu napędowego pojazdu PRT konstrukcji ECO Mobilność – napęd za pomocą indukcyjnego silnika liniowego, zasilanie bezstykowe dynamiczne oraz układ rekuperacji z zastosowaniem superkondensatora. Zaprezentowano mapy sprawności elektrycznej silnika linowego i układu zasilania bezstykowego. Przedstawiono sposób ich wykorzystania w obliczeniach zużycia energii trakcyjnej metodą przejazdów teoretycznych. Przedstawiono wyniki obliczeń symulacyjnych dla toru próbnego w skali. Przedstawiono wyniki obliczeń projektowych parametrów układu zasilania dla planowanej linii demonstratora o wymiarach rzeczywistych.

GUO C, LYU C, CHEN J, ZHOU. **A design approach based on a correlative relationship between maintainability and functional construction**. Eksploatacja i Niezawodnosc – Maintenance and Reliability 2018; 20 (1): 115–124, http://dx.doi.org/10.17531/ein.2018.1.15.

As an important quality characteristic, maintainability is the ability of a product to be repaired efficiently and economically. Because it is mainly determined at the design stage, maintainability is mostly affected by the construction of a product. Traditional product design methods put more focus on design for function and production, neglecting design for maintainability, which causes a gap between functional construction design and maintainability design. The delay of maintainability design results in huge costs for design changes and even irrevocable design flaws. Because of the weak relationship between functional construction and maintainability in product design, the influence of maintainability design on the product is limited. To resolve this problem, this paper proposes a design approach considering the relationship between maintainability and functional construction. First, maintainability design factors (MDFs) and functional construction design factors (FCDFs) are defined and classified. Second, based on topology graphic theory, a correlative relationship model is constructed by graphically combining the MDFs and FCDFs into a network diagram. Third, to determine primary design factors, a quantization matrix is developed to perform importance evaluation of the correlative relationship. Finally, a practical case is studied by implementing the proposed approach for the lubrication system of an armoured vehicle. The results validate the effectiveness and feasibility of the approach.

GUO C, LYU C, CHEN J, ZHOU. **Podejście projektowe oparte na korelacyjnym związku między konserwowalnością a funkcjonalną budową produktu**. Eksploatacja i Niezawodnosc – Maintenance and Reliability 2018; 20 (1): 115–124, http://dx.doi.org/10.17531/ein.2018.1.15.

Konserwowalność to ważna charakterystyka jakościowa, którą można zdefiniować jako możliwość wydajnej i ekonomicznej naprawy produktu. Ponieważ o konserwowalności produktu decydują głównie wybory dokonane na etapie projektowania, największy wpływ na nią ma budowa produktu. Tradycyjne metody projektowania produktów kładą większy nacisk na projektowanie funkcji i produkcji, zaniedbując projektowanie pod kątem łatwości konserwacji, co powoduje powstanie luki między projektowaniem funkcjonalnej budowy produktu a projektowaniem jego konserwowalności. Opóźnienie etapu projektowania konserwowalności generuje ogromne koszty związane z koniecznością zmian projektu i może nawet prowadzić do nieodwracalnych wad projektowych. Ze względu na słabą zależność między budową funkcjonalną a konserwowalnością w projektowaniu produktu, wpływ projektowania konserwowalności na produkt jest ograniczony. Aby rozwiązać ten problem, w niniejszej pracy zaproponowano podejście projektowe uwzględniające związek między konserwowalnością a budową funkcjonalną wyrobu. Po pierwsze, zdefiniowano i sklasyfikowano czynniki konstrukcyjne (projektowe) dotyczące konserwowalności (MDF) oraz czynniki konstrukcyjne związane z budową funkcjonalną produktu (FCDF). Po drugie, w oparciu o teorię graficznej reprezentacji topologii, zbudowano model zależności korelacyjnych między MDF i FCDF w postaci diagramu sieciowego. Po trzecie, w celu określenia podstawowych czynników konstrukcyjnych, opracowano macierz kwantyzacji, pozwalającą na ocenę ważności relacji korelacyjnych. Wreszcie, przeanalizowano przypadek układu smarowania pojazdu opancerzonego jako przykład zastosowania proponowanego podejścia w praktyce. Wyniki potwierdzają skuteczność omawianego podejścia oraz możliwość jego praktycznego wykorzystania.

KNOPIK L, MIGAWA K. **Multi-state model of maintenance policy**. Eksploatacja i Niezawodnosc – Maintenance and Reliability 2018; 20 (1): 125–130, http://dx.doi.org/10.17531/ein.2018.1.16.

Preventive replacement is applied to improve the device availability or increase the profit per unit time of the maintenance system. In this paper, we study age-replacement model of technical object for n-state system model. The criteria function applied in this paper describe profit per unit time or coefficient of availability. The probability distribution of a unit's failure time is assumed to be known, and preventive replacement strategy will be used over very long period of time. We investigate the problem of maximization of profit per unit time and coefficient availability for increasing the failure rate function of the lifetime and for a wider class of lifetime. The purpose of this paper is to obtain conditions under which the profit per unit time approaches a maximum. In this paper we shows that the criteria function (profit per unit time or coefficient availability) can be expressed using the matrix calculation method. Finally, a numerical example to evaluate an optimal replacement age is presented.

KNOPIK L, MIGAWA K. **Wielostanowy model decyzji eksploatacyjnych**. Eksploatacja i Niezawodnosc – Maintenance and Reliability 2018; 20 (1): 125–130, http://dx.doi.org/10.17531/ein.2018.1.16.

Wymiany prewencyjne stosuje się w celu podnoszenia gotowości systemów eksploatacji maszyn i wzrostu dochodu na jednostkę czasu systemu eksploatacji. W pracy analizuje się model wymian obiektów technicznych według wieku dla n-stanowego systemu. Funkcja kryterialna stosowana w pracy wyraża zysk przypadający na jednostkę czasu lub współczynnik gotowości. Zakłada się, że rozkład prawdopodobieństwa czasu do uszkodzenia obiektu technicznego jest znany i strategia wymian prewencyjnych będzie stosowana na długim przedziale czasowym. Bada się problem maksymalizacji zysku na jednostkę czasu i współczynnika gotowości dla rosnącej funkcji intensywności uszkodzeń lub funkcji intensywności z szerszej klasy. Celem tej pracy jest sformułowanie warunków, przy których zysk na jednostkę czasu osiąga maksimum. W pracy pokazano, że badaną funkcję kryterialną (zysk na jednostkę czasu lub współczynnik gotowości) można wyrazić za pomocą metod rachunku macierzowego. Na końcu pracy przedstawiono przykład numeryczny oceny optymalnego wieku wymiany dla rzeczywistego procesu eksploatacji.

STANIK W, JAKÓBIEC J, MAZANEK A. **Engine tests for coking and contamination of modern multi-injection injectors of high-pressure fuel supplies compression-ignition engine**. Eksploatacja i Niezawodnosc – Maintenance and Reliability 2018; 20 (1): 131–136, http://dx.doi.org/10.17531/ein.2018.1.16.

The paper presents the results of engine tests for contamination and coking of modern multi-injection injectors of high-pressure fuel supplies compression-ignition engines. The subject of research is base diesel fuel with 7% (v / v) FAME, and effectiveness of the detergent-dispersant additives plays a key role. The engine tests were performed according to the CEC procedure F-98-08 PSA DW-10, it was essential for the coking and contamination of modern multi-injection injectors of high-pressure fuel supplies compression-ignition engines and for the conclusions.

STANIK W, JAKÓBIEC J, MAZANEK A. **Badania silnikowe dotyczące koksowania i zanieczyszczenia nowoczesnych wielootworowych wtryskiwaczy wysokociśnieniowego układu zasilania paliwem silników ZS**. Eksploatacja i Niezawodnosc – Maintenance and Reliability 2018; 20 (1): 131–136, http://dx.doi.org/10.17531/ein.2018.1.16.

W pracy przedstawiono wyniki badań silnikowych dotyczących zanieczyszczenia i koksowania nowoczesnych wielootworowych wtryskiwaczy wysokociśnieniowego układu zasilania paliwem silników o zapłonie samoczynnym (ZS). W zapobieganiu tym zjawiskom wiodącą rolę odgrywa skuteczność działania dodatków detergentowo-dyspergujących o odpowiednim poziomie dozowania. Przedmiotem badań jest bazowy olej napędowy z udziałem 7%(v/v) FAME. W celu sprawdzenia skuteczności działania badanych dodatków wykonano testy silnikowe zgodne z procedurą CEC F-98-08 PSA DW-10 pod kątem koksowania i zanieczyszczenia nowoczesnych wielootworowych wtryskiwaczy wysokociśnieniowego układu zasilania silników o ZS oraz sformułowano wnioski.

BUCHACZ A, BAIER A, HERBUŚ K, OCIEPKA P, GRABOWSKI Ł, SOBEK M. **Compression studies of multi-layered composite materials for the purpose of verifying composite panels model used in the renovation process of the freight wagon's hull**. Eksploatacja i Niezawodnosc – Maintenance and Reliability 2018; 20 (1): 137–146, http://dx.doi.org/10.17531/ein.2018.1.18.

The paper presents the procedure sequence for modelling multilayer composite materials using PLM Siemens NX software. Virtual studies were referring to three-point and four-point flexural test of composite material samples. Composite materials containing fiber reinforced epoxy resin composites were considered. Within the carried out research, a virtual experiment to test composite samples composed of 5, 7 and 10 layers was conducted. Then the virtual model was matched to the results obtained during the stationary tests. As a result of matching the composite material model to the real model, correct results of the virtual bending experiment of composite samples were obtained. The presented procedure sequence for modelling composite material was used to analyse the MES of the scaled side of the freight wagon. The modification consisted in the use of composite panels as reinforcing elements of the wagon's hull from inside to extend its life. The presented modelling approach enabled the initial strength verification of the modified side of the freight wagon's hull.

BUCHACZ A, BAIER A, HERBUŚ K, OCIEPKA P, GRABOWSKI Ł, SOBEK M. **Badania porównawcze wielowarstwowych materiałów kompozytowych na potrzeby weryfikacji modelu paneli kompozytowych stosowanych do renowacji poszycia wagonów towarowych**. Eksploatacja i Niezawodnosc – Maintenance and Reliability 2018; 20 (1): 137–146, http://dx.doi.org/10.17531/ein.2018.1.18.

W pracy przedstawiono sposób postępowania przy modelowaniu wielowarstwowych materiałów kompozytowych z zastosowaniem oprogramowania PLM Siemens NX. Badania wirtualne odnosiły się do próby trójpunktowego i czteropunktowego zginania próbek kompozytowych. Rozważano materiały kompozytowe będące kompozycją żywicy epoksydowej ze wzmocnieniem włóknistym. W ramach prowadzonych badań przeprowadzono wirtualny eksperyment badania próbek kompozytowych będących kompozycją złożoną z 5, 7 i 10 warstw. Następnie dopasowano wirtualny model do wyników otrzymanych na drodze badań stanowiskowych. W wyniku dopasowania modelu materiału kompozytowego uzyskano poprawne wyniki wirtualnego eksperymentu zginania próbek kompozytowych. Zaprezentowany tok postępowania odnośnie modelowania materiału kompozytowego zastosowano do analizy MES pomniejszonego fragmentu zmodyfikowanej burty bocznej wagonu. Modyfikacja polegała na zastosowaniu paneli kompozytowych jako elementów wzmacniających poszycie wewnętrzne wagonu mających na celu wydłużenie jego czasu eksploatacji. Przedstawiony sposób modelowania umożliwił wstępną weryfikację wytrzymałościową zmodyfikowanego fragmentu burty bocznej wagonu towarowego.

TABASZEWSKI M, FIRLIK B. **Assessment of the track condition using the Gray Relational Analysis method**. Eksploatacja i Niezawodnosc – Maintenance and Reliability 2018; 20 (1): 147–152, http://dx.doi.org/10.17531/ein.2018.1.19.

The article concerns the developed methodology for assessing the technical condition of a tramway track. Thanks to the data collected from multiple tram journeys equipped with an on-board vibration recording system, it was possible to create profiles of crossings through track sections in different technical condition. In order to identify the track condition, an algorithm based on the gray-scale modeling was proposed, and a similarity comparison between the obtained track profiles. A new measure of similarity has been proposed that has not been used so far in gray-scale modeling. The obtained results confirm the applicability of the proposed methodology.

TABASZEWSKI M, FIRLIK B. **Ocena stanu torowiska z wykorzystaniem metody Grey Relational Analysis**. Eksploatacja i Niezawodnosc – Maintenance and Reliability 2018; 20 (1): 147–152, http://dx.doi.org/10.17531/ein.2018.1.19.

Praca dotyczy opracowanej metodyki do oceny stanu technicznego toru tramwajowego. Dzięki zgromadzonym danym z wielokrotnych przejazdów tramwaju wyposażonego w pokładowy system rejestracji drgań, udało się stworzyć profile przejazdów przez odcinki torów w różnym stanie technicznym. W celu identyfikacji stanu toru zaproponowano algorytm oparty na metodzie modelowania szarych systemów oraz badanie podobieństwa pomiędzy uzyskanymi profilami przejazdów. Zaproponowano także nową miarę podobieństwa nie stosowaną do tej pory w zagadnieniach modelowania szarych systemów. Uzyskane wyniki potwierdzają aplikacyjność zaproponowanej metodyki.

ŁUKASZEWSKI K. **Adaptive reliability structures of heat exchange surface in turbine condenser**. Eksploatacja i Niezawodnosc – Maintenance and Reliability 2018; 20 (1): 153–159, http://dx.doi.org/10.17531/ein.2018.1.20.

In this paper adaptive reliability structures of heat exchange surface in turbine condenser was proved from the angle of effective heat exchange in variable conditions of its exploitation. Then, determinant factors for design and exploitation in assessment of reliability of pipe subsystem in turbine condenser were suggested. The influence of change of scheme of the pipes, constituting the surface of heat exchange, which

ŁUKASZEWSKI K. **Adaptacyjne struktury niezawodnościowe powierzchni wymiany ciepła skraplacza turbiny parowej**. Eksploatacja i Niezawodnosc – Maintenance and Reliability 2018; 20 (1): 153–159, http://dx.doi.org/10.17531/ein.2018.1.20.

W artykule wykazano adaptację struktur niezawodnościowych powierzchni wymiany ciepła skraplacza turbiny parowej z punktu widzenia efektywnej wymiany ciepła w zmiennych warunkach jego eksploatacji. Następnie, wskazano istotne uwarunkowania projektowo-eksploatacyjne oszacowania niezawodności podsystemu rur skraplacza turbiny parowej.

stems from the matter of regulating the surface in an attempt to both condense the given amount of steam and maintain the given pressure in the condenser in variable conditions of its exploitation on the reliability of the pipe subsystem was determined. The surface of heat exchange is regulated by enabling and disabling the flow of cooling water through given amount of pipes, in a given way, that is by enabling or disabling possible combination of given pipes in given exploitation conditions. An algorithm to assess the reliability of the pipe subsystem in the condenser in given exploitation conditions, means of regulating the surface and up-to-date technical condition was put forward. The reliability of pipe subsystem has a significant influence either on reliability of the condenser while exploited or in the further course, indirectly on sustaining the requested reliability in the power system therein. Effective operation of the condenser in technical power system is performed by sustaining the given pressure of steam condensation, which is vital in maintaining the required energy efficiency of technical power system in variable exploitation conditions. The exemplification of the aspects put forward in the paper pertains to steam turbine condensers.

Wykazano wpływ zmian układów rur stanowiących powierzchnię wymiany ciepła, które wynikają ze sposobu regulacji tej powierzchni w celu skroplenia zadanej ilości pary wodnej i utrzymywania zadanej wartości ciśnienia w skraplaczu w zmiennych warunkach jego eksploatacji, na niezawodność podsystemu rur. Powierzchnię wymiany ciepła reguluje się poprzez włączanie i wyłączanie przepływu wody chłodzącej przez zadaną liczbę rur, w określony sposób tzn. poprzez włączanie albo wyłączanie możliwych kombinacji określonych układów rur w zadanych warunkach eksploatacyjnych. Przedstawiono algorytm oszacowania niezawodności podsystemu rur skraplacza względem określonych warunków eksploatacyjnych, sposobu regulacji tej powierzchni i aktualnego stanu technicznego. Niezawodność podsystemu rur ma istotny wpływ na niezawodność skraplacza turbiny parowej w czasie jego eksploatacji, a dalej pośrednio na utrzymywanie wymaganej niezawodności systemu energetycznego, w którym występuje. Efektywne funkcjonowanie skraplacza w technicznym systemie energetycznym jest realizowane poprzez utrzymywanie zadanego stałego ciśnienia skraplania pary wodnej, co jest istotne z punktu widzenia utrzymywania wymaganej sprawności energetycznej technicznego systemu energetycznego w różnych warunkach eksploatacyjnych. Egzemplifikacja zawartych w pracy zagadnień odnosi się do rurowych skraplaczy turbin parowych.

Article citation info:
KOWALSKI S. The influence of selected PVD coatings on fretting wear in a clamped joint based on the example of a rail vehicle wheel set. Eksploatacja i Niezawodnosc – Maintenance and Reliability 2018; 20 (1): 1–8, http://dx.doi.org/10.17531/ein.2018.1.1.

Sławomir KOWALSKI

THE INFLUENCE OF SELECTED PVD COATINGS ON FRETTING WEAR IN A CLAMPED JOINT BASED ON THE EXAMPLE OF A RAIL VEHICLE WHEEL SET

WPŁYW WYBRANYCH POWŁOK PVD NA ZUŻYCIE FRETTINGOWE W POŁĄCZENIU WTŁACZANYM NA PRZYKŁADZIE MODELU ZESTAWU KOŁOWEGO POJAZDU SZYNOWEGO*

In this article, laboratory test results concerning the influence of selected PVD coatings on the initiation and development of fretting wear in clamped joints are presented. TiN and CrN+a-C:H:W coatings were applied to shafts, and the results of wear tests compared with those for uncoated shafts. Wear tests were conducted at a test bed which simulated the operation conditions of the wheel sets of rail vehicles moving along a straight track. The sample elements for testing were assembled by forcing the sleeve onto the shaft with the tolerance of 0.02 mm. To assess fretting at shaft top layers being tested, macroscopic observations, microscopic observations with the use of a scanning microscope, x-ray microanalysis of the chemical composition by means of the EDS method and the measurement of the top layer topography in the place of wear were performed. Test results presented concern the shaft top layer because it is that layer which mainly determines the life of a clamped joint. The results of the macroscopic observations of the sleeve hub top layer were presented, too, for comparison of the image of wear between mating surfaces.The results of the observations of the various shaft top layers indicate the mitigation of the development of fretting wear in the case of shafts with coatings; CrN+a-C:H:W coatings influence the mitigation of fretting wear better indeed. The main damage comprised by fretting in all the samples being tested is material build-up occurring as a result of adhesion. That build-up undergoes oxidation during operation. Micropits and microabrasion of the top layer are observed in places.

***Keywords**: clamped joint, fretting wear, PVD coating.*

W artykule zaprezentowano wyniki badań laboratoryjnych dotyczące wpływu zastosowania wybranych powłok PVD na inicjację i rozwój zużycia frettingowego w połączeniach wtłaczanych. Na wały nałożono powłoki TiN a także CrN+a-C:H:W, wyniki badań zużyciowych porównano z wynikami badań wałów bez powłok. Badania zużyciowe wykonywano na stanowisku badawczym, które symulowało warunki pracy zestawów kołowych pojazdów szynowych poruszających się po torze prostym. Montaż elementów próbki przeznaczonej do badań wykonano przez wtłoczenie tulei na wał z wartością wcisku 0,02mm. W celu oceny zjawiska frettingu dla badanych warstw wierzchnich wałów wykonano obserwacje makroskopowe, mikroskopowe przy użyciu mikroskopu skaningowego, mikroanalizę rentgenowską składu chemicznego metodą EDS oraz pomiar topografii warstwy wierzchniej w miejscu zużycia. Zaprezentowane wyniki badań dotyczą warstwy wierzchniej wałów, ponieważ to ona w głównej mierze determinują trwałość połączenia wtłaczanego. Zaprezentowano również wyniki obserwacji makroskopowych warstwy wierzchniej piasty tulei, w celu porównania obrazu zużycia pomiędzy współpracującymi powierzchniami.Wyniki obserwacji poszczególnych warstw wierzchnich wałów wskazują na ograniczenie rozwoju zużycia frettingowego w przypadku wałów z zastosowanymi powłokami, przy czym powłoki CrN+a-C:H:W korzystniej wpływają na zmniejszenie zużycia frettingowego. Głównym uszkodzeniem składającym się na zjawisko frettingu we wszystkich badanych próbkach są nalepienia materiału, powstałe w wyniku zjawiska adhezji. W czasie eksploatacji nalepienia te ulegają utlenianiu. Lokalnie obserwuje się mikrowżery i mikrowytarcia warstwy wierzchniej.

***Słowa kluczowe**: *połączenie wtłaczane, zużycie frettingowe, powłoki PVD.*

1. Introduction

Clamped joints are one of the most frequently used methods of element joining. This is related to the simplicity of assembly and therefore low costs of the process. The possibility of transferring relatively high loads causes clamped joints to connect elements working in various, sometimes tough operation conditions.

Rail vehicle wheel sets are one of the examples in which elements are connected by pressing. The assembly process takes place at a press equipped with a force recorder, thus the joint is protected from undesirable damage. Wheel sets are one of the most important rail vehicle elements. They directly influence passenger safety. Any damage oc-

(*) Tekst artykułu w polskiej wersji językowej dostępny w elektronicznym wydaniu kwartalnika na stronie ***www.ein.org.pl***

curring during operation may be the cause of a rail crash, that is why appropriate damage risk reducing methods should be used.

The effective elimination of damage and wear of wheel sets is not an easy task because of the peculiar conditions of their operation. Wheel sets are subjected to static forces following from the vertical load depending on the vehicle weight and to dynamic forces at the wheel/rail contact point which result from the rolling of a wheel set along a track. Vertical forces will cause axle deflection; in relation to that, during operation, as a result of the operation of dynamic forces, oscillatory tangential displacement will occur between mating surfaces. Such operation conditions cause damage not only to the rolling wheel surface or to the rails, but also in the area of the wheel/axle clamped joint. The following may be included among the most frequent kinds of wear and damage: adhesion-related damage to the axle, the shift of track wheels in relation to the axle, axle fretting and fatigue wear leading to cracks. The primary focus of this article is fretting wear because its development mechanism has not been fully recognised yet.

Fretting wear is counted among the tribological kinds of wear, and the necessary condition for the development of fretting wear is oscillatory microdisplacement, with the amplitude of 25-150 μm according to some authors, of mating elements. Because of the complexity of physical and chemical phenomena accompanying fretting wear, the unambiguous definition of that concept has not been given so far. Fretting wear may be demonstrated by corrosion traces at the surface of the elements, the increase of surface roughness, as well as by pits and microcracks.

The development of fretting wear is influenced by many various factors, however, it is difficult to give their exact number in view of the complexity of the phenomenon and because of its development mechanism which has not been fully investigated yet. The author of [5] made a tabular schedule of the most frequent factors influencing the development of fretting wear. He indicated, among other things, surface hardness and roughness, the number of cycles and air temperature and humidity. The authors of [15], among others, investigated the influence of roughness on the development of fretting wear. They suggested a large-scale procedure for the investigation of the roughness effect with the use of the finite element method. The influence of surface roughness on the development of the corrosion and fretting wear of pure titanium used for medical implants was examined in [3]. The authors of [10] state that the initial topography of the top layer has significant influence on the development and intensity of fretting wear. Research was conducted for several slip amplitude values. The influence of temperature on fretting wear was investigated by, among others, the authors of [8, 13].

It follows from the review of literature that most research into fretting wear concerns the elements pressed against each other with a normal force, and only few authors undertook research into the development of fretting wear in push fit joints. That kind of joint does, however, accumulate in it all the factors conducive to the development of fretting wear. There is a specific pressure between the surfaces of the connected elements, and the relative displacement of those surfaces occurs. This happens when one of the elements is loaded with a variable turning force or when the joint operates in the conditions of rotary bending or twisting with a variable moment [5]. The probable cause of the small volume of research into fretting wear in clamped joints is the problem with joint disassembly. Traditional forcing of one element from the other may damage the fretting wear occurrence zone and thus distort the wear image. In relation to that, an appropriate process enabling safe joint disassembly should be developed. In the case of rail vehicle wheel sets, such a process is related to high costs because wheel set dimensions require the creation of an appropriate test bed and appropriately long disassembly time.

Among the works concerning fretting wear testing in a push fit joint based on the example of rail vehicle wheel sets, research work [6] may be mentioned, for example, in which the author investigated the influence of the way of making the joint (a forced-in joint or thermocompression bonding), the value of the tolerance and the surface roughness of the elements before the joint was made on the development and intensity of fretting wear. The authors of [17] conducted the analysis of axle damage at the point of connection with the wheel. They demonstrated that fretting comprises abrasive and oxidation wear and delamination. Research conducted by the authors of [19] demonstrated that fretting wear intensity strongly depends on normal loads and slip amplitude. In that case, too, fretting is the combination of abrasive and corrosive wear and of delamination with distinct plastic deformation. Work [14] concerning wear processes and the way of their mitigation in rotary joints is also worth noting. As an example of such a joint, that work mentions a rail vehicle wheel set with automatic wheel track changing. Whilst the work does not concern wear tests in clamped joints, the fretting wear development mechanism in the joint under analysis is very similar. The author suggests selected processes to mitigate fretting wear. It follows from test results referred to that only molybdenum coatings mitigate fretting effectively.

The cited works concerned mainly the determination of the place and range of fretting wear development, and also the indication of the kinds of wear comprised by fretting. Research into an attempt to eliminate wear has not been conducted, however. Works [7] and [9] may be pointed out in that regard. In the first one, the authors analysed the influence of surface strengthening treatment (thermal improvement, grit blasting, nitriding, surface hardening) on the fatigue strength of samples with an engineering notch. Research did not concern the influence of the above technologies on the development of fretting wear directly. The other work pertained to the influence of selected shaft surface finish processes such as nitriding, rolling and surface hardening on the development of fretting wear in clamped joints. Test results demonstrated an insignificant influence of those processes on the mitigation of fretting wear development. It follows from the review of literature that research into the application of PVD coatings with a view to mitigating fretting wear has not been conducted. That is why such tests of the shaft/sleeve clamped joint in which the shaft was covered with TiN and CrN+a-C:H:W coatings were conducted in this article.

PVD coatings were initially used to extend the life of cutting tools. It was already then that the positive tribological properties of those coatings were noticed. With the passage of time, the range of applications of the coatings extended, and they are used as a protection against tribological wear more and more commonly at present. PVD coatings are distinguished by their high hardness and resistance to wear and corrosion, and they have good fatigue properties. Several works confirming those properties may be found in literature. Work [11] in which the author tested the tribological properties of a-C:H:W coatings with TiN and CrN intermediate layers may be mentioned as an example. Test results confirmed the improvement of the tribological properties of the elements to which coatings were applied. The aim of tests presented in [2] was to determine the mechanisms of damage arising on stainless steel used for the manufacture of olive oil presses and the assessment of the properties of TiN coatings influencing the mitigation of those mechanisms. Test results demonstrated the excellent wearing resistance of the coatings. In work [1], a-C:H:W coatings applied over a steel base surface were investigated. Test results demonstrated the good tribological properties of coatings in that case as well. Further works [4, 12, 16, 18] concerning research on the properties of multi-layer a-C:H:W coatings and of WC/C coatings also confirm the reduction of the wear of the elements to which low-friction coatings were applied.

2. Properties of the tested shaft top layer

The research programme assumed the assessment of fretting wear in a clamped joint in which selected PVD coatings were applied to shafts.

As part of the tests, the following alternatives of the shaft top layer finish were used:

- shaft with an uncoated top layer – (sample number: S_02),
- shaft with the top layer coated with titanium nitride (TiN) – (sample number: S_06),
- shaft with the top layer to which a low-friction coating (CrN+a-C:H:W) was applied – (sample number: S_14).

The basic properties of coatings used in further tests are shown in table 1.

Table 1. Coating properties according to Oerlikon Balzers catalogue data

Properties	Coating	
Coating composition	TiN	CrN+a-C:H:W
Microhardness [HV0.05]	2300	1500
Coefficient of friction against steel when dry, μ	0,4	0,1-0,2
Coating thickness [μm]	1-4	1-2
Coating temperature [°C]	180-500	180-350
Residual compressive stresses [GPa]	−2,5	−1
Colour	gold	anthracite

In the case of examination of fretting wear in clamped joints, the input roughness and hardness of the top layer of the mating elements play an important role in fretting wear development. The diagrams of roughness and waviness profiles of the shaft top layer in the function of length are shown in fig. 1, and the values of roughness parameters in table 2.

Table 2. Results of the measurement of top layer roughness parameters

Roughness parameter	Wartość zmierzona [μm]			
	Uncoated shaft	Shaft with a TiN coating	Shaft with a CrN+a-C:H:W coating	Sleeve
				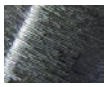
Ra	1,16	1,34	1,68	2,78
Rz	6,25	7,09	11,57	14,55

It follows from table 2 and fig. 1 that the top layer of coated shafts has greater roughness parameters in relation to the surface of uncoated shafts. This is related to the structure of the coatings, which is distinguished by porosity. The pores are the natural outcome of the coating application process. Those are cavities in the coating in the form of narrow channels filled with substances which do not constitute the coating. Those substances may include air or other gases. Various liquids or solids are sometimes found as well.

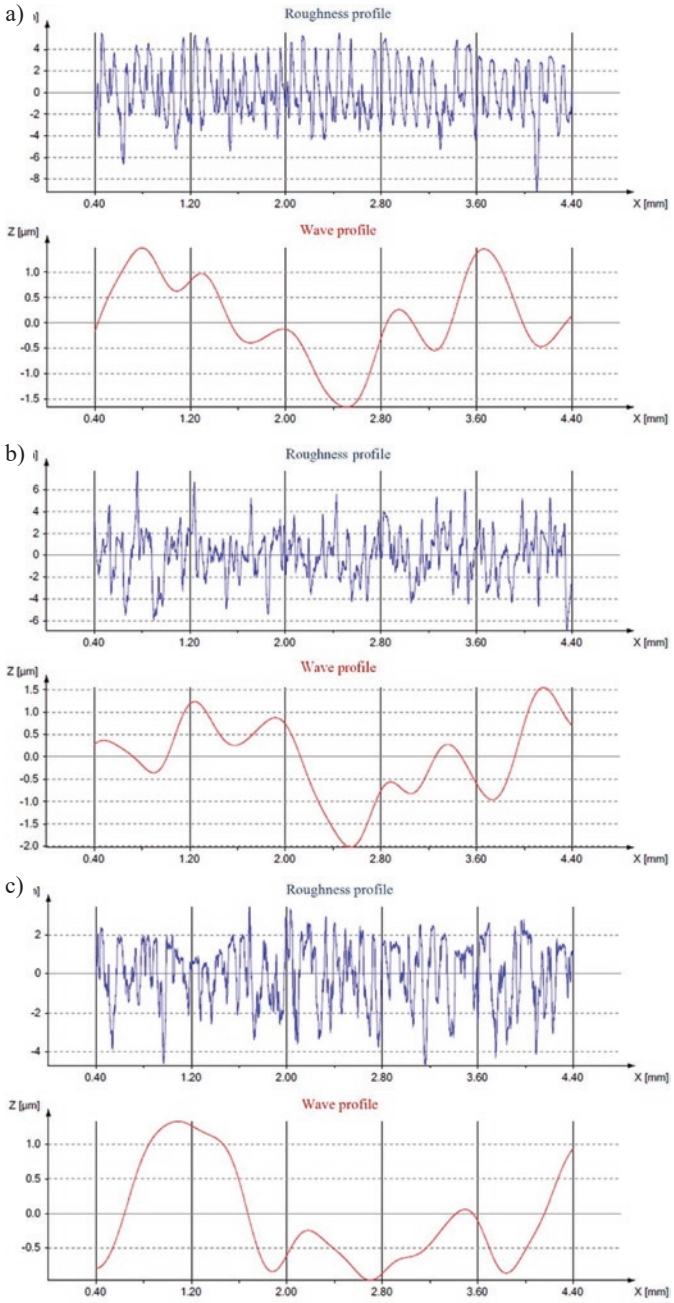

Fig. 1. Diagram of the roughness and waviness profile of a) an uncoated shaft, b) a shaft with a TiN coating, c) a shaft with a CrN+a-C:H:W coating

3. Test methodology

Coatings commonly used as the protection of cutting and pressing tools was conducted to mitigate the development of fretting wear in a clamped joint.

Experimental tests concerned:

- determination of the actual condition of the top layer of the mating elements after wear tests,
- determination of the influence of coatings on the development and intensity of fretting wear.

While selecting a wear test bed and samples, it was assumed that the tests were to simulate the operation conditions of a rail vehicle wheel set. For that purpose, an appropriate fatigue testing machine was chosen and the dimensional similarity at the place of connection of sample elements retained.

The sample for testing consisted of a sleeve, whose hub top layer had the hardness of 160 HB and of the shaft with the top layer hardness of 170 HB. The joint was assembled by pressing the sleeve onto the shaft with the tolerance ensuring joint durability.

Sample dimensions are presented in fig. 2. The shaft length and diameter depended on test bed dimensions. Dimensional proportions between the joint diameter and length, and the value of the tolerance in relation to the dimensions of the rail vehicle wheel set were retained, however.

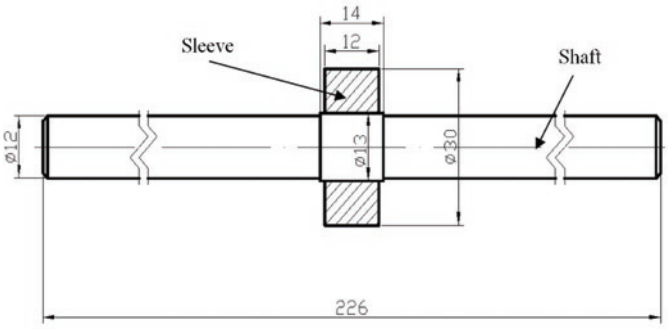

Fig. 2. Dimensions of the sample subjected to wear tests

The similarity did not pertain to the dimensions only, with the same structural materials having been used, too. The shaft was made of C45 steel, and the sleeve of P58 steel.

Wear tests were conducted at a UB-M fatigue testing machine ensuring the parameters simulating the actual operation conditions of a wheel set. The fatigue testing machine structure permits the generation of a periodically variable load on the sample with pure rotational bending.

The load on the sample should generate a bending moment which will cause shaft deflection. In such a situation, during operation, oscillatory tangential displacement of the sleeve in relation to the shaft will occur, which is a necessary condition for the initiation of fretting wear.

In fig. 3, the test bed for wear testing of the sample, the way of sample loading and the resultant bending moment are shown schematically. A similar bending moment distribution is obtained in the case of wheel sets loaded with the weight of a rail vehicle body at a straight track.

During wear tests, samples were loaded with the force of 550 N. As a result of such a load, normal stresses of 102 MPa occur at the sleeve/shaft contact surface. That value is close to the range of normal stresses at the axle seat surface of the real wheel set. Under the assumption of the typical operation conditions of a rail engine wheel set at a straight track, normal stresses at the axle surface are, according to the UIC regulations, 98 MPa.

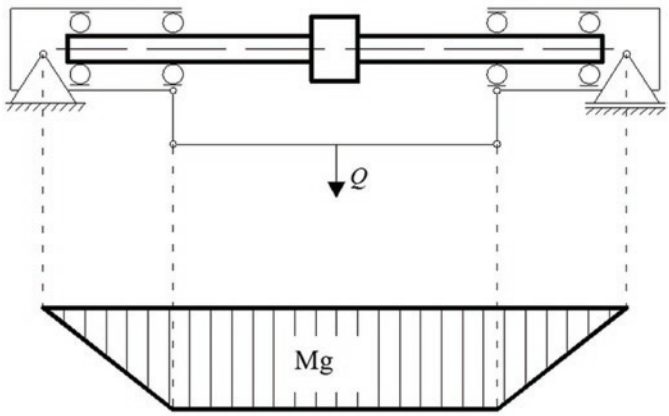

Fig. 3. Diagram showing sample fixing in the fatigue testing machine and the load, Mg – Bending moment

A strength analysis conducted in the ANSYS software demonstrated that loading with the force of 550 N would cause the maximum shaft deflection of 0.52 mm (fig. 4), and the maximum reduced stresses of 356 MPa (fig. 5) without causing plastic deformation at the same time. Such strength parameters will enable, during tests, oscillatory tangential displacement initiating the development of fretting wear to be obtained. The other parameters of wear tests are summarised in table 3.

Following wear tests, several laboratory tests were carried out to determine the influence of coatings on the development of fretting. Among other things, the tests of the topography of the models and the microscopic observations with the use of an electronic scanning microscope, type JEOL JSM-6460LV, equipped with an EDS spectrometer, were conducted. Tests were possible only after the samples were prepared as appropriate. Traditional forcing of the sleeve from the shaft would cause the destruction of fretting wear which has arisen, which would prevent its in-depth analysis. Hence, a joint disassembly technology was developed, which consists in cutting the joint parallel to the shaft axis. As a result, three samples were obtained whose observations permitted drawing relevant conclusions concerning the use of the coatings under analysis to extend the shaft's life.

Table 3. Summary of wear test parameters

Sample No.	Force pressing the sleeve onto the shaft N	Load on the sample N	Bending moment Nm	Stress amplitude MPa		Number of cycles 10^6
				ϕ 12 mm	ϕ 13 mm	
S_02	4800	550	27,5	162	128	8
S_06	7000	550	27,5	162	128	16
S_14	6600	550	27,5	162	128	10

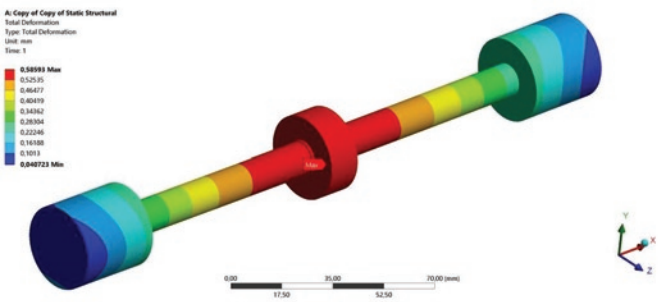

Fig. 4. Distribution of the sample deflection line

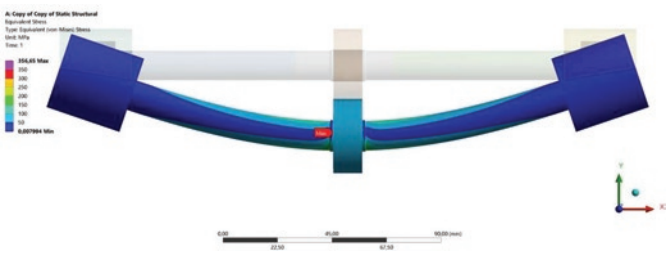

Fig. 5. Distribution of reduced stresses occurring in a sample loaded with the force of 550 N

4. Results of experimental tests

First, test results for an uncoated shaft are presented. They are a reference base for the remaining samples under analysis. A similar fretting wear image is observed at the surface of the axle and wheel in the wheel/axle joint of the wheel set. In the further part of this article,

the results of wear tests for shafts with coatings applied to them are presented.

4.1. Shaft with an uncoated top layer

The results of the macrographic tests of the top layer demonstrated the occurrence of fretting wear on either side of the shaft axle seat and sleeve hub (fig. 6). The location of wear, close to joint edges, should be explained by the mechanism of the development of fretting in clamped joints, which was discussed in detail in [5].

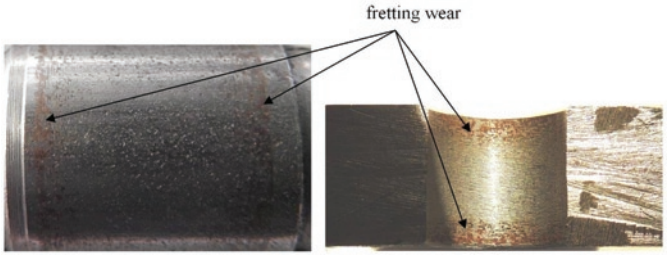

Fig. 6. Fretting wear at the surface of an uncoated shaft and sleeve hub

Wear occurs in the form of a ring at the entire circumference of the shaft axle seat. The width of the area affected by wear is approx. 2-3 mm on either side and that area is located approx. 2 mm from the axle seat edge.

The tests of the topography of the top layer at the place of fretting wear indicated a considerable increase of roughness parameters. The Ra parameter at the place of fretting wear is 3.23 µm. The sample

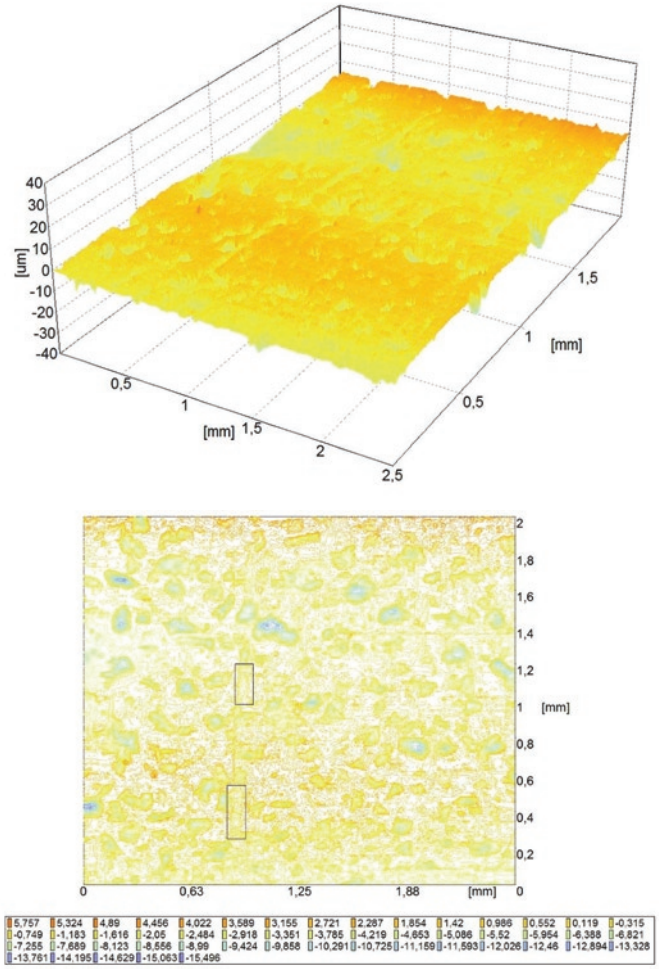

Fig. 7. Results of the testing of top layer topography at the place of fretting wear

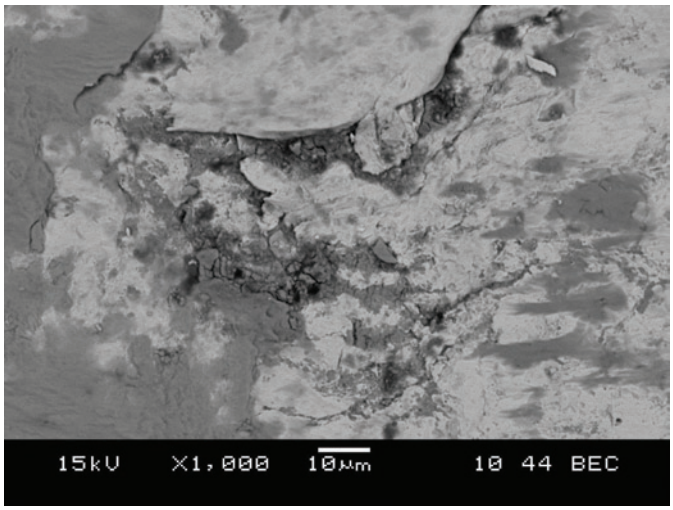

Fig. 8. Image of the shaft surface in the fretting wear zone as seen under a scanning microscope

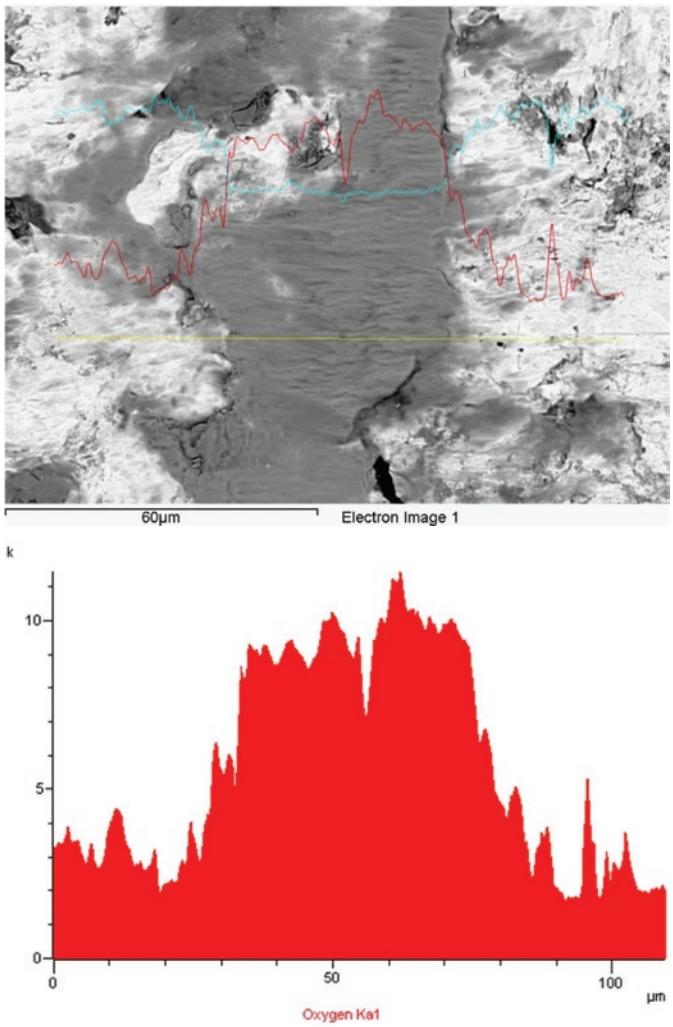

Fig. 9. Results of x-ray examinations of the chemical composition conducted by means of the EDS method at the shaft surface in the fretting wear zone

results of the testing of top shaft layer topography at the place of fretting wear, achieved with the use a TOPO 01P contact profilometer equipped with an induction measuring head with the radius of 2 µm and cone angle of 90°, are presented in fig. 7.

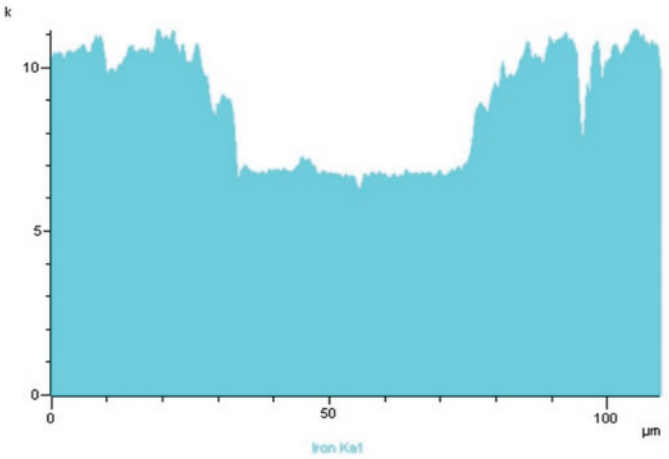

Fig. 9. (continued) Results of x-ray examinations of the chemical composition conducted by means of the EDS method at the shaft surface in the fretting wear zone

The increase of roughness parameters is mainly related to material build-up. That build-up is the wear products which came into being during the process of forcing the sleeve onto the shaft, when the microprojections of the top layer of the elements with a smaller hardness gradient were being torn off and moved continuously until the completion of the forcing process. The source of wear products and formation of the build-up is adhesion.

In fig. 8, the sample image of the shaft surface at the place of fretting wear is shown as seen under a scanning microscope. In that image, widespread damage in the form of material build-up as well as micropits and microcracks of the top layer can be observed.

During operation, as a result of oscillatory tangential displacement of the mating surfaces, the build-up undergoes plastic deformation and then oxidation thus creating an image which is typical of iron corrosion. In fig. 6, that is visible in the form of a brown ring at the place of fretting wear. The oxidation of the deformed build-up takes place as a result of oxygen penetration into worn-out places through fissures which came into being as a result of shaft deflection. To confirm the above statement, the analysis of oxygen and iron concentration in the area affected by wear was conducted. X-ray examinations of the chemical composition were carried out by means of the EDS method, and the results of those examinations are presented in figure 9.

4.2. The shaft with a TiN coating

The macrographic observations of the coated shaft surface demonstrated the occurrence of fretting wear in the form of a ring comprising the entire circumference of the axle seat on either side. Wear intensity is considerably smaller in relation to the shaft without a coating. Fretting wear is also observed at the surface of the sleeve hub on its both edges, and wear intensity is definitely greater in relation to the shaft with a TiN coating (fig. 10).

Fretting wear is distinguished by different intensity at each side of the axle seat. The width of the area affected by wear is approx. 1 mm

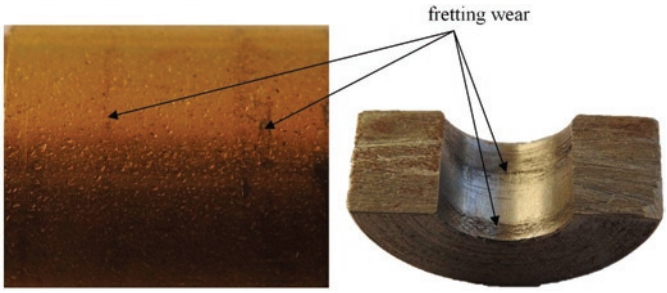

Fig. 10. Fretting wear at the surface of the shaft with a TiN coating and at the sleeve hub

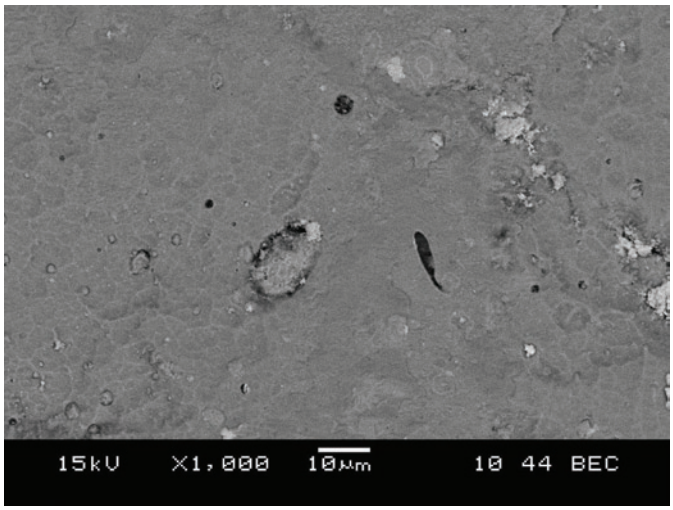

Fig. 11. Fretting wear traces at the surface of the shaft with a TiN coating

at the left side and that area starts approx. 4 mm from the axle seat edge. On the right side, the width of the wear area is approx. 2-3 mm and that area starts approx. 5-6 mm from the joint edge.

In the case of the sleeve hub, the start of fretting wear is observed as early as next to the edges and the wear area is considerable. The width of the „strip" varies from 3 to 4 mm on either side.

As was the case with a clamped joint with an uncoated shaft, here the main kind of wear also comprised by fretting is, too, material build-up which originates from the shearing of the microprojections

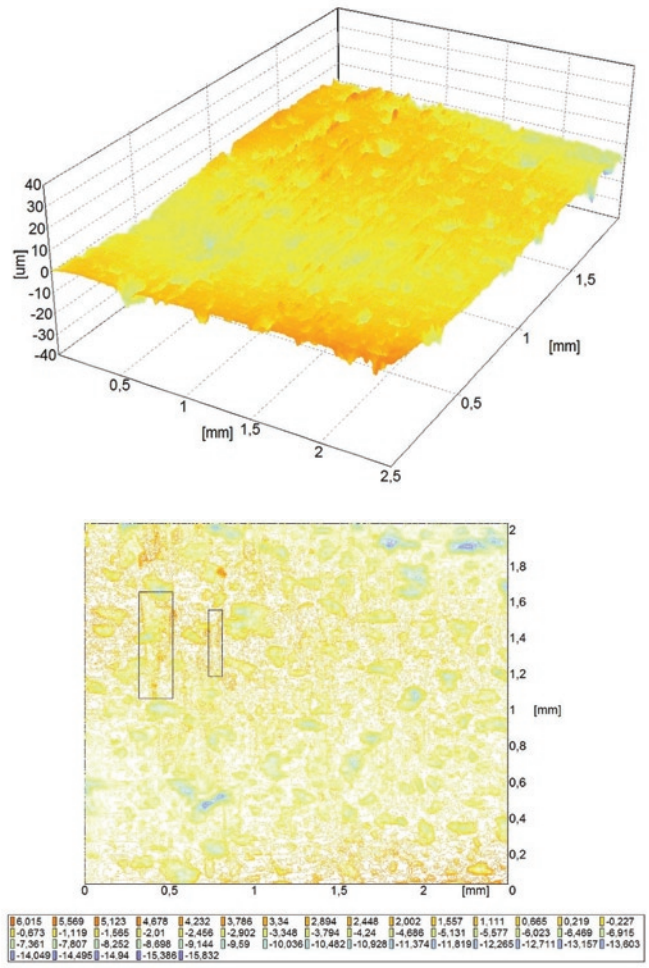

Fig. 12. Results of the testing of top layer topography at the place of fretting wear

of the sleeve hub surface (fig. 11). That build-up undergoes plastic deformation and oxidation during operation. A big difference in the shaft surface hardness gradient in relation to the sleeve surface causes mainly the sleeve to become damaged.

The testing of roughness parameters at a place distinguished by a greater intensity of fretting wear did not show significant differences in relation to the state before wear tests. This follows from the small height of damage which mainly coincides with the microirregularities at the axle seat surface. A sample result of the measurement of roughness parameters at the place of fretting wear is presented in fig. 12.

4.3. The shaft with a CrN+a-C:H:W coating

The macrographic examinations of the top layer of the shafts demonstrated the occurrence of fretting wear to a small extent. In the case of the sleeve hub top surface, fretting wear is also observed in places. As in previous cases, damage occurs close to joint edges (fig. 13). Damaged areas are distributed randomly at the circumference of the shaft axle seat.

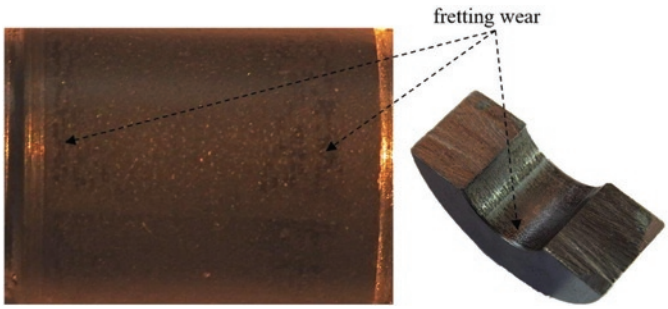

Fig. 13. Fretting wear at the surface of the shaft with a CrN+a-C:H:W coating and at the sleeve hub

The area of the biggest noted traces of fretting wear is approx. 2-2.5 mm^2. Fretting wear zones are distinguished by their brown colour.

Wear occurs mainly in the form of wear product build-up, a fact confirmed by the images from the scanning microscope. A sample image of the shaft top layer in the fretting wear zone is shown in fig. 14.

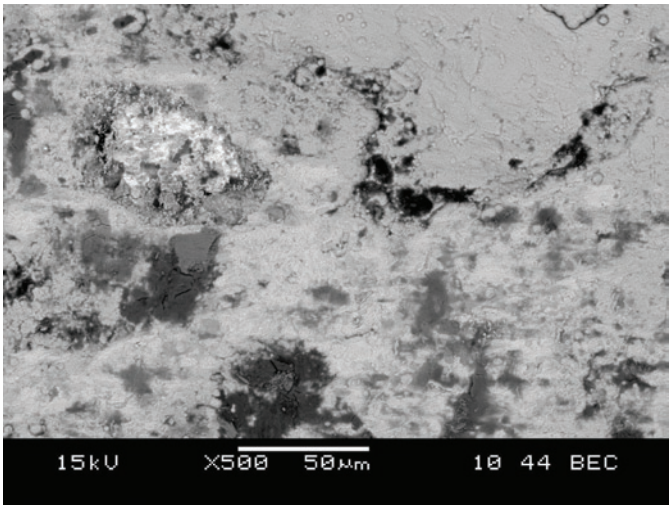

Fig. 14. Fretting wear traces at the surface of the shaft with a CrN+a-C:H:W coating

The access of oxygen to the damaged zones causes wear products to oxidise. This is confirmed by chemical element distribution maps for the shaft surface in the fretting wear zone as shown in fig. 15.

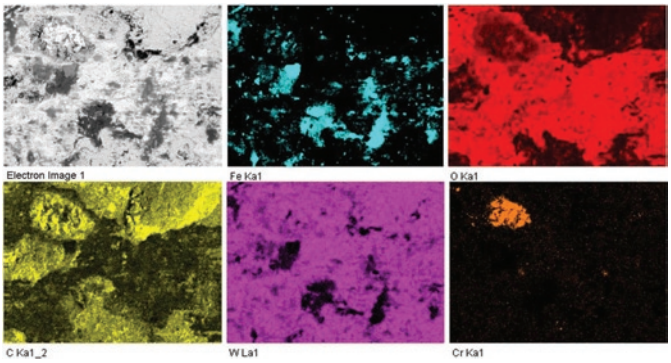

Fig. 15. Chemical element distribution maps for the shaft surface in the fretting wear zone

Oxygen occurs in 90% of the surface being tested thus forming oxides with other chemical elements.

5. Conclusion

The aim of this article was to present the results of research on the mitigation of the development of fretting wear in clamped joints. It follows from the review of literature that the mitigation of wear in that kind of joints is connected with the elimination of adhesion. This is possible in the case of matching the elements distinguished by the appropriate geometry and hardness of the top layer.

Shafts without PVD coatings and shafts with TiN and CrN+a-C:H:W coatings were subjected to wear tests. Coatings were applied to shaft surfaces because in a real joint between the wheel and axle of a rail vehicle wheel set it is the axle which is the element determining the life of the entire wheel set.

The results of the tests of the uncoated shaft surfaces demonstrate the intensive image of fretting wear, which confirms the susceptibility of the joint to the creation of adhesive bonds. Fretting wear occurs at the entire shaft circumference in the form of a ring 2-3 mm wide on either side of the axle seat. The area affected by wear starts approx. 3 mm from the joint edge.

In the case of shafts with a TiN coating, the smaller wear intensity is observed, however, also in the form of a ring, 1 mm wide for the left side and 2-3 mm on the right side of the axle seat. The different geometry and hardness of the shaft and sleeve causes the occurrence of fewer places prone to the creation of adhesive bonds.

Out of the proposed coatings, CrN+a-C:H:W ones have the greatest influence on the mitigation of the development of fretting wear. Despite smaller hardness and roughness in relation to TiN coatings, wear on shafts covered with the former coating is less intensive. In that case, wear occurs in places and each time occupies the area of 2-2.5 mm^2. This may be due to the chemical composition of the coating. Good anti-wear properties of hydrogenated amorphous carbon are completed by tungsten. Hence, that coating is distinguished by the small coefficient of friction of the steel surfaces thus reducing damage to those.

Microscopic examinations demonstrated that fretting comprises mainly material build-up from the shearing of microprojections of the sleeve top surface, which build-up sticks to the shaft surfaces. In relation to the top layers of shafts with coatings, the sleeve top layer has the smallest hardness, therefore that layer will be more susceptible to damage. Research also demonstrated that, during operation, the build-up undergoes plastic deformation as a result of the occurrence of oscillatory tangential displacement of the mating surfaces and oxidation as a result of contact with atmospheric air. The quantitative examinations of the chemical composition of the wear products demonstrated 40% concentration of oxygen and 50% concentration of iron. The remaining 10% of the chemical composition is constituted by the elements comprised by the top layer of the shafts. Moreover,

micropits and microcracks, particularly visible at uncoated shafts, are observed in wear zones.

In this article, the results of research on fretting wear based on the example of rail vehicle wheel sets have been presented, but those results may also be referred to other examples of clamped joints operating in rotational bending conditions.

Acknowledgement:
This work was done as part of research project No. PB.501-1/2017 financed by the Higher Vocational School in Nowy Sącz.

References

1. Astrid Gies, Thomas Chudoba, Norbert Schwarzer, Jürgen Becker. Influence of the coating structure of a-C:H:W coatings on their wear-performance: A theoretical approach and its practical confirmation. Surface and Coatings Technology 2013; 237: 299-304, https://doi.org/10.1016/j.surfcoat.2013.07.065.
2. Bahri A, Kaçar E, Akkaya S S, Elleuch K, Ürgen M. Wear protection potential of TiN coatings for 304 stainless steels used in rotating parts during olive oil extraction. Surface and Coatings Technology 2016; 304: 560-566, https://doi.org/10.1016/j.surfcoat.2016.07.067.
3. Bose Sivakumar, Lokesh Chandra Pathak, Raghuvir Singh. Role of surface roughness on corrosion and fretting corrosion behaviour of commercially pure titanium in Ringer's solution for bio-implant application. Applied Surface Science 2017; 401: 385-398, https://doi.org/10.1016/j.apsusc.2017.01.033.
4. Dong-Wook Kim, Kyung-Woong Kim. Tribological characteristics of Cr/CrN/a-C:H:W/a-C:H coating under boundary lubrication conditions with glycerol mono-oleate (GMO) and molybdenum dithiocarbamate (MoDTC). Wear 2015; 342-343: 107-116.
5. Guzowski S. Analiza zużycia frettingowego w połączeniach wciskowych na przykładzie osi zestawów kołowych pojazdów szynowych. Wydawnictwo Politechniki Krakowskiej, Kraków, 2003.
6. Guzowski S. Warunki rozwoju zużycia frettingowego w połączeniu koło-oś zestawu kołowego. Zeszyty Naukowe Politechniki Śląskiej, Transport 1995; 27: 111-118.
7. Karwala K, Kulikowski H, Tułecki A. Technologiczne problemy trwałości zestawów kołowych pod kątem przystosowania pojazdów szynowych do zwiększonych prędkości. Rozprawa doktorska, Kraków, 1991.
8. Kesavan D, Vamshidhar Done, Sridhar M R, Ronald Billig, Daniel Nelias. High temperature fretting wear prediction of exhaust valve material. Tribology International 2016; 100: 280-286, https://doi.org/10.1016/j.triboint.2016.02.011.
9. Kowalski S, Guzowski S. Wpływ procesów technologicznych na zużycie frettingowe w połączeniu wciskowym. Tribologia 2010; 3: 85-94.
10. Lenart A, Pawlus P, Dzierwa A, Sęp J, Dudek K. The effect of surface topography on dry fretting in the gross slip regime. Archives of Civil and Mechanical Engineering 2017; 17 (4): 894-904, https://doi.org/10.1016/j.acme.2017.03.008.
11. Madej M. The effect of TiN and CrN interlayers on the tribological behavior of DLC coatings. Wear; 2014; Volume 317, Issues 1-2: 179-187 https://doi.org/10.1016/j.wear.2014.05.008
12. Matteo Benedetti, Vigilio Fontanari, Elisa Torresani, Christian Girardi, Lorenzo Giordanino. Investigation of lubricated rolling sliding behaviour of WC/C, WC/C-CrN, DLC based coatings and plasma nitriding of steel for possible use in worm gearing. Wear 2017; 378-379: 106-113, https://doi.org/10.1016/j.wear.2017.02.029.
13. Mi X, Cai Z B, Xiong X M, Qian H, Tang L C, Xie Y C, Peng J F, Min-Hao Zhu. Investigation on fretting wear behavior of 690 alloy in water under various temperatures. Tribology International 2016; 100: 400-409, https://doi.org/10.1016/j.triboint.2016.05.012.
14. Michnej M. Proces zużycia w połączeniu obrotowym na przykładzie modelu zestawu kołowego z samoczynną zmianą rozstawu kół. Praca doktorska 2012; Kraków.
15. Pereira K, Yue T, Abdel Wahab M. Multiscale analysis of the effect of roughness on fretting wear. Tribology International 2017; 110: 222-231, https://doi.org/10.1016/j.triboint.2017.02.024.
16. Richert M, Zawadzka P, Mazurkiewicz A, Smolik J, Leszczyńska-Madej B, Nejman I, Pałka P, Pietrzyk S. Deposition of W/a-C:H:Zr and W/a-C:H:W multilayer coatings on substrate made of porous graphite by arc - Electron beam hybrid method. Surface and Coatings Technology 2016; 300: 19-24, https://doi.org/10.1016/j.surfcoat.2016.05.035.
17. Song C, Shen M X, Lin X F, Liu D W, Zhu M H. An investigation on rotatory bending fretting fatigue damage of railway axles. Fatigue & Fracture of Engineering Materials & Structures 2014; 37: 72-84, https://doi.org/10.1111/ffe.12085.
18. Stefan Nißen, Jan Heeg, Mareike Warkentin, Detlef Behrend, Marion Wienecke. The effect of deposition parameters on structure, mechanical and adhesion properties of a-C:H on Ti6Al4V with gradient Ti-a-C:H:Ti interlayer. Surface and Coatings Technology 2017; 316: 180-189, https://doi.org/10.1016/j.surfcoat.2017.03.020.
19. Zheng J F, Luo J, Mo J L, Peng J F, Jin X S, Zhu M H. Fretting wear behaviors of a railway axle steel. Tribology International 2010; 43 (5-6): 906-911, https://doi.org/10.1016/j.triboint.2009.12.031.

Sławomir KOWALSKI
Technical Institute
State Higher Vocational School in Nowy Sącz
ul. Zamenhofa 1a, 33-300 Nowy Sącz, Poland

E-mail: skowalski@pwsz-ns.edu.pl

Article citation info:
SZUDROWICZ M. Layered composite increasing the resistance of patrol and intervention vehicles to the impact of improvised explosive devices (IED) from below. Eksploatacja i Niezawodnosc – Maintenance and Reliability 2018; 20 (1): 9–15, http://dx.doi.org/10.17531/ein.2018.1.2.

Marek SZUDROWICZ

LAYERED COMPOSITE INCREASING THE RESISTANCE OF PATROL AND INTERVENTION VEHICLES TO THE IMPACT OF IMPROVISED EXPLOSIVE DEVICES (IED) FROM BELOW

KOMPOZYT WARSTWOWY ZWIĘKSZAJĄCY ODPORNOŚĆ SAMOCHODÓW PATROLOWYCH I INTERWENCYJNYCH NA ATAK IMPROWIZOWANYCH ŁADUNKÓW WYBUCHOWYCH (IED) OD DOŁU*

Model layered composites were made of polyester resin reinforced with layers of glass fibre and aramid fibre fabrics. The fabrics for the study were selected in a manner enabling the comparison of their ballistic resistance depending on the material type and density. Additionally, aluminium plates were used to produce the composites.The study examined the resistance of the model composites to 1.1 g fragment simulating projectile (FSP) penetration, their susceptibility to deformation caused by shock waves produced by pure TNT charges, and their resistance to the effects of detonation of model improvised explosive devices (IED) containing fragments in the form of bearing balls. The analysis and optimisation of the test results enabled the selection of a layer configuration combining the materials studied that has the lowest area density and that protects car bottom structures against perforation in the case of a detonation of a small improvised explosive device.

***Keywords**: polymer composites, terminal ballistics, ballistic resistance, 1.1 g FSP, improvised explosive devices.*

Wykonano modelowe kompozyty warstwowe do budowy których wybrane zostały: żywica poliestrowa zbrojona warstwami tkanin z włókien szklanych i aramidowych. Tkaniny do badań dobrano w sposób umożliwiający porównanie odporności balistycznej w zależności od rodzaju materiału i gęstości. Dodatkowo do konstrukcji kompozytów użyto blachy aluminiowej. Zbadano odporność wykonanych modeli kompozytów na przebicie pociskami symulującymi odłamek (FSP) o masie 1,1 g, ich podatność na deformację w wyniku oddziaływania fali uderzeniowej czystych ładunków trotylu, odporność na detonację modelowych improwizowanych urządzeń wybuchowych IED, zawierające odłamki w postaci kulek łożyskowych. Analiza i optymalizacja wyników badań eksperymentalnych pozwoliła dobrać układ warstwowy, będący kombinacją badanych materiałów, o najmniejszej gęstości powierzchniowej chroniący dno samochodów przed przebiciem w przypadku detonacji małego improwizowanego ładunku wybuchowego.

***Słowa kluczowe**: kompozyty polimerowe, balistyka końcowa, odporność balistyczna, odłamek FSP 1,1 g, improwizowane ładunki wybuchowe.*

1. Introduction

Patrol and intervention cars are used in regions threatened by terrorism for purposes such as:

- patrolling areas where there is a risk of fire attacks and explosions of explosive charges;
- intervention activities, in particular combating terrorist groups;
- peace-keeping operations, separating belligerents, and restoring and maintaining public order;
- transporting officers and other persons and cargoes requiring special protection;
- transporting and ensuring the functioning of devices and apparatus used for reconnaissance, identification, and recording.

As for the detonation of small fragmentation explosive charges, i.e.: anti-personnel mines, hand grenades, and improvised charges, two major types of impact that endanger the lives and health of personnel can be distinguished. These are: the impact of fragments and the impact of the shock wave. The most unfavourable situation is an under-vehicle explosion. Due to the small distance from the target (at the moment, the clearance in passenger off-road vehicles is approx. 0.3÷0.5 m), fragments hit the floor material, which is pre-loaded with the shock wave. Very frequently, in such types of cars, the personnel keep their legs directly on the floor and the seats are made of thin textiles.

Requirements for the ballistic protection of cars should be considered in parallel with requirements concerning their mobility [15]. This necessitates the use of light materials for ballistic protection covers. On the other hand, such protections are usually required to perform the function of structural components, e.g. due to the manner of their installation, which is why the materials should be characterised by appropriate strength and rigidity. Modern materials for automotive applications, including ballistic covers for special cars, need to satisfy the requirements of multifunctionality and cost-effectiveness in the areas of production, operation, and disposal [9,10,11,25,29].

The purpose of the study was to develop an additional, self-supporting ballistic cover for car bottoms, mounted on the outside to prevent the perforation of the base floor. In currently-used cars, the floor is usually made of ordinary steel sheets having a thickness of 1÷1.5 mm. New models have floors made of thicker plates (approx. 3 mm). A self-

(*) Tekst artykułu w polskiej wersji językowej dostępny w elektronicznym wydaniu kwartalnika na stronie ***www.ein.org.pl***

supporting cover should have a weight and thickness enabling its use in non-armoured vehicles such as: Land Rover, Toyota, and Mercedes.

These assumptions were based on an analysis of damage to steel plates (used for the production of car floors — Fig. 1), performed after preliminary tests of resistance to detonation of small IEDs. Information about the existence of such damage and its structure was obtained from officers of Independent Anti-Terrorist Subunits (SPAT). An analysis of the mass distribution of fragments generated during detonation of F1 grenades, POMZ anti-personnel mines (Противопехотная Осколочная Мина Заграждения), and pipe bomb IEDs showed that statistically most fragments have a mass of approx. 1 g and heavier fragments are only generated singularly.

An additional cover installed under the floor will protect it against:

- deformation caused by the shock wave,
- perforation by fragments, as the cover, even if perforated, will reduce the kinetic energy of fragments sufficiently to prevent the perforation of the base floor material.

It was also assumed that raw minerals used for the production of said covers should be available and produced domestically.

Light-weight materials that can be used in ballistic covers of this type include: strong steel, aluminium-based alloys, magnesium- and titanium-based alloys, and metal and polymer matrix composites [6, 7, 13, 17, 18, 23, 26].

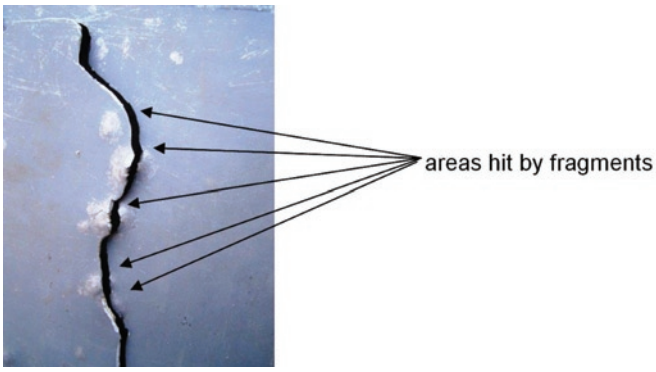

Fig. 1. Failure of a steel plate caused by the simultaneous impact of a shock wave and fragments Source: WITPiS, author's own work.

As fibre-reinforced polymer composites combine light weight with very good mechanical properties, they are used in demanding structural applications. Composites combine the strength and rigidity of the reinforcing fibres with the protective properties of the polymer matrix, which transfers loads among fibres [14, 27].

The materials that are currently used most commonly in composite ballistic covers are mainly glass-, aramid-, and carbon-fibre fabrics combined with a polymer matrix. Individually, these materials are not good structural materials, however, combined together, they offer properties that often surpass the properties of traditional metallic materials [8,33,36,38].

Layered composites have been studied under various load conditions, including shock wave loads. It was shown that for composites and monolithic materials having the same area density, composites are stronger [4, 31, 39, 40, 41].

There are several types of glass fibres. The most popular are E-type fibres. The advantages of this type of glass fibres include: high strength, good chemical and thermal resistance, easy processing, and low prices. Carbon fibres are reinforcements used in advanced structural composites due to their good mechanical properties and light weight. They are available in a number of varieties offering different properties and they are classified mainly according to their elastic modulus (fibres having a low, medium, and high elastic modulus). Aramid fibres are light-weight and very strong. They have a high energy absorption capacity, which is why they are widely used in applications such as impact-resistant products, including ballistic applications. Their additional advantage in applications such as ballistic protections is their good fire resistance — they are a self-extinguishing material. Due to their relatively low shear strength, it is recommended that hybrid fabrics (e.g. with glass fibres) be used in special applications. The recommended matrix for composites are epoxy or polyester resins [19, 21, 37].

Polymer composites are sensitive to loads that are perpendicular to the surface (to which ballistic protections are exposed), as their mechanical properties in this direction are much worse than in the layer plane [12, 28, 30]. Damage to such composites depends on:

- the properties of the reinforcement and matrix materials,
- the proportion, form, and orientation of the reinforcement,
- the adhesive forces between the matrix and the reinforcement,
- the impact energy.

In general, a material's capacity for effective counteracting of ballistic impacts depends on the material hardness, which is critical for the phenomenon of projectile deformation, and the strain at which damage is inflicted, due to the material's capacity for absorbing energy through brittle fracture, in the case of ceramics and composites, and plastic deformation, in the case of some metals [35].

In the case of composites in which fibres are bound by a polymer matrix, the composite damage process can be divided into two phases (Fig. 3). Initially, the projectile, as it penetrates the material, causes damage due to the compression and shear on the upper layers. In the second phase, when the velocity of the penetrating projectile has decreased, the material is damaged due to delamination and due to fibres being pulled out from the matrix as a result of stretching [1, 22, 24, 32].

A composite, being an anisotropic material, undergoes complex states of stress and strain when subjected to impact. Due to the existing diversity of composites, the unlimited freedom in the selection of configurations of components and the complex damage mechanism, depending on the impact energy, it is very difficult to estimate the damage resistance based on existing fragmentary hypotheses [5, 20].

Study [16] examined the effect of type of reinforcement and stacking sequence in a composite on low velocity impact damage tolerance. The impact strength was determined using the compression after impact strength criterion. The criterion can also be referred to as low velocity impact damage tolerance. No major differences concerning the examined strength properties and impact damage tolerance were observed between the tested carbon-glass composites. Thus, the decisive factor in the selection of one of those materials may be the price. Taking into account the properties examined and the price, aramid-glass fabric composites behave in a similar manner to glass and carbon fabric-reinforced composites.

The main reason for using composites is the ability to reduce the weight of structural elements. However, high strength properties entail high production costs. Thus, reducing the production costs is currently one of the most important challenges in the area of polymer composite production.

A major advantage of using a unidirectional fibre arrangement is the ability to produce composites having precisely the required number of appropriately oriented layers. In comparison with woven fabrics, unidirectional layers have better mechanical properties due to the fact that individual fibres are not bound (tied up). Unidirectional fibres for use in composites are available in two forms. The first form are fibres arranged unidirectionally in a layer, pre-impregnated with resin enabling the preservation of the geometry and layout of a plate (prepregs) and the other form are adhesive-bonded (e.g. using elastomers) fabrics. Elements made of arranged prepregs are cured in autoclaves. This technology enables obtaining composites having

very good mechanical properties, especially in the composite plane. An alternative to the use of prepregs in the production of composites is adhesive bonding of individual layers in order to obtain an integrated fibre structure [2, 3, 34].

Table 1. Test materials

Material name	Material designation		Specimen area density [10^3 g/m^2]
glass composite (flammable resin)	A	A1	10.4
		A2	16.2
		A3	21.0
glass composite (resin with flame-retardant additives)	B	B1	20.0
		B2	26.0
		B3	32.0
aramid composite (elastomer bonding)	C	C1	5.0
		C2	10.0
		C3	15.0
aramid composite (prepregs)	D	D1	4.4
		D2	10.4
		D3	16.3
Aluminium-based alloy	E	E1	8.4
		E2	14.0
		E3	22.4
Steel plate (armoured)	F	F1	19.5
		F2	23.4
		F3	31.2
Steel plate	G	G1	7.8
		G2	15.6
		G3	23.4

Materials characterised by fragment penetration resistance and shock wave-inflicted damage resistance were selected from among products offered by domestic companies. The materials include glass fabric and aramid fabric composites, aluminium alloy plates, and armour steel plates (Table 1).

Rowings used in the production of glass fabrics by domestic companies are covered with a chemically-active substance that makes it possible to use those fabrics directly in the production of composites (without any additional application of the necessary surface finishes), at the same time ensuring good polymer-glass adhesion. The range of products offered comprises balanced and oriented fabrics. Unidirectional glass fabrics having a grammage of 500 g and fibre orientation [0,45] were used to produce the composites. The selection of the resin was made with a view to ensuring the price competitiveness of the product and thus the Polimal polyester resin, with and without flame-retardant additives, was selected for use in the tests. Due to the high viscosity of resins with additives, the polyester-glass composite production technology was manual lamination. Their density was 1.8 g/cm^3, tensile strength – 210 MPa, and elongation – 10%.

No aramid fabrics are produced domestically. Two companies produce aramid composites based on imported unidirectional fabrics and used in the production of ballistic protections (vest inserts, helmets, composite armours). Each of the companies produces the composites using a different technology, i.e. prepreg pressing and adhesive bonding of individual fabric layers using elastomers. Their density was 1.1 g/cm^3, tensile strength – 460 MPa, and elongation – 40%.

Plates of various thickness made of an aluminium-based alloy that is produced domestically and has parameters similar to the parameters of foreign alloys that are referred to as ballistic alloys were selected for the tests. The density was 2.8 g/cm^3, tensile strength – 380 MPa, and elongation – 14%.

The armour steel plate selected for the tests was characterised by a density of 7.8 g/cm^3, tensile strength of 1550 MPa, and elongation of 8%.

Additionally, low-alloy steel plates of several different thicknesses were prepared for the tests as reference material. The density was 7.8 g/cm^3, tensile strength – 395 MPa, and elongation – 25%.

2. Test stand testing

The following tests were performed at test stands:

- resistance to penetration by explosive weapons: hand grenades, anti-personnel mines, small IEDs (selected from among actual threats according to SPAT's information),
- resistance to penetration by 1.1 g fragment simulating projectiles (FSP),
- susceptibility to deformation caused by shock waves,
- resistance to penetration by model IEDs.

As for fragment resistance, a recognised test allowing the comparison of different materials, primarily in terms of their area density, is the determination of the V50 ballistic limit using a 1.1 g fragment simulating projectile, referred to as the standard fragment in Polish standards (Fig. 2). The test is described in the Polish standard PN-V-87000: "Light ballistic protections. Bullet- and fragment-proof vests. General requirements and testing." The basic NATO document setting out requirements concerning this test is STANAG 2920: "Ballistic test method for personal armour."

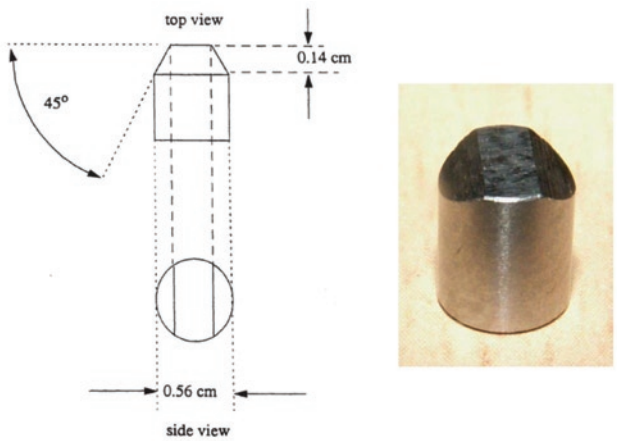

Fig. 2. 1.1 g fragment simulating projectile. Source: STANAG 2920.

The V50 ballistic limit is determined as the average of six perpendicular impact velocities (three lowest velocities with complete penetrations and three highest velocities with partial penetrations). In the determination of ballistic limits, the maximum permissible difference between the lowest and highest FSP impact velocities is 20 m/s. Only in cases where the lowest velocity with a complete penetration

is more than 20 m/s lower than the highest velocity with a partial penetration, the ballistic limit is calculated as the average of 10 velocities (five lowest velocities with complete penetrations and five highest velocities with partial penetrations). In this case, the velocity range is limited to the lowest possible level (as close to 20 m/s as possible).

V50 tests with the use of 1.1 g fragment simulating projectiles will mainly be used to compare the fragment resistance of individual layers comprising the composite, made of different materials.

Fragment resistance tests were performed with the use of 1.1 g FSPs and the characteristics of the prepared materials were established. A diagram of the test stand is shown in Figure 3.

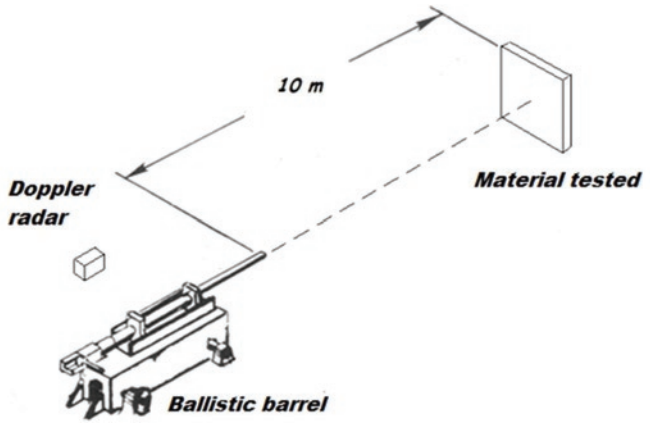

Fig. 3. Test stand diagram

Another test performed for the purpose of selecting materials was a self-developed test of material resistance to deformation during the explosion of a pure 75 g TNT charge placed 250 mm under the material tested, with the specimen measuring 500x500 mm.

The extent of material deformation was measured using witness plates: 0.5 mm aluminium alloy plates placed directly behind the material tested.

The next test involved the use of model IED charges and enabled evaluating particular materials under reproducible conditions combining the impact of the shock wave and fragments.

A separate issue addressed in relation to that method was the development of a model charge. The need to develop such a charge stemmed from the fact that assessment of a material's fragment resistance only on the basis of tests with the use of FSPs does not reflect the actual conditions of fragments hitting the material multiple times with the simultaneous action of the shock wave. Moreover, there is a great number and diversity of currently produced grenades and anti-personnel mines. The objective was to obtain a model charge enabling testing materials' resistance to penetration under the same repeatable conditions.

The charge proposed in the NATO Standardization Agreement STANAG 4569 "Protection Levels for Occupants of Logistic and Light Armored Vehicles" (Fig. 4), in which the casing is made of an aluminium-based alloy and the fragments are minimum 750 steel bearing balls having a diameter of 4.762 mm and a mass of 0.4 g, was

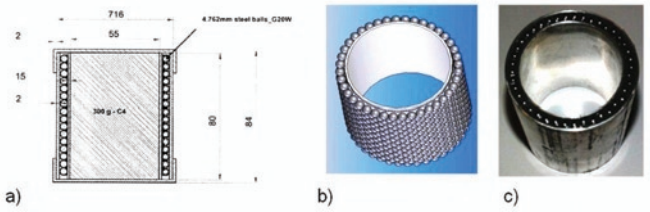

Fig. 4. a) diagram of an improvised explosive device presented in STANAG 4569; b) diagram of the ball arrangement in an IED model; c) IED model.

used as the model improvised explosive device. The content of the C4 explosive material was 300 g. STANAG 4569 states that fragments generated from a model charge should have a velocity of approx. 1200 m/s (Fig. 4).

3. Results and discussion

When a fragmentation charge explodes within a short distance, the material is subjected to the combined action of a shock wave and fragments.

In order to develop a layered composite that is resistant to such action, preliminary tests were performed in separate experiments: fragment resistance tests with the use of 1.1 g FSPs and pure 75 g TNT charge explosion resistance tests. The tests were followed by verification tests with the use of a model IED charge complying with STANAG 4569 Annex B Level 1.

In the preliminary fragment resistance tests with the use of 1.1 g FSPs, the V50 ballistic limit was determined for three different area densities of the prepared materials. The relation between the ballistic limit and the area density was plotted for each of those materials (Fig. 5).

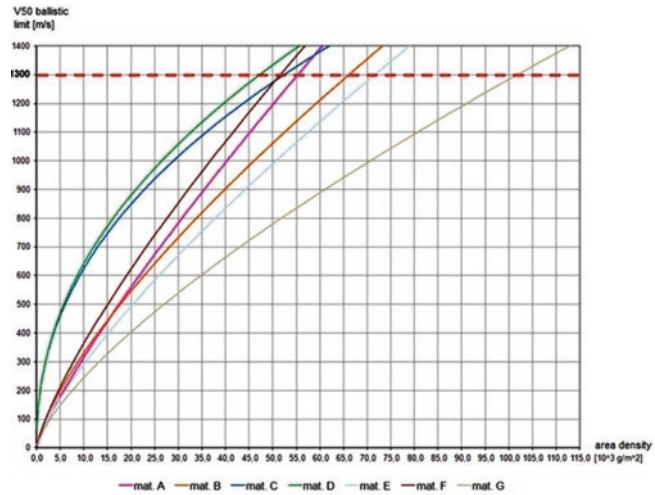

Fig. 5. Results of the fragment resistance tests with the use of 1.1 g FSPs, relation between the ballistic limits of the materials tested and their area densities, with the trend lines drawn. Source: WITPiS, author's own work

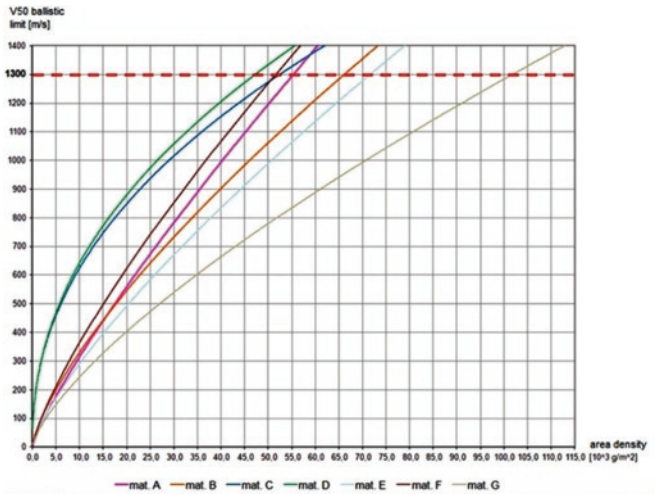

Fig. 6. Relation between the ballistic limits of the materials tested and their area densities. Source: WITPiS, author's own work.

Based on the graphs, area density values corresponding to the ballistic limits at 1300 m/s were evaluated (Fig. 6). This velocity is the maximum velocity of IED model fragments recorded during military field tests and was adopted as the criterion for comparative tests of the materials' fragment resistance.

The results obtained indicate that for the glass composite, the V50 ballistic limit for 1.1 g FSPs is 1300 m/s when the area density is $55 \cdot 10^3$ g/m^2. As for the other materials, the following values were obtained: aramid composite — $47 \cdot 10^3$ g/m^2, aluminium-based alloy — $72 \cdot 10^3$ g/m^2, armour steel plate — $52 \cdot 10^3$ g/m^2, and steel plate — $102 \cdot 10^3$ g/m^2.

The fragment resistance results obtained were analysed for the purpose of optimising two-layer and three-layer material configurations. Two conditions were imposed with regard to the optimisation: the sum of the area densities of individual layers should be minimum and at the same time, the sum of the ballistic limit values of those layers should not be smaller than 1300 m/s. Tables 2 and 3 show examples of the optimisation for selected layer configurations. The minimum area density values of particular layer configurations for which the ballistic limit is 1300 m/s are marked in yellow.

The optimisation performed showed that the lightest layer configuration that meets the conditions is the three-layer configuration. The area density of the configuration is $31.5 \cdot 10^3$ g/m^2. The information presented in the tables can also be used to determine the thickness of the configuration, as the area densities of the individual layers in the configuration are known, and to evaluate the costs of the materials.

The fragment resistance tests with the use of 1.1 g FSPs made it possible to select the individual layers making up the composite. However, they did not indicate the layer stacking sequence in the composite. For this purpose, the pure 75 g TNT charge explosion resistance tests were performed.

As the area density of materials increases, their deformation caused by a TNT explosion decreases. The witness plate, made of an aluminium-based alloy, placed behind the material tested, becomes deformed together with the material. After each test, the extent of witness plate deformation was measured in two perpendicular directions. Figure 7 shows examples of witness plate deformation after tests on 1 mm, 2 mm, and 3 mm thick steel plates.

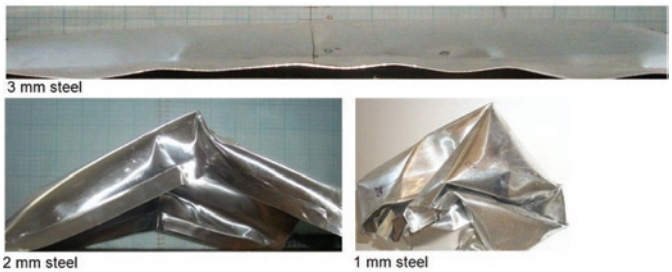

Fig. 7. Witness plate deformation after tests on steel plates of various thickness.
Source: WITPiS, author's own work.

Figure 8 presents the characteristics of the materials tested with the use of pure 75 g TNT charges. The tests conducted enabled arranging the materials based on their resistance to deformation caused by a pure TNT charge explosion. The material that was deformed to the smallest degree was the glass composite.

The results of the preliminary tests made it possible to determine the sequence in which the materials were to be stacked in the layered composite. It was decided that due to its highest resistance to deformation caused by TNT explosions and its high fragment resistance, expressed by the value of the V50 ballistic limit, the first material would be the glass composite. The last material would be the aramid

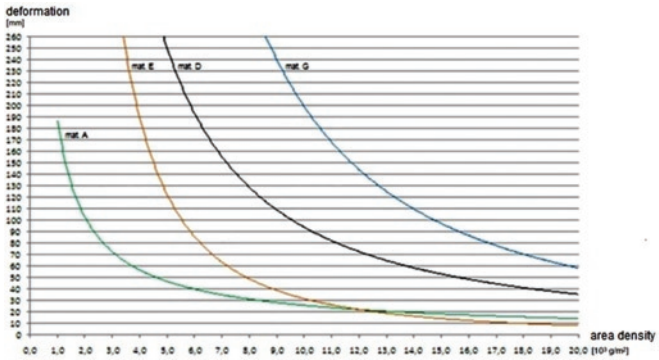

Fig. 8. Relation between the deformation of selected materials and their area densities.
Source: WITPiS, author's own work. Source: WITPiS, author's own work.

composite. It is characterised by a lower deformation resistance than the glass composite, however, it has the best fragment resistance.

IED models were used in the verification tests. The tests were military field tests. The IED models were placed on a concrete slab, 300 mm below the specimen tested.

The reference material for the test was a 480 HB steel plate, i.e. the so-called "armoured" steel plate. In the case of 4 mm thick plates ($32 \cdot 10^3$ g/m^2), up to 5 penetrations were obtained. Under these test conditions, effective protection was provided by the 6 mm thick plate ($48 \cdot 10^3$ g/m^2).

The resistance of selected two- and three-layer models was tested. 1 mm thick auto-body sheet metal that simulated the car floor was placed behind the material tested as a witness panel. Figure 9 shows the influence of the IED model on the developed three-layer composite ($31.5 \cdot 10^3$ g/m^2). The composite was not perforated.

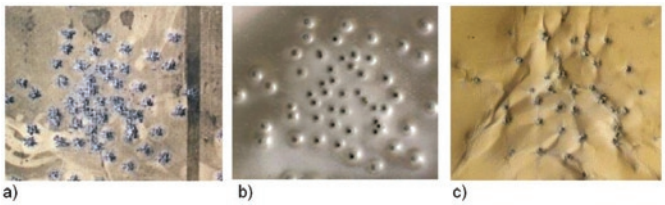

Fig. 9. Front sides of particular materials from the three-layer configuration: a) glass composite, b) aluminium plate, c) aramid composite. Source: WITPiS, author's own work.

Summary

A material configuration for an additional bottom cover for non-armoured and light-armoured patrol and intervention cars was developed. The cover is a layered composite (the first layer being a 6 mm thick glass composite, due to the lowest degree of deformation during the tests with the use of TNT charges, and the second and third layers being a 2.5 mm thick aluminium plate and a 12.5 mm thick aramid composite) mounted on the bottom of the car, protecting occupants of the car against injury or death and the car floor structure against damage caused by detonation of small fragmentation charges.

Bearing in mind the type of application, it is recommended that the cover be produced by screwing together the particular layers. The rationale behind this recommendation is that:

- it is possible that in the case of detonation of lower-impact charges or as a result of mechanical damage related to moving over a difficult terrain, only the first layer of the cover, i.e. the glass composite, will be damaged. If this is the case, the other layers, in particular the expensive aramid composite, can continue to be used in the cover structure after the glass composite is replaced. This approach necessitates developing non-invasive methods of inspecting composite integrity,

- screwing particular layers together enables arranging the cover layers in any sequence depending on the anticipated dangers (and their anticipated impact),
- particular layers of the cover can be worked mechanically more easily than a three-layer configuration. There is no need to order ready custom-made cover templates. The user can cut out any shapes from large sheets of particular materials, according to the current needs, e.g. in field conditions.

The three-layer cover provides protection against perforation by fragments of F1 grenades, POMZ anti-personnel mines, and small IEDs at STANAG 4569 Level 1. The area density of the protection cover is $31.5 \cdot 10^3$ g/m^2.

The technology has been partially introduced (production of the glass composite). Additional protection covers for the bottoms of patrol and intervention cars used by the Armed Forces of the Republic of Poland were produced.

References

1. Abrate S. Impact on composite structures. Cambridge: Cambridge University Press, 1998, ISBN 0-521-01832-3.
2. Abrate S. Impact on Laminated Composite Materials. Applied Mechanics Reviews 1991; 44(4): 155-190, https://doi.org/10.1115/1.3119500.
3. Amparo G, Graciani E, Paris F. Prediction of in-plane stiffness properties of Non-Crimp Fabric laminates by means of 3D Finite Element analysis. Composites Science and Technology 2008; 68(1): 121-131.
4. Andrews E W, Moussa N A. Failure mode maps for composite sandwich panels subjected to air blast loading. International Journal of Impact Engineering 2009; 36(3): 418-425, https://doi.org/10.1016/j.ijimpeng.2008.08.005.
5. Bogusz P, Ochelski S, Panowicz R, Niezgoda T, Barnat W. Influence of loading rate on energy absorption performance of epoxy composites reinforced with glass fabric. Composites Theory and Practice 2012; 12(2): 110-114.
6. Borvik T, Dey S, Clausen A H. Perforation resistance of five different high-strength steel plates subjected to small-arms projectile. International Journal of Impact Engineering 2009; 36(7): 948-964.
7. Borvik T, Langseth M, Hopperstad O S, Malo K A. Ballistic penetration of steel plates. International Journal of Impact Engineering 1999; 22(9): 855-886.
8. Committee on High-Performance Structural Fibers for Advanced Polymer Matrix Composites, National Research Council. Report: High-Performance Structural Fibers for Advanced Polymer Matrix Composites. Washington: The National Academies Press, 2005, ISBN: 0-309-54943-4.
9. Committee on Materials Research for Defense After Next, National Research Council. Report: Materials Research to Meet 21st Century Defense Needs. Washington: The National Academies Press, 2003, ISBN: 0-309-50572-0.
10. Committee on Lightweight Materials for 21st Century Army Trucks, National Research Council. Report: Use of Lightweight Materials in 21st Century Army Trucks. Washington: The National Academies Press, 2003, ISBN:0-309-50646-8.
11. Ernest S C. Army focused research team on functionally graded armor composites. Materials Science and Engineering 1999; A259: 155-161.
12. Fahmy A A. Report AD-A281587: Deformation, strength, and failure modes of laminated conventional and hybrid polymer-matrix composites loaded in the thickness direction. Defense Technical Information Center, 1994.
13. Galanis K. Hull construction with composite materials for ships over 100 m in length. Massachusetts Institute of Technology, 2002.
14. Gürdal Z, Haftka R T, Hajela P. Design and Optimization of Laminated Composite Materials. John Wiley & Sons, 1999, ISBN: 978-0-471-25276-4.
15. Hogg P J. Composites for Ballistic Applications. Proceedings of Composite Processing, 2003.
16. Imielińska K, Wojtyra R. Wpływ rodzaju zbrojenia i kolejności ułożenia warstw na tolerancję zniszczeń wywołanych udarami o małej prędkości laminatów epoksydowych zbrojonych włóknem węglowym, szklanym, kevlarowym i hybrydowych. Kompozyty - Composites 2002; 5: 364-368.
17. Jena P K, Mishra B, Ramesh Babu M, Singh A K, Sivakumar K, Bhat T B. Effect of heat treatment on mechanical and ballistic properties of a high strength armour steel. International Journal of Impact Engineering 2010; 37(3): 242-249, https://doi.org/10.1016/j.ijimpeng.2009.09.003.
18. Jensen R E, Mcnight S H, Quesenberry M J. Report ARL-TR-2655: Strength and Durability of Glass Fiber Composites Treated With Multicomponent Sizing Formulations. Army Research Laboratory, 2002.
19. Kang T J, Kim C. Impact energy absorption mechanism of largely deformable composites with different reinforcing structures. Fibers and Polymers 2000; 1(1): 45-54.
20. Kant S, Verma S L. A Review on Analysis and Design of Bullet Resistant Jacket - Ballistic Analysis. International Advanced Research Journal in Science, Engineering and Technology 2017; 4(3): 71-80.
21. Kevlar Technical Guide. DuPont.
22. Kirkwood J E, Kirkwood K M, Lee Y S, Egres R G, Wagner N J, Wetzel E D. Report ARL-CR-538: Yarn pull-out as a mechanism for dissipating ballistic impact energy in KevlarR KM-2 fabric: part II: predicting ballistic performance. Army Research Laboratory, 2004.
23. Lane R, Craig B, Babcock W. Materials for blast and penetration resistance. The Amptiac Quarterly 2002; 6(4): 39-45.
24. Liu D. Characterization of impact properties and damage process of glass/epoxy composite laminates. Journal of Composite Materials 2004; 38(16): 1425-1442, https://doi.org/10.1177/0021998304042741.
25. Madhu V, Balakrishna Bhat T. Armour Protection and Affordable Protection for Futuristic Combat Vehicles. Defence Science Journal 2011; 61(4): 394-402.
26. Mamalis A G, Spentzas K N, Manolakos D E, Ioannidis M B. Composite and hybrid materials for next generation road and rail vehicles. Proceeding Synenergy Forum Conference, National Technical University of Athens 2008: 9-16.
27. Marston C, Gabbitas B, Adams J. The effect of fibre sizing on fibres and bundle strength in hybrid glass carbon fibre composites. Journal of Materials Science 1997; 32(6): 1415-1423, https://doi.org/10.1023/A:1018537530192.
28. McMahon P E, Ying L. Report 3607: Effects of fibre/matrix interactions on the properties of graphite/epoxy composites. NASA 1982.
29. MIL-HDBK-1002/6. Aluminum structures, composites structures, structural plastics, and fiber-reinforced composites. Department of Defence USA
30. MIL-HDBK-17. Composite Materials Handbook. Department of Defense USA.

31. Nurick G N, Langdon G S, Chi Y, Jacob N. Behavior of sandwich panels subjected to intense air blast - part 1: experiments. Composite Structures 2009; 91(4): 433-441.
32. Patel B P, Bhola S K, Ganapathi M, Makhecha D P. Penetration of Projectiles in Composite Laminates. Institute of Armament Technology. Defence Science Journal 2004; 54(2): 151-159, https://doi.org/10.14429/dsj.54.2027.
33. Pike R A, Novak R C. Report CR-134763: Design, fabrication and test of multi-fiber laminates. NASA 1975.
34. Randjbaran E, Zahari R, Majid D, Jalil N, Vaghei R and Ahmadi R. The Effects of Stacking Sequence Layers of Hybrid Composite Materials in Energy Absorption under the High Velocity Ballistic Impact Conditions: An Experimental Investigation. Journal of Material Sciences & Engineering 2013, 2(4): 1-8.
35. Razali N, Sultan M T H, Mustapha F, Yidris N, Ishak M R. Impact Damage on Composite Structures - A Review. International Journal of Engineering and Science (IJES) 2014; 3(7): 8-20.
36. Report ETL 1110-2-548: Composite materials for civil engineering structures, U.S. Army Corps of Engineers, 1997.
37. Schuster D. Ballistic impact on composites. Transactions on Engineering Sciences 1994; 4: 175-181.
38. Surowska B. Materiały funkcjonalne i złożone w transporcie lotniczym. Eksploatacja i Niezawodnosc - Maintenance and Reliability 2008; 3: 30-40.
39. Tekalur S A, Bogdanovich A E, Shukla A. Shock loading response of sandwich panels with 3-D woven E-glass composite skins and stitched foam core. Composites Science and Technology 2009; 69(6): 736-753, https://doi.org/10.1016/j.compscitech.2008.03.017.
40. Wang E, Gardner N, Shukla A. The blast resistance of sandwich composites with stepwise graded cores. International Journal of Solids and Structures 2009; 46(18-19): 3492-3502.
41. Zhu F, Lu G. A review of blast and impact of metallic and sandwich structures. Electronic Journal of Structural Engineering 2007; Special Issue: Loading on Structures: 92-101.

Marek SZUDROWICZ
Military Institute of Armored and Automotive Technology (WITPiS)
Okuniewska 1, 05-070 Sulejówek, Poland

E-mail: marek.szudrowicz@witpis.eu

Article citation info:
PIELECHA I, CIEŚLIK W, SZAŁEK A. Operation of electric hybrid drive systems in varied driving conditions. Eksploatacja i Niezawodnosc – Maintenance and Reliability 2018; 20 (1): 16–23, http://dx.doi.org/10.17531/ein.2018.1.3.

Ireneusz PIELECHA
Wojciech CIEŚLIK
Andrzej SZAŁEK

OPERATION OF ELECTRIC HYBRID DRIVE SYSTEMS IN VARIED DRIVING CONDITIONS

EKSPLOATACJA ELEKTRYCZNYCH UKŁADÓW NAPĘDOWYCH POJAZDÓW HYBRYDOWYCH W ZRÓŻNICOWANYCH WARUNKACH RUCHU*

Hybrid vehicles allow an increase in the powertrain efficiency thanks to their design. One such factor is the use of increased voltage supplying electric motors to the voltage supplying the high voltage battery. The battery voltage is increased several times in the inverter (boost) system to increase the final electric power supplied to the electric motor. The article presents the possibilities of using such a voltage boost in urban and non-urban driving conditions. The tests were performed on the latest generations of parallel hybrid drive systems in Lexus NX 300h and Toyota RAV4 hybrid vehicles. It has been shown that the boost system is used in about 30–40% of the urban drive distance (up to 20% of the driving time). The power supply voltage boost of the electric motors of both vehicles is used throughout the entire engine speed range of these machines at high torque values. Research has shown that the maximum voltage gain – approximately three times (up to 650 V) – is within the maximum torque range of the electric motors and allows for doubling the torque generated by the drive.

***Keywords**: electric motor, current generator, hybrid drive, voltage boost, energy flow, high voltage battery.*

Pojazdy z napędem hybrydowym dzięki swojej konstrukcji, pozwalają na zwiększenie sprawności układu napędowego. Jednym z takich czynników jest stosowanie zwiększonego napięcia zasilającego silniki elektryczne w stosunku do napięcia zasilającego akumulator wysokonapięciowy. Napięcie akumulatora zostaje zwiększone kilkukrotnie w układzie inwertera (boost) w celu zwiększenia końcowej mocy elektrycznej doprowadzonej do silnika elektrycznego. W artykule przedstawiono możliwości wykorzystania takiego wzmocnienia napięcia w warunkach jazdy miejskiej i pozamiejskiej. W badaniach wykorzystano najnowsze generacje układów napędu hybrydowego równoległego w pojazdach Lexus NX 300h oraz Toyota RAV4 hybrid. Wykazano, że układ wzmocnienia napięcia w warunkach miejskich wykorzystany jest w około 30–40% dystansu (do 20% czasu jazdy). Wzmocnienie napięcia zasilającego maszyny elektryczne obu pojazdów wykorzystane jest w całym zakresie prędkości obrotowej tych maszyn przy dużych wartościach momentu obrotowego. Badania wykazały, że maksymalne wzmocnienie napięcia – około trzykrotne (do wartości 650 V) – występuje w zakresie maksymalnego momentu obrotowego silników elektrycznych i pozwala na ponad 2-krotne zwiększenie generowanego momentu obrotowego układu napędowego.

***Słowa kluczowe**: silnik elektryczny, generator prądu, napęd hybrydowy, wzmocnienie napięcia, przepływ energii, akumulator wysokonapięciowy.*

1. Introduction

The variety of hybrid drives available from most passenger vehicles manufacturers means that the interest in the energy flow in such vehicles is very high. Vehicle hybrid drives have been dominated by parallel drives with independent internal combustion engine or electric motor propulsion. Parallel systems with the electric motor supporting the internal combustion engine – despite their simpler construction – are much less common. This is due to the less universal nature of such a hybrid drive solution in everyday urban and non-urban traffic [5].

Tests of vehicles powered with alternative fuels or with alternative propulsion systems are carried out with respect to their respective harmful components emissions [6, 8, 9]. Increasingly more often, these studies refer to conditions of energy flow in hybrid [12] or electrical systems [3]. The theoretical and road analysis of the increased energy recovery potential through the use of different gearing reduction strategies is described in [4]. There are currently many models of hybrid drive systems [1, 2, 11, 13], but road tests of such systems are the basis for the verification of simulation test results.

Current hybrid drive solutions, despite the use of batteries with rated voltages between 200 V and 250 V, allow the electric motors to operate on up to 650 volts. This input voltage gain allows for a 2.5 to 3 times increase in the nominal voltage. Voltage converters are described in [7, 10], among others.

Previous studies have not dealt with the issue of the effect of changes in the electric motor supply voltage to its operating conditions. Taking this into account, the authors have divided the voltage boost value into several compartments:

a) $U < 300$ V,
b) $300 \text{ V} \le U < 400$ V,
c) $400 \text{ V} \le U < 500$ V,
d) $500 \text{ V} \le U < 600$ V,
e) $U \ge 600$ V.

2. Motivation

Varied solutions used in passenger vehicles with hybrid drive systems make the comparison of their mechanical or electrical characteristics ineffective. The use of identical hybrid drive systems allows

(*) Tekst artykułu w polskiej wersji językowej dostępny w elektronicznym wydaniu kwartalnika na stronie ***www.ein.org.pl***

for increased comparability, especially when mounted on two similar vehicles. The mechanical and electrical similarities of powertrain systems do not allow for the unambiguous affirmation of the similarity of their characteristics in terms of differentiated vehicle driving conditions. Thus, the motivation for the study was to analyze the driving characteristics of vehicles with hybrid drive systems. In addition, considering the increase in the supply voltage, the use of this voltage increase and its effect on the flow of energy in the hybrid drive systems of vehicles has been analyzed.

3. Methodology

The purpose of the research was to analyze the energy flow in vehicles equipped with the same hybrid powertrain system, taking the following aspects into account:

1. Analysis of electric vehicles working conditions during driving and regenerative braking.
2. Determining the conditions for using the increased voltage supply value for the electric motors.
3. Determining the flow of electric power in a hybrid vehicle including consumption and energy recovery in different driving conditions.

Analysis of these specific objectives was conducted using vehicles with a full hybrid (parallel) drive system. These vehicles also used an additional rear axle drive system with an electric motor. The only difference between the test vehicles was their curb mass (Table 1).

The research objectives, in addition to the research objects in the form of two hybrid vehicles, required the use of an instrument that would allow making measurements of the main electric parameters of their drive systems. Acquisition of the measured data at 16–38 Hz has been made, which allows for accurate estimation of the changes in the drive systems operation. The study was conducted using a dedicated TechStream diagnostic system for acquisition of measurement data from Toyota and Lexus vehicles (Figure 1).

Table 1. Technical parameters of the test vehicles

Parameter	Unit	Lexus NX 300h	Toyota RAV4 hybrid
Combustion engine			
Displacement	dm^3	2.494	←
Torque	Nm at rpm	206 at 4400–4800	←
Power	kW at rpm	114 at 5700	←
Electric drive system – front			
Torque	Nm at rpm	270 at 0–1800	←
Power	kW at rpm	105 at 4500	←
Electric drive system – back			
Torque	Nm	139	←
Power	kW	50	←
Electric energy storage system			
Battery	–	NiMH	←
Capacity	kW·h	1.59	←
Battery voltage	V	244.8	←
Maximum inverter voltage	V	650	←
Vehicle			
Curb weight	kg	1860	1735

a)

b)

Fig. 1. Vehicle test conditions using on-board diagnostic system reader designed for analysis of vehicles with hybrid drive systems

4. Research conditions

Analyzes of the vehicle propulsion systems were made using road tests in urban and non-urban areas in and around Warsaw. Using the technique of driving one after another (so-called following the leader) – Figure 2, it was found that both drives have similar parameters. The travel distance was 14.8 km (about 2450 s) in urban driving condi-

a)

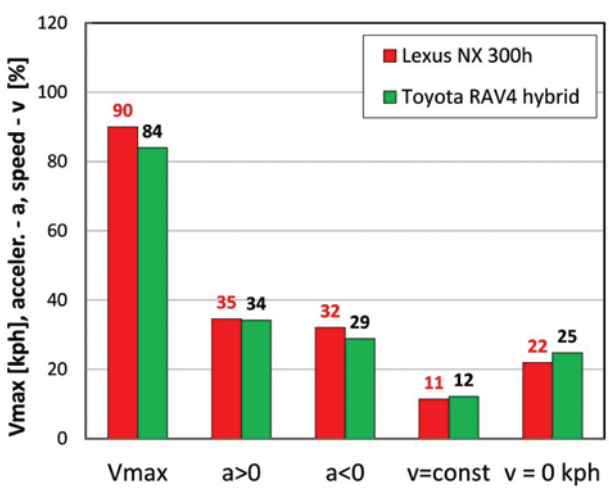

Fig. 2. Tested vehicles speed comparison: a) in urban driving conditions

b)

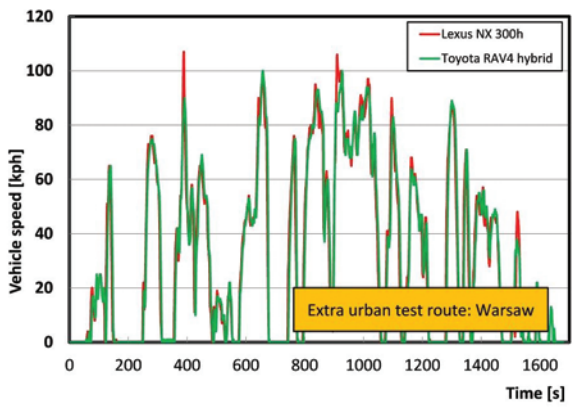

Fig. 2. Tested vehicles speed comparison: b) in non-urban driving conditions

a)

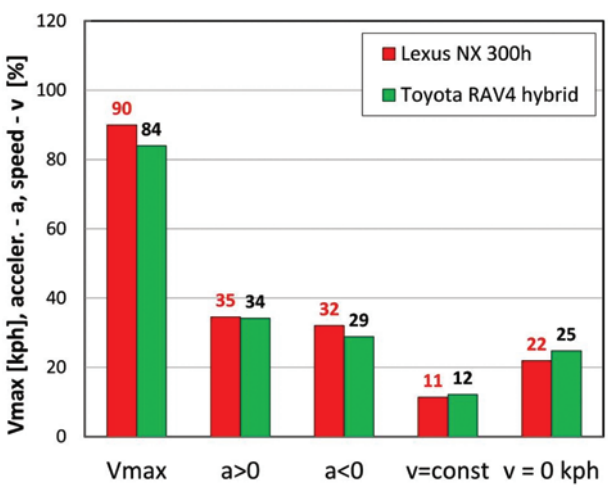

b)

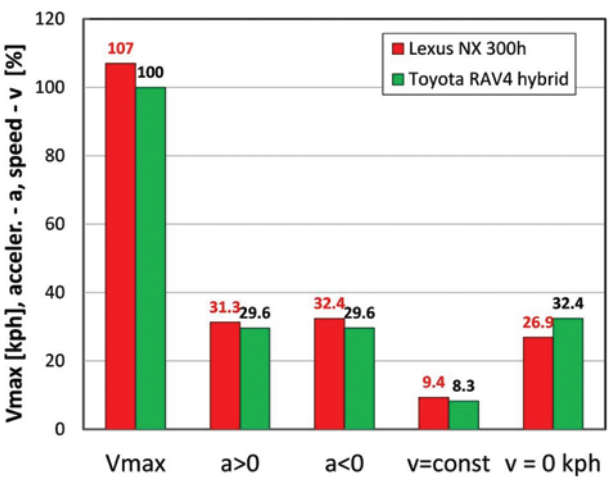

Fig. 3. Characteristic measured values of the test drives: a) in urban driving conditions, b) in non-urban driving conditions

tions and 14.6 km (about 1770 s) in non-urban driving conditions. In the first one the average speed was 24 km/h, while for the second case the speed was 33 km/h.

The similarity of the drives was further confirmed in the analysis of the maximum speed values as well as the time shares of accelerating and driving at constant speed. In urban traffic the maximum speed difference was 7% (Figure 3a). The same difference value was obtained in non-urban traffic (Figure 3b). Relative acceleration time in urban traffic was about 35%, while in non-urban traffic – about 30%. There was about a 5% difference. Relative braking time was about 30% in all test drives. Driving time at a steady speed was short and reached about 10% – slightly longer in urban driving. The drive time share of the vehicle being stationary was 22–25% in urban traffic, and 27–32% in non-urban traffic.

The analysis of these measured parameters allows determining the similarity of the two drives. This is a prerequisite for further analysis and the comparison of the operating conditions of two hybrid drives in urban and non-urban driving conditions. This analysis was carried out in the next chapter.

5. Operation of electric motors at variable voltage conditions

5.1. Comparison of the electric motors operating conditions during vehicle operation

The hybrid vehicles operation analysis was conducted mainly in relation to the electric systems of the vehicle drive. The analysis of the electric motors operation was carried out in the aspect of motor voltage supply intervals. According to the above-mentioned data, higher supply voltage values should be used at high torque values. An analysis of the electric motors performance characteristics of tested vehicles indicates the use of high voltages in the high torque range at medium engine speed (Figure 4 above 600 V). As the engine speed increases, the value of its supply voltage increases. Note that in non-urban driving conditions (higher driving speeds), a wider field of operating point values is used with higher voltages. In urban driving conditions (Figure 4a and 4b), the high density of operating points is visible for tor-

a)

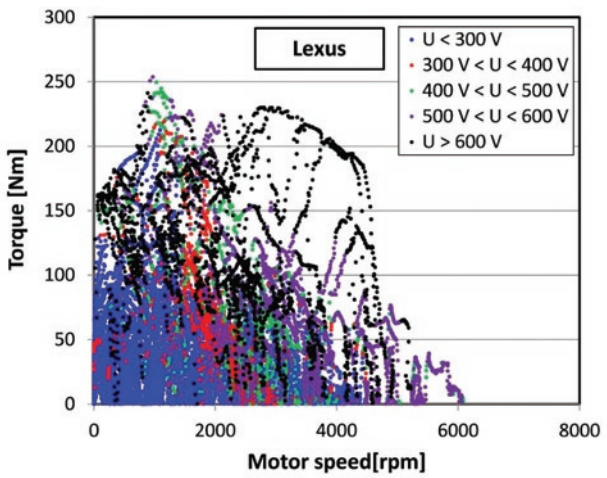

b)

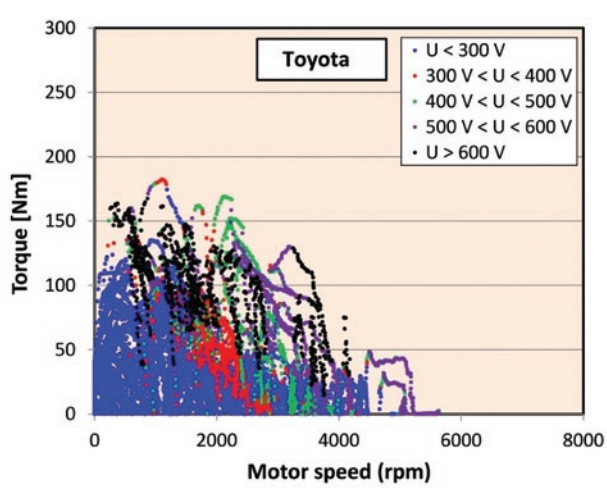

Fig. 4. Electric motors characteristics of the tested vehicles: a–b) in urban driving conditions relative to the supply voltage

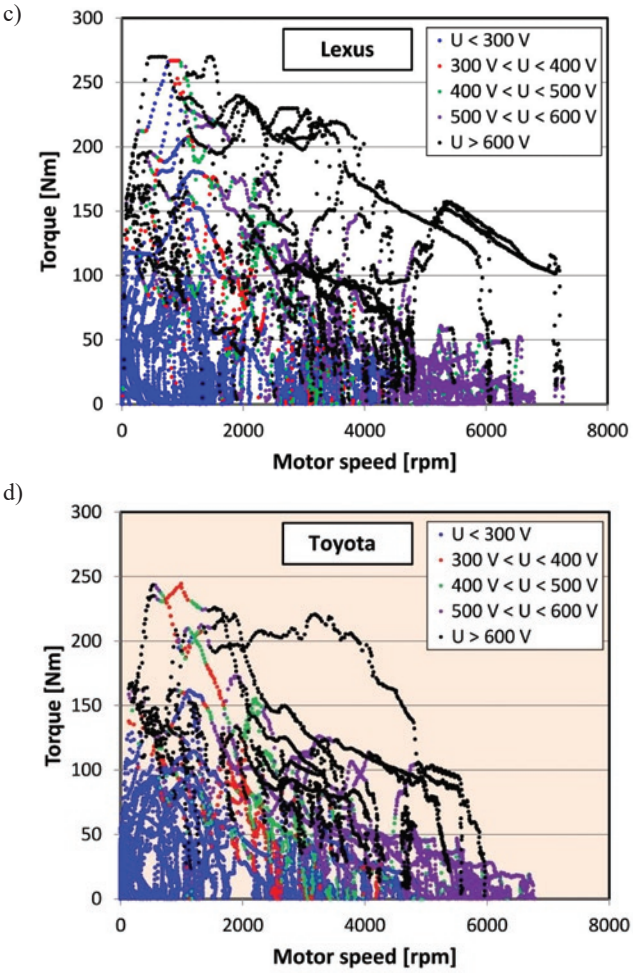

Fig. 4. Electric motors characteristics of the tested vehicles: c–d) in non-urban driving conditions relative to the supply voltage

ques up to 150 Nm and engine speed up to 6000 rpm. Higher values of maximum torque were observed when driving a Lexus car than for the Toyota vehicle. The analysis of this speed characteristic of the electric motor shows that at the given speed it is possible to supply the motor with different voltage values. This voltage increases proportionally to the required torque value. Increasing the supply voltage increases the electric motor power.

The characteristics of the power system means that the vehicle driving speed is proportional to the speed of the motor. It follows that with the driving speed increase in non-urban areas the engine speeds increase as well (Figure 4c and 4d). In non-urban driving conditions the differences in the areas used for the electric motors characteristics show smaller variations than in urban driving. The high torque values in the mean electric motor speed range values lead to the maximum electric motor output power in this range of motor speed. These maximum power values are generated at high voltages. Otherwise, according to the equation Ne = U × I, the powers would be limited (at the same current and a smaller voltage value).

5.2. Electric motors operating conditions comparison during regenerative braking

Recovering energy during braking allows observing the typical conditions of electric voltage change that lead to changes in the energy stored in the high-voltage battery.

The previous section has shown that the maximum values of the electric motor supply voltage occur at their maximum power. The conditions of voltage change during energy recovery are different (Figure 5). During braking, the voltage change from the current gen-

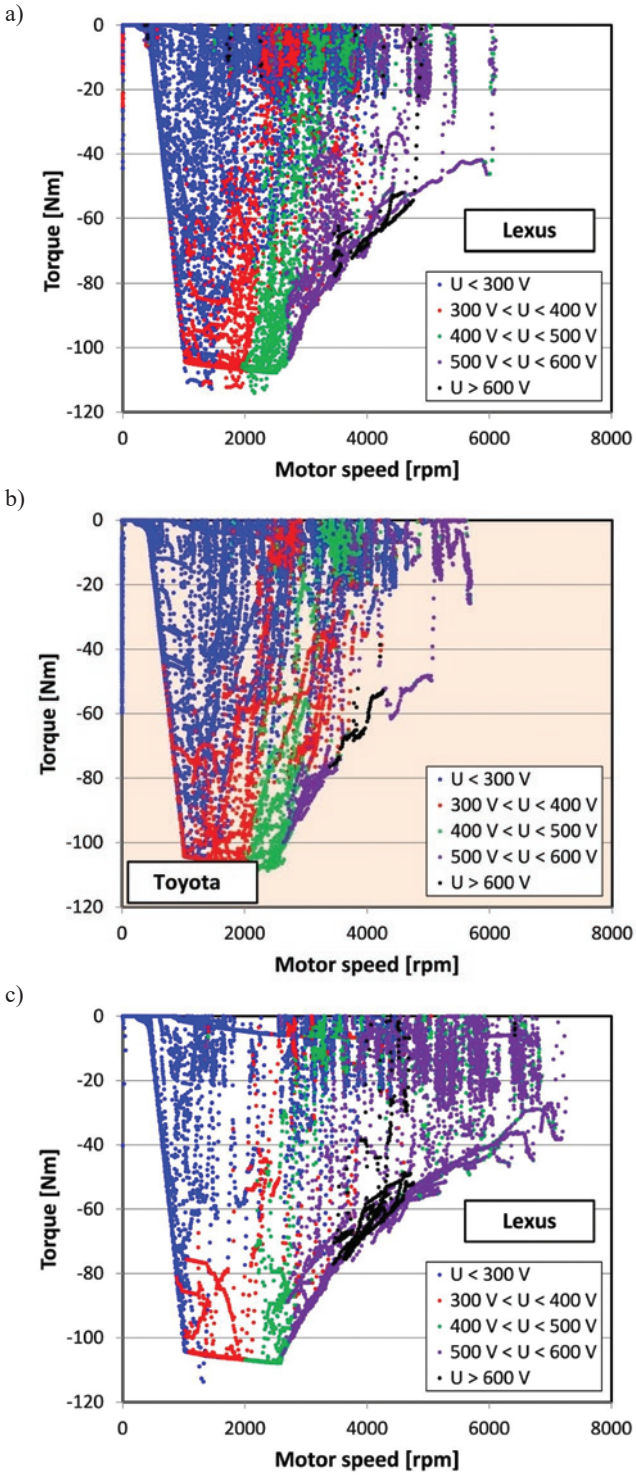

Fig. 5. Electric motor characteristics of the tested vehicles during regenerative braking: a–b) in urban driving conditions, c–d) in non-urban driving conditions relative to the supply voltage

erator is proportional to its rotational speed. High speed values result in the higher voltage values. From the energy recovery characteristic it follows that the generated voltage values depend only on the rotational speed and not on the torque. Such a rule applies when changing the voltage from the battery supply voltage (about 240 volts) to 600 volts. Above this value (600–650 volts) the voltage is only obtained for maximum power range generated during braking. These conditions apply to all test route variants used in the study.

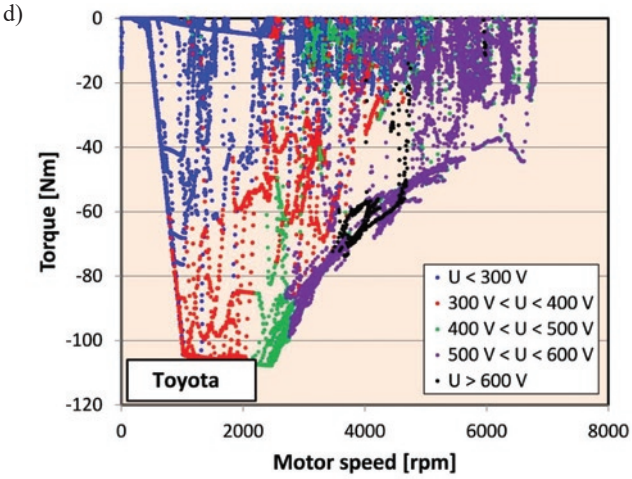

Fig. 5. Electric motor characteristics of the tested vehicles during regenerative braking: d) in non-urban driving conditions relative to the supply voltage

When analyzing the torque value during braking, supplemented by engine rotational speed, it is possible to determine the flow of energy using the equation:

$$E = 2\pi \int_{t=0}^{t=tm} Tndt \tag{1}$$

where: T – braking torque of the electric motor, n – engine speed.

With this equation the energy during regenerative braking was determined along with the voltage generator divisions into intervals. According to Figure 5 and after application of equation (4) it was found that the largest share of regenerative braking in urban areas is at voltage of up to 300 volts. This represents over 40% of the driving time for the Lexus and over 50% of the Toyota test drives (Figure 6a). It is characteristic that the increased voltage in the Lexus vehicle while recovering energy increases further for greater voltages. This is true for both urban and non-urban driving (Figure 6b).

In urban driving conditions the contribution of higher voltages in the overall operating time decreases. The largest share of voltage in non-urban conditions (around 30% of regenerative braking time) is between 500 and 600 V, which can be explained by increased driving speeds and the ability to process higher kinetic energy values into electricity. As shown in Figure 5, this range applies to the highest electric motor speed during regenerative braking.

5.3. Analysis of the energy flow through the battery in vehicle operation

An important aspect of conducting road tests is the initial charge level of high voltage batteries called SOC (state of charge). It indicates the amount of energy stored in the battery at the start of the test – at the same time it gives information on the possibility of using electric motors without having to start the combustion engine.

The SOC value in both urban and non-urban drives in the study was similar, at approximately 45% (Figure 7). Both drives were characterized by a similar energy flow, as the final battery charge in both cases was comparable. In urban driving conditions, it was about 57% for both vehicles (ΔSOC = 12%). While in non-urban driving conditions the value was higher, at 60% (ΔSOC = 15%). This is another confirmation of the comparability of the test drives made by the two vehicles.

The energy flow conditions were also analyzed, these confirm the similarity of energy flow management in both tested vehicles. The value of energy changes is similar, but the final energy stored in the

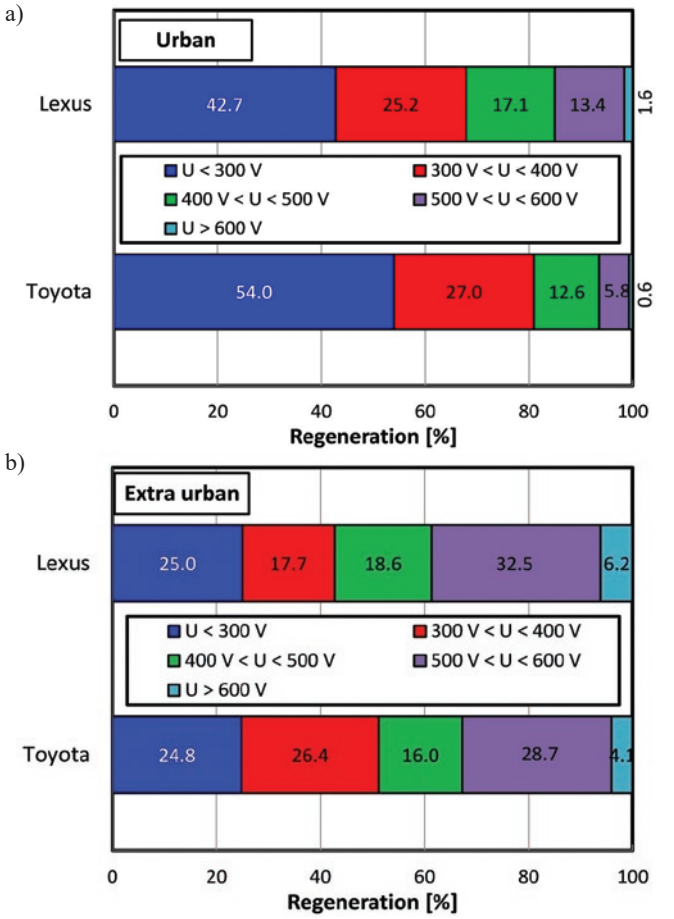

Fig. 6. Analysis of relative energy recovery time shares taking into account the electric generator voltage of the tested vehicles: a) in urban driving conditions, b) in non-urban driving conditions

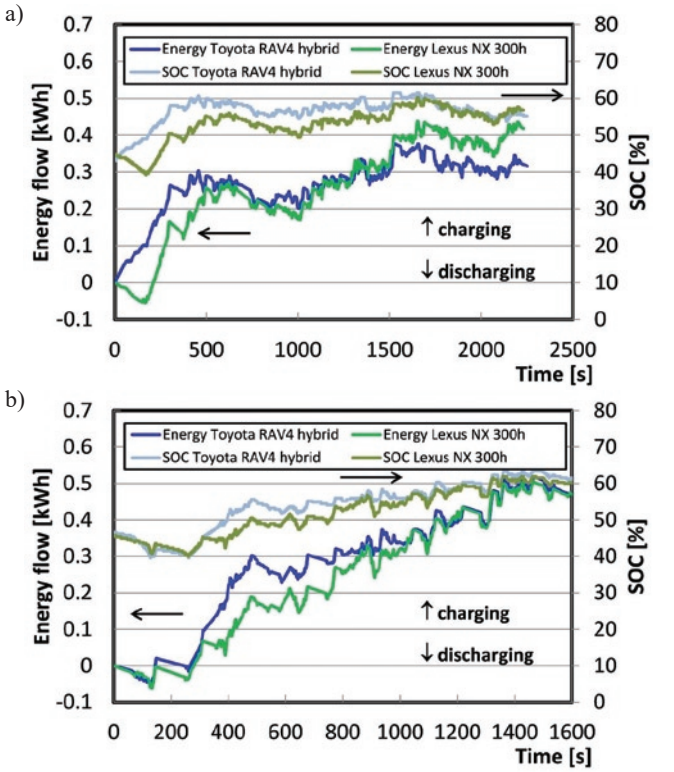

Fig. 7. Analysis of energy flow and battery charge of the vehicles during the drives: a) in urban driving conditions, b) in non-urban driving conditions

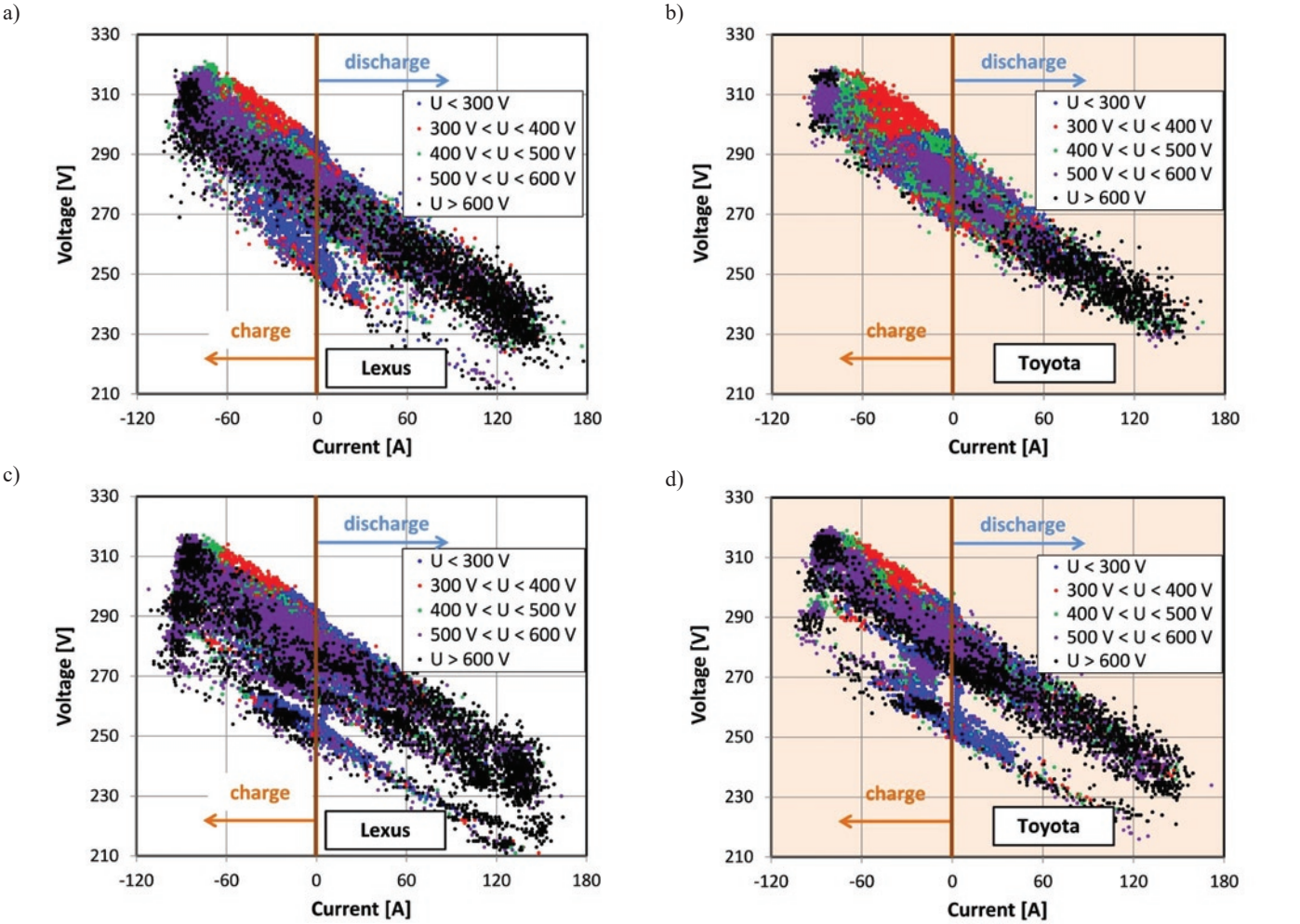

Fig. 8. Charging and discharging voltage characteristics of high-voltage batteries: a–b) in urban driving conditions, c–d) in non-urban driving conditions relative to the supply voltage of the electric motors

battery is greater for the Lexus than for the Toyota. These changes in favor of the Lexus vehicle may result from greater vehicle weight (which is visible in early stages of the drives from the battery discharge rate), but also results in greater braking energy recovery as described by:

$$E = m \int_{t=0}^{t=tm} v dt \tag{2}$$

where the weight of the vehicle affects the value of kinetic energy converted to electricity.

Analysis of SOC changes in urban drive conditions indicates no continuous recharging of the battery to maximum values. At the beginning of the route, after obtaining a SOC of 60%, it is then discharged down to about 50%. Therefore, it has been asserted that the typical SOC values in urban environments oscillates in the range of 50–60%. In non-urban driving conditions, the use of the electric motor's boost mode for the combustion engine is more frequent, indicating a lower battery charge rate. In this case, the battery SOC of 60% was achieved only in the final section of the test drive route, which is typically an urban stretch allowing for increased energy recovery.

4. Analysis of high-voltage battery operation in different driving conditions

Battery performance analysis indicates that higher battery currents and lower voltages relate to battery discharging (Figure 8). Analysis of voltage changes in electric motors during charging and discharging of the battery indicates a certain pattern. The lowest voltage value (less than 300 V) is used at low current flow through the battery. As the current increases, the voltage boost is increased. This is a characteristic feature of these systems, regardless of the direction of current flow (charging or discharging the battery).

5. Energy flow analysis during vehicle operation

The previously analyzed aspects of the eclectic motors and accumulators operating conditions allow making a comparison of the energy flow in hybrid drive systems in road conditions.

The collected measurement data allowed to specify the following phases of energy flow:

- discharge of high-voltage batteries (power drained from the high-voltage battery – IB > 0),
- charging in typical conditions (current flow into the battery IB < 0 and no regenerative braking Th < 0),
- charging with regenerative braking (current flow into the battery IB < 0 and negative torque on motor Th < 0).

These conditions made it possible to determine the energy values of the three vehicle driving modes. The sum of all energy values al-

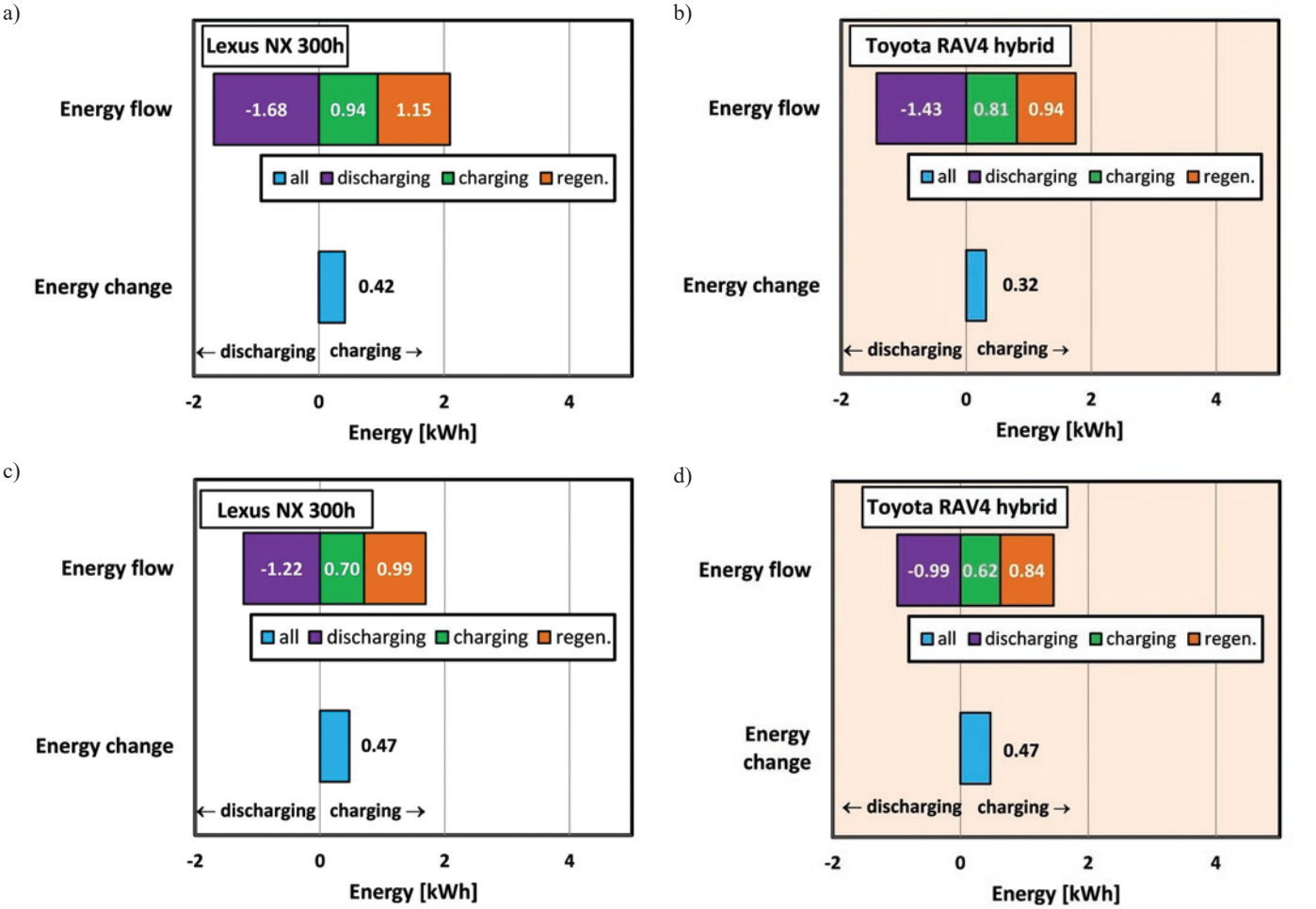

Fig. 9. The energy flow and total change of battery charge analysis during driving: a–b) in urban driving conditions, c–d) in non-urban driving conditions, including charging, high-voltage discharge and regenerative braking

lows to determine the energy changes to the final energy value stored in the battery. In urban driving conditions, the Lexus vehicle (1.68 kWh) had a higher battery discharge rate (15.6%) than in the case of the Toyota (1.43 kWh) battery (Figures 9a and 9b). Similarly, an increased value of recovered energy – 14% higher, was recorded for the same vehicle. Taking into account the battery charging from the internal combustion engine, the battery charge change in the Lexus NX 300h was 0.42 kWh (additional battery charge). In the same urban driving conditions, the change in battery power in Toyota was 0.32 kWh. The 24% greater value of the energy accumulated in the battery is the result of all analyzed values presented above (discharge, charge, regeneration) being higher for the Lexus vehicle.

Non-urban driving analysis shows similar differences in battery discharge – in the Lexus NX 300h this value is 19% higher than for the Toyota RAV4 hybrid (Figure 9c and 9d). Taking into account the fact that the Lexus NX 300h has acquired more energy from battery charging (11%) and energy recovery (5%), the total amount of energy change in batteries was exactly the same (0.47 kWh).

It can thus be stated that in non-urban driving conditions, the amount of extra energy in the battery did not depend on the vehicle type (that is, the weight of the vehicle, since the other parameters are equivalent).

6. Conclusions

An analysis of hybrid vehicles operating conditions leads to the conclusion that their characteristics in urban and non-urban environments are different. This results in different energy flows and the charging and discharging rates of the high-voltage batteries. Detailed conclusions are given below:

- Using this electric motor speed characteristic analysis it can be seen that it is possible to supply the motor with different voltage values at any given rotational speed. This voltage increases with the required torque value. Increasing the supply voltage increases the power of the motor.
- During braking the generator voltage changes in proportion to the rotational speed. High rotational speed results in the highest voltage values. The energy recovery characteristic indicates that the voltage values depend only on the rotational speed and not on the torque.
- Changes in battery charge range vary between 50–60% in the urban driving conditions. In non-urban driving conditions, the electric motor's boost mode is used more, indicating a lower battery charge rate. Battery charge of up to 60% was reached only at the end of the route.
- The battery charge value changes during the test drives are similar, but the final energy accumulated in the battery at the end of the route is greater in the Lexus NX 300h than in the Toyota RAV4 hybrid. These differences in favor of the Lexus vehicle could be caused by different vehicle weights (higher for the Lexus) that affect the amount of kinetic energy converted into electricity.
- The smallest voltage value (less than 300 V) is used at low battery current. As the current increases, the voltage boost is increased. This is a characteristic feature of these systems, re-

gardless of the current flow direction (charging or discharging the battery).

The above studies were carried out with the same level of battery charge in both urban and non-urban drive conditions. The next stage of this research is the operational analysis of such drives with respect to the different initial conditions of stored energy in the batteries of these vehicles. This way the characteristics of these drives should be significantly different.

References

1. Hu X, Jiang J, Egardt B, Cao D. Advanced power-source integration in hybrid electric vehicles: multicriteria optimization approach. IEEE Transactions on Industrial Electronics 2015; 62 (12): 7847–7858, http://dx.doi.org/10.1109/TIE.2015.2463770.
2. Hu X, Moura S J, Murgovski N, Egardt B, Cao D. Integrated optimization of battery sizing, charging, and power management in plug-in hybrid electric vehicles. IEEE Transactions on Control Systems Technology 2016; 24 (3): 1036–1043, http://dx.doi.org/10.1109/TCST.2015.2476799.
3. Kasprzyk L. Modelling and analysis of dynamic states of the lead-acid batteries in electric vehicles. Eksploatacja i Niezawodnosc – Maintenance and Reliability 2017; 19 (2): 229–236, http://dx.doi.org/10.17531/ein.2017.2.10.
4. Li L, Wang X, Xiong R, He K, Li X. AMT downshifting strategy design of HEV during regenerative braking process for energy conservation. Applied Energy 2016; 183: 914–925, http://dx.doi.org/10.1016/j.apenergy.2016.09.031.
5. Merkisz J, Pielecha I. Układy mechaniczne napędu hybrydowego. Wydawnictwo Politechniki Poznańskiej, Poznań 2015.
6. Michel P, Charlet A, Colin G, Chamaillard Y, Bloch G, Nouillant C. Optimizing fuel consumption and pollutant emissions of gasoline-HEV with catalytic converter. Control Engineering Practice 2017; 61: 198–205, http://dx.doi.org/10.1016/j.conengprac.2015.12.010.
7. Navamani J D, Vijayakumar K, Jegatheesan R. Non-isolated high gain DC-DC converter by quadratic boost converter and voltage multiplier cell. Ain Shams Engineering Journal 2016, in press, http://dx.doi.org/10.1016/j.asej.2016.09.007.
8. Pielecha J, Merkisz J, Markowski J, Jasinski R. Analysis of passenger car emission factors in RDE tests. E3S Web of Conferences 10, UNSP 00073 (2016), http://dx.doi.org/10.1051/e3sconf/20161000073.
9. Stroe N, Colin G, Ben-Cherif K, Olaru S, Chamaillard Y. Towards a generic control-oriented model for HEV predictive energy management. IFAC 2016; 49 (11): 259–264, http://dx.doi.org/1.1016/j.ifacol.2016.08.039.
10. Tani A, Camara M B, Dakyo B, Azzouz Y. DC/DC and DC/AC converters control for hybrid electric vehicles energy management-ultracapacitors and fuel cell. IEEE Transactions on Industrial Informatics 2013; 9 (2): 686–696, http://dx.doi.org/10.1109/TII.2012.2225632.
11. Wei Z, Xu J, Halim D. HEV power management control strategy for urban driving. Applied Energy 2017; 194: 705–714, http://dx.doi.org/10.1016/j.apenergy.2016.10.023.
12. Wei Z, Xu Z, Halim D. Study of HEV power management control strategy based on driving pattern recognition. Energy Procedia 2016; 88: 847–853, http://dx.doi.org/10.1016/j.egypro.2016.06.062.
13. Zhu L, Yu F R, Ning B, Tang T. Optimal charging control for plug-in electric vehicles in smart microgrids fueled by renewable energy sources. International Journal of Green Energy 2013; 10 (9): 924–943, http://dx.doi.org/10.1080/15435075.2012.727364.

Ireneusz PIELECHA
Wojciech CIEŚLIK
Institute of Combustion Engines and Transport
Poznan University of Technology
ul. Piotrowo 3, 60-965 Poznań, Poland

Andrzej SZAŁEK
Toyota Motor Poland
ul. Konstruktorska 5, 02-673 Warszawa, Poland

E-mails: Ireneusz.Pielecha@put.poznan.pl,
Wojciech.Cieslik@put.poznan.pl, Andrzej.Szalek@toyota.pl

Article citation info:
VAIČIŪNAS G, BUREIKA G, STEIŠŪNAS S. Research on metal fatigue of rail vehicle wheel considering the wear intensity of rolling surface. Eksploatacja i Niezawodnosc – Maintenance and Reliability 2018; 20 (1): 24–29, http://dx.doi.org/10.17531/ein.2018.1.4.

Gediminas VAIČIŪNAS
Gintautas BUREIKA
Stasys STEIŠŪNAS

RESEARCH ON METAL FATIGUE OF RAIL VEHICLE WHEEL CONSIDERING THE WEAR INTENSITY OF ROLLING SURFACE

BADANIE ZMĘCZENIA METALU KOŁA POJAZDU SZYNOWEGO Z UWZGLĘDNIENIEM INTENSYWNOŚCI ZUŻYCIA POWIERZCHNI TOCZNEJ

The article overviews scientific research studies that examine the interaction between railway vehicle wheel and rail, and the phenomena of wear on wheel rolling surface. Unique experimental research has been conducted, in which regularity of weariness on rolling surface of exploitable locomotive wheel and phenomena of metal fatigue on wheel were researched. A hypothesis is made, that according to the differences in weariness intensity of wheel rolling surface it is possible to determine the start of metal fatigue. The inequality of wear intensity of different locomotive wheels is assessed by the Sharpe ratio, adapting it to describe the wheel wear intensity criteria. Based on the results of research, the authors propose a simplified and reliable methodology for determining metal fatigue on locomotive wheels at initial stages. The uneven wear on rolling surface of different wheels of wheelset inevitably changes the values of Sharpe ratio, which can accurately describe the conditions in which the critical metal fatigue on wheels begins to emerge.

***Keywords**: rail vehicle, wheel-set, wheel rolling surface, wear intensity, metal fatigue, Sharpe ratio.*

W artykule omówiono badania naukowe dotyczące wzajemnych oddziaływań między kołem pojazdu szynowego a szyną oraz zjawiska zużycia powierzchni tocznej kół. Przeprowadzono nowatorskie badania eksperymentalne, w których zbadano prawidłowości dotyczące zużywania się powierzchni tocznej eksploatowanego koła lokomotywy oraz zjawisko zmęczenia metalu koła. Założono hipotezę, że na podstawie różnic w intensywności zużycia powierzchni tocznej kół można określić początek procesu zmęczenia metalu. Różnice w intensywności zużycia różnych kół lokomotywy oceniano na podstawie współczynnika Sharpe'a, dostosowując go do opisu kryteriów intensywności zużycia kół. Na podstawie wyników badań autorzy zaproponowali uproszczoną, rzetelną metodologię określania zmęczenia metalu kół lokomotywy na początkowym etapie tego procesu. Nierównomierne zużycie powierzchni tocznej różnych kół zestawu kołowego zmienia wartości współczynnika Sharpe'a, które można wykorzystać do precyzyjnego opisu warunków, w jakich dochodzi do krytycznego zmęczenia metalu kół.

***Słowa kluczowe**: pojazd szynowy, zestaw kołowy, powierzchnia toczna koła, intensywność zużycia, zmęczenie metalu, współczynnik Sharpe'a*

1. Introduction

One of the most commonly analysed technical issue related to the safety usage of railway vehicle is the interaction between wheel and rail. Rolling stability, train traffic safety and continuity of wagons depend on technical condition of wheelset. During the exploitation of railway vehicles, one of the rolling stability and safety ensuring parameter, which must be constantly monitored and controlled, is the weariness of wheel rolling surface. Two parts in the interaction between railway vehicle wheel and rail wear the most: the rolling surface and the flange. Weariness gets particularly intensive when vehicle is rolling on track curves or railroad switches, when wheel and rail is in contact with both rolling surface and flange. The regularity of weariness on these contacting surfaces are constantly researched by scientists Nielsen [8], Shackleton and Iwnicki [16], Polách [10]. It should be noted that evaluations of scientists are different from the approach carried in practice, which states that the contact between wheel and rail is only in one or two points. Researchers Ren, Iwnicki and Xie [11]examine the regularity of linear and "stepped" load distribution on different wheel/rail contact areas. The same assumption, that the load in the wheel-rail contact is evenly distributed on rail-wheel surface area, is made by scientists Sichani [17] and Nielsen [8]. It should be noted, that scientists in these articles are analysing only vertical forces occurring in wheel-rail interaction. The variation of roughness/unevenness of the rail must be evaluated in order to assess the interaction between wheel and rail more accurately [22].

Exploitation of railway vehicle and intense weariness of wheel rolling surface lead to radical changes in geometrical parameters of the wheel. When the lowest critical values of these parameters are reached, the wheelset rolling imbalance increases due to worse wheel/rail contact conditions and the derailment threat increases [15]. It should be noted that, wheel dimensions are regularly and carefully monitored and registered during the vehicle exploitation [20-21]. A very significant technological dimension is the thickness of wheel flange. When it decreases to a critical value, the threat of wheel derailment increases, so it is important to turn new wheel rolling surface. Another important parameter for locomotives is the thickness of rim. The rim that is too thin heats up and expands considerably, during locomotive's traction or braking, when wheels are towing or sliding on rails. The loose rim skids on wheel disc and the locomotive no longer generates the required traction or braking force. Other critical damages of wheelset wheel are the rolling surface damages, such as cracks, scaling and splits, which are caused by metal fatigue.

The detection of metal fatigue is a particularly challenging task at the initial stage [6].

The condition of vehicle wheel rolling surface (whether there are no rolling surface damages) is controlled by trackside automated control equipment (hereinafter TACE), which determines the values of vertical wheel impact on rail [1, 23]. The devices show the critical values that exceed vertical impact forces, when there are wheel damages. The size of wheel impact force is completely stochastic, so the specialists of railway vehicle exploitation are faced with problems of repeatability and reliability of measuring equipment readings [3, 19]. The problem is that dynamic measuring equipment (TACE) shows different vertical impact forces, after passing with the same damaged wheel through the same rail point.

Another important aspect of interaction between wheel and rail is the provision of wheel's adhesion with rail during the traction for locomotives [7] and braking for the train [2]. The quality adhesion between wheel and rail is significantly dependant on the accuracy of geometrical wheel/rail rolling surface, level of weariness and the contamination of interacting surfaces.

A vertical static load of more than 180 kN is present on one of its wheels while the locomotive is still, and it can grow up to 2-3 times when rolling on rails. In addition, horizontally (longitudinal and transverse) dynamic forces appear on wheel/rail contact, when the vehicle is rolling, due to the wheelset oscillation process and the geometric inequalities of the railway track [14]. Due to these dynamic creepage loads, both the rolling surface of the wheel and the rail surface are heavily worn. It is noteworthy, that wheel metal fatigue appears due the cyclicality of these relative slip loads. The study of Shackleton & Iwnicki [16] is valuable because the authors describe multiple methodologies used for examination of interaction between wheel and rail surfaces, and provide examples of their implementation in different software packages. One of the results of this study is the regularity of the displacement of the wheel / rail contact surface. Wheel - rail interaction is explored similarly in the article by researchers Ferrara, Leonardi & Jourdan [4]. The authors analyse the regularity of the variation of the rail oscillation acceleration. During the exploitation, the major factor, which determines wear in railway vehicle wheel, is the elastic and plastic deformation of the rolling surface. It causes metal fatigue and changes in physical properties. The phenomenon of wheel and rail surface deformation has been thoroughly examined by scientists Sebès, Chevalier, Ayasse & Chollet [12]. This article presents examples of modelling of wheel and rail contact. It should be noted that most of the consequences of the primary metal fatigue (cracks, scaling and splits) is rubbed with pads, when the locomotives are braked by pressing the brake pads against the rolling surface of the wheel. Thus, the effects of fatigue during the exploitation of the vehicle are eliminated or significantly reduced.

In the last century, scientific researches on the development of railway vehicle wear reduction measures and evaluation of their effectiveness have been intensively carried out, which laid the foundations for the breakthrough of modern scientific and technological achievements in this area. From the scientific point of view, researches on individual cases of wheel and rail interaction, for example, in railway switches, are innovative. The interaction between wheel and rail is highly influenced by design of railway switches. The results of such studies are presented in the Pålsson's article [9]. The author proposed a methodology for modelling profile of railway switch cross in order to minimize the dynamic load on the wheel.

The variety and complexity of the factors that cause the fatigue to the vehicle wheel rolling surface listed above, reduce the chances of vehicle exploitation specialist success on determining wheel metal fatigue in the early stages. In solving this problem, the regularity of the wear of the wheel surface was studied in detail, considering metal fatigue phenomena. Different wear in wheels of the same bogie are found between the wheel casts, with the increase in the mileage (periodicity) of the vehicles. This different wheel wear appears not only due to the wear of the rolling surface, but also due to metal fatigue. In this article, the authors analyse the possibilities of applying more abstract interdisciplinary research methods, by using knowledge and methods of related fields of science.

New methods must be applied in order to forecast intensity of wheelset wheel wear and metal fatigue, due to increasingly sophisticated trouble-shooting equipment. During vehicle exploitation, it would be rational to evaluate both the average intensity of wheel wear and the discretion of this wear depending on the location of wheelset in bogie. Such evaluation may be a criterion for the design of a running gear in the future, to ensure the even wear of wheels during exploitation. The problem gets an aspect of comparison of changes in element value (quality). In this article, the authors assume that, it is possible to use methods for comparing change of value (quality) that are used in other fields of science, in order to examine and forecast vehicle wheel wear. The following article describes the adaptation of the Sharpe ratio in order evaluate intensity of rolling surface weariness distribution on different wheels [13]. In this research, the Sharpe ratio is considered as a complex indicator of the technical condition (quality) of wheelsets, adapting it to describe the wear intensity parameters.

2. Methodology for the assessment of wheelset wheel weariness and metal fatigue

One of the most researched and methodically applied qualitative methods in the financial sciences is the evaluation of changes in the investment value (for example, stock portfolio). This qualitative change in value is perceived as the return on investment. Mathematically, both of the processes mentioned above can be examined as identical, just in opposite directions. One of the best-performing indicators that evaluates (compares) the return on investment is Sharpe ratio [5]. The higher the Sharpe ratio is; the sooner the fund compensates for the risks involved [18]. The Sharpe ratio is calculated from the investment return rate minus the risk-free rate of return and dividing the result by the average standard deviation of the investment risk:

$$SR = \frac{R_f - R_n}{\sigma}; \tag{1}$$

where: R_f – the average annual rate of return on the investment fund; R_n – rate of return on risk-free investment; σ – average standard deviation of the average annual rate of return fund.

The risk-free return rate on investment R_f is defined as the average return on investment over a long period (about 10 years). Typically, all of these values are measured in monetary terms, and their ratio in the formula (1) is dimensionless. This is one of the essential features of similarity criteria. Thus, this attribute of the Sharpe ratio allows it to be adapted to control the change of value (quality) in other areas of activity. When solving engineering problems, it is often necessary to compare the changes in technical condition of wearing parts and value (residual resources or other qualitative indicators). When examining the wear of wheelset wheels, it is assumed that weariness of wheel rolling surface reduces the qualitative value of the wheels.

3. Analysis of vehicle wheel weariness and metal fatigue processes

Vehicle wheel weariness can be distinguished in two main directions: wear of rolling surfaces and metal fatigue. Wheel wear researches can be divided in wheel rolling surface weariness and wheel flange weariness.

Fig. 1. Visual attributes of metal fatigue on rolling surface of wheel

The visual attributes of metal fatigue on rolling surface of wheel are shown in Figure 1.

The defective wheel rolling surface is covered with a special high-penetration pigment. If the surface of the wheel is intact, the pigment cleanses away from it, and if it contains cracks, the pigment penetrates into them and does not come off. This can be used to detect cracks that usually occur due to metal fatigue. These defects appear, when the wheel has minor wear and after the wheel surface turning the vehicle has driven through a mileage of 150 – 200 thousand kilometres. Defects are usually overlooked, when wheel surface wears more intensively and after the wheel surface turning the vehicle has driven through a mileage of 100 – 150 thousand kilometres. Metal fatigue layer is cut off from the wheel rolling surface. Therefore, if the wheel reaches such a mileage that metal fatigue appears, this is considered to be a result of proper operating conditions in the aspect of wheel wear. Such defects in locomotive wheels were observed on Lithuanian railways, when the new generation of German locomotives SIEMENS ER20CF were put into operation in 2008 instead of Russian freight locomotives, and travelled a respective mileage. Lithuanian scientists Jastremskas et al describe this more thoroughly in the article (2010). These new generation reliable locomotives do not always reach more than 150,000 kilometres without casting wheels. The wear intensity of wheel surface is determined not only by the quality of the locomotive (wheel slip control system, accuracy of parts, wheel flange lubrication system), but also by other conditions during exploitation (locomotive control quality, railroad curves and switches, working culture). Traction and braking forces determine the wear of wheel rolling surface. These forces depend on the train's acceleration and mass. The wear of the flange forms on the railroad curves and switches. Sometimes the wheel is in contact with the rail by both the rolling surface and the flange. These two surfaces rotate at the same angular speed when the wheel rolls, but the linear speed differs. As a result, inevitably one of them slips (skids) and, of course, gets damage. This process is illustrated in Figure 2.

Rail contact with wheel rolling surface is marked by symbol B and contact with flange is marked by symbol A. β is the angle between wheel-rail rolling surface, a – the distance between points of rail contact with rolling surface and rail contact with flange. In proper vehicle operating conditions, wheel flange does not lean on rail at point A and due to that it does not wear. Two wheels are fastened on the axle, both of which rotate at the same angular speed with the axle. The linear velocity (along the train's direction) of each wheel centre is proportional to the diameter of rolling wheel surface. Wheel usually does not climb on the rail if one of the wheelset wheel is getting closer to the rail and the other one is moving away from it. It starts to roll at a larger diameter of the surface cone and other wheelset wheel – at a smaller diameter. The linear speed of its centre begins to increase as compared to the linear speed of another wheel. The wheelset then turns in the direction of the decelerating wheel. If another wheelset wheel is approaching to the rail, the same happens in the opposite direction. This way the direction of the rolling wheelset on rails is continuously adjusted and the wheelset tilts in the track gauge. This adjustment is called wheelset oscillation.

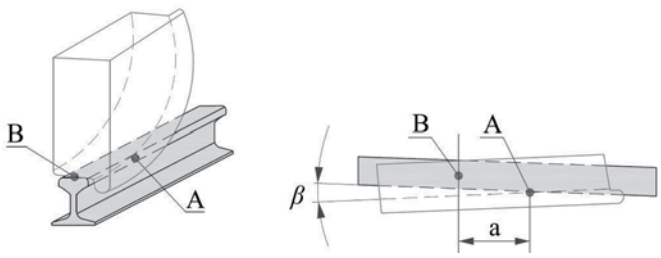

Fig. 2. Rail in contact with wheel rolling surface and flange

Due to the oscillation phenomena, longitudinal and transverse forces of relative slip arise between wheel and rail. These cyclic nature forces cause metal fatigue in contacting surfaces. In straight railway track, oscillation is approximately symmetrical, in the curved track – the required ratio of rolling wheel diameters is adjusted. Due to this phenomenon, the wheel does not lean on the rail with the flange. However, if the wheel systematically leans on the rail with the flange (and therefore flange wears), this is considered that the exploitation is not completely normal. It is true that this happens in some of the more primitive structures or lower production culture vehicles. The wheel flange on modern and properly operated locomotives is only a fuse for special occasions for example, when curve radii are smaller than foreseen or when traveling through railroad switches. For such cases, a flange lubrication system is also provided. As a result, the wear is systematically found in the rolling surface of the wheel, but not in the wheel flange. During exploitation, it is noticeable that the weariness on rolling surfaces of the wheels on the same locomotive varies. The difference in intensity of rolling surface wear in different wheelset wheels was researched in Lithuanian railways. Four SIEMENS "ER20CF" freight locomotives were used for the research. The main technical data of the mentioned locomotives is given in Table 1.

Table 1. The main technical data of the SIEMENS "ER20CF" diesel locomotive (http://www.siemens.fi/pool/lithuania)

Parameter	Parameter value
Wheel arrangement	Co'Co'
Track gauge, mm	1520
Weight, kN (tf)	1354 (138)
Axle load, kN (tf)	225 (23)
Length over couples, mm	22850
Wheel diameter (new / worn), mm	1100 / 1020
Maximum speed, km/h	120
Diesel engine power, kW	2000
Power at the wheel rim., kW	1600
Starting tractive effort, kN	450
Electric braking power, kW	1600 kW / with self-loading capability
Ambient temperature range, ° C	from –34 up to +40

Locomotive *SIEMENS "ER20CF"* has two bogies, each of which has three driven wheelsets. The numeration of wheelsets starts from the beginning of the locomotive. During this study, weariness of the vehicle wheelset wheel's rolling surface has been periodically meas-

ured. Changes of wheelset wheel wear measured are different mileages are shown in Figure 3.

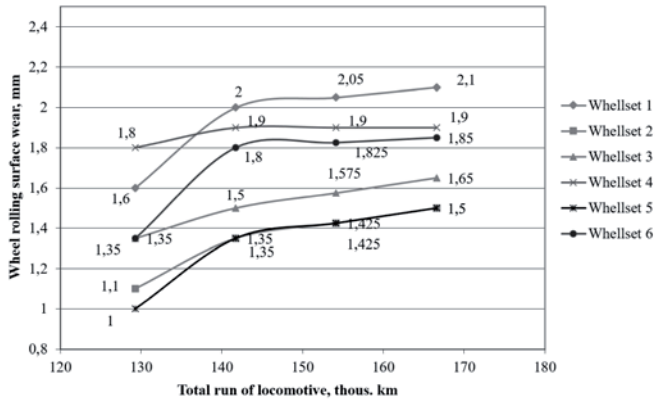

Fig. 3. Wheel rolling surface wear of different wheelset wheels

The wear of each locomotive wheel is measured three times (in different locations, every 120°) and the average for both wheelset wheels is calculated. From Figure 3 it can be seen that 1st, 3rd, 4th, 6th wheelset wheel rolling surfaces are getting the most weariness and the middle wheelsets of the bogie 2nd, 5th - wear the least. This happens, because the wheelsets of triaxle bogies, which are located on the edges (1st, 3rd, 4th and 6th wheelsets) get the most load, when rolling into track curves, railway switches and when braking.

4. Applying the sharpe ratio to forecast metal fatigue

To use the Sharpe ratio for assessment of wear unevenness on locomotive wheel rolling surface, the following measures for evaluation of wear are taken into account instead of normal structure of the formula (1):

$$SR_i^w = \frac{W_i - \overline{W}}{\sigma_w}; \qquad (2)$$

where: SR_i^w – Sharpe ratio, used to evaluate the intensity of wear on wheel of *i*-th wheelset; W_i –average of wear on wheel of *i*-th wheelset, mm; $\overline{W}$ – average wear of locomotive wheels, mm; σ_w – average standard deviation of wear on locomotive wheel rolling surface.

After evaluation of wheel wear intensity data of four Siemens "ER20CF" locomotives obtained over mileage of 165 thousand kilometres and by using the same data, which has been used in *Figure 3*, the Sharpe ratio distribution on wheelset diagram has been created

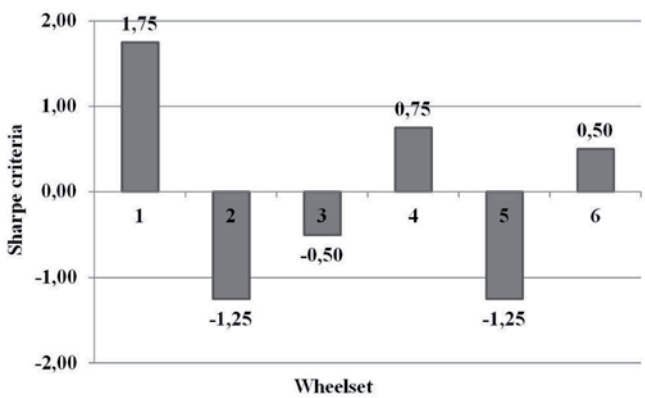

Fig. 4. Evaluation of weariness on the wheel rolling surface using the Sharpe ratio

(the wheelsets are numbered from the front of locomotive). The diagram is shown in Figure 4.

Results of analysis, obtained by using different methods, but using the same data, are provided in Figure 3 and Figure 4. Results of regression analysis presented in Figure 3 reflect the general tendencies of weariness of locomotive wheel rolling surface. The differences in the intensity of wear on the locomotive wheels are shown in Figure 4, in 165 thousand kilometres within the mileage range, which means that Sharpe ratio highlights the level of wear on the wheel rolling surface. Sharpe ratio value that is greater than 1.0 or less than -1.0 indicates that the difference between the average wear W_i on wheel rolling surface of *i*-th wheelset and average wear $\overline{W}$ on locomotive wheels, exceeds the standard deviation σ_w. The diagrams in Figure 3 show that the wear on the surface of the locomotive wheels is not equal throughout the mileage interval. It is noteworthy that when the mileage is 140 thousand kilometres this intensity lowers. This means that the intensity of the wear of the different axle wheels should be compared in different mileage intervals. Based on data in Figure 3, it is convenient to distinguish these mileage intervals: 0–130, 130-140, 140-150 and 150-160 thousand kilometres. Sharpe ratio for these mileage intervals is shown in Figure 5. The end of interval is shown

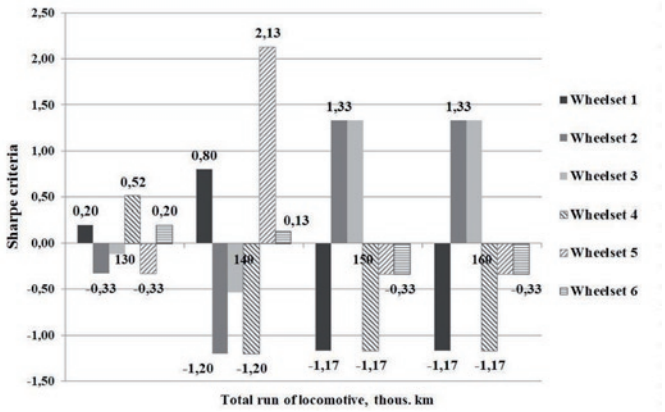

Fig. 5. Assessment of difference in wear of wheel rolling surface in mileage interval, by using Sharpe ratio

on abscissa axis for example: 130 means mileage interval from 0 to 130 thousand kilometres.

After looking at data in Figure 3, it was expected that the indicators of wheel wear may change after a mileage of 130 thousand kilometres. From the data of Figure 5, it is necessary to realize that the changes of distribution of wear intensity between different wheelset wheels is as important as changes in average wear intensity. Differences in wear, which are significantly (up to 2 times) greater than the average deviation of wear intensity at the mileage interval, emerge after 130 thousand kilometres of mileage. This is indicated by the value of the Sharpe ratio in Figure 5. The increased values of Sharpe ratio determine the mileage in which metal fatigue in rolling surface begins to appear.

From the described facts, it is reasonable to raise the hypothesis that by the values of Sharpe ratio it is possible to determine the possible start of metal fatigue in wheel rolling surface. The intensity on wheel wear, the size of the wear and the regularity of the wear dependence on the mileage may vary, depending on the exploitation conditions of vehicle. The wear of wheels (the size of wheel wear per unit of mileage) is determined by the railway track curves, pulled train weight, the vibrations and accelerations of the vehicle elements, the braking intensity and the climatic conditions. The authors of the study suggest that regardless of the impact of exploitation on locomotive wheel parameters, it is possible to determine the

start of metal fatigue on the rolling surface of a locomotive based on the Sharpe ratio values.

5. Conclusions

1. A large number of scientific publications that examine the interaction between the railway vehicle wheel and rail do not eliminate the large gap between theoretical research and the objectives of practical research. It is necessary to more effectively apply results of theoretical research in order to solve relevant exploitation problems of railway vehicle, such as forecasting the metal fatigue on railway vehicle wheels by using the simplified method.
2. Problem of vehicle wheel flange wear is significantly reduced by using vehicle wheel flange lubrication systems, compared to the problem of wheel rolling surface wear and metal fatigue. Currently, one of the most pressing problems is the metal fatigue on the rolling surface of the wheel and its timely detection.
3. It is easy to calculate the uneven wheel wear on different wheels by using the dimensions (wear data) of railway vehicle wheel rolling surface during exploitation. According to the critical values of this dimension, the initial formation of metal fatigue on rolling surface of the wheel can be determined. Thus, by the values of Sharpe ratio it is possible to determine the possible start of metal fatigue in locomotive wheel rolling surface.
4. The probability of fatigue on wheel rolling surface appears when deviations in wear intensity of wheel rolling surface are significantly larger or smaller than average deviation of wear intensity of bogie wheelset wheels.
5. The results of experimental research carried out by the authors show that the signs of primary metal fatigue on the rolling wheel surface appear when the values of the Sharpe ratio calculated for the bogie wheelset wheels are greater than 1.0 or less than minus 1.0.

References

1. Bogdevičius M, Žygienė R, Bureika G, Dailydka S. An analytical mathematical method for calculation of the dynamic wheel–rail impact force caused by wheel flat. Vehicle system dynamics 2016; 54 (5): 689-705, https://doi.org/10.1080/00423114.2016.1153114.
2. Bureika G. A mathematical model of train continuous motion uphill. Transport 2008; 23 (2): 135-137, https://doi.org/10.3846/1648-4142.2008.23.135-137.
3. Bureika G, Levinzon M.; Dailydka S, Steišūnas S, Žygienė R. Evaluation criteria of wheel/rail interaction measurement results by track-side control equipment. Int. J. Heavy Vehicle Systems 2017.
4. Ferrara R, Leonardi G, Jourdan F. 2013. A contact-area model for railpads connections in 2-D simulations: sensitivity analysis of train-induced vibrations. Vehicle System Dynamics, 51 (9): 1342-1362, https://doi.org/10.1080/00423114.2013.801996.
5. Israelsen C. A refinement to the Sharpe ratio and information ratio. Journal of Asset Management 2005; 5 (6): 423-427, https://doi.org/10.1057/palgrave.jam.2240158.
6. Jastremskas V, Vaičiūnas, G, Černašėjus O, Rudzinskas V. Investigation into the mechanical properties and metal creaks of a diesel locomotive wheel. Transport 2010; 3: 287-292, https://doi.org/10.3846/transport.2010.35.
7. Liudvinavičius L, Bureika G. Theoretical and practical perspectives of diesel locomotive with DC traction motors wheel-sets' slipping and sliding control. Transport 2011; 26, (4): 335-343, https://doi.org/10.3846/16484142.2011.633339.
8. Nielsen J C O. High–frequency vertical wheel–rail contact forces—Validation of a prediction model by field testing. Wear 2008; 265: 1465–1471, https://doi.org/10.1016/j.wear.2008.02.038.
9. Pålsson B A. Optimisation of railway crossing geometry considering a representative set of wheel profiles. Vehicle System Dynamics 2015; 53 (2): 274-301, https://doi.org/10.1080/00423114.2014.998242.
10. Polách O. Optimierung moderner Lok-Drehgestelle durch fahrzeugdynamische Systemanalyse, EI-Eisenbahningenieur 2002; 53 (7): 50–57.
11. Ren Z, Iwnicki S D, Xie G. A new method for determining wheel–rail multi-point contact. Vehicle System Dynamics 2011; 49 (10): 1533-1551, https://doi.org/10.1080/00423114.2010.539237.
12. Sebès M, Chevalier L, Ayasse J-B, Chollet H. A fast-simplified wheel –rail contact model consistent with perfect plastic materials. Vehicle System Dynamics 2012; 50 (9): 1453-1471, https://doi.org/10.1080/00423114.2012.669483.
13. Sharpe F W. Mutual funds' performance. Journal of Business 1966; 39 (1): 119−138, https://doi.org/10.1086/294846.
14. Shabana A A, El–Ghandour A I, Zaazaa K E. Study of the effect of the spiral geometry on wheel/rail contact forces. Journal of Multi–body Dynamics 2011; 225 (2): 111–125, https://doi.org/10.1177/1464419311406626.
15. Shabana A A, Rathod C. Geometric coupling in the wheel/rail contact formulations: a comparative study. Journal of Multi–body Dynamics 2007; 221 (2): 147–160, https://doi.org/10.1243/14644193JMBD103.
16. Shackleton P, Iwnicki, S. Comparison of wheel–rail contact codes for railway vehicle simulation: an introduction to the Manchester Contact Benchmark and initial results Vehicle System Dynamics 2008; 46 (1-2): 129-149, https://doi.org/10.1080/00423110701790749.
17. Sichani M Sh, Enblom R, Berg M. A novel method to model wheel–rail normal contact in vehicle dynamics simulation. Vehicle System Dynamics 2014; 52 (12): 1752-1764, https://doi.org/10.1080/00423114.2014.961932.
18. Stankevičienė J, Mencaitė E. The evaluation of bank performance using a multicriteria decision making model: a case study on Lithuanian commercial banks. Technological and economic development of economy 2012; 18 (1): 189-205, https://doi.org/10.3846/20294913.2012.668373.
19. Steišūnas S. Research on dynamics processes of wagon wheelsets with flat impact on rail. Doctoral dissertation. Vilnius: Technika, 2017.
20. Vaičiūnas G, Bureika G. Approach modelling of constant inter-failure process of renewal multi-unit fleet. Eksploatacja i Niezawodnosc – Maintenance and Reliability 2014; 16 (3): 415-421.
21. Vaičiūnas G, Lingaitis L P, Mikaliūnas Š. Determining major factors causing the wear of wheelset tyres. Solid State Phenomena: Mechatronic Systems and Materials: a collection of papers from the 1st international conference MSM 2005. Uetikon-Zurich: Trans Tech Publications, 2006, https://doi.org/10.4028/3-908451-21-3.425.
22. Xie G, Iwnicki S. Simulation of wear on a rough rail using a time-domain wheel–track interaction model. Wear 2008; 265 (11–12):1572-1583, https://doi.org/10.1016/j.wear.2008.03.016.

23. Žygienė R. Research on the dynamic processes of the interaction between the damaged wheels of railway vehicle and rails. Doctoral dissertation. Vilnius: Technika, 2015.

Gediminas VAIČIŪNAS
Stasys STEIŠŪNAS
Department of Mobile Machinery and Railway Transport
Vilnius Gediminas Technical University
Plytinės g. 27, LT-10105, Vilnius, Lithuania

Gintautas BUREIKA
Competence Centre of Transport and Logistics
Vilnius Gediminas Technical University
Saulėtekio al. 11, LT-10223 Vilnius, Lithuania

E-mails: gediminas.vaiciunas@vgtu.lt, stasys.steisunas@vgtu.lt, gintautas.bureika@vgtu.lt

Article citation info:
KAJZER W, JAWORSKA J, JELONEK K, SZEWCZENKO J, KAJZER A, NOWIŃSKA K, HERCOG A, KACZMAREK M, KASPERCZYK J. Corrosion resistance of Ti6Al4V alloy coated with caprolactone-based biodegradable polymeric coatings. Eksploatacja i Niezawodnosc – Maintenance and Reliability 2018; 20 (1): 30–38, http://dx.doi.org/10.17531/ein.2018.1.5.

Wojciech KAJZER
Joanna JAWORSKA
Katarzyna JELONEK
Janusz SZEWCZENKO
Anita KAJZER
Katarzyna NOWIŃSKA
Anna HERCOG
Marcin KACZMAREK
Janusz KASPERCZYK

CORROSION RESISTANCE OF Ti6AL4V ALLOY COATED WITH CAPROLACTONE-BASED BIODEGRADABLE POLYMERIC COATINGS

ODPORNOŚĆ KOROZYJNA STOPU Ti6AL4V POKRYTEGO BIODEGRADOWALNYMI POWŁOKAMI POLIMEROWYMI NA BAZIE KAPROLAKTONU*

The aim of this study was to determine the influence of long-term exposure of Ringer's solution on degradation of the anodically oxidated Ti6Al4V alloy coated with a biodegradable polymer coating. Polymeric coatings made of poly(glycolide-ε-caprolactone) – G-Cap and poly(glycolide- ε-caprolactone-lactide) – G-Cap-L were applied by a dip-coating method. Degradation was assessed on the basis of the results of pitting corrosion resistance and density of metal ions infiltrating to the solution. Studies were conducted for samples after 3, 6, 8, 10 and 12 weeks of exposure to the corrosive environment. In addition, topography of the surface of the polymer coating was assessed. As a result of potentiodynamic studies, the value of the polarization resistance and corrosion potential for the G-Cap and G-Cap-L coated samples were significantly decreased while simultaneous reduction of the density of metal ions infiltrating to the solution throughout the whole study period. There was also observed a faster degradation of the G-Cap coating compared to G-Cap-L, which showed local discontinuity after 12 weeks of exposure. The obtained results provide the basis for the development of polymeric coatings on surface of metal implants with predictable time / kinetics of degradation by selecting the composition of polymers while simultaneous limitation of metal ions infiltration into surrounding tissues.

***Keywords**: corrosion resistance, metal biomaterials, Ti6Al4V alloy, biodegradable polymeric coatings.*

Celem pracy było określenie wpływu długotrwałego oddziaływania rozworu Ringera na proces degradacji utlenianego anodowo stopu Ti6Al4V pokrytego powłoką biodegradowalnego polimeru. Powłoki polimerowe wykonane z poli(glikolido- ε-kaprolaktonu) – G-Cap oraz poli(glikolido ε-kaprolaktono- laktydu) – G-Cap-L naniesiono metodą zanurzeniową (dip-coating). Proces degradacji w funkcji czasu oceniano na podstawie wyników badań odporności na korozję wżerową oraz gęstości masy jonów metalowych przenikających do roztworu. Badania przeprowadzono dla próbek po 3, 6, 8, 10 i 12 tygodniach ekspozycji na środowisko korozyjne. Ponadto oceniano topografię powierzchni powłoki polimerowej. W wyniku przeprowadzonych badań potencjodynamicznych stwierdzono wyraźne obniżenie wartości oporu polaryzacyjnego i potencjału korozyjnego dla próbek z naniesionymi powłokami G-Cap i G-Cap-L przy jednoczesnym wyraźnym ograniczeniu gęstości jonów metalowych przenikających do roztworu w całym okresie badawczym. Stwierdzono również szybszą degradację powłoki typu G-Cap w porównaniu do G-Cap-L, dla której po 12 tygodniu ekspozycji stwierdzono lokalnie występujące przerwania ciągłości. Uzyskane wyniki dają podstawę do opracowywania na powierzchni implantów metalowych powłok polimerowych o przewidywalnym czasie/określonej kinetyce degradacji, poprzez dobór składu polimerów z jednoczesnym ograniczeniem możliwości przenikania jonów metalowych do otaczających tkanek.

***Słowa kluczowe**: odporność korozyjna, biomateriały metalowe, stop Ti6Al4V, biodegradowalne powłoki polimerowe.*

1. Introduction

The use of polymeric biomaterials, which are the subject of continuous, intensive research, is still widening. This is because of their good functionality and biocompatibility in the tissue environment. In particular, the large interest of researchers is focused on a group of synthetic bioresorbable polymers such as polylactide (PLA), poly (ε-caprolactone) (PCL), polyglycolide (PGA), etc. [6, 9, 10, 17]. The wide range of applications of bioresorbable polymers in medicine is primarily concerned with the possibility of shaping their mechanical and physicochemical properties. Controlled degradation of polymers allows them to be used as carriers of drug substances to provide drug dosing with the desired kinetics until the desired therapeutic effect is

(*) Tekst artykułu w polskiej wersji językowej dostępny w elektronicznym wydaniu kwartalnika na stronie ***www.ein.org.pl***

reached [14]. These polymers have a confirmed biocompatibility [17] and their final degradation products in the form of lactic, glycolic and hydroxyhexanoic acids are inert to the body and metabolized in the Krebs cycle [16].

The main limitation associated with the use of biodegradable polymers in medicine is related to the changing mechanical properties. This feature in some applications, for example, orthopedic implants for traumatic surgery may be unfavorable. In the absence of positive effects of treatment, the impaired implant ceases to function as a stabilizer. This may lead to a renewal of the injury. This will result in the need for a revision operation involving the removal of a fully degraded, mechanically impaired implant and replacing it with a new one. Revision check due to the progressive degradation of polymeric material may involve severe complications leading to much more traumatisation of the surrounding tissue compared to the original implantation procedure. Therefore, despite continuous development of material engineering, resulting in the development of a variety of biomaterials, metal materials in many applications are still the dominant group.

Their universality is the result of many years of clinical experience and low cost of use. Because of its good and long-lasting mechanical properties, they allow long-term support and stabilization of implantation areas. However, metal biomaterials are characterized by limited biocompatibility in the human body. When subjected to synergistic influence of corrosive environments and mechanical factors they degrade [8, 13]. Among the wide range of metal biomaterials, titanium alloys are becoming increasingly popular. In particular Ti6Al4V ELI alloy is widely used for manufacturing of orthopedic prostheses. It exhibits good mechanical properties adapted to carry static and dynamic loads, high biocompatibility and corrosion resistance in the tissue environment. However, as a base material for endoprostheses and medical implants, it often causes allergic reactions due to the presence of vanadium, aluminum, and, less frequently, titanium [15, 20]. Therefore, in order to improve the biocompatibility of Ti alloys, a Ti6Al7Nb alloy was developed. By replacing the toxic vanadium with the inert niobium, the corrosion resistance and biocompatibility of the degradation products have been increased. However, the toxic / allergic effects of aluminium and titanium remain unresolved. Hence, the basic direction of research currently being developed is to modify the surface layer of Ti6Al4V alloy or apply coatings so that it is characterized by greater biocompatibility [20]. A common method of modifying the surface of titanium alloys is anodic oxidation. Interesting results were obtained by applying sol-gel and ALD coatings on titanium alloys [1, 2, 12, 15, 19]. However, despite numerous studies, the problem of harmful effects of metal biomaterial degradation products is still not fully resolved.

Therefore, the use of biodegradable polymeric coatings is an interesting way to modify the surface of metal implants to ensure the correct course of treatment. The metal substrate will ensure the mechanical stability of the treated tissue structures throughout the treatment period. The polymer coating, on the other hand, will be a barrier to the degradation of the metal biomaterial. In addition, it can support the process of treatment through local, controlled release of active substances. Local delivery of therapeutic substances will contribute to its effectiveness, while limiting the amount of while limiting the amount of used active substances compared to conventional pharmacotherapies [14, 19].

In the previous studies the influence of polymeric coatings on the corrosion resistance of metal substrates was mainly analyzed on coatings made of non-biodegradable polymers [3, 4, 5]. There are few reports on the influence of biodegradable coatings on the corrosion resistance of metal substrates [11, 18, 19].

Therefore, the principal aim of the work was to determine the influence of polymer coatings on the corrosion resistance of Ti6Al4V ELI alloy. Long-lasting exposure of titanium alloy with the polymer coatings made of poly(glycolide-ε-caprolactone) and poly (glycolide-ε-caprolactone-lactide) in Ringer's solution was analyzed. In addition, the barrier properties of polymer coatings were evaluated based on the corrosion resistance of the metal substrate and the density of metal ions infiltrating to the solution. Based on microscopic observations, the polymer coating degradation process was evaluated as a function of time of exposure to the corrosive solution.

2. Material and methods

2.1. Material

Ti6Al4V ELI alloy samples were taken from a rod of 6 mm in diameter with chemical composition, structure and mechanical properties in accordance with ISO5832-3 [7]. The surface of the samples was subjected to modifications. They included grinding on 120 grit sandpaper and anodic oxidation. The anodic oxidation was performed in a bath containing phosphoric and sulfuric acid (Titan Color by Poligrat) at room temperature for 2 minutes at 97 V. The surfaces of the modified samples were characterized by a surface roughness Ra = 0.65±0.05 μm. Alloy samples were coated with biodegradable poly(glycolide-ε-caprolactone) (G-Cap) copolymer with comonomer ratio of 10:90 or poly (glycolide-ε-caprolactone-lactide) (G-Cap-L) 10:15:75. In both cases a bactericidal substance, ciprofloxacin, was placed in the polymer matrix. Biodegradable G-Cap and G-Cap-L polymers releasing ciprofloxacin were synthesized in the Center of Polymer and Carbon Materials of the Polish Academy of Sciences in Zabrze. Polymers were obtained by ring opening polymerization using non-toxic coordination initiator zirconium acetylacetonate $Zr(acac)_4$ [6, 23]. Biodegradable polymeric coatings of G-Cap and G-Cap-L type were applied to metal implants by dip coating. In the first stage, the copolymers were dissolved in methylene chloride (1% by weight of polymer). Ciprofloxacin (10% by weight relative to the polymer) was added to the solution and thoroughly mixed. In such prepared solution, the sample was immersed using Dip Coater PTL-OV6P, MTI CORPORATION (immersion rate: 1500 mm / min, immersion time: 30 s, 1 dipping cycle). The implants with biodegradable coatings were dried in air for 48 h and then 72 h under vacuum.

2.2. Potentiodynamic studies

Pitting corrosion resistance studies were performed by potentiodynamic method in the Ringer's solution at T = 37°C. The tests were performed using the VoltaLab PGP201 potentiometer, the reference electrode was a saturated calomel electrode (SCE), an auxiliary electrode was the platinum wire. Corrosion studies were started with the determination of the E_{OCP} open circuit potential in currentless conditions for 2h. Polarization curves were recorded from $E_{start} = E_{OCP} - 100$ mV. The potential rate was equal to 3 mV/s. After reaching the anode current density of 1 mA/cm^2 or the potential of 4000 mV, the direction of polarization was changed. Based on the obtained curves using the Stern method, the values of the corrosion potential E_{corr} and the polarisation resistance R_p were determined.

2.3. Study of metal ions release

Concentrations of metal ions releasing into the solution were tested using a Yobin-Yvon JY 2000 spectrometer using the Inductively Coupled Plasma – Atomic Emission Spectrometry (ICP-AES) method.

Corrosion resistance and metal ion release tests were carried out on the samples at the initial state, and with the polymer coatings, both non-exposed and exposed to the Ringer's solution (pH = 7,0±0,2) for 3, 6, 8, 10 and 12 weeks. During the exposure, the samples were kept in the heating chamber Binder FD 115 at T = 37°C. The mass concentration of metal ions releasing into the solution was converted to mass density.

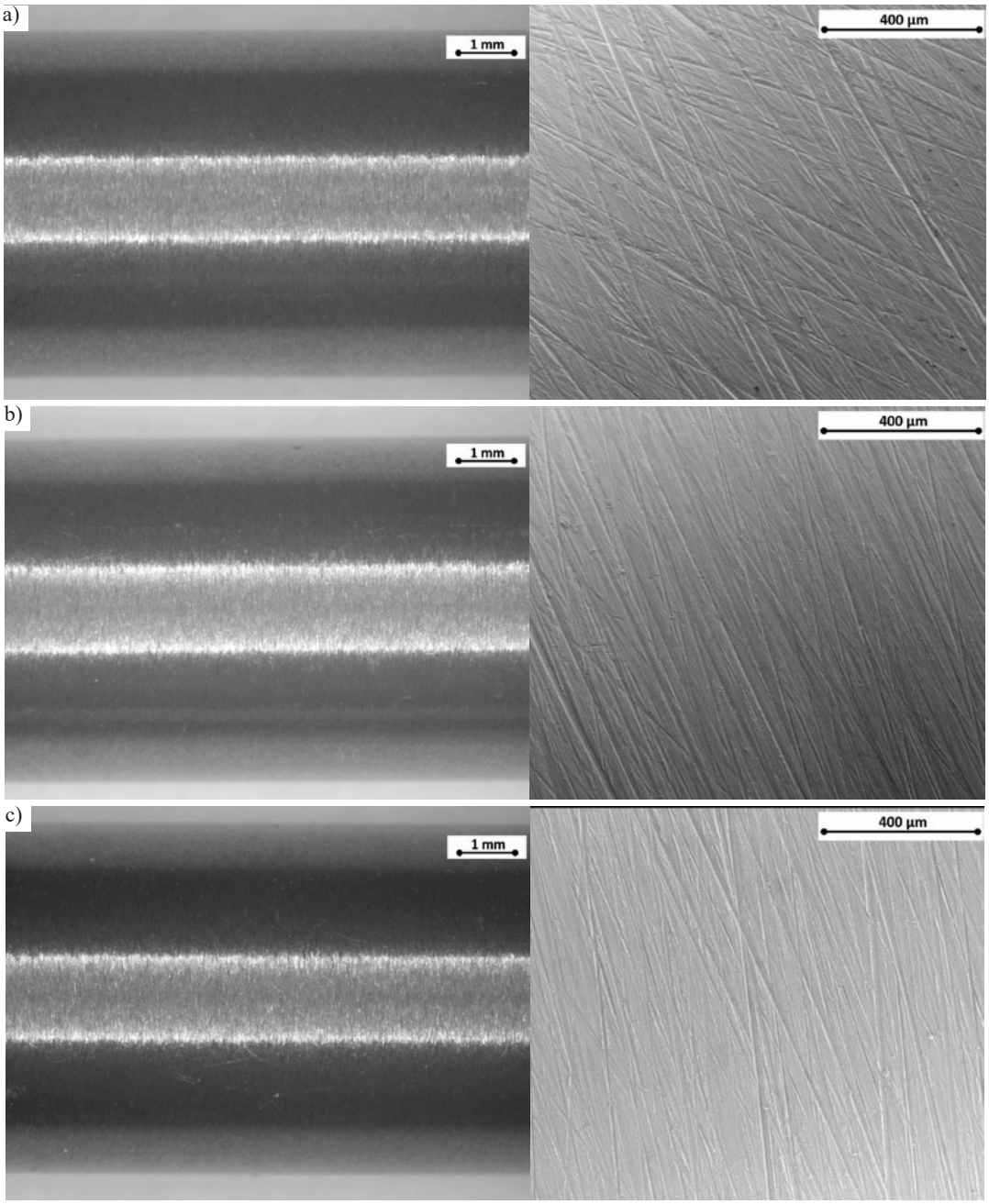

Fig. 1. Exemplary images of the samples' surface in the initial state (stereoscopic microscope – left; SEM – right): a) Ti6Al4V 97V, b) Ti6Al4V 97V + G-Cap, c) Ti6Al4V 97V + G-Cap-L

2.4. Surface observations

Observations of samples surface before and after corrosion tests and the exposure to the Ringer's solution were performed using the scanning electron microscope (SEM, Quanta 250 FEG, FEI Company, Oregon, USA) and the stereoscopic Zeiss Stereo Discovery V8 microscope with MC5s camera.

3. Results and discussion

3.1. Results of macro and microscopic observations of the samples in the initial state

After anodization, the prepared samples were characterized by uneven coloration – Fig. 1. Macro and microscopic observations of the samples in the initial state showed the occurrence of scratches resulting from the mechanical treatment (grinding on sandpaper 120). Furthermore, it was found that the applied biodegradable coatings, G-Cap (Fig. 1b) and G-Cap-L (Fig. 1c), are homogeneous and continuous. The coatings are characterized by transparency, absence of air bubbles and dirt. Moreover, no detachment of the polymeric coating from the metal substrate was observed.

3.2. Results of pitting corrosion studies

Results of pitting corrosion tests of Ti6Al4V alloys and with the coatings made of the poly(glycolide-ε-caprolactone) – G-Cap) and poly(glycolide-ε-caprolactone-lactide) – G-Cap-L in the initial state and after the long-time exposure to Ringer's solution are summarized in Table 1 and Fig. 2.

For all the analyzed samples, polarization curves were recorded for which no breakdown potential was observed. This testifies the

resistance to pitting corrosion, which was confirmed during microscopic observation of the surface of the tested samples, in which no corrosion damage was observed. For all tested variants, the recorded potentiodynamic curves are characterized by a flat course showing the ideal passivity throughout the measuring range (+ 4000mV) – Fig. 2.

Detailed analysis of the obtained results of potentiodynamic studies showed diverse values of parameters describing corrosion resistance of the tested samples depending on time of exposure to the Ringer‘s solution. The anodicaly oxidized samples and the samples with biodegradable polymers in the initial state (not exposed to the Ringer’s solution) were characterized by the highest values of corrosion potential E_{corr} and polarization resistance R_p (Table 1). The exposure to the Ringer’s solution resulted in the decrease of both corrosion potentials as well as polarization resistances. In the case of corrosion potential, no clear tendency of the obtained potential values in the function of exposure time was observed. Regardless of the time of exposure (3, 6, 8, 10 and 12 weeks), the polarization resistance R_p was more than 5 times lower than recorded for the samples in the initial state. For all study periods, the recorded values of the polarization resistance R_p were close to each other – Table 1.

a)

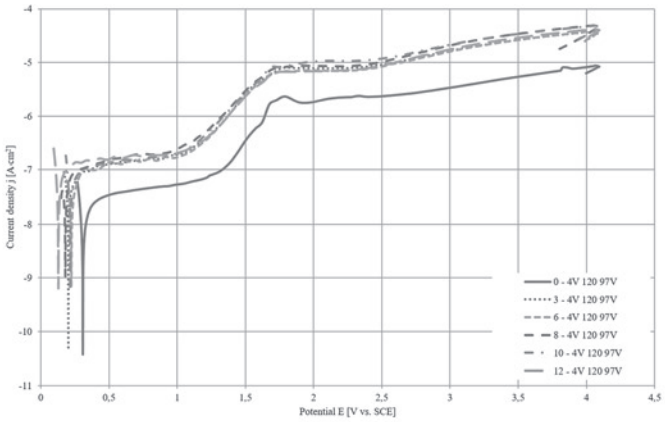

b)

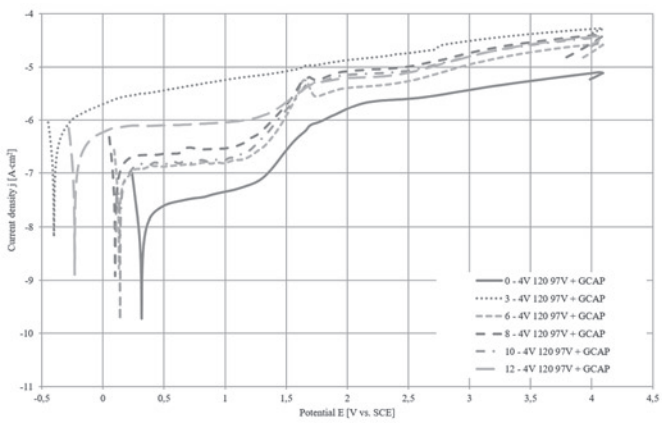

c)

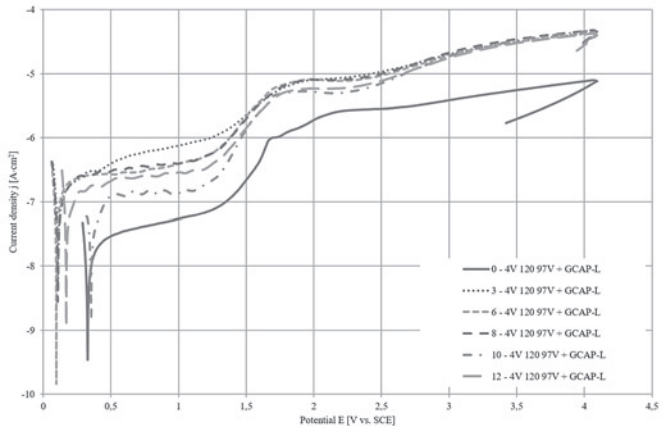

Fig. 2. Exemplary polarization curves for samples after different times of exposure to Ringer’s solution: a) Ti6Al4V 97V, b) Ti6Al4V 97V + G-Cap, c) Ti6Al4V 97V + G-Cap-L

Table 1. Results of pitting corrosion studies

No.	Sample	Time of exposure, weeks	Corrosion potential E_{corr}, mV	SD	Polarization resistance R_p, MΩcm^2	SD
1	4V 120 97V	0	311	51	2,11	0,25
2		3	156	68	0,400	0,030
3		6	177	99	0,42	0,14
4		8	147	51	0,308	0,070
5		10	204	17	0,360	0,080
6		12	191	83	0,360	0,080
7	4V 120 97V + GCAP	0	350	42	3,08	0,36
8		3	-328	86	0,169	0,060
9		6	85	145	0,35	0,20
10		8	13	129	0,210	0,090
11		10	200	83	0,52	0,15
12		12	-128	98	0,22	0,11
13	4V 120 97V + GCAP-L	0	323	35	2,03	0,29
14		3	105	66	0,250	0,040
15		6	207	97	0,210	0,020
16		8	163	73	0,303	0,080
17		10	289	93	0,42	0,10
18		12	173	33	0,210	0,080

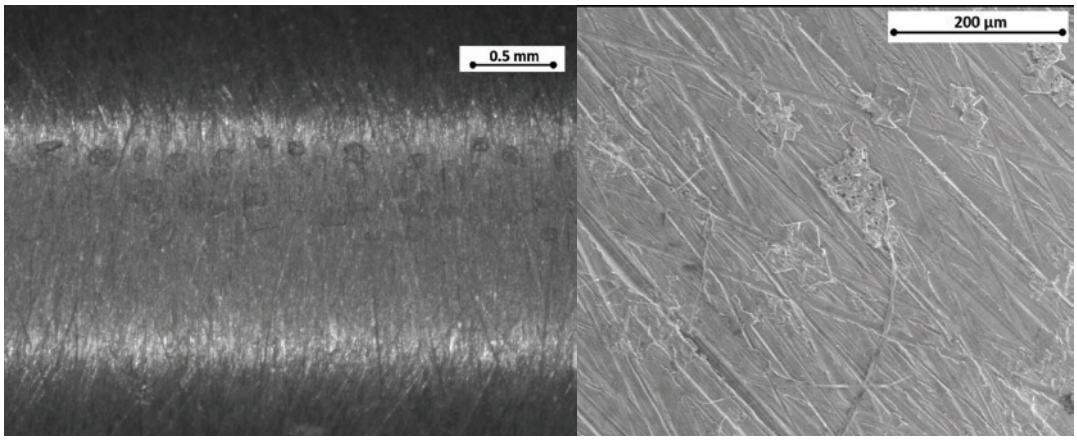

Fig. 3. Exemplary images (stereoscopic and SEM) of the surface of a Ti6Al4V-97V sample subjected to a 12-week exposure to Ringer's solution after pitting corrosion study

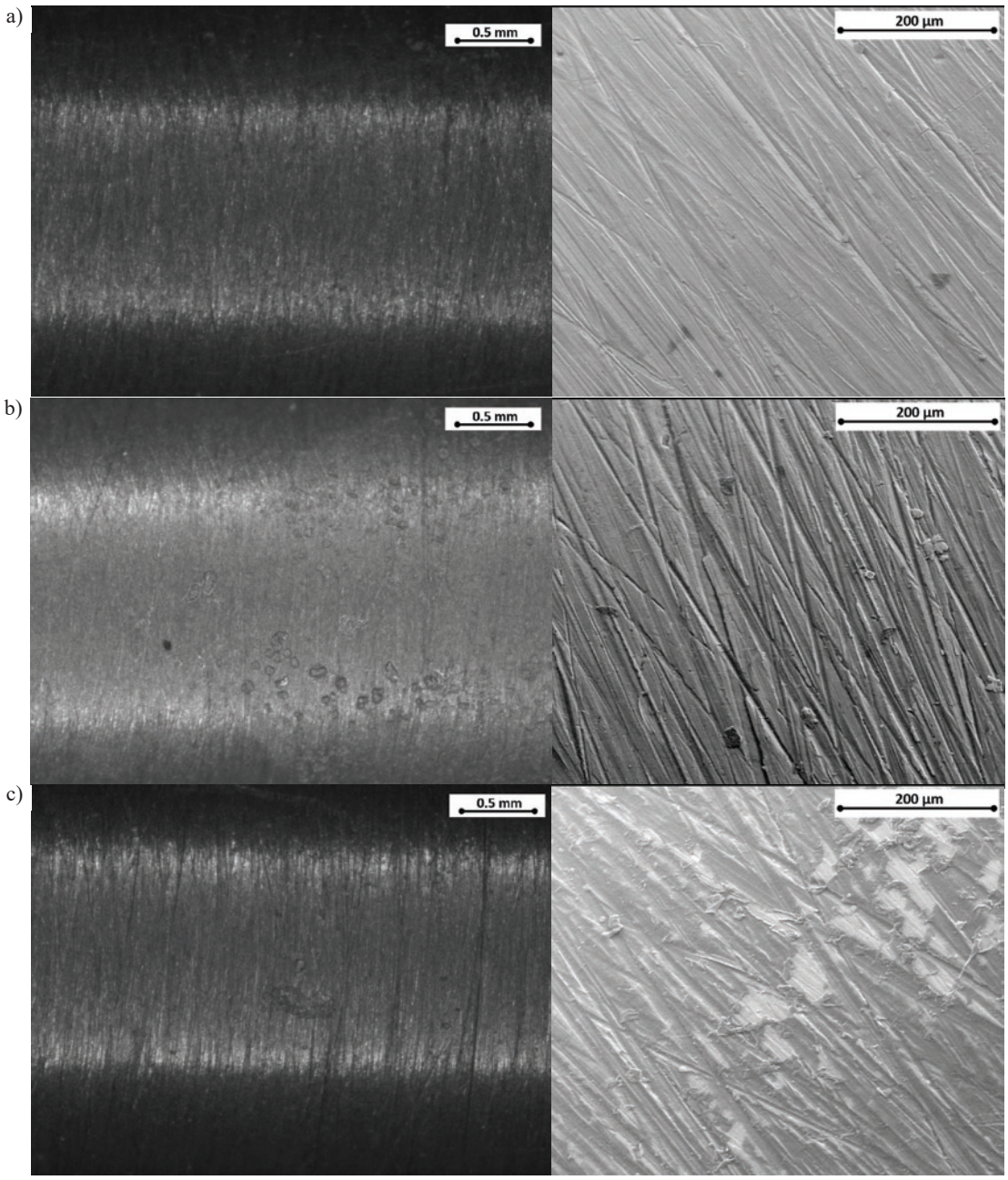

Fig. 4. Exemplary images (stereoscopic and SEM) of the sample surface of Ti6Al4V-97V + G-Cap after pitting corrosion study: a) after 3 weeks of exposure, b) after 8 weeks of exposure, c) after 12 weeks of exposure to the Ringer's solution

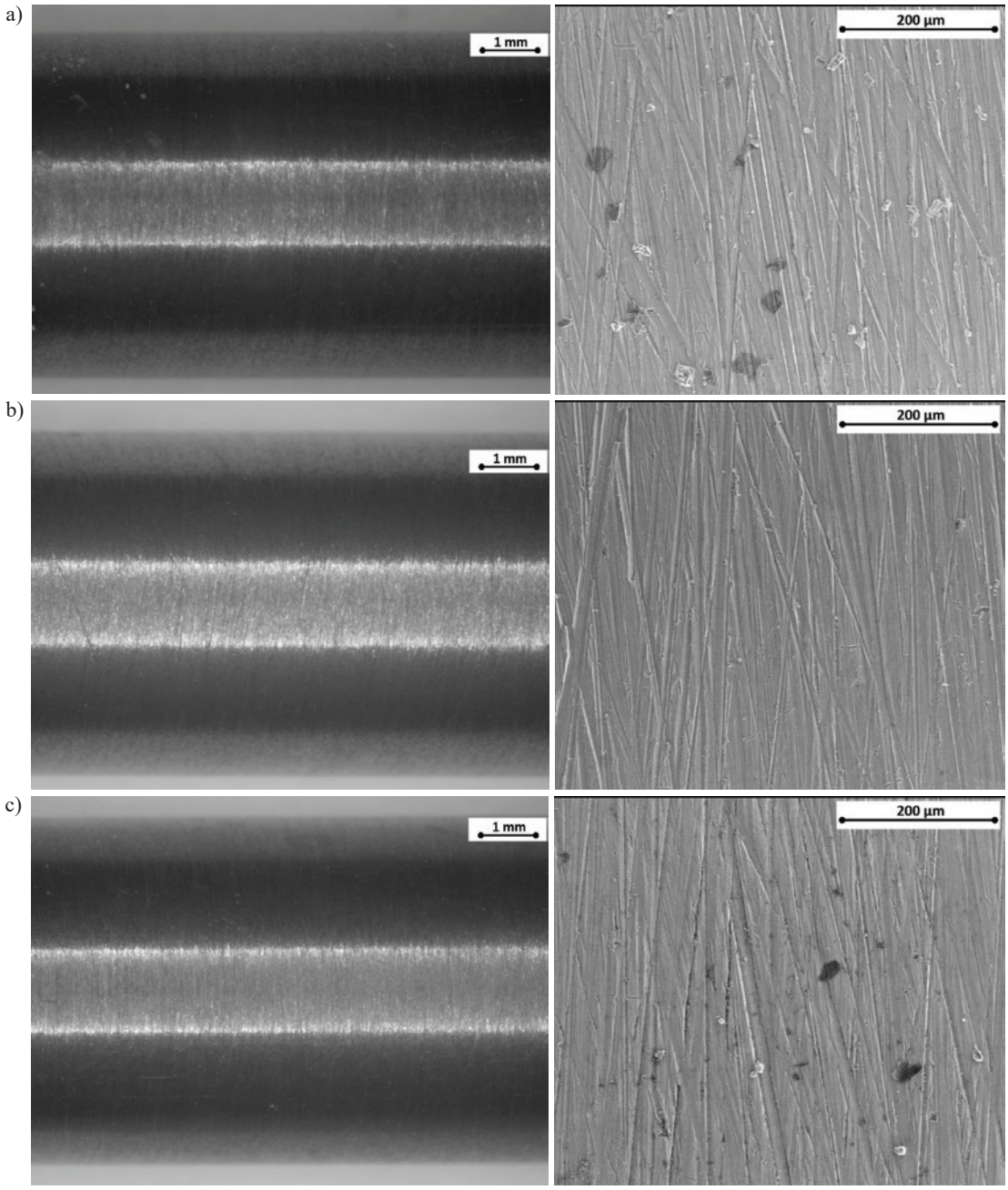

Fig. 5. Exemplary images (stereoscopic and SEM) of the sample surface of Ti6Al4V-97V + G-Cap-L after pitting corrosion study: a) after 6 weeks of exposure, b) after 10 weeks of exposure, c) after 12 weeks of exposure to the Ringer's solution

3.3. Macro and microscopic observations after long-term exposure to Ringer's solution and potentiodynamic studies

Both stereoscopic and scanning electron microscope observations have shown the presence of salt crystals on the surface dervied form the Ringer's solution – Fig. 3. Moreover, observations did not show the presence of corrosion pits on the surface of the samples, thus confirming the results of the potentiodynamic tests. In the case of Ti6Al4V-97V + G-Cap samples, the polymer coating was discontinued at 12 weeks of exposure (Figure 4c). Macro and microscopic observations of the G-Cap-L coated samples showed no damage throughout the study period - up to 12 weeks – Fig. 5.

3.4. Results of metal ions release

The density of metal ions mass in the Ringer's solution after 3, 6, 8, 10 and 12 weeks of exposure is shown in Fig. 7. Analysis of the results showed that the highest density of metal ions (Ti, Al, V) permeating into the Ringer's was obtained for Ti6Al4V-97V alloy not coated with polymer coating - Fig. 4a, b, c. Deposiotion of the G-Cap oraz G-Cap-L coatings resulted in a decrease of the density of metal ions mass. This shows that application of the polymer coatings is a protective barrier to the penetration of metal degradation products into the Ringer's solution.

However, in the case of the G-Cap coating, the presence of metal substrate degradation products correlates with the observed discontinuity of the polymer coating. A similar relationship was observed in our earlier work on Ti6Al4V and Ti6Al7Nb alloys coated with Poly(Lactide-co-Glycolide) - PLGA, which contributed to a signifi-

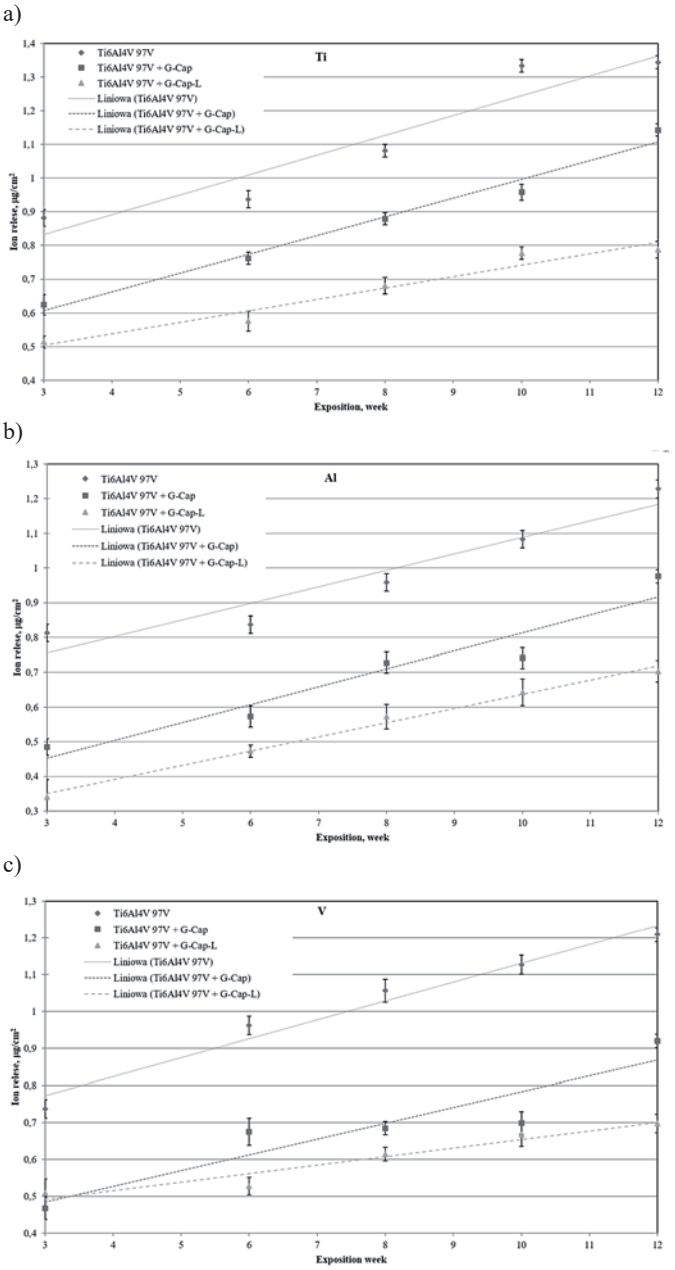

Fig. 6. Density of metal ion mass penetrating to the Ringer's solution: a) Ti ions, b) Al ions, c) V ions

cant decrease in the density of metal ions mass at a similar time, after 90-day exposure to the Ringer's solution [12].

From all the analyzed polymer coatings, the G-Cap-L was characterized by the best barrier properties. Furthermore, for both the G-Cap and G-Cap-L coatings a significant increase in the density of metal ions was observed in the last study periods (12 weeks) in comparison to the previous study periods (Fig. 6). This was caused by the local surface disintegration of the coating that exposed the metal substrate.

The obtained results were confirmed by the microscopic observations, where polymer coatings were locally discontinued after 12 weeks of exposure – Fig 3d.

4. Summary

The proposed surface treatment with the use of the biodegradable polymers poly(glycolide-ε-caprolactone) – G-Cap and poly(glycolide-ε-caprolactone-lactide) – G-Cap-L reduces the release of degradation products from the metal substrate, which *in vivo* conditions may result in the increase of biocompatibility. The polymer coatings on Ti6Al4V alloys are characterized by continuity, translucency, homogeneity, lack of air bubbles or contaminations. The potentiodynamic curves for all variants of surface modification in the initial state were characterized by a lack of hysteresis loops showing the resistance of the examined samples to pitting corrosion. Furthermore, it was found that deposition of the polymer coating did not contribute to a significant increase of the polarization resistance R_p (Table 1). As a result of exposure to the Ringer's solution, regardless of the applied surface modification method (anode oxidized samples and polymeric coatings), the course of the potentiodynamic curves has not changed. However, a significant decrease in the value of the polarisation resistance R_p was found. Over time, this value remained constant. Observations of the surface of the metal substrate after the potentiometric tests for both the samples in the initial state and the samples with the polymeric coatings showed no corrosion damage, which, together with the course of the potentiometric curves, clearly demonstrates the corrosion resistance of the anodized oxidized samples and the G-Cap and G-Cap-L coatings. Scratches visible on the surface are the effect of the performed surface modification.

The results of potentiodynamic studies do not show the unambiguously advantageous influence of the polymer coating on the corrosion resistance of the titanium alloy. The obtained results for both the G-Cap and G-Cap-L coatings are comparable to those of the anodized oxidized samples. This was observed regardless of the exposure time.

Observations of the polymer coating showed a diverse in the function of time course of coating disintegration. The course is also dependent on the type of polymer. It was found that the G-Cap [poly(glycolide-caprolactone)] coating was visibly disintegrating compared to the G-Cap-L [poly(glycolide-caprolactone-lactide)]. After 12 weeks of exposure to the Ringer's solution, discontinuity of the G-Cap coating (Fig. 4) was observed while the G-Cap-L coating was continuous.

The study of the release of metal substrate ions into the Ringer's solution carried out for different periods of exposure showed a diverse course of substrate degradation. The highest values of density of ions mass (Ti, Al, V) were recorded for the samples not coated with the polymer coatings. Deposition of the polymeric coatings has contributed to lowering the density of ions mass. The G-Cap-L coatings (Fig. 6) were characterized by better barrier properties (Fig. 6).

Analysis of the obtained results shows the beneficial influence of the polymer coatings deposited on Ti6Al4V alloy on biocompatibility of the substrate, characterized by the amount of metal ions released to the solution. As a result of the exposure of the G-Cap and G-Cap-L coatings, no deterioration of the corrosion resistance was observed compared to the corrosion resistance of the anodically oxidized samples. It has been found, however, that the polymer coatings reduce the kinetics of ion release. Good barrier properties of the G-Cap and G-Cap-L coatings with ciprofloxacin, and lack of negative influence on corrosion resistance of the metal substrate indicate their potential applications in medicine.

Acknowledgements:

The work is the result of the research project No. 2015/19/B/ST5/03431 funded by the National Science Centre.

References

1. Basiaga M, Paszenda Z, Walke W, Karasiński P, Marciniak J. Electrochemical Impedance Spectroscopy and corrosion resistance of SiO2 coated cpTi and Ti-6Al-7Nb alloy. Information Technologies in Biomedicine, Advances in intelligent Systems and Computing, Springer 2014; 284: 411-420, https://doi.org/10.1007/978-3-319-06596-0_39.
2. Basiaga M, Walke W, Paszenda Z, Kajzer A. The effect of EO and steam sterilization on the mechanical and electrochemical properties of titanium Grade 4. Materials and technology 2016; 50(1): 153-158, https://doi.org/10.17222/mit.2014.241.
3. Cieślik M, Engvall K, Pan J, Kotarba A. Silane-parylene coating for improving corrosion resistance of stainless steel 316L implant material. Corrosion Science 2011; 53: 296-301, https://doi.org/10.1016/j.corsci.2010.09.034.
4. Cieślik M, Kot M, Reczyński W, Engvall K, Rakowski W, Kotarba A. Parylane coatings on stainless steel 316L Surface for medical applications – Mechanical and protective properties. Materials Science and Engineering C 2012; C32: 31-35, https://doi.org/10.1016/j.msec.2011.09.007.
5. Cieślik M, Zimowski S, Gołda M, Engvall K, Pan J, Rakowski W, Kotarba A. Engineering of bone fixation metal implants biointerface – Application of parylene C as versatile protective coating. Materials Science and Engineering C 2012; C32: 2431-2435, https://doi.org/10.1016/j.msec.2012.07.018.
6. Dobrzynski P, Li S M, Kasperczyk J, Bero M, Gasc F, Vert M. Structure-property relationships of copolymers obtained by ring-opening polymerization of glycolide and epsilon-caprolactone. Part 1. Synthesis and characterization, Biomacromolecules 2005; 6(1): 483-488, https://doi.org/10.1021/bm0494592.
7. ISO 5832-3:2017-02 – Implants for surgery -- Metallic materials -- Part 3: Wrought titanium 6-aluminium 4-vanadium alloy.
8. Kajzer A, Kajzer W, Gołombek K, Knol M, Dzielicki J, Walke W. Corrosion resistance, EIS and wettability of the implants made of 316 LVM steel used in chest deformation treatment. Archives of Metallurgy and Materials 2016; 61(2): 767-770, https://doi.org/10.1515/amm-2016-0130.
9. Kasperczyk J, Hu Y, Jaworska J, Dobrzyński P, Wei J, Li S. Comparative Study of the Hydrolytic Degradation of Glycolide/l-actide/Caprolactone Terpolymers Initiated by Zirconium(IV) Acetylacetonate or Stannous Octoate. Journal of Applied Polymer Science, 2008; 107: 3258-3266, https://doi.org/10.1002/app.27404.
10. Kasperczyk J, Li S, Jaworska J, Dobrzyński P, Vert M. Degradation of copolymers obtained by ring-opening polymerization of glycolide and ε-caprolactone: A high resolution NMR aand ESI-MS study. Polymer Degradation asd Stability 2008; 93: 990-999, https://doi.org/10.1016/j.polymdegradstab.2008.01.019.
11. Kazek-Kęsik A, Jaworska J, Krok-Borkowicz M, Gołda-Cępa M, Pastusiak M, Brzychczy-Włoch M, Pamuła E, Kotarba A, Simka W. Hybrid oxide-polymer formed on Ti-Mo alloy surface enhancing antibacterial and osseointegration functions. Surface & Coatings Technology 2016; 302: 158-165, https://doi.org/10.1016/j.surfcoat.2016.05.073.
12. Kiel-Jamrozik M, Szewczenko J, Basiaga M, Nowińska K. Technological capabilities of surface layers formation on implant made of Ti-6Al-4V ELI alloy. Acta of Bioengineering and Biomechanic 2015; 1: 31-37.
13. Krauze A, Ziębowicz A, Marciniak J. Corrosion resistance of intramedullary nails used in elastic osteosynthesis of children. Journal of Materials Processing Technology 2005; 162-163: 209-214, https://doi.org/10.1016/j.jmatprotec.2005.02.191.
14. Ma X, Xia Y, Xu H, Lei K, Lang M. Preparation, degradation and in vitro release of ciprofloxacin-eluting ureteral stents for potential antibacterial application. Materials Science and Engineering C 2016; 66: 92-99, https://doi.org/10.1016/j.msec.2016.04.072.
15. Makuch K, Koczorowski R. Biokompatybilność tytanu oraz jego stopów wykorzystywanych w stomatologii. Dent Med Probl, 2010; 47: 81-88.
16. Marciniak J, Szewczenko J, Kajzer W. Surface modification of implants for bone surgery. Archives of Metallurgy and Materials 2015; 60(3B): 13-19, https://doi.org/10.1515/amm-2015-0357.
17. Maurus P B, Kaeding C C. Bioabsorbable implant material review. Oper Techn Sport Med 2004; 12(3): 158-160, https://doi.org/10.1053/j.otsm.2004.07.015.
18. Orchel A, Jelonek K, Kasperczyk J, Dobrzyński P, Marcinkowski A, Pamuła E, Orchel J, Bielecki I, Kulczycka A. The influence of chai microstructure of biodegradable copolyesters obtained with low-toxic zirconium initiator to in vitro biocompatibility. Hindawi Publishing Corporation. BioMed Reserch International. 2013; Article ID 176946: 12.
19. Park M, Lee J, Park Ch, Lee S, Seok H, Choy Y. Polycaprolactone coating with varying thyicknesses for controlled corrosion of magnesium. Journal of Coatings Technology and Research 2013; 10(5): 695-706, https://doi.org/10.1007/s11998-013-9474-6.
20. Rusinek B, Stobiecka A, Obtułowicz K. Alergia na tytan i implant. Alergia Immunologia 2008; 5: 5-7.
21. Szewczenko J, Kajzer W, Grygiel-Pradelok M, Jaworska J, Jelonek K, Gawliczek M, Libera M, Marcinkowski A, Kasperczyk J. Corrosion resistance of PLGA-coated biomaterials. Acta of Bioengineering and Biomaechanics 2017; 19(1): 173-179.
22. Szewczenko J, Nowinska K, Marciniak J. Influence of initial surface treatment on corrosion resistance of Ti6Al4V ELI alloy after anodizing. Przegląd Elektrotechniczny 2011; 87(3): 228-231.
23. Zini E, Scandola M, Dobrzynski P, Kasperczyk J, Bero M. Shape memory behavior of novel (L-Lactide- glycol ide-trimethylene carbonate) terpolymers, Biomacromolecules 2007; 8(11): 3661-3667, https://doi.org/10.1021/bm700773s.

Wojciech KAJZER
Department of Biomaterials and Medical Devices Engineering,
Faculty of Biomedical Engineering,
Silesian University of Technology,
Roosevelta 40, 41-800 Zabrze, Poland

Joanna JAWORSKA
Centre of Polymer and Carbon Materials of the Polish Academy of Sciences,
M. Curie-Skłodowskiej 34, 41-819 Zabrze, Poland,

Katarzyna JELONEK
Centre of Polymer and Carbon Materials of the Polish Academy of Sciences,
M. Curie-Skłodowskiej 34, 41-819 Zabrze, Poland,

Janusz SZEWCZENKO
Department of Biomaterials and Medical Devices Engineering,
Faculty of Biomedical Engineering,
Silesian University of Technology,
Roosevelta 40, 41-800 Zabrze, Poland

Anita KAJZER
Department of Biomaterials and Medical Devices Engineering,
Faculty of Biomedical Engineering,
Silesian University of Technology,
Roosevelta 40, 41-800 Zabrze, Poland

Katarzyna NOWIŃSKA
Institute of Applied Geology, Faculty of Mining and Geology,
Silesian University of Technology,
Akademicka 2, Gliwice, Poland.

Anna HERCOG
Centre of Polymer and Carbon Materials of the Polish Academy of Sciences,
M. Curie-Skłodowskiej 34, 41-819 Zabrze, Poland,

Marcin KACZMAREK
Department of Biomaterials and Medical Devices Engineering,
Faculty of Biomedical Engineering,
Silesian University of Technology,
Roosevelta 40, 41-800 Zabrze, Poland

Janusz KASPERCZYK
Centre of Polymer and Carbon Materials of the Polish Academy of Sciences,
M. Curie-Skłodowskiej 34, 41-819 Zabrze, Poland,

E-mails: wojciech.kajzer@polsl.pl, jjaworska@cmpw-pan.edu.pl,
kjelonek@cmpw-pan.edu.pl, janusz.szewczenko@polsl.pl, anita.kajzer@polsl.pl,
katarzyna.nowinska@polsl.pl, marcin.kaczmarek@polsl.pl,
jkasperczyk@cmpw-pan.edu.pl

Article citation info:
POSZWA P, SZOSTAK M. Influence of scale deposition on maintenance of injection molds. Eksploatacja i Niezawodnosc – Maintenance and Reliability 2018; 20 (1): 39–45, http://dx.doi.org/10.17531/ein.2018.1.6.

Przemysław POSZWA
Marek SZOSTAK

INFLUENCE OF SCALE DEPOSITION ON MAINTENANCE OF INJECTION MOLDS

WPŁYW ODKŁADANIA SIĘ KAMIENIA NA EKSPLOATACJĘ FORM WTRYSKOWYCH*

The cooling system of an injection mold serves a substantial role in the process of plastic injection. It is responsible for efficient dissipation of heat from the injection mold, generated by the plasticized material which during the injection phase is introduced into the mold. Apart from rapid heat dissipation, it is important to achieve uniform distribution of temperatures on the surface of the molding cavity. This study focuses on the phenomenon of lime scale deposition in injection mold cooling systems. Lime scale deposition results in reduction of the cooling canal's section diameter, as well as a clear reduction in cooling efficiency due to its lowered thermal conductivity. The study specifies the influence of many factors (geometry of the cooling system and molded piece, coolant temperature, type of plastic material) on the utilization of the injection mold as a result of the occurrence of lime scale in the cooling system. The conducted numerical simulations have allowed to account for the impact of the deposit layer's thickness on the distribution of temperatures on the molding cavity's surface, the average injection mold temperature, as well as the time required to solidify the plastic material products.

Keywords: *injection mold, cooling phase, lime scale, fouling.*

Układ chłodzenia formy wtryskowej odgrywa niebagatelną rolę w procesie wtryskiwania tworzyw sztucznych. Odpowiada on za sprawny odbiór ciepła z formy wtryskowej dostarczonego przez uplastycznione tworzywo, które w fazie wtrysku jest wprowadzone do formy. Oprócz szybkiego odbioru ciepła istotne jest, aby rozkład temperatury na powierzchni gniazda formującego był równomierny. W niniejszej pracy skupiono się na zjawisku osadzania się kamienia w układach chłodzących form wtryskowych. Kamień powoduje zarówno zwężenie przekroju kanału chłodzącego, jak i wyraźny spadek wydajności chłodzenia ze względu na jego niską przewodność cieplną. W pracy określono wpływ wielu czynników (geometria układu chłodzenia oraz wypraski, temperatura cieczy chłodzącej, rodzaj tworzywa) na eksploatację formy wtryskowej w wyniku pojawienia się kamienia w układzie chłodzącym. Przeprowadzone symulacje numeryczne pozwoliły uwzględnić wpływ grubości warstwy osadu na rozkład temperatury na powierzchni gniazda formującego, średnią temperaturę formy wtryskowej, a także czas potrzebny do zestalenia wyrobów produkowanych z tworzyw sztucznych.

Słowa kluczowe*: injection mold, cooling phase, limescale, fouling.*

1. Introduction

Injection molding is one of the most popular methods of plastic processing. It involves cyclical plasticizing of the material, injecting it under pressure into a mold, filling out defects associated with its solidification, cooling and removal of the finished product from the mold. The longest part of the injection molding cycle is the cooling phase, whose duration is a result of the insulating properties of plastic materials. An optimally designed cooling system enables efficient heat dissipation from the plastic material [9, 12].

Apart from the cooling system's geometry, the efficiency of heat dissipation is affected by the type of material used to manufacture the injection mold and its elements. The parameter responsible for heat dissipation is heat conductivity of mold material, coolant type and its flow rate. In order to increase the rate of heat dissipation, inserts are used which are made out of copper alloys, e.g. beryl bronze, Ampco 940, Ampco 944, MoldMax XL. These allow to increase the speed of heat dissipation, resulting in the ability to achieve the same mold temperature within up to 29% less time through the use of an appropriate insert material [6].

During utilization of an injection mold water flows through the cooling system, where the precipitation of scale and its deposition on the surface of cooling canals occurs. Lime scale is characterized by very low heat conductivity, comparable or slightly higher compared to the heat conductivity of plastic materials. Scale deposition results in the generation of additional resistance on the heat flow path from the plasticized plastic to the surface of cooling canals, from where it is further removed on the heat flow path [13].

Depending on the chemical composition of water used for cooling, different types of scale with varying thermal properties may be deposited. Regardless of the type, their heat conductivity is 5-600x lower than the conductivity of steel (approx. 30 W/m/K), which is presented in Table 1. This means that a layer of scale deposit with a thickness of 1 mm is equal respectively to 5-600 mm of steel. This illustrates how important it is to ensure high heat conductivity of the injection mold.

There are multiple models which describe the deposition of scale over time. In the case of canals with a circular section, the deposit thickness may reach very high values [7, 10] – which in the case of molds utilized over long periods of time may cause significant issues with cooling efficiency. This is especially important in the case of injection molds which do not have temperature sensors installed, and the only factor measured during the cooling process is the liquid temperature in the thermostat.

No studies have been found regarding the issue of scale layer deposition in the cooling canals of injection molds and the impact of such a layer on the cooling process. On the other hand, it is a notion very

(*) Tekst artykułu w polskiej wersji językowej dostępny w elektronicznym wydaniu kwartalnika na stronie ***www.ein.org.pl***

Table 1. Heat conductivity of different types of scale deposits [1]

Scale Type	Calcium Carbonate Scale	Calcium Sulphate Scale	Calcium Silicate Scale	Organic Sediment	Soot
Thermal Conductivity [W/mK]	0,6 – 6	2,3	0,3	0,1	0,2

widely discussed in process engineering, as it has a key effect on the efficiency of heat removal [3, 5, 11]. An example may be petroleum distillation equipment, where the impact of scale deposits on cooling efficiency has been determined. After a year of system operation without the use of compounds halting the deposition of scale, the efficiency of such equipment was reduced by over 40% [3].

For correct performance of injection mold cooling, the liquid flow rate should be high enough in order for the difference between its temperature at the input and output should be lower than 3°C [2]. Unfortunately, the measurement method does not provide diagnostic information regarding the utilization of the injection mold, as the scale will cause minor coolant liquid temperature reductions at the output due to a reduction of the cooling efficiency (provided a properly selected volume flow intensity). The lack of a mold temperature monitoring tool (especially in the case of less expensive solutions) may lead to the occurrence of an issue with the manufacture of molded piece with the desired dimension tolerances.

3. Discussion of the Issue

This study involved the performance of a range of numerical analyses with the objective of indicating the impact of clogged injection mold cooling canals on cooling efficiency. For the purpose of comparison, an analysis of heat transmission averaged over time was incorporated, using the Autodesk Moldflow® software. The software enables 2 types of analysis – with a defined cooling time and with its automatic determination. Analysis with a defined cooling time involves specification of a temperature field with the assumption of a given temperature of the injected plastic material and initial mold temperature (40°C by default). With the above data, the software determines the average temperature distribution, which is substituted in the subsequent equation instead of the default mold temperature. The process is iteratively repeatable for as long, as the difference between subsequent cycles (which are the de facto injection cycles) is below 0,1°C. In the case of seeking to establish the cooling time, the software commences the search from the initially assumed cooling time (30 s) and conducts an iterative analysis verifying the fraction of the solidified plastic material, its temperature and temperature distribution on the mold's surface. After achieving the assumed convergence (difference of temperatures between cycles below 0,1°C) the software evaluates, whether the criteria presented above have been fulfilled. If not, the software modifies the cooling time and conducts an iterative analysis in order to arrive at the expected values. After receiving the expected values, the analysis is stopped.

The simulation assumes that the entire molding cavity is filled with plastic material (this simplification arises from the fact that the time of cavity filling by the material compared to the cooling time is relatively short).

In order to acquire the fullest extent of information, analyses were conducted by introducing modifications to the base model. Changes were made to:

- the geometry of the cooling system, the molded piece and mold (diameter of cooling canals, distance between cooling canals, distance from the cooling canals to the molded piece surface, molded piece thickness and shape, injection mold thickness),

Table 2. Compilation of constant parameters

Dimensions of the injection mold base [mm]	156 x 156
Dimensions of the molded piece base in the shape of the base [mm]	100 x 100
Dimensions of the molded piece in the shape of the edge [mm]	51,5 x 51,5 x 100
Molded piece thickness in the shape of the edge [mm]	3
Set Parameters	
Volume based flow intensity [l/min]	3,387 (for a cooling canal diameter of 8mm) 2,54 (for a cooling canal diameter of 6mm)
Mold opening time [s]	1
Analyzed cycle time (without the mold opening time) [s]	20
Cooling time selection criteria	
Exit temperature of the molded piece from the mold [°C]	103 (Moplen HP500N) 148 (Tarnamid T27 natural)
Percentage of solidified plastic material during removal of the molded piece from the mold	100%
Scale deposit material properties	
Density [g/cm^3]	1,4
Specific heat [J/kgC]	500
Heat conductivity [W/mC]	0,5
Tool steel material properties	
Density [g/cm^3]	7,8
Specific heat [J/kgC]	460
Heat conductivity [W/mC]	29

- the type of plastic material and set parameters (plastic material temperature, coolant liquid temperature, assumed injection mold temperature).

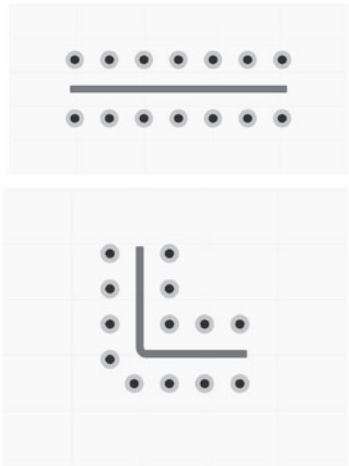

Fig. 1. Geometry of analyzed molded pieces, injection molds and cooling systems with scale deposit layers.

Within the scope of the analyses one modification was performed at a time to make it possible to illustrate the influence of a given factor on the studied aspects. An exception was found in the change of the plastic material type, where the impact of the coolant liquid temperature was investigated. It is assumed that the coolant liquid temperature should be 10–20°C lower than the expected mold temperature. In order to gain a full perspective of the situation, in the case of the second plastic material liquids with a temperature 10 and 20°C lower than the mold temperature were used, as well as with a temperature assumed for the base plastic material. All constant values are presented in Tab. 2, while all variable values are presented in Tab. 3 (base values emphasized with a bold font). Fig. 1 illustrates a view of the geometry which was subject to modification. The molded pieces have been placed in such a way, that they are located in the exact middle of the mold (taking into consideration their dimensions).

The analyses assumed the introduction of a layer of lime scale of varying thickness injection mold cooling channels in order to illustrate the impact of the lime scale layer size on the cooling system's efficiency. The averaged material data of the lime scale deposit have been established on the basis of Tab. 1 and scientific studies [3, 4, 8] and also presented in Tab. 2.

The initial cooling time was determined for the base model, so that the entire molded piece is subject to solidification (rounded up to full seconds). In order to compare the influence of a layer of lime scale, the following results have been compared: the minimum, maximum and average temperature of the molding cavity, average temperature of the injection mold, percentage of the solidified plastic material, as well as the time to which the cooling process should be extended in order to achieve complete solidification of the molded piece and the assumed mold temperature.

The above results are significant to the utilization of the mold as a tool used for manufacturing of a product which meets assumed quality criteria. The average molding cavity temperature impacts the size of distortions associated with plastic material contraction – this is directly associated with the time required to cool the molded piece. The longer the cooling time, the more significant the contraction inside the molded piece, which leads to problems with maintaining the assumed dimensional tolerances. On the other hand, the difference between the minimum and maximum mold temperature results in non-uniform contraction, which further intensifies molded piece deformations. The average mold temperature, on the other hand, has a very significant effect on the utilization of the mold itself and its reliability. As the mold's temperature rises, its dimensions increase due to the material's thermal expansion. This has a very significant effect on its utilization and reliability. On the one hand, the increase of the mold's linear dimensions causes a change in the linear dimensions of the molding cavity, which leads to manufactured products with dimensions different from the ones assumed in case of a properly cooled mold. On the other hand, an increase in tool temperature leads to problems with fitting the individual moving elements of the mold (e.g. slides, ejectors), which may result in decreased longevity of such elements. The percentage of solidified plastic material tells indicates what scale layer thickness can lead to large distortions of the molded piece, which without support in the form of the molding cavity will be able to freely deform during solidification outside the mold. The time to which the cooling process should be extended is a measure of the cooling system's degree of degradation in the event of its utility with a given layer of scale deposit.

3.1. Numerical calculation results

In this study results were analyzed in 3 areas divided by the type of modification to the base model (change to the cooling system's geometry, molded piece and mold, as well as change of the plastic material and set parameters).

The first analyzed aspect was the average temperature on the surface of the molding cavity. Within the studied scope for each modification implemented to the base model it is possible to approximately assume (R>0,95) a linear correlation between the scale deposit thickness and the increase of the mold's average temperature (Fig. 2). In the case of no scale deposit, depending on changes to the geometry, it ranged from 38 to 42°C. The differences became clearer only with a scale deposit thickness equal to 1 mm, to then reach larger variations with a scale deposit thickness of 2 mm. The smallest change to the average cavity surface temperature was observed for the removal of cooling canals away from the molded piece surface and thickening of the injection mold. A significant rise of the average cavity temperature

Table 3. Compilation of variable parameters

Diameter of the cooling canal c [mm]	Distance between cooling canals c_s [mm]	Distance from the cooling canal to the molded piece surface c_d[mm]	Molded piece thickness g_t [mm]
6, **8**	**16**,24	**12**, 18	**3**, 5
Molded piece geometry g	Injection mold height m_h [mm]	Plastic material type p	Plastic material injection temperature p_t [°C]
base, edge	**88 (126 in the case of the edge)**, 126	Moplen HP500N,	**235**, 250
		Tarnamid T27 natural	270
Coolant temperature m_{ct} [°C]		Assumed cavity surface temperature m_t [°C]	
15, **25**		**35**, 50	
25, 60,70		80	

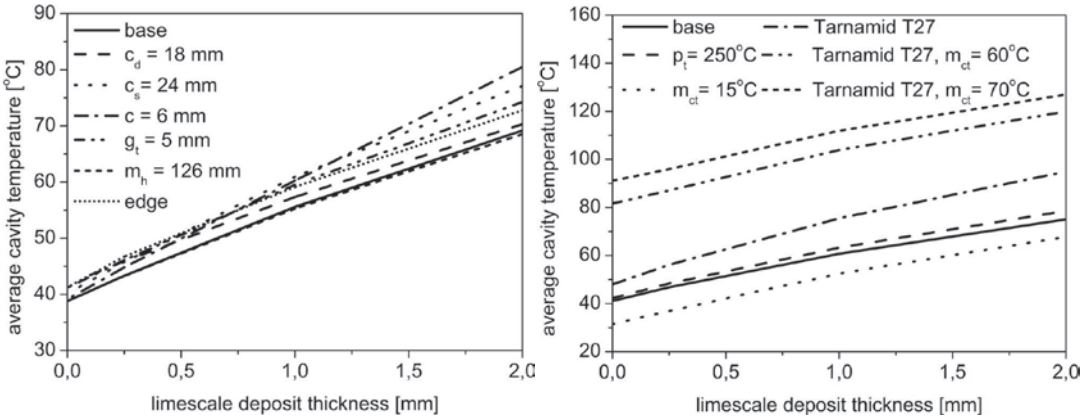

Fig. 2. Graph of the average temperature on the molding cavity surface

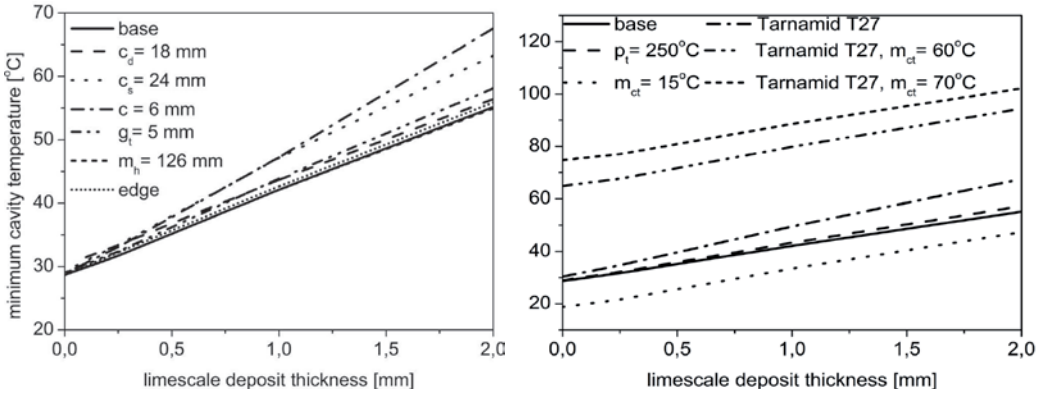

Fig. 3. Graph of the minimum temperature on the molding cavity surface

was observed in the case of modifying the molded piece geometry from a base to an edge, which resulted from the fact of hindered heat dissipation from the edge area. An even greater rise was observed in the case of molded piece thickening (the increase arises from a greater degree of heat needed to be dissipated during the cycle). The greatest changes were observed in the case of increasing the distance between canals (approx. 10°C) and reduction of the canal's diameter (approx. 15°C). In both cases the number of heat dissipation sources was reduced measurably (smaller area of the cooling canal in the case of diameter reduction and smaller number of cooling canals in the case of larger distances between canals). Were the number of cooling canals maintained, the average temperature increase on the cavity's surface would be less than 5°C.

In case of modifications to the set parameters and the plastic material it was possible to observe more significant differences in the average mold temperature. Increasing the temperature of the plastic material had the smallest impact. Lowering the coolant liquid temperature for Moplen by 10°C resulted in a balanced reduction of the molding cavity minimum temperature. Changing the plastic material to Tarnamid did not cause any significant change to the minimum cavity temperature in the case of no scale deposit, however with a deposit thickness of 2 mm, the difference was approx. 15°C (maintaining the same coolant liquid temperature). In the case of incorporating a coolant liquid temperature 10-20°C lower than the assumed cavity temperature, a very distinct rise of the minimum cavity temperature was observed, however the change was proportionate to the change of the coolant liquid temperature.

Another analyzed criterion was the minimum temperature on the surface of the molding cavity. In the case of modifying the geometry for the zero scale deposit thickness, the average temperature was equal to approx. 26-30°C. After increasing the thickness to 0,25 mm the average temperature was raised by approx. 5-7°C to 32-37°C (on a case by case basis). Larger discrepancies occurred with further increases of scale deposit thickness. For a 1 mm layer a significantly larger increase was observed in the average temperature of the cooling canal with a smaller diameter and a cooling system with larger distances between canals. This difference would further increase when raising the scale layer thickness to 2 mm. Reducing the heat dissipation area resulted in an increase of the average mold temperature by respectively 10°C (change of the distance between canals) and 20°C (change of the canal diameter). Maintaining the base number of cooling canals would result in the abovementioned temperature rise to be non-existent. In the case of other geometry changes the scale deposit thickness increase results in approximate linear temperature changes with the same straight line slope ratio value.

Changing the plastic material or set parameters resulted only in the upward shift of temperature values, while maintaining the separations between individual graphs, such as in the case of the average molding cavity surface temperature.

In the case of the maximum molding cavity surface temperature a significant deviation was observed for the molded piece geometry change to the edge (even in the case of no scale deposit). This arises from the fact that within the boundaries of the edge heat dissipation is significantly hindered. For that reason the highest maximum temperature is observed for the edge within the full scope of scale deposit thickness. Similarly to the two prior parameters, increasing the mold thickness and distance of cooling canals from the mold surface does not result in changes in relation to the base model. Increasing the molded piece thickness, increasing the distance between cooling canals and reducing the cooling canal diameter also provides the same result as in the case of remaining parameters. Non-removal of cooling canals in the case of spreading them out results in a decrease of the maximum temperature by 6°C in relation to the value presented on the graph for the scale deposit layer thickness.

In order to compare the changes in temperature distribution, Fig. 5 was prepared which marks the minimum and maximum temperature range for a given model. In the analyzed case it can clearly be seen that the application of a smaller cooling canal diameter and a larger distance between canals leads to an increase in difference between the minimum and maximum temperature on the molding cavity surface. Increasing the mold's thickness resulted in a slight reduction of the temperature difference, while increasing the molded piece thickness and raising the temperature of the injected plastic material resulted in a slight increase in the degree of difference. Changing the geometry to a more complex one (edge) resulted in a significant increase in differences between the minimum and maximum temperature, similarly to changing the plastic material type without changing the coolant liquid

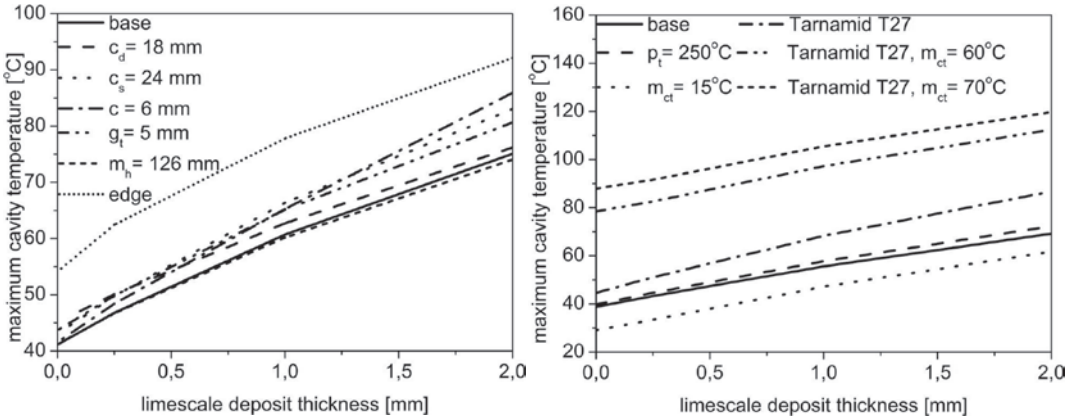

Fig. 4. Graph of the maximum temperature on the molding cavity surface

temperature. This shows that the use of an excessively cold coolant liquid results in large temperature differences between individual locations in the injection mold, which will further result in additional deformations associated with non-uniform contraction. Changing the coolant liquid temperature resulted only in a shift of the minimum and maximum temperature ranges.

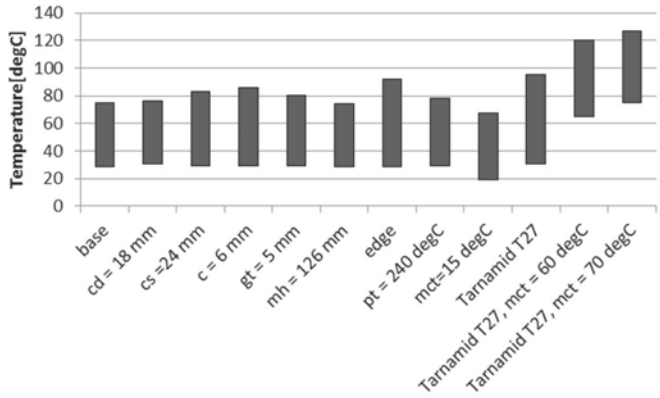

Fig. 5. Graph of the minimum and maximum temperature on the molding cavity surface for a scale deposit layer of 2 mm

Another important parameter is also the average mold temperature. Its value versus the scale deposit thickness is presented in Fig. 6. Similar changes (as in the case of previously analyzed parameters) were observed for increasing the distance between cooling canals and the surface and increasing the mold's thickness. The result for an increased mold volume provides very significant information – regardless of the mold's size, its average temperature remains constant versus the scale deposit thickness. This has a significant impact on the utility of the injection mold, in which an increase of individual linear dimensions occurs due to the rise in temperature.

For other changes in the mold's geometry changes were observed only in the case of narrowing the canal and increasing the distance between canals – in terms of the average mold temperature the highest value was reached in the case of spreading out the cooling canals (and not reducing the cooling canal diameter). In the case of non-removal of cooling canals located further away from the mold's surface the temperature would have been 5°C lower.

In case of changing the set parameters the largest temperature changes were observed when using Tarnamid T27 and maintaining the original coolant liquid temperature (a slightly smaller change was observed in the case of spreading out the cooling canals) and was equal to approx. 27°C. Assuming a linear expandability ratio for P20 tool steel (40CrMnMo9) equal to 0,000012, an increase of the mold's linear dimension was determined for the largest temperature rise. The linear dimension change was equal to approx. 0,04 mm for the 156 mm side o the mold. Knowing that standard injection molds are significantly larger, it was concluded that raising the mold temperature by merely 20°C may result in significant changes to the injection mold cavity size, which would in turn have a significant impact on the dimensional accuracy of manufactured plastic elements. Further, the mold temperature increase has an impact on the injection mold's operational reliability, as issues may occur with the fitting of the injection mold's moving elements, resulting in their excessive wear.

The deposition of scale in cooling systems affects not only temperature distribution of the injection mold, but also the solidification of the plastic material during the cooling phase. In the event of geometry changes for all cases with the exception of molded piece thickness increases, it was concluded that a scale deposit layer of 0,25 mm does not extend the time needed to solidify the molded piece (in all cases the scale deposit did not cause a reduction of the solidified plastic fraction below 100%). A significant reduction was observed for a scale deposit layer of 1 mm. Depending on the system, from 70 to 80% of the molded piece was subject to solidification. Similarly to the previous parameters, minor differences were observed when increasing the mold thickness and increasing the distance of cooling canals to the mold surface. For a scale layer thickness of 2 mm the lowest percentage of solidified plastic material was observed for smaller canals (slightly greater in case of spreading out the cooling canals). In this case non-removal of excess cooling canals would cause an increase of solidified plastic to 55% (despite the fact that these canals are significantly far removed from the molded piece surface).

In the case of set parameters, it was possible to observe significantly larger differences in the amount of solidified plastic. Increasing the plastic

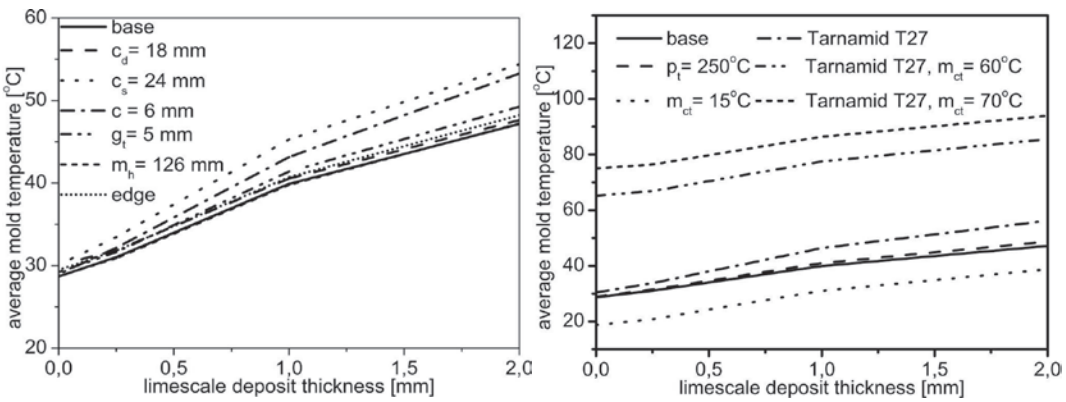

Fig. 6. Graph of the average injection mold temperature

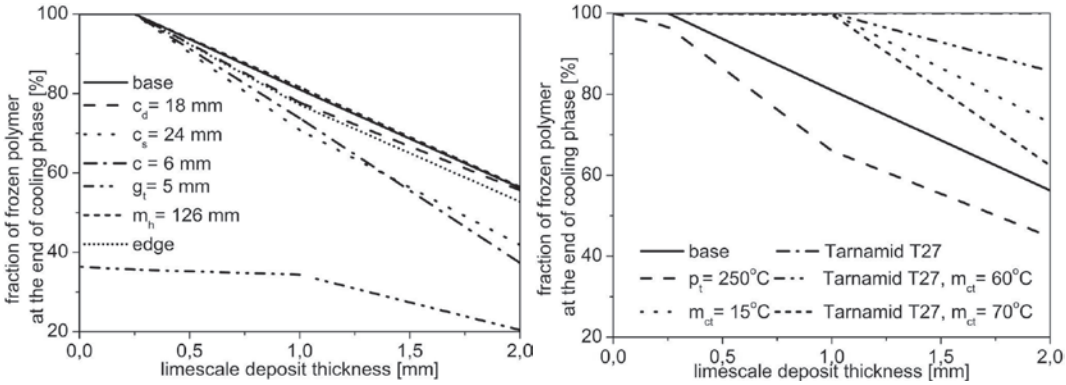

Fig. 7. Graph of the frozen plastic fraction at the end of the cooling phase

material temperature to 250°C resulted in that for even a thin layer of scale equal to 0,25 mm the molded piece is not subject to complete solidification before removal from the mold. The use of a lower coolant liquid temperature resulted in complete solidification of the entire molded piece prior to removal from the injection mold even with a 1 mm layer of scale. In the case of changing the plastic material to Tarnamid, regardless of the scale deposit layer, it was possible to solidify the molded piece within the assumed cooling time (without increasing the coolant liquid temperature). In the case of raising the coolant liquid temperature to 60°C complete solidification of the molded piece was observed with a scale deposit thickness of 1 mm (for a coolant liquid temperature of 70°C 99,71% of the molded piece was solidified).

The final analyzed aspect was the theoretical cooling time needed to solidify the entire molded piece and cool down the mold to the assumed temperature. In the case of geometry changes it was observed that in certain instances the increase in scale deposit thickness over 1 mm does not significantly extend the cooling time. This result occurred in the case of a change in the injection mold thickness, distance from the cooling canals to the molded piece surface and changes to the molded piece geometry. In other cases further scale deposit thickness increases caused significant cooling time extensions.

It should be taken into consideration that such a long cooling time was not a result of issues with plastic material solidification, but with issues connected with cooling the mold to the assumed temperature. The longest time required for molded piece solidification did not exceed 30 seconds, however it assumed appropriate cooling of the injection mold.

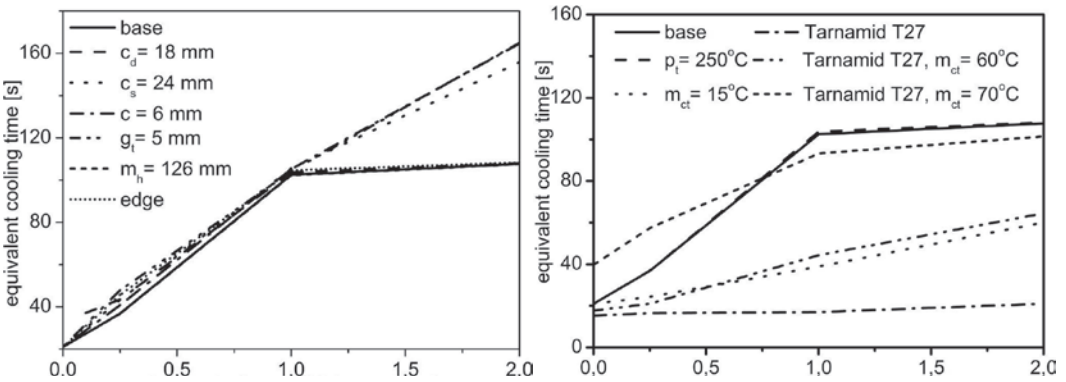

Fig. 8. Graph of the equivalent cooling time, in which the entire plastic material becomes solidified and the mold achieves the assumed cavity temperature.

Changing the plastic material temperature to 250°C gave results similar to the base model. Reducing the temperature of the coolant liquid to 15°C allowed to cool the injection mold down to the assumed temperature much faster (a nearly 50% cooling time reduction). When using Tarnamid, setting the coolant liquid temperature to 70°C resulted in a correlation between the cooling time and lime scale deposit layer thickness more similar to the correlation for Moplen at 25°C. The use of liquid with a temperature 10°C lower resulted in a correlation similar to using Moplen with a temperature of 15°C. This means that it is not the coolant liquid temperature, but relative difference between the assumed mold temperature and liquid temperature which has a significant impact on the required cooling time. The use of a cooling liquid of 25°C for Tarnamid resulted in the cooling time of slightly over 13 seconds (with approx. 19,5 s for Moplen), which is connected with the solidification temperature of Tarnamid. Even with a 2 mm layer of lime scale, the require cooling time was slightly over 20 s (while the molded piece solidification time was approx. 19,2 s).

4. Conclusion

The conducted analyses have shown a significant impact of lime scale deposited in the cooling system on the injection mold's utilization. Due to its low conductivity, the deposited scale causes issues with proper heat dissipation from the injection mold.

In the case of a thicker layer of lime scale (1 mm), its very significant impact on all studied aspects was observed. From the perspective of utility and reliability of the injection mold, the most important factor is the temperature of the mold, which is subject to expansion as a result of temperature increases. This may lead to issues with the fitting of moving elements, leading to reduction of the mold's longevity as a tool. On the other hand, the distribution of temperatures on the cavity surface and cooling efficiency had a very significant impact on the reliability of the injection mold as a tool, which is intended to mold the product within a specified time and with specified parameters. A non-uniform temperature distribution on the mold's surface may lead to increased molded piece deformations and resulting problems with maintaining tolerances. An inefficient cooling system extends the process duration and results in the molded piece not solidifying correctly after removal from the mold, which also causes further deformations. Changes to the mold's dimensions as a result of increasing its average temperature will impact individual dimensions, which ma cause failure to maintain the previously assumed tolerances.

Calculations have shown that the plastic material temperature, distance of the canals to the mold surface, as well as size of the mold have a minor impact on the course of the cooling process. This means that the use of an excessively large injection mold will result in additional issues with dimensional tolerance. A larger

impact was recorded for the molded piece thickness due to the fact of a larger amount of heat needing to be dissipated from the plastic material, which has insulating properties. A very large impact, on the other hand, was shown for the diameter of cooling canals, especially in conditions of hindered heat dissipation, similarly as for the number of cooling canals. In the conducted analysis spreading out the cooling canals resulted in some of them being located in a large distance from the molded piece, therefore, in term of industrial practice, they would not be drilled. Their absence together with the increase of the lime scale deposit thickness, caused a much larger increase in the average injection mold temperature, in comparison to instances in which such cooling canals had been drilled. This shows that the introduction of additional cooling canals in areas which would normally not take part in heat dissipation, in the case of the appearance of lime scale may reduce its negative impact on the injection mold's utilization.

The analysis takes into consideration two types of plastic materials in order to compare their influence in connection with different coolant liquid temperatures. For a material requiring a high mold temperature there is a theoretical possibility of applying a much colder cooling liquid compared to the assumed mold temperature, which results in significant reduction of the cooling time, reduction of the average mold temperature, but would introduce non-uniformity in temperature distribution in the molding cavity, which in the case of more complex molded pieces would result in deformations. In the case of a plastic material requiring lower mold temperatures, reduction of the coolant liquid temperature is problematic due to the increased cost of the cooling process of the medium itself.

It is necessary to be aware that analyses have been conducted for a very simple molded piece geometry, which is a base and edge. Currently elements manufactured using the injection mold method are very complex, often featuring thick walls (especially in the automotive industry), due to which in an actual situation of average mold temperature increases may reach even several dozen degrees. In certain circumstances a complex system of ejectors makes it impossible to use an efficient cooling system, due to the fact that cooling canals would intersect with the ejector locations. This means that the magnitude of linear dimension changes may reach up to 0,5 mm, which would have a significant negative impact on the utility of the injection mold, which is characterized by very narrow dimensional tolerances.

References

1. Autodesk Inc., 11 factors for efficient mold cooling - Balancing speed and quality to reduce cycle time, 2016.
2. Autodesk Inc., Autodesk Moldflow Insight, San Rafael, CA. 94903, USA, 2017.
3. Bott T B. Fouling of Heat Exchangers, Amsterdam-Lausanne-New York-Oxford-Shannon-Tokyo: Elsevier, 1995.
4. Gane P A C, Cathy J, Ridgway C J, Schoelkopf J. Heat transfer through calcium carbonate-based coating structures: observation and model for a thermal fusing Process. Omya Development AG, University of Maine.
5. Garrett-Price B A, Smith S A, Watts R L, Knudsen J G. Fouling of Heat Exchangers: Characteristics, Costs, Prevention, Control, and Removal, Parkdridge, NJ: Noyes Publications, 1985
6. Kelly A. L., Mulvaney-Johnson L., Coates P. D., Effect of copper alloy mold tooling on cycle time and product quality. 67th Annual Technical Conference of the Society of Plastics Engineers 2009, Brookfield, Conn: Society of Plastics Engineers, 2009 .
7. Kocsis D. Modeling and vibration analysis of lime scale deposition in geothermal pipes. Environmental Engineering and Management Journal, 2014; 13 (11): 2817-2824.
8. Mostafa M.A. Fouling of Heat Transfer Surfaces, Heat Transfer - Theoretical Analysis, Experimental Investigations and Industrial Systems, Prof. Aziz Belmiloudi (Ed.), InTech 2011, https://doi.org/ 10.5772/13696.
9. Pepliński K, Bieliński M. Prototype modular inserts to boost the cooling of mold cavities in polymer processing. Polimery, 2015; 60 (11-12): 747-750 http://dx.doi.org/10.14314/polimery.2015.747.
10. Saifi A, Amiri A E, Elhassnaoui A, Obbadi A, Errami Y, Sahnoun S. Thermography model for detecting the scale thickness in water pipes. 3rd International Renewable and Sustainable Energy Conference (IRSEC), pp. 1-4, Marrakech, 2015.
11. Shah R K, Sekulic D P. Fundamentals of Heat Exchanger Design, Hoboken, NJ: John Wiley & Sons, 2003.
12. Sikora R., Processing of Macromolecular Plastic Materials, Warszawa: Wydawnictwo Edukacyjne Zofii Dobkowskiej (Zofia Dąbkowska Educational Publishing), 1993.
13. Zhang Z, Zhang B, Li Z. Study on the prediction model of heat transfer coefficient during tube digestion. Light Metals 2015: ,http://doi.org/10.1007/978-3-319-48248-4_6.

Przemysław POSZWA
Marek SZOSTAK
Faculty of Mechanical Engineering and Management
Poznan University of Technology
ul. Piotrowo 3, 60-965 Poznań, Poland

E-mails: przemyslaw.b.poszwa@doctorate.put.poznan.pl, marek.szostak@put.poznan.pl

Article citation info:
ROMANIUK M. Optimization of maintenance costs of a pipeline for a V-shaped hazard rate of malfunction intensities. Eksploatacja i Niezawodnosc – Maintenance and Reliability 2018; 20 (1): 46–56, http://dx.doi.org/10.17531/ein.2018.1.7.

Maciej ROMANIUK

OPTIMIZATION OF MAINTENANCE COSTS OF A PIPELINE FOR A V-SHAPED HAZARD RATE OF MALFUNCTION INTENSITIES

OPTYMALIZACJA KOSZTÓW EKSPLOATACYJNYCH RUROCIĄGU DLA V-KSZTAŁTNEJ FUNKCJI INTENSYWNOŚCI USZKODZEŃ*

In this paper I focus on an evaluation of maintenance costs of a water distribution system (WDS), if a concept of a value of money in time is taken into account. Contrary to more classical approaches, instead of a constant yield, a strictly stochastic process (i.e., the one-factor Vasicek model) of an interest rate is assumed. Such an assumption presents uncertain, future behaviour of the yield in a more correct, realistic way. Moments of failures of connections in a WDS are generated using the Monte Carlo simulations via a new kind of a convex hazard rate function (HRF), which is proposed in this paper. Moreover, quality of a pipeline and a number of previous failures have direct influence on statistical properties of this introduced HRF. Apart from an analysis of the simulated output (like the maintenance costs), the Kiefer-Wolfowitz method is used for a better adjustment of one of parameters of a WDS – deterministic and unconditional replacement (i.e., planned replacement) time of each pipe. Algorithms, for both the simulations of the failure moments for the introduced HRF and the optimization step, are also provided. Additionally, some examples of a WDS for a crisp and a fuzzified settings are statistically analysed.

Keywords: *water distribution system, maintenance costs, convex hazard rate function, Monte Carlo simulations, present value of money, Kiefer-Wolfowitz method, one-factor Vasicek model.*

W niniejszej publikacji skupiam się na obliczeniu kosztów eksploatacji wodociągu (water distribution system – WDS), jeśli pod uwagę zostanie wzięta wartość pieniądza w czasie. W przeciwieństwie do klasycznego podejścia, zamiast stałej wartości stopy procentowej, zakładam stochastyczny proces stopy procentowej (w postaci jednoczynnikowego modelu Vasicka). Założenie to przedstawia niepewne, przyszłe zachowanie stopy procentowej w bardziej dokładny i realistyczny sposób. Momenty awarii połączeń w WDS generowane są z wykorzystaniem metody Monte Carlo poprzez zastosowanie nowego typu funkcji intensywności uszkodzeń (hazard rate function – HRF), który zaproponowany został w niniejszej publikacji. Ponadto, jakość połączenia oraz ilość wcześniejszych uszkodzeń ma bezpośredni wpływ na statystyczne właściwości wprowadzonej HRF. Oprócz analizy wygenerowanych za pomocą symulacji wyników (takich jak koszty eksploatacji), użyta została metoda Kiefera-Wolfowitza w celu lepszego dopasowania jednego z parametrów WDS – deterministycznego i bezwarunkowego momentu wymiany każdego z połączeń (czyli wymiany planowanej). Zaprezentowane zostały również algorytmy zarówno dla symulowania momentów uszkodzeń przy użyciu zaproponowanej HRF, jak i dla kroku optymalizacyjnego. Ponadto, wykonana została analiza statystyczna kilku przykładów WDS dla dokładnych („crisp") i rozmytych („fuzzy") wartości parametrów.

Słowa kluczowe: *system dystrybucji wody, koszty eksploatacji, wypukła funkcja intensywności uszkodzeń, wartość obecna pieniądza, metoda Kiefera-Wolfowitza, model jednoczynnikowy Vasicka.*

1. Introduction

From the customers' point of view, the main aim of a water distribution system (which is further abbreviated as WDS) is to deliver water, moreover – water of desirable quality and in necessary quantity. Therefore, different maintenance services have to be performed, e.g., broken or simply malfunctioned pipes or other parts of a WDS should be repaired or replaced. Because water is an indispensable good for humans, therefore also scientific literature devoted to reliability of water distribution systems is abundant. Firstly, let us mention reviews of various methods, approaches and literature, which can be found in, e.g., [15,28,29]. The papers themselves are very varied – some of them concern hydraulic and physical characteristics of parts of a WDS (see, e.g., [4,17]), other discuss rather a "macro-management" of a WDS rehabilitation problem (see, e.g., [12,22]) or only a "micro-management" scale (e.g., for a single building, see [1]). Even some monitoring systems for failures detection in a WDS are proposed (see, e.g., [23]).

Usually, if maintenance costs for a WDS are considered, planning for a relatively long-time horizon should be taken into account. Such a time interval covers 20, 50 or even 60 years (see, e.g., [12]). Of course, one unit of money, which is paid now, and the same unit in 50-60 years, are not equal. Therefore, an influence of a future / present value of the money onto a calculation of the maintenance costs should be taken into account. However, most of the authors apply only a constant interest rate, as a discount factor, to calculate a present value of future cash flows. Such an assumption is, of course, too strong and unrealistic in practical situations. Therefore, in this paper I adopt a more realistic and complex model – a variable interest rate, which is described by the widely known one-factor Vasicek model.

Moreover, some model for intensities of malfunctions of parts of a WDS has to be assumed. As it is proposed in literature, it can be based on selected physical aspects of a pipe and numerical equations (like the Hazen-Williams equation, see, e.g., [12]), it can be described with some type of Markov or semi-Markov process (see, e.g., [13, 16, 26]) or malfunctions are randomly generated using a hazard rate function (HRF). A

(*) Tekst artykułu w polskiej wersji językowej dostępny w elektronicznym wydaniu kwartalnika na stronie ***www.ein.org.pl***

multilateral review of various HRFs can be found in [29]. In this paper I propose a new kind of a HRF, which can be easily adapted to real-life data and which is very efficient during the Monte Carlo simulations.

Very often in literature, some optimization procedure for minimization of the maintenance costs of a WDS is proposed. For example, the total costs of a renewal, risk and an unavailability of a WDS is given as one function of time and then minimised (see, e.g., [24]), different scenarios with and without replacement of pipes for the installation and repair costs with a damage and inconvenience cost multiplier are considered (see, e.g., [18]) etc. In the following, I also propose an optimization approach. During this procedure, the Kiefer-Wolfowitz algorithm is applied to find a minimum of the maintenance costs, if an unconditional replacement age of a pipe is our variable parameter.

Also some model of the previously mentioned maintenance costs has to be adopted. In literature, these costs are related to various sources and models, like a rehabilitation of a pipe and breakage repair costs (see, e.g., [12]), an extra energy, water losses and a loss of revenues (see, e.g., [11]) etc. In this paper the costs are modelled using their constant and variable part. This second element is related to time, which is necessary to conduct a repair or a replacement of a malfunctioned pipe. However, in some papers such a concept (i.e., time of a service) is completely neglected. Such a simplification is possible (see, e.g., [29] for a more detailed discussion), but usually the relevant period is modelled by some random variable (like the exponential distribution, see, e.g., [11]). In the following, I also assume, that a time, which is necessary for a repair or a replacement, is given by some random distribution.

This paper can be seen as a further development of some ideas, which were previously discussed in [25,26], but it is also a proposition of completely new ones. Hence, my current contribution is fourfold.

Firstly, I propose a new kind of a hazard rate function, which describes the intensities of malfunctions of pipes in a WDS. Many different HRFs were discussed in literature, however, each of them has some significant disadvantages (see, e.g., [29] for a comprehensive review). The HRF, which is introduced in this paper, has some appealing features. It is V-shaped, so it models two different states of a connection: a starting burn-in period (immediately after a repair or an installation of a pipe) and a later wear-out period (when an intensity of malfunctions for a connection is higher than during its starting phase). This HRF also depends on a number of previous repairs of the given pipeline, so an increasing deterioration of a material, which is caused by recurring stresses of repairs, can be taken into account. Moreover, a relevant algorithm for a random generation of intervals of times between malfunctions is numerically very efficient and straightforward. Therefore, the Monte Carlo simulations, which are then based on this HRF, can be directly applied to simulate behaviour of a whole WDS. Furthermore, the parameters of this HRF can be easily fuzzified, which enables us to introduce an additional source of an imprecision and an uncertainty, other than a strictly probabilistic one. These features should be highlighted, as important ones, when the introduced hazard rate function is compared to other HRFs.

Secondly, I adapt the Kiefer-Wolfowitz algorithm to find a minimum of the total maintenance costs. This method allows me to decide about an optimal value of a deterministic and unconditional replacement age, i.e., when it is better to replace a connection instead of its next, future repair. Because the mentioned algorithm directly utilizes stochastic nature of simulations, the Monte Carlo method can be directly used to calculate necessary estimators in this approach. In this paper, I focus on the unconditional replacement age as a variable, which is considered in the optimization problem, but the presented approach can be extended to other parameters, which are important for decision makers. Because an output, which is simulated in the analysis, behaves in a very varied and unpredictable way, I propose some practical alternation of the standard Kiefer-Wolfowitz algorithm. As it is pointed out in presented numerical examples, this optimization procedure can significantly lower the maintenance costs.

Thirdly, apart from a crisp case, I discuss a possible fuzzifaction of the parameters of the introduced HRF and of a model of the costs. As it is known (see, e.g., [3,6]), data can be imprecise and uncertain in real life situations. Moreover, sometimes it can not be appropriately modelled, if only a probabilistic approach is used. Therefore, I further develop an idea, which was discussed in [26], and some parameters of the assumed models are described by fuzzy numbers. It means, that they are not completely precise (i.e., "crisp") but they are, in some way, imprecise ("near to / about") and can be given as experts' opinions (even in a form of linguistic variables). For example, a cost of a repair is rather stated as "about 50 thousand (some unit of money)", than as a total and accurate value before this repair will take place. And a fuzzy setting is widely used in an analysis of possible financial decisions (see, e.g., [20,21]).

Fourthly, in contrary to [25,26], a more sophisticated model of time intervals of transitions between the states of a pipeline is proposed now. The intervals between the malfunctions are generated using the introduced HRF, and the times of repairs and replacements can be drawn from various probabilistic distributions. For a simplicity of the analysis, I focus on the exponential distribution, but other densities can be easily applied in the proposed simulation approach. Moreover, this model of the states is directly related to a model of costs of maintenance services. I distinguish two types of these costs (separately for a repair and a replacement) with two parts for each of them – a constant part (which is independent of length of time of a service) and a variable part (which depends on a random value of time of a repair or a replacement). Therefore, the considered model is closer to practical situations.

It should be pointed out, that the stochastic model of the interest rate (i.e., the one factor-Vasicek model, which is assumed in this paper) is directly embedded into the Monte Carlo simulations, as in [26]. To the best knowledge of the author, such an approach is still a new idea, which is not even considered in other papers. Whereas, there are significant differences in estimated values of costs and in other important results between models with a constant yield and with a variable discount factor, which is, of course, a more realistic assumption. Some of these discrepancies were already highlighted in [26]. Now I continue this analysis and show, that a simplified approach (i.e., with a constant yield) leads to different solutions and statistical results for the calculated maintenance costs. Therefore, future decisions can be also invalid, if such a too simplified model is assumed.

This paper is organized as follows. In Section 2, a new type of a hazard rate function, which describes times of the failures of a connection, is presented. A random generation procedure for a relevant density, which is based on this HRF, is also discussed. In Section 3, a model of possible states of an each connection with an additional parameter – deterministic and unconditional replacement age – is introduced. Section 4 is devoted to a description of maintenance costs, which are divided into constant and variable parts. Section 5 presents the Kiefer-Wolfowitz algorithm, which is then applied to optimize the discounted value of the maintenance costs in examples in Section 6. Apart from a numerical analysis of an example in a crisp case, a proposition of fuzzification of some parameters of the model is also examined using the Monte Carlo simulations. Results, which are obtained in these examples, are statistically summarized then. The paper is concluded in Section 7 with some final remarks.

2. Model of failure intensities

Let us suppose, that a WDS is modelled by a graph of connections G. In this graph, each connection (i.e. a pipeline which is a part of the whole WDS) is represented as an edge, and possible sources or outflows are denoted by nodes. In the following, I focus only on the

edges of the graph G, i.e. the connections of the considered WDS. Let us assume, that these connections behave in a statistically independent way, i.e. there is no "information flow" between the connections and time of a malfunction of one pipe does not influence on quality and possible malfunctions of other connections.

Firstly, I assume that times of the failures for an each connection are described by a hazard rate function (HRF or simply a hazard function) $\lambda(x|n_r)$, given by the formula:

$$\lambda(x|n_r)=\begin{cases}-a_0 x+a_0 x^*+y^*+\alpha_r n_r & if \quad x\in\left[0,x^*\right)\\ a_1 x+y^*-a_1 x^*+\alpha_r n_r & if \quad x\geq x^*\end{cases}, \qquad (1)$$

where $a_0>0, a_1>0, x^*>0, y^*>0, \alpha_r>0$ are parameters, which are related to the given type of a connection. Strictly speaking, such a HRF has a V-curve, linear shape (see Figure 1), for which:

- $-a_0$ is a directional component of a descending, linear part of the HRF (i.e., a left hand side of the function, for which $x\in\left[0,x^*\right)$),
- a_1 is a directional component of an ascending, linear part of the HRF (i.e., a right hand side of the function, for which $x\geq x^*$),
- $\left(x^*,y^*\right)$ is a point, where the HRF becomes an ascending linear function, instead of being a descending one,
- α_r is a parameter of deterioration of the connection related to a single, previous malfunction,
- n_r is a number of previous malfunctions of the connection, if there were repairs afterwards.

It is assumed that, when some connection is replaced with a completely new component, then $n_r=0$ is set for such a part. Hence, the parameter α_r reflects a level of fatigue, which is caused by previous malfunctions and repairs, without a replacement of such a connection. It directly increases a value of the hazard function $\lambda(x|n_r)$. The point $\left(x^*,y^*\right)$, and especially the value x^*, depends on time, when the HRF (1) changes its behaviour. In this point, instead of a burn-in period after some repair (or an installation of a new pipe), the connection reaches its wear-out period (see also, e.g., [5] for a more detailed descriptions of such states). It means, that for the first part of (1) an intensity of the malfunctions decreases, and for the second part this value increases with passing time, which approximates real-life situations in better way. Hence, the proposed function (1) can be used in straightforward manner to describe the intensity of malfunctions, taking into account two completely different quality states and progress of connection fatigue, which is also related to the number of previous repairs n_r. Therefore, this HRF can be better adjusted to real-life data.

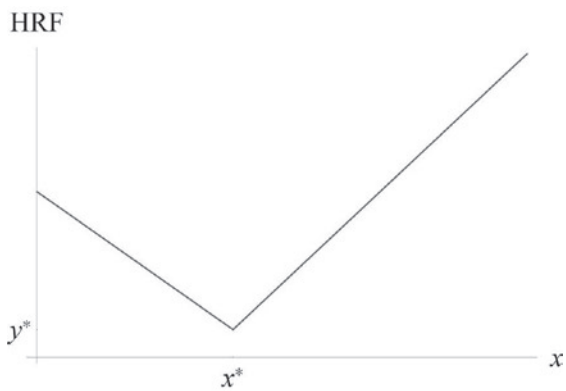

Fig. 1. Exemplary plot of the introduced HRF

From now on, for a simplicity of formulas, I use abbreviations:

$$b_0=a_0 x^*+y^*+\alpha_r n_r \;,\; b_1=y^*-a_1 x^*+\alpha_r n_r \;.$$

For a HRF, we have a general formula:

$$\lambda(x)=\frac{f(x)}{R(x)},$$

where $f(x)$ is a pdf (probability density function), $R(x)=1-F(x)$ and $F(x)$ is a cdf (cumulative density function), then in the case of (1), we get:

$$f(x)=\begin{cases}(-a_0 x+b_0)\exp\left(\frac{1}{2}a_0 x^2-b_0 x\right) & if \quad x\in\left[0,x^*\right)\\ (a_1 x+b_1)\exp\left(-\frac{1}{2}a_1 x^2-b_1 x-c_1\right) & if \quad x\geq x^*\end{cases}, \qquad (2)$$

where:

$$c_1=-\frac{1}{2}a_1\left(x^*\right)^2-b_1 x^*-\frac{1}{2}a_0\left(x^*\right)^2+b_0 x^*.$$

An exemplary plot of this density can be found in Figure 2. As it is seen, $f(x)$ is a continuous function with a visible point of a change of its behaviour (which is given by the parameters $x^*=0.5, y^*=1$ in this case).

Fig. 2. Exemplary plot of the introduced density

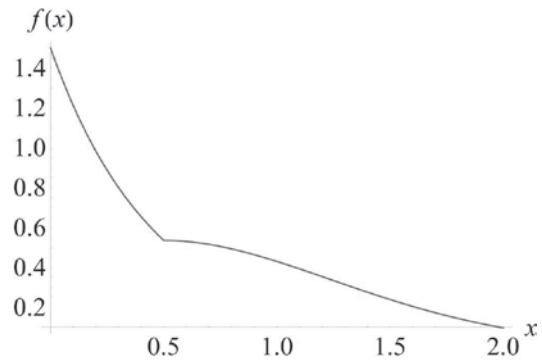

In Section 6, an analysis of a simulated output for times of malfunctions given by the density (2) is presented. Therefore, it is necessary to provide an efficient algorithm for a generation of random variables for such a pdf. It can be done using the composition method and the inversion method (see, e.g., [27] for an introduction and a review). In the composition method, a pdf $f(x)$ is decomposed as:

$$f(x)=\sum_{i=1} f_i(x)p_i \;,$$

where, for an each $i = 1, 2, \ldots$, $f_i(x) \geq 0$ is some density and $p_i \geq 0$ is a discrete probability. In the case of (2), we have:

$$p_1 = P\left(X \in \left[0, x^*\right)\right) = 1 - \exp\left(\frac{1}{2} a_0 \left(x^*\right)^2 - b_0\, x^*\right)$$

$$p_2 = P\left(X \geq x^*\right) = 1 - p_1, \tag{3}$$

and the pdfs $f_1(x)$ (for $x \in \left[0, x^*\right)$), $f_2(x)$ (for $x \geq x^*$) lead to relevant inversions of their cdfs, which are equal to:

$$F_1^{-1}(y) = \frac{b_0 - \sqrt{b_0^2 + 2a_0 \ln(1 - p_1 y)}}{a_0},$$

$$F_2^{-1}(y) = \frac{-b_1 + \sqrt{\left(a_1 x^* + b_1\right)^2 - 2a_1 \ln(1 - y)}}{a_1}. \tag{4}$$

Therefore, a simulation of random times of the failures is straightforward (see Algorithm 1). Moreover, because the inversion method is applied, the whole algorithm is numerically very efficient. None of the randomly generated points are rejected, as it is commonly seen in, e.g., the ROU (ratio-of-uniforms) method.

Algorithm 1 (Generation procedure for the HRF)
Input: A set of the parameters of the HRF (1).
Output: A random time of a failure *X*.

Calculate p_1, p_2 *, which are given by (3);*
Generate independent random values U, Y *from the uniform standard distribution* $U[0;1]$*;*
if $U \leq p_1$
$X = F_1^{-1}(Y)$ *(see (4));*
else
$X = F_2^{-1}(Y)$ *(see (4));*
end
return *X*

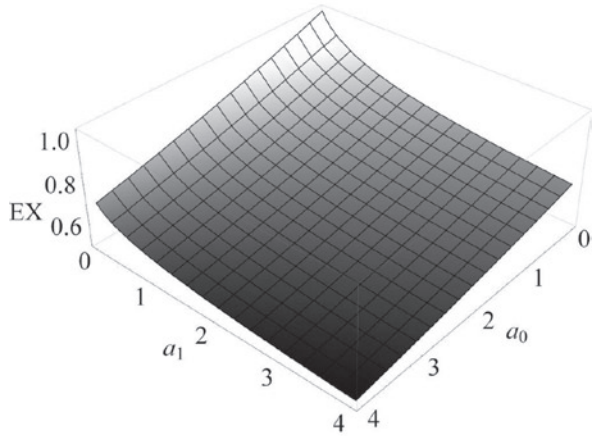

Fig. 3. Plot of the expected value (EX) for the introduced density as a function of a_0 *and* a_1 *.*

Because of a few parameters, which describe the formula (1), the introduced model of time of a failure can be applied in many various cases. Exemplary plots of the expected values for the relevant density (2) can be found in Figure 3, Figure 4 and Figure 5. As it is seen, the expected value of time of a failure is both a linear and non-linear function, which simplifies an adjustment to complex real-life data.

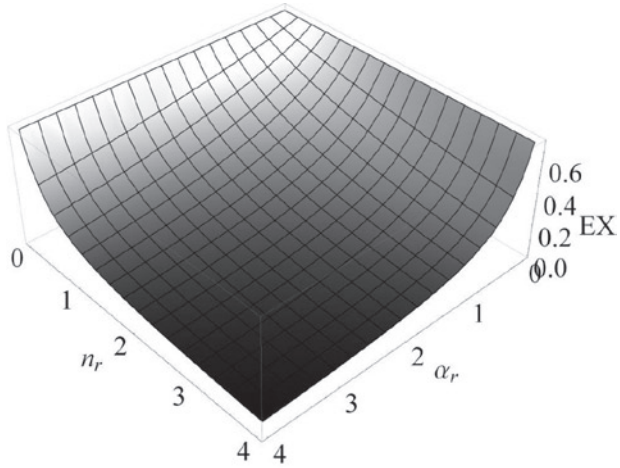

Fig. 4. Plot of the expected value (EX) for the introduced density as a function of α_r *and* n_r *.*

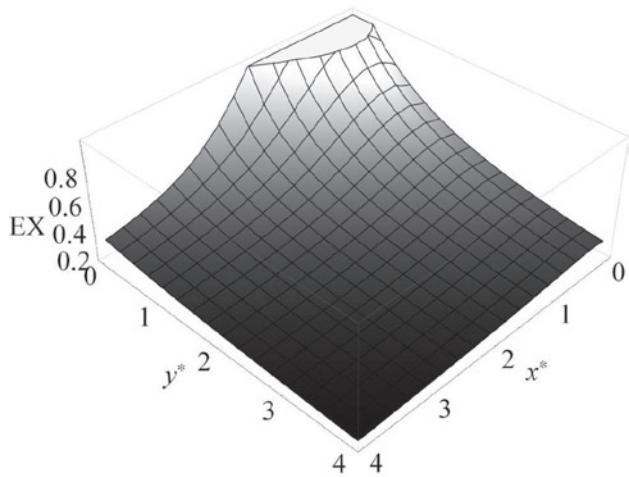

Fig. 5. Plot of the expected value (EX) for the introduced density as a function of x^* *and* y^**.*

3. States of a connection

An each connection in time *t* can be in one of the following states: *working, under repair, under replacement*. It means, that immediately after some failure, a connection is repaired or replaced by a new one.

A random length of working time WT_i, after a repair or a replacement of the pipe and before a next malfunction, is given by (2). A length of repairing time RT_i (after a malfunction, when a connection is being repaired) can be modelled by various random distributions, e.g. the exponential distribution or the lognormal one. Of course, this distribution and its parameters should be fitted to real-life data, e.g. using statistical methods. The same applies for a length of replacement time PT_i (i.e., after a malfunction, when a connection is being replaced with a new one).

As in [26], I introduce a deterministic and unconditional replacement age P^*. This value is used to decide, if instead of one more repair, the connection in question should be rather replaced. It means that, when:

$$\sum_{i=1}^{j} WT_i + RT_i > P^*, \tag{5}$$

where $WT_1,\ldots,WT_j$ and $RT_1,\ldots,RT_j$ are working and repairing times after the last replacement of a connection, then this connection is replaced with a new one. Afterwards, $n_r = 0$ is set in (1), so such a replacement "restarts" a deterioration process.

4. Maintenance costs

As it was noted in Section 2, it is possible to directly simulate the periods of the working times WT_i of the considered connection for the pdf given by (2). Also, if numerically feasible distributions for the repairing times RT_i and the replacement times PT_i are selected (like, e.g., the lognormal distribution), then the Monte Carlo approach can be applied. Furthermore, the replacement condition (5) can be easily embedded in such a setup, without a necessity of conducting of complex theoretical probabilistic calculations.

Hence, the MC approach can be applied to generate the subsequent states of each connection *j*, and then, in a similar way, to simulate behaviour of the whole WDS. From now on, I assume, that these connections behave in a statistically independent way. However, if there is some kind of dependency, the MC procedure can be also used. Easily seen, apart from WT_i, RT_i and PT_i, exact times of the malfunctions can be found, when the necessary maintenance services (i.e., replacements or repairs) begin. In the following, these times are denoted by $t_1, t_2, \ldots$.

In this paper I focus only on the maintenance costs related to the replacements and the repairs. Of course, other types of costs (like costs of water losses, loss of revenues etc. – see, e.g., [5,11,12,18]) are commonly considered in the literature. Among others, I should also mention restoration and diagnostic costs. They are very important, especially for long time horizon of an analysis. Some of the mentioned costs can be easily taken into consideration using the MC approach. It seems, that this is also possible for the restoration and the diagnostic costs. However, due to nature of further assumptions in this paper, these costs can be rather related to the HRF itself, instead of time of a service (like a repair or a replacement). For example, after a restoration of a connection, a value of n_r can be lowered or values of a_0 and a_1 can be respectively changed for this connection. And an aim of such a change would be to increase length of a period to a next malfunction given by (1). But still the simulation approach is appropriate in this case. Of course, incorporation of other types of the costs (like restoration costs) can have some influence on the obtained results.

I assume, that the mentioned costs depend on a type of a service (i.e., if it is a replacement or a repair), length of such a service and a type of the considered connection. Therefore we have:

$$c^{(j)}(t_i) = c^{(j)}_{R,const} + c^{(j)}_{R,Var}(RT_i)$$

or

$$c^{(j)}(t_i) = c^{(j)}_{P,const} + c^{(j)}_{P,Var}(PT_i),$$

where $c^{(j)}(t_i)$ denotes a total sum of costs for the given j-th connection and time t_i, when a necessary service begins, $c^{(j)}_{R,const}$ is a constant value independent of length of a period for a repair (or for a replacement in the case of $c^{(j)}_{P,const}$), i.e. it is a fixed cost, and $c^{(j)}_{R,Var}(.)$ denotes a variable cost of a repair (or a replacement for $c^{(j)}_{P,Var}(.)$), i.e. some function of length of this service. If the MC approach is applied, then the variable costs can be modelled in various ways, e.g., an additional random distribution, which is related to RT_i or PT_i, can be used.

As it was mentioned, I assume that the value of money depends on time in the considered setting. Therefore, the concept of a present value (or a future value), which is widely known in financial mathematics, is applied (see, e.g., [7,27]). It is especially useful, if we are interested in a long time horizon T (like 20 or even 50 years) for which the estimated costs of the maintenance services should be calculated. And these costs, for different management decisions and possible scenarios, can be easily compared for the same, present time, i.e. $t = 0$. It leads to a straightforward way to select the best decision, taking into account a financial risk.

To calculate the present value of the total sum of the costs of repairs and replacements:

$$PV(c) = \sum_{i,j} PV\left(c^{(j)}(t_i)\right), \tag{6}$$

some model of an interest rate should be used, in order to find a discounting factor $PV(.)$ for each $c^{(j)}(t_i)$. In the following, the one-factor Vasicek model (see, e.g., [7]):

$$dr_t = a(b - r_t) + \sigma dW_t, \tag{7}$$

is used, where r_t is a value of the interest rate at time *t*, W_t is the standard Brownian motion, and a, b, σ are parameters of this model. Moreover, *b* characterizes a long term mean level (i.e. the trajectory of r_t is directed to this value during its long run), *a* reflects speed of reversion towards *b*, and σ is an instantaneous volatility (variability) of the trajectory introduced by the random component W_t.

In the MC setting, a relevant iterative scheme for a generation of increments Δr_t of the process (7) should be used (see, e.g., [7]). The values of r_t for the fixed moments $0 = t_0 < t_1 < \ldots < t_n$ are given by:

$$r_{t_{i+1}} = exp\left(-a(t_{i+1} - t_i)\right) r_{t_i} + b\left(1 - exp\left(-a(t_{i+1} - t_i)\right)\right) + \sigma\sqrt{\frac{1 - \exp\left(-2a(t_{i+1} - t_i)\right)}{2a}} Z_i,$$

where $Z_1, Z_2, \ldots, Z_n$ are *iid* samples from *N(0,1)*. Also a cumulative factor:

$$fv_{(t_i, t_{i+1})} = \int_{t_i}^{t_{i+1}} r_s ds,$$

which is necessary to evaluate the present value, can be easily approximated (see, e.g., [7,26,27] for a more detailed discussion).

As it is pointed out in [26], if a variable interest rate is assumed (like the one-factor Vasicek model in this paper), then obtained results

are different from an output for a model with a constant interest rate. I will also show these differences in examples in Section 6.

5. Optimization procedure

In numerical examples, which are presented in Section 6, I am interested in various statistical measures, which are important for an analysis of the maintenance costs. In practical situations, a decision maker is also confronted with different scenarios, concerning values of some parameters. Because of stochastic nature of the introduced process of the interest rate (7) and behaviour of the WDS itself, a relevant optimization procedure is necessary. There are various methods, which can be used to solve the mentioned min-max problem with a stochastic background (see, e.g., [9]). However, in the following, I apply the Kiefer-Wolfowitz (KW) algorithm (see, e.g., [2]) with some alternations, which are necessary for the considered setting.

In general, an iteration scheme of the KW algorithm is based on a formula:

$$X_{n+1} = X_n - a_n \left(\hat{f}\left(X_n + c_n\right) - \hat{f}\left(X_n - c_n\right) \right) / c_n \ , \tag{8}$$

where X_1 is an initial value, a_n and c_n are two real-valued, deterministic tuning sequences, and $\hat{f}\left(X_n + c_n\right)$, $\hat{f}\left(X_n - c_n\right)$ are estimators (which are usually based on the MC approach) of a goal function $f(.)$ for $X_n + c_n$ and $X_n - c_n$. The aim of the sequence (8), which is produced by this algorithm, is to minimize the value of $f(x)$, taking into account the decision parameter *x*. Speed and quality of a convergence to this minimum depend on the tuning sequences a_n and c_n (see, e.g., [2] for a more detailed discussion of some necessary requirements for these sequences).

Usually, the estimators $\hat{f}\left(X_n + c_n\right)$, $\hat{f}\left(X_n - c_n\right)$ are based on only single Monte Carlo samples, which are drawn from the relevant functions $f\left(X_n + c_n\right), f\left(X_n - c_n\right)$. But in some cases, a more sophisticated approach is necessary. As in the considered setting, a function $f(x)$ can behave in a very varied and unpredictable way, because of its stochastic nature. Therefore, the mentioned estimators, which are calculated as standard Monte Carlo averages, should be based on larger samples. Additionally, it can be profitable to store estimated values of $f(.)$ for previous steps of the algorithm, not only for the last one.

In the following, the numerical experiments are focused on an optimization of the maintenance costs, if the unconditional replacement age P^* is a decision parameter in (8). Strictly speaking, my aim is to find:

$$\min_{P^*} EPV(c) \ , \tag{9}$$

i.e. a minimum of the expected, present value of the total sum (6), if P^* is a decision parameter. From a practical point of view, the unconditional replacement age is very significant for a decision maker, especially if a long time horizon is taken into account. Of course, other characteristics of the WDS can be also treated as decision parameters, but the presented approach is applicable in these cases, too.

6. Example of numerical analysis

Now I apply the KW algorithm and the Monte Carlo simulations to find an optimum value of the unconditional replacement age P^*, which is a solution of the problem (9). In order to do this, I present a simplified example, but similar to a real-life case. In this analysis, the HRF, given by (1), is used to simulate times of the failures.

I will start from a general description of the parameters in Section 6.1. Then, in Section 6.2, I will present assumed numerical values of these parameters for a strictly crisp case. These values are used further, in Section 6.3, to find an optimal value of P^* in the considered optimization problem. Also some other statistical measures of the maintenance costs are estimated there. In Section 6.4, I will discuss possible problems with suboptimality of the obtained solution. A dependency between the assumed model of an interest rate and the optimal solution for P^* is also considered there. Then, in Section 6.5, I will recall basic definitions and notation concerning a fuzzy approach. This fuzzy approach will be used in two analyses afterwards: firstly, when some parameters of the introduced HRF are fuzzified (Section 6.6), and secondly, to decide, if the estimated output is more prone to impreciseness related to the constant or to the variable parts of the costs (Section 6.7). The results of all of the analyses will be summarized in Section 6.8. I will conclude this example with some remarks about a possibility of using the presented approach in practical application (Section 6.9).

6.1. General description of the parameters

Taking into account the previous considerations, the parameters of the whole model, which are used in simulations, can be divided into four groups:

1. parameters of the given type of the connection, which are related to the HRF given by (1), i.e. $a_0, a_1, x^*, y^*, \alpha_r, n_r$,
2. parameters, which depend on the type of the connection, its location etc., and they are related to the maintenance costs $c_{R,const}, c_{P,const}, c_{R,var}(.), c_{P,var}(.)$ or to the lengths of times of necessary services (i.e. repairs and replacements), like parameters of the random distributions for RT_i and PT_i,
3. parameters of the interest rate model, which are related to the financial setup (7), i.e. r_0, a, b, σ,
4. other parameters, like P^* and time range for the whole simulation *T*.

6.2. Applied parameters for the crisp case

Firstly, I focus on the strictly crisp case. In a further numerical analysis, to simplify my considerations, I model a WDS, which consists of 20 connections of one type of a pipe. Let us assume, that one year is time unit, and $x^* = 0.5, y^* = 1$. It means, that after half of a year, the HRF of the time to a failure changes its behaviour and after a burn-in period, a connection is in its wear-out period. In general, these values can be given by some expert. And such a source combines an insight knowledge with a classical, probabilistic approach.

I also assume, that $a_0 = a_1 = 1$. It means, that the linear parts in the function (1) lean at an angle of 45 degrees and, if there is no previous repairs, the expected value of time to a next malfunction is equal to 0.715 of a year. This value can be easily found using numerical software, like, e.g., *Mathematica*. As it is seen from (1), if there are some previous repairs, the whole HRF shifts upward by a multiplication of the parameter α_r and the number of the previous repairs n_r. Let us assume, that $\alpha_r = 0.2$. Then, after one repair, the time to a next malfunction is shortened to 0.635 (about 11%).

The next set of the parameters is related to the maintenance costs. In the following analysis, I apply one monetary unit assumption and set $c_{R,const}=1, c_{P,const}=3, c_{R,var}(t)=100t, c_{P,var}(t)=100t$. Then, the constant cost of a replacement is three times greater than the constant cost of a repair, and the variable costs are linear functions of time, which is necessary for these services. Also, the variable cost of a replacement is the same as the relevant cost of a repair, which is equal to about 0.274 per day (plus the constant cost, which is paid once). Additionally, time of the maintenance service should be also modelled in some way. In the following, I apply the exponential random variable to describe both the time of a repair (with a parameter λ_R for its density) and the time of a replacement (with a parameter λ_P, respectively). Other random distributions, like, e.g., the lognormal distribution, are also useful and have a significantly practical meaning in this area. In this case, I set $\lambda_R=365$ (so, the expected value of the time of a repair is equal to one day) and $\lambda_P=182.5$ (then, the expected value of the time of a replacement is equal to 2 days).

Of course, in practical applications the relevant parameters of the considered connections should be estimated from real data (or based on the experts' opinions).

The last group of the parameters, which is mentioned in Section 6.1, describes the interest rate model. For the one-factor Vasicek model, which is analysed in this paper, it is assumed that

$$a=0.1, b=0.05, r_0=0.04, \sigma=0.001$$

and a very long fifty years horizon of the financial analysis of the maintenance costs is considered (i.e., $T=50$). Therefore, comparing with [26], even longer time period is taken into account.

6.3. Results of the optimization procedure in the crisp case

Now, when all of the necessary parameters are set, the KW algorithm for finding the solution of the problem (9) can be started.

In the following analysis, I use $P_0^*=5$ as an initial value. As it was mentioned in Section 5, because of stochastic nature of the estimators $\hat{f}\left(P_n^*+c_n\right)$, $\hat{f}\left(P_n^*-c_n\right)$, the KW algorithm has to be slightly modified. Therefore, to calculate the values $\hat{f}\left(P_n^*+c_n\right)$, $\hat{f}\left(P_n^*-c_n\right)$, $m=100000$ simulations are conducted for each of them and the relevant Monte Carlo averages are found.

After 50 steps of the KW algorithm, an optimal value of P^*, which solves the problem (9) is achieved. In the considered case, it is equal to 3.58. Now, let us compare various statistical measures of the maintenance services for this optimal value $P^{**}=3.58$ and the starting point $P_0^*=5$. I examine an estimator of the discounted costs of services ($\widehat{PV}(c)$), an average number of repairs ($\bar{x}_R$) and unconditional replacements ($\bar{x}_P$), a minimum cost of a repair ($\min c_R$) and an unconditional replacement ($\min c_P$), an average cost of repairs ($\bar{c}_R$) and replacements ($\bar{c}_P$), a maximum cost of a repair ($\max c_R$) and a replacement ($\max c_P$), a standard deviation of costs of repairs ($sd(c_R)$) and replacements ($sd(c_P)$).

As it is seen from Table 1, ($\widehat{PV}(c)$) is reduced about 3.39%, if the optimal value of P^* is used and a value of $\bar{x}_R$ is reduced even more, about 14.21%. It means, that the overall discounted costs are now smaller and the repairs are more rare. In contrary, a value of $\bar{x}_P$ is greater for P^{**} about 44.44%. Therefore, in this case, the more often unconditional replacements lead to a decrease of the number of repairs. Statistics for the cost of a single repair or a replacement are very similar for the both values of P^*, so they do not affect the obtained conclusions.

Table 1. Comparison of statistical measures of the maintenance services for the optimal value and the starting point

Measure	$P^{**}=3.58$	$P_0^*=5$
$\widehat{PV}(c)$	1307.52	1353.36
$\bar{x}_R$	1929.56	2266.41
$\bar{x}_P$	260	180
$\min c_R$	1	1
$\max c_R$	6.39567	6.22472
$\bar{c}_R$	1.27371	1.27373
$sd(c_R)$	0.273725	0.273755
$\min c_P$	3	3
$\max c_P$	12.3977	12.4351
$\bar{c}_P$	3.54815	3.54807
$sd(c_P)$	0.547971	0.548069

6.4. The optimization procedure – additional remarks

Of course, if the KW algorithm is applied, it is possible, that instead of an optimal point, some suboptimal value is found. However, it is not a case in the considered example. In Figure 6, $\widehat{PV}(c)$ is plotted as a function of P^* and denoted by circles. As it is seen, this function has a clear U-shape. On the other hand, Figure 7 allows us to analyse behaviour of the averages $\bar{x}_R$ (a plot denoted by squares)

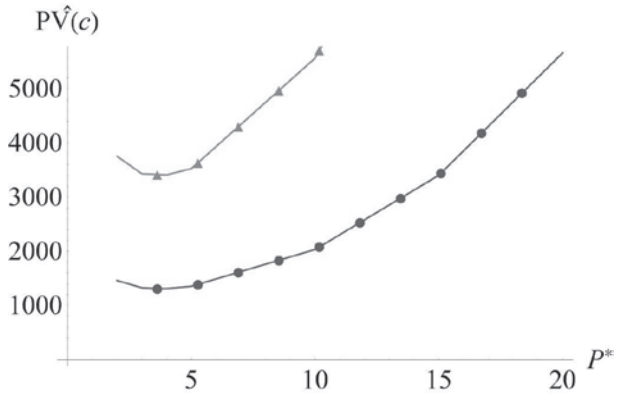

Fig. 6. Plot of $\widehat{PV}(c)$ for the one-factor Vasicek model (circles) and a nominal value (triangles) as a function of P^*

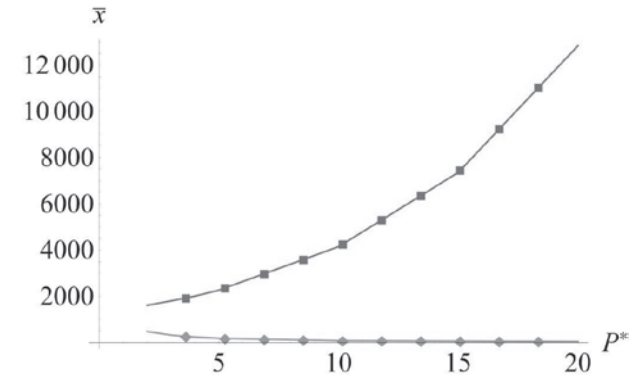

Fig. 7. Plot of $\bar{x}_R$ (squares) and $\bar{x}_P$ (diamonds) as functions of P^*

and $\bar{x}_P$ (a plot denoted by diamonds). The average number of repairs grows rapidly fast, if it is compared to a slow decrease of the average number of replacements. Then, clearly, it is fruitful for a decision maker to choose the calculated optimal value of P^*, instead of greater or lower one.

It was noticed in [26], that if a nominal value of the cash flow or a model with a constant yield is used, this leads to an incorrect estimation of the costs of the maintenance services. Because now I consider an optimization approach, a similar problem should be formulated – if other optimal value of P^* will be found, when the model, which describes the cash flows, is changed? I apply the KW approach also for the model with nominal values of the cash flows (i.e., a value of one unit of money is constantly the same, there is no discounting). Then, the optimal value of P^* is calculated as 3.34, which is about 6.7% lower than $P^{**} = 3.58$.

Also averages of the costs can be compared. In Figure 6, apart from $\widehat{PV}(c)$, for the one-factor Vasicek model, a similar average for a nominal value of the cash flow as a function of P^* is plotted and denoted by triangles. As it is easily seen, if a value of money is not taken into account, the nominal average cost of the maintenance services is overestimated and the optimal value of P^* is shifted to the left hand side.

6.5. Fuzzy approach – basic notation and definitions

As it is noticed in many papers (see, e.g, [6,8,10,26]), some sources of impreciseness can be easily modelled by a fuzzy approach, so a value of such an imprecise parameter can be based on expert's knowledge. This approach is especially very important, when data is sparse and various data analysis methods, like statistics, are not usable or even not possible. Then, taking into account opinions of the experts, the necessary parameters of the model can be described, e.g., as "the value of this parameter is about 5". Because these opinions have not completely precise forms (like real numbers), fuzzy numbers are an obvious model to describe such statements.

In [26], an important step in an application of a fuzzy setting for simulations of the maintenance costs was made. Now, I conduct similar analysis, but for the new model of time of the failures, which was proposed in Section 2.

I start form basic definitions and notation concerning the fuzzy approach, which will be used in the further part of the paper. Additional details can be found in, e.g., [14].

For a fuzzy subset $\tilde{A}$ of the set of real numbers R I denote by $\mu_{\tilde{A}}$ its membership function $\mu_{\tilde{A}} : R \to [0,1]$ and by $\tilde{A}[\alpha] = \{x : \mu_{\tilde{A}}(x) \geq \alpha\}$ the α-level set of $\tilde{A}$ for $\alpha \in (0,1]$. Then $\tilde{A}[0]$ is the closure of the set $\{x : \mu_{\tilde{A}}(x) > 0\}$.

A fuzzy number $\tilde{a}$ is a fuzzy subset of R for which $\mu_{\tilde{A}}$ is a normal, upper-semicontinuous, fuzzy convex function with a compact support. Then for each $\alpha \in [0,1]$, the α-level set $\tilde{a}[\alpha]$ is a closed interval of the form $\tilde{a}[\alpha] = [a_L[\alpha], a_U[\alpha]]$, where $a_L[\alpha], a_U[\alpha] \in R$ and $a_L[\alpha] \leq a_U[\alpha]$.

A left-right fuzzy number (which is further abbreviated as a LRFN) is a fuzzy number with the membership function of the form:

$$\mu_{\tilde{a}}(x) = \begin{cases} L\left(\dfrac{x-a}{b-a}\right), & x \in [a,b] \\ 1, & x \in [b,c] \\ R\left(\dfrac{d-x}{d-c}\right), & x \in [c,d] \\ 0, & otherwise \end{cases},$$

where $L, R : [0,1] \to [0,1]$ are non-decreasing functions, such that $L(0) = R(0) = 0$ and $L(1) = R(1) = 1$. A triangular fuzzy number, denoted further by $[a,b,c]$, is a LRFN with the membership function of the form:

$$\mu_{\tilde{a}}(x) = \begin{cases} \dfrac{x-a}{b-a}, & x \in [a,b] \\ \dfrac{x-c}{b-a}, & x \in [b,c] \\ 0, & otherwise \end{cases}.$$

In my further investigation, behaviour of a function $f(x)$ plays a crucial role. In order to approximate a fuzzy output $\tilde{f}(\tilde{x})$ for some fuzzy parameter $\tilde{x}$, monotonicity of $f(x)$ should be checked. If $f(x)$ is an non-decreasing function, then for the given α, the left end point $f_L[\alpha]$ is approximated using the crisp value $x_L[\alpha]$. The same applies for $f_U[\alpha]$ and $x_U[\alpha]$. In contrary, if $f(x)$ is an non-increasing function, $x_U[\alpha], x_L[\alpha]$ are applied to evaluate $[f_L[\alpha], f_U[\alpha]]$ (see, e.g., [19,26]).

6.6. Numerical analysis for the fuzzified parameters x^*, y^*

After the strictly crisp case, its fuzzy counterpart can be discussed. First, I assume that x^*, y^* are modelled by triangular fuzzy numbers and all of other parameters are given as crisp values, which are the same as in Section 6.2. As it was indicated, both x^* and y^* can be based on experts' knowledge, therefore fuzzy numbers are obvious tool to model these parameters. In the following, I set $\tilde{x}^* = [0.25, 0.5, 0.75]$ and $\tilde{y}^* = [0.5, 1, 1.5]$. It means, that a horizontal coordinate of the point, where the introduced HRF (1), changes its

behaviour is "about 0.5", and its vertical coordinate is "about 1", with impreciseness equal to "plus / minus 50%". Using these fuzzy values $\tilde{x}^*, \tilde{y}^*$, the Monte Carlo estimator of the discounted cost of services $\widehat{PV}(c)$ for the previously estimated optimal point P^{**} can be found. As it is seen in Figure 8, the output is a LRFN, which is slightly right-skewed. Its support is equal to $[979.649, 1769.21]$, which is -25% and +35%, if this interval is compared to a core of $\widetilde{PV}(c)$ (and, at the same time, the crisp value of $\widehat{PV}(c)$, which was estimated in Section 6.2). Therefore, the parameters x^*, y^* have important impact on the estimated discounted costs.

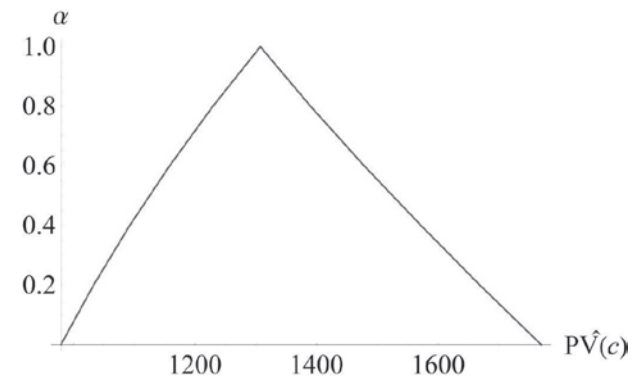

Fig. 8. Plot of $\widehat{PV}(c)$ as a fuzzy number for $\tilde{x}^* = [0.25, 0.5, 0.75]$ and $\tilde{y}^* = [0.5, 1, 1.5]$

Moreover, a fuzzification of the parameters x^*, y^* has an impact on the average number of the repairs. As it is seen in Figure 9, for $\tilde{x}^* = [0.25, 0.5, 0.75]$ and $\tilde{y}^* = [0.5, 1, 1.5]$, the relevant fuzzy average $\tilde{x}_R$ is also a LRFN, which is slightly right-skewed. Its support is equal to $[1271.46, 2859.13]$, which is -34% and +48%, if this interval is compared to the core of $\tilde{x}_R$. Therefore, a variability of $\tilde{x}_R$ is higher than for $\widetilde{PV}(c)$. It also means, that an optimal value of P^* should be found for each single analysed set of x^*, y^*. For example, 0-cut (i.e., α-cut of a fuzzy number, for which $\alpha = 0$) of $\tilde{P}^*$ is equal

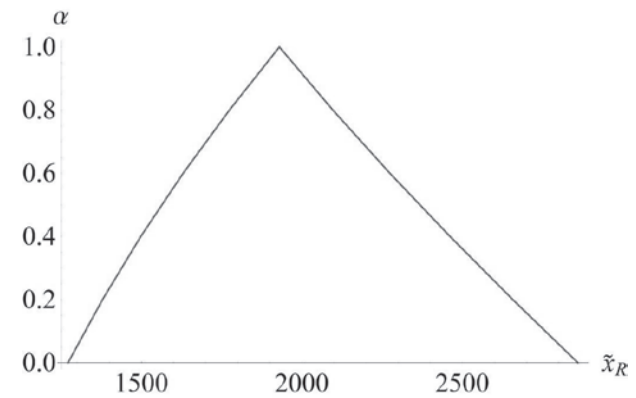

Fig. 9. Plot of $\tilde{x}_R$ as a fuzzy number for $\tilde{x}^* = [0.25, 0.5, 0.75]$ and $\tilde{y}^* = [0.5, 1, 1.5]$

Table 2. Comparison of statistical measures of the maintenance services for the left and the right end of $\tilde{P}^*[0]$.

Measure	$P_L[0] = 3.15$	$P_U[0] = 4.45$
$\widehat{PV}(c)$	1758.44	968.028
$\bar{x}_R$	2720.12	1389.72
$\bar{x}_P$	300	220
$\min c_R$	1	1
$\max c_R$	6.32746	6.01543
$\bar{c}_R$	1.27363	1.27373
$sd(c_R)$	0.273637	0.273719
$\min c_P$	3	3
$\max c_P$	12.2116	12.3969
$\bar{c}_P$	3.54795	3.54803
$sd(c_P)$	0.547883	0.548142

to $[3.15, 4.45]$ for the previously mentioned values of $\tilde{x}^*$ and $\tilde{y}^*$. Estimators of $PV(c)$ and statistical measures of the costs of repairs and replacements for the left and the right end of this 0-cut can be found in Table 2.

6.7. Numerical analysis for the fuzzified parameters of the costs

Apart from the parameters of the HRF, an influence of a fuzzification of other values can be analysed. For example, a decision maker can be interested in finding an answer, if the constant values of repairs and replacements or their variable counterparts are more prone to an impreciseness in an expert's opinion. Once again, the Monte Carlo simulations lead to a straightforward solution of this problem, which can be seen in Figure 10. In this case, I assume, that the relevant costs are "about plus / minus 10%", i.e. $\tilde{c}_{R,const} = [0.9, 1, 1.1]$, $\tilde{c}_{P,const} = [2.7, 3, 3.3]$ (the plot for the fuzzified constant values, which is labelled with squares) and $\tilde{c}_{R,var} = [90, 100, 110]$, $\tilde{c}_{P,var} = [90, 100, 110]$, (the plot with circles, for the fuzzified variable parts). As it is easily seen, the constant parts of the maintenance costs have more important impact on the estimated total costs. In both cases, the outputs are triangular fuzzy numbers. For the considered fuzzy constant costs, its support is given by +/− 1.98% (if it is compared to the "crisp" estimator of $PV(c)$) and in the case of the fuzzy variable costs, its support is more wider (+ / − 8%).

Of course, more than one source of impreciseness, which is modelled by a fuzzy approach, can be analysed. Using the Monte Carlo simulations, it is possible to observe interactions among many sources, e.g., the parameters of the HRF, the costs etc.

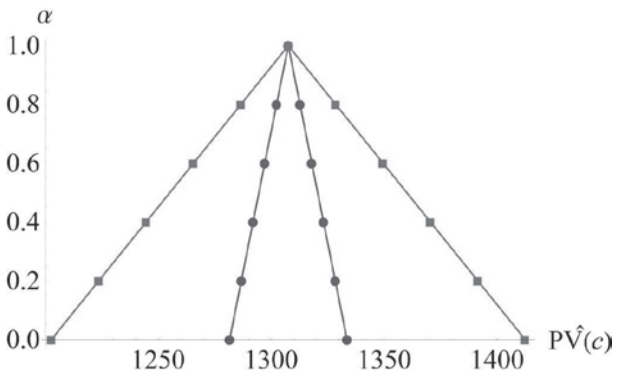

Fig. 10. Plot of $\widehat{PV}(c)$ *as a fuzzy number for* $\tilde{c}_{R,const} = [0.9,1,1.1]$, $\tilde{c}_{P,const} = [2.7,3,3.3]$ *(squares) and* $\tilde{c}_{R,var} = [90,100,110]$, $\tilde{c}_{P,var} = [90,100,110]$ *(circles)*

6.8. Summary of the results

Taking into account the previous analyses, some remarks about their results can be highlighted:

- In the considered case, the overall discounted costs of the services are smaller (about 3.39%) and the repairs are even more rare (about 14.21%) for the optimal solution. The costs of a single repair or a replacement are not affected by the optimization procedure.
- It is possible, that application of nominal values of the cash flow, instead of a more realistic model with a variable interest rate, leads to incorrect results for the optimization procedure just like other statistics of the costs.
- A fuzzification of various parameters of the introduced models is possible. For example, fuzzy values of $\tilde{x}^*$ and $\tilde{y}^*$ have a significant impact on the estimated discounted costs and the evaluated average number of repairs. Additionally, the optimization procedure should be applied for each single analysed set of these parameters.
- Using simulations and the fuzzy approach, many practical problems can be solved. In the considered fuzzy case, it turns out, that the constant parts of the maintenance costs have greater impact on the estimated total costs than their variable counterparts.

6.9. Towards a practical application

As it was mentioned, the previously presented example is a simplified one. However, some of its aspects can be directly carried to a real life application. For example, instead of only 20 connections of one type, a few hundreds or even a few thousands of connections together with many types can be considered. It can be achieved using the Monte Carlo simulations, because the HRF, which is introduced in this paper, is a numerically very efficient algorithm. The same applies for the optimization procedure, which is linearly dependent on the number of the samples (i.e. connections).

It seems, that a more complex problem is related to an estimation procedure for the applied parameters. If many connections are considered, then it can be quite laborious to estimate the necessary parameters of the HRF for each single type of a connection. In practical situations, it is also possible, that other kinds of the costs (see also the discussion in Section 4) and other effects (like a requirement to repair a whole group of connections in one time) should be taken into account. This directly leads to a more complicated model and longer time of the necessary simulations.

7. Conclusions

In this paper, a new kind of a hazard rate function for time between malfunctions of a pipeline is proposed. This HRF is a V-shape function, which also depends on number of previous repairs of the given connection. Moreover, times of malfunctions can be easily generated with the Monte Carlo simulations, if this HRF is applied. Then, a model of costs, which is related to a type of a performed service and its length, is also introduced.

These costs are dived into two parts, which facilitates an application of this approach in real-life situations. To calculate a present values of the maintenance costs, the one-factor Vasicek model is used. It is noticed during a more detailed analysis, that the obtained results strictly depend on the assumed type of a discount factor (i.e. if it is variable interest rate or a constant yield). During this numerical analysis, a behaviour of the whole WDS is simulated using the Monte Carlo approach. Afterwards, the costs of the maintenance services (i.e. repairs and replacements) are evaluated and statistically summarized. In this paper, a main aim of the conducted simulations is to minimize these maintenance costs. Therefore, an optimization procedure, which is based on the Kiefer-Wolfowitz algorithm, is applied. Apart from the strictly crisp setup, fuzzification of some parameters of the introduced models is also considered. Such an application of fuzzy numbers leads to a better incorporation of the experts' knowledge and more proper, closer to real-life situations, modelling of these uncertain parameters. Some relevant examples of the simulated output for both the crisp and the fuzzy settings are also provided.

References

1. Amani N, Ali N M, Mohammed A H, Samat R A. Maintenance and management of wastewater system components using the condition index system, prediction process and costs estimation. Eksploatacja i Niezawodnosc – Maintenance and Reliability 2013; 15(2): 161–168.
2. Broadie M, Cicek D, Zeevi A. General bounds and finite-time improvement for the Kiefer-Wolfowitz stochastic approximation algorithm. Operations Research 2011; 59(5): 1211–1224, https://doi.org/10.1287/opre.1110.0970.
3. Buckley J J. Simulating Fuzzy Systems. Berlin Heidelberg: Springer-Verlag, 2005, https://doi.org/10.1007/b100371.
4. Clark R M, Thurnau R C. Evaluating the risk of water distribution system failure: A shared frailty model. Front. Earth Sci. 2011; 5(4): 400–405.
5. Fadaee M J, Tabatabaei R. Estimation of failure probability in water pipes network using statistical model. Engineering Failure Analysis 2011; 18: 1184–1192, https://doi.org/10.1016/j.engfailanal.2011.02.013.
6. Gil M A, Hryniewicz O. Statistics with Imprecise Data. In: Meyers R A (ed.). Encyclopedia of Complexity and Systems Science. New York: Springer-Verlag, 2009.
7. Glasserman P. Monte Carlo Methods in Financial Engineering. New York: Springer, 2004.
8. Gonzalez A, Pons O, Vila M A. Dealing with uncertainty and imprecision by means of fuzzy numbers. International Journal of Approximate Reasoning 1999; 21: 233–256, https://doi.org/10.1016/S0888-613X(99)00024-9.

9. Homem-de-Mello T, Bayraksan G. Monte Carlo sampling-based methods for stochastic optimization. Surveys in Operations Research and Management Science 2014; 19: 56–85, https://doi.org/10.1016/j.sorms.2014.05.001.
10. Hryniewicz O, Kaczmarek K, Nowak P. Bayes statistical decisions with random fuzzy data – An application for the Weibull distribution. Eksploatacja i Niezawodnosc – Maintenance and Reliability 2015; 17(4): 610–616, https://doi.org/10.17531/ein.2015.4.18.
11. Kanakoudis V K, Tolikas D K. Assessing the performance level of a water system. Water, Air, and Soil Pollution 2004; 4: 307–318, https://doi.org/10.1023/B:WAFO.0000044807.41719.c7.
12. Kleiner Y, Adams B J, Rogers J S. Long-term planning methodology for water distribution system rehabilitation. Water Resources Research. August 1998; 34(8): 2039–2051, https://doi.org/10.1029/98WR00377.
13. Kumar G, Jain V, Gandhi O P. Steady-state availability analysis of repairable mechanical systems with opportunistic maintenance by using semi-Markov process. Int J Syst Assur Eng Manag. 2014; 5(4): 664–678, https://doi.org/10.1007/s13198-014-0231-8.
14. Lee K H. First Course on Fuzzy Theory and Applications. Berlin Heidelberg: Springer, 2005.
15. Liu Z, Kleiner Y, Rajani B, Wang L, Condit W. Condition Assessment Technologies for Water Transmission and Distribution Systems. Washington DC: U.S. Environmental Protection Agency, 2012; EPA/600/R-12/017.
16. Malinowski J. A newly developed method for computing reliability measures in a water supply network. Operations Research and Decisions 2016; 26(4): 49–64.
17. Marchionni V, Cabrala M, Amadoa C, Covasa D. Water supply infrastructure cost modelling. Procedia Engineering 2015; 119: 168–173, https://doi.org/10.1016/j.proeng.2015.08.868.
18. Neelakantan T R, Suribabu C R, Lingireddy S. Optimisation procedure for pipe-sizing with break-repair and replacement economics. Water SA. April 2008; 34(2): 217–224.
19. Nguyen H T. A Note on the Extension Principle for Fuzzy Sets. Journal Mathematical Analysis and Applications 1978; 64: 369–380, https://doi.org/10.1016/0022-247X(78)90045-8.
20. Nowak P, Romaniuk M. Application of Levy processes and Esscher transformed martingale measures for option pricing in fuzzy framework. Journal of Computational and Applied Mathematics 2014; 263: 129–151, https://doi.org/10.1016/j.cam.2013.11.031.
21. Nowak P, Romaniuk M. Catastrophe bond pricing for the two-factor Vasicek interest rate model with automatized fuzzy decision making. Soft Computing 2017; 21(10): 2575–2597, https://doi.org/10.1007/s00500-015-1957-1.
22. Pietrucha-Urbanik K, Studziński A. Case study of failure simulation of pipelines conducted in chosen water supply system. Eksploatacja i Niezawodnosc – Maintenance and Reliability 2017; 19 (3): 317–322, https://doi.org/10.17531/ein.2017.3.1.
23. Rojek I, Studziński J. Comparison of different types of neuronal nets for failures location within water-supply networks. Eksploatacja i Niezawodnosc – Maintenance and Reliability 2014; 16 (1): 42–47.
24. Rokstad M M, Ugarelli R M. Minimising the total cost of renewal and risk of water infrastructure assets by grouping renewal interventions. Reliability Engineering and System Safety 2015; 142: 148–160, https://doi.org/10.1016/j.ress.2015.05.014.
25. Romaniuk M. Application of Markov chain and interest rate process for forecasting of costs of maintenance of pipelines. In: Wittmann J, Wieland R. (eds.) Simulation in Umwelt- und Geowissenschaften. Workshop Müncheberg 2015. Aachen: Shaker Verlag, 2015.
26. Romaniuk M. On simulation of maintenance costs for water distribution system with fuzzy parameters. Eksploatacja i Niezawodnosc – Maintenance and Reliability 2016; 18(4): 514–527, https://doi.org/10.17531/ein.2016.4.6.
27. Romaniuk M, Nowak P. Monte Carlo methods: theory, algorithms and applications to selected financial problems. Warszawa: ICS PAS, 2015.
28. Røstum J. Statistical modelling of pipe failures in water networks. Ph.D. dissertation. 2000.
29. Scheidegger A, Leitão J P, Scholten L. Statistical failure models for water distribution pipes – A review from a unified perspective. Water Research 2015; 83: 237–247, https://doi.org/10.1016/j.watres.2015.06.027.

Maciej ROMANIUK
Systems Research Institute, Polish Academy of Sciences
ul. Newelska 6, 01-447 Warszawa, Poland
and
The John Paul II Catholic University of Lublin,
ul. Konstantynów 1 H, 20-708 Lublin, Poland

E-mail: mroman@ibspan.waw.pl

Article citation info:
SAWCZUK W. Analytical model coefficient of friction (COF) of rail disc brake on the basis of multi-phase stationary tests. Eksploatacja i Niezawodnosc – Maintenance and Reliability 2018; 20 (1): 57–67, http://dx.doi.org/10.17531/ein.2018.1.8.

Wojciech SAWCZUK

ANALYTICAL MODEL COEFFICIENT OF FRICTION (COF) OF RAIL DISC BRAKE ON THE BASIS OF MULTI-PHASE STATIONARY TESTS

MODEL ANALITYCZNY ZMIENNOŚCI WSPÓŁCZYNNIKA TARCIA KOLEJOWEGO HAMULCA TARCZOWEGO NA PODSTAWIE WIELOFAZOWYCH BADAŃ STANOWISKOWYCH*

Similarly to road vehicles, a disc brake remains the main friction brake in rail vehicles. Due to the increasing train speeds, a disc brake has already replaced the traditional clasp brake that is however, still used in cargo trains. In the process of long-term operation of the brake pad-brake disc friction pair, the parameters of the braking process such as the curve of the coefficient of friction are changed, which extends the braking distance. The paper presents the results of several years of investigations on the railway disc brake in different wear conditions in the aspect of the requirements set by the UIC (International Union of Railways) related to the brake pads approval for use.

***Keywords**: railway disc brake, organic brake pad, coefficient of friction, multiple regression.*

W pojazdach szynowych, podobnie jak w samochodowych, podstawowym hamulcem roboczym jest cierny hamulec tarczowy. Ze względu na coraz większe prędkości jazdy, hamulec tarczowy w wielu pojazdach kolejowych jak i tramwajowych wyparł już hamulec klockowy, który niezmiennie jeszcze jest stosowany w pociągach towarowych. W procesie dłuższej eksploatacji pary ciernej tarcza-okładzina główne parametry procesu hamowania jak przebieg współczynnika tarcia obniża się, co w konsekwencji wydłuża drogę hamowania. W artykule przedstawiono wyniki kilkuletnich badań kolejowego hamulca tarczowego w różnych stanach jego zużycia z uwzględnieniem między innymi wymagań stawianych przez Międzynarodowy Związek Kolei UIC w zakresie dopuszczenia okładzin hamulcowych do eksploatacji.

***Słowa kluczowe**: kolejowy hamulec tarczowy, współczynnik tarcia, regresja wieloraka.*

1. Introduction

Due to the nature of friction in the disc brake (dry friction), it is possible to apply this brake to different friction models. In case of vehicle standstill, it is possible to refer to static friction models such as Karnopp [21], Quinn, Awrejcewicz [4, 12], Adams [8] or Wojewody [55]. These models are based on the Coulomb model. However, dynamic braking models (derived from the Dahl model) such as the LuGre model [34, 40], the Leuven model [30] and the GMS model [2] are used during the braking process from set speed to stop. The operating range of the disc brake is very complex in terms of speed or load as well as the state of the transition between the friction and the kinetic friction. A large number of variable parameters hinder the process of friction modeling in the brake system, resulting in significant model development and longer computational time.

The friction pair of a railway disc brake must meet a variety of regulatory requirements before it is approved for use. TSI (Technical Inter-operation Specifications) regulations related to the UIC sheets are applicable for the brake pads and for the brake discs PN-EN standards apply. This is sometimes validated with several days of testing on test stands. In order to most efficiently reproduce the conditions of a train braking with a disc brake, the tests are carried out in the 1:1 scale on actual objects. Due to the size of the test stand and the costs of its maintenance there are only a few such tests stands in Europe, contrary to the tests stands designed for road vehicles (most often owned by brake pad manufacturers). The friction pads of the disc brake are made of an organic material consisting of thermo hardened resins, synthetic elastomers, friction modifiers and metallic fibers [25, 52]. The second typical friction pad material is metallic sintered composites containing a number of matrix and non-metal metallic components in the form of sliding, friction and filler additives [23, 25]. In the case of motor vehicles, there are also ceramic friction pads [38, 39, 54] characterized by a more stable friction coefficient compared to the composite material.

Validation tests on test stands are preceded by laboratory tests on the friction material samples and simulations in the ANSYS or ABAQUS environment [6, 22, 36]. Tests provide the possibility of evaluation of the temperature distribution on the brake disc as presented in [9, 20, 42]. In terms of temperature distribution, many researchers deal with the problems of explanation and modeling of the phenomenon of hot spots occurring on the surface of the brake discs or vehicle clutches, as discussed in [23, 29]. A separate problem raised by many researchers [19, 23, 49, 57] is the process of fatigue cracking of brake discs by cyclical heating during braking and cooling of the disc after braking (disc spectrum). As a result of the rapid increase of the disk temperature and its equally rapid (in the case of ventilated discs) or slow (for full discs) cooling, there are surface cracks occurring on the surface of friction disc in the form of microcrystalline grids. Figure 1 shows the typical damage to the brake discs in terms of single cracks on the friction surface and microcracks on a substantial portion of the disc surface.

The phenomenon of thermal cracking is identifiable only after a series of brakings (approx. 300 and more) on the test stand or during operation (heavy-duty trucks in particular). A separate phenomenon occurring in the operation of the disc brake is the uneven wear of the

(*) Tekst artykułu w polskiej wersji językowej dostępny w elektronicznym wydaniu kwartalnika na stronie ***www.ein.org.pl***

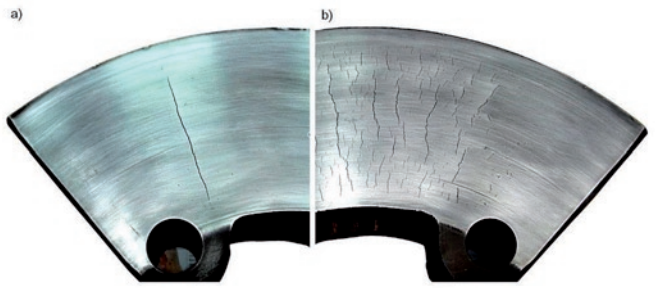

Fig. 1. View of friction disc brake discs after several years of use: a) with one crack, b) with surface cracks

friction pads due to the poor alignment of the pads relative to the disc. In the paper [19] the results of friction brake discs wear from the operation of double-deck passenger rail cars type Bmnopux. The work presents examples of uneven wear of friction linings such as higher wear on the outer radius of the disc relative to the inner radius of the disc, edge defects and cracking or tearing of the entire lining parts from the bearing plate. In this respect, works are underway on such a selection of the friction pair materials as to ensure a compromise among the costs of manufacturing (additional thermal and chemical processes when making the casts of the brake discs), the component wear and the friction mechanical properties of the friction pair, as described in [1, 3, 10, 13, 14, 42]. On the other hand, [7, 11, 37] presents problems related to friction models and friction wear modeling of brake system components based on operational tests. A separate issue raised by many researchers in [24, 31, 52] is the vibration and noise generated by brakes during braking. In papers [17, 18, 50, 51], vibroacoustic signals in the time domain, amplitudes and frequencies have been analyzed, allowing for the evaluation of rotary machines, brakes and identification of faults.

The aim of this article is to present a model for estimating the mean friction coefficient of the disc brake in terms of braking parameters as well as some parameters of the design and operation of the friction pair of disc brake discs. Modeling of the coefficient of friction using multiple regression was carried out on the basis of several years of examination of the rail brake disk at the brake position in terms of both momentary and average friction coefficient. It should be emphasized that the current provisions for the admission of such brake system components as brake disc and friction lining are reduced to a positive test result at a certified brake position only for new (unused) brake discs and lining without frictional characteristics for parts or completely worn out.

2. Requirements set for the disc brake friction pair

In railway vehicles, two types of brake linings are applied made from either organic or sintered materials, as shown in Fig. 2.

Depending on the applied brake lining, during tests on approved test stands, appropriate characteristics of the curve of instantaneous and average coefficient of friction are developed.

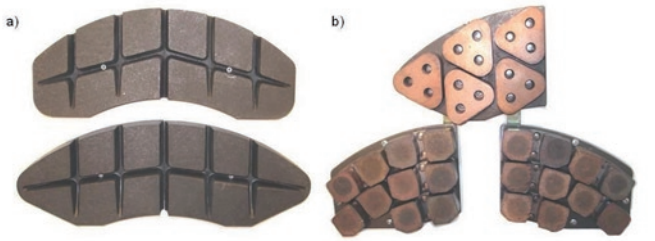

Fig. 2. View of the brake pads used in a railway disc brake: a) organic material, b) sintered material

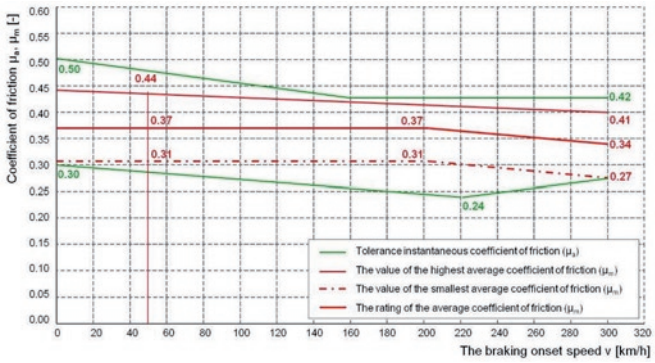

Fig. 3. Range of tolerance of the coefficients of friction of a friction pair of a railway disc brake during the tests on the test stand according to [26]

A brake lining made from an organic and sintered material according to [26] must ensure a curve of the coefficient of friction of a friction pair in a dry condition on the level of 0.37. The tolerance ranges of the instantaneous and average coefficients of friction have been shown in Fig. 3. Besides, the main requirement for the railway brake linings according to UIC 541-3 is an absolute restriction on the application of blue asbestos. UIC 541-3 does not recommend the use of lead, zinc and other materials whose dust or gas generated during braking may have an adverse effect on the passengers and be hazardous to their health.

The brake lining material should be selected to ensure a balance between:

- friction properties of the friction pair,
- wear and durability of the brake pads,
- negative impact on the brake disc.
- Besides, the coefficient of friction of the friction pair in a disc brake should possibly be independent from:
- braking onset speeds,
- clamping force of the brake pads on the brake disc,
- the run-in condition of the brake pads,
- atmospheric conditions (rain, snow),
- temperature of the surface of the disc brake.

Under the influence of humidity, snow or ice a slight deviation of the average coefficient of friction is allowed compared to braking performed under dry conditions. The average coefficient of friction under these conditions may vary in relation to the braking performed under dry conditions in the range of ± 15%. The average coefficient of friction of a friction pair when braking under dry conditions until a full halt performed at the temperature of the friction surface of above 140°C may be different than a braking performed on a cold disc (max. 60°C) not more than 15% [26].

During continuous braking (simulation of a coast down) with the maximum power of up to 43 kW per friction pair, the coefficient of friction should meet the following requirements [26]:

- The average coefficient of friction from the entire braking process should fall between 0.25 and 0.50,
- The amplitude of the course of instantaneous coefficient of friction should not exceed 0.15.

The above requirements should be met by the organic friction material up to 400°C (the disc temperature) and 550°C when the brake linings are made from metallic sinters [26].

Besides, the TSI regulations and sheets [26, 27, 47, 48], related to the requirements for brake linings of a discs brake, state that the friction material must meet requirements related to the tolerance of instantaneous and average coefficient of friction in the entire range of admissible brake pad wear level, i.e. 5 mm from the 35 mm thickness of a new pad.

For brake discs complying to the [43, 45] standards, depending on the program of research, the requirements pertain to the dissipated en-

ergy, braking power, braking onset speeds, decelerated mass per single brake disc and brake delay. Depending on the program of research simulating the braking of a light railcar or, in an extreme scenario, a locomotive or a traction set from high speeds, the required energy to be dissipated falls in the range of 4.6÷37 MJ. The braking powers during braking should fall in the range 400÷667 kW at the braking onset speeds falling in the range of 120÷400 km/h. During the stationary investigations, the decelerated masses are 6÷10 t depending on the type of braking, while the braking delays during the investigations should not exceed 0.8÷1.2 m/s^2. In the most recent editions of standard [45] more requirements were introduced related to the energy absorbed by the ventilated brake discs when disengaged and rotating (simulation of a train drive at a steady speed without braking) and the noise generated by the disc brake during the tests. Depending on the applied ventilated brake disc, the power used during its rotation should not exceed 5kW. Schedule B to standard [45] contains the methodology of the noise measurement without not-to-exceed boundary values related to the disc brake during braking. In regulation 90 [53] related to the brake discs (despite the fact that this pertains to road vehicles) additional requirements are included as to the content of carbon, silicon, manganese, chromium and copper, depending on the disc type (cast iron, cast steel, carbon or alloy). Besides, the regulation states the ranges of hardness (for cast iron discs 190÷248 HBW) and geometrical quantities of the discs to be met after mechanical processing (change of thickness, axial run out, surface perpendicularity, flatness and roughness). For railway brake discs, the geometrical quantities are provided only in the Operation and Maintenance Manual of a given vehicle (locomotive, traction set or railcar).

3. Methodology and object of investigations

Investigations related to the determination of selected braking characteristics depending on the conditions of the disc brake friction pair were performed based on the assumptions of an active experiment [32, 35]. During the tests, the input parameters (brake condition) were purposefully modified in a predefined way and their influence on the change of the output parameters was observed.

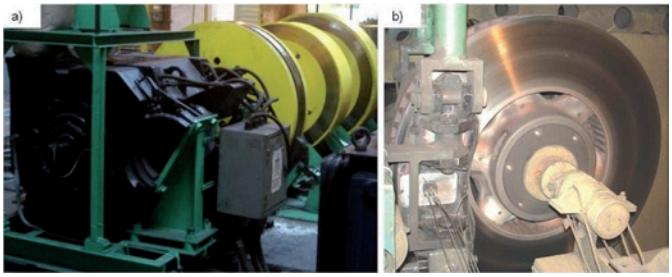

Fig. 4. View of the research object on the test stand: a) view of the driving section of the test stand with the rotating masses, b) 610×110 brake disc fitted on the test stand

Investigations of a tribological nature were performed on an inertia test stand presented in Fig. 4. On the said test stand, clasp brakes and disc brakes can be tested reproducing the rail vehicle actual braking conditions.

Two ventilated 610×110 gray cast iron brake discs were tested. The first disc was new and the other was worn to 105 mm from 110 mm (prior to tests). The worn disc was subject to turning. The brake disc masses were m_{T1}=116.0 kg (new disc) and m_{T2}=111.5 kg (disc worn). Both discs were prepared for the tests as per standard [44]. Fig. 5 presents the brake discs during the tests. In the tests, organic brake linings were applied.

The brake pads, according to the manufacturer's procedure and requirements contained in [26], were made from thermo bonded resin, synthetic elastomer, metal and organic fiber as well as friction modi-

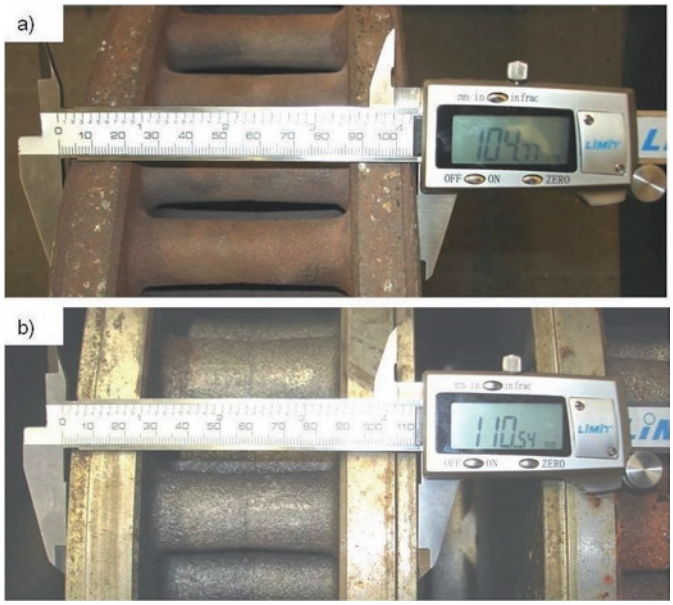

Fig. 5. View of the brake discs used during the tests: a) disc worn to 104 mm after tests on the test stand, b) new disc of the thickness of 110 mm

fiers. Three sets of brake pads were used per disc for the tests stand investigations (the first, new set of brake pads (4 pieces) - G_1=35 mm and the two sets of pads worn to G_2=25 mm and G_3=15 mm). Masses of friction pads were m_{G1}=1.75 kg (new pad), m_{G2}=1.45 kg (pad worn to 25 mm thickness), m_{G3}=1.02 kg (pad worn to 15 mm thickness). The applied brake pads have been shown in Figure 6.

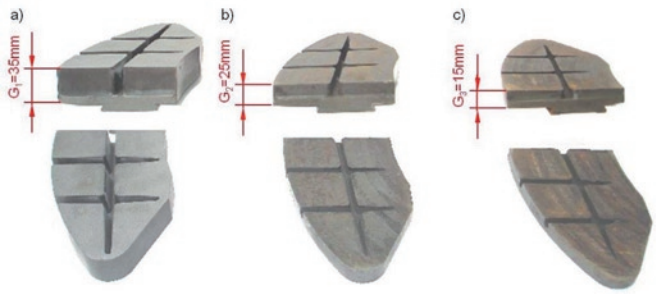

Fig. 6. View of the brake pads used during the tests: a) new brake pads, 35 mm, b) pads worn to 25 mm, c) pads worn to 15 mm

The tests stand investigations have been performed according to the UIC 541-3 sheet. Each research program refers to specific conditions of the brake operation throughout the vehicle life cycle. In order to reproduce the actual braking conditions with a disc brake of a passenger railcar, research program *C* has been selected – fast driving.

The modified parameters during the tribological tests were:

- conditions of the brake disc: new – 110 mm and worn – 105 mm,
- thickness of the brake pad: G_1=35 mm, G_2=25 mm and G_3=15 mm,
- Braking onset speed: v= 50, 80, 120, 160 and 200 km/h,
- clamping force of the pad on the disc: p= 28 and 44 kN,
- Decelerated mass per disc: M= 4.4 and 7.5 t.

Prior to the commencement of the main tribological investigations a series of brakings was performed to run in the brake pads. According to [26] initial braking needs to be continued until the surface is refreshed (exceeding 75% of the surface before running in.)

During the investigations on the inertia test stand, instantaneous coefficient of friction μ_a was recorded at each moment of braking [52]:

$$\mu_a = \frac{F_t}{F_b} \tag{1}$$

where: F_t – instantaneous tangential force related to the braking radius r,
F_b – total instantaneous clamping force on the brake disc.

Then, the average coefficient of friction μ_m was calculated determined from the definite integral of the instantaneous coefficient of friction throughout the braking distance s_2 [26]:

$$\mu_m = \frac{1}{s_2}\int_0^{s_2} \mu_a ds \tag{2}$$

Prior to the tests stand tribological investigations (upon running in of the brake pads), a series of 30 brakings were performed for statistical evaluation. The test aimed at determining of the minimum number of repetitions that would ensure the results on a satisfactory level of confidence of 95% at the adopted level of significance of α=0.05, at which the smallest coefficient of variation is observed. The value of the average slide coefficient of friction μ_m was subjected to analysis measured in 30 trials at an unchanged braking onset speed of 120 km/h. The measurement was performed upon running in of the brake pads according to the requirements contained in the UIC 541-3 sheet. Each subsequent braking was preceded by chilling of the disc through its free rotation, which also simulated the train driving at the speed of 100 km/h. Upon reducing of the disc temperature to 60°C, the chilling was stopped and subsequent braking was performed. In order to determine the minimum number of brakings, relations of the following statistical formulas were used: average value, standard deviation, half interval of confidence, bottom and top limit of the confidence interval and the coefficient of variation W based on [16, 28].

Fig. 7 presents the value of the coefficient of friction obtained from a given braking and the average value of the coefficient of friction taking into account the top and the bottom limits of the confidence interval with the assumed significance level of α=0.05 for two tested brake discs.

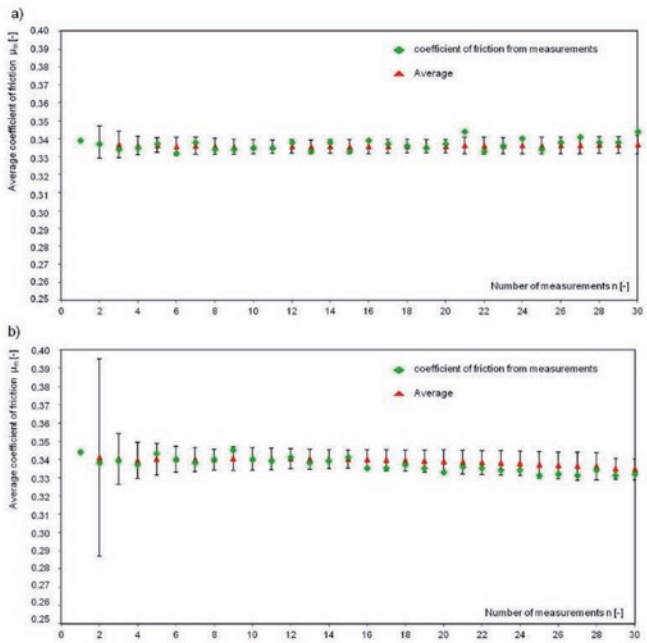

Fig. 7. Curve of the coefficient of friction between the brake pad and the brake disc and its average value obtained on the 610×110 disc: a) new, b) worn (turned)

Fig. 8 presents the percentage curve of coefficient of variation W determined in the measurement of the coefficient of friction, based on which the determination of the number of measurements was possible. Based on Fig. 7, upon performance of 30 brakings, it was observed that the minimum number of braking repetitions ensuring the obtainment of the average coefficient of friction in the expected confidence interval at the assumed level of significance of α=0.05, is 5 for the new disc and 8 for the worn one (turned).

Based on the statistical analysis of the obtained results of the measurement of the average coefficient of friction, disc temperature, braking distance and time, it was assumed that for the main investigations on the test stand 8 repetitions must be performed. For this number of brakings, a satisfactory coefficient of variance was obtained in the expected confidence interval and at the assumed level of significance. Since the values of the coefficient of variation for the measurements of the average coefficient of friction according to [16] did not exceed 10%, a negligible statistical difference of the analyzed quantities was observed.

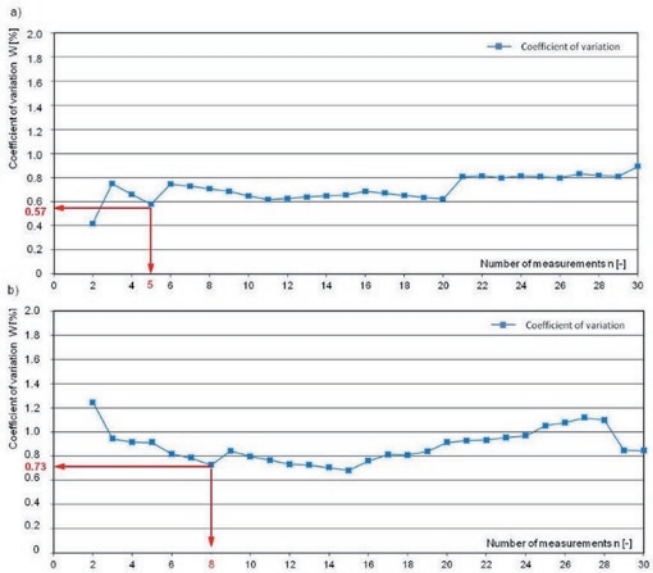

Fig. 8. Curve of the coefficient of variation obtained from the statistical calculations for the brake disc: a) new, b) worn (turned)

During tribological research, 780 brake applications were performed, not counting the brakes related to the lining of the friction lining. In order to validate the multiple regression model described by the relation (3) and presented in Chapter 5, further 384 inhibition was performed.

4. Results and analysis

The aim of the test stand investigations was to determine the curves of instantaneous and average coefficients of friction as per relations (1) and (2) with reference to the applicable regulations on the approval of brake pads of a disc brake for use.

The results of the investigations of the instantaneous coefficient of friction for three brake pads (35, 25 and 15 mm) and two brake discs have been presented in Figs. 9-12 allowing for the top and the bottom limits of the instantaneous coefficient of friction for rail vehicles in compliance with sheet [26]. By using relation (2), upon integrating of the value of instantaneous coefficient of friction on braking distance s, the average value of the coefficient of friction was obtained. The relations of the average coefficient of friction for the same braking parameters as in the instantaneous coefficient of friction have been shown in Figs. 13-16 The results have been referred to the top and

the bottom deviation of the average coefficient of friction, which also remained in compliance with sheet [26].

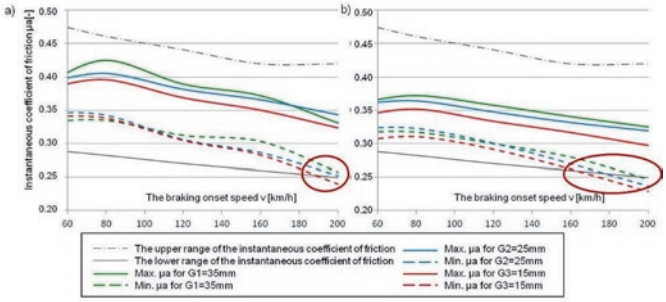

Fig. 9. Dependence of instantaneous coefficient of friction μ_a on the braking onset speed at N=44 kN, M=7.5 t: a) for a new disc, b) for a worn disc

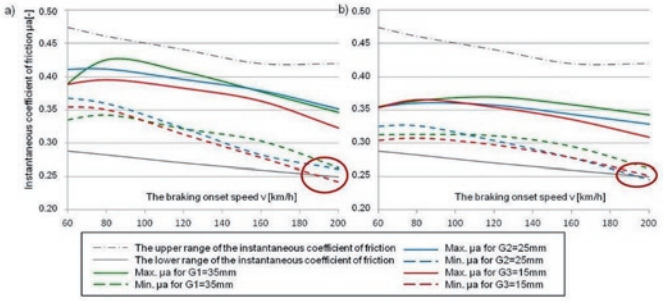

Fig. 10. Dependence of instantaneous coefficient of friction μ_a on the braking onset speed at N=28 kN, M=7.5 t: a) for a new disc, b) for a worn disc

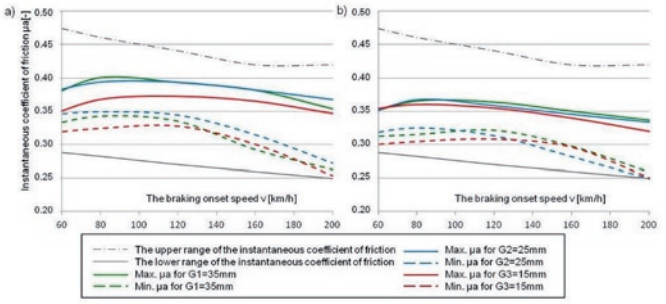

Fig. 11. Dependence of instantaneous coefficient of friction μ_a on the braking onset speed at N=44 kN, M=4.4 t: a) for a new disc, b) for a worn disc

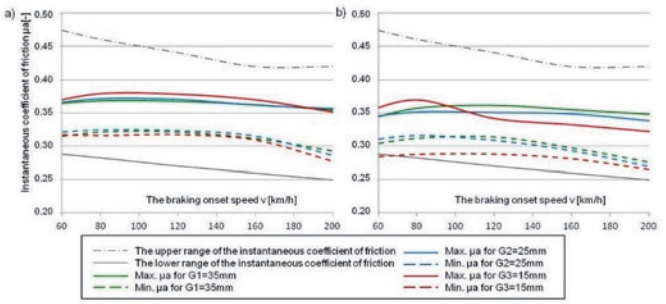

Fig. 12. Dependence of instantaneous coefficient of friction μ_a on the braking onset speed at N=28 kN, M=4.4 t: a) for a new disc, b) for a worn disc

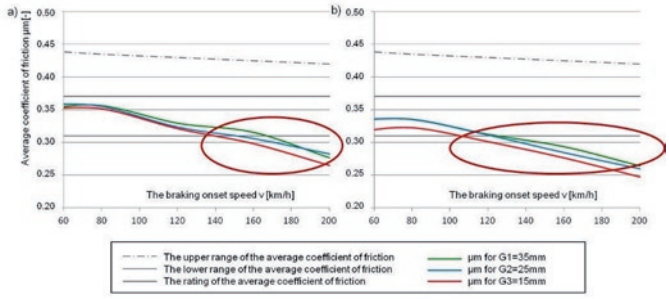

Fig. 13. Dependence of average coefficient of friction μ_m on the braking onset speed at N=44 kN, M=7.5 t: a) for a new disc, b) for a worn disc

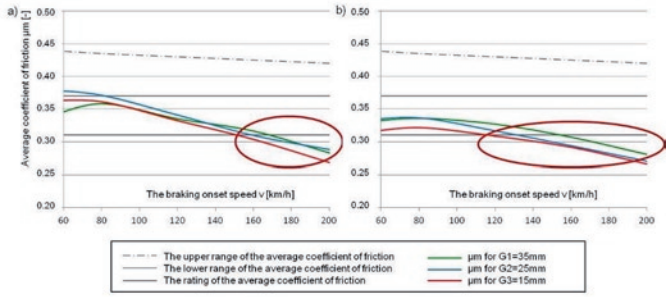

Fig. 14. Dependence of average coefficient of friction μ_m on the braking onset speed at N=28 kN, M=7.5 t: a) for a new disc, b) for a worn disc

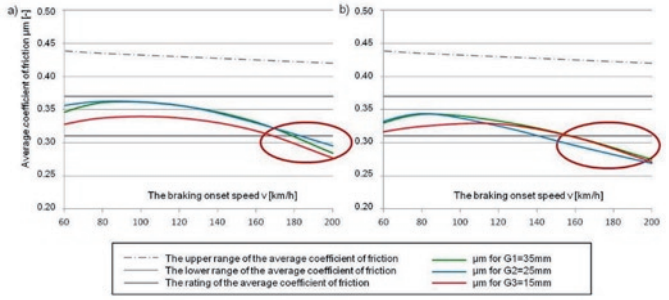

Fig. 15. Dependence of average coefficient of friction μ_m on the braking onset speed at N=44 kN, M=4.4 t: a) for a new disc, b) for a worn disc

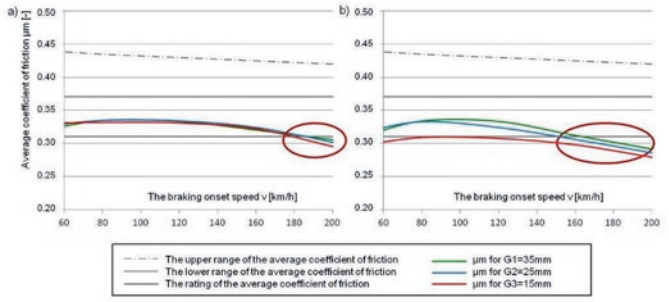

Fig. 16. Dependence of average coefficient of friction μ_m on the braking onset speed at N=28 kN, M=4.4 t: a) for a new disc, b) for a worn disc

Upon analysis of the curves of the instantaneous coefficient of friction presented in Figs. 9-12 one can observe that in some combinations of the clamping force and decelerated mass, the obtained values of the minimum coefficient of friction exceed the minimum required range μ_a of instantaneous coefficient of friction according to sheet [26]. This is particularly the case for a disc worn to 105 mm cooperating with brake pads worn to 15 mm while braking with high

clamping force (N=44 kN) and decelerated mass of M=7.5 t simulating the braking process of a railcar with a maximum load at the speed of v=200 km/h. For the brakings performed on a new disc, only worn brake pads influence the instantaneous coefficient of friction at the bottom tolerance limit μ_a at the braking onset speed of 200 km/h. It is to be expected though, that at higher braking onset speeds (from 200 to 300 km/h), as provided in sheet UIC 541-3, the bottom limit of instantaneous coefficient of friction will be exceeded, as provided in the above sheet.

Upon analysis of the curves of average coefficient of friction obtained during the investigations, it can be observed that for all braking scenarios the bottom deviation of the average coefficient of friction is exceeded for both new and worn discs, for all brake pad configurations (new and worn). Only in the case of low clamping force braking and low decelerated mass (N=28 kN and M=4.4 t) on a new disc and new brake pads up to the braking onset speed of v=200 km/h was the non-excess of the average coefficient of friction above its bottom value observed. For the braking with a high value of the clamping force and a high decelerated mass (N=44 kN and M=7.5 t), the analyzed case of braking using a new disc and worn brake pads results in a non-compliance with the bottom limit of the average coefficient of friction starting from the braking onset speed of v=140 km/h and, in the case of a worn disc and worn pads, from the speed of v=100 km/h. It is noteworthy that in the investigations no extreme case of maximum admissible disc and brake pad wear was considered. Based on the Operation and Maintenance Manual [15, 46], it is allowed to use a brake disc worn to 102 mm (repetitive turning) and brake pads worn to 5 mm based on sheet [26]. In the tests the author used a disc of the thickness of 104 mm and brake pads worn to 15 mm.

5. Modeling of the variation of the coefficient of friction

Based on the results of the investigations of average coefficient of friction $\mu_{m,}$ modeling of its variation was attempted based on such input parameters as disc thickness, brake pad thickness, braking onset speed, clamping force of the pad on the disc and decelerated mass per one disc.

Multiple regression (otherwise referred to as multinomial regression) was applied to model the variation of the average coefficient of friction. This is a method, in which the value of a random variable Y depends on k-th dependent attributes ($X_1, X_2, \ldots X_k$). Based on a given sample of the results, according to [16], determination of the invariable parameters $\alpha_0, \alpha_1, \ldots \alpha_k$ was performed using the method of least squares. The following relation was proposed to determine the coefficient of friction:

$$\mu_m = \alpha_1 G_T + \alpha_2 G_O + \alpha_3 v^2 + \alpha_4 v + \alpha_5 N + \alpha_6 M + \alpha_0 \tag{3}$$

where: G_T – thickness of the brake disc (new 110 mm, worn to 105 mm),
G_O – thickness of the brake pads (new G_1=35 mm, worn to G_2=25 mm and G_3=15 mm),
v – braking onset speed (v=50, 80, 120, 160 and 200 km/h),
N – clamping force of the brake pad on the disc (N=28 and 44 kN),
M – decelerated mass per one disc (M=4.4 and 7.5 t).

Calculated multiple regression parameters for the model (3) obtained at the determinant R^2=0.81 are summarized in Table 1.

Then, the Pearson linear correlation coefficient was validated according to relation (4) for the analyzed variables i.e. disc thickness, thickness of the brake pads, braking onset speeds, clamping force of the brake pads on the disc and decelerated mass.

Table 1. Coefficient of multiple regression

Coefficient	Value
α_1	$3.72 \cdot 10^{-3}$
α_2	$5.09 \cdot 10^{-4}$
α_3	$-3.78 \cdot 10^{-6}$
α_4	$5.66 \cdot 10^{-4}$
α_5	$-4.92 \cdot 10^{-5}$
α_6	$-8.81 \cdot 10^{-4}$
α_0	$-90.2 \cdot 10^{-3}$

$$r = \frac{\sum_{i=1}^{n}(x_i - \bar{x})(y_i - \bar{y})}{\sqrt{\sum_{i=1}^{n}(x_i - \bar{x})^2 \sum_{i=1}^{n}(y_i - \bar{y})^2}} \tag{4}$$

where:
$\bar{y}$, $\bar{x}$ – average values of attribute x and attribute y,
y_i, x_i – descriptive values.

Table 2 presents the correlation matrix (Pearson) for the analyzed variables. Upon analysis of the correlation coefficient from table 2 it was observed that the changes of the average coefficient of friction are most heavily influenced by the braking onset speeds (r=0.79) and the clamping force of the brake pads on the disc (r=0.0146) while the decelerated mass (R=0.0507) has the least influence. The model written with relation (3) may be simplified by eliminating the influence of two variables i.e. the clamping force and the decelerated mass.

Figs. 17-20 present the validation of the model of regression as per relation (3) against the results of investigations of the average coefficient of friction obtained on the test stand.

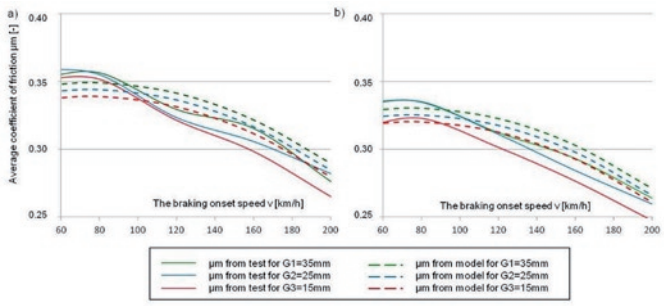

Fig. 17. The relation between the average coefficient of friction obtained in the tests and that allowing for the model of multiple regression when braking with N=44 kN, M=7.5 t: a) new disc, b) worn disc

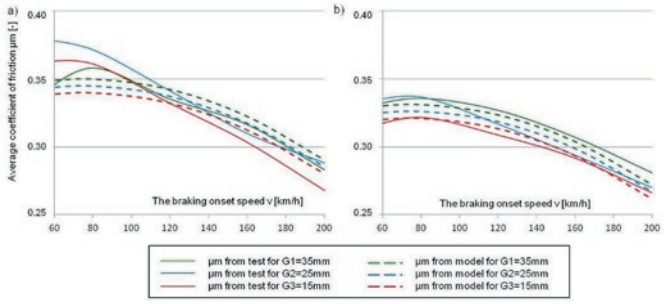

Fig. 18. The relation between the average coefficient of friction obtained in the tests and that allowing for the model of multiple regression when braking with N=28 kN, M=7.5 t: a) new disc, b) worn disc

Table 2. Correlation matrix

Variable	Disc sickness G_T	Brake pad thickness G_O	Speed v^2	Speed v	Brake pad clamping force N	Decelerated mass M	Correlation coefficient
Disc thickness G_T	1.0	0	0	0	0	0	0.3449
Brake pad thickness G_O	0	1.0	0	0	0	0	0.1542
Speed v^2	0	0	1.0	0.9855	0	0	−0.7998
Speed v	0	0	0.9855	1.0	0	0	−0.7557
Brake pad clamping force N	0	0	0	0	1.0	0	−0.0146
Decelerated mass M	0	0	0	0	0	1.0	−0.0507
Correlation coefficient	0.3449	0.1542	−0.7998	−0.7557	−0.0146	−0.0507	1.0

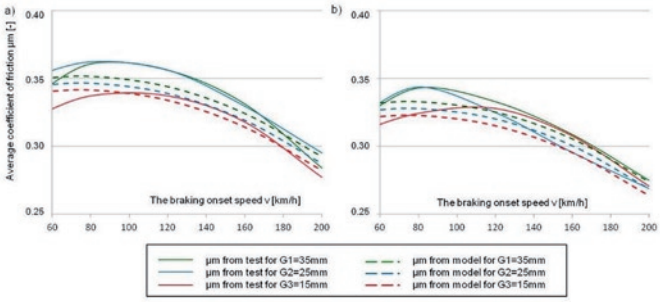

Fig. 19. The relation between the average coefficient of friction obtained in the tests and that allowing for the model of multiple regression when braking with N=44 kN, M=4.4 t: a) new disc, b) worn disc

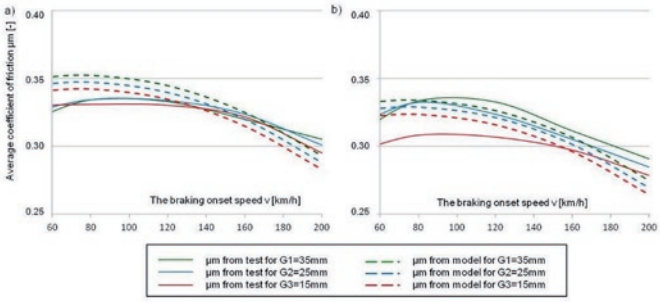

Fig. 20. The relation between the average coefficient of friction obtained in the tests and that allowing for the model of multiple regression when braking with N=28 kN, M=4.4 t: a) new disc, b) worn disc

Then, according to relation (5) the relative percentage error was determined [28] of the fitting of the model of multiple regression of the average coefficient of friction to the results of the investigations.

$$\delta = \frac{|x - x_z|}{x} \cdot 100\% \tag{5}$$

where: x – value μ_m obtained in the tests on the test stand,
x_z – value μ_m determined from the model of multiple regression (relation (3)).

Due to the sample size of $n>30$, based on inequality (6) a number of k classes was set in order to determine the distribution of the relative percentage error [16].

$$k \le 5 \ln n \tag{6}$$

Upon the application of relation (6) the number of k classes was 10. Based on the relative error data, the maximum value of variable x_{max}=9.8 and the minimum value x_{min}=0.009 were determined, which allowed the calculation of the data spread of 9.79. Fig. 21 shows the histogram of the relative percentage error size for 10 classes.

Upon the analysis of the histogram presented in Fig. 21 it can be observed that the greatest is the relative error resulting

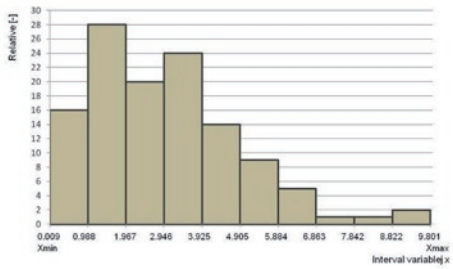

Fig. 21. Histogram of the relative percentage error size of the fitting of the model of average coefficient of friction to the results of the investigations

from the non-fitting of the model of multiple regression to the results in the range of up to 2% that occurred in 44 cases out of 120 observations. The error in the range of up to 5% occurred in 88 cases.

6. Model validation

In order to check the proposed model of estimation of the average coefficient of friction, a model validation was performed from equation (3) on subsequent brake discs. The tests were performed on two brake discs (new and regenerated) obtained from different suppliers and brake pads made from organic material. During the investigations, three types of brake pads were prepared (FR20H.2), one set of new brake pads (4 pieces) and two sets of pads worn to 25 and 15 mm. The number of brake pads tested on two brake discs totaled 24. Fig. 22 presents the brake discs. Additionally, thermal images have been recorded of the discs revealing microcracks in the case of the regenerated disc (turned from 110 mm to 108 mm).

During the main investigations, two 610 mm brake discs were tested. In the subsequent tests, a different research program was applied. In the main investigations this was program C with a clamping force of N=28 and 44 kN and a decelerated mass 4.4 and 7.5 t. During the validation tests, research program B was applied from the UIC sheet according to [26]. During the research, for the 590 mm disc, a clamping force of 25 and 36 kN was applied with a decelerated mass of 5.7 t while for the 640 mm disc, a clamping force of 16 and 26 kN and a decelerated mass of 4.7 and 6.7 t was applied.

Figs. 23-25 present the validation of the model of regression according to relation (3) for the results of average coefficient of friction obtained on the test stand.

Then, according to relation (5) the relative percentage error [28] was determined of the fitting of the model of multiple regression of average coefficient of friction to the results of tests on a new 590×110

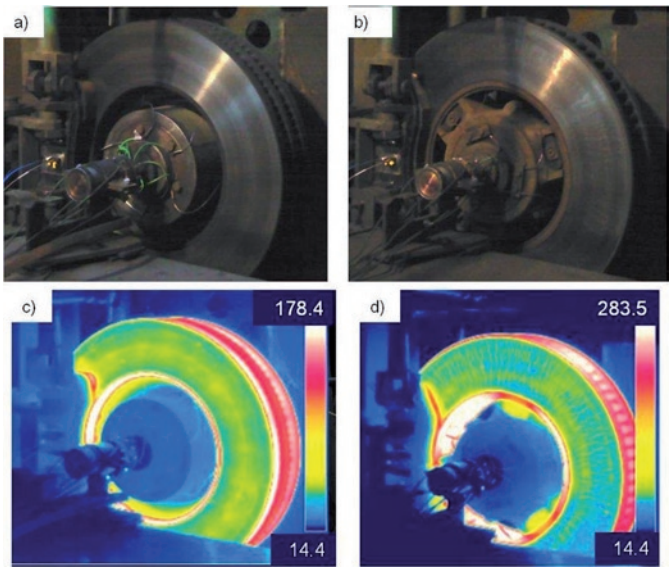

Fig. 22. Object of the investigations on the test stand: a) 590×110 brake disc (new), b) 640×110 brake disc (worn to 108 mm), c) thermal image of a 590×110 brake disc, d) thermal image of the 640×110 brake disc

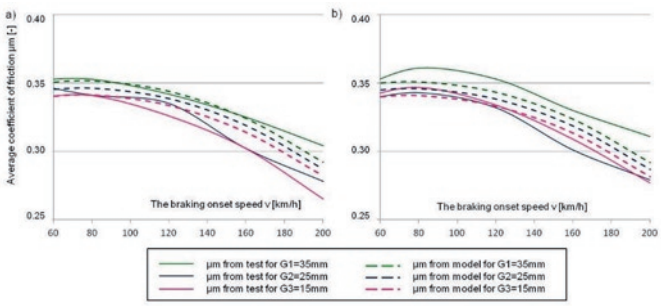

Fig. 23. The relation between μm obtained in the tests and that allowing for the model of multiple regression when braking with a new 590×110 disc with: a) N=25 kN and M=5.7 t, b) N=36 kN and M=5.7 t

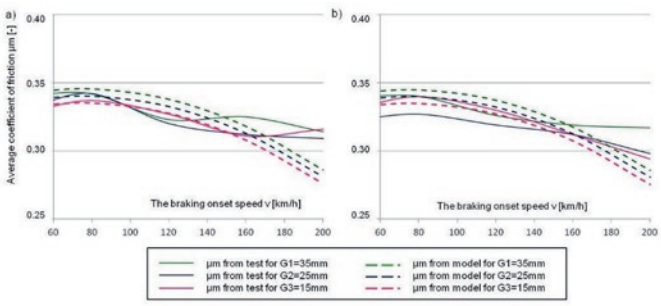

Fig. 24. The relation between μm obtained in the tests and that allowing for the model of multiple regression when braking with a worn 640×110 disc with: a) N=16 kN and M=4.7 t, b) N=26 kN and M=4.7 t

brake disc. Due to the size of the sample *n>30* (149 brakings) based on inequality (6) the number of classes was ascertained (*k=10)* in order to determine the distribution of the relative percentage error [16]. Based on the relative error data, the maximum x_{max}=13.4 and the minimum value x_{min}=0.03 of the variable was determined, which allowed calculating the data spread of 13.37. Fig 26 presents the percentage of the size of the relative percentage error for 10 classes for the new brake disc.

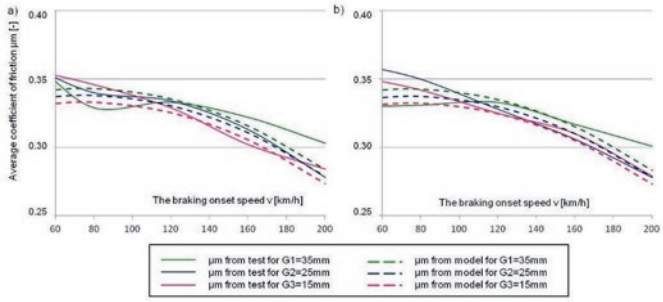

Fig. 25. The relation between μ_m obtained in the tests and that allowing for the model of multiple regression when braking with a worn 640×110 disc with: a) N=28 kN and M=6.7 t, b) N=40 kN and M=6.7 t

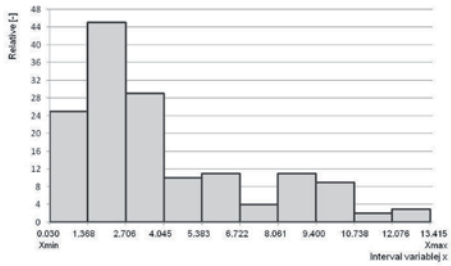

Fig. 26. The histogram of the size of the relative percentage error of the fitting of the model of multiple regression of average coefficient of friction to the results of the tests on a new 590×110 brake disc

Upon the analysis of the histogram presented in Fig. 26, it can be observed that the greatest is the relative percentage error resulting from the non-fitting of the model of multiple regression to the test results in the range of up to 4% that occurred in 60 cases out of 146 observations.

Also, for the regenerated disc, according to relation (5), the relative percentage error [28] was determined of the fitting of the model of multiple regression of the average coefficient of friction (3) to the results of the tests on the 640×110 brake disc. For 237 brakings with different clamping forces and decelerated masses, based on inequality (6) the number of classes was ascertained (*k=11)* in order to determine the distribution of the relative percentage error. Based on the error data, the maximum value x_{max}=14.6 and the minimum value x_{min}=0.05 of the variable were determined, which allowed calculating the data spread of 14.55. Fig. 27 presents the histogram of the size of the relative percentage error for 11 classes for the regenerated brake disc.

Upon analysis of the histogram presented in Fig. 27 it can be observed that the greatest is the relative percentage error resulting from the non-fitting of the model of multiple regression to the test results in the range of up to 7% that occurred in 188 cases out of 237 observations.

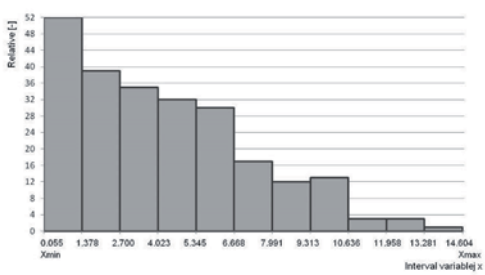

Fig. 27. The histogram of the size of the relative percentage error of the fitting of the model of multiple regression of average coefficient of friction to the results of the tests on a worn 640×110 brake disc

7. Conclusions

The investigations of the friction pair of a disc brake on an approved test stand at Institute of Rail Vehicles 'Tabor' in Poznan have shown that, aside from the preset braking parameters, the coefficient of friction decreases upon wear of both the brake pads and the brake disc below the adopted tolerances according to applicable regulations. The excess of the bottom tolerance of instantaneous and average coefficient of friction already takes place when testing a friction pair of a new brake disc and worn brake pads. This is particularly the case in some braking scenarios i.e. significant clamping forces of the pads on the disc and great decelerated masses. In the extreme cases of the tests, i.e. worn discs and worn brake pads, the reduction of the coefficient of friction is even more conspicuous. It is noteworthy, however, that under actual operation, the wear range is much wider then in the tests. It is to be expected that the values of the coefficient of friction will be even lower for extreme wear of the brake pads (5 mm) and the thickness of the brake disc after regeneration (turning from 110 to 102 mm).

The changes of the coefficient of friction can be modeled to estimate its value by using a series of variable parameters such as the braking onset speed or the decelerated mass. Additionally, it is possible to incorporate the wear of the friction pair components (brake pads and brake disc) in the model of multiple regression. The clamping force on the disc, however, and the decelerated mass have the least significant impact on the changes of the average coefficient of friction.

The tests performed on the test stand on the applied friction pair (organic brake lining and cast iron brake disc) have shown that the requirement of ensuring a constant coefficient of friction in the set ranges was not met. Even though the brake pads made from organic material of an alternative manufacturer were not tested (brake pads currently manufactured and applied in domestic rail vehicles were used) it is justified to include in the brake pad approval regulations a stipulation on the necessity of brake pad testing under an extreme wear scenario in order to validate its variability.

Besides, the results of the tests, based on which the model of changes of the average coefficient of friction was developed, may turn out useful in determining the characteristics of the coefficient of friction depending on the input parameters and wear of the friction pair. Today, when designing vehicle-specific brake calipers, the average value of the coefficient of friction given in sheet UIC 541-3 is introduced, based on which, *inter alia*, the braking distance is calculated. The introduction of a single value μ_m will result in a significant error of the calculated braking distance, where, instead of the imposed value of 0.37, the coefficient of friction assumes values in the range from 0.247 to 0.380.

During the works, the results of which have been presented in the paper, 780 brakings were carried out in order to determine the model of the multiple regression for the average coefficient of friction and 384 brakings to validate the model on subsequent brake discs.

The project has been financed by National Research and Development Centre, project LIDER V, contract number LIDER/022/359/L-5/13/NCBR/2014

References

1. Abbasi S, Teimourimanesh S, Vernersson T, Sellgren U, Olofsson U, Lundén R. Temperature and thermoelastic instability at tread braking using cast iron friction material. Wear 2014; 314: 171-180, https://doi.org/10.1016/j.wear.2013.11.028.
2. Al-Bender F, Lampaert V, Swevers J. The generalized Maxwell-Slip Model: A novel model for friction simulation and compensation. IEEE Transactions on Automatic Control 2005; 50(11): 1883-1887, https://doi.org/10.1109/TAC.2005.858676.
3. Aranganathan N, Jayashree B. Development of copper-free eco-friendly brake-friction material using novel ingredients. Wear 2016; 352-353: 79-91, https://doi.org/10.1016/j.wear.2016.01.023.
4. Awrejcewicz J, Grzelczyk D, Pyryev Y. A novel friction modeling and its impact on differential equations computation and Lyapunov exponents estimation, Vibromechanika. Journal of Vibroengineering 2008; 10(4): 475-482.
5. Bagnoli F, Dolce F, Bernabei M. Thermal fatigue cracks of fire fighting vehicles gray iron brake disc. Engineering Failure Analysis 2009; 16: 152-163, https://doi.org/10.1016/j.engfailanal.2008.01.009.
6. Baranowski P, Damaziak K, Małachowski J. Brake system studies using numerical methods. Eksploatacja i Niezawodnosc – Maintenance and Reliability 2013; 15(4): 337–342.
7. Baranowski P, Damaziak K, Małachowski J Sergienko V.P. Bukharov S N. Modeling of Abrasive Wear by the Meshless Smoothed Particle Hydrodynamics Method. Journal of Friction and Wear 2016; 37(1): 94–99, https://doi.org/10.3103/S1068366616010037.
8. Basic ADAMS Full Simulation Training Guide, http://support.mscsoftware.com
9. Belhocine A, Bouchetara M. Thermomechanical modelling of dry contacts in automotive disc brake. International Journal of Thermal Sciences 2012; 60: 161-170, https://doi.org/10.1016/j.ijthermalsci.2012.05.006.
10. Betancourt S J, Cruz A. Friction and wear in sliding contact of cast iron against phenolic resin composites reinforced with carbonaceous fibres from plantain fibre bundles. Lubrication Science 2013; 25: 163-172, https://doi.org/10.1002/ls.1186.
11. Chichinadze A V. Theoretical and practical problems of thermal dynamics and simulation of the friction and wear of tribocouples. Journal of Friction and Wear 2009; 30: 199–215, https://doi.org/10.3103/S106836660903009X.
12. Canadus de Wit C, Olson H, Åström K J, Lischinsky P. A new model for control of systems with friction. IEEE Transactions on Automatic Control 1995; 40(3): 419-425, https://doi.org/10.1109/9.376053.
13. Collignon M, Regheere G, Cristol A.L, Desplanques Y, Balloy D. Braking performance and influence of microstructure of advanced cast irons for heavy goods vehicle brake discs. Journal of Engineering Tribology 2013; 227(8): 930-940, https://doi.org/10.1177/1350650113484212.
14. Crăciun A. Evolution of materials for motor vehicles brake discs, ANNALS of Faculty Engineering Hunedoara. International Jurnal of Engineering 2015; 13(3): 149-154.
15. Dokumentacja Systemu Utrzymania – czteroosiowy piętrowy wagon pasażerski 2 klasy typu DBme serii Bmnopux nr DSU-DBme 0130-1. Przewozy Regionalne spółka z o. o. Warszawa 2010; 12: 70-76.
16. Gajek L, Kałuszka M. Wnioskowanie statystyczne – modele i metody. WNT, Warszawa 2000: 90-95.
17. Głowacz A, Głowacz W, Glowacz Z, Kozik J. Early fault diagnosis of bearing and stator faults of the single-phase induction motor using acoustic signals, Measurement 2018; 113: 1-9, https://doi.org/10.1016/j.measurement.2017.08.036.

18. Głowacz A, Głowacz Z. Diagnosis of stator faults of the single-phase induction motor using acoustic signals. Applied Acoustics Part A 2017; 117: 20-27, https://doi.org/10.1016/j.apacoust.2016.10.012.
19. Gruszewski M. Wybrane zagadnienia eksploatacji hamulca tarczowego. Technika transport szynowego 1995; 6-7: 84-86.
20. Grzes P, Oliferuk W, Adamowicz A, Kochanowski K, Wasilewski P, Yevtushenko A.A. The numerical-experimental scheme for the analysis of temperature field in a pad-disc braking system of a railway vehicle at single braking. International Communications in Heat and Mass Transfer 2016; 75: 1-6, https://doi.org/10.1016/j.icheatmasstransfer.2016.03.017.
21. Kikuuwe R, Takesue N, Sano A, Mochiyama H, Fujimoto H. Fixed-step friction somulation: from classical Coulomb model to modern continuous models. Proceedings of IEEE/RSJ International Conference on Intelligent Robots and Systems 2005: 3910-3917.
22. Kamiński Z, Kulikowski K. Determination of the functional and service characteristics of the pneumatic system of an agricultural tractor with mechanical brakes using simulation methods. Eksploatacja i Niezawodnosc – Maintenance and Reliability 2015; 17(3): 355–364, https://doi.org/10.17531/ein.2015.3.5.
23. Kasem H, Brunel J.F, Dufrénoy P, Siroux M, Desmet B. Thermal levels and subsurface damage induced by the occurrence of hot spots during high-energy braking. Wear 2011; 270: 355-364, https://doi.org/10.1016/j.wear.2010.11.007.
24. Kinkaid N.M, O'Reilly O.M, Papadopoulos P. Automotive disc brake squeal. Journal of sound and vibration 2003; 267: 105-166. https://doi.org/10.1016/S0022-460X(02)01573-0
25. KNORR-BREMSE Brake Disc and Pads. Application freight cars, high-speed train, light rail vehicles, locomotives, metros, passenger coaches, regional and commuter trains. P-1264-EN. 2014; 9:1-4.
26. Kodeks UIC 541–3. Hamulec–Hamulec tarczowy i jego zastosowanie. Warunki dopuszczenia okładzin hamulcowych. Wydanie 7, czerwiec 2010: 10-24.
27. KOMISJA Decyzja komisji z dnia 28 lipca 2006 r. dotycząca technicznej specyfikacji dla interoperacyjności odnoszącej się do podsystemu tabor kolejowy – wagony towarowe transeuropejskiego systemu kolei konwencjonalnych 2006/861/WE, Załącznik I, podpunkt I.9: 242-243.
28. Krysicki W, Włodarski L. Analiza matematyczna w zadaniach, Wydawnictwo PWN, Warszawa 2007: 412-426.
29. Kumar M, Boidin X, Desplanques Y, Bijwe J. Influence of various metallic fillers in friction materials on hot-spot appearance during stop braking. Wear 2011; 270: 371-381, https://doi.org/10.1016/j.wear.2010.11.009.
30. Lampaert V, Swevers J, Al-Bender F. Modyfication of the Leuven integrated friction model structure. IEEE Transactions on Automatic Control 2002; 47(4): 683-687, https://doi.org/10.1109/9.995050.
31. Lang A.M, Smales H. An approach to the solution of disc brake vibration problems, in: Braking of Road Vehicles. Automobile Division of the Institution of Mechanical Engineers, Mechanical Engineering Publications Limited, Suffolk, England 1993: 223-231.
32. Leszek W. Wybrane zagadnienia metodyczne badań empirycznych. Instytut Technologii Eksploatacji, Radom 2006: 142-153.
33. Li Z, Han J, Yang Z, Li W. Analyzing the mechanisms of thermal fatigue and phase change of steel used in brake discs. Engineering Failure Analysis 2015; 57: 202-218, https://doi.org/10.1016/j.engfailanal.2015.07.002.
34. Liang J, Fillmore S, Ma O. An extended bristle friction force model with experimental validation. Mechanism and Machine Theory 2012; 56, 2012: 123-137.
35. Mańczak K. Technika planowania eksperymentu, Wydawnictwo Naukowo-Techniczne, Warszawa 1976: 76-84.
36. Meierhofer A, Hardwick C, Lewis R, Six K, Dietmaier P. Third body layer-expermental results and a model describing its influence on the traction coefficient. Wear 2014; 314: 148-154, https://doi.org/10.1016/j.wear.2013.11.040.
37. Müller M, Ostermeyer G.P. A cellular automaton model to describe the three dimensional friction and wear mechanism of brake systems. Wear 2007; 263: 1175–1188, https://doi.org/10.1016/j.wear.2006.12.022.
38. Nosal S, Orłowski T. Wpływ wybranych napełniaczy na właściwości ciernych materiałów hamulcowych. Tribologia 2009; 2: 119-126.
39. Nosal S, Orłowski T. Wpływ rodzaju użytego grafitu I koksu naftowego na właściwości tarciowo-zużyciowe materiałów ciernych. Tribologia 2010; 2: 85-93.
40. Padthe A. K, Oh J, Bernstein D S. On the LuGre model and friction-induced hysteresis. Proceedings of the 2006 American Control Conference, Minneapolis, Minnesota, USA 2006: 3247-3252, https://doi.org/10.1109/ACC.2006.1657218.
41. Panier S, Dufrénoy P, Weichert D. An experimental investigation of hot spots in railway disc brakes. Wear 2004; 256: 764-773, https://doi.org/10.1016/S0043-1648(03)00459-9.
42. Peveca M, Oder G, Potrč I, Šraml M. Elevated temperature low cycle fatigue of grey cast iron used for automotive brake discs. Engineering Failure Analysis, 2014; 42: 221-230, https://doi.org/10.1016/j.engfailanal.2014.03.021.
43. Polska Norma PN-EN 14531-1, Kolejnictwo – Metody obliczania dróg hamowania do zatrzymania lub do określonej prędkości oraz metody obliczania hamulca postojowego – Część 1: Algorytmy ogólne z zastosowaniem średniej wartości obliczeniowej dla pociągów lub pojedynczych pojazdów. Warszawa luty 2016: 11-19.
44. Polska Norma PN-EN 14535-1, Kolejnictwo – tarcze hamulcowe kolejowych pojazdów szynowych – Część 1: Tarcze hamulcowe wtłaczane lub mocowane skurczowo na osiach zestawów tocznych lub napędnych, wymiary i wymagania dotyczące jakości, Warszawa 2006: 22-23.
45. Polska Norma PN-EN 14535-3 Kolejnictwo – Tarcze hamulcowe kolejowych pojazdów szynowych – Część 3: Tarcze hamulcowe, właściwości tarczy i pary ciernej, klasyfikacja. Warszawa luty 2016: 12-16.
46. Rail Consult Gesellschaft für Verkehrsberatung mbH, Wagon osobowy Z1 02 – układ jezdny–tom2. Dokumentacja Techniczno-Ruchowa: 46-59.
47. Rozporządzenie Komisji (UE) NR 321/2013 z dnia 13 marca 2013 r. dotyczące technicznej specyfikacji interoperacyjności odnoszącej się do podsystemu Tabor- wagony towarowe systemu kolei w Unii Europejskiej i uchylające decyzję 2006/861/WE: 17-18.
48. Rozporządzenie Komisji (UE) NR 1302/2014 z dnia 18 listopada 2014 r. w sprawie technicznej specyfikacji interoperacyjności odnoszącej się do podsystemu Tabor – lokomotywy i tabor pasażerski systemu kolei w Unii Europejskiej, Dodatek J Nr indeksu 24: 272-274, 388-389.
49. Saumweber E. Auslegung und Leistungsgrenzen von Scheibenbremsen. ZEV-Glasses Annalen 1988; 112(4): 139-143.
50. Szymanski G M, Josko M, Tomaszewski F, Filipiak R. Application of time-frequency analysis to the evaluation of the condition of car suspension. Mechanical System and Signal Processing 2015; 58-59: 298-308, https://doi.org/10.1016/j.ymssp.2014.12.017.
51. Szymanski G M, Josko M, Tomaszewski F. Diagnostics of automatic compensators of valve clearance in combustion engine with the use of vibration signal. Mechanical System and Signal Processing 2016; 68-69: 479-490, https://doi.org/10.1016/j.ymssp.2015.07.015.

52. Ścieszka S.F. Hamulce cierne. Zagadnienia materiałowe, konstrukcyjne i tribologiczne. Wydawnictwo Gliwice-Radom 1998: 11-19.
53. UNITED NATIONS Regulation No. 90, Addendum 89: Uniform provisions concerning the approval of replacement brake lining assemblies, drum brake linings and discs and drums for power-driven vehicles and their trailers. E/ECE/324/Rev.1/Add.89/Rev.3-E/ECE/TRANS/505/Rev.1/Add.89/Rev.3, 17 February 2012: 17-21.
54. Webside http://breck.pl/pl/produkty/klocki-breck-hs/
55. Wojewoda J, Stefański A, Wiercigroch M, Kapitaniak T. Hysteretic effects in dry friction: modelling and experimental studies. Philosophical Transactions of the Royal Society A 2008: 366: 753-757, https://doi.org/10.1098/rsta.2007.2125.
56. Wu S C, Zhang S Q, Xu Z W. Thermal crack growth-based fatigue life prediction due to braking for a high-speed railway brake disc. International Journal of Fatigue. 2016; 87: 359-369, https://doi.org/10.1016/j.ijfatigue.2016.02.024.
57. Wirth X., Improving the Performance of Disc Brakes on High-speed Rail Vehicles with a Novel Types of Brake Pad: Isobar. RTR 1998; 1: 24-29.

Wojciech SAWCZUK
Institute of Combustion Engines and Transport
Poznan University of Technology
ul. Piotrowo, 60-965 Poznań, Polska

E-mail: wojciech.sawczuk@put.poznan.pl

Article citation info:
KONTREC N, PANIĆ S, PETROVIĆ M, MILOŠEVIĆ H. A stochastic model for estimation of repair rate for system operating under performance based logistics. Eksploatacja i Niezawodnosc – Maintenance and Reliability 2018; 20 (1): 68–72, http://dx.doi.org/10.17531/ein.2018.1.9.

Nataša KONTREC
Stefan PANIĆ
Milena PETROVIĆ
Hranislav MILOŠEVIĆ

A STOCHASTIC MODEL FOR ESTIMATION OF REPAIR RATE FOR SYSTEM OPERATING UNDER PERFORMANCE BASED LOGISTICS

STOCHASTYCZNY MODEL DO SZACOWANIA INTENSYWNOŚCI NAPRAW DLA SYSTEMU DZIAŁAJĄCEGO W WARUNKACH LOGISTYKI WYDAJNOŚCIOWEJ

Performance Based Logistics (PBL) concept has an aim to improve the system availability and it has been extensively researched in the recent years. These researches showed that inventory level does not impact system availability as much as component reliability and repair time in repairable system operating under PBL contract. Based on that, in this paper, we propose a new stochastic model for determination of annual repair rate for critical aircraft components in such system in order to achieve desired availability. The result obtained could be used for planning of base stock level and capacity of repair facilities.

***Keywords**: repair rate, availability, stochastic model, performance based logistic.*

Koncepcja Logistyki Opartej na Wydajności (Performance Based Logistics, PBL), której celem jest poprawa gotowości systemów, została w ostatnich latach szeroko zbadana. Badania te wykazały, że w przypadku systemów działających w warunkach PBL, poziom zapasów nie wpływa na gotowość systemu w tak dużym stopniu jak niezawodność elementów składowych oraz czasy napraw. Opierając się na tej obserwacji, w niniejszym artykule proponujemy nowy model stochastyczny do określania rocznej intensywności napraw krytycznych elementów samolotu tworzących system tego typu. Model ten pozwala na osiągnięcie pożądanej gotowości. Uzyskany model może być wykorzystany do planowania bazowego poziomu zapasów oraz przepustowości zakładów remontowych.

***Słowa kluczowe**: intensywność napraw, gotowość, model stochastyczny, logistyka oparta na wydajności.*

1. Introduction

The concept of Performance Based Logistics (PBL) originates from the military aircraft industry. It refers to acquiring cost-effective weapon system support. PBL is a strategy which has an aim to improve the performance and to lower the total operating cost of the complex system (especially in aviation and defense industry) during the post production phase of their life-cycle [21].

This system was succeeded by numerous commercial companies [20, 5]. In practice, the principle works as follows – e.g. when servicing aircraft engines under the PBL contract, the maintenance and service are not charged by the number of used spare parts, the number of repairs or activities, but the number of flight hours that the engine's operator makes instead [17].

The availability is one of the crucial criteria in the PBL contracts [28] and can be largely affected by factors such as reliability and number of spare parts. Control of all factors is vital for contract users. Many researchers have tried to provide mathematical models which will answer the question: How do supply management, parts reliability and maintenance affect the availability?

One of the most utilized, and at a later stage most perfected, is the METRIC model, as a first practical mathematic model from this area [23]. It is based on the Poisson distribution with the mean value estimated by a Bayesian procedure and uses "one-for-one" policy of filling out the storage and modeling the system on the basis of mean repair time rather than its distribution. Other models based on the METRIC model have appeared later, such as VARI-METRIC [24] and MOD-METRIC model [15] which provided better results in simulations than the initial model.

Regarding the aspect of expenses and production order, this problem was examined in paper [2] by considering the failure rate as a function that depends on the number of machines and determining the optimum supplies for expensive, critical parts with low demand. This topic was further elaborated in paper [3] but in conditions of limited capacity related to repairs of spare parts and in paper [26] in relation to systems with the condition based maintenance strategy. Furthermore, the supplies of repairable spare parts in the case of non-stationary Poisson demand have been examined in paper [12] with the goal to minimize system's expenses. Similarly, with minor corrections, this problem was also examined in papers [27, 25] with the goal to reduce the delivery time, delays and transport costs. The aforesaid models proved to be far superior in relation to the original Sharebrook's METRIC model.

Kang et al. examined systems for inventory management under the PBL contracts [7]. They have developed a methodology which determines the system's availability based on reliability of its components/parts and maintenance possibilities. They concluded that mean time to failures (MTBF), number of spare parts and mean time to repair (MTTR) have the greatest impact on availability. Some modifications of this model are presented in papers [8, 9, 10, 18 and 19].

This problem was examined further, by relaxing assumptions such as fixed repair rate, fixed failure rate and infinitive repair in paper [14]. The results that were achieved in this research proved that the level of supplies of reparable spare parts does not affect the system

availability as much as reliability and repair rate. The authors advise to focus on the component reliability and repair system efficiency to improve system availability.

Based on the aforesaid research, the model presented in this paper observes the repair rate as a stochastic process and has an aim to determine this parameter for preferred level of availability. The need for stochastic modeling of repairable systems has been justified and explained in paper [1].

2. Model for assessment of expected time to repair

In this paper we are observing system that alternates between two states – system is operative at certain time and non-operative otherwise. In the literature, this approach is known as alternating renewal process [4]. We assumed that at the start system is operative. It remains in that state for a period of time T (failure time), then it stops operating for time R (repair time) and after being repaired system is back in operative state. The duration of the renewal cycle is $T+R$. We also assumed that perfect repair has been carried out at the constant rate after which system behaves the same as the new one. In this case we are observing the system in which failure time has Rayleigh distribution and the goal is to determine the repair rate in order to optimize performance of the system i.e. to determine repair rate for desired level of system availability in the case when mean time between failures (MTBF) is known. MTBF is reliability measure of repairable system and includes only operational time between failures and not the repair time. Main purpose of PBL contracts is to optimize system availability. Steady state availability is often used availability measure in repairable system and according to definitions is equal to:

$$A = \lim_{t\to\infty} A(t). \tag{1}$$

According to key renewal theorem the limited probability that system is available can be expressed as ratio of the mean of period when system is operative and mean of the period which represents one renewal cycle [22]:

$$\lim_{t\to\infty} A(t) = \frac{E[T]}{E[T]+E[R]}, \tag{2}$$

where E is the expected value operator. Based on this relation is derived a well known formula for availability:

$$A = \frac{MTBF}{MTBF + MTTR}. \tag{3}$$

MTTR is mean time to repair i.e. expected time needed to repair a failed component. If there exists probability density function $p(t)$, than the $MTBF$ can be defined as:

$$MTBF = \int_0^\infty t p(t) dt. \tag{4}$$

Since we assumed that failure time has Rayleigh distribution with probability density function (shortly written PDF) $p(t) = {2t}/{x} \exp\left(-{t^2}/{x}\right), t > 0$ [6] where the distribution parameter x is determined by relation $E\left(t^2\right) = x$, the previous equation is:

$$MTBF = \int_0^\infty \frac{2t^2}{x} \exp\left(-\frac{t^2}{x}\right) dt. \tag{5}$$

By solving the previous integral we obtained following equation:

$$MTBF = \frac{1}{2}\sqrt{\pi x}. \tag{6}$$

The rate of repair can be observed as a reciprocal value of MTTR [16]. So, in order to simplify further calculation we introduce the changes:

$$u = 1 / MTBF = 2 / \sqrt{\pi x}, \tag{7}$$

where such defined u denotes the failure rate and:

$$\mu_r = 1 / MTTR,$$

where μ_r denotes repair rate.

According to (7) Rayleigh's random variable x is:

$$x = \frac{4}{\pi u^2} \tag{8}$$

and the availability formula (3) can now be expressed as:

$$A = \frac{\mu_r}{u + \mu_r}. \tag{9}$$

Equation (9) will be further used in order to determine repair rate for desired level of availability in case when MTBF is known. We could use eq. (3) and define availability through MTBF and MTTR. In that case we would observe MTTR as a stochastic process and we would determine its characteristic PDF and other parameters for certain predefined availability but, according to our opinion observing 1/MTTR, rate of repair, as stochastic process, is more significant for the entire repair process planning and managing.

Due to complexity of process of estimating the components' failure rate in relation to time, as well as a stochastic nature of the observed process, the parameter x could also be considered as a random variable that changes significantly slower than random variable t described with the Rayleigh's model. Since we already know from the stochastic theory [13], for cases when the changes of variable t are described by the Rayleigh's model and when $x \approx t^2$, slow changes of variable x can be described with the stochastic process with exponential distribution with the use of:

$$p_x(x) = \frac{\exp\left(-{x}/{x_0}\right)}{x_0}, \quad x > 0, \tag{10}$$

where $x_0 = E(x)$.

Since the goal of this paper is to determinate the repair rate for desired level of availability in case when MTBF is known and we already expressed Rayleigh's random variable x in (8), than the following transformation is applicable:

$$p(u) = p_x\left(\frac{4}{\pi u^2}\right)|J|, \tag{11}$$

where $|J|$, Jacobian transformation of random variable x, is stated in (12):

$$|J| = \left|\frac{dx}{du}\right| = \frac{8}{\pi u^3}. \tag{12}$$

By replacing (12) into (11), we get

$$p(u) = \frac{8}{u^3 \pi x_0} \exp\left(-\frac{4}{u^2 \pi x_0}\right). \tag{13}$$

Now, based on (9) the repair rate μ_r can be presented as $\mu_r = \frac{Au}{1-A}$ with PDF function:

$$p(\mu_r) = p_u\left(\frac{Au}{1-A}\right)|J|, \tag{14}$$

where Jacobian transformation is:

$$|J| = \frac{du}{d\mu_r} = \frac{A}{1-A}. \tag{15}$$

According to previous, PDF function of repair rate can be stated as:

$$p(\mu_r) = \frac{8A^2}{(1-A)^2 \mu_r^3 \pi x_0} \exp\left(\frac{-4A^2}{(1-A)^2 \mu_r^2 \pi x_0}\right). \tag{16}$$

This is a major contribution of this paper, exact mathematical characterization of MTTR random process. By using this PDF expression an exact modeling of repair rate process can be obtained by generating exact repair rate sample values for corresponding values of availability and MTBF. In such way, simulation of repair rate process through generating its samples could serve for dynamical prediction of system performances.

Now, let present cumulative distribution function (shortly written CDF) of repair rate as:

$$F(\mu_r) = \int_0^{\mu_r} p(\mu_r) d\mu_r = 1 - \exp\left(\frac{-4A^2}{\left(1-A^2\right)\mu^2 \pi x_0}\right) \tag{17}$$

With the use of inverse sampling $y = F(\mu_r)$, the inverse CDF is $F^{-1}(\mu_r) = y^{-1}$ and repair rate samples μ_r can be expressed as:

$$\mu_r = \sqrt{\left(-\frac{\left(1-A^2\right)\pi x_0}{4A^2} \ln\left(1 - F^{-1}(\mu_r)\right)\right)} = \sqrt{\left(-\frac{\left(1-A^2\right)\pi x_0}{4A^2} \ln(1-y)\right)}, \tag{18}$$

where y is uniformly distributed in interval [0, 1]. By introducing change $U = 1 - y$, (18) can be reduced to:

$$\mu_r = \sqrt{\left(-\frac{\left(1-A^2\right)\pi x_0}{4A^2} \ln U\right)}$$

where U is uniformly distributed in interval [0, 1].

Further, based on the equation (16), we can determine the expected repair rate of component $\bar{\mu}_r$ in relation to the preferred level of availability as:

$$\bar{\mu}_r = \int_0^{+\infty} \mu_r p(\mu_r) d\mu_r \tag{19}$$

After replacing (16) into (19) the previous expression is reduced to:

$$\bar{\mu}_r = \frac{2A}{(1-A)\sqrt{\pi}\sqrt{x_0}}. \tag{20}$$

This measure that characterizes MTTR random process is in that way for the first time expressed as the function of availability and MTBF and can be observed as their function.

3. Numerical results

In order to verify our model we are using data that originate from [7, 14], where the system of unmanned aerial vehicles consisting of four air vehicles, two ground-control stations, modular mission payloads, data links, remote data terminals and an automatic landing subsystem were observed. The concept of an unmanned aerial vehicle (UAV) is not new but it has not been utilized in civilian sector due to the insufficient level of reliability of current solutions that leads to high probability of failure occurrence [11].

The following critical repairable components: aircraft's engine, propeller and avionics, are taken into consideration. Known parameters examined in the system are:

- Each aircraft has 120 flight hours per month, i.e. 1440 (120*12) flight hours per year.
- Mean time between failures (MTBF is 750 flight hours for the aircraft engine, 500 for the propeller and 1000 for avionics.
- Based on that it is possible to determine the MTBF as follows:
  - for the aircraft engine $MTBF_e = 750/1440$
  - for the aircraft propeller $MTBF_p = 500/1440$
  - for the avionics $MTBF_a = 1000/1440$

Based on the model presented in previous section, a numerical analysis was conducted with the goal to calculate the annual expected time for repair in order to acquire availability of A=0.85, A=0.9, A=0.95 by emphasizing the stochastic nature of this process. A similar analysis can also be conducted for other values of parameter A.

Fig.1 represents the probability of engine's repair rate depending on time for cases when it is expected that availability of this component is 85%, 90% and 95%. Likewise, Fig.2 provides data related to the propeller, while Fig.3 refers to system's avionics.

Fig. 4 provides graphics data on repair rate in relation to availability on annual level. The availability parameter was set in interval [0.5 – 1] and according to previous equations we can calculate the annual repair rate for aircraft engine, propeller and avionics. It can be seen that the repair rate increases with the increase of required level of availability. Complete set of graphic data is presented in the following table:

Table1. Level of annual repair rate in relation to availability

Availability	Propeller	Electronics	Engine
0.50	1.92	2.88	1.44
0.55	2.35	3.52	1.76
0.60	2.88	4.32	2.16
0.65	3.57	5.35	2.67
0.70	4.48	6.72	3.36
0.75	5.76	8.64	4.32
0.80	7.68	11.52	5.76
0.85	10.88	16.32	8.16
0.90	17.28	25.92	12.96
0.95	36.48	54.72	27.36
0.97	62.08	93.12	46.56

4. Conclusion

According to previous PBL studies, the base stock level does not influence system availability as much as repair rate and reliability, so in this paper we proposed a model for determination of expected repair rate on annual level by observing it as a stochastic process, for the first time. The presented model can be used for estimation of other significant maintainability parameters. Further, by setting the availability parameter at required values and assuming the base stock level was fixed at some constant value, we can determine the repair rate, not just for critical components mentioned in this paper, but for any other repairable system that meets the accepted assumptions. By using this PDF expression an exact modeling of repair rate process can be obtained by generating exact repair rate sample values for corresponding values of availability and MTBF. In such way simulation of repair rate process through generating its samples could serve for dynamical prediction of system performances. This modeling procedure could be used for planning implementation of new service stations or increasing any other capacity required for reparable spare parts servicing in order to increase repair system efficiency. The potential area of further research is optimization of cost that these modifications could bring, such as optimizing the number of repair stations.

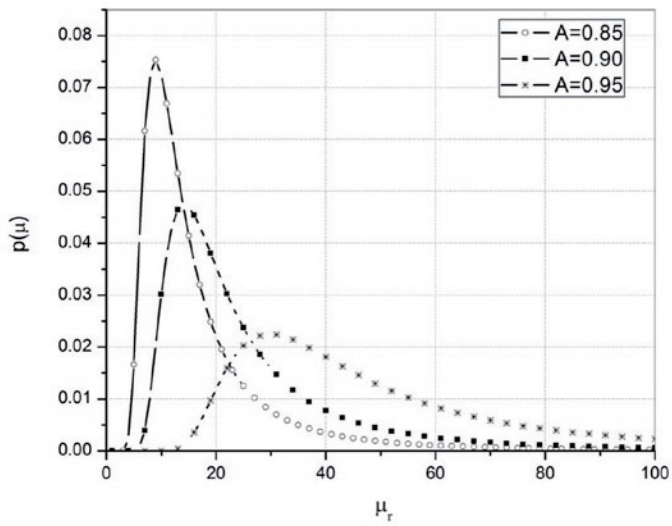

Fig. 1. PDF of engine repair rate

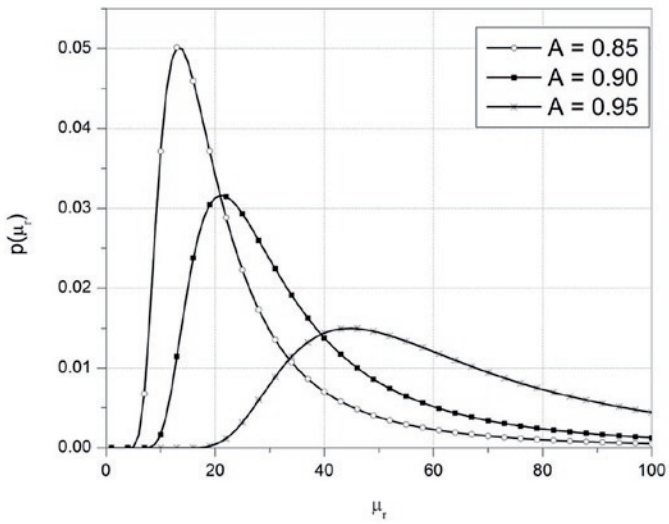

Fig. 2. PDF of propeller repair rate

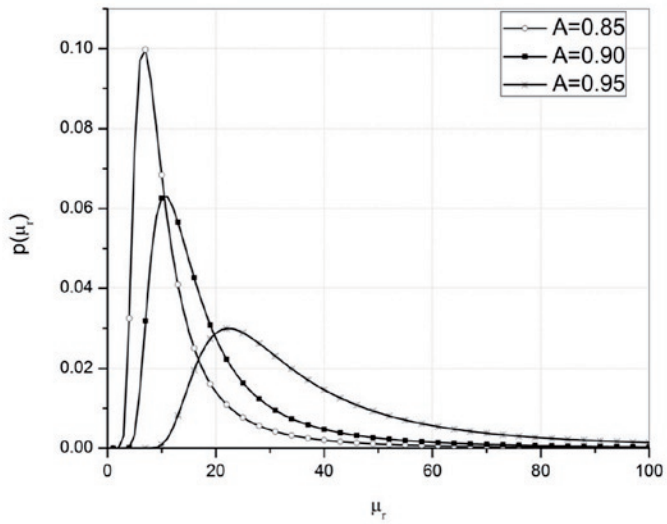

Fig. 3. PDF of aircraft's avionics repair rate

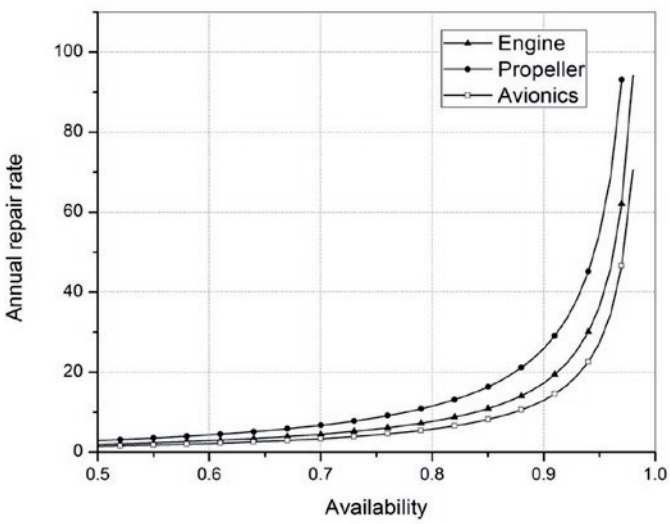

Fig. 4. Annual level of repair rate in relation to availability

References

1. Andrzejczak K. Stochastic modelling of the repairable system. Journal of KONBiN. 2015; 35 (1): 5-14, https://doi.org/10.1515/jok-2015-0034.
2. Dhakar T S, Schmidt C, Miller D M. Base stock level determination for high cost low demand critical repairable spares. Computers & Operation Research 1994; 21 (4): 411-420, https://doi.org/10.1016/0305-0548(94)90028-0.
3. Diaz A, Fu M. Multi-echelon inventory systems for repairable items with limited repair facilities. European Journal of Operations Research 1997; 97 (3): 480-492, https://doi.org/10.1016/S0377-2217(96)00279-2.
4. Gamiz M L, Kulasekera K B, Limnios N, Lindqvist B H. Applied Nonparametric Statistics in Reliability. Springer-Verlag London 2011; ISBN 978-0-85729-117-2, https://doi.org/10.1007/978-0-85729-118-9.
5. Geary S. Ready for combat. DC Velocity 2006; 4 (7): 75-80.
6. Hoffman D, Karst O. J. The theory of the Rayleigh distribution and some of its applications. Journal of Ship Research 1975; 19 (3).
7. Kang K, Doerr K. H, Boudreau M, Apte U. A decision support model for valuing proposed improvements in component reliability. Working paper, Naval Postgraduate School 2005.
8. Kang K, Doerr K H, Sanchez S M. A Design of Experiments Approach to Readiness Risk Analysis. Simulation Conference WSC 06. Proceedings of the Winter 2006: 1332-1339, https://doi.org/10.1109/WSC.2006.323232.
9. Kim S H, Cohen M A, Netessine S. Performance contracting in fter-sales service supply chains. Management Science. 2007; 53 (12):1843-1858, https://doi.org/10.1287/mnsc.1070.0741.
10. Kim S H, Cohen M A, Netessine S. Reliability or inventory? Contracting strategies for after-sales product support. Proceedings of 2007 International Conference on Manufacturing & Service Operations Management 2007.
11. Krawczyk M. Conditions for Unmanned Aircraft Reliability Determination. Eksploatacja i Niezawodnosc - Maintenance and Reliability 2013; 15 (1): 31-36.
12. Lau H C, Song H. Two-echelon repairable item inventory system with limited repair capacity under nonstationary demands. Proceedings of 35th Meeting of the Decision Sciences Institute (DSI). USA: Boston 2004: 1901-1908.
13. Leemis L, McQueston J. Univariate distribution relationships The American Statistician 2008; 62: 45-53, https://doi.org/10.1198/000313008X270448.
14. Mirzahosseinian H, Piplani R. A study of repairable parts inventory system operating under performance-based contract. European Journal of Operational Research 2011; 214 (2): 256-261, https://doi.org/10.1016/j.ejor.2011.04.035.
15. Muckstadt J. A. A model for a multi-item, multi-echelon, multi-indenture inventory system. Management Science 1973; 20: 472-481, https://doi.org/10.1287/mnsc.20.4.472.
16. Muralidharan K, and Syamsundar A. (2012). Statistical Methods for Quality, Reliability and Maintainability, PHI Learning PVT, India ISBN-978-81-203-4543-0.
17. Ng I C L, Maull R, Yip N. Outcome-based contracts as a driver for systems thinking and service-dominant logic in service science: evidence from the defense industry. European Management Journal 2009; 27 (6): 377-387, https://doi.org/10.1016/j.emj.2009.05.002.
18. Nowicki D, Kumar U D, Steudel H J, Verma D. Spares provisioning under performance-based logistics contract: profit-centric approach. Journal of the Operational Research Society 2008; 59 (3): 342-352, https://doi.org/10.1057/palgrave.jors.2602327.
19. Öner K B, Kiesmüller G P, van Houtum J. Optimization of component reliability in the design phase of capital goods. European Journal of Operational Research 2010; 205 (3): 615-624, https://doi.org/10.1016/j.ejor.2010.01.030.
20. Phillips E H. Performance based logistics: a whole new approach. Aviation Week and Space Technology 2005; 163 (17): 52-55.
21. Randall W, Pohlen T, Hanna J. Evolving a theory of performance-based logistics using insights from service dominant logic, Journal of Business Logistics 2010; 31 (2): 35-61, https://doi.org/10.1002/j.2158-1592.2010.tb00142.x.
22. Ross S M. Applied probability models with optimization applications. Courier Corporation; 2013 Apr 15.
23. Sherbrooke C C. METRIC: a multi-echelon technique for recoverable item control. Operational Research 1968; 16: 122-141, https://doi.org/10.1287/opre.16.1.122.
24. Sherbrooke C C. VARI-METRIC: improved approximations for multi-indenture, multi-echelon availability models. Operations Research 1986; 34: 311-319, https://doi.org/10.1287/opre.34.2.311.
25. Tao N, Wen S. Simulation of a closed loop multi-echelon repairable inventory system. Proceedings of the 16th International conference on Management Science & Engineering 2009: 663-668.
26. Wang Y, Zhao J, Cheng Z, Yang Z. Integrated decision on spare parts ordering and equipment maintenance under condition based maintenance strategy. Eksploatacja i Niezawodnosc - Maintenance and Reliability 2015; 17 (4): 591- 599, http://dx.doi.org/10.17531/ ein.2015.4.15.
27. Wong H, Cattrysse D, Van Oudheusden D. Stocking decisions for repairable spare parts pooling in a multi-hub system. International Journal of Production Economics 2005; 93: 309-317, https://doi.org/10.1016/j.ijpe.2004.06.029.
28. Wynne M. W. Performance based logistics: purchasing using performance based criteria. The Under Secretary of Defense, Memorandum for Secretaries of the Military Departments 2004.

Nataša KONTREC
Stefan PANIĆ
Milena PETROVIĆ
Hranislav MILOŠEVIĆ
Faculty of Sciences and Mathematics
University of Pristina
Lole Ribara 29, Kosovska Mitrovica, Serbia

E-mails: natasa.kontrec@pr.ac.rs, stefan.panic@pr.ac.rs, milena.petrovic@pr.ac.rs, hranislav.milosevic@pr.ac.rs

Article citation info:
TAHA R. On system reliability of increasing multi-state linear k-within-(m,s)-of-(m,n):F lattice system. Eksploatacja i Niezawodnosc – Maintenance and Reliability 2018; 20 (1): 73–82, http://dx.doi.org/10.17531/ein.2018.1.10.

Radwan TAHA

ON SYSTEM RELIABILITY OF INCREASING MULTI-STATE LINEAR *k*-WITHIN-(*m,s*)-OF-(*m,n*):F LATTICE SYSTEM

ZWIĘKSZANIE NIEZAWODNOŚCI WIELOSTANOWYCH SYSTEMÓW LINIOWYCH TYPU *k*-W- (*m,s*) -Z- (*m,n*):F O STRUKTURZE KRATOWEJ

A "multi-state linear k-within-(m,s)-of-(m,n):F lattice system" (MS L(k,m,s,n:F)) comprises of m×n components, which are ordered in m rows and n columns. The state of system and components may be one of the following states: 0, 1, 2, ..., H. The state of MS L(k,m,s,n:F) is less than j whenever there is at least one sub-matrix of the size m×s which contains k_l or more components that are in state less than l for all $j \le l \le H$. This system is a model for many applications, for example, tele communication, radar detection, oil pipeline, mobile communications, inspection procedures and series of microwave towers systems. In this paper, we propose new bounds of increasing MS L(k,m,s,n:F) reliability using second and third orders of Boole-Bonferroni bounds with i.i.d components. The new bounds are examined by previously published numerical examples for some special cases of increasing MS L(k,m,s,n:F). Also, illustration examples of modelling the system and numerical examples of new bounds are presented. Further, comparisons between the results of second and third orders of Boole-Bonferroni bounds are given.

Keywords: *network reliability, reliability engineering, structural reliability, system failure modelling, reliability optimization, probabilistic methods.*

"Wielostanowy system liniowy k-w- (m, s) -z- (m, n):F o strukturze kratowej" (MS L(k, m, s, n:F)) składa się z m × n elementów, uporządkowanych w m wierszach i n kolumnach. Stan systemu i elementów może być jednym z następujących stanów: 0, 1, 2, ..., H. Stan MS L (k, m, s, n: F) jest mniejszy niż j, gdy istnieje co najmniej jedna pod-matryca o rozmiarze m × s, która zawiera kl lub więcej elementów, które znajdują się w stanie mniejszym niż l dla wszystkich $j \le l \le H$. System ten stanowi model dla wielu zastosowań, na przykład w telekomunikacji, detekcji radarowej, rurociągach naftowych, komunikacji mobilnej, procedurach przeglądu oraz systemach wież radiolinii. W niniejszym artykule proponujemy nowe granice zwiększania niezawodności MS L (k, m, s, n: F) z wykorzystaniem drugiego i trzeciego stopnia nierówności Boole'a–Bonferroniego z niezależnymi elementami o jednakowym rozkładzie. Nowe granice omówiono na podstawie poprzednio publikowanych przykładów numerycznych dla niektórych szczególnych przypadków zwiększania MS L (k, m, s, n: F). Przedstawiono także przykłady ilustrujące modelowanie systemu oraz numeryczne przykłady nowych granic. Ponadto porównano wyniki uzyskane dla drugiego i trzeciego stopnia nierówności Boole'a–Bonferroniego.

Słowa kluczowe: *niezawodność sieci, inżynieria niezawodności, niezawodność konstrukcyjna, modelowanie uszkodzeń systemu, optymalizacja niezawodności, metody probabilistyczne.*

Notations

m,s,n,k,p_j system parameters.

N $= n - s + 1$.

H highest state for the system and components.

k_j minimum number of components that must be in state less than j in the sub matrix of the size $m \times s$, $j = 1, 2, \ldots, H$.

k_j^G minimum number of components that must be in state greater than or equal j in the sub matrix of the size $m \times s$, $j = 1, 2, \ldots, H$; $k_j^G = (m \times s) - k_j + 1$.

k a vector of k_j-s.

k_j^G a vector of k_j^G-s.

δ_j number of components that are in state less than j inside the sub-matrix of the size $m \times s$.

$x_{i,j}$ the state of the component, which are located in the row i and the column j, $x_{i,j} \in \{0,1,\ldots,H\}$.

x the states of all components, $x = \begin{pmatrix} x_{1,1} & x_{1,2} & \cdots & x_{1,n} \\ x_{2,1} & x_{2,2} & \cdots & x_{2,n} \\ \vdots & \vdots & \vdots & \vdots \\ x_{m,1} & x_{m,2} & \cdots & x_{m,n} \end{pmatrix}$.

$\varphi(x)$ the structure function of the system, $\phi(x) \in \{0,1,2,\ldots,H\}$.

p_j probability that state of the component is j, $\sum_{i=0}^{H} p_i = 1$.

P_j probability that state of the component is greater than or equal j, $P_j = \sum_{i=j}^{H} p_i$.

Q_j probability that state of the component is less than j, $Q_j = 1 - P_j$.

$A_{i,j}$ an event that at least k_l components in state less than l, $j \le l \le H$, of the sub-matrix with the size $m \times s$, that begin with the component (1, i) and end with the component (m, $i + s - 1$).

μ denote the random number of events among $A_{1,j}, A_{2,j}, \ldots, A_{N,j}$ which occur.

$S_{1,j}, S_{2,j}, S_{3,j}$: the binomial moments of μ.

$S_{1,j}$ $\sum_a \Pr(A_{a,j})$, for $1 \le a \le N$.

$S_{2,j}$ $\sum_{a,b} \Pr(A_{a,j} A_{b,j})$, for $1 \le a < b \le N$.

$S_{3,j}$ $\sum_{a,b,c} \Pr(A_{a,j} A_{b,j} A_{c,j})$, for $1 \le a < b < c \le N$.

R_j probability that state of the system is greater than or equal j.

F_j probability that state of the system is less than j, $F_j = 1 - R_j$.

$\lfloor z \rfloor$ the lower integer part for z.

E_j maximum error of the estimation of R_j and F_j.

UB_j the upper bound of R_j.

LB_j the lower bound of R_j.

i.i.d independent identically distributed.

MS multi-state.

L(k,m,s,n:F) linear k-within-(m,s)-of-(m,n):F lattice system

L(k^G,m,s,n:G) linear k-within-(m,s)-of-(m,n):G lattice system

1. Introduction

A binary L(k,m,s,n:F) is a two dimensional grid. Its components have only the state 1 (operating) or state 0 (failed), and arranged in m rows and n columns. This system fails if at least one (m,s) sub-matrix of its components contains k or more failed components. Many papers studied its reliability, such as [13-16, 21, 23]. In the last few years, many systems generalized to MS systems, because the MS models give more limberness for modelling the equipment conditions. Such as, MS consecutive k-out-of-n:F system [9, 22, 24], MS k-out-of-n:F system [1, 10, 20], MS consecutive k-out-of-r-from-n: F system [8, 19] and MS L(k,m,s,n:F) [7]. In this paper, we study MS L(k,m,s,n:F). This system is a model for many applications. The system definition and illustration examples of modelling the system are given in section 2. The Boole-Bonferroni bounds are generalized in section 3, that will used for evaluation the proposed bounds. In section 4, the proposed bounds and an illustration example are given. The numerical results are presented in section 5.

2. The MS L(k,m,s,n:F)

The MS L(k,m,s,n:F) contains $m \times n$ components, that are ordered as a matrix of the degree $m \times n$. The possible states of MS L(k,m,s,n:F) and its components are: 0, 1, …,H. The state of MS L(k,m,s,n:F) is less than j whenever there is at least one sub-matrix of the size $m \times s$ which contains k_l or more components that are in state less than l for all $j \le l \le H$. In other words, $\phi(x) < j$ if at least one sub-matrix of the size $m \times s$ is in state less than j. The state of a sub-matrix of the size $m \times s$ is less than j if all the following inequalities are satisfied:

$$\delta_j \ge k_j,$$
$$\delta_{j+1} \ge k_{j+1},$$
$$\delta_{j+2} \ge k_{j+2},$$
$$\vdots$$
$$\delta_H \ge k_H.$$

The values of k vector, $k_1, k_2, \ldots, k_H$, categorize the MS L(k,m,s,n:F) to three cases:

Case1: When $k_1 \ge k_2 \ge \ldots \ge k_H$, the system is called a decreasing MS L(k,m,s,n:F). The exact reliability of decreasing MS L(k,m,s,n:F) evaluated in Ref. [7].

Case2: When $k_1 \le k_2 \le \ldots \le k_H$, the system is called an increasing MS L(k,m,s,n:F). In this case, that is more difficulty, new lower and upper bounds are proposed.

Case3: When $k_1 = k_2 = \ldots = k_H$, the system is called a constant MS L(k,m,s,n:F). This system is a special case of the increasing MS L(k,m,s,n:F) and decreasing MS L(k,m,s,n:F).

As with the binary system, the MS L(k,m,s,n:F) and the MS L(k^G,m,s,n:G) are considered as mirror images of each other. Further, the decreasing MS L(k,m,s,n:F) is an increasing MS L(k^G,m,s,n:G). The following examples illustrate this system.

Example 1:

A decreasing MS linear (k_1 = 4, k_2 = 3, k_3 = 2)-within-(2,2)-of-(2,4):F lattice system, which is an increasing MS linear ($k_1^G = 1, k_2^G = 2, k_3^G = 3$)-within-(2,2)-of-(2,4):G lattice system, consists of 8 components, that arranged in 2 rows and 4 columns. This system contains 3 sub-matrices of the degree 2×2. The state of any one of them is:

- less than 1, if $\delta_1 \ge 4$, $\delta_2 \ge 3$ and $\delta_3 \ge 2$,
- less than 2, if $\delta_2 \ge 3$ and $\delta_3 \ge 2$,
- less than 3, if $\delta_3 \ge 2$.

For state 1:

$\phi(x) < 1$, if at least one sub-matrix of the degree 2×2 is in state less than 1. For example, when $x = \begin{pmatrix} 0 & 0 & 2 & 3 \\ 0 & 0 & 3 & 1 \end{pmatrix}$:

- The state of $\begin{pmatrix} 0 & 0 \\ 0 & 0 \end{pmatrix}$ is less than 1, such that $\delta_1 = \delta_2 = \delta_3 = 4$.
- The state of $\begin{pmatrix} 0 & 2 \\ 0 & 3 \end{pmatrix}$ is less than 3, such that $\delta_1 = \delta_2 = 2$ and $\delta_3 = 3$.
- The state of $\begin{pmatrix} 2 & 3 \\ 3 & 1 \end{pmatrix}$ is less than 3, such that $\delta_1 = 0$, $\delta_2 = 1$ and $\delta_3 = 2$.

Then $\phi\begin{pmatrix} 0 & 0 & 2 & 3 \\ 0 & 0 & 3 & 1 \end{pmatrix} < 1$. Similarly, $\phi\begin{pmatrix} 3 & 0 & 0 & 1 \\ 3 & 0 & 0 & 1 \end{pmatrix} < 1$, $\phi\begin{pmatrix} 1 & 3 & 0 & 0 \\ 2 & 1 & 0 & 0 \end{pmatrix} < 1$, $\phi\begin{pmatrix} 2 & 0 & 0 & 0 \\ 1 & 0 & 0 & 0 \end{pmatrix} < 1$, etc.

For state 2:

$\phi(x) < 2$, if at least one sub-matrix of the degree 2×2 is in state less than 2. For example, when $x = \begin{pmatrix} 0 & 1 & 1 & 3 \\ 2 & 3 & 1 & 0 \end{pmatrix}$:

- The state of $\begin{pmatrix} 0 & 1 \\ 2 & 3 \end{pmatrix}$ is less than 3, such that $\delta_1 = 1$, $\delta_2 = 2$ and $\delta_3 = 3$.
- The state of $\begin{pmatrix} 1 & 1 \\ 3 & 1 \end{pmatrix}$ is less than 2, such that $\delta_1 = 0$, $\delta_2 = \delta_3 = 3$.
- The state of $\begin{pmatrix} 1 & 3 \\ 1 & 0 \end{pmatrix}$ is less than 2, such that $\delta_1 = 1$, $\delta_2 = \delta_3 = 3$.

Then $\phi\begin{pmatrix} 0 & 1 & 1 & 3 \\ 2 & 3 & 1 & 0 \end{pmatrix} < 2$. Similarly, $\phi\begin{pmatrix} 1 & 0 & 2 & 3 \\ 1 & 0 & 2 & 2 \end{pmatrix} < 2$, $\phi\begin{pmatrix} 2 & 0 & 2 & 2 \\ 1 & 1 & 2 & 2 \end{pmatrix} < 2$, $\phi\begin{pmatrix} 3 & 3 & 3 & 1 \\ 3 & 3 & 1 & 1 \end{pmatrix} < 2$, etc.

For state 3:

$\phi(x) < 3$, if at least one sub-matrix of the degree 2×2 is in state less than 3. For example, when $x = \begin{pmatrix} 3 & 3 & 1 & 2 \\ 1 & 3 & 2 & 0 \end{pmatrix}$:

- The state of $\begin{pmatrix} 3 & 3 \\ 1 & 3 \end{pmatrix}$ is 3, such that $\delta_1 = 0$, $\delta_2 = \delta_3 = 1$.
- The state of $\begin{pmatrix} 3 & 1 \\ 3 & 2 \end{pmatrix}$ is less than 3, such that $\delta_1 = 0$, $\delta_2 = 1$ and $\delta_3 = 2$.
- The state of $\begin{pmatrix} 1 & 2 \\ 2 & 0 \end{pmatrix}$ is less than 3, such that $\delta_1 = 1$, $\delta_2 = 2$ and $\delta_3 = 4$.

Then $\phi\begin{pmatrix} 3 & 3 & 1 & 2 \\ 1 & 3 & 2 & 0 \end{pmatrix} < 3$. Similarly, $\phi\begin{pmatrix} 2 & 2 & 3 & 2 \\ 2 & 2 & 3 & 0 \end{pmatrix} < 3$, $\phi\begin{pmatrix} 3 & 2 & 3 & 3 \\ 2 & 1 & 3 & 3 \end{pmatrix} < 3$, $\phi\begin{pmatrix} 3 & 2 & 3 & 3 \\ 2 & 1 & 2 & 0 \end{pmatrix} < 3$, etc.

Example 2:

An increasing MS linear ($k_1=2, k_2=3, k_3=4$)-within-(2,2)-of-(2,4):F lattice system, that is a decreasing MS linear ($k_1^G = 3, k_2^G = 2, k_3^G = 1$)-within-(2,2)-of-(2,4):G lattice system, consists of 8 components, that arranged in 2 rows and 4 columns. This system contains 3 sub-matrices of the degree 2×2. The state of any one of them is:

- less than 1, if $\delta_1 \geq 2$, $\delta_2 \geq 3$ and $\delta_3 \geq 4$,
- less than 2, if $\delta_2 \geq 3$ and $\delta_3 \geq 4$,
- less than 3, if $\delta_3 \geq 4$.

For state 1:

$\phi(x) < 1$, if at least one sub-matrix of the degree 2×2 is in state less than 1. For example, when $x = \begin{pmatrix} 1 & 0 & 1 & 2 \\ 0 & 1 & 2 & 2 \end{pmatrix}$:

- The state of $\begin{pmatrix} 1 & 0 \\ 0 & 1 \end{pmatrix}$ is less than 1, such that $\delta_1 = 2$ and $\delta_2 = \delta_3 = 4$.
- The state of $\begin{pmatrix} 0 & 1 \\ 1 & 2 \end{pmatrix}$ is less than 2, such that $\delta_1 = 1$, $\delta_2 = 3$ and $\delta_3 = 4$.
- The state of $\begin{pmatrix} 1 & 2 \\ 2 & 2 \end{pmatrix}$ is less than 3, such that $\delta_1 = 0$, $\delta_2 = 1$ and $\delta_3 = 4$.

Then $\phi\begin{pmatrix} 1 & 0 & 1 & 2 \\ 0 & 1 & 2 & 2 \end{pmatrix} < 1$. Similarly, $\phi\begin{pmatrix} 0 & 0 & 0 & 0 \\ 0 & 0 & 0 & 0 \end{pmatrix} < 1$, $\phi\begin{pmatrix} 1 & 1 & 1 & 1 \\ 0 & 0 & 1 & 1 \end{pmatrix} < 1$, $\phi\begin{pmatrix} 3 & 3 & 0 & 0 \\ 3 & 3 & 0 & 0 \end{pmatrix} < 1$, etc.

For state 2:

$\phi(x) < 2$, if at least one sub-matrix of the degree 2×2 is in state less than 2. For example, when $x = \begin{pmatrix} 0 & 1 & 1 & 3 \\ 2 & 1 & 1 & 1 \end{pmatrix}$:

- The state of $\begin{pmatrix} 0 & 1 \\ 2 & 1 \end{pmatrix}$ is less than 2, such that $\delta_1 = 1$, $\delta_2 = 3$ and $\delta_3 = 4$.
- The state of $\begin{pmatrix} 1 & 1 \\ 1 & 1 \end{pmatrix}$ is less than 2, such that $\delta_1 = 0$ and $\delta_2 = \delta_3 = 4$.
- The state of $\begin{pmatrix} 1 & 3 \\ 1 & 1 \end{pmatrix}$ is 3, such that $\delta_1 = 0$ and $\delta_2 = \delta_3 = 3$.

Then $\phi\begin{pmatrix} 0 & 1 & 1 & 3 \\ 2 & 1 & 1 & 1 \end{pmatrix} < 2$. Similarly, $\phi\begin{pmatrix} 1 & 0 & 3 & 2 \\ 0 & 2 & 0 & 0 \end{pmatrix} < 2$, $\phi\begin{pmatrix} 2 & 0 & 2 & 2 \\ 1 & 1 & 2 & 2 \end{pmatrix} < 2$, $\phi\begin{pmatrix} 3 & 3 & 1 & 1 \\ 3 & 3 & 1 & 1 \end{pmatrix} < 2$, etc.

For state 3:

$\phi(x) < 3$, if at least one sub-matrix of the degree 2×2 is in state less than 3. For example, when $x = \begin{pmatrix} 3 & 2 & 1 & 3 \\ 2 & 1 & 2 & 0 \end{pmatrix}$:

- The state of $\begin{pmatrix} 3 & 2 \\ 2 & 1 \end{pmatrix}$ is 3, such that $\delta_1 = 0$, $\delta_2 = 1$ and $\delta_3 = 3$.
- The state of $\begin{pmatrix} 2 & 1 \\ 1 & 2 \end{pmatrix}$ is less than 3, such that $\delta_1 = 0$, $\delta_2 = 2$ and $\delta_3 = 4$.
- The state of $\begin{pmatrix} 1 & 3 \\ 2 & 0 \end{pmatrix}$ is 3, such that $\delta_1 = 1$, $\delta_2 = 2$ and $\delta_3 = 3$.

Then $\phi\begin{pmatrix} 3 & 2 & 1 & 3 \\ 2 & 1 & 2 & 0 \end{pmatrix} < 3$. Similarly, $\phi\begin{pmatrix} 3 & 2 & 1 & 3 \\ 2 & 1 & 2 & 0 \end{pmatrix} < 3$, $\phi\begin{pmatrix} 2 & 1 & 2 & 0 \\ 2 & 3 & 2 & 1 \end{pmatrix} < 3$, $\phi\begin{pmatrix} 3 & 3 & 0 & 0 \\ 3 & 3 & 2 & 2 \end{pmatrix} < 3$, etc.

Example 3: *A Surveillance Cameras System*

Given, a surveillance cameras system consists of 20 cameras that arranged in 4 rows and 5 columns. This system has 4 different surveillance levels:

- Good surveillance (state 3).
- Medium surveillance (state 2).
- Low surveillance (state 1).
- Non surveillance (state 0).

Each camera also has 4 different surveillance levels:

- Good surveillance, in the first time (state 3).
- Medium surveillance, after some time (state 2).
- Low surveillance, after more time (state 1).
- Non surveillance, the camera not works (state 0).

Then:

- The system state is less than 1, if at least one sub-matrix of the degree 4×3 contains at least 6 components in state less than 1.
- The system state is less than 2, if at least one sub-matrix of the degree 4×3 contains at least 4 components in state less than 2.
- The system state is less than 3, if at least one sub-matrix of the degree 4×3 contains at least 2 components in state less than 3.

We can represent such a system by a decreasing MS linear (6,4,2)-within-(4,3)-of-(4,5):F lattice system (or an increasing MS linear ($k_1^G = 7, k_2^G = 9, k_3^G = 11$)-within-(4,3)-of-(4,5):G lattice system).

Example 4: *A Radar Detection System*

Given, a radar detection system consists of 25 radar stations that arranged in 5 rows and 5 columns. This system has 4 different surveillance levels:

- Good detection (state 3).
- Medium detection (state 2).
- Low detection (state 1).
- Non detection (state 0).

Each station also has 4 different detection levels:

- Good detection, in the first time (state 3).
- Medium detection, after some time (state 2).
- Low detection, after more time (state 1).
- Non detection, the station not works (state 0).

Then:

- The system state is less than 1, if at least one sub-matrix of the degree 5×3 contains at least 3 components in state less than 1, at least 5 components in state less than 2 and at least 7 components in state less than 3.
- The system state is less than 2, if at least one sub-matrix of the degree 5×3 contains at least 5 components in state less than 2 and at least 7 components in state less than 3.
- The system state is less than 3, if at least one sub-matrix of the degree 5×3 contains at least 7 components in state less than 3.

We can represent such a system by an increasing MS linear (3,5,7)-within-(5,3)-of-(5,5):F lattice system (or a decreasing MS linear ($k_1^G = 13, k_2^G = 11, k_3^G = 9$)-within-(5,3)-of-(5,5):G lattice system).

3. Generalization of Boole-Bonferroni Bounds

The technique of Boole-Bonferroni bounds was derived by Prékopa and Boros [2, 17], and improved by many papers such as [2-5, 11, 12, 17]. This technique depends on the solution of the linear programming problem according to the definition of the binomial moments.

Let μ denote the random number of the events among $A_{1,j}, A_{2,j}, ..., A_{N,j}$ which occur. Then:

$$S_{i,j} = E\left[\binom{\mu}{i}\right] = \sum_{l=1}^{N} \binom{l}{i} b_l, \qquad i = 1,2,\ldots,N \quad (1)$$

where $b_l = \Pr(\mu = l)$ and $\binom{l}{i} = 0$, if $i > l$.

The proof of the definition of the expected value in formulae (1) can be found by Prékopa [18]. The value $S_{i,j}$ is called the ith binomial moment of μ.

If we take $b_1, b_2 \ldots, b_N$ as variables and compute $S_{1,j}, S_{2,j}, ..., S_{V,j}$; $V \prec N$, then we have two linear programming problems as follow:

$$\text{Minimize } \{b_1 + b_2 + \ldots + b_V + \ldots + b_N\} \quad (2)$$

Subject to:

$$\begin{aligned} b_1 + \binom{2}{1} b_2 + \ldots + \binom{V}{1} b_V + \ldots + \binom{N}{1} b_N &= S_{1,j} \\ b_2 + \ldots + \binom{V}{2} b_V + \ldots + \binom{N}{2} b_N &= S_{2,j} \\ \ddots \vdots \\ b_V + \ldots + \binom{N}{V} b_N &= S_{V,j} \end{aligned}$$

$$b_1 \geq 0, b_2 \geq 0, ..., b_V \geq 0, ..., b_N \geq 0$$

$$\text{Maximize } \{b_1 + b_2 + \ldots + b_V + \ldots + b_N\} \quad (3)$$

Subject to:

$$\begin{aligned} b_1 + \binom{2}{1} b_2 + \ldots + \binom{V}{1} b_V + \ldots + \binom{N}{1} b_N &= S_{1,j} \\ b_2 + \ldots + \binom{V}{2} b_V + \ldots + \binom{N}{2} b_N &= S_{2,j} \\ \ddots \vdots \\ b_V + \ldots + \binom{N}{V} b_N &= S_{V,j} \end{aligned}$$

$$b_1 \geq 0, b_2 \geq 0, ..., b_V \geq 0, ..., b_N \geq 0$$

The solutions of these problems give us the best possible lower and upper bounds respectively on the value of

$$\Pr(\mu \geq 1) = \Pr(A_{1,j} + \ldots + A_{1,N}) = F_j \quad (4)$$

These bounds are called Boole-Bonferroni bounds. In the following, we give the known explicit solutions of the linear programming problems for $V = 2$ (the second order) and $V = 3$ (the third order).

3.1. The Second Order of Boole-Bonferroni Bounds:

By putting V=2 in the aforesaid linear programming problems and calculation $S_{1,j}$ and $S_{2,j}$, j = 1, 2, 3,…, H, then the lower bound of F_j is:

$$F_j \geq \frac{2}{u_j + 1} S_{1,j} - \frac{2}{u_j(u_j + 1)} S_{2,j}. \quad (5)$$

Where:

$$u_j = 1 + \left\lfloor \frac{2S_{2,j}}{S_{1,j}} \right\rfloor \quad (6)$$

And the upper bound of F_j is:

$$F_j \le S_{1,j} - \frac{2}{N} S_{2,j}. \tag{7}$$

3.2. The Third Order of Boole-Bonferroni Bounds:

By putting V=3 in the aforesaid linear programming problems and calculation $S_{1,j}$, $S_{2,j}$ and $S_{3,j}$, j = 1, 2, 3,…, H, then the lower bound of F_j is:

$$F_j \ge \frac{1}{N(\lambda_j+1)}\left[(\lambda_j+2N-1)S_{1,j} - \frac{2(2\lambda_j+N-2)}{\lambda_j}S_{2,j} + \frac{6}{\lambda_j}S_{3,j}\right] \tag{8}$$

Where:

$$\lambda_j = 1 + \left\lfloor \frac{-6S_{3,j} + 2(N-2)S_{2,j}}{-2S_{2,j} + (N-1)S_{1,j}} \right\rfloor \tag{9}$$

And the upper bound of F_j is:

$$F_j \le Min\left\{1, S_{1,j} - \frac{2}{\omega_j(\omega_j+1)}\left[(2\omega_j-1)S_{2,j} - 3S_{3,j}\right]\right\} \tag{10}$$

Where:

$$\omega_j = 2 + \left\lfloor \frac{3S_{3,j}}{S_{2,j}} \right\rfloor \tag{11}$$

4. System Reliability of the Increasing MS L(*k*,*m*,*s*,*n*:F)

From the definition of $A_{i,j}$, $i = 1,2,...,N$, the increasing MS L(k,m,s,n:F) is in state less than j, if at least one event $A_{i,j}$, $i = 1,2,...,N$, occurred. Then:

$$F_j = \Pr\left\{\bigcup_{i\in\Omega} A_{i,j}\right\} \text{ for all } \Omega = \{1,2,...,N\} \tag{12}$$

Calculation F_j in equation (12) is very difficult, so we will propose an approximation for lower and upper bounds of increasing MS L(*k*,*m*,*s*,*n*:F) using Boole-Bonferroni bounds. Calculation these bounds required the knowledge of $S_{1,j}$, $S_{2,j}$ and $S_{3,j}$, that will be suggested in the following sections. Further, we can have the lower bounds and upper bounds of R_j as follows:

$$\text{LBj} = 1\text{- (the upper bounds of } F_j\text{)}, \tag{13}$$

$$\text{UBj} = 1\text{- (the lower bound of } F_j\text{)}. \tag{14}$$

Estimation R_j by one value can be given by the following formula:

$$\hat{R}_j = \frac{LB_j + UB_j}{2}. \tag{15}$$

The maximum error is:

$$E_j = UB_j - \hat{R}_j = \hat{R}_j - LB_j. \tag{16}$$

4. 1. Calculation the Binomial Moment $S_{1,j}$

The binomial moment $S_{1,j}$ can be given by:

$$\begin{aligned} S_{1,j} &= \Pr(A_{1,j}) + \Pr(A_{2,j}) + ... + \Pr(A_{N,j}) \\ &= N \times \Pr(A_{1,j}) \end{aligned} \tag{17}$$

Where:

$$\Pr(A_{1,j}) = \sum_{y=k_j}^{m\times s} \binom{m\times s}{y} Q_j^y \beta_j(m\times s, y), \tag{18}$$

$$\beta_j(m\times s, y) = \prod_{e=0}^{M-j-1} \sum_{i_e=0}^{\min(m\times s-y-I_e, m\times s-k_{M-e}-I_e)} \binom{m\times s-y-I_e}{i_e} \times p_{M-e}^{i_e} . p_j^{m\times s-y-I_{M-j}}, \quad j < H \tag{19}$$

$$\beta_M(m\times s, y) = p_M^{m\times s-y}, \tag{20}$$

$$I_0 = 0,\ I_a = I_a(i_0, i_1, ..., i_{a-1}) = \sum_{b=0}^{a-1} i_b, \text{ for } a = 1, 2, \ldots, H - j. \tag{21}$$

4. 2. Calculation the Binomial Moment $S_{2,j}$

The binomial moment $S_{2,j}$ can be given by:

$$\begin{aligned} S_{2,j} &= \sum\nolimits_{a,b} \Pr(A_{a,j}A_{b,j}), \quad 1 \le a < b \le N. \\ &= \sum_{a=1}^{N-1}\sum_{b=a+1}^{N} \Pr(A_{a,j}A_{b,j}) \\ &= \sum_{t=2}^{N} (N-t+1) \times \Pr(A_{1,j}A_{t,j}) \end{aligned} \tag{22}$$

The $\Pr(A_{a,j}A_{b,j})$, $1 \le a < b \le N$, can be calculated through the following two cases:

Case 1: If *b*-*a* > *s*-1, then:

$$\Pr(A_{a,j}A_{b,j}) = \left(\Pr(A_{a,j})\right)^2. \tag{23}$$

Case 2: If *b*-*a* ≤ *s*-1, then:

$$\Pr(A_{a,j}A_{b,j}) = \sum_{y_1=t_1}^{m_1} \binom{m_1}{y_1} Q_j^{y_1} . \Psi_j(m_1, y_1) . \left[\sum_{y_2=t_2}^{m_2} \binom{m_2}{y_2} Q_j^{y_2} . \Psi'_j(m_2, y_2, I_{M-j})\right]^2, \tag{24}$$

$$\Psi_j(m_1,y_1)=\prod_{e=0}^{M-j-1}\sum_{i_e=0}^{m_3}\binom{m_1-y_1-I_e}{i_e}p_{M-e}^{i_e}.p_j^{m_1-y_1-I_{M-j}},\ j<M, \quad (25)$$

$$\Psi_M(m_1,y_1)=p_M^{m_1-y_1}, \quad (26)$$

$$\Psi'_j(m_2,y_2,I_{M-j})=\prod_{g=0}^{M-j-1}\sum_{i'_g=0}^{m_4}\binom{m_2-y_2-I'_g}{i'_g}p_{M-g}^{i'_g}.p_j^{m_2-y_2-I'_{M-j}},\ j<M, \quad (27)$$

$$\Psi'_M(m_2,y_2,I_0)=p_M^{m_2-y_2}, \quad (28)$$

$$I'_0=0,\ I'_a=I'_a(i'_0,i'_1,...,i'_{a-1})=\sum_{b=0}^{a-1}i'_b,\ \text{for } a=1,2,\ldots,M\text{-}j, \quad (29)$$

$t_1=\max(0,k_j+m(a-b))$, $\quad m_1=m(s-b+a)$,

$t_2=\max(0,k_j-y_1)$, $\quad m_2=m(b-a)$,

$m_3=\min(m_1-y_1-I_e,m\times s-k_{M-e}-I_e)$,

$m_4=\min(m_2-y_2-I'_g,m\times s-k_{M-g}-I_{g+1}-I'_g,...,m\times s-k_{j+1}-I_{M-j}-I'_g)$.

4. 3. Calculation the Binomial Moment $S_{3,j}$

The binomial moment $S_{3,j}$ can be given by:

$S_{3,j}=\sum_{a,b,c}\Pr(A_{a,j}A_{b,j}A_{c,j})$, for all $1\le a<b<c\le N$.

$$=\sum_{a=1}^{N-2}\sum_{b=a+1}^{N-1}\sum_{c=b+1}^{N}\Pr(A_{a,j}A_{b,j}A_{c,j}) \quad (30)$$

The $\Pr(A_{a,j}A_{b,j}A_{c,j})$, $1\le a<b<c\le N$, can be calculated through the following five cases:

Case 1: *c-a* ≤ *s*-1

In this case, all the events $A_{a,j}$, $A_{b,j}$ and $A_{c,j}$ have common components. The number of common components between the events $A_{a,j}$, $A_{b,j}$ and $A_{c,j}$ is $m\times(s+a-c)$ components. Then:

1- When *j* < *M*,

$$\Pr(A_{a,j}A_{b,j}A_{c,j})=\prod_{e=1}^{5}\sum_{x_e=t_e}^{m_e}\binom{m_e}{x_e}Q_j^{x_e}.\left[\prod_{L=0}^{M-j-1}\sum_{d_{e,L}=0}^{g_{e,L}}\binom{m_e-x_e-D_{e,L}}{d_{e,L}}p_{M-L}^{d_{e,L}}\right].p_j^{m_e-x_e-D_{e,M-j}} \quad (31)$$

2- When *j* = *M*,

$$\Pr(A_{a,j}\ A_{b,j}A_{c,j})=\prod_{e=1}^{5}\sum_{x_e=t_e}^{m_e}\binom{m_e}{x_e}Q_j^{x_e}.p_j^{m_e-x_e}, \quad (32)$$

where:

$t_1=\max(0,\ k_j+m(a-c))$, $\quad m_1=m(s+a-c)$,

$t_2=\max(0,\ k_j-x_1+m(a-b))$, $\quad m_2=m_5=\mathrm{m}(c-b)$

$t_3=t_4=\max(0,\ k_j-x_1-x_2)$, $\quad m_3=m_4=m(b-a)$

$t_5=\max(0,k_j-x_1-x_3)$

$d_{e,M-j}=m_e-x_e-D_{e,M-j}$, $D_{i,L}=\sum_{y=0}^{L-1}d_{i,y}$, $\quad i=1,2,\ldots,5$

$g_{1,L}=\mathrm{Min}\left(m_1-x_1-D_{1,L},\ m\times s-k_{M-L}-D_{1,L}\right)$

$g_{2,L}=\mathrm{Min}\left(m_2-x_2-D_{2,L},\ m\times s-k_{M-L}-D_{2,L}-D_{1,L+1},\ldots,m\times s-k_j-D_{2,L}-D_{1,M-j+1}\right)$

$g_{3,L}=\mathrm{Min}\left(m_3-x_3-D_{3,L},m\times s-k_{M-L}-D_{3,L}-D_{1,L+1}-D_{2,L+1},\ldots,m\times s-k_j-D_{3,L}-D_{1,M-j+1}-D_{2,M-j+1}\right)$

$g_{4,L}=\mathrm{Min}\left(m_4-x_4-D_{4,L},\ m\times s-k_{M-L}-D_{4,L}-D_{1,L+1}-D_{2,L+1},\ldots,m\times s-k_j-D_{4,L}-D_{1,M-j+1}-D_{2,M-j+1}\right)$

$g_{5,L}=\mathrm{Min}\left(m_5-x_5-D_{5,L},\ m\times s-k_{M-L}-D_{5,L}-D_{1,L+1}-D_{3,L+1},\ldots,m\times s-k_j-D_{5,L}-D_{1,M-j+1}-D_{3,M-j+1}\right)$

Case 2: *c-a* > *s*-1, *b-a* ≤ *s*-1, *c-b* ≤ *s*-1

In this case the events $A_{a,j}$, $A_{b,j}$ have common components, and so the events $A_{b,j}$, $A_{c,j}$. The number of common components between the events $A_{a,j}$, $A_{b,j}$ is $m\times(s+a-b)$ components and between $A_{b,j}$, $A_{c,j}$ is $m\times(s+b-c)$ components. But there are no any common components between the events $A_{a,j}$, $A_{c,j}$.

We can use the formulas (31) and (32) to calculate the $\Pr(A_{a,j}\ A_{b,j}A_{c,j})$ in this case, but with the following data:

$t_1=\max(0,\ k_j+m(c-a-2\mathrm{s}))$, $\quad m_1=m(c-a-s)$

$t_2=\max(0,\ k_j-x_1+m(c-b-s))$, $\quad m_2=m(a-b+s)$

$t_3=\max(0,\ k_j-x_1-x_2)$, $\quad m_3=m(b-c+s)$

$t_4=\max(0,\ k_j-x_2)$, $\quad m_4=m(b-a)$

$t_5=\max(0,\ k_j-x_3)$, $\quad m_5=m(c-b)$

$d_{e,M-j}=m_e-x_e-D_{e,M-j}$

$D_{i,L}=\sum_{y=0}^{L-1}d_{i,y}$, $\quad i=1,2,\ldots,5$

$g_{1,L}=\mathrm{Min}\left(m_1-x_1-D_{1,L},\ m\times s-k_{M-L}-D_{1,L}\right)$

$g_{2,L}=\mathrm{Min}\left(m_2-x_2-D_{2,L},m\times s-k_{M-L}-D_{2,L}-D_{1,L+1},\ldots,m\times s-k_j-D_{2,L}-D_{1,M-j+1}\right)$

$g_{3,L}=\mathrm{Min}\left(m_3-x_3-D_{3,L},m\times s-k_{M-L}-D_{3,L}-D_{1,L+1}-D_{2,L+1},\ldots,m\times s-k_j-D_{3,L}-D_{1,M-j+1}-D_{2,M-j+1}\right)$

$g_{4,L}=\mathrm{Min}\left(m_4-x_4-D_{4,L},\ m\times s-k_{M-L}-D_{4,L}-D_{2,L+1},\ldots,m\times s-k_j-D_{4,L}-D_{2,M-j+1}\right)$

$g_{5,L}=\mathrm{Min}\left(m_5-x_5-D_{5,L},\ m\times s-k_{M-L}-D_{5,L}-D_{3,L+1},\ldots,m\times s-k_j-D_{5,L}-D_{3,M-j+1}\right)$

Case 3: *c-a* > *s*-1, *b-a* ≤ *s*-1, *c-b* > *s*-1

In this case the events $A_{a,j}$, $A_{b,j}$ have common components. But the two events $A_{b,j}$, $A_{c,j}$ and so the two events $A_{a,j}$, $A_{c,j}$ are disjoint. The number of common components between the events $A_{a,j}$ and $A_{b,j}$

is $m\times(s + a - b)$ components. So, we can find the $\Pr(A_{a,j}\ A_{b,j}A_{c,j})$ by the following formula:

$$\Pr(A_{a,j}\ A_{b,j}A_{c,j}) = \Pr(A_{a,j}\ A_{b,j})\times\Pr(A_{c,j}) \tag{33}$$

Such that, the $\Pr(A_{a,j}\ A_{b,j})$ can be obtained by formulas (23), (24) and the $\Pr(A_{c,j})$ can be obtained by formula (18).

Case 4: ***c-a > s-1, b-a > s-1, c-b ≤ s-1***

In this case the two events $A_{a,j}$, $A_{b,j}$ and so the two events $A_{a,j}$, $A_{c,j}$ are disjoint. The events $A_{b,j}$ and $A_{c,j}$ have common components. The number of common components between the events $A_{b,j}$ and $A_{c,j}$ is $m\times(s + b - c)$ components. So, we can find the $\Pr(A_{a,j}\ A_{b,j}A_{c,j})$ by the following formula:

$$\Pr(A_{a,j}\ A_{b,j}A_{c,j}) = \Pr(A_{a,j})\times\Pr(A_{b,j}A_{c,j}) \tag{34}$$

Such that, the $\Pr(A_{b,j}\ A_{c,j})$ can be obtained by formulas (23), (24) and the $\Pr(A_{a,j})$ can be obtained by formula (18).

Case 5: *c-a > s-1, b-a > s-1, c-b ≤ s-1*

In this case, all the events $A_{a,j}$, $A_{b,j}$, $A_{c,j}$ are disjoint.

So, we can find the $\Pr(A_{a,j}\ A_{b,j}A_{c,j})$ by the following formula:

$$\Pr(A_{a,j}\ A_{b,j}A_{c,j}) = \Pr(A_{a,j})\times\Pr(A_{b,j})\times\Pr(A_{c,j}) \tag{35}$$

Such that, the $\Pr(A_{a,j}),\Pr(A_{b,j}),\Pr(A_{c,j})$ can be obtained by formula (18).

Example 5.

Consider an increasing MS L(*k*,*m*,*s*,*n*:F) with the following data: $n = 5$, $m = 2$, s = 2, $H = 3$, the k vector is $(k_1,k_2,k_3) = (1, 2, 3)$, and the state distribution of components is $(p_0,p_1,p_2,p_3) = (0.1, 0.2, 0.4, 0.3)$. So that, $(Q_1,Q_2,Q_3) = (0.1, 0.3, 0.7)$. In the following, we illustrate the calculations of $S_{1,j},S_{2,j},S_{3,j}$. The results of this example are listed in table 4.

At state 3:

$$\Pr(A_{1,3}) = \sum_{y=3}^{4}\binom{4}{y}(0.7)^y\beta_3(4,y) = 0.6517\ ,$$

$$\Pr(A_{1,3}A_{2,3}) = \sum_{y_1=1}^{2}\binom{2}{y_1}(0.7)^{y_1}.(0.3)^{2-y_1}.\left[\sum_{y_2=3-y_1}^{2}\binom{2}{y_2}(0.7)^{y_2}.(0.3)^{2-y_2}\right]^2 = 0.506611$$

$$\Pr(A_{1,3}A_{3,3}) = \Pr(A_{1,3}A_{4,3}) = \left[\Pr(A_{1,3})\right]^2 = 0.4247129$$

$$\Pr(A_{1,3}A_{2,3}A_{3,3}) = \sum_{x_1=0}^{0}\sum_{x_2=1}^{2}\sum_{x_3=3-x_2}^{2}\sum_{x_4=3-x_2}^{2}\sum_{x_5=3-x_3}^{2}\binom{0}{0}\binom{2}{x_2}\binom{2}{x_3}\binom{2}{x_4}\binom{2}{x_5}$$
$$\times(0.7)^{x_2+x_3+x_4+x_5}(0.3)^{8-(x_2+x_3+x_4+x_5)} = 0.3823593$$

$$\Pr(A_{1,3}A_{2,3}A_{4,3}) = \Pr(A_{1,3}A_{2,3})\times\Pr(A_{4,3}) = \Pr(A_{1,3}A_{2,3})\times\Pr(A_{1,3}) = 0.506611\times0.6517$$
$$= 0.3301584$$

$$S_{1,3} = 4\times0.6517 = 2.6068$$

$$S_{2,3} = 3\times\Pr(A_{1,3}A_{2,3}) + 2\times\Pr(A_{1,3}A_{3,3}) + \Pr(A_{1,3}A_{4,3})$$
$$= 3\times0.506611\ +\ 2\times0.4247129\ +\ 0.4247129 = 2.7939717$$

$$S_{3,3} = \Pr(A_{1,3}A_{2,3}A_{3,3}) + \Pr(A_{1,3}A_{2,3}A_{4,3}) + \Pr(A_{1,3}A_{3,3}A_{4,3}) + \Pr(A_{2,3}A_{3,3}A_{4,3})$$
$$= 2\times\Pr(A_{1,3}A_{2,3}A_{3,3}) + 2\times\Pr(A_{1,3}A_{2,3}A_{4,3})$$
$$= 2\times0.3823593 + 2\times0.3301584 = 1.4250354$$

$u_3 = 3$, $\lambda_3 = 2$, $\omega_3 = 3$

At state 2:

$$\Pr(A_{1,2}) = \sum_{y=2}^{4}\binom{4}{y}(0.3)^y\beta_2(4,y) = 0.2997\ ,$$

$$\Pr(A_{1,2}A_{2,2}) = \sum_{y_1=0}^{2}\binom{2}{y_1}(0.3)^{y_1}.\beta_2(2,y_1).\left[\sum_{y_2=2-y_1}^{2}\binom{2}{y_2}(0.3)^{y_2}.\beta_2'(2,y_2,I_1)\right]^2$$
$$= 0.159795$$

$$\Pr(A_{1,2}A_{3,2}) = \Pr(A_{1,2}A_{4,2}) = \left[\Pr(A_{1,2})\right]^2 = [0.2997]^2 = 0.0898201$$

$$\Pr(A_{1,2}A_{2,2}A_{3,2}) = \sum_{x_1=0}^{0}\binom{0}{0}(0.3)^0\sum_{d_{1,0}=0}^{0}\binom{0}{0}(0.3)^0(0.4)^0$$
$$\times\sum_{x_2=0}^{2}\binom{2}{x_2}(0.3)^{x_2}\sum_{d_{2,0}=0}^{g_{2,0}}\binom{2-x_2-D_{2,0}}{d_{2,0}}(0.3)^{d_{2,0}}(0.4)^{2-x_2-D_{2,1}}$$
$$\times\sum_{x_3=2-x_2}^{2}\binom{2}{x_3}(0.3)^{x_3}\sum_{d_{3,0}=0}^{g_{3,0}}\binom{2-x_3-D_{3,0}}{d_{3,0}}(0.3)^{d_{3,0}}(0.4)^{2-x_3-D_{3,1}}$$
$$\times\sum_{x_4=2-x_2}^{2}\binom{2}{x_4}(0.3)^{x_4}\sum_{d_{4,0}=0}^{g_{4,0}}\binom{2-x_4-D_{4,0}}{d_{4,0}}(0.3)^{d_{4,0}}(0.4)^{2-x_4-D_{4,1}}$$
$$\times\sum_{x_5=2-x_3}^{2}\binom{2}{x_5}(0.3)^{x_5}\sum_{d_{5,0}=0}^{g_{5,0}}\binom{2-x_5-D_{5,0}}{d_{5,0}}(0.3)^{d_{5,0}}(0.4)^{2-x_5-D_{5,1}}$$
$$= 0.0719061$$

$$\Pr(A_{1,2}A_{2,2}A_{4,2}) = \Pr(A_{1,2}A_{2,2})\times\Pr(A_{4,2}) = \Pr(A_{1,2}A_{2,2})\times\Pr(A_{1,2}) = 0.159795\times0.2997$$
$$= 0.0478906$$

$$S_{1,2} = 4\times0.2997 = 1.1988$$

$$S_{2,2} = 3\times\Pr(A_{1,2}A_{2,2}) + 2\times\Pr(A_{1,2}A_{3,2}) + \Pr(A_{1,2}A_{4,2})$$
$$= 3\times0.159795\ +\ 2\times0.0898201\ +\ 0.0898201 = 0.7488453$$

$$S_{3,2} = \Pr(A_{1,2}A_{2,2}A_{3,2}) + \Pr(A_{1,2}A_{2,2}A_{4,2}) + \Pr(A_{1,2}A_{3,2}A_{4,2}) + \Pr(A_{2,2}A_{3,2}A_{4,2})$$
$$= 2\times\Pr(A_{1,2}A_{2,2}A_{3,2}) + 2\times\Pr(A_{1,2}A_{2,2}A_{4,2})$$
$$= 2\times0.0719061 + 2\times0.0478906 = 0.2395934$$

$u_2 = 2$, $\lambda_2 = 1$, $\omega_2 = 2$

At state 1:

$$\Pr(A_{1,1}) = \sum_{y=1}^{4}\binom{4}{y}(0.1)^y\beta_1(4,y) = 0.1797\ ,$$

$$\Pr(A_{1,1}A_{2,1}) = \sum_{y_1=0}^{2}\binom{2}{y_1}(0.1)^{y_1}.\beta_1(2,y_1).\left[\sum_{y_2=\max(0,1-y_1)}^{2}\binom{2}{y_2}(0.1)^{y_2}.\beta_1'(2,y_2,I_2)\right]^2$$
$$= 0.078995$$

$$\Pr(A_{1,1}A_{3,1}) = \Pr(A_{1,1}A_{4,1}) = \left[\Pr(A_{1,1})\right]^2 = [0.1797]^2 = 0.0322921$$

$$\Pr(A_{1,1}A_{2,1}A_{3,1}) = \sum_{x_1=0}^{0}\binom{0}{0}(0.1)^0 \sum_{d_{1,0}=0}^{0}\binom{0}{0}(0.3)^0 \sum_{d_{1,1}=0}^{0}\binom{0}{0}(0.4)^0(0.2)^0$$
$$\times \sum_{x_2=0}^{2}\binom{2}{x_2}(0.1)^{x_2} \sum_{d_{2,0}=0}^{g_{2,0}}\binom{2-x_2-D_{2,0}}{d_{2,0}}(0.3)^{d_{2,0}} \sum_{d_{2,1}=0}^{g_{2,1}}\binom{2-x_2-D_{2,1}}{d_{2,1}}(0.4)^{d_{2,1}}(0.2)^2$$
$$\times \sum_{x_3=\max(0,1-x_2)}^{2}\binom{2}{x_3}(0.1)^{x_3} \sum_{d_{3,0}=0}^{g_{3,0}}\binom{2-x_3-D_{3,0}}{d_{3,0}}(0.3)^{d_{3,0}} \sum_{d_{3,1}=0}^{g_{3,1}}\binom{2-x_3-D_{3,1}}{d_{3,1}}(0.4)^{d_{3,1}}(0.2)^{2-x_3-D_{3,2}}$$
$$\times \sum_{x_4=\max(0,1-x_2)}^{2}\binom{2}{x_4}(0.1)^{x_4} \sum_{d_{4,0}=0}^{g_{4,0}}\binom{2-x_4-D_{4,0}}{d_{4,0}}(0.3)^{d_{4,0}} \sum_{d_{4,1}=0}^{g_{4,1}}\binom{2-x_4-D_{4,1}}{d_{4,1}}(0.4)^{d_{4,1}}(0.2)^{2-x_4-D_{4,2}}$$
$$\times \sum_{x_5=\max(0,1-x_3)}^{2}\binom{2}{x_5}(0.1)^{x_5} \sum_{d_{5,0}=0}^{g_{5,0}}\binom{2-x_5-D_{5,0}}{d_{5,0}}(0.3)^{d_{5,0}} \sum_{d_{5,1}=0}^{g_{5,1}}\binom{2-x_5-D_{5,1}}{d_{5,1}}(0.4)^{d_{5,1}}(0.2)^{2-x_5-D_{5,2}}$$
$$= 0.0234413$$

$$\Pr(A_{1,1}A_{2,1}A_{4,1}) = \Pr(A_{1,1}A_{2,1}) \times \Pr(A_{4,1}) = \Pr(A_{1,1}A_{2,1}) \times \Pr(A_{1,1}) = 0.078995 \times 0.1797$$
$$= 0.0141954$$

$$S_{1,1} = 4 \times 0.1797 = 0.7188$$

$$S_{2,1} = 3 \times \Pr(A_{1,1}A_{2,1}) + 2 \times \Pr(A_{1,1}A_{3,1}) + \Pr(A_{1,1}A_{4,1})$$
$$= 3 \times 0.078995 + 2 \times 0.0322921 + 0.0322921 = 0.3338613$$

$$S_{3,1} = \Pr(A_{1,1}A_{2,1}A_{3,1}) + \Pr(A_{1,1}A_{2,1}A_{4,1}) + \Pr(A_{1,1}A_{3,1}A_{4,1}) + \Pr(A_{2,1}A_{3,1}A_{4,1})$$
$$= 2 \times \Pr(A_{1,1}A_{2,}A_{3,1}) + 2 \times \Pr(A_{1,1}A_{2,1}A_{4,1})$$
$$= 2 \times 0.0234413 + 2 \times 0.0141954 = 0.0752734$$

$$u_1 = 1,\ \lambda_1 = 1,\ \omega_1 = 2$$

5. Numerical Results

The numerical calculations of increasing MS L(k,m,s,n:F) reliability are carried out using Visual Basic Program. The computer codes were written very carefully. The new bounds and computer codes examined by previously published numerical examples for some special cases of increasing MS L(k,m,s,n:F), as shown in tables 1-3.

- When m=1, the increasing MS L(k,1,s,n:F) becomes the increasing MS consecutive-k-out-of-s-from-n: F system. An example of increasing MS consecutive-k-out-of-s-from-n: F system in Ref [19] is examined by our bounds and given in table 1.
- When H=1 and m=1, the increasing MS L(k,1,s,n:F) becomes the binary consecutive-k-out-of-s-from-n: F system. An example of binary consecutive-k-out-of-s-from-n: F system in Ref [6] is examined by our bounds and given in table 2.
- When m=1 and s = n, the increasing MS L(k,1,n,n:F) becomes the increasing MS k-out-of-n:F system. An example of MS k-out-of-n:F system in Ref [10] is examined using formula (18) and given in table 3.

The bounds of the increasing MS L(k,m,s,n:F) reliability with H=3 and variant values of p_j, k_j, m, s, n are given in tables 4-7. These bounds are evaluated using second and third orders of Boole-Bonferroni bounds. The comparison between the results of second and third orders of Boole-Bonferroni bounds explained in tables 2-7 and figures 1-4. This comparison shows that the third order Boole-Bonferroni bounds are the best.

Table 1. n = s = 4, m=1, H = 4, k_1 = 1, k_2 = 2, k_3 = 3, k_4 = 4, p_0=0.1, p_1=0.2, p_2=0.3, p_3=0.3, p_4=0.1

State (j)	0	1	2	3	4
R_j	1	0.8669	0.7813	0.6112	0.3439

Table 2. n =15, m=1, s=10, H=4, k_1=4, k_2=6, k_3=7, k_4=9, p_0=0.1, p_1=0.2, p_2=0.3, p_3=0.3, p_4=0.1

Bounds	**S_1- S_2 based**	S_1- S_3 based	$\hat{R}_j$	E_j
LB_1	0.9786406	0.9820220	0.9838254	0.0018034
UB_1	0.9884654	0.9856288		
LB_2	0.8541696	0.8862806	0.8993991	0.0131184
UB_2	0.9270848	0.9125175		
LB_3	0.1880035	0.3577432	0.42207593	0.0643328
UB_3	0.5517231	0.4864087		
LB_4	0	0.0628391	0.1072802	0.0444411
UB_4	0.1957316	0.1517213		

Table 3. n =50, m=1, s=40, H=1, k_1=28, p_0=0.5, p_1=0.5

Bounds	**S_1- S_2 based**	S_1- S_3 based	$\hat{R}_j$	E_j
LB_1	0.9560414	0.9696965	0.9764474	0.0067509
UB_1	0.9863147	0.9831983		

Table 4. n =5, m =2, s =2, k_1 =1, k_2 =2, k_3 =3, p_0 =0.1, p_1 =0.2, p_2 =0.4, p_3 =0.3

Bounds	S_1- S_2 based	S_1- S_3 based	$\hat{R}_j$	E_j
LB_1	0.4481306	0.5397878	0.5491970	0.0094092
UB_1	0.6150613	0.5586062		
LB_2	0.1756226	0.3104519	0.3404011	0.0299492
UB_2	0.4504151	0.3703502		
LB_3	0	0.0089921	0.0473096	0.0383175
UB_3	0.1622619	0.0856270		

Table 5. n =10, m =3, s =6, k_1 =13, k_2 =14, k_3 =15, p_0 =0.3, p_1 =0.3, p_2 =0.2, p_3 =0.2

Bounds	**S_1- S_2 based**	S_1- S_3 based	$\hat{R}_j$	E_j
LB_1	0.9988797	0.9990029	0.9990196	0.0000166
UB_1	0.9990861	0.9990362		
LB_2	0.7064799	0.7559996	0.7767656	0.0207660
UB_2	0.8306766	0.7975315		
LB_3	0.0000000	0.1815675	0.2344687	0.0529012
UB_3	0.3740597	0.2873698		

Table 6. n =20, m =2, s =16, k_1 =18, k_2 =20, k_3 =21, p_0 =0.3, p_1 =0.2, p_2 =0.2, p_3 =0.3

Bounds	**S_1- S_2 based**	S_1- S_3 based	$\hat{R}_j$	E_j
LB_1	0.9944228	0.9951706	0.9955345	0.0003639
UB_1	0.9967637	0.9958983		
LB_2	0.7542582	0.7968765	0.8128056	0.0159291
UB_2	0.8527955	0.8287347		
LB_3	0.0047005	0.0967175	0.1186511	0.0219336
UB_3	0.1724146	0.1405848		

Table 7. n =25, m =2, s =22, k_1 =36, k_2 =38, k_3 =40, p_0 =0.3, p_1 =0.2, p_2 =0.3, p_3 =0.2

Bounds	**S_1- S_2 based**	S_1- S_3 based	$\hat{R}_j$	E_j
LB_1	0.9969130	0.9973025	0.9973999	0.0000974
UB_1	0.9979420	0.9974973		
LB_2	0.7189426	0.7519136	0.7601564	0.0082428
UB_2	0.7928078	0.7683991		
LB_3	0.0214187	0.0456554	0.0503207	0.0046653
UB_3	0.0643166	0.0549860		

6. Conclusions.

In this paper, we proposed new lower and upper bounds for increasing MS L(k,m,s,n:F) reliability with i.i.d components using second and third orders Boole-Bonferroni bounds. The new bounds are examined by previously published numerical examples for some special cases of increasing MS L(k,m,s,n:F). The comparison between the results of second and third orders of Boole-Bonferroni bounds shows that the third order Boole-Bonferroni bounds are the best.

References

1. Amari V, Zuo M J, Dill G. A fast and robust reliability evaluation algorithm for generalized multi-state k-out-of-n systems. IEEE Transactions on reliability 2009; 58 (1): 88-97, https://doi.org/10.1109/TR.2008.2011684.
2 Boros E, Prékopa A. Closed form two-sided bounds for probabilities that exactly r and at least r out of n events occur. Math. Oper. Res. 1989; 14: 317-342, https://doi.org/10.1287/moor.14.2.317.
3. Dawson D, Sankoff A. An inequality for probabilities. Proc. Am. Math. Soc. 1967; 18: 504-507, https://doi.org/10.1090/S0002-9939-1967-0211424-0.
4. Galambos J, Simonelli I. In: Gani J, Heyde CC, Kurtz TG, editors., Bonferroni-type inequalities with applications. Probability and its application, a series of applied probability trust, Berlin, New York, Heidelberg: Springer, 1996.
5. Galambos J. Bonferroni inequalities. Annals of Prob. 1977; 5: 577-581, https://doi.org/10.1214/aop/1176995765.
6. Habib A, Szantai T. New bounds on the reliability of the consecutive k-out-of-r-from-n:F system. Reliability Engineering and System Safety 2000; 68 (2): 97-104, https://doi.org/10.1016/S0951-8320(99)00021-6.
7. Habib A, Alseedy R, Elsherbeny A, Radwan T. Generalization for Lattice System with Equal Components. Applied Mathematical Sciences 2009; 3: 1479 - 1486.
8. Habib A, Al-Seedy R, Radwan T. Reliability Evaluation of Multi-state Consecutive k-out-of-r-from-n: G system. Applied Mathematical Modelling 2007; 31: 2412-2423, https://doi.org/10.1016/j.apm.2006.09.006.
9. Huang J, Zuo M J, Fang Z. Multi-State consecutive k-out-of-n systems. IIE Transactions 2003; 35: 527-534, https://doi.org/10.1080/07408170304418.
10. Huang J, Zuo M J, Wu Y. Generalized Multi-State k-out-of-n:G Systems. IEEE Transactions on reliability 2000; 49 (1): 105-111, https://doi.org/10.1109/24.855543.
11. Kwerel S M. Bounds on the probability of a union and intersection of m events. Adv. Appl. Prob. 1975; 7: 431-448, https://doi.org/10.1017/S000186780004605X. 12. Kwerel S M. Most stringent bounds on aggregated probabilities of partially specified dependent probability systems. J. Am. Stat. Assoc. 1975; 70: 472-479, https://doi.org/10.1080/01621459.1975.10479893.
13. Lin D, Zuo M J. Reliability Evaluation of A linear k-within-(r,s)-of-(m,n):F lattice system. Probability in the Engineering and Informational Sciences 2000; 14: 435-443, https://doi.org/10.1017/S0269964800144031.
14. Makri F S, Psillakis Z M. Bounds for reliability of k-within connected-(r, s)-out-of-(m, n) failure systems. Microelectron. Reliab. 1997; 37 (8): 1217-1224, https://doi.org/10.1016/S0026-2714(96)00289-2.
15. Makri F S, Psillakis Z M. Bounds for reliability of k-within two-dimensional consecutive-r-out-of-n failure systems. Microelectron. Reliab. 1996; 36 (3): 341-345, https://doi.org/10.1016/0026-2714(95)00102-6.
16. Malinowski J, Preuss W. Lower & Upper Bounds for the Reliability of Connected-(r,s) -out-of-(m,n) : F Lattice Systems. IEEE Transactions on Reliability 1996; 45 (1): 156-160, https://doi.org/10.1109/24.488935.
17. Prékopa A. Boole-Bonferroni inequalities and linear programming. Operations Research 1998; 36: 145-162, https://doi.org/10.1287/opre.36.1.145.
18. Prékopa A. Stochastic programming. Dordrecht: Kluwer Academic,1995, https://doi.org/10.1007/978-94-017-3087-7.
19. Radwan T, Habib A, Alseedy ., Elsherbeny A. Bounds for increasing multi-state consecutive k-out-of-r-from-n:F system with equal components probabilities. Applied Mathematical Modelling 2011; 35: 2366-2373, https://doi.org/10.1016/j.apm.2010.11.059.
20. Tian Z, Richard C M, Zuo M J, Huang H. Reliability Bounds for Multi-State k-out-of-n Systems. IEEE Transactions on reliability 2008; 57(1): 53-58, https://doi.org/10.1109/TR.2007.909766.
21. Yamamoto H, Akiba T. Evaluating methods for the reliability of a large 2- dimensional rectangular k-within-consecutive-(r,s)-out-of-(m,n):F system. Naval Research Logistics2005; 52 (3): 243-252, https://doi.org/10.1002/nav.20067.
22. Yamamoto H., Zuo M J, Akiba T, Tian Z. Recursive formulas for the reliability of multi-state consecutive-k-out-of-n: G systems. IEEE Trans. Reliability 2006; 55 (1): 98-104, https://doi.org/10.1109/TR.2005.863792.
23. Zuo, M J, Lin D, Wu Y. Reliability evaluation of combined k-out-of-n:F, consecutive-k-out-of-n:F and linear connected-(r, s)-out-of-(m, n):F lattice system structures. IEEE Transactions on Reliability 2000; 49 (1): 99-104, https://doi.org/10.1109/24.855542.
24. Zuo M J, Fang Z, Huang J, Xu X. Performance evaluation of decreasing multi-state consecutive-k-out-of-n: G systems. Int. J. of Reliability, Quality and Safety Eng. 2003; 10 (3): 345-358, https://doi.org/10.1142/S0218539303001184.

Radwan TAHA
Department of Mathematics and Statistics
Port Said University
Port Said, EGYPT

E-mail: taha_ali_2003@hotmail.com

Article citation info:
PIELECHA I, SKOWRON M, MAZANEK A. Evaluation of the injectors operational wear process based on optical fuel spray analysis. Eksploatacja i Niezawodnosc – Maintenance and Reliability 2018; 20 (1): 83–89 http://dx.doi.org/10.17531/ein.2018.1.11.

Ireneusz PIELECHA
Maciej SKOWRON
Aleksander MAZANEK

EVALUATION OF THE INJECTORS OPERATIONAL WEAR PROCESS BASED ON OPTICAL FUEL SPRAY ANALYSIS

OCENA EKSPLOATACYJNEGO ZUŻYCIA WTRYSKIWACZY NA PODSTAWIE ANALIZY OPTYCZNEJ ROZPYLENIA PALIWA*

The diagnostics of combustion engine components currently requires the integration of many technical and scientific fields in order to quickly and accurately locate faults or pinpoint the causes of malfunction. This article analyzes the wear of injectors based on the geometric indicators of the fuel spray. Using a number of available parameter data, a selection has been made to best judge the wear of injectors in their operating conditions. Optical fuel spray tests were used to assess the injector wear. Various geometric indicators of the fuel stream have been presented, indicating their diagnostic utility and applicability. In conclusion, it was found that the current injection systems require the combination of mechanical injector diagnostics and advanced optical fuel spray diagnostics.

***Keywords**: fuel injection, fuel spray, fuel jet cone angle, optical diagnostics.*

Diagnostyka elementów silnika spalinowego wymaga obecnie integracji wielu dziedzin techniki i nauki w celu szybkiej i trafnej lokalizacji uszkodzenia lub poszukiwania przyczyn niesprawności. Artykuł dotyczy analizy zużycia wtryskiwaczy na podstawie wskaźników geometrycznych strugi rozpylanego paliwa. Na podstawie kilku dostępnych wielkości badawczych dokonano wyboru pozwalającego najlepiej ocenić zużycie wtryskiwaczy w warunkach ich eksploatacji. Do oceny diagnostycznej zużycia wtryskiwaczy wykorzystano badania optyczne rozpylenia paliwa. Przedstawiono różne wskaźniki geometryczne strugi paliwa, wskazując na ich użyteczność diagnostyczną oraz możliwość zastosowania. W podsumowaniu stwierdzono, że badania obecnych układów wtryskowych wymagają połączenia mechanicznych metod diagnostyki wtryskiwaczy oraz zaawansowanej diagnostyki optycznej rozpylenia paliwa.

***Słowa kluczowe**: wtrysk paliwa, rozpylenie paliwa, kąt stożka strugi, badania optyczne.*

1. Introduction

The diagnostics of combustion engine components currently requires the integration of many technical and scientific fields in order to quickly and accurately locate faults or pinpoint the causes of malfunction. The injection system is one of the most sensitive engine systems, which in compression-ignition engines requires more rigorous performance and fit regimes than in spark ignition engines. Evaluation of the injection system components and in particular of the injectors is carried out by analyzing the degree of their contamination by external or internal deposits resulting from the combustion of fuels and lubricating oil [16].

The use of additives for diesel fuels aims to limit the formation of such deposits.

Studies on the use of detergent-dispersant additives were conducted by Beck et al. [1]. They have shown that these additives are suitable for increasing the oxidation resistance of pure diesel and biodiesel blends. With respect to the fuel samples tested - biodiesel, diesel and their mixtures, the reduction of oxidation stability due to prolonged shelf life may be partially compensated by the use of selected dispersant-detergent additives. Additives prevent the formation of radicals and neutralize carboxylic acids and thus increase the oxidation stability of the fuel samples.

When analyzing the effects of detergent-dispersant additives Żak et al. [19] have shown that they have a significant effect both on the state of the compression-ignition combustion engine fuel supply equipment as well as on the reduction of exhaust gas emissions (mainly for particulate matter).

Khalife et al. [5] analyzed the effects of various additives on fuel consumption and emissions, and showed that oxidation additives have the most significant impact on these values. They increase fuel consumption while reducing CO, HC and PM emissions, while slightly increasing NO_x emissions. It has also been shown that non-metallic additives (such as carbon nanotubes) have the least notable impact on these values.

Nano-additives to fuels are becoming increasingly important. Shaafi et al. presented their full characteristic in [15]. This revealed the impact of the use of metal nano-additives, metal oxides, magnetic fluids, carbon nanotubes and mixtures thereof on engine performance and emissions. It has been found that using mixtures of nano-additives into pure diesel fuel increases nitrogen oxide emissions, due to the increase in the combustion chamber maximum temperature. It has been shown that emulsification (the use of water) is the best way to reduce NO_x emissions, but also limits the engine performance.

Reducing the buildup of residues can lead to changes in fuel spraying and combustion in the combustion chamber. Hence the need to study the fuel stream geometric parameters, not only as a result of

(*) Tekst artykułu w polskiej wersji językowej dostępny w elektronicznym wydaniu kwartalnika na stronie ***www.ein.org.pl***

the engine operation of the wear of components, but also as a result of using fuel additives.

Fuel stream research is used mainly to determine the main spray indicators, such as the stream range, the area of the jet (defined as flat image exposure) and the jet incidence angle. Many studies employ fixed volume chambers to study these quantities using halogen lamps [13], LED [7] or laser light [18].

The study of fuel streams geometric indicators is usually performed using optical methods. They allow for precise determination of the stream range in different temperature conditions of the medium. They also often include images from varying view angles to allow for corrections in determining the stream. Flat image exposure is used to determine the area of the fuel stream. There are methods of masking each stream to individually determine their parameters. The stream cone angle is determined using several methods. The basic methods allow to determine it at any distance from the atomizer, analyzing the width of the stream in a given cross section [8]. Others are based on the averaging of such magnitudes after taking into account several stream width values. The latest method, which allows for some level of automation, was devised by Naber and Siebers [8]. It enables determining the cone angle based on the knowledge of the stream surface area and its range [10]. So, to determine the stream cone angle, it is necessary to know the value of these several parameters.

Ghahremani et al. [2] determined the geometry of the fuel stream based on experimental studies. Equations describing the range and surface area of the stream were determined (fuel and medium density, kinematic viscosity and surface tension of fuel) using the physical and chemical properties of the fuel (bio-diesel). The maximum range error was 9% and for the area it was 12%.

2. Research motivation

Studies of fuel spray indicators conducted with respect to injectors in compression-ignition engines are primarily concerned with the assessment of changes in the stream geometric parameters resulting from their operation. The aim of this article was to determine the influence of different fuels on these indicators in addition to obtaining the indicator values themselves. Another issue was the estimation of fuel atomization time, with which it is possible to determine the described changes in geometric parameters.

3. Research methodology

3.1. Test objects

The study of the fuel stream geometric parameters for different fuels was performed using three groups of injectors and two types of fuel. New injectors (designated n1) and injectors previously used in vehicles (designated u1 and u2) were used. Their characteristics are shown in Table 1. The tested injectors were characterized by an 8-pore atomizer with a 162° angle between the fuel jets.

Base diesel fuel (B7 fuel labeled as #1) and diesel fuel with a set of additives (labeled #2) are included in the study.

Table 1. Characteristics of the injectors used in the tests

Injector	Fuel	Notes	Injector mileage [km]
n1	#1	New injector	0
n1	#2	New injector	0
u1	#1	Used injector/vehicle 1	80 000
u2	#2	Used injector/vehicle 2	80 000

Table 2. Selected properties of the base and modified diesel fuel

Test type	Unit	Result	
		Diesel oil B7	Diesel oil with INIG additives
Cetane index	–	57.6	57.8
Cetane number	–	53.3	54.7
Density at 15°C	kg/m^3	828.7	828.6
Content of polycyclic aromatic hydrocarbons	% (m/m)	1.1	
Sulfur content	mg/kg	below 5	below 3.0
Ignition temperature	°C	88	87.5
Coking residue (with 10% distillation residue)	% (m/m)	0.062	0.074
Incineration residue	% (m/m)	0.001	0.004
Water content	% (m/m)	0.005	0.0005
Impurities content	mg/kg	2.1	6.7
Corrosion test on steel (3 h, in the temperature of 38°C)	corrosion degree	trace B^{++}	corrosion trace
Fatty acids methyl esters (FAME)	% (V/V)	5.6	–
Oxidation resistance	hg/m^3	35.97	2.0
Lubricity, corrected average wear trace diameter (WS 1.4) at 60°C	µm	180	337
Kinematic viscosity at 40°C	mm^2/s	2.7175	2.711
Fractional composition at temperature up to 250°C distills at temperature up to 350°C distills 95% (V/V) distills at temperature	 % (V/V) % (V/V) °C	 27.3 97.7 333.0	 26.3 97.2 328.0

3.2. Research apparatus

A fixed volume chamber with a set backpressure value was used to determine the fuel stream geometry, using a diesel fuel injection (the exact description of the chamber can be found in [14]). Fuel injection at 35 MPa (corresponding to idle and low load conditions) and injection time of 0.3 ms were used in the research. For these conditions it is possible to accurately determine the stream geometric parameters. At the same time it also becomes possible to determine the effect of the injectors used on the change of the spray parameters. High fuel pressure values result in high flow rates, which results in fewer data records being recorded in a given measurement range. The measurement range is due to the size of the video window of the fixed

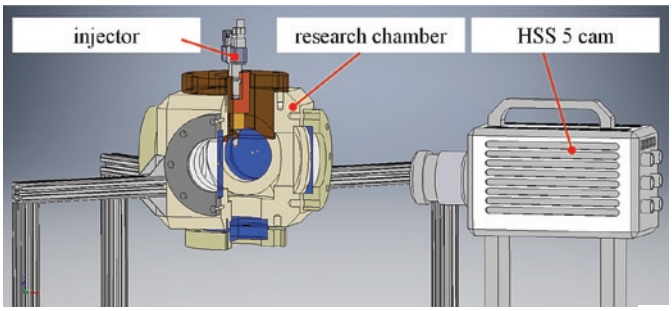

Fig. 1. Test bench

volume chamber [13]. The size of the quartz window used was 90 mm – Fig. 1.

Fuel injection into a fixed volume chamber was performed using an oil injection system along with its conditioning – STPiW3 from Mechatronics. The system uses a CP4.1 pump with a maximum fuel injection pressure of 200 MPa. In order to provide comparable testing conditions, the fuel temperature was maintained at 42°C.

The optical analysis of the fuel injection and atomization process was carried out using LaVision's high speed, monochrome HSS5 camera, with the 10 kHz (Δt = 100 µs) frequencies at a resolution of 512 × 512 pixels (examples are shown in [12]). The work area was 410 pixels, which, at the size of the measuring window (90 mm), allows for a 1 pixel = 220 µm imaging (or 1 mm = 4.55 pixels). This value is sufficient to carry out accurate analyzes of the fuel stream geometric parameters.

3.3. Results analysis

The recorded images were further processed to obtain fuel injection indicators from injectors with different mileage (new and used).

The study of injection indicators was carried out independently for each of the eight fuel sprays and the parameters determined included:

a) stream range; it is defined as the maximum distance from the atomizer to the adopted luminance boundary of the fuel stream image. Preparation of the images to evaluate the fuel stream range consisted of selecting the test area (applying masking of the image) and subtracting the background (measured noise). The fuel stream range was determined individually for each stream.
b) fuel stream area; it is defined as the number of pixels within the specified luminance intensity range. These tests were performed by determining the coordinates of triangles on each of the fuel streams.
c) the fuel stream cone angle; this value was determined using the method devised by Naber and Siebers [8]. It is possible to use typical algorithms to search for the stream cone based on the edges of the fuel jet streams, but this method is used increasingly less often due to the low accuracy and lack of precise guidelines for determining the rules of such methods. The Naber and Siebers method can be used for any injector in compression-ignition engines with different fuel outflow angles [9]. This algorithm requires determining the range of the fuel stream and then using half of that value and determining the fuel stream area for that range value. With this method it is possible to determine half of the stream cone angle value:

$$tg\left(\frac{\alpha}{2}\right)=\frac{P_{\Delta}}{(S/2)^2}$$

where: α – fuel stream cone angle, P_{Δ} – triangle surface area, S – maximum fuel stream range (Fig. 2).

The method of image processing and determination of individual spray indicators is shown in Fig. 3. The results obtained with this method (for each stream and for the full atomization time) mean that the results of initial values obtained for the fuel stream development will be subject to a large error resulting from the small developed fuel stream area value. With the development of the stream, the value of the resulting cone angle of the stream should be constant.

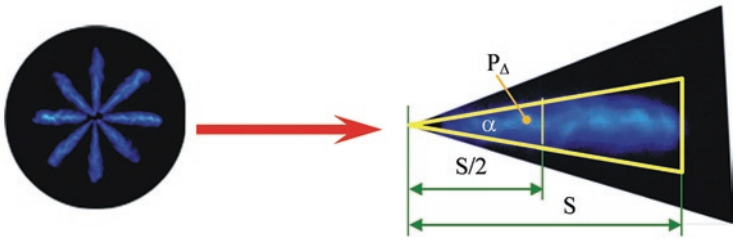

Fig. 2. Method for determining the fuel stream cone angle

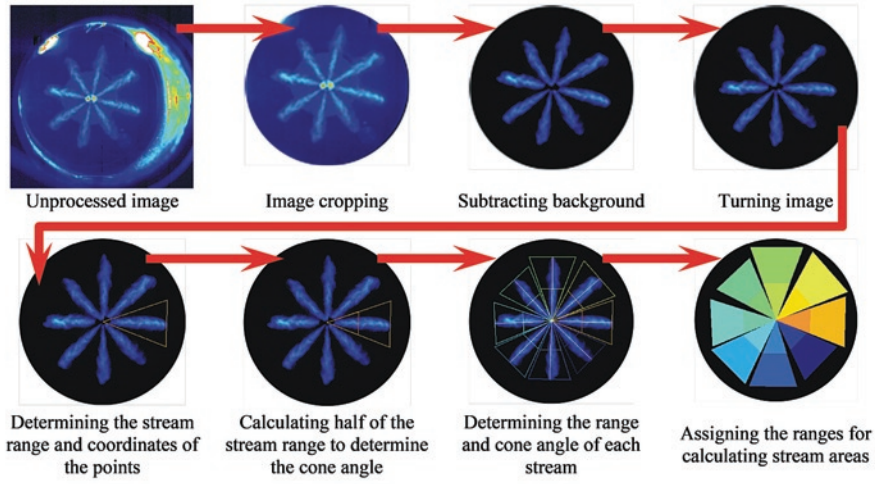

Fig. 3. Image processing and determining the geometric indicators of the fuel stream

4. Analysis of fuel spray geometric parameters and selection of the comparative index

4.1. Assessment of individual fuel spray indicator values

The methodology described above was used to determine the range of individual fuel streams. An average of these values was calculated, and presented in the form of lines without any visible measured points (Fig. 4a). Conducted research indicates the similarity of the range of individual fuel streams. It can also be concluded that analyzing each of the streams individually is necessary, since the arbitrary choice of one fuel stream does not permit full analysis of such atomization. Representative streams can be indicated in the analyzed results – similar to the average values. However, this selection is pos-

sible only after individual stream analysis. There were no significant differences in the range of individual fuel streams using standard fuel (diesel). In the analysis of the modified fuel range, however, it was found that there are two streams that differ significantly from the others. Such cases occurred during the stream range analysis of both, the new and the used injectors. It is not possible to deduce the difference in the wear level of the injectors or to change this value by using different fuels based on the analysis of individual stream ranges.

Analysis of the injected fuel stream surface area indicates the existence of significant differences when determining this value. Using this indicator, it is possible to assess the operational wear of the injector, as the stream surface area is significantly smaller (Figure 4b). It was thus also found that the analysis results of only one fuel stream could not be representative of the injectors operational changes.

The assessment of the fuel stream cone angle (Fig. 4c) indicates the existence of the lowest scatter values (spread at t = 1.6 ms between the new injectors is 4 percentage points). Analyzing this angle indicates a high repeatability of this measurement for each fuel stream. It is also possible to determine the injector wear, since as the injector mileage increases the fuel stream cone angle decreases.

4.2. Assessment of fuel spray indicators limits

Due to the discrepancies in the fuel spray indicators of different streams mentioned previously, their limit values were determined. Stream range analysis indicates an increase in the differences with the streams development. The fuel spray limit values are similar (Figure 5a). At time up to 0.6 ms, the differences in the stream ranges are small and are about 14.9% for new injectors regardless of fuel type. After this time, however, these values increase to 30.5% for the injection of both fuels (at atomization time t = 1.6 ms after injection start time). The spread of values obtained for the used injectors #1 and #2 are: 17.5% and 22% respectively (0.6 ms after injection start) and 26.9% and 33% (at 1.6 ms) respectively.

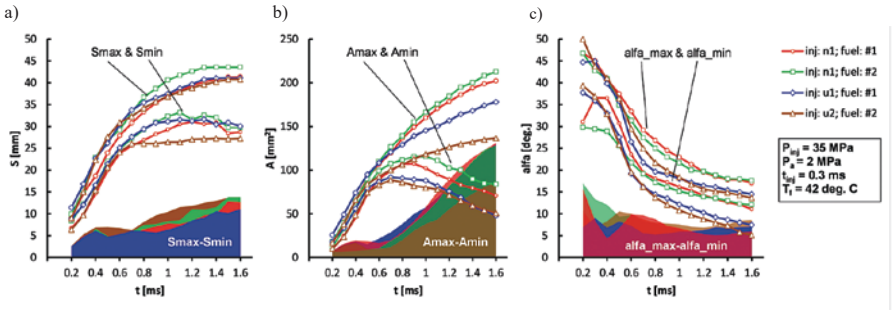

Fig. 5. Evaluation of limit values and differences of these values during fuel injection: a) stream range – S, b) stream surface area – A, c) stream cone angle – alpha

The boundary values of the stream surface areas vary more significantly (Figure 5b). The investigations of new injectors indicate a much smaller spread between them than observed for the used injectors. However, the absolute value analysis allows to conclude that the differences in this case are smaller (between used injectors fed with different fuels). The smaller fuel stream surface area is caused by injector wear and tear (smoldering of atomizer holes), the smaller differences in values are due to the same level of injector wear. New injectors were characterized by increased differences in manufacturing and machining and were not subjected to several hours of operation. Up until 0.6 ms time the stream surface area differences were small and amounted to 15–19%. In both cases, the final stream surface area values (at t = 1.6 ms after injection start) were found to be in the range of 60–75%. This result may be due to the different manufacturing accuracy of the injector holes. The change in the range of stream area value analysis (t = 1.6 ms) does not exceed 5 percentage points (new

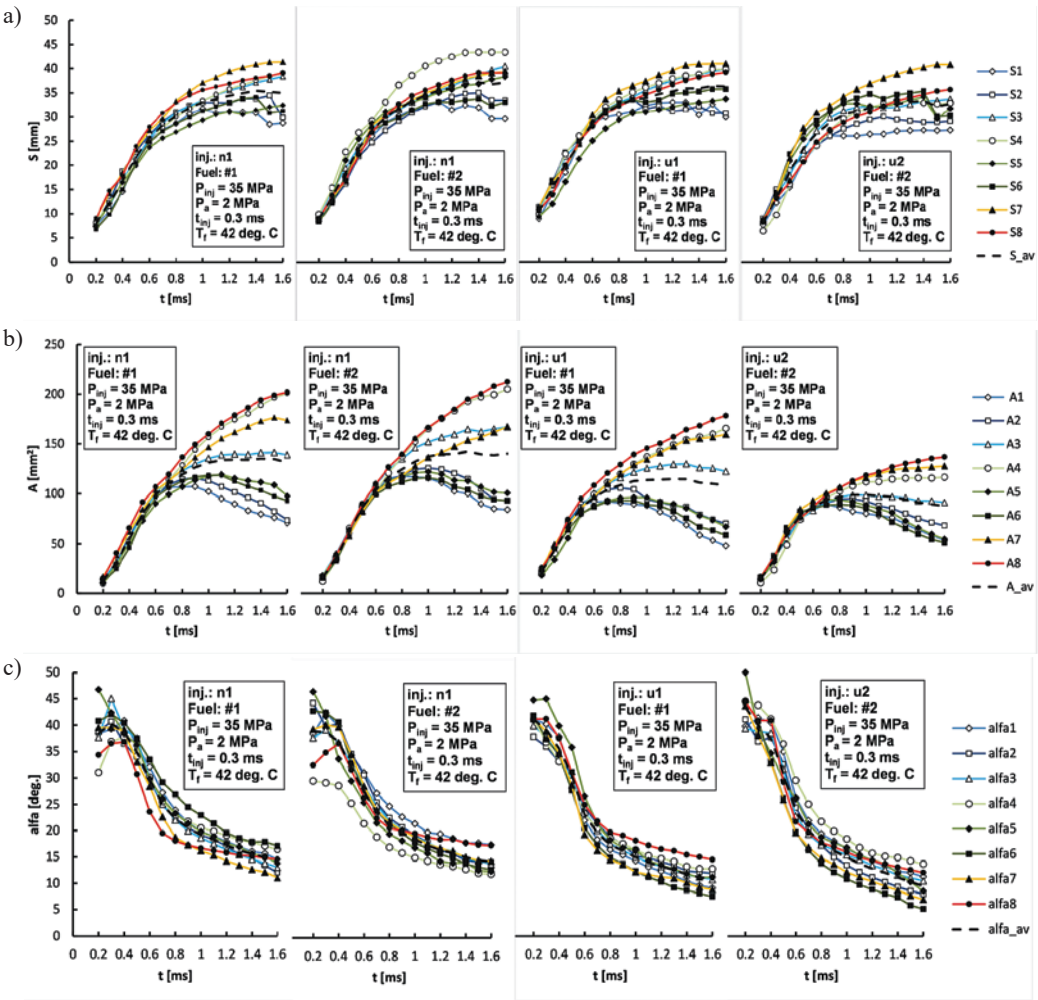

Fig. 4. Results of fuel spray indicator tests: a) fuel stream range – S, b) fuel stream area – A, c) stream cone angle – alpha

injectors) and 11 percentage points when analyzing injectors previously used.

Changes in the fuel stream cone angle are quite uniform throughout the injection period. The initial large angle values are due to the low corresponding fuel range value. Later on in fuel injection, similar changes for each test are observed. Up to 0.68 ms the difference in the stream range values is about 30%. After this time the values are still around 30% (at time t = 1.6 ms). Thus it can be stated, that this indicator is characterized by limited value changes with the time after injection. But also, for all the performed tests, the stream cone angle value spread decreases, resulting in a steady values after about 1 ms (range of angle between streams less than 10 degrees).

4.3. Average fuel spray rate evaluation

Due to the described discrepancies in the individual stream spray indicators, their averaged values were determined (Fig. 6).

Fuel injection using the new injectors indicates a greater stream range is obtained by fuel with additives (5% greater range). The operating conditions produce ambiguous results (Figure 6a). The stream range for injectors using base diesel fuel increased by 6%, while for diesel fuel with additives the range decreased by 11%. As can be seen from the above results, there is no clear conclusion, which indicates the need for additional fuel stream geometry analyzes to determine the fuel atomization differences between the various injectors and the use of different fuels.

The mean fuel stream area values analysis indicates the possibility of evaluating both the injectors wear degree as well as the fuel type used (Figure 6b). This is due to significant changes in the analyzed quantities. Larger fuel stream areas are observed for new injectors (regardless of the fuel type used). These values are higher by 20% (fuel #1) and 60% (fuel #2) compared to used injectors. Larger spray values (6%) were achieved with fuel #2 for new injectors. In the case of used injectors, the larger stream area was observed for fuel #1 – by 24%. Inclusion of the stream surface area in the fuel stream geometric analysis is a measure that allows the identification of the mileage and wear of the injectors as well as to determine the differences when spraying different types of fuels.

Analysis of the average stream cone angle values indicates the high usefulness of this indicator for evaluating fuel spray of the operating injectors (Figure 6c). This analysis of the average stream cone angle reveals significant differences in the evaluation of new and used injectors. Operating conditions deteriorate the performance of the injectors (sintering and coking of the injector holes), resulting in a reduced stream cone angle. The difference between new and used injectors is about 30%. It can be noted that after some time (about 0.8 ms from the start of the injection) the values of these differences are constant. In the case of tested fuels it is not possible to effectively distinguish the difference in fuel spray from new or used injectors (the difference in spray angle for used injectors is only about 5% higher). The results of the fuel stream cone angle analysis by this method are convergent (with respect to the trend of changes during injection and atomization) with the results obtained in the studies of the mixture of n-pentanol and diesel oil by Ma et al. [7].

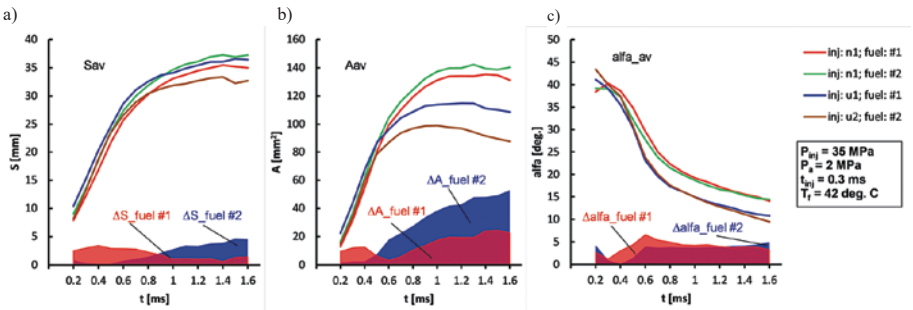

Fig. 6. Evaluation of average fuel spray indicators with limit values and value ranges: a) stream range – S, b) stream surface area – A, c) stream cone angle – alpha

5. Selection of test conditions for the assessment of fuel spray indicators

Using the average fuel spray indicator values obtained, the coefficient of variation (as the standard deviation of the mean value) was determined for each fuel injection time. Because the value of the standard deviation itself depends on the mean value, this means that as the stream range increases, this value will also increase, an indicator that is independent of the mean has been selected. Thus it became possible to determine the time after which indicator value only increases. In combustion engine studies, it is assumed that the value of the coefficient of variation compared to the average indicated pressure should not exceed 3.5%–5% [6, 17] or the value of 10% [4]. Due to the much lower repeatability of the stream cone angle measurement results, it is assumed that in such tests it can reach values of up to 40% [3]. Taking these assumptions into account, an analysis is presented, including the determination of the minimum coefficient of variation value. It has been shown that there is a time after which the value of a given fuel geometry indicator only increases (Figure 7). With these assumptions, it is assumed that the minimum fuel spray analysis time, after which it is possible to determine the difference in the fuel atomization method, is 0.6 ms from the start of the injection. Only after such a time, changes in the range of the stream, the stream surface area and the stream cone angle are visible. Adopting a higher time value makes it valid, but the best form of evaluation consists of the knowledge of the whole fuel spray pattern.

6. Conclusions

Conducting research on the fuel streams geometry requires the use of optical tests in which it is important to consider several different parameters. Determining the geometric indicators of the fuel stream requires the use of procedures that determine the parameters of each stream separately and then averaging the results. It is necessary to analyze each stream individually, because choosing one stream for analysis does not allow for a full fuel spray and atomization analysis. Because of the large variation between

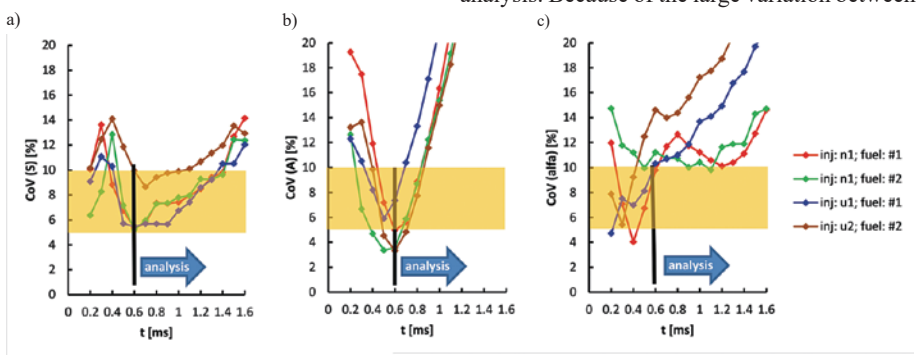

Fig. 7. Choice of analysis time for fuel spray coefficients based on the coefficient of variation: a) stream range – CoV (S), b) stream surface area – CoV (A), c) stream cone angle – CoV (alpha)

the different atomizer holes, the atomized fuel parameter values can vary greatly for each fuel stream.

In order to determine the effect of the fuel type used for the same injectors, it is necessary to determine the surface area occupied by the fuel stream as well as the stream cone angle. Due to the close similarity of the physical characteristics of the tested fuels, the range of the fuel stream does not indicate any changes that would allow to differentiate the fuel used based on the observed values.

Evaluation of the injectors wear level requires knowledge of the fuel stream surface area and the stream cone angle. In this case, the cone angle of the injected fuel stream is a significant indicator of the stream geometry, whose changes can be observed as a result of the operation and wear of the injector.

Detailed conclusions on the fuel stream geometric indicators were formulated in relation to the mean values obtained from the analysis of each stream:

1) in terms of stream range:
   a) the similarity in the physical characteristics of the analyzed fuels causes the differences in stream range from the new injectors to be small reaching about 5% in favor of the additive-rich fuel,
   b) during the analysis of the used injectors, different results were obtained: fuel injection using base diesel fuel increased the stream range by 6%, while using diesel fuel with additives led to a range decrease of 11%,
   c) the fuel injection characteristics and operational changes of the injectors cannot be evaluated or tested using the values of fuel stream range.
2) in terms of fuel stream surface area:
   a) new injectors (regardless of the fuel used) have a much larger stream area than the used injectors; which had a mileage of 80,000 km, the area has decreased both during base diesel fuel injection (20%) and during the additive-rich fuel injection (60%),
   b) when fuel is injected using the new injectors, the stream area is slightly larger for fuel with additives (by 6%); it is significantly smaller for base diesel fuel (by 24%) when using the already worn out injectors,
   c) the analysis of the mean stream area values indicates the applicability of this indicator, both to the assessment of the injectors wear and mileage and to identify the injection of different fuels (even with similar physical characteristics); this is due to significant changes in the values of analyzed parameters,
3) in terms of fuel stream cone angle:
   a) the difference between new and used injectors is about 30%,
   b) in the case of the tested fuels, it is not possible to determine the difference of fuel spray from new or used injectors (the difference in stream cone angle for used injectors reaches only up to 5%),
   c) the analysis of the results indicates the usefulness of this indicator for assessing the fuel atomization for the analysis of both new and used injectors.

The results of the conducted research indicate very high possibility of evaluating the degree of wear of the injectors. However, full analysis of the impact of different fuels on their geometric indicators should be complemented with combustion studies. Such studies, which are the next planned stage in the authors research, on the recognition of the various fuels injection effects, should be used to supplement the knowledge on the possibility of evaluating different fuel types, in the aspect of their effect on the operation of injectors, in compression-ignition engines.

Acknowledgement

The research presented in this paper was performed within the statutory work, project no. 05/52/DSMK/0265.

References

1. Beck Á, Pölczmann G, Eller Z. et al. Investigation of the effect of detergent–dispersant additives on the oxidation stability of biodiesel, diesel fuel and their blends. Biomass and Bioenergy 2014; 66: 328–336, https://doi.org/10.1016/j.biombioe.2014.03.050.
2. Ghahremani A R, Saidi M H, Hajinezhad A, Mozafari A A. Experimental investiga-tion of spray characteristics of a modified bio-diesel in a direct injection combustion chamber. Experimental Thermal and Fluid Science 2017; 81: 445–453, http://dx.doi.org/10.1016/j.expthermflusci.2016.09.010.
3. Hassen N S, Sidik N A C, Sheriff J M. Effect of nozzle type, angle and pressure on spray volumetric distribution of broadcasting and banding application. Journal of Me-chanical Engineering Research 2013; 5(4): 76–81, https://doi.org/10.5897/JMER2013.0272.
4. Heywood J B. Internal combustion engine fundamentals. New York, McGraw-Hill 1988.
5. Khalife E, Tabatabaei M, Demirbas A, Aghbashlo M. Impacts of additives on perfor-mance and emission characteristics of diesel engines during steady state operation. Progress in Energy and Combustion Science 2017; 59: 32–78, http://dx.doi.org/10.1016/j.pecs.2016.10.001.
6. King J, Böcker O. Multiple injection and boosting benefits for improved fuel con-sumption on a spray guided direct injection gasoline engine. Proceedings of the FISI-TA 2012 World Automotive Congress. Lecture Notes in Electrical Engineering 2013; 189, Springer, Berlin, Heidelberg, https://doi.org/10.1007/978-3-642-33841-0_18.
7. Ma Y, Huang S, Huang R, Zhang Y, Xu S. Spray and evaporation characteristics of -pentanol–diesel blends in a constant volume chamber. Energy Conversion and Man-agement 2016; 130: 240–251, http://dx.doi.org/10.1016/j.enconman.2016.10.063.
8. Naber J, Siebers D. Effects of gas density and vaporization on penetration and disper-sion of diesel sprays.SAE Technical Paper 1996, 960034, http://dx.doi.org/10.4271/960034.
9. Payri R, Gimeno J, Bardi M, Plazas A. Effect of injection rate shaping over diesel spray development in non reacting evaporative conditions. ASME 2012 Internal Com-bustion Engine Division Spring Technical Conference 2012; 347–356, http://dx.doi.org/10.1115/ICES2012-81206.
10. Payri F, Payri R, Salvador F J, Bardi M. Effect of gas properties on Diesel spray pene-tration and spreading angle for the ECN injectors. ICLASS 2012, 12th Triennial Inter-national Conference on Liquid Atomization and Spray Systems, Heidelberg, Germany, September 2-6, 2012.
11. Payri R, Viera J P, Gopalakrishnan V, Szymkowicz P G. The effect of nozzle geome-try over the evaporative spray formation for three different fuels. Fuel 2017; 188: 645–660, http://dx.doi.org/10.1016/j.fuel.2016.10.064.
12. Pielecha I. Analysis of the repeatability of fuel spray indexes in a spray-guided spark-ignited direct-injection engine. Combustion Engines 2016; 164(1): 49–55.

13. Pielecha I. Modeling of gasoline fuel spray penetration in SIDI engines. International Journal of Automotive Technology 2014; 15(1): 47–55, http://dx.doi.org/10.1007/s12239-014-0005-y.
14. Pielecha I, Wisłocki K, Borowski P, Cieślik W. Thermodynamical evaluation of use-fulness of future hydrocarbon fuels for use in compression ignition engines. Journal of Thermal Analysis and Calorimetry 2015; 122(1): 473–485, http://dx.doi.org/10.1007/s10973-015-4735-5.
15. Shaafi T, Sairam K, Gopinath A, Kumaresan G, Velraj R. Effect of dispersion of vari-ous nanoadditives on the performance and emission characteristics of a CI engine fuelled with diesel, biodiesel and blends—A review. Renewable and Sustainable En-ergy Reviews 2015; 49: 563–573, http://dx.doi.org/10.1016/j.rser.2015.04.086.
16. Stępień Z. A study of factors influencing the formation of harmful deposits in the die-sel engine injectors. Eksploatacja i Niezawodnosc – Maintenance and Reliability 2017; 19(3): 331–337, http://dx.doi.org/10.17531/ein.2017.3.3.
17. Subic A, Wellnitz J, Leary M, Koopmans L. Sustainable automotive technologies 2012: Proceedings of the 4th International Conference, Springer Science & Business Media 2012; 404.
18. Wei M, Gao Y, Yan F, Chen L, Feng L, Li G, Zhang C. Experimental study of cavita-tion formation and primary breakup for a biodiesel surrogate fuel (methyl butanoate) using transparent nozzle. Fuel 2017; 203: 690–699, http://dx.doi.org/10.1016/j.fuel.2017.05.022.
19. Żak G, Ziemiański L, Stępień Z, Wojtasik M. Engine testing of novel diesel fuel de-tergent–dispersant additives. Fuel 2014; 122: 12–20, http://dx.doi.org/10.1016/j.fuel.2013.12.055.

Ireneusz PIELECHA
Maciej SKOWRON
Institute of Combustion Engines and Transport
Poznan University of Technology
ul. Piotrowo 3, 60-965 Poznan, Poland

Aleksander MAZANEK
Department of Performance Testing
Oil and Gas Institute - National Research Institute
ul. Lubicz 25A, 31-503 Cracow, Poland

E-mails: Ireneusz.Pielecha@put.poznan.pl, Maciej.Skowron@put.poznan.pl, MazanekA@inig.pl

Article citation info:
ZELIĆ A, ZUBER N, ŠOSTAKOV R. Experimental determination of lateral forces caused by bridge crane skewing during travelling. Eksploatacja i Niezawodnosc – Maintenance and Reliability 2018; 20 (1): 90–99, http://dx.doi.org/10.17531/ein.2018.1.12.

Atila ZELIĆ
Ninoslav ZUBER
Rastislav ŠOSTAKOV

EXPERIMENTAL DETERMINATION OF LATERAL FORCES CAUSED BY BRIDGE CRANE SKEWING DURING TRAVELLING

EKSPERYMENTALNE WYZNACZANIE SIŁ POPRZECZNYCH WYWOŁANYCH SKRĘTEM SUWNICY PODCZAS JAZDY

Crane condition depends on the large number of variables randomly changing in time. Due to the large number of parameters, skewing forces have stochastic character. Though in standards treated as occasional loads, their dynamic action in certain cases can cause fatigue damage of the crane travelling mechanisms, structure and runway components. Current European Norms have left the question of skewing forces influence upon the fatigue damage occurrence unresolved. The paper presents an experimental determination of lateral forces acting on the vertical wheels of a bridge crane using two different solutions of transducers for the direct measurement on the wheels of the cranes in operation, without changing the way of lateral guiding. As an illustration, few records of the measured wheel lateral force vs. time are shown. Presentation of such records in the form of a loading spectrum (e.g. using the software nCode), obtained during long-lasting or continuous monitoring of cranes in operation, is the first step in finding the relevant answer to the previously unresolved question.

***Keywords**: bridge crane skewing, lateral force transducer, load spectrum, fatigue.*

Stan suwnicy pomostowej zależy od dużej liczby zmiennych losowo zmieniających się w czasie. Ze względu na dużą liczbę parametrów, siły skośne mają charakter stochastyczny. Chociaż w normach traktowane są one jako obciążenia sporadyczne, ich dynamiczne oddziaływanie w niektórych przypadkach może powodować zmęczeniowe uszkodzenie mechanizmu jazdy suwnicy, jak również jego konstrukcji oraz elementów toru jezdnego. Obecnie obowiązujące normy europejskie pozostawiają bez rozwiązania kwestię wpływu sił skośnych na występowanie uszkodzeń zmęczeniowych. W pracy przedstawiono metodę eksperymentalnego wyznaczania sił poprzecznych działających na koła pionowe suwnicy pomostowej. Metoda ta polega na użyciu dwóch różnych rozwiązań przetworników do bezpośredniego pomiaru sił na kołach pracującej suwnicy, bez zmiany sposobu prowadzenia bocznego . Dla ilustracji pokazano kilka zapisów pomiarów siły poprzecznej koła w funkcji czasu. Przedstawienie takich zapisów w postaci widma obciążenia (np. za pomocą oprogramowania nCode), uzyskanego podczas długotrwałego lub ciągłego monitorowania suwnicy w trakcie jej eksploatacji, stanowi pierwszy krok do znalezienia rozwiązania nierozwikłanego do tej pory problemu.

***Słowa kluczowe**: skręt suwnicy, przetwornik siły poprzecznej, widmo obciążenia, zmęczenie.*

1. Introduction

The separate group of cyclically operating load transporting machines includes cranes, travelling along the invariable railway consisting of two parallel rails fastened onto the corresponding steel or concrete supporting beams, or onto the foundation on the ground. Some typical representatives of this group are bridge, gantry and semi-gantry cranes, ship-to-shore container gantry cranes, and slewing jib portal or semi-portal cranes.

All the loads acting upon the crane are transmitted from the points of their action through the structure and wheels or guide rollers, to the runway rails. Crane wheels derailment is usually mechanically prevented under constraint by the guiding means, such as wheel flanges, or horizontal side rollers. Manufacturers of transducer technologies have already offered various electronic contactless guiding systems. However, their application is limited to the newer and valuable cranes. Nowadays in use are mainly bridge and gantry cranes without any additional electronic guiding devices.

During the operation of slewing jib portal cranes, due to the slewing of their turntable, and derricking the jib, the position of the center of gravity projecting point upon the supporting plane is constantly altered. Asymmetric allocation of gravity forces at bridge and gantry cranes is caused by the loaded trolley traversing. Consequently, the general rule applies to all the previously mentioned cranes where during the load handling, vertical loads acting on the crane wheels and resistance forces change their values, thus causing the crane structure skewing in the horizontal plane. Their vertical wheels are rolling without disturbance in the „natural direction“, causing the deviation of the direction of resulting crane motion from the runway rail direction. However, the direction of motion alters when the guiding means comes into the contact with the rail head, and the crane keeps coming back into the runway direction. Such forced guiding along the runway realized by the successive interaction among the guiding means and the rail, causes complex planar motion of the crane, termed as skewing.

The purpose of this research is to propose the concept of forming the experimental data basis concerning the influence of crane skewing on the fatigue of its structure elements and traveling drive components. Such data basis is indispensible for further advancement of probabilistic calculations of cranes.

The paper gives the short survey of typical damages of crane wheels and rails caused by the undesirable consequences of excessive skewing. The main goal of the paper is to outline one of the possible ways of measuring the values of lateral forces due to skewing, without altering the function, the composition, or the form of the standard-

ized crane wheel assembly. Two different forms of force transducers were designed for the purpose of measuring the lateral forces. The proposed technical solution was tested at the single-girder bridge crane. The obtained records of the measured wheel lateral force vs. time were processed by using the software nCode. The final results were obtained in the form of the lateral forces spectra per wheel for the period of measurement.

2. Short reference to the problems of bridge crane skewing

Forces arising in the interaction among the wheel and the rail, and corresponding velocities (projected onto the contact plane) are shown in Fig. 1. The natural direction of a crane vertical wheel rolling deviates from the rail direction, and the deviation is expressed as the skewing angle α_w.

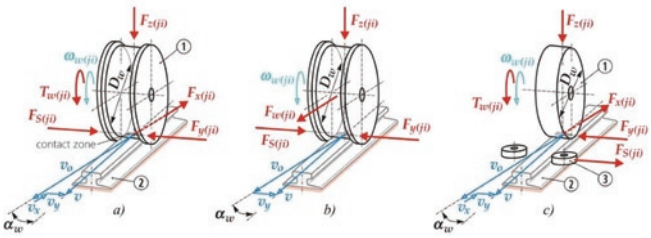

Fig. 1. Velocities and forces corresponding to the skewed crane wheel: a) driven flanged wheel; b) non-driven flanged wheel; c) driven flangeless wheel (1- vertical crane wheel; 2 - rail; 3 - horizontal guiding roller)

Driven wheel i on the rail j, Fig. 1.a, loaded with vertical force $F_{z(ji)}$ and driven by the torque $T_{w(ji)}$, rolls along the rail with tangential velocity $v_o = (D_w/2)\cdot\omega_{w(ji)}$, where D_w denotes the nominal wheel diameter. Due to its elastic slip, the driven wheel slips tangentially with the velocity v_x. When its flange comes upon the rail head, due to the axial slip with the velocity v_y, the wheel abandons its „natural direction" and starts rolling in the rail direction with the resulting velocity v. The corresponding forces due to the tangential and axial slips are $F_{x(ji)}$ and $F_{y(ji)}$, and the skewing force $F_{S(ji)}$ arises in the contact point of wheel flange and rail head.

Non-driven wheel, Fig. 1.b, is driven by the crane structure, pulling its axle with force $F_{w(ji)}$, and rolls with the angular velocity $\omega_{w(ji)}$. In this case, no elastic slip occurs, and consequently there exists neither velocity v_x, nor force $F_{x(ji)}$.

In case of a crane with flangeless vertical wheels, Fig. 1.c, guiding along the runway rails is performed by horizontal rollers. The skewing force occurs in the contact point of the roller and the rail.

The occurrence of skewing phenomena is not equally noticeable at each of the mentioned crane types. Skewing forces at portal slewing cranes with derricking jib and container portal cranes are of no exceptional importance for the dynamic behavior and structure fatigue, because the travelling of these cranes is a mere auxiliary movement (changing the operation location). However, for gantry and bridge cranes with wider spans, the steady tendency to skewing during travelling is one of the important issues.

The most significant factors having impact on the crane motion stability and its dynamic behavior in the process of skewing, as well as on the occurrence frequency, amplitude values and history of skewing force, are [8, 17]:

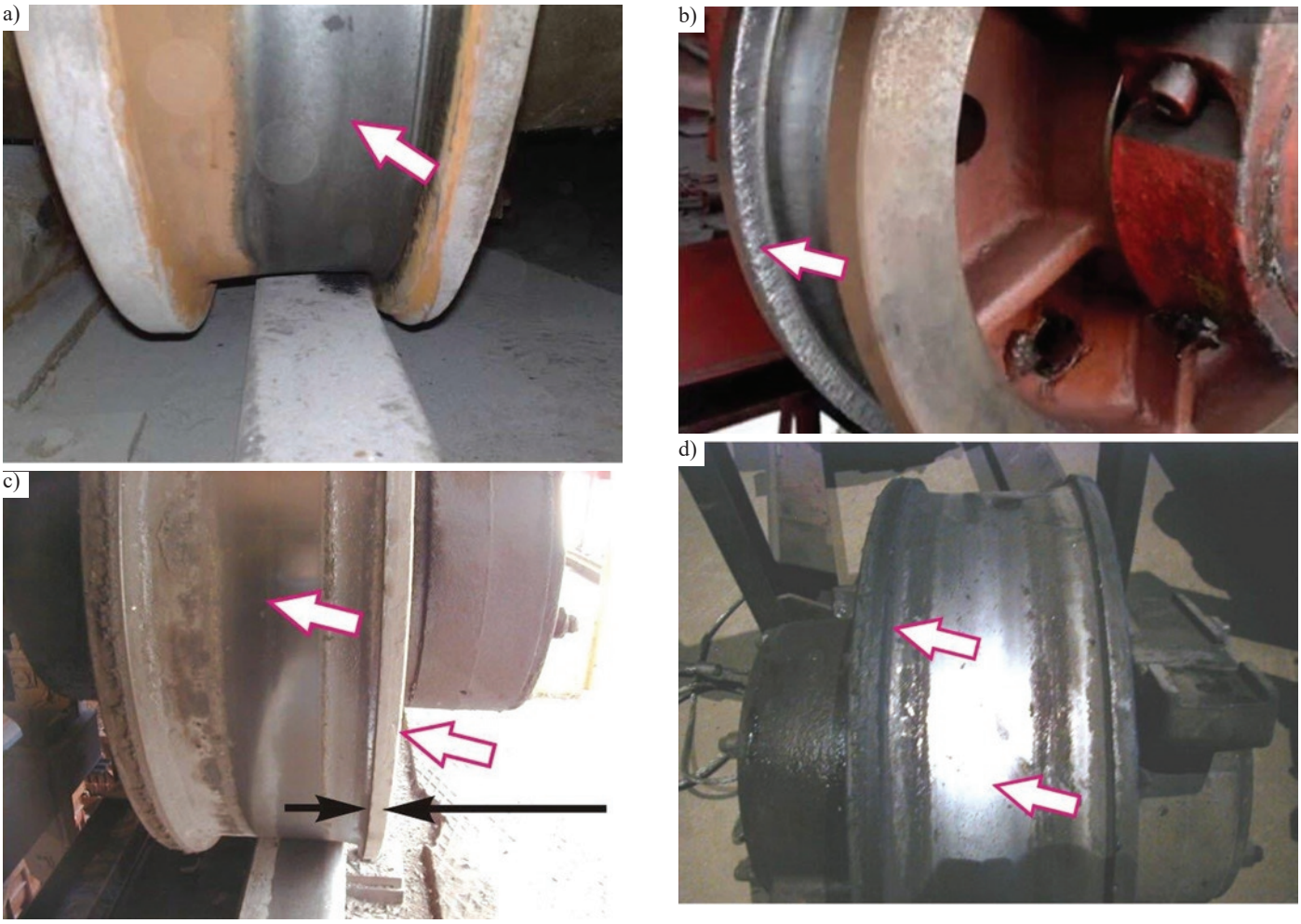

Fig. 2. (a–d) Examples of typical damage of crane vertical wheels and horizontal guiding rollers

Fig. 2. (e–i) Examples of typical damage of crane vertical wheels and horizontal guiding rollers

– factors and phenomena depending on the crane configuration, operation regimes, and environmental conditions, and cannot be altered by means of technical or technological actions,
– geometrical imperfections and deviations made during manufacturing and installation of crane vertical wheels assemblies,
– improper arrangement of horizontal guiding roller assemblies, geometrical imperfections and deviations made during installation of their components,
– geometrical imperfections made during manufacturing and installation of crane runway rails,
– deviations made during installation of crane structure elements,
– unequal angular velocities of driven wheels on both end carriages,
– irregular and incompetent maintenance of a crane and its rail track, and
– errors in crane design due to insufficient knowledge of crane skewing problems.

Undesired consequences of crane skewing are usually shown as various types of damage on vertical wheels and horizontal rollers, rails and crane structure elements. Extreme lateral loads caused by

enormous skewing can even cause frequent failures, rail track degradation, demolition or plastic deformation of crane driving mechanism components, or even crane structure collapse.

Fig. 2.a and 2.c show the wheel tread (rolling surface) with clearly distinguishable lighter surfaces with metal glitter from the corroded surfaces, [10, 11]. The difference among the conditions of these surfaces indicates that the crane doesn't use the whole width of the wheel tread. In case of constant contact between the wheel flange and the same rail head, the crane travels in a straight line without any „waddling". During a longer period, this leads to wearing of only one rail head side and its corresponding wheel flange. Shallow traces of wearing on the inner wheel flange surface, Fig. 2.b, are the signs of wheel flange tending to climb onto the rail head, [2]. The examples of worn-out wheel tread and altered wheel flange geometry, [10], are shown in Fig. 2.d. Such traces occur mainly at driven wheels due to the tangential and axial slip. If wheel maintenance and condition check are not regularly carried out, the flange thickness can be considerably reduced, thus leading to its fracture, Fig. 2.f, even by minor lateral load acting, [15].

Sometimes skewing forces cause plastic deformations of a thinned wheel. In case of inadequately designed and poorly maintained wheels, these deformations can be accompanied by the occurrence of recess along the wheel circumference, in-depth hairline cracks in tread surface, and worn-out flange, Fig. 2.g, [23]. These damages arise as a result of joint action of exceptionally large vertical and lateral loads during crane operation. In case of inadequate wheel heat-treatment, vertical and lateral forces can induce flaking by layers of wheel tread surface, Fig. 2.h, especially in the case of a high temperature in the working environment (iron foundries, ironworks, rolling mills, etc.),

Fig. 3. (a-d) Examples of typical damage of crane runway rails

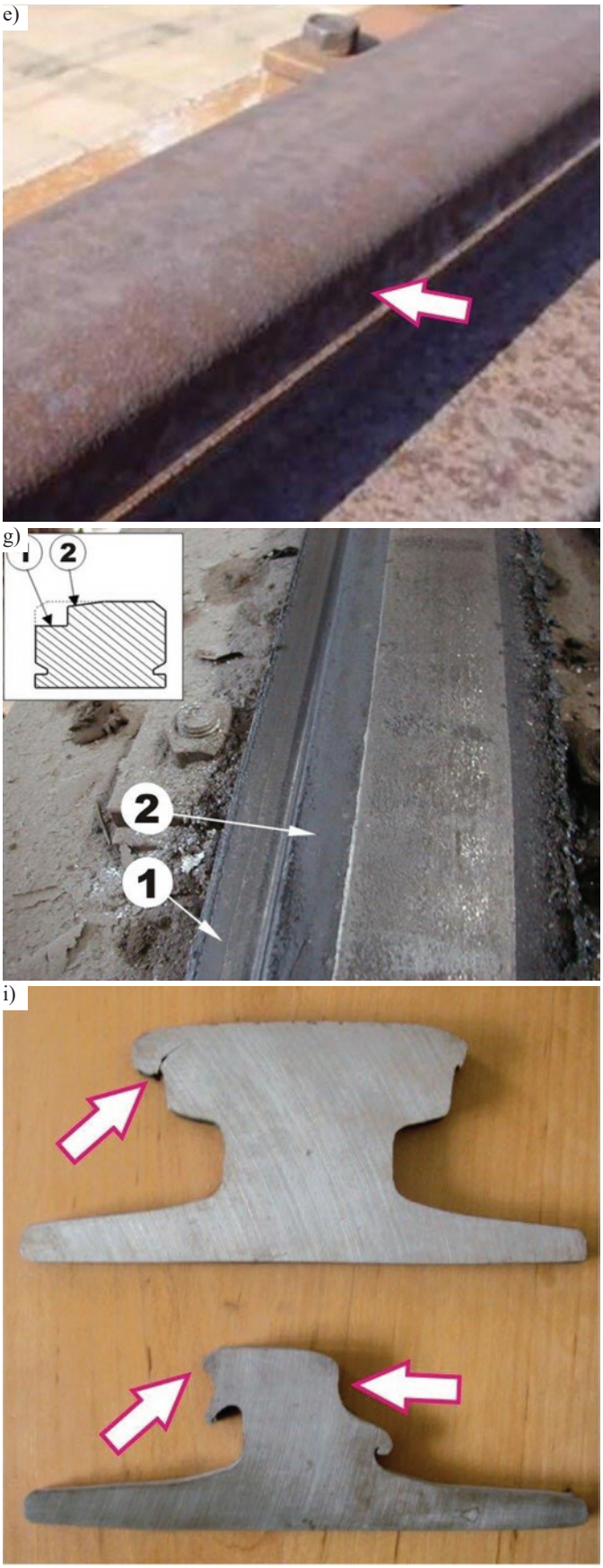

[2]. Loads due to the skewing of gantry cranes with wide spans can cause flaking of rolling surfaces even on the horizontal guiding rollers, Fig. 2.i, [25].

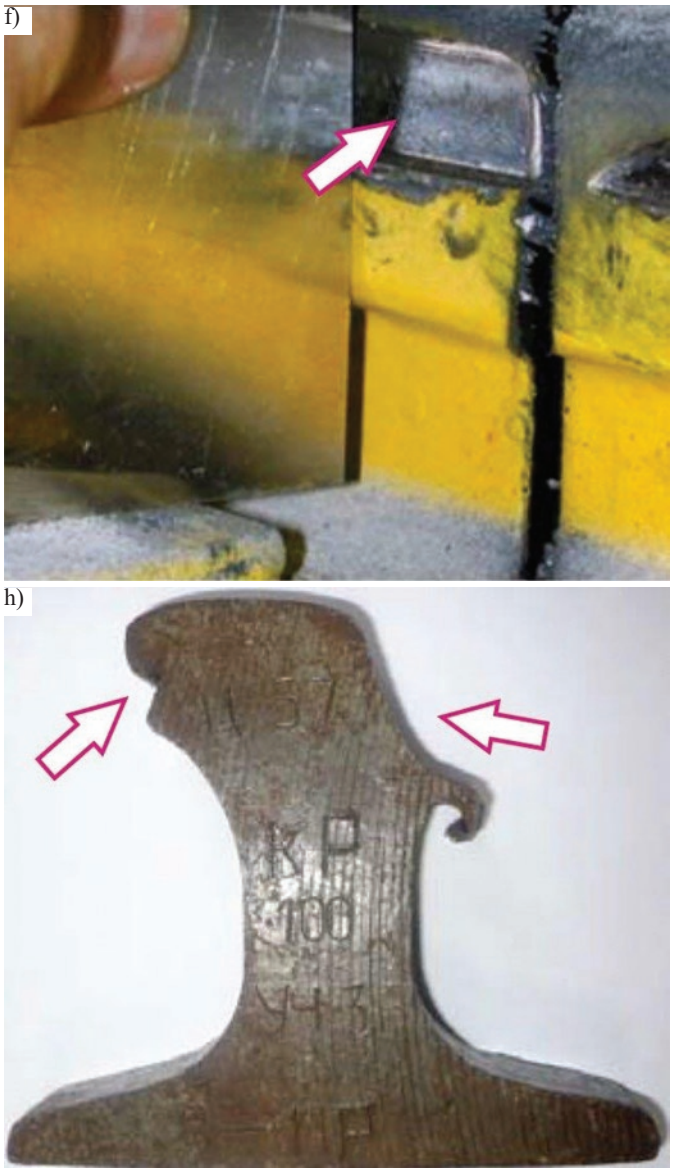

Fig. 3. (e-i) Examples of typical damage of crane runway rails

The most frequent patterns of crane rails damage are shown in Fig. 3. Lateral loads often cause rail deformations, Fig. 3.a, on certain track sections (primarily at gantry cranes), [25]. Due to the increased pressure in the contact point of wheel flange and rail head, wearing traces arise at both of them. When the deviations from the rail direction exceed the tolerable values, difficulties occur during travelling, even crane „wedging-in". Vertical and horizontal offset between the adjoining rail sections obstruct the normal crane travelling. Vertical offset is usually the result of errors in installation, and wheel crossing over the so developed step causes the additional high-impact loads and crane structure vibrations. Lateral loads can even cause the rail joint „opening". The horizontal rail offset occurs mainly at crane tracks with free supported rails. An example of a deformed step-like formed rail joint is shown in Fig. 3.b. The horizontal offset between the rail sections joining at an angle is shown in Fig. 3.c, [2]. Damage pattern shown in Fig. 3.d, [1], occurs mainly at rails with small roundness radius of a head edge. In case of wheels mounted at an angle, due to steady skewing the wheel flange tends to climb onto the rail head, and in extreme cases to cause the crane wheels derailment. During that process the sharp edge of wheel flange mechanically damages the rail head edge.

At the same time, bumping of skewed wheel flange into the rail edge in a joint with perpendicularly cut rail ends causes strong impact leading to flange and rail damage. In case when the crane guiding is only realized by means of one rail head side, and mainly by the same flange, flange and rail head geometry alter quickly, and traces of intensive wearing arise, 3.e, f, and g, [10, 18, 19]. During operation of heavy bridge cranes at increased temperature, e.g. in foundries and ironworks, easy recognizable patterns of rail head deformation appear, as an effect of vertical and horizontal loads acting, Fig. 3.h, and i, [11, 24].

The skewing forces can cause fatigue hairline cracks in structure elements, mainly at the end carriages of bridge cranes close to wheel bearing assemblies, main girder ends and their connections with end carriages or with rigidly connected gantry crane legs. A notable number of accidents are described in [9]. In the majority of these accidents the excessive skewing had caused the derailment of crane wheels and even the collapse of a complete crane structure.

3. Forces caused by crane skewing – Occasional or regular loads?

Majority of withdrawn national standards, e.g. PN-86/M-06514, and international guidelines, e.g. earlier versions of [7], proposed a very simple procedure for the calculations of lateral forces acting perpendicularly to the direction of a crane/trolley motion. According to the requirements of these standards, the skewing loads were not taken into account in calculations of stresses induced by varying loads able to induce the fatigue of material.

In accordance with the effective norms [3, 6], calculations of amplitude of axial friction force acting on the vertical wheel, and skewing force, [6, 18, 26], are even now treated on the basis of a simplified static model, although the results of a few theoretic and extensive experimental researches, [17], confirm that the dynamic effects of induced loads have to be taken into account for the qualitative and quantitative description of skewing.

Crane as a whole, its structure elements, and driving mechanisms components are subjected to various loads, which can be classified on the basis of the occurrence frequency and character of varying in time. According to [3], they are classified in regular, occasional, and exceptional, and skewing forces are classified as occasional loads (in general, occurring in load combination B, which covers regular loads combined with occasional loads), and pursuant to that, are as a rule neglected in fatigue evaluation. However, in the chapter considering the calculation of skewing forces, the next paragraph is quoted: "Skewing loads as described above are usually taken as occasional loads but their frequency of occurrence varies with the type, configuration, and accuracies of wheel axle parallelism and service of the crane or trolley. In individual cases, the frequency of occurrence will determine whether they are taken as occasional or regular loads. Guidance for estimating the magnitude of skewing loads and the category into which they are placed is given in the European Standards for specific crane types." In accordance with the previously cited, if in certain case it has been proved that skewing forces are to be treated as regular loads, then these loads are to be taken into account in the analyses and proofs of crane structure fatigue. In [4] it is also pointed out that in certain cases loads generally taken into account only in load combination B can occur often enough to request their integration into the estimation of fatigue. In addition to that, it has been requested that the stresses occurring in structure elements due to these occasional loads are to be treated in the same way as stresses induced by regular loads.

However, neither [3], nor [6] give any further guideline of defining some indicator as the basis for determination of occurrence frequency relevant for classifying skewing forces into the group of regular loads. Solely [5] unambiguously specifies that by determining the design contact force for fatigue evaluation, skewing forces acting on the guiding rollers shall be considered as regular loads.

Analyses and proofs of fatigue strength of crane structure elements are impracticable without knowledge of loading history. Identification of relevant influences upon the fatigue and having a detailed knowledge of values of varying loads (or stresses) during usage (i.e. of designed crane lifetime) are necessary for forming the load or stress spectrum and further calculations (e.g. accumulated damage, remaining fatigue lifetime of a structure, etc.), [12].

Load spectrum is a collection of loads arranged according to the load amplitudes and frequency of their occurrence. It can be determined on the basis of:

- joining in accordance with indicators, to the one of the *norm spectra*,
- self-obtained records of a measurement on a crane in operation, or
- results of a conducted computer simulation of a tested crane during operation.

Nevertheless, the norm spectra of skewing forces still are not defined in literature. The computer simulation of a complex planar motion of a bridge crane under the action of skewing loads is difficult to conduct, due to the large number of influencing parameters of stochastic character. The most reliable results can be gathered by observing and recording the variables of interest (loads, stresses, vibrations, etc.) during long-lasting usage (especially when crane operation regime alters in time), or only during shorter, but representative periods of time. Estimation of integrity and lifetime on the basis of long-lasting crane monitoring is of ever more growing importance in design and maintenance of heavy machines, [20, 21].

Engineers and researchers have been engaged in the problem of crane skewing for almost six decades, [17]. However, the need for developing more adequate methods for determination of the dynamic loads and the probabilistic approach to the analysis of crane structure fatigue and stimulates the development of new research directions.

4. Experimental determination of lateral forces acting on bridge crane wheels

Up to these days, experimental determinations of lateral forces acting on the vertical wheels were carried out on the special redesigned laboratory bridge cranes. Almost all proposed and realized measuring methods demanded an extensive redesign of crane structure, such as additional horizontal rollers (they alter the structure of positive guiding system, and are practically useless for the certain crane types due to the implicitly requested rail track redesign), or redesign of end carriages, or additional wheel processing, etc, [8, 14, 16]. Design modifications are rarely acceptable for the crane user, or even inadmissible according to crane regulations. Due to these reasons and considerably higher expenses, the number of conducted experiments on the cranes engaged in real operation conditions is greatly reduced. The known solutions with wheel assemblies designed to be in the same time transducers for lateral forces, considerably deviate from the standardized assemblies. Their permanent usage in real operational conditions cannot insure the reliable crane usage. Consequently, the validity of obtained results is limited, and any generalization of drawn conclusions is arguable, especially in any consideration of existing cranes in long-lasting usage.

The authors have carried out an extensive series of experimental tests on a single-girder bridge crane with the rated capacity $m_Q = 3.2$ t and span $l = 8.91$ m, Fig. 4. The crane is designed for the general application in workshops with a light regime operation and an average relative loading. The weight of the crane structure and travelling mechanisms is $m_c \approx 1.3$ t, and the weight of the trolley including traversing and hoisting mechanisms is $m_t \approx 1.15$ t.

Fig. 4. Measurement of lateral forces acting on the wheels of a single-girder bridge crane

Crane structure is supported by four vertical flanged wheels (nominal diameter 200 mm) on the track runway. Both end carriages are equipped with one driven and one non-driven wheel, each one with two spherical roller bearings. All the components of wheel assemblies are manufactured in accordance with the (still in effect) Serbian standards. The design of a wheel bearing permits negligible lateral (axial) shifting. Track rails with square cross-section 40x40 mm, are intermittently welded to the upper flanges of rolled steel beams with INP 340 cross section. Crane runway beams are supported at 3.3 meters distances by cantilever overhangs on reinforced concrete columns of the lab hall and by screw connections fastened to it. Positive lateral crane guiding is obtained by the flanges of vertical wheels, with the total lateral clearance s_g = 20 mm between the wheel flange and rail head (although the recommended minimal value is 10 mm, according to [6]). The crane wheelbase is w_b = 1.5 m, and the relation of crane span to the distance of end guiding means is l/w_b = 5.94 (according to the recommendations it has to be $l/w_b \leq 6$).

Crane travelling along the rail track (at the rated velocity 30 m/min) is realized by independent end carriage drives. Asynchronous 3-phase squirrel-cage brake geared motors (with rated power 1.1 kW) of travelling mechanisms are DOL (direct-on-line) supplied, with starting softened by the „KUSA-Schaltung“. Motors are neither mechanically nor electrically synchronized, but the connection can be simply enabled by supplying them through the frequency converter Danfoss VLT 302, in order to synchronize the driven wheels of both crane end carriages as well as to „soften” crane starting and stopping.

The authors have designed two different special force transducers for the measurement of lateral forces occurring in the contact point of wheel tread and upper rail head surface, and skewing forces in the contact point of wheel flange and rail head. The aim was to develop the technical solution that enables reliable monitoring of values of these forces, on newly erected, as well as on existing cranes in usage, and that would demand only minor altering/addition in a wheel assembly.

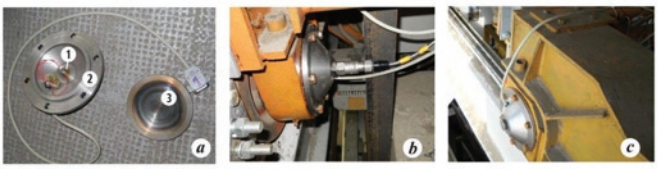

Fig. 5. Force transducer type CST: a) components; b) CST with a mounted accelerometer, fitted in the non-driven wheel bearing housing; c) CST fitted in the non-driven wheel bearing housing on the wall side

The first transducer type denoted as CST (**C**entral **S**crew **T**ransducer) is basically a screw, with a partly removed thread, shaped into the thin-walled cylinder (pos. 1 in Fig. 5.a).

The threaded hole is drilled through the screw head to enable the accelerometer mounting, Fig. 5.b. Four strain gauges are bonded to the processed surface and connected into the full Wheatstone bridge. The element is screwed into the threaded aperture, in the conically shaped cover of bearing housing, with the possibility of later fine tuning of its position (pos. 2 in Fig. 5.a). The screw top end presses the disc element (pos. 3 in Fig. 5.a) onto the outer wheel bearing ring. Transducers of this type are installed in the bearing housings of non-driven wheels, Fig. 5.b and c.

The second transducer type, denoted as HDT (**H**ollow **D**isc **T**ransducer) is shown in Fig. 6.

Fig. 6. Force transducer type HDT: a) components, b) HDT fitted in the driven wheel bearing housing - the cogwheel side; c) HDT fitted in the driven wheel bearing housing - the wall side

Strain gauges connected into the full Wheatstone bridge are bonded on a measuring element shaped as a disc with a thicken rim and a round aperture in the middle (pos. 1 in Fig. 6.a). In the mounted position the disc is pressed by the cover of bearing housing, through the four adjustable screws (pos. 2 in Fig. 6.a) onto the outer wheel bearing ring. Transducers of this type are mounted in the bearing housings of driven wheels, Fig. 6.b and c. The wheel shaft end with the driven cog-wheel of an open wheel-pair passes through the bearing housing, hence the covers on this housing side have round aperture in the middle, Fig. 6.b.

Shape and dimensions of elastic elements of both transducers were optimized on the basis of FEM analysis, in order to achieve the required sensitivity. The stress distribution in the measuring element of a CST is shown in Fig. 7.

The both transducer types have been calibrated in an accredited laboratory.

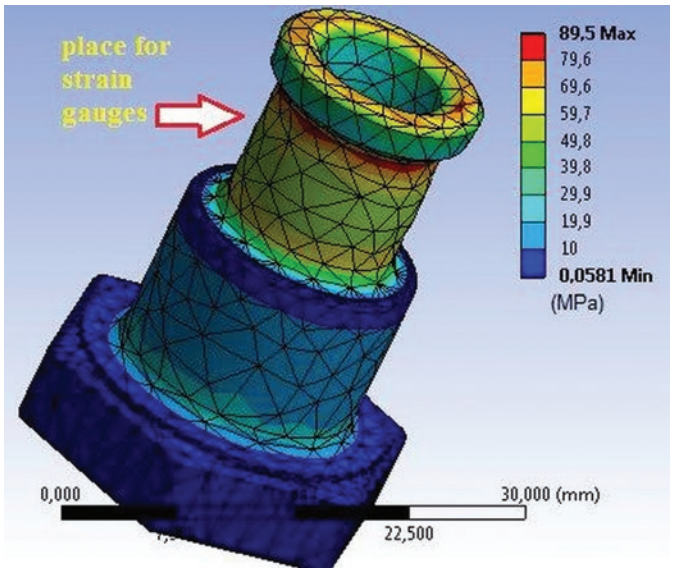

Fig. 7. Stress distribution in the measuring element of the CST, obtained using FEM software (transducer here presented without the steel bit at the top end)

Schematic outline of the system used for measuring the lateral forces and vibrations on the crane vertical wheels shown in Fig. 4. is given in Fig. 8. Due to space limitations, vibrations were registered only on the inner track sides of non-driven wheels. The data acquisition was conducted using two mutually connected and synchronized measuring amplifiers QuantumX (HBM, Germany). All the lateral force transducers were connected to the inputs of one amplifier, and accelerometers (type AC102-1A, CTC, USA) to the inputs of another one. Corresponding signals of force transducers are denoted as FY(CST1) ÷ FY(CST4) and FY(HDT1) ÷ FY(HDT4), and accelerometers as AC1 and AC2. Measurement process was controlled using the software package Catman® (HBM, Germany).

Experimental determination of lateral forces acting on the vertical wheels has been carried-out in accordance with 18 different measuring scenarios defined by varying 3 parameters: load weight, trolley position, and the way of supplying the electric motors of crane travel driving mechanisms. Calibrated casted iron weights were used as a load. Crane travelling was performed: without load, with load total weight: m_L = 700 kg and m_L = 1400 kg. Three trolley positions (R - right, M - span middle, L - left) were defined by the distances: y_R = 2.2 m, y_M = 4.45 m, and y_L = 7 m, Fig. 8. The trolley position remained unaltered during each crane travelling. For each combination of load weight and trolley position, crane travel driving electric motors were supplied DOL and through the frequency converter.

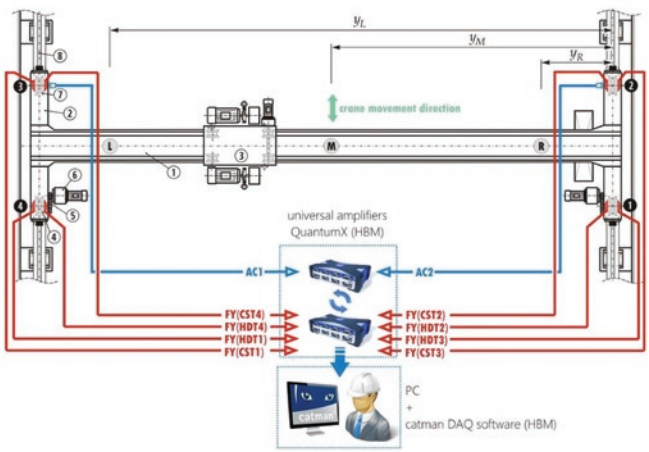

Fig. 8. Schematic outline of the used system for measuring the lateral forces and vibrations on the vertical wheels of a single-girder bridge crane, the top view positions: 1 - main girder, 2 - end carriage, 3 - trolley, 4 - driven wheel, 5 - cogwheel pair, 6 - geared electric motor with brake, 7 - non-driven wheel, 8 - track rail

5. Results and discussion

Generally, the described transducers can be also fitted into the wheel assemblies designed according to other national standards (e.g. DIN, TGL, PN, etc.). Minor redesign has to be carried out only regarding the measures and perhaps the shapes of transducer measuring element and bearing housing cover.

The results of 180 crane travels have been put on record during the experiment realization. As an illustration, the history of the lateral force acting on the wheel Nº 2, Fig. 8, during one crane travelling is shown in Fig. 9. The crane wheels were already before the start in the slanted position in relation to the rail direction. Electric motors of crane travelling drives were DOL supplied, with the load m_L = 1.4 t and the trolley in the position R, Fig. 8.

The complete experimental data processing has been carried out using the software nCode GlyphWorks (HBM, Germany). The most important statistical indicators necessary for conducting the fatigue analysis of structure elements have been determined. Distribution of force amplitudes corresponding with the recording shown in Fig. 9.a is presented in Fig. 9.b. The rain-flow matrix of loads, Fig. 9.c, can be used for the calculative determination of corresponding stress spectrum in the chosen point of the individual crane structure element. The joint distribution histogram shown in Fig. 9.d can be used as the basis for determination of a correlation between the force amplitudes and the acceleration.

a)

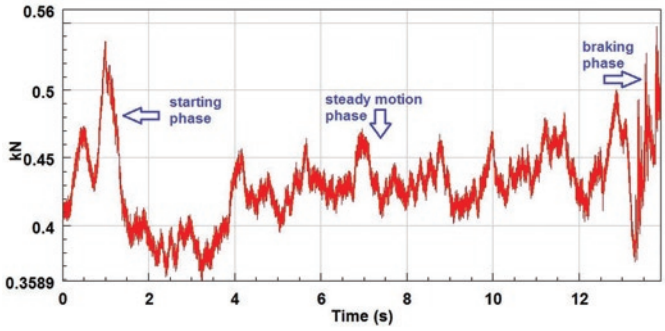

b)

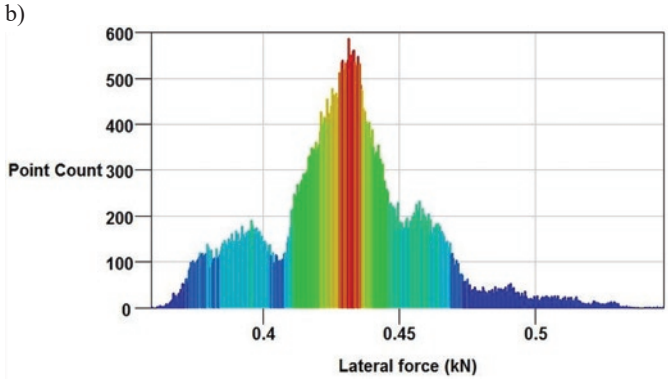

c)

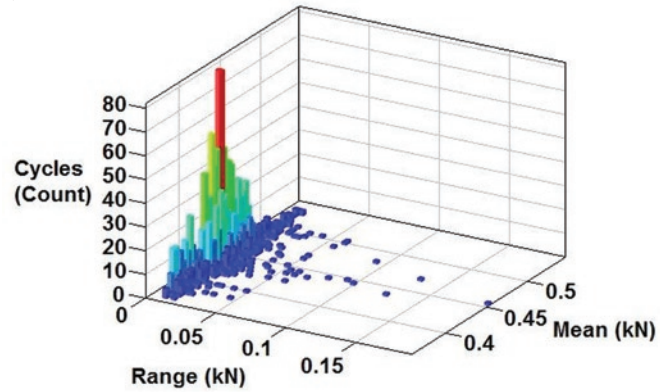

d)

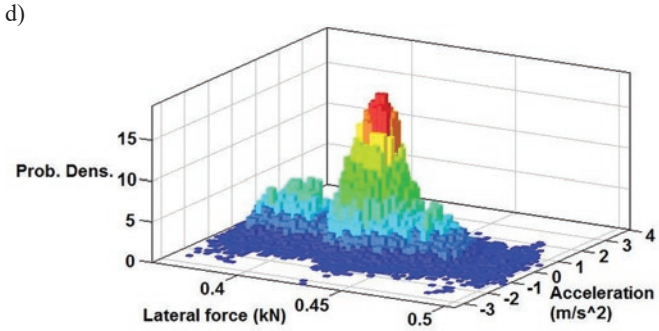

Fig. 9. The recording of wheel No2 loading history, trolley in position R, load mL = 1.4 t a), and the processed results in software package nCode: b) distribution of force amplitudes, c) rain-flow matrix of loads, and d) joint distribution histogram (force amplitudes and acceleration)

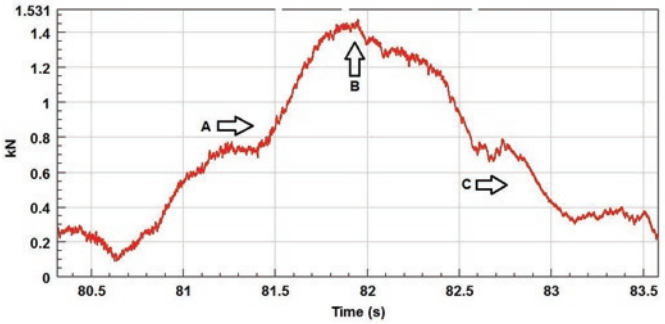

Fig. 10.The recording of wheel №4 loading history (m_L = 0, motors DOL supplied, trolley position M)

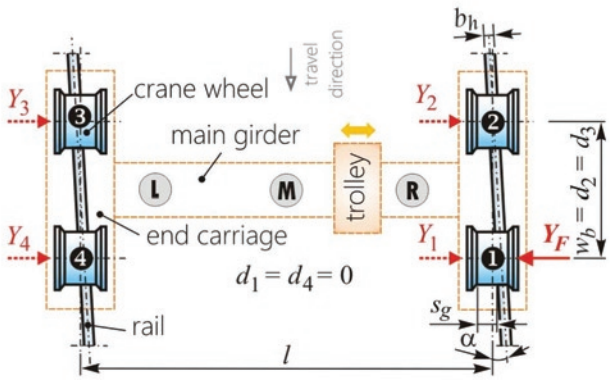

Fig. 11. Model for the rigid calculation method, according to [6]

Table 1. The resume of the calculated values of lateral, i.e. skewing forces

Load, [t]			m_L = 0			m_L = 0.7			m_L = 1.4			m_L = 3.2		
Trolley position:			L	M	R	L	M	R	L	M	R	L	M	R
Force, [kN]	lateral (due to axial slip)	Y_1	0.85	1.16	1.44	0.99	1.49	1.93	1.13	1.82	2.43	1.50	2.67	3.72
		Y_2	0.00	0.00	0.00	0.00	0.00	0.00	0.00	0.00	0.00	0.00	0.00	0.00
		Y_3	0.00	0.00	0.00	0.00	0.00	0.00	0.00	0.00	0.00	0.00	0.00	0.00
		Y_4	1.47	1.16	0.88	1.99	1.49	1.05	2.51	1.82	1.21	3.85	2.68	1.63
	skewing	Y_F	2.32	2.32	2.32	2.98	2.98	2.98	3.64	3.64	3.64	5.35	5.35	5.35

The values of wheel lateral forces were considerably higher in the starting and braking phases of crane travelling, Fig. 9.a. These impacts were less expressed during transitional phases with the travelling drive motors supplied through the frequency converter. During crane travelling with a steady velocity, the lateral force values varied within a relatively narrow range. Nevertheless, in this phase the abrupt value changes due to the interaction between the wheel flange and the rail head can be noticed, too. The recording detail is shown in Fig. 10, where the wheel flange run into the rail head can be clearly spotted (force value increase in period A), followed by hitting the top value of skewing force (in period B), and the gradual wheel flange separating from the rail head (in period C).

According to the experimental results, the trolley position influence on the values of measured lateral forces was practically irrelevant. This can be partly explained by the narrow crane span. Before drawing any conclusion on this subject, it is necessary to carry out a series of experimental researches on the heavier cranes with wider spans.

The results also confirmed the relevant influence of the way of supplying the electric motors of travelling drives on the skewing force value, especially in transient motion phases.

Experimentally defined values of lateral forces acting upon the wheels of the single-girder bridge crane are lower than the values calculated on the basis of the crane model according to [6], Fig. 11 and Tab. 1. The calculated values of lateral forces acting on some of the wheels are equal to zero, but that does not correspond with the actual values, especially when the bearing prevents the wheel from lateral movement. So, the experimentally measured force values are not in a consistence with the values calculated according to [6].

6. Conclusion

The most suitable and probably the only possible way to comprehend the influence of skewing on the fatigue of crane structure and traveling drives is to form a „catalog“ of skewing forces spectra. For that purpose, an extensive systematic experimental research carried out on cranes of various types and operating in realistic conditions, is indispensible.

The presented technical solution for the monitoring of lateral loads can be incorporated into the more complex systems for monitoring the crane structure condition (mainly of special importance and value) during its usage, if it is technically and economically justified. Simultaneous measuring of lateral forces and vibrations on crane vertical wheels is realized in order to initiate the development of faster, simpler, and more efficient way of gathering the data needed for the forming of corresponding crane structure load spectra.

On the basis of results obtained through the experiments conducted on a single-girder bridge crane with the capacity 3.2 t, and the span 8.9 m, with used 2 transducer types and varied 3 parameters (load weight, trolley position and electric motors supply source), the next conclusions have been drawn:

- both transducer types were reliable in operation, and turned out to be suitable for fitting into a new/existing standardized crane wheel assembly without changing its structure or function, with just a minor redesign,
- experimental data processing was carried out, and the main statistical indicators needed for the fatigue analysis of crane structure were calculated, using the software package nCode GlyphWorks,
  - experimentally defined values of lateral forces acting on crane wheels were lower than the values calculated according to the rigid calculation method, [6],
  - the influence of the trolley position on the values of measured forces was practically irrelevant, possibly due to the short crane span, low crane capacity and light load weights, and
  - the results confirmed the influence of the type of supply source (frequency converter or DOL) of travelling drives electric motors on the force values, especially in transient phases of motion.

Acknowledgement

The paper is a part of the project TR 35036 (Application of IT in harbours of Serbia - from machines monitoring to the network system of EU environment), financially supported by Serbian Ministry of Science and Technological Development.

References

1. Crane Rail Inspection, Gantrex Technical Bulletin No. TB47; https://www.yumpu.com/en/document/view/42642970/gantrex-technical-bulletin-47-crane-rail-inspection/3 (access: April 08, 2016)
2. Demag Laser-Mess-System zum präzisen Vermessen von Kranbahnen und Bodenschienen; https://wn.com/demag_laser-mess-system_zum_präzisen_vermessen_von_kranbahnen_ und_bodenschienen (access: April 09, 2016)
3. EN 13001-2:2014. Crane safety - General design - Load actions. Brussels: CEN, 2014.
4. EN 13001-3-1:2012+A1:2013. Cranes - General Design - Limit States and proof competence of steel structure. Brussels: CEN, 2013.
5. EN 13001-3-3:2014. Cranes - General design - Limit states and proof of competence of wheel/rail contacts. Brussels: CEN, 2014.
6. EN 15011:2011+A1:2014. Cranes - Bridge and gantry cranes. CEN, 2014.
7. FEM 1.001. Rules for the design of hoisting appliances - Booklet 2: Classification and loading on structures and mechanisms. Courbevoie: Fédération Européenne de la Manutention.
8. Hannover H.-O. Untersuchung des Fahrverhaltens der Brückenkrane unter Berücksichtigung von Störgrößen. PhD thesis. Braunschweig: Fakultät für Maschinenbau und Elektrotechnik, 1970.
9. Котельников В С, Шишков Н А. Аварийность и травматизм при эксплуатации грузоподъемных кранов. Москва: Федеральное государственное унитарное предприятие Научно технический центр по безопасности в промышленности Госгортехнадзора России, 2004.
10. Kulka J, Mantic M, Fedorko G, Molnar V. Failure analysis of increased rail wear of 200 tons foundry crane truck. Engineering Failure Analysis 2016; 67: 1-14, https://doi.org/10.1016/j.engfailanal.2016.05.032.
11. Кузнецов Е С. Обоснование необходимости рихтовки рельсовых путей кранов мостового типа. Журнал ВСЕ КРАНЫ 2010; 3/33: 22-25.
12. Lee Y-L, Barkey M., Kang H-T. Metal Fatigue Analysis Handbook. London: Elsevier, 2012.
13. Mitrović N, Kostić V, Petronijević M, Jeftenić B. Practical Implementation of Load Sharing and Anti Skew Controllers for Wide Span Gantry Crane Drives. Strojniški vestnik - Journal of Mechanical Engineering 2010; 56(3): 207-216.
14. Musílek J. Příčné horizontální síly mezi mostovým jeřábem a jeřábovou drahou. PhD thesis. Praha: České vysoké učení technické v Praze - Fakulta stavební, 2008.
15. Reducing crane wheel failures; http://www.hoistmagazine.com/features/reducing-crane-wheel-failures/ (access: 09. 04. 2016.)
16. Sanders D. Rechnerisches Modell und vergleichende experimentelle Untersuchung zur spurgeregelten Fahrt des Brückenkranes. PhD thesis. Darmstadt: Technische Hochschule, 1991.
17. Scheffler M, Feyrer K, Matthias K. Fördermaschinen - Hebezeuge, Aufzüge, Flurförderzeuge. Braunschweig/Wiesbaden: Vieweg, 1998.
18. Seeßelberg C. Kranbahnen - Bemessung und konstruktive Gestaltung. Berlin: Bauwerk Verlag, 2009.
19. Seeßelberg C. Zum Entwurf von Kranbahnträgern für Laufkrane. FRILO - Magazin 2005; 20-30
20. Stevanov B, Zuber N, Šostakov R, Tešić Z, Bojić S, Georgijević M, Zelić A. Reengineering the Port Equipment Maintenance Process. International Journal of Industrial Engineering and Management 2016; 7(3): 103-109
21. Zuber N, Bajrić R. Application of artificial neural networks and principal component analysis on vibration signals for automated fault classification of roller element bearings. Eksploatacja i Niezawodnosc – Maintenance and Reliability 2016; 18 (2): 299-306, https://doi.org/10.17531/ein.2016.2.19.
23. Tanasković D. Otpornost prema habanju i lomu reparaturno navarenih točkova kranskih dizalica. PhD thesis. Belgrade: Faculty of mechanical engineering, 2016.
24. Thoß R. Steuerbare Einwirkungen auf Kranbahnen. Stahlbau 2011; 80(1): 39-45.
25. Viiala O. Development of the guide roller system of portal gantry crane. Lappeenranta: Faculty of Technology, 2008.
26. Żmuda J. Konstrukcje wsporcze dźwignic. Warszawa: Wydawnictwo Naukowe PWN, 2013.

Atila ZELIĆ
Ninoslav ZUBER
Rastislav ŠOSTAKOV
Faculty of Technical Sciences
University of Novi Sad
Trg Dositeja Obradovića 6, Novi Sad, Serbia

E-mails: zelic@uns.ac.rs, zuber@uns.ac.rs, sostakov@uns.ac.rs

Article citation info:
BUREK R, WYDRZYŃSKI D, SĘP J, WIĘCKOWSKI W. The effect of tool wear on the quality of lap joints between 7075 T6 aluminum alloy sheet metal created with the FSW method. Eksploatacja i Niezawodnosc – Maintenance and Reliability 2018; 20 (1): 100–106, http://dx.doi.org/10.17531/ein.2018.1.13.

Rafał BUREK
Dawid WYDRZYŃSKI
Jarosław SĘP
Wojciech WIĘCKOWSKI

THE EFFECT OF TOOL WEAR ON THE QUALITY OF LAP JOINTS BETWEEN 7075 T6 ALUMINUM ALLOY SHEET METAL CREATED WITH THE FSW METHOD

WPŁYW ZUŻYCIA NARZĘDZIA NA JAKOŚĆ POŁĄCZEŃ ZAKŁADKOWYCH BLACH ZE STOPU ALUMINIUM 7075 T6 WYKONANYCH METODĄ FSW*

The article concerns the issues of tool wear effect on the quality of a friction stir welding joint quality. The experiment used aluminum alloy 7075 T6 sheet metal, which is used primarily in the aerospace industry. 1.0mm and 0.8mm thick lap joints were tested. Tool wear was determined based on multiple readings on a multisensory machine. The tool wear evaluation was done on the basis of a static tensile strength test and metallographic sections of the joints. The pin of the tool works in more demanding conditions and is more exposed to friction. This results from tooling operations performed at full depth dive in the jointed material. When also considering the small dimensions of the pin such as the diameter and the great forces occurring in this process, it is easy to see why this element is most susceptible to tool wear. The welding process causes the tool to undergo friction wear, which is the cause of reduced tool dive depth in the jointed material. As a result, it is paramount to constantly control the tool extension to achieve the desired quality parameters of the joint. After creating 200m of joints, a decrease in the strength of joints was observed as well as the repeatability of the results connected to a change in the stirring conditions in the material. The change in joint strength and tool wear is also confirmed in the metallographic analysis, which states that the continued degradation of the tool makes it subject to a decrease in size of the characteristic sizes of the thermoplastic zone that is the main determining factor of the joint strength.

***Keywords**: friction stir welding, FSW, Al 7075 T6 Alloy.*

Opracowanie podejmuje problematykę wpływu zużycia narzędzia na jakość zgrzeiny otrzymanej metodą zgrzewania tarciowego z przemieszaniem FSW. Do badań użyto stopu aluminium Al 7075 T6, stosowanego głównie w przemyśle lotniczym. Badano połączenia zakładkowe blach o grubości 1,0mm i 0,8mm. Zużycie narzędzia oceniano na podstawie pomiarów na maszynie multisensorycznej. Ocenę wpływu zużycia przeprowadzono w oparciu o statyczną próbę rozciągania oraz analizę zgładów metalograficznych wykonanych połączeń.Trzpień narzędzia pracuje w trudniejszych warunkach i jest bardziej narażony na ścieranie. Wynika to z pracy przy pełnym zagłębieniu w łączonym materiale. Zważywszy również na stosunkowo małe wymiary trzpienia tj. jego średnicę i duże siły występujące w procesie to ten element jest najbardziej narażony na zużycie. W procesie zgrzewania narzędzie ulega zużyciu ściernemu, co jest powodem zmniejszania zagłębienia narzędzia w materiale łączonym. W związku z powyższym konieczna jest ciągła kontrola wysunięcia narzędzia dla uzyskania pożądanych parametrów jakościowych zgrzeiny. Po wykonaniu 200m zgrzeiny zauważono zmniejszenie wytrzymałości zgrzeiny, jak również powtarzalności wyników związany ze zmianą warunków mieszania materiału. Zmiana wytrzymałości zgrzeiny oraz zużycia narzędzia ma również potwierdzenie w badaniach metalograficznych, z których wynika, iż w związku z postępującą degradacją narzędzia zmniejszeniu ulegają wymiary charakterystyczne strefy termo–plastycznej odpowiedzialnej w główniej mierze za wytrzymałość zgrzeiny.

***Słowa kluczowe**: zgrzewanie tarciowe z przemieszaniem, FSW, Al 7075 T6.*

1. Introduction

One of the methods of joining metal elements, which is becoming more and more popular in recent times is friction stir welding (FSW). Friction stir welding was developed by Mr. Wayne Thomas in the Welding Institute (UK) in 1991 to join light metal [25]. The technique is based on joining material in the solid state, which makes it possible to produce constant joints in materials that were considered difficult or impossible to weld. Compared to other welding methods of joining metals, FSW is energy efficient, universal, and ecological [6, 17, 20, 28]. The quality of welded joints is dependent on the process parameters. A weld results from localized heating of the material by the tool's rotation as well as tool dive to a desired depth and its translation along a specified tool path at a selected rate. The plasticized material, resulting from the friction between the material and tool, moves around the pin. The element becomes joined as result friction stirring of the semisolid state material [9]. Besides the process parameters, it is also critical to specify additional parameters like tool geometry, mounting system, welding direction etc. [5, 21, 27]

Due to the high strength of FSW joints, this method can easily compete with traditional joining methods. The applications of this method instead of traditional welding or riveting is appealing because it lowers the manufacturing costs and the mass of the product. Due

(*) Tekst artykułu w polskiej wersji językowej dostępny w elektronicznym wydaniu kwartalnika na stronie ***www.ein.org.pl***

to these reasons, FSW has been classified as a key technology in the production of airplane fuselages and wings [15, 32]. The list of material used in aircraft skins is primarily populated by aluminum alloys [4, 23, 30]. Aluminum alloys, especially 2xxx and 7xxx series are difficult to weld because of their weak solidification and porosity in the joint area. However, these materials are relatively easily joined through FSW [8, 11].

These joints have their own advantages such as not having typical defects that can be observed in joints resulting from traditional welding methods like gas pores, shrinkage, thermal cracking and many others. Like all joining methods of this type, FSW has its limitations related to the difficulties in jointing elements with complex geometries and defects related directly to the strength of the joint and the repeatability of the process. The most common defects that can be observed from this method include contact line deformation, porosity, which results from the geometry of the tool [12-14, 16, 31].

There are very few publications concerned with the usage problems of tools used for friction welding. Most of works are focused primarily on the mechanism that cause wear in the friction welding process [22, 24, 29] and prediction tool wear with numerical methods [10]. The main problem of friction welding is tool pin wear. Wear is caused by excessive contact between the tool and welded material. The tool geometry has a significant effect on its resistance to erosive wear [3]. Without a doubt, the topics covered in the articles are valuable from the weld quality point of view, which should be characterized by identical strength parameters across the entire life of the tool. The use of PVD coatings on FSW tools is a promising approach to improve their effectiveness and lifespan, and thus improving the economics of the process. Coated tools are not as susceptible to dimensional variation as noncoated tools [1].

The research conducted by several authors aimed to present the phenomena occurring during friction stir welding with tools of various materials. The pin of the tool underwent a more detailed study because the works determined that the pin works in the most demanding conditions and is more susceptible to wear. The research does not cover topics that are very important for industrial applications like tool lifespan as a function of welding distance, which has, without a doubt, a significant meaning for manufacturing critical structural parts. When constructing an aircraft, the skin is traditionally joined using methods like resistance welding, riveting or gluing. Introducing a new sheet metal joining method like friction stir welding requires conducting several studies and attaining multiple certification that would allow for this technology to be widely used. Familiarity of the usage possibilities of FSW tools will assist in implementing this technology.

The fundamental goal of the study was determining the total welding length before reaching the critical wear criterium. Predicting the tool wear as a function of time or distance is a complex task. Having constant parameters through the entire operating range is not clear with equal tool wear. Several interferences cause variable tool lifespan. The results of tribological processes as well as heat and chemical influences affecting the tool pin, which has the greatest effect on tool lifespan. The assumptions of the study regarding the wear of the pin regard determining the welding distance for maintaining the strength parameters in a determined range. The reason for such wear criterium is the occurrence of significant tool deformation caused by the welded material affecting the tool pin. Thus, it is a technological criterium, which is wear that the tool will work in a stable manner and the weld quality meets the technological requirements. In the case of tool geometry variance caused by wear, the characteristics of the weld change, which would also be the subject of analysis in further studies.

2. Materials and Experiment Methods

2.1. Fundamental FSW concepts

Creating a weld using the FSW method is done by introducing a rotating tool with a specially designed pin into the contact area of two joined parts and then moving it along the length of the edges of the joined parts. The process of FSW being used to join two parts is illustrated in figure 1.

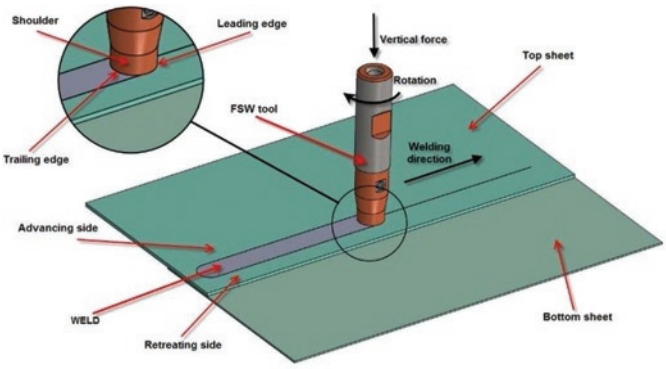

Fig. 1. The Friction Stir Welding Process

To properly complete the operation, the parts that are to be joined must be fixed securely and pressed firmly together. During the welding process, the rotating shoulder of the rotating tool heats up the parts, while the tool pin stirs the material to create a joint. When describing the friction welding process, concepts like the advancing side and retreating side should be specified. The advancing side is the side where the welding direction and rotation direction are the same. The retreating side's name suggests that the liquid material retreats in its direction. It is the side where the tool rotation direction is opposite to the welding direction.

As a result of the friction welding process, a solid weld appears where the materials were joined. The shape and properties of the weld are affect by a few factors like the shape of the tool and parameters like feed rate and rotational speed. Thermoplastic deformations can be observed in the transverse section of the weld. The effect of these process properties is the appearance of a complex microstructure that has a significant effect on the mechanical properties of the joint. A FSW weld can be divided into a few zones (Fig. 2).

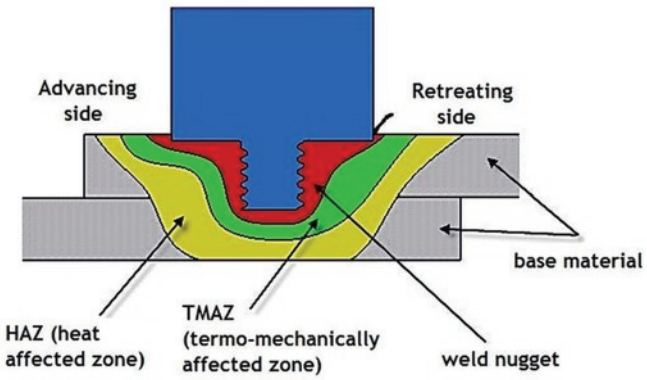

Fig. 2. The microstructure zones of the FSW process

Fig. 2. Presents the following zones of the weld:

- Parent material (PM): the part of the material that is the farthest away from the center of the weld, which does not undergo any deformation or change in a mechanically and structurally.
- Heat affected zone (HAZ): the part of the material that neighbors the weld where the material underwent the effects of heats, which resulted in a change of structure and mechanical properties. This zone does not undergo plastic deformation.
- Thermoplastic deformation zone: the zone where the material is affected by the tool resulting in mechanical and heat reactions. Aluminum alloys can undergo significant plastic deformation in this zone without the material recrystallizing. This is where the border between the non-crystallized material and weld core is found.
- Weld core: The area that undergoes full recrystallization. The weld is characterized by a small, axially distributed grain that is barely a few micrometers large (aluminum alloys). This is the area where the FSW tool pin travelled through.

The parameters of the weld like the size, shape, and zone size depend primarily on the size and shape of the tool.

2.2. Material and Samples

The experiment was conducted using 7075-T6 alloy sheet metal that was plated on both sides. The chemical composition is presented in Table 1. It was additionally examined using an X-ray spectrometer. 7xxx series aluminum alloys are characterized by high strength in comparison to other series of alloys. The compression strength and resistance to fatigue are the critical parameters in aircraft skin, wing, and empennage element design. The high strength of 7075-T6 aluminum alloy is key in using this material in aircraft structures based on its strength to weight ratio, machinability, and relative low cost [7, 26].

Aluminum alloys are susceptible to corrosion, which obviously decreases the lifespan of aircraft components. A negative phenomenon that lowers the lifespan of aircraft is corrosion and material fatigue [18]. As a result, aluminum alloy sheet metal producers use plating, a process of coating the sheet metal in pure aluminum to prevent corrosion [19]. The thickness of layer of pure aluminum is 40μm in accordance with AMS–QQ–A–250/13. The microstructure of plated Al 7075-T6 is presented in Figure 3.

Fig. 3. The microstructure of plated 7075-T6 aluminum alloy [2].

One of the stages of tool wear analysis was determining its effect on the static strength of the joint as a function of welding distance. To conduct strength tests, samples with the dimensions presented in Figure 4. were prepared.

The thickness of the welded sheet metal was composed of a 1mm thick top sheet and a 0.8mm thick bottom sheet, which matches the thickness of an aircraft's skin and longerons respectively.

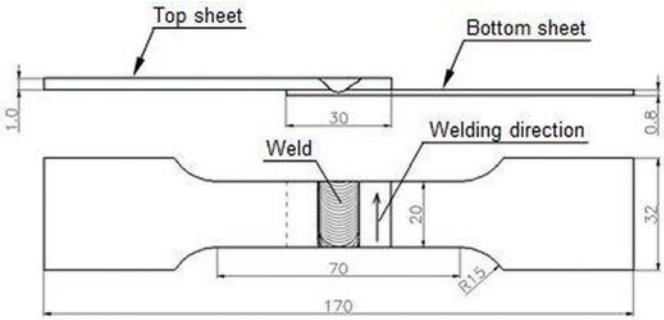

Fig. 4. Welded joint sample dimensions

3.3. Experiment

The experimental trails were conducted on a DMC 104V mill with an ISO 40 mounting system (Fig. 5a) using a commercial Schilling 10–S–4–Z–G–O tool with a hardness of 54-56HRC (Fig. 5b). The tool is characterized by a concave mainstay and cylindrical pin.

The trails were conducted on 320 mm long joints, which were cut into 4 samples for strength tests and one sample used for microscope analysis. The course of the process is presented in Fig. 6.

The following parameters were selected to perform the process:
- Rotation speed – 1000 RPM
- Feed rate – 200mm/min
- Pin extension – 1.2mm

The control samples were made every 20m up to 100m of weld, next every 40m. The geometric measurements of the pin were conducted ever 100m on a OGP Smart Scope FLASH 200 multisensory machine. To ensure repeatability of mounting the pin for making measurements, a fixture was made for indexing that precisely positions the measured pin. The measurements were conducted in two planes. After each measurement, the pin was set with an extension that accounted for the wear of the face surface (its extension was shorter than the initial value by amount defined as Δl) in comparison to the initial setting.

4. Results Analysis

The measurements showed that the wear for 100m≈2%; 200m≈4%; 300m≈10%; 400m≈12% pin material erosion. When considering the tool measurements and the wear of the face surface, there was not a significant amount of material erosion; however, the wear of the face surface was Δl≈0,06mm after 300m and Δl≈0,08 mm after 400m (Fig. 7)

Adjusting the pin extension from the mainstay of the tool allows for greater confidence and repeatability of results; however, it does not change the shape of the face surface undergoes constant advancing degradation (Fig. 8).

The wear of the tool influences the strength of the joint, which effected by the contribution of the pin (its dive depth and extension) in stirring the material (Fig. 9)

Table 1. 7075-T6 Aluminum Alloy Chemical Composition (wt.%)[2].

source	Chemical composition(wt.%)									
	Si	Fe	Cu	Mn	Mg	Cr	Zn	Ti	other	Al
Standard	max 0.4	max 0.5	1.2~2.0	max 0.3	2.1~2.9	0.18~0.28	5.1~6.1	0.3	0.05 0.15	remainder
Tested	–	0.10	1.35	0.06	2.61	0.26	5.6	0.05	– –	remainder

a)

b)

Fig. 5. (a)DMC 104V Mill, b) Schilling tool

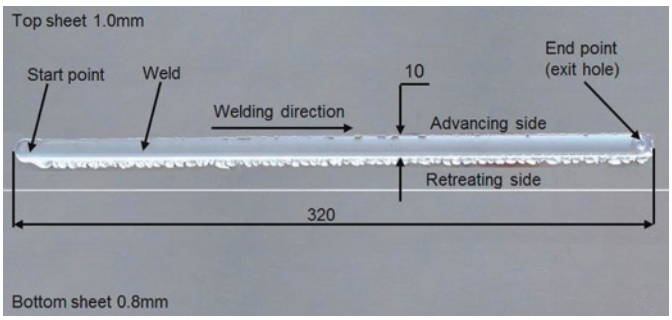

Fig. 6. FSW Process Course

a)

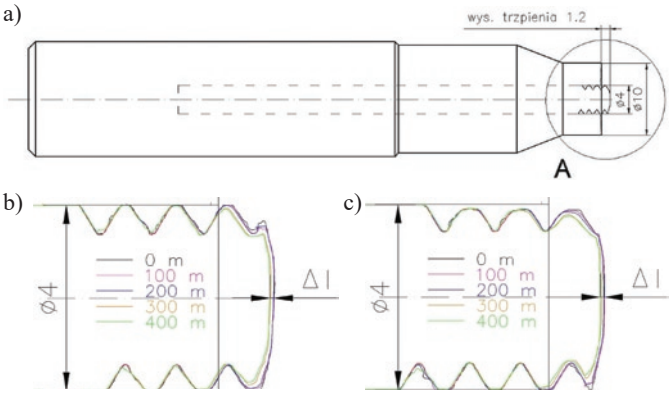

Fig. 7. The tool pin measurement results: a) characteristic dimensions b) 0°plane measurement c) 90° plane measurement

a)

b)

c)

d)

e)

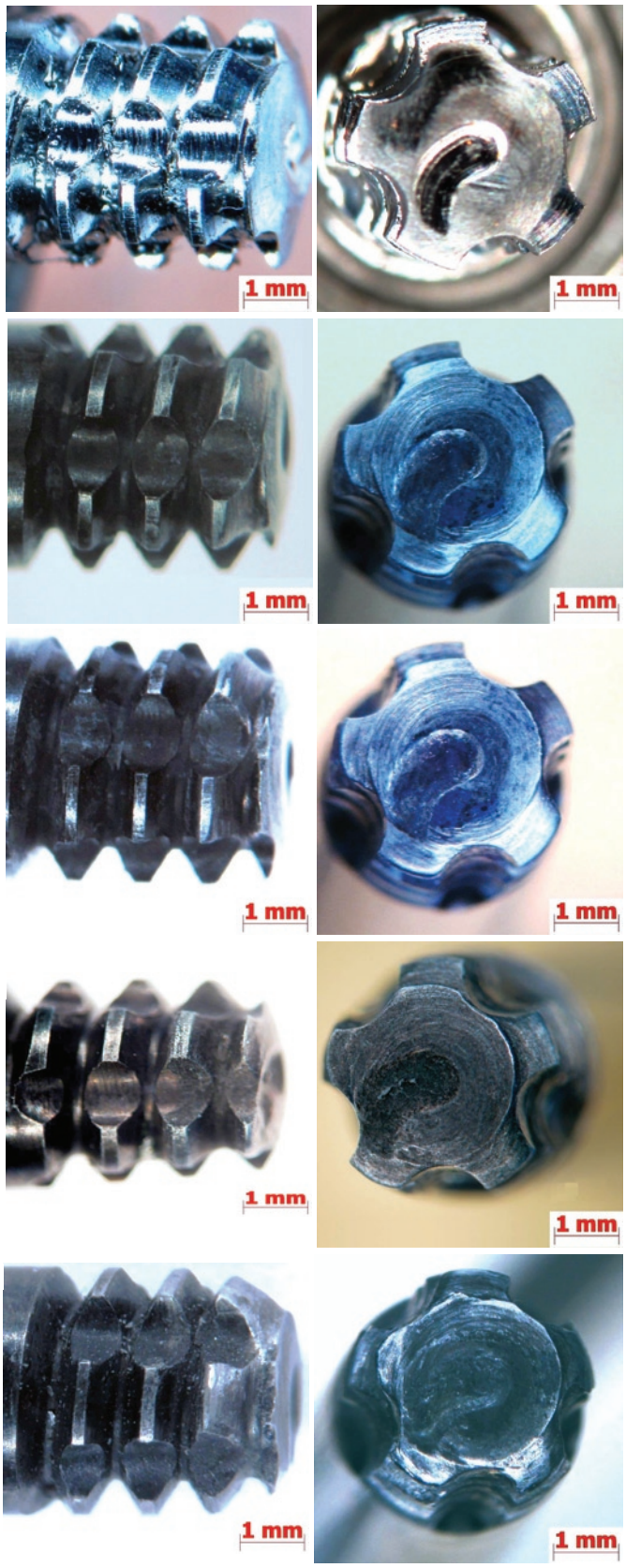

Fig. 8. Macroscopic wear analysis of the tool from the side and face for the following welding distances: a) 0m, b) 100m, c) 200m d) 300m, e) 400m.

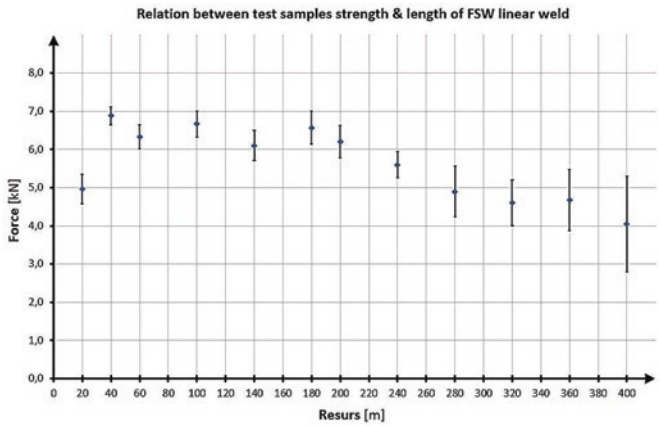

Fig. 9. The tearing force as a function of tool welding distance.

The results of the strength test trails show that the initial stage of the tool wear tests does not significantly increase the strength. This is related to the break-in period of the tool, which can be blatantly observed with an increase in strength in the 20m/40m welding distance control point. The following samples show a relatively comparable strength until reaching a welding distance of 200m. After that distance there is a decrease in strength and a lower rate of sample failure force repeatability can be observed (standard deviation value increase).

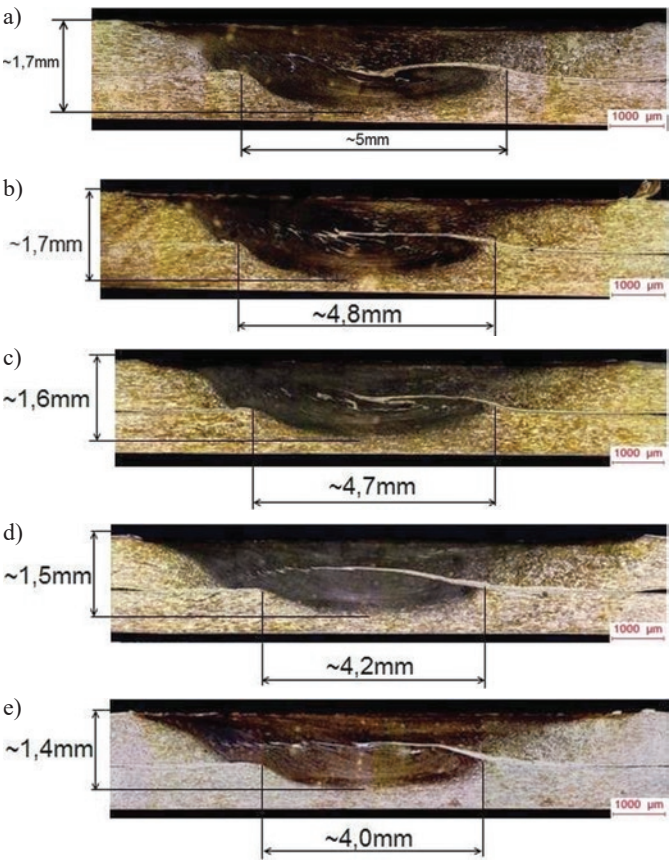

Fig. 10. Cross section and weld microstructure at: a) 40m, b) 100m, c) 200m, d) 300, e) 400m.

This is due to tool wear on the helical thread and surface face.

Thread wear also causes a decrease in stirring width on the contact line and stirring depth, which can be observed in Fig. 10.

It can be easily seen that the weld width decreases to 4mm and its depth decreases to 1.4mm after 400m of welding distance.

Based on the results, the aim of the study was to determine the welding distance where the critical wear value is reached. The wear of the pin has the greatest effect on the lifespan of the tool, which results from the tribological processes, heat, and chemical reactions. The accepted wear criterium is justified by the occurrence of significant tool deformation resulting from reactions of the welded material on the tool pin. Thus, this a technological criterium, or in other words, wear limit that the tool performs stable manner and the weld quality meets the technological requirements. The tendencies observed in this study are concurrent with those in similar publications [1, 3] concerning tool wear.

5. Conclusions

1. The tool pin performs in the most difficult conditions and is most susceptible to wear. This results from work at full dive depth in the joined material. The relatively small dimensions of the pin like its 4mm width and the large forces (5kN) that occur during process cause this part to be the most susceptible to wear. In addition, thread wear increases the chances of damage that can also weak the tool core.
2. Face surface and circumferential wear (Δl) of the tool was observed during the welding process that was proportional to the welding distance. As a result, it is paramount to control the pin extension to ensure the desired weld quality parameters during the process.
3. During the initial welding stages, the tool underwent a break in period over the first 40m of welding that was characterized by decreased strength. After this distance, the strength values stabilize at around ~6.5kN. After 200m of welding, the welds' strength begins to decrease by about 30% and the repeatability of the results also deteriorate because of a change in the stirring conditions of the material (thread wear affects the transport of the plasticized material). The repeatability of the results is critical from the aircraft construction point of view.
4. A change in the strength of the weld and tool wear is also confirmed by metallographic analysis, which confirms that the degradation of tool's dimensions results in a change in the dimensions of the characteristic thermoplastic zone that is the most significant factor of weld strength. The first 200m of welding resulted in dimensions that varied around ~1.6mm depth and ~4.8mm width.
5. The study presents the effect of tool wear on the strength parameters of welded samples. In order to perform this study, over 400m of welds had to be made, which resulting in the research being time consuming and costly.

Acknowledgements

The was financed using funds from the National Center for Research and Development, European Union and PZL Mielec, A Sikorsky Company under the European Regional Development Fund Project entitled "Advanced Manufacturing Techniques of Fuselage Structural Parts Using the Innovative FSW Technology" Nr INNOLOT/I/4/NCBR/2013.

References

1. Adesina A. Y., Gasem Z. M., Al-Badour F. A. Characterization and evaluation of AlCrNcoated FSW tool: A preliminary study. Journal of Manufacturing Processes 2017; 25: 432-442, https://doi.org/10.1016/j.jmapro.2016.12.019.
2. AMS-QQ-A-250/13Aluminum Alloy Alclad 7075, Plate and Sheet (2007).
3. Bist A., Saini J. S., Sharma B. A review of tool wear prediction during friction stir welding of aluminium matrix composite. Transactions Nonferrous Metals Society of China 2016; 26: 2003-2018, https://doi.org/10.1016/S1003-6326(16)64318-2.
4. Cascada W., Liu J., Staley J. Aluminium alloys for aircraft structures. Advanced Materials and Processes 2002; 160(12):27-9.
5. Colegrove P. Airbus evaluates friction stir welding. <http://www.comsol.com/
6. Derry C.G., RobsonJ.D., Characterisation and modelling of toughness in 6013-T6 aerospace aluminium alloy friction stir welds. Materials Science and Engineering: A. 2008; 490(1-2): 328-334, https://doi.org/10.1016/j.msea.2008.01.044.
7. Dursun T., Soutis C.Recent developments in advanced aircraft aluminium alloys. Materials and Design 2014; 56: 862-871, https://doi.org/10.1016/j.matdes.2013.12.002.
8. Elangovan, K., Balasubramanian V. Influences of post-weld heat treatment ontensile properties of friction stir-welded AA6061 aluminum alloy joints. Materials Characterization 2008; 59(9): 1168-1177, https://doi.org/10.1016/j.matchar.2007.09.006.
9. Gibson B. T., Lammlein D. H., Prater T. J., Longhurst W. R., Cox C. X.,Ballun M. C., Dharmaraj K. J., Cook G. E., Strauss A. M. Friction stir welding: process, automation and control. Journal of Manufacturing Processes 2004;16: 56-73, https://doi.org/10.1016/j.jmapro.2013.04.002.
10. Hasan A. F., Bennett C. J., Shipway P. H., Cater S., Martin J. A numerical methodology for predicting tool wear in Friction Stir Welding. Journal of Materials Processing Technology 2017; 241: 129-140, https://doi.org/10.1016/j.jmatprotec.2016.11.009.
11. Heinz B., Skrotzki B. Characterization of a Friction Stir Welded AluminumAlloy 6013. Metallurgical and Materials Transactions B 2002; 33B: 489-498, https://doi.org/10.1007/s11663-002-0059-5.
12. Huijie Z., Huijie L. Characteristics and formation mechanisms of welding defects in underwater friction stir welded aluminium alloy. Metallography, microstructure and analysis 2012; 1:269-281, https://doi.org/10.1007/s13632-012-0038-4.
13. JanakiR. P., GaneshN. R., Kailash Satish V.,Jayachandra R. Internal defect and process parameter analysis during friction stir welding of Al 6061 sheets. International Journal of Advanced Manufacturing Technology 2013; 65: 1515-1528, https://doi.org/10.1007/s00170-012-4276-z.
14. Kadlec M., Ruzek R., Novakova L. Mechanical behaviour of AA 7475 friction stir welds with the kissing bond defects.International Journal of Fatigue 2015; 74: 7-19, https://doi.org/10.1016/j.ijfatigue.2014.12.011.
15. Kafali H., Nuran A. Y. Mechanical Properties of 6013-T6 Aluminium Alloy Friction Stir Welded Plate. 13th International Conference on Aerospace Sciences & Aviation Technology. ASAT-13-MS-14.
16. Kumar R., ChAttopadhyaya S., Hloch S., Krolczyk G., Legutko S. Wear characteristics and defects analysis of friction stir welded joint of aluminium alloy 6061-T6. Eksploatacja i niezawodnosc - Maintenance and Reliability 2016; 18(1): 128-135, https://doi.org/10.17531/ein.2016.1.17.
17. Mishra R.S., Ma Z. Y., Friction stir welding and processing. Materials Science and Engineering: R: Reports 2005; 50 (1-2): 1-78, https://doi.org/10.1016/j.mser.2005.07.001.
18. Necsulescu D.A. The effects of corrosion on the mechanical properties of aluminum alloy 7075-T6. Universitatea Politehnica Bucuresti Science Bulletin 2011; 73(1): 223-229.
19. Pantelakis S.G., Chamos A.N., Kermanidis A. A critical consideration of use of Alcladding for protecting aircraft aluminium alloy 2024 against corrosion. Theoretical and Applied Fracture Mechanics 2012; 57: 36-42, https://doi.org/10.1016/j.tafmec.2011.12.006.
20. Rai1 R., De A., Bhadeshia H. K. D. H., DebRoy T. Review: friction stir welding tools. Science and Technologyof Welding and Joining 2011; 16(4): 325-342, https://doi.org/10.1179/1362171811Y.0000000023.
21. Rodrigues, D. M., Loureiro A., Leitao C., Leal R. M., Chapparo B. M., Vilaca P. Influence of friction stir welding parameters on the microstructural and mechanical properties of AA 6016-T4 thin welds. Materials and Design 2008. In Press.
22. Sahlot P., Jha K., Dey G. K., Arora A. Quantitative wear analysis of H13 steel tool during friction stir welding of Cu-0.8%Cr-0.1%Zr alloy. Wear 2017; 378-379: 82-89, https://doi.org/10.1016/j.wear.2017.02.009.
23. Starke E.A., Staley J.T. Application of modern aluminium alloys to aircraft. Progress in Aerospace Science 1996; 32: 131-72, https://doi.org/10.1016/0376-0421(95)00004-6.
24. Tarasov S. Y., Rubtsov V. E., Kolubaev E. A. A proposed diffusion-controlled wear mechanism of alloy steel friction stir welding (FSW) tools used on an aluminum alloy. Wear 2014; 318: 130-134, https://doi.org/10.1016/j.wear.2014.06.014.
25. Thomas W.M., Nicholas E.D., Needhan J.C., Murch M.G., Templesmith P., Dawes C.J. International patent application PCT/GB92/02203 and GB patent application
26. Troeger L.P., StarkeE.A. Microstructural and mechanical characterization of asuperplastic 6xxx aluminum alloy. Materials Science and Engineering A 2000; 277(1-2): 102-113, https://doi.org/10.1016/S0921-5093(99)00543-2.
27. Vilaça P., Thomas W. Friction stir welding technology. Advanced Structural Material 2011; 8: 85-124, https://doi.org/10.1007/8611_2011_56.
28. Wang D., Xiao B. L., Ni D. R., Ma Z. Y. Friction Stir Welding of Discontinuously Reinforced Aluminum Matrix Composites: A Review. ActaMetallurgicaSinica2014, 27(5): 816-824, https://doi.org/10.1007/s40195-014-0143-2.
29. Wang J., Su J., Mishra R. S., Xu R., Baumann J. A. Tool wear mechanisms in friction stir welding of Ti-6Al-4V alloy. Wear 2014; 321: 25-32, https://doi.org/10.1016/j.wear.2014.09.010.

30. Williams J.C., Starke E.A. Progress in structural materials for aerospace systems. ActaMaterialia, 2003, 51(19): 5775-5799, https://doi.org/10.1016/j.actamat.2003.08.023.
31. Won-Bae L., Chang-Yong L., Myoung-Kyun K., Jung-Il Y., Young-Jig K., Yun-Mo Y., Seung-Boo J. Microstructures and wear property of riction stir welded AZ91Mg/SiC particle reinforced composite. Composites Science and Technology 2006; 66: 1513-1520, https://doi.org/10.1016/j.compscitech.2005.11.023.
32. Zhang Y. N., Cao X., Larose S., Wanjara P. Review of tools for friction stir welding and processing. Canadian Metallurgical Quarterly 2012; 51(3): 250-261, https://doi.org/10.1179/1879139512Y.0000000015.

Rafał BUREK
Development Projects Office DTR/B
Polskie Zakłady Lotnicze Sp. z o.o.
ul. Wojska Polskiego 3, 39-300 Mielec, Poland

Dawid WYDRZYŃSKI
Jarosław SĘP
Faculty of Mechanical Engineering and Aeronautics
Rzeszow University of Technology
al. Powstańców Warszawy 12, 35-959 Rzeszów, Poland

Wojciech Więckowski
Faculty of Mechanical Engineering and Computer Science
Czestochowa University of Technology
al. Armii Krajowej 21, 342-201 Częstochowa, Poland

E–mails: rafal.burek@lmco.com, dwydrzynski@prz.edu.pl, jsztmiop@prz.edu.pl, wieckowski@itm.pcz.pl

Article citation info:
NIKONIUK M, KOZŁOWSKI M. Energy properties of a contactless power supply in PRT (Personal Rapid Transit) laboratory model. Eksploatacja i Niezawodnosc – Maintenance and Reliability 2018; 20 (1): 107–114, http://dx.doi.org/10.17531/ein.2018.1.14.

Marcin NIKONIUK
Maciej KOZŁOWSKI

ENERGY PROPERTIES OF A CONTACTLESS POWER SUPPLY IN PRT (PERSONAL RAPID TRANSIT) LABORATORY MODEL

WŁASNOŚCI ENERGETYCZNE UKŁADU ZASILANIA BEZSTYKOWEGO MODELU LABORATORYJNEGO POJAZDU PRT (PERSONAL RAPID TRANSIT)*

The article presents the results of research on the operational properties of contactless power supply system used in the PRT vehicle demonstration model, made within the framework of the ECO Mobility project. The area of transport applications of the PRT automated rail transport system is presented. Elements of the ECO Mobility PRT Drive System have been described – an inductive linear motor, dynamic contactless power supply, and supercapacitor recuperation system. Electrical performance maps of the linear motor and contactless power system were presented. Also shown was the method of their use in calculation of traction energy consumption by means of theoretical journeys. The results of the simulation calculations for the trial track were presented. The results of design calculations of the power supply parameters for the planned line of the demonstrator with real dimensions are presented.

***Keywords**: PRT, contactless power supply, simulation, assumed operating traffic conditions.*

Artykuł prezentuje wyniki badań własności eksploatacyjnych układu zasilania bezstykowego zastosowanego w modelu demonstracyjnym pojazdu PRT, wykonanym w ramach projektu ECO Mobilność. Przedstawiono obszar zastosowań transportowych systemu szynowego automatycznych środków transportu PRT. Opisano rozwiązanie układu napędowego pojazdu PRT konstrukcji ECO Mobilność – napęd za pomocą indukcyjnego silnika liniowego, zasilanie bezstykowe dynamiczne oraz układ rekuperacji z zastosowaniem superkondensatora. Zaprezentowano mapy sprawności elektrycznej silnika linowego i układu zasilania bezstykowego. Przedstawiono sposób ich wykorzystania w obliczeniach zużycia energii trakcyjnej metodą przejazdów teoretycznych. Przedstawiono wyniki obliczeń symulacyjnych dla toru próbnego w skali. Przedstawiono wyniki obliczeń projektowych parametrów układu zasilania dla planowanej linii demonstratora o wymiarach rzeczywistych.

***Słowa kluczowe**: PRT, układ zasilania bezstykowego, symulacja, zakładane eksploatacyjne warunki ruchu.*

1. Introduction

Transportation solutions using PRT (Personal Rapid Transit) vehicles are not new [1]. The PRT is a mode of automatic rail transport. PRT vehicles usually run on rubber-tired wheels at special track systems [26]. Also in Poland, PRT transport applications have been subject to exhaustive analyses [5]. At present, however, there has been a renewed interest in such modes of transport, due to the concept of "pod car", which is the idea of extending the use of this type of automatic rail vehicle to public circuits [27]. Introduction of this concept can be based on two different levels of motion control automatics. At the lower level, usually designated Level 3 [29], vehicles move on separate lanes of public roads called "virtual roads" due to the need to build a special V2I communication infrastructure and communication system [10]. At the highest level, marked Level 5, vehicles should move as autonomous vehicles. PRT vehicles moving in line with the idea of "pod car" also on public roads will become part of automated transport networks (ATN) in urban areas [8]. In the future, vehicles of this type will be the synthesis of an automatic rail and wheel vehicle. In dense areas with heavy traffic, they will be able to navigate the dedicated tracks built specifically for them so that traffic infrastructure can be used in suburban areas with low traffic.

This article is devoted to the description of the power supply used in the "Polish" PRT version, made as a physical model in scale within the framework of the ECO Mobility project. This project has not yet been implemented for transport applications but has nevertheless been tested on a test track for scale vehicles. A fragment of track in scale was recently presented at the Hannover Fair at the SciTech Poland "scientific" Polish stand [7, 28].

The already mentioned power supply is a contactless, dynamic power system, which means that it can deliver energy to the vehicle in motion as opposed to stationary systems where energy is delivered only when the vehicle is stationary. The drive motor is a linear induction motor. This system solution illustrates one of the many possibilities that can be applied to the driving and powering of this type of vehicle. The power supply can also be made as a contact one with power points at parking places. Propulsion motors can be made as brushless, induction and wheeled or as central units. On the other hand, the contactless power supply has the advantage of being a safe system [23, 30]. The supply energy is transmitted inductively from the primary winding distributed along the track - similarly to the third rail in the metro. The fundamental difference between the contact supply by means of the third rail and the contactless induction is that the contact rail "power" is isolated and thus safe.

(*) Tekst artykułu w polskiej wersji językowej dostępny w elektronicznym wydaniu kwartalnika na stronie ***www.ein.org.pl***

2. Power Transmission System for PRT with contactless power supply, linear motor, and supercapacitor

The layout of the PRT drive system with the contactless power supply, the linear motor and the supercapacitor is shown in Fig. 1, where the following are marked:

– stationary part - traction substation: SE - electricity grid, TS network transformer, PS - diode mains rectifier, PR - resonant converter, KR1 - resonant circuit capacitors on the primary side, TD - matching transformer
– vehicle part: contactless power supply (CET), SZ – primary winding of the contactless energy transfer system, UW - secondary winding of the non-contact energy transfer system, KR2 – resonant circuit capacitors on the secondary side, PD – diode rectifier, FN – drive inverter, PM – bi-directional converter for energy storage and brake resistor converter, SC – supercapacitor tray, RH – braking resistor, linear induction motor (SIL)

Fig. shows a diagram of the energy increments that can be associated with separate circuits during vehicle movement. In addition, it was assumed that:

- The energy of the CET transformer is the electrical energy of a single-phase sinusoidal non-distorted 50 kHz transformer. The increments of this type of energy are indicated by the following symbols: dE_Z – CET primary power supply, dE_{CET} – CET secondary site, dE_{CS} – supercapacitor discharge, dE_{DC} – supercapacitor charge, ΔE_{CET} – CET system losses, ΔE_{CET} – supercapacitor losses.
- The energy supplying the motor is the electric current of the three-phase sinusoidal variable non-deformed variable frequency controlled by the inverter. Increments of this type of energy are denoted by: dE_{conv} - motor power, dE_R - recuperation, ΔE_{SIL} - engine loss, ΔE_R - recuperation.

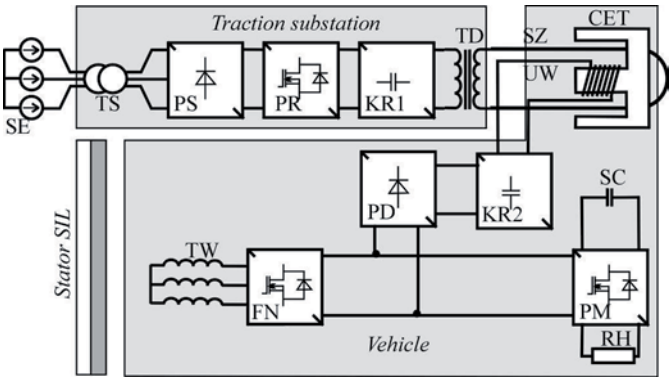

Fig. 1. Block diagram of the power supply – stationary and vehicle

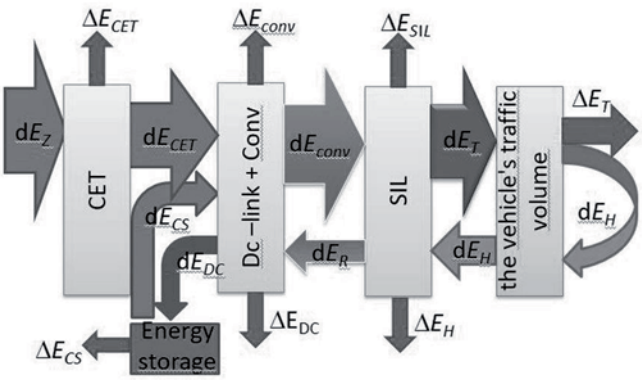

Fig. 2. Diagram of Power Transmission System for the PRT vehicle

- Propulsion energy is a form of mechanical energy. Energy increments are: dE_T - traction, dE_H - kinetic, ΔE_T - mechanical losses.

Fig. 3 presents a 1:4 physical model of PRT vehicle at the laboratory stand for the laboratory study of the power supply and motion control at the Faculty of Transport. The vehicle shown on the picture is on the crossover. On the side of the vehicle, there is a CET transformer with an open magnetic E-shaped circuit. The magnetic circuit is open so that the vehicle can freely exit the loop of the primary winding. The primary winding section is visible behind the vehicle. The vehicle travels the road section on the crossover in the power mode by superconductor energy storage.

Fig. 3. Physical model of a PRT vehicle in a laboratory station

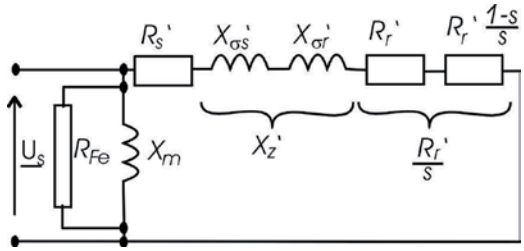

Fig. 4. Simplified peripheral circuit diagram describing the linear motor model adopted for the calculation

3. Model of linear induction motor

The energy characteristics of the steady-state drive system components can be described by efficiency, power factor and power loss as follows:

$$\eta = \frac{P_m}{P_c} \tag{1}$$

$$\cos\phi = \frac{P_c}{\sqrt{P_c^2 + Q_c^2}} \tag{2}$$

$$P_c = P_m + \Delta P \tag{3}$$

where: P_m – power on the shaft, P_c – total active power, ΔP – power losses, Q_c – reactive power.

The mechanical power of the linear motor can also be defined as the product of force and velocity:

$$P_m = F_{lin} v_{lin} \tag{4}$$

The theoretical description of the above relationships has been applied to the peripheral model of the simplest motor, known from the static modelling of the rotary engine operating state for sinusoidally variable non-distorted current supply conditions. The diagram of electrical circuit of the model substitute is shown in Fig. 4. The parameters listed are as follows: R_s - primary winding resistance, R_r - secondary winding resistance, X_z - secondary substitution reactance (consisting of scattering and stator and rotor reactances), R_{FE} - replacement resistance in iron (for vortex currents and hysteresis), X_m - magnetization reactance. Index ‘ means the conversion of the value of the secondary side parameter to the value of the primary side. The use of such a simple model was determined through its usefulness, understood here as the ability to obtain a sufficiently small divergence in the description of the traction-energy characteristics of the engine used in the propulsion system at the laboratory. However, it should be noted that the linear motor (in contrast to the rotary motor) has an open magnetic circuit. Marginal and edge parasitic phenomena are very important in linear motors, which can be omitted in rotary motors. The magnetic gap of the linear motor is much wider than the gap in the rotary engine. The effect of these phenomena is the reduction of the efficiency of linear induction motors and increase in the demand for reactive power to produce magnetic flux. The mathematical model of linear induction motor describing these additional phenomena is a complex process which has been found in many theoretical papers [20], also in the area of control theory [2, 24, 11].

For the accepted substitution scheme, it is possible to formulate the following set of formulas:

a) Total active power consists of rotor electromagnetic power and power loss in the iron:

$$P_c = P_m + \Delta P = F_l V_s + pm\frac{U_s^2}{R_{Fe}} \tag{4}$$

b) Reactive power is charged to the formation of the magnetizing stream and diffusion streams:

$$Q_c = \frac{sF_l V_s}{s_K} + pm\frac{U_s^2}{X_m} \tag{5}$$

c) Strength is a slip function described by the Kloss formula:

$$F_l = \frac{2F_K}{\frac{s_K}{s} + \frac{s}{s_K}} = \frac{2F_K s_K s}{\left(s_K^2 + s^2\right)} \tag{6}$$

where: V_s – synchronous linear speed, m – number of phases, p – number of poles, U_s – stator voltage. F_K – critical power, s_K – critical slip, s - slip

For the accepted method of describing the active and reactive power, the determination of efficiency (1) and power factor (2) can be reduced to:

$$\eta = \frac{V_l}{V_s + m\frac{U_s^2}{F_l R_{Fe}}} \tag{7}$$

$$\cos\phi = \frac{F_l V_s + m\frac{U_s^2}{R_{Fe}}}{\sqrt{\left(F_l V_s + m\frac{U_s^2}{R_{Fe}}\right)^2 + \left(\frac{sF_l V_s}{s_K} + m\frac{U_s^2}{X_{mi}}\right)^2}} \tag{8}$$

4. Map of linear induction motor model efficiency

Table 1 shows the linear induction motor ratings of a 1:4 vehicle [12, 25]. Table 2 shows the variation of the parameters for the change in the nominal width of the air gap in a permissible construction range of 2-4 mm. Parameters of the peripheral motor model were identified by analysing the waveforms of the theoretical and laboratory-measured characteristics. This was done using the least distance method. The calculated parameters are presented in Table 3. The theoretical characteristics obtained are shown in Fig. 5: a) mechanical, b) efficiency, c) power factor.

Table 1. SIL rated characteristics

Parameter	Symbol	Unit	Value
Length of inductor	L	m	0,27
Number of pairs of poles	p	-	3
Number of phases	m	-	3
Rated gap	g_m	mm	3
Supply voltage	U_1	V	230
Rated frequency	f_n	Hz	45
Rated linear speed	V_{ln}	[m/s]	3,375
Rated power	P_{cn}	W	433
Active power	P_{1n}	W	966
Apparent power	S_{1n}	[VA]	7250

Table 2. Parameters of continuous motor operation in conditions of changing the length of the air gap in the range of 2-4 mm.

Parameter	Symbol	Unit	2	2,5	3	3,5	4,0
Slip	s_n	-	0,143	0,160	0,167	0,180	0,1901
Linear speed	V_{ln}	[m/s]	3,470	3,402	3,375	3,32	3,28
Continuous force	F_{cn}	[N]	166	148	128	116	103
Power on the shaft	P_{cn}	[W]	575	504	433	385	338
Active power	P_{1n}	[W]	1148	1053	966	1006	1039
Apparent power	S_{1n}	[VA]	7250	7250	7250	7250	7250
Efficiency	η_N	-	0,50	0,48	0,448	0,38	0,32
Power factor	$\cos\varphi_N$	-	0,158	0,146	0,133	0,14	0,14
Energy factor	$\eta_N * \cos\varphi_N$	-	0,079	0,070	0,060	0,053	0,047

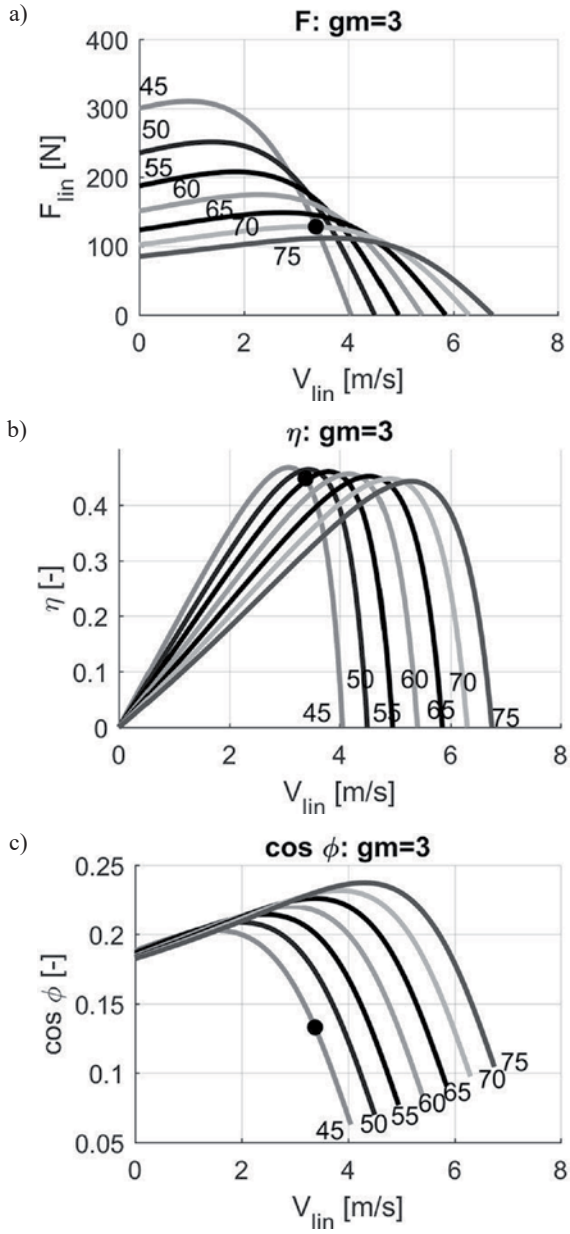

Fig. 5. SIL natural characteristics: mechanical, efficiency (η) and power factor (cos ϕ) for different values of supply voltage frequency

Table 3. Parameters of the replacement scheme for different air gap widths

Symbol	Unit	2	2,5	3	3,5	4,0
X_Z'	[Ω]	151	170	189	213	235
R_r'	[Ω]	97	121	146	174	207
X_m	[Ω]	68	68	67	67	66
R_{Fe}	[Ω]	998	1051	1066	888	767

Fig. 6 shows a map of the efficiency and power factor of the motor for the gap width of 3 mm. The parameters listed in Table 3 provide maps for the remaining slot widths.

5. Model of contactless power supply

The basic element of the contactless power supply system is the high frequency CET transformer, whose primary and secondary windings are maintained in the resonant state - using additional capacitors

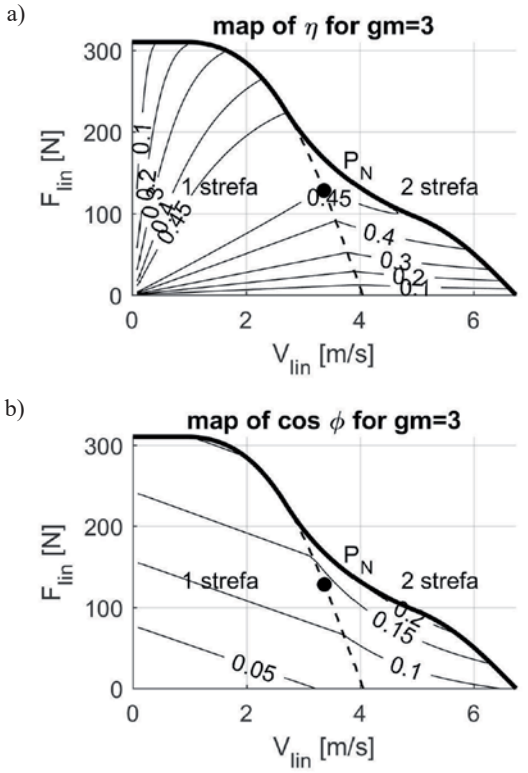

Fig. 6. SIL performance and power factor charts for the laboratory drive for a slot width of 3 mm

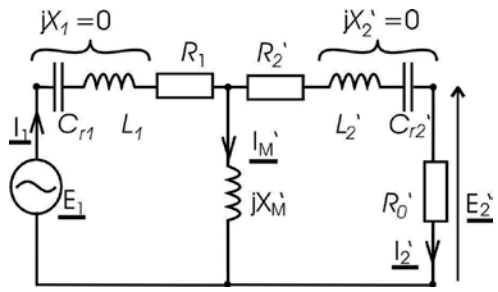

Fig. 7. Diagram of substitution circuit of CET transformer

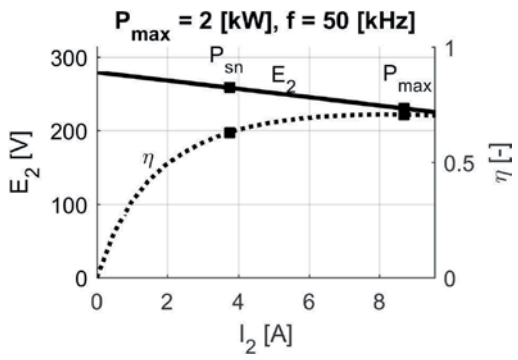

Fig. 8. Contactless power supply diagrams: external $E_2(I_2)$ and efficiency $\eta(I_2)$

(X1 = X2 = 0) [3, 9, 13, 14, 22]. The circuit diagram used to describe the steady-state condition of the sine wave voltage supply [4, 21] is shown in Fig. 7.

Marked: R_1 – primary winding resistance, R_2' – secondary winding resistance reduced to primary side, R_0' – receiver resistance reduced to primary side, L_1 – inductance of primary winding, L_2' – inductance

of secondary winding reduced to primary side, C_{r1} – capacitance of the primary compensation capacitor, C_{r2}' – capacitance of the secondary compensation capacitor reduced to primary side, X_M' – magnetic coupling reactance reduced to primary side, X_1 – replacement reactance of serial connection $L_1 – C_{r1}$, X_2' – replacement reactance of serial connection $L_2 – C_{r2}$ reduced to primary side, I_1 – primary current, I_2' – secondary current reduced to primary side, E_1 – primary power supply voltage, E_2' – receiver voltage reduced to primary side.

The power allocated at the receiver is determined by the formula:

$$P_{out} = (I_2')^2 R_0' \tag{9}$$

The power output from the source is the sum of the power output at all resistances of the circuit:

$$P_{in} = P_{out} + \Delta P = I_1^2 R_1 + (I_2')^2 \left(R_2' + R_0'\right) \tag{10}$$

Electrical efficiency is defined by the formula:

$$\eta = \frac{P_{out}}{P_{in}} = \frac{(I_2')^2 R_0'}{(I_1)^2 R_1 + (I_2')^2 \left(R_2' + R_0'\right)} \tag{11}$$

The reactive power of the system is only taken to produce a magnetizing stream:

$$Q_{in} = (I_M')^2 X_M' \tag{12}$$

The power factor is defined by the formula:

$$cos\varphi = \frac{P_{in}}{S_{in}} = \frac{(I_1)^2 R_1 + (I_2')^2 \left(R_2' + R_0'\right)}{\sqrt{\left((I_1)^2 R_1 + (I_2')^2 \left(R_2' + R_0'\right)\right)^2 + \left((I_M')^2 X_M'\right)^2}} \tag{13}$$

The output voltage of the contactless power system is determined by the formula:

$$\underline{E_0} = \underline{E_2}' + \underline{Z_w}' \underline{I_2}' \tag{14}$$

where: $\underline{E_0}$ – is idle voltage, $\underline{Z_w}$' – is internal impedance of the power supply.

The formula for external characteristic describes the cosine pattern, which after transformations takes the following form:

$$E_0^2 = (E_2')^2 + (Z_w' I_2')^2 + 2(E_2')(Z_w' I_2')\cos\psi_w \tag{15}$$

where additionally: ψ_W – phase angle between current and voltage in internal impedance.

Based on the calculated design calculations and measurements of CET transformer parameters for the vehicle power supply, the following parameters of the peripheral model were adopted: $M = 5 \cdot 10^{-6}$ H, $R_1 = 18 \cdot 10^{-3}$ Ω, $R_2 = 20 \cdot 10^{-3}$ Ω, υ =1/18, f = $50 \cdot 10^3$Hz [19]. The required maximum power of the motor $P_{max} = 2 \cdot 10^3$ W is developed at a voltage of U_s = 230 V, under voltage conditions of E_1 = 280/18 V. Fig. 8 shows the characteristics of a contactless power supply system: external $E_2(I_2)$ designated E_2 (converted to secondary side) and efficiency $\eta(I_2)$ designated η. Two selected work points are indicated in the drawing: P_{sn} – the load point of the system with the active power corresponding to the rated operating conditions of the motor with a 3mm magnetic slot (966 W – table 1) and P_{max} – the maximum load point with the active power.

6. Theoretical analysis of the energy properties of the power supply system for the assumed operating conditions of the laboratory vehicle.

The starting point for the analysis of the energy consumption of the vehicle drive system is the analysis of demand for power (energy) mechanical, popularly known as traction power. The diagram of the applied traction power calculation method is shown in Fig. 9 [18], where: Speed – predetermined instantaneous speed, Route – predetermined path and path profile, P_K – increase in kinetic energy over time, P_V – power to overcome aerodynamic motion resistance, $F_R \cdot v_{lin}$ – power to overcome the forces of additional resistance (corners). In the presented method the power component of the motion resistance is the function of the arc radius R and the velocity v_{lin}, determined interpolatively on the basis of the results obtained through simulation [15] using the vehicle dynamics models [15, 16]. Fig. 10 shows a diagram of a laboratory track, where the symbols H mark the stops, K – switches, L – track connections. Fig. 11 depicts the interstitial distribution travel speed in the H4 – H2 fragment (as a function of the road), determined from the solutions of the computational model of the structure shown in Fig. 9. The dashed line indicates speed limits on the corners. The limitations of traction forces in the form of the characteristics shown in Fig. 6 and the influence of the forces of motion resistance (basic from speed and additional curvature of the trajectory) are taken into account in determining the course of speed. Fig. 12 shows the driving force of the SIL motor (as a function of time) on the analysed road segment.

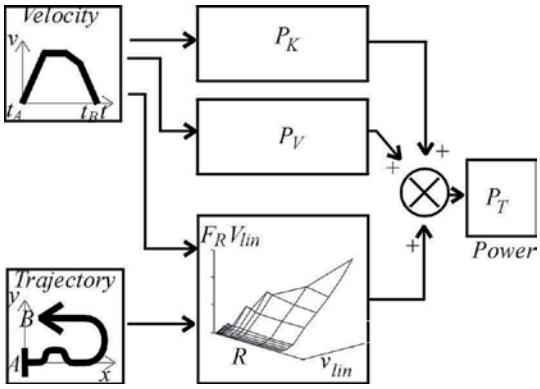

Fig. 9. Diagram of determination of traction power

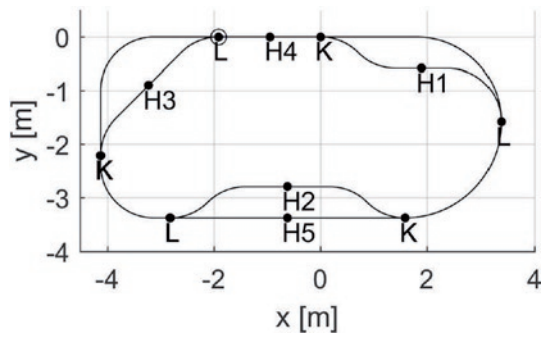

Fig. 10. Track diagram for occupational tests (Faculty of Transport lab)

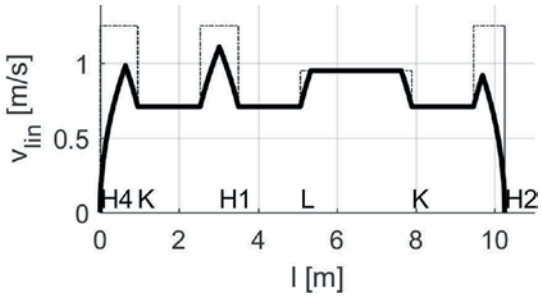

Fig. 11. Distribution of speed as a function of road while passing on the interstitial section of road H4-H5

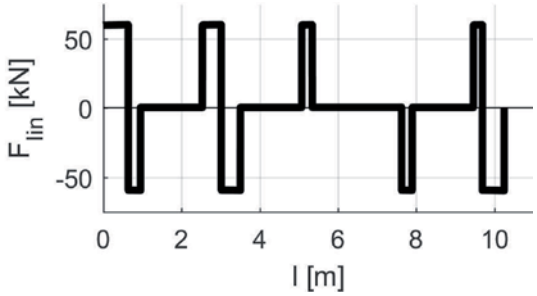

Fig. 12. Waveform of driving force SIL as a function of time on the section of road H4-H5

The above forces and velocities are the basis for determining the power supply of the SIL motor. The calculation takes into account the efficiency of the motor function of the map shown in Fig. 6. The calculation of power output is shown in Fig. 13. The graphs are marked: 1 - the instantaneous power of SIL motor, - 2 the instantaneous power to be delivered from the PD rectifier (fig.1) when a supercapacitor is used in the system. The negative values of power in diagram 1 correspond to the possibility of applying the electric braking of the vehicle. According to the diagram of Fig. 2, the recuperation process is based on the accumulation of braking energy in the supercapacitor and the equalization of the starting power. The calculations take into account the share of the energy loss in the supercapacitor system.

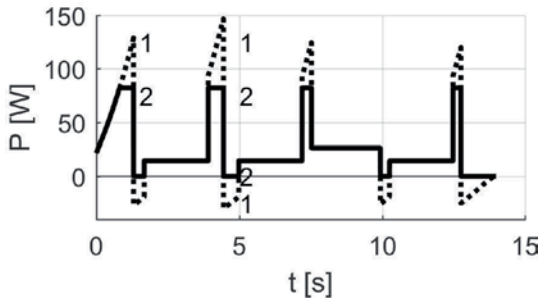

Fig. 13. Power of the SIL power supply. Diagrams are: 1 - without energy storage on the vehicle, 2 - in a system with supercapacitor

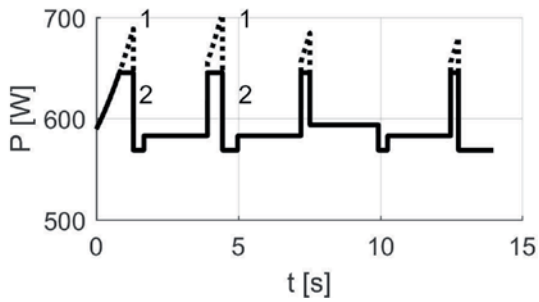

Fig. 14. Power cycle of the laboratory vehicle power supply on the CET contactless power supply terminals. Diagrams are marked: 1 - without energy storage on the vehicle, 2 - in the system with supercapacitor

7. Theoretical analysis of the energy properties of the power supply system for the assumed operating conditions of the vehicle with actual dimensions.

One of the locations considered for the construction of the PRT is the city of Rzeszow. At this stage of the discussions, the type of electric motors used for the drive and the way the vehicle will be powered for that location are not yet determined. However, traction calculations show that a train of actual size and a max. speed of 50 km/h will require a drive with a nominal capacity of approx. 16 kW. Brushless motors located in the wheels of a vehicle which are already used in the car's ECO pre-processor, can be used to implement the drive, for example. The power loss maps of this engine are shown in publication [17]. Equally good is the use of 5-phase induction motors in wheel hubs. This type of engine dedicated to automotive applications was recently presented by HCP at the Hannover Fair. In the already completed ECO Mobility project, a linear induction motor design was implemented [12]. The performance map of this motor is shown in Fig. 15. Fig. 16 shows the external characteristics and performance characteristics of the contactless power system designed in this solution. Fig. 17 shows a diagram of the track line of one of the route sections in the planned location. Fig. 18 shows the driving speeds of the forcing drive - minimum time at this section of the road. Speed limits result from both the limits of the maximum permissible axial acceleration on the curvature of the tracks and the speed limits for direct driving conditions. The exponential acceleration and motion delays result from the possibility of obtaining maximum traction forces (described in the form of the F-V relation in Fig. 15). Fig. 19 shows the course of traction forces on the analysed section of the road, and Fig. 20 shows the power flow patterns. In this figure, the waveforms are shown in two possible variants of the vehicle power supply solution: black diagram - waveform without additional power source, blue - with supercapacitor system for braking energy return (recupera-

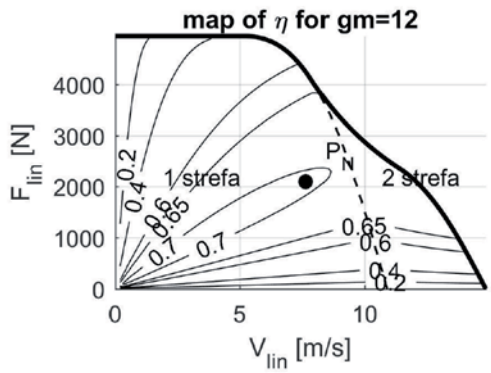

Fig. 15. SIL performance charts for vehicles with actual dimensions at a gap width of 12 mm

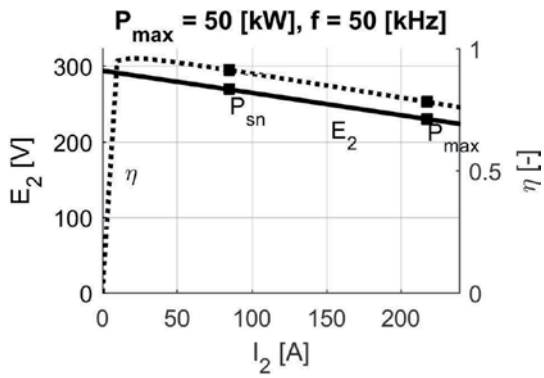

Fig. 16. Contactless power supply diagrams: external E2(I2) and efficiency η(I_2)

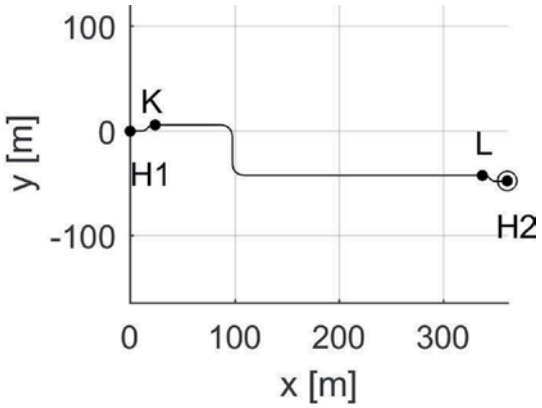

Fig. 17. Diagram of the track line of the first section of the route for the planned location of the PRT track in Rzeszow

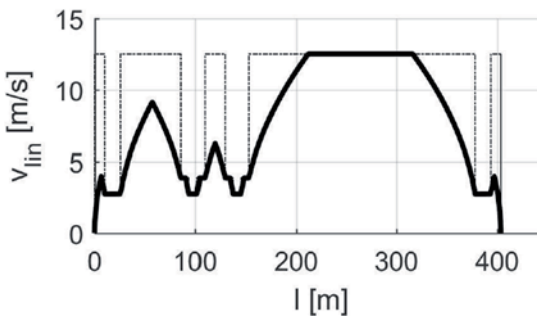

Fig. 18. Distribution of speed as a function of road during the passage of the section in the city of Rzeszow

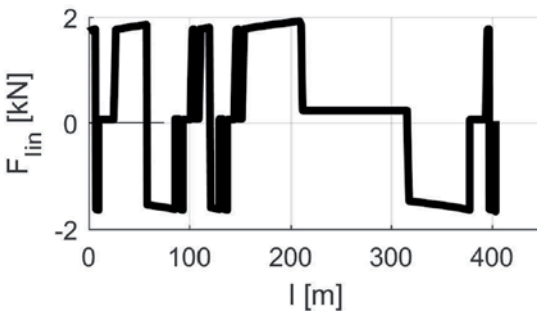

Fig. 19. Distribution of SIL driving force as a function of the road section of the city of Rzeszow

tion system). Fig. 21 shows power draws on the primary source side of the CET transformer. When using an energy recovery system, the maximum input power of the system is approximately 12 kW.

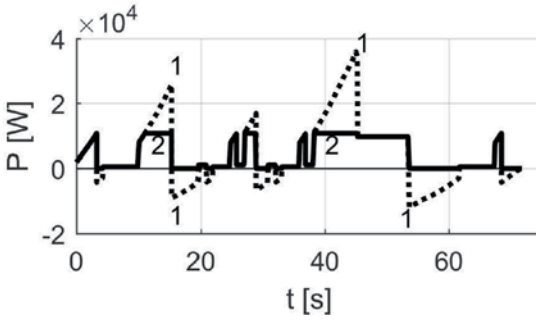

Fig. 20. Power step at the output of the PD rectifier (fig. 1). Diagrams are: 1 - without energy storage on the vehicle, 2 - in the system with supercapacitor

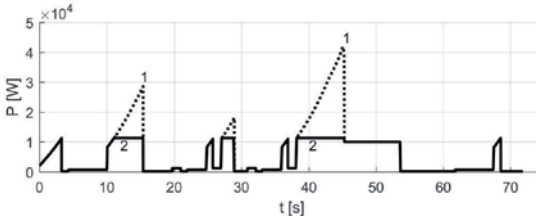

Fig. 21. The power of the vehicle power supply on the terminals of the contactless power supply CET for the section in the city of Rzeszow. Diagrams are: 1 - without energy storage on the vehicle, 2 - in the system with supercapacitor

8. Conclusions

The conducted analysis of the PRT drive and the laboratory tests of vehicles on a test scale showed that dynamic contactless power may be considered as one of the methods of supplying electricity to vehicles of actual size. This type of power supply is ideal for small vehicles moving in urban infrastructure, where safety considerations are particularly important. Results of analyses and studies also show that low power linear induction motors are characterized by low values of energy coefficients (both efficiency and power factor). The 16kW engine designed for the vehicle with actual dimensions is also characterized by poorer operating conditions than rotary motors. The use of linear motors also excludes the possibility of moving this PRT vehicle on public roads intended for wheeled vehicles. For this reason, the second generation of currently-developed PRT vehicles will be equipped with rotary motors. These vehicles will be able to have a contactless power supply system as a rail system, supplemented by electrochemical energy storage on board the vehicle. During the rail traffic, the contactless power supply system will provide the energy required to track the path and the energy to charge the electrochemical battery, which will be a source of power during the period of moving on the public road.

References

1. Anderson J E. A Review of the State of the Art of Personal Rapid Transit. Journal of Advanced Transportation 2000; 34(1): 3-29, https//doi.org/10.1002/atr.5670340103.
2. Berrin S, Vedat M. Karsli. Direct Thrust Controlled Linear Induction Motor Including End Effect. 13th International Power Electronics and Motion Control Conference 2008.
3. Böttigheimer M, Parspour N, Zimmer M, Lusiewicz A, Design of a Contactless Energy Transfer System for an Electric Vehicle, PCIM Europe 2016; ISBN 978-3-8007-4186-1
4. Boys J, Kazmierkowski M P, Lomonova E, Madawala U, Covic G. Special Section on "Contactless Energy Transfer Systems " IEEE Transactions on Industrial Electronics 2013; 60(1): 212, https://doi.org/10.1109/TIE.2012.2203489.
5. Chormański W. Systemy transportowe PRT. Wydawnictwa Komunikacji i Lacznosci - Transport and Communication Publishers 2015: 38.
6. Codziennypoznan.pl: Powstanie innowacyjny elektryczny samochód dostawczy z silnikiem opracowanym w Zakładach Cegielskiego w Poznaniu, http://www.codziennypoznan.pl/artykul/2017-04-27/powstanie-innowacyjny-elekt ryczny-samochod-dostawczy-z-silnikiem-opracowanym-w-zakladach-cegielskiego-w-poznaniu [2017-07-13]
7. Dziennik naukowy.pl. Polskie technologie i wynalazki na targach Hannover Messe 2017 http://dzienniknaukowy.pl/nauka-w-polsce/olskie-

technologie-hannover-messe- 2017/ [2017-07-13]
8. Furman B, Fabian L, Ellis S, Muller P, Swenson R. Automated Transit Networks (ATN): A Review of the State of the Industry and Prospects for the Future, MTI Report 2014
9. Judek S., Karwowski K.: Contactless electrical energy transfer system via magnetically coupled air coils. Gdańsk: Wyd. Politechniki Gdańskiej, 2013, ISBN 978-83-7348-501-3
10. Jurgen R K. V2V/V2I Communications for Improved Road Safety and Efficiency, SAE International. Product Code of PT-154 2012, ISBN of 978-0-7680-7725-4, https://doi.org/10.4271/PT-154.
11. Kamiński B, Nikoniuk M, Drązikowski Ł. A concept of propulsion and power supply systems for PRT vehicles. Archiwum Transportu - Archives of Transport 2013; 27(3-4): 81-93.
12. Kamiński G., Przyborowski W., Staszewski P., Biernat A., Kupiec E., Design and testing of Laboratory Model of Linea Induction Motor for Automation Personal Urban Transport PRT, Przeglad Elektrotechniczny -Electrical Review 2017; 93(3): 276-283.
13. Kazmierkowski M P, Miskiewicz R M, Moradewicz A J. Inductive coupled contactless energy transfer systems - a review. Selected Problems of Electrical Engineering and Electronics (WZEE) 2015.
14. Kazmierkowski M P, Moradewicz A J, Duarte J, Lomonova E, Sonntag Ch. Chapter 35 "Contactless Energy Transfer" in The industrial Electronics Handbook, Part II: Power Electronics and Motor Drives, Second Edition, Edited by B. M. Wilamowski, J. David Irvin, CRC Press 2011.
15. Kozłowski M, Choromański W, Kowara J. Analysis of dynamic properties of the PRT vehicle-track system. Bulletin of the polish academy of sciences, Technical sciences 2015; 63(3): 799-806, https://doi.org/10.1515/bpasts-2015-0091.
16. Kozłowski M, Choromański W, Kowara J. Parametric sensitivity analysis of ATN-PRT vehicle (automated transit network - personal rapid transit). Journal of Vibroengineering 2015; 17(3): 1436 1451
17. Kozłowski M, Tomczuk K, Szczypior J. Methodology of determining basic technical parameters of electric-drive car, Przeglad Elektrotechniczny - Electrical Review 2011; 87(10): 299-304.
18. Kozłowski M. Simulation method for determining traction power of ATN - PRT (Automated Transit Network - Personal Rapid Transit) vehicle, Transport 2016; ISSN 1648-4142.
19. Krawczyk Z, Nikoniuk M, Starzyński J, Chaber B, Kamiński B. A prototype transformer for inductive contactless energy transfer system: numerical models verified by measurement. Przegląd Elektrotechniczny - Electrical Review 2014; 90(5): 56-60.
20. Lu G, Li Q, Liu Z, Fan Y, Li G. The Analytical Calculation of the Thrust and Normal Force and Force Analyses for Linear Induction Motor, ICSP 2008; Proceedings
21. Mecke R, Rathage C. High frequency resonant converter for contactless energy transmission over large air gap. PESC iEEE 2004; 1737-1743.
22. Moradewicz A J, Kazmierkowski M P. High efficiency contactless energy transfer system with power electronic resonant converter. Bulletin Of The Polish Academy of Sciences, Technical Sciences 2009; 57(4): 375-381, https://doi.org/10.2478/v10175-010-0141-0.
23. Nam P. Suh . Dong Ho Cho (Editors): The On-line Electric Vehicle. Wireless Electric Ground Transportation Systems. Springer 2017. ISBN 978-3-319-51182-5
24. Nikoniuk M., Kamiński B., Yaremoff O.: Zagadnienia regulacji sił ciągu i prędkości silnika indukcyjnego liniowego. rozdział 6.9, w: Ekomobilność. Innowacyjne i ekologiczne środki transportu / Choromański Włodzimierz (red.), Wydawnictwa Komunikacji i Lacznosci - Transport and Communication Publishers 2015, 1: 160-179.
25. Nikoniuk M., Kozłowski M., Model strat mocy układu napędu pojazdu PRT (Personal Rapid Transit), Prace Naukowe Politechniki Warszawskiej. Seria Transport. OWPW 2016; 112: 301-311,
26. Personal Rapid Transit. Website from Wikipedia: http://en.wikipedia.org/wiki/Personal_rapid_transit, [2017-07-13]
27. Podcar city & advanced transit conference 2017. Smart Cities, Smart Transportation, Smart Energy. Las Vegas USAr 8-10 November 2017. Website at: http://www.advancedtransit.org/library/news/podcar-city-advanced-transit-con ference-2017/ [2017-07-13]
28. Politechnika Warszawska Badania i Nauka, Reprezentanci Politechniki Warszawskiej na targach Hannover Messe, Web Site: 2017 https://www.pw.edu.pl/Badania-i-nauka/Aktualnosci/Reprezentanci-Politechniki -Warszawskiej-na-targach-Hannover-Messe-2017 [2017-07-13]
29. Radovanovic D, Muoio D. This is what the evolution of self-driving cars looks like, Finance on line, Business Insider, http://www.businessinsider.com/what-are-the-different-levels-of-driverless-cars-2016-10?IR=T/#-1 [2017-07-13]
30. Worek C. Bezstykowy przesył energii elektrycznej oparty o szeregowo-równoległe układy rezonansowe http://ptetis.agh.edu.pl/CWorek.pdf. 2013 [2017-07-13]

Marcin NIKONIUK
Maciej KOZŁOWSKI
Department of Information Technology and Mechatronics in Transport
Warsaw University of Technology,
Faculty of Transport,
ul. Koszykowa 75, 00-662 Warszawa, Poland

Emails: marcin.nikoniuk@wt.pw.edu.pl, mkozlo@wt.pw.edu.pl

Article citation info:
GUO C, LYU C, CHEN J, ZHOU. A design approach based on a correlative relationship between maintainability and functional construction. Eksploatacja i Niezawodnosc – Maintenance and Reliability 2018; 20 (1): 115–124, http://dx.doi.org/10.17531/ein.2018.1.15.

Chunhui GUO
Chuan LYU
Jiayu CHEN
Dong ZHOU

A DESIGN APPROACH BASED ON A CORRELATIVE RELATIONSHIP BETWEEN MAINTAINABILITY AND FUNCTIONAL CONSTRUCTION

PODEJŚCIE PROJEKTOWE OPARTE NA KORELACYJNYM ZWIĄZKU MIĘDZY KONSERWOWALNOŚCIĄ A FUNKCJONALNĄ BUDOWĄ PRODUKTU

As an important quality characteristic, maintainability is the ability of a product to be repaired efficiently and economically. Because it is mainly determined at the design stage, maintainability is mostly affected by the construction of a product. Traditional product design methods put more focus on design for function and production, neglecting design for maintainability, which causes a gap between functional construction design and maintainability design. The delay of maintainability design results in huge costs for design changes and even irrevocable design flaws. Because of the weak relationship between functional construction and maintainability in product design, the influence of maintainability design on the product is limited. To resolve this problem, this paper proposes a design approach considering the relationship between maintainability and functional construction. First, maintainability design factors (MDFs) and functional construction design factors (FCDFs) are defined and classified. Second, based on topology graphic theory, a correlative relationship model is constructed by graphically combining the MDFs and FCDFs into a network diagram. Third, to determine primary design factors, a quantization matrix is developed to perform importance evaluation of the correlative relationship. Finally, a practical case is studied by implementing the proposed approach for the lubrication system of an armoured vehicle. The results validate the effectiveness and feasibility of the approach.

Keywords: *maintainability design, correlative relationship, functional construction design factors, maintainability design factors.*

Konserwowalność to ważna charakterystyka jakościowa, którą można zdefiniować jako możliwość wydajnej i ekonomicznej naprawy produktu. Ponieważ o konserwowalności produktu decydują głównie wybory dokonane na etapie projektowania, największy wpływ na nią ma budowa produktu. Tradycyjne metody projektowania produktów kładą większy nacisk na projektowanie funkcji i produkcji, zaniedbując projektowanie pod kątem łatwości konserwacji, co powoduje powstanie luki między projektowaniem funkcjonalnej budowy produktu a projektowaniem jego konserwowalności. Opóźnienie etapu projektowania konserwowalności generuje ogromne koszty związane z koniecznością zmian projektu i może nawet prowadzić do nieodwracalnych wad projektowych. Ze względu na słabą zależność między budową funkcjonalną a konserwowalnością w projektowaniu produktu, wpływ projektowania konserwowalności na produkt jest ograniczony. Aby rozwiązać ten problem, w niniejszej pracy zaproponowano podejście projektowe uwzględniające związek między konserwowalnością a budową funkcjonalną wyrobu. Po pierwsze, zdefiniowano i sklasyfikowano czynniki konstrukcyjne (projektowe) dotyczące konserwowalności (MDF) oraz czynniki konstrukcyjne związane z budową funkcjonalną produktu (FCDF). Po drugie, w oparciu o teorię graficznej reprezentacji topologii, zbudowano model zależności korelacyjnych między MDF i FCDF w postaci diagramu sieciowego. Po trzecie, w celu określenia podstawowych czynników konstrukcyjnych, opracowano macierz kwantyzacji, pozwalającą na ocenę ważności relacji korelacyjnych. Wreszcie, przeanalizowano przypadek układu smarowania pojazdu opancerzonego jako przykład zastosowania proponowanego podejścia w praktyce. Wyniki potwierdzają skuteczność omawianego podejścia oraz możliwość jego praktycznego wykorzystania.

Słowa kluczowe: *projektowanie konserwowalności, związek korelacyjny, czynniki konstrukcyjne dotyczące funkcjonalnej budowy, czynniki konstrukcyjne dotyczące konserwowalności.*

1. Introduction

The quality level determines to a great extent if a product can achieve performance continuously and effectively. Maintainability is an important product quality characteristic that reflects the ability for fast, easy and economical maintenance of a product [12, 20]. Therefore, it is crucial to improve product maintainability, which helps increase the quality level of a product. To achieve this purpose, maintainability design is an effective and feasible way. Recently, a large body of literature has been published on maintainability design.

Repair time is an important quantitative design factor. Several papers have proposed improving maintainability design by the rational planning of repair time. D Khandelwal et al. presented an optimal maintainability strategy for machines by switching the maintainability time and the end time using the optimal periodic control theory [14]. T Dohia et al. proposed a new graphical method to estimate optimal repair-time limits with incomplete repair and discounting [9]. D Zhou et al. proposed an improved method of maintainability allocation based on time characteristic [29]. Y Yin et al. emphasized that arrangement of maintainability times by means of CON and SLK time allocation methods optimizes maintainability frequency and location

of maintainability operations [27]. Reasonable allocation for repair time can improve maintainability design and avoid waste. However, these methods mainly concentrate on quantitative aspects, rather than the entire maintainability design.

Maintenance strategy optimization is also a research focus. Zhen, F et al. proposed a modelling method for maintenance design of product level reuse using the approach of house of quality [28]. Liu, W. and Y.U. Shui-Jun established a computer technology-based decision support system to make maintenance decisions quickly and effectively [16]. QS Jia used a simple value function representation for engine maintenance strategy optimization [13]. Peng, W. et al. developed a preventive maintenance decision model for series-parallel systems subject to reliability [21]. A Saxena et al. used a hybrid reasoning architecture based on knowledge of vehicle maintenance to solve vehicle maintenance problems [22]. Bohlin, M., et al. used condition monitoring and dynamic planning to reduce vehicle maintenance [4]. Deloux, E. constructed a specific maintenance policy, which combines a classical condition-based maintenance policy for the system state with a condition monitoring method to track environmental changes [8]. D Mazurkiewicz described the most popular diagnostic systems used in the maintenance of internal transport conveyor systems [19]. Baidya, R. et al. presented strategic maintenance options using the benefits of combined quality function deployment, analysis of hierarchical processes and scepticism technical selection [2]. Maintenance strategy optimization can effectively improve the utilization of maintenance manpower and reduce maintenance time. Research on maintenance strategy is an optimization of maintenance processes, rather than optimization of the product itself.

Several researchers considered maintainability evaluation. Chang, L., et al. performed reliability and maintainability analysis of vehicle anti-tank missiles [5]. Lu, Z. et al. presented maintainability fuzzy evaluation by virtual simulation for aircraft systems [17]. Senivongse T. and A. Puapolthep presented a maintainability assessment model for determining whether a service-oriented system is maintainable by using several metrics [23]. Guo, L performed research on equipment maintainability forecast methods based on support vector machine [11]. Ertas, et al. proposed a diagnostic approach to quantify the maintainability of a commercial off-the-shelf based system by analysing the complexity of the deployment of the system components [10]. Maintainability evaluation is an effective way to analyse the maintainability of a product and feedback suggestions on design changes. However, compared with active design of function and construction, it is a passive feedback design and requires time to complete several design loops.

However, repair time plan, maintenance strategy optimization and maintainability evaluation mainly concern more about later stage of product design. It results in the maintainability design lags to the product design. Thus, the effection of maintainability design requirements to product design is limited.

To resolve the lag issue, more scholars and experts put concerns on optimization of traditional maintainability and product design. Yau, S.S. and J.S. Collofello discussed several factors affecting the software maintainability process and important software quality attributes [26]. Ali, A. et al. presented optimized maintainability design using simulation to analyse the capability of auto part manufacturing production systems[1]. Barabadi, A. et al. used point process models to analyse maintainability of equipment solving the lack of on-site maintainability data [3]. These optimization methods are helpful to maintainability design in early stage. However, these methods are not ideal and comprehensive maintainability design, which cannot significantly improve product maintainability.

To comprehensively design maintainability in early stage, it should be combined with product design. Concurrent engineering, emphasising on maintainability design and traditional functional construction design in parallel, is proposed and developed[24]. D Zhou et al have proposed the use of digital prototyping and virtual environment to achieve parallel engineering[30]. H Zhou et al put forward the view that the maintainability model is integrated into the design process[31]. These methods proposed new insights that maintainability and product functional construction are parallel design.

To consider maintainability design in detail, several studies examine the relationship of maintainability design factors (MDFs). Li, Q. et al. analysed the relationship between maintainability qualitative factors [15]. Luo, X. et al. described the priority of maintainability qualitative factors [18]. Da, X.U. et al. studied qualitative index systems of equipment maintainability [7]. Maintainability and functional construction are closely linked. Yang, Y. presented maintainability-based facility layout optimum design of ship cabins [25]. Although maintainability design factors and their relationships are considered, little of the relationship between maintainability and functional construction is analysed.

Much of the current research on improving product maintainability is related to improvement of some special aspect. In the current approach to product design, function and construction are designed first. Next, maintainability design is considered, which means that maintainability design lags behind function and construction design. This lag results in the requirements of maintainability design having little effect on product design and limiting the improvement of product maintainability. Because product maintainability is mostly determined at the design stage, the cost is high to correct the design, even leading to irrevocable defects if not enough attention is paid to the influence of maintainability design at the initial design stage [6]. Product maintainability focuses on design factors related to function and construction, such as layout and visibility, which indicates that the design of function and construction has a significant effect on maintainability design. Therefore, it is crucial to integrate maintainability, function and construction design at the design stage.

To correlate maintainability and functional construction design, this paper presents a design approach for maintainability and functional construction using three steps: definition and classification, modelling relationship and importance evaluation. The main contributions of this paper is to propose a concurrent design method, which combines maintainability design and product functional construction design through considering the relationship between two types of design factors. Because the design factors contain quantitative and qualitative aspects of maintainability, the approach can comprehensively design maintainability in the early product stage. In addition, modelling the relationship between maintainability design factors and functional construction design factors, the maintainability requirements can affect the functional construction design of products. Finally, to validate the proposed approach, it is applied to the practical case of the lubrication system of an armoured vehicle.

2. Methodology

To bridge the gap between maintainability design and functional construction design, a design approach is proposed; its framework is shown in *Fig. 1*. The approach consists of three parts: Definition and classification of MDFs and functional construction factors (FCDFs), modelling the relationship between MDFs and FCDFs, and importance evaluation of the relationship. First, MDFs and FCDFs are defined and classified into system-level and unit-level. Second, based on topology graphic theory, a correlative relationship model is constructed by combining MDFs and FCDFs into a network diagram. Third, the importance of the correlative relationship is evaluated by a quantization matrix (QM).

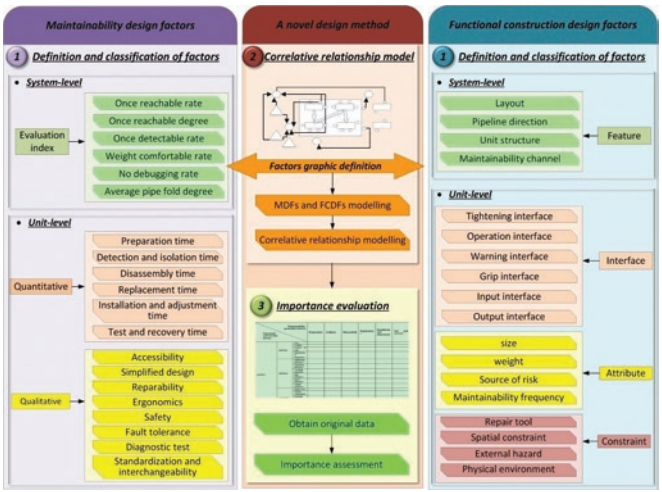

Fig. 1. Framework of the proposed methodology

2.1. Definition and classification of factors

To express product design concepts, design factors are defined and classified into maintainability design factors (MDFs)and functional construction design factors (FCDFs).

2.1.1. Maintainability Design Factors

Different design levels lead to different design considerations. System and unit are two design levels. At the system level, it is more important to consider the overall design of the system, while at the unit level, detailed design factors require more attention. MDFs are divided into two types, system level and unit level.

1) System level

As shown in Table 1, for product system maintainability, six design factors are defined as a system maintainability evaluation index, which are reachability ratio, degree of accessibility, detectable rate, weight comfort rate, free debugging rate and average pipe fold separately.

2) Unit level

Table 1. Definition of system level MDFs

Factors	Definition
Once reachable rate	It refers to the ratio of the number of units, which can be accessed and repaired without taking apart other units (excluding the normally installed cover or door, etc.) by the total number of units in the system.
Once reachable degree	It refers to the power of 1/2 of the product of the value, which is the failure rate of once reachable unit by the total failure rate of the system, and ORR.
Once detectable rate	It refers to the rate of the number of units, which can be monitored and diagnosed without taking apart other units (excluding the normally installed cover or door, etc.) by the total number of units in the system.
Weight comfortable rate	It refers to the rate of the number of units, which do not exceed 16 kg by the total number of units in the system.
No debugging rate	It refers to the rate of the number of units, which do not require debugging after maintenance by the total number of units in the system.
Average pipe fold degree	It refers to the average value of pipe folds in the system. When bending degree is greater than 90°, it is not a fold. When bending degree is less than 90°, it is counted as two folds.

Table 2. Definition of maintainability quantitative factors

Factors	Definition
Preparation time	Time for products to be repaired or maintenance tools to reach a repairable state, not including logistical delays.
Detection and isolation time	Time for fault identification, fault location, determination of fault cause and fault isolation.
Disassembly time	Time for product disassembly.
Replacement time	Time to restore the ability of a faulty product to perform a specified function.
Installation and adjustment time	Time of product installation and adjustment.
Test and recovery time	Time for checking whether a product can perform the specified function after maintenance.

Table 3. Definition of maintainability qualitative factors

Factors	Definition
Accessibility	Accessibility is the degree of difficulty in approaching different components of a product.
Simplified design	Simplified design refers to the simplification of functional construction and maintenance process.
Reparability	Reparability refers to the degree of difficulty in repairing expensive parts and battlefield parts.
Ergonomics	Ergonomics is the study of the relationship of human factors and product maintenance, and how to improve maintenance efficiency, quality and reduce human fatigue.
Maintenance safety	Maintenance safety refers to a design feature, which avoids casualties or damage to products when implementing maintenance.
Errors prevention	Error prevention means to take appropriate measures to avoid or prevent maintenance operation error at the design stage.
Diagnostic test	Diagnostic test means measures or activities taken to find fault cause and location guarantee the performance, characteristics, applicability of a product or system.
Standardization and interchangeability	Standardization is a design feature limiting viable changes to the minimum range under conditions that requirements are met. Interchangeability is a design feature that products can be physically and functionally interchangeable.

According to the traditional maintainability design and analysis method, design factors at the unit-level are divided into two types, quantitative factors and qualitative factors.

Based on maintainability design requirements, the quantitative and qualitative factors are defined and shown separately as Table 2 and Table 3. Quantitative factors are preparation time, detection and isolation time, disassembly time, replacement time, installation and adjustment time, and test and recovery time. Qualitative factors are accessibility, simplified design, reparability, ergonomics, maintenance safety, error prevention, diagnostic test, and standardization and interchangeability.

2.1.2. Functional Construction Design Factors

By analysing the maintenance process, maintenance programme and design process of maintainability, this paper summarizes various design factors of function and construction influencing maintainability. These factors are also divided into system and unit level. There are four design factors at the system level, which are layout, pipeline direction, unit structure and maintenance channel. There are three classes of design factors at the unit level interface class, attribute class and constraint class. More detailed definition and classifications are shown in Table 4.

2.2. Correlative relationship model

To solve the problem of the complex relationship of maintainability and functional construction, a correlative relationship model is built based on topology graphic theory to define the influence relationship.

Topology requires that the geometry or space after a continuous change remains unchanged. Topology takes into account only positional relationships between objects regardless of their shape and size. Topology is a branch of geometry, but it is different from plane geometry and three-dimensional geometry. Plane geometry and three-dimensional geometry are concerned with the positional relationships between points, lines, and planes, and their measurement properties. The length, size, area and volume are irrelevant to topology, which only focuses on the relationship between objects. High system reliability, relative ease to expand and each node linked with multi-points are the advantages of network topology. Considering that modelling method is designed to express relationships, not specific product size and weight, this paper uses network topology as the model basis.

Before model construction, to clearly define the meaning of graphic units and structure the model, elements in the model are defined as shown in Table 5.

To construct the relationship model, there are four steps, as shown in *Fig. 2*: (1) product structure modelling (2) FCDFs modelling (3) MDFs modelling (4) correlative relationship modelling.

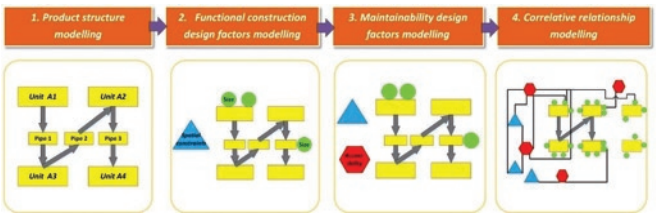

Fig. 2. Framework of modelling the relationship of MDFS and FCDFs

1) Product structure modelling

The first step of modelling the relationship is to analyse the product structure and the exchange of material, energy and information between units. As shown in the first phase of Fig. 2, a product system, which contains four product units and three pipes, and the interaction of the units are described. In the system, four units and three pipes are defined as product units and expressed by solid line rectangles. Each product unit is defined as a line replaceable unit, which indicates the

Table 4. Definition of FCDFs

FCDFs		Specific functional structural factors	Definition
System level	System feature class	Layout	Spatial relationship of product parts in the system.
		Pipeline direction	Line direction of transmission of material, energy and information.
		Unit structure	Types of units making up a system.
		Maintenance channel	A set of paths to pass in the maintenance process.
Unit level	Interface class	Tightening interface	A fixed way of tightening two or more parts to be an entirety.
		Operating interface	Operating port between the user and the device which is convenient for users, detecting electronic and machinery devices.
		Warning interface	Display devices, including warnings, reminders, logos and cautions, used for environmental, safety, operational and technical states, etc.
		Grip interface	Parts, including handles, spreaders and pedals, used for equipment moving and personnel climbing in maintenance process.
		Input interface	Ports used for passing external material, energy and information to the internal system or unit.
		Output interface	Ports used for passing internal material, energy and information to the external system or unit.
	Attribute class	Size	Shape data of the unit or system.
		Weight	Physical quality of the unit or system.
		Source of risk	Features of potential harm to personnel and equipment in the unit.
		Maintenance frequency	Number of repairs over a period of time.
	Constraint class	Repair tool	A set of tools used for maintenance process.
		Spatial constraint	A set of space constraints for maintenance operations in maintenance process.
		External hazard feature	Features of potential harm to personal, devices in the unit or system.
		Space and physical environment	Physical or non-entity environment of the facilities.

Table 5. Definition of model elements

Name	Specific meaning	Graphic definition	Legend
Product unit	Units making up the system	Solid line rectangle	
Virtual unit	External unit associated with the system	Dashed line rectangle	
System level	An entity to complete a function		
Physical relationship	Material and energy flow between units	Double line arrows	
FCDF	System-level and unit level design factors (not included in constraint class)	Solid line circle attached to a rectangle	
	Design factors of constraint class	Solid line triangle	
MDF	System-level and unit level	Solid line hexagon	
Correlative relationship	Associated impact between factors	Solid line	

unit can be replaced when a failure occurs, rather than repairing it after disassembling the whole product system. From the figure, the flow direction of material, energy and information is from unit A1 to unit A4.

2) Functional Construction Design Factors modelling

Nodes are widely used in different fields. In network topography theory a node is the end of any branch in the network or the common node linking two or more branches in a system, representing attributes, design features and interfaces of a product or system. Usually, the node is attached to the edge of a unit or system, showing a subordinate relationship. Nodes can be added according to need and there is no quantitative requirement.

In this model, FCDFs are defined as nodes and represented by solid line circles attached to the target product unit. Because there are many internal and external constraints in maintenance operations, design factors of the constraint class in the model are represented by solid line triangles. As shown in the second phase of *Fig. 2*, the circle marked with size attached to the rectangle indicates the size design factor of that product unit.

3) Maintainability Design Factors modelling

MDFs are modelled and defined as solid line hexagons, which surround the product units to construct a relationship. As shown in the third phase of *Fig. 2*, an MDF, accessibility, is constructed in the model and surrounds the product units.

4) Correlative relationship modelling

The final step to build the model is to construct correlative relationships between MDFs and FCDFs. The relationship is defined and represented by a solid line. Theoretically, if there is a relationship between an MDF and an FCDF, a solid line would connect the two factors. However, a system contains many product units, which means that the model is usually very large and complex, resulting in intricate lines and nodes. Therefore, to make the model more practical and easier to understand, the system usually selects strong relationships and uses nodes in the model. Because the construction of relationships depends on the deep understanding of product design, it is the most important step. As shown in the fourth phase of *Fig. 2*, the relationship is constructed, and the model is completed.

2.3. Importance evaluation

After constructing the model, the relationship between maintainability and functionality can be graphically expressed. To describe more accurately the strength of the relationship and provide effective data to guide design and improve maintainability, an importance evaluation method is developed based on a QM and described as follows.

1) Collection of original data

To obtain original data of the relationship, three data tables are designed and shown as Table 6, Table 7 andTable 8. To quantify the basic relationships, the three tables are filled by experts and designers according to the scoring rule, which uses a scoring method of 9 points. In this rule, 1, 3, 5, 7, 9 points indicate little correlation, a certain correlation, a strong correlation, stronger correlation, the strongest correlation, and 2, 4, 6, 8 are the scaling values of the intermediate states between the two adjacent numerical judgements.

2) Importance evaluation

Step 1: Construct a QM. The collected data from the tables can be abstracted into a QM, keeping the original data position unchanged. a_{ij} in the matrix is the collected data from the tables and represents the strength of relationships between FCDFs and MDSs:

$$QM = \begin{bmatrix} a_{11} & a_{12} & \cdots & a_{1n} \\ a_{21} & \ddots & \cdots & \vdots \\ \vdots & \cdots & \ddots & \vdots \\ a_{m1} & \cdots & \cdots & a_{mn} \end{bmatrix} = \begin{bmatrix} F_1 \\ F_2 \\ \vdots \\ F_m \end{bmatrix} = \begin{bmatrix} M_1 & M_2 & \cdots & M_n \end{bmatrix}, a_{ij} > 0 (i = 1,2\ldots m; j = 1,2\ldots n) \tag{1}$$

Step 2: Obtain the importance degree of every FCDF to MDF.

In this approach, assuming that the weight of each factor is equal, thus the average value is used to evaluate importance. The importance degree matrix of every FCDF to MDF (IDM_1) can be calculated by equations (2) and (3):

$$f_i = average(F_i)/9, f_i > 0 (i = 1,2\ldots m) \tag{2}$$

$$IDM_1 = \begin{bmatrix} f_1 & f_2 & \cdots & f_m \end{bmatrix} \tag{3}$$

The value of f_i is between 0 and 1, reflecting the importance degree of every FCDF to MDF. If the value is larger, the importance degree is larger.

Step 3: Obtain the importance degree of every MDF to FCDF.

In this approach, assuming that the weight of each factor is equal, thus the average value is used to evaluate importance. The importance degree matrix of every MDF to FCDF (IDM_2) can be calculated by equations (4) and (5):

$$m_i = average(M_i)/9, m_i > 0 (i = 1, 2 \ldots n) \tag{4}$$

$$IDM_2 = [m_1 \quad m_2 \quad \cdots \quad m_m] \tag{5}$$

The value of m_i is between 0-1, reflecting the importance degree of every MDF to FCDF. If the value is larger, the importance degree is larger.

3. Case Study

Because it is army equipment, an armoured vehicle requires efficient and easy repair to restore combat capacity as soon as possible when a failure occurs. This results in high demand for the maintainability of armoured vehicles. However, due to complexity of armoured vehicles in function and construction, maintainability design usually lags behind function and construction design and affects little of the design. As a result, difficulty in maintenance of armoured vehicles bothers soldiers and reduces the availability of vehicles, as shown in Fig. 3.

To validate the proposed approach, a practical case of an armoured vehicle's lubrication system is studied. As a typical system of an armoured vehicle, the lubrication system consists of mechanical and electric units, and has many typical maintenance problems.

Fig. 3. Maintenance activities of armoured vehicles

3.1. Modelling relationship

Relationships of the two levels are analysed. At the unit level, the oil tank is selected as the study object. The entire lubrication system is selected as the study object at the system level. By analysing the traditional design process, maintenance problems and maintenance procedures in use, the relationship models of the oil tank and the system are built following the modelling approach described in section 2.2 and shown as Fig. 5 and Fig. 7.

At the unit level, the simple structure of the oil tank is shown as Fig. 4. Materials, such as water, oil and gas, are input from the input pipe A to the oil tank and subsequently output through the output pipe B. The input pipe A and output pipe B represent the oil pipe, water pipe and ventilator. Therefore, these pipes are regarded as external product units and represented by virtual units. The model is built and shown

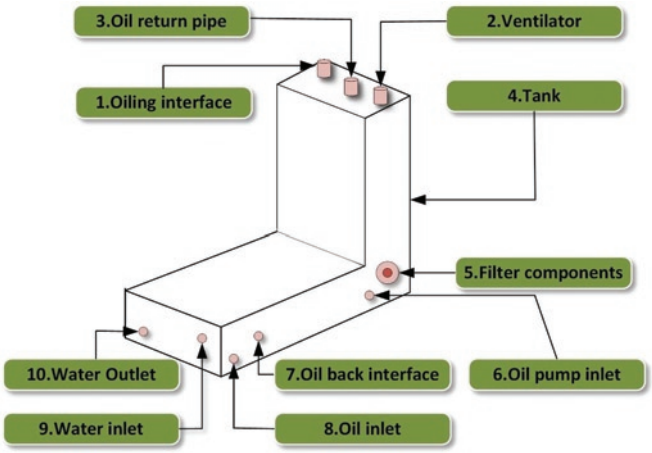

Fig. 4. Simple structure of an oil tank

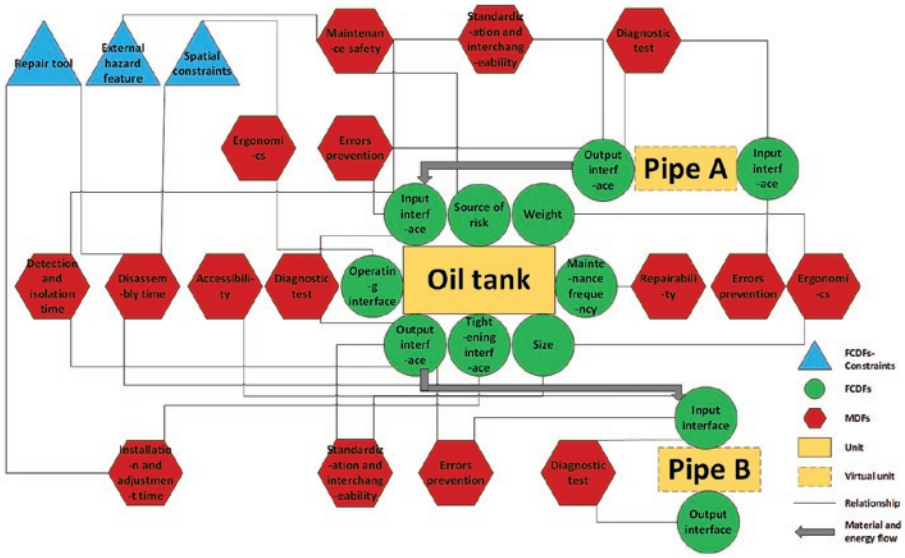

Fig. 5. Correlative relationship model of the oil tank

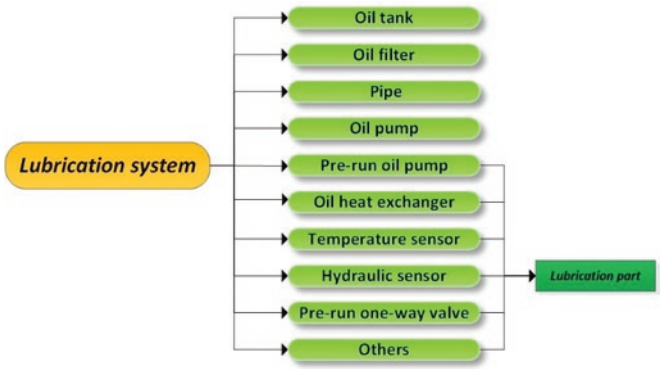

Fig. 6. Unit structure of a lubrication system

in Fig. 5. The main FCDFs of the oil tank related to the MDFs are the input interface, source of risk, weight, maintainability frequency, size, tightening interface, output interface, operating interface, repair tools, external hazard features and spatial constraints. Main MDFs and relationships with FCDFs are modelled in the figure. By constructing the model, the relationships are modelled and clear.

At the system level, the unit structure of the system is shown in *Fig. 6*. Units of a lubrication system include an oil tank, oil filter, pipe, oil pump, pre-run oil pump, oil heat exchanger, temperature sensor,

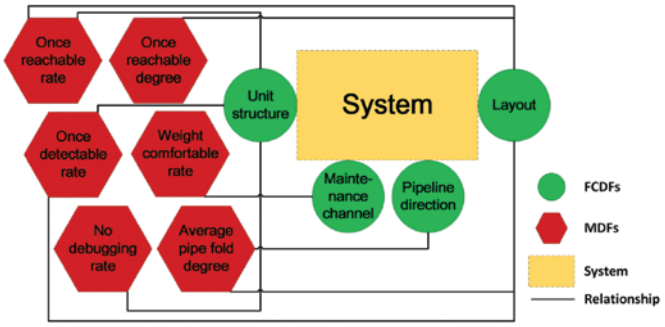

Fig. 7. Correlative relationship model of the lubrication system

hydraulic sensor, pre-run one-way valve and others. The model is built and shown as Fig. 7. The main FCDFs and MDFs of the system are four system level features and six system level evaluation indexes.

3.2. Evaluating importance

By modelling the relationship of MDFs and FCDFs at system and unit levels, the relationships are expressed graphically and clearly. To evaluate the importance of factors, three tables are provided to collect original scoring data shown as Table 6, Table 7 and Table 8. According to the approach, the three tables are filled by more than 20 experts and designers. Each sample obtained from the experts and designers is independent. Therefore, the average value of these data samples is obtained to construct the QM and shown as the Table 6, Table 7 and Table 8. The results in Table 6 and Table 7 are the importance of the relationship between MDFs and FCDFs at the unit level. The results in Table 8 are the importance of the relationships at the system level.

Three quantification matrixes are constructed and represent the importance relationships of quantitative MDFs and FCDFs at the unit level, qualitative MDFs and FCDFs at the unit level, and MDFs and FCDFs at the system level. Applying the importance evaluation method described in section 2.3 to these three matrixes, six IDMs are obtained and shown as *Fig. 8*, *Fig. 9* and *Fig. 10*.

1) Importance degree of relationship between quantitative MDFs and FCDFs at the unit level

For relationships between quantitative MDFs and FCDFs at the unit level, the evaluation results can be found in *Fig. 8*. As shown in the figure, in terms of importance degree of FCDFs to quantitative MDFs, tightening interface and repair tool are the two most important FCDFs; the corresponding importance degrees reach 0.556 and 0.5, which indicates when designing the oil tank, tightening interface and repair tool are the two most important FCDFs and warrant further investigation. For quantitative MDFs to FCDFs, disassembly time and installation and adjustment time are the two most influential quantitative MDFs; the corresponding importance degrees are both 0.484.

From engineering experience there are many maintenance problems n tightening interfaces of an oil tank, which is the oil supply device of lubrication system. Because several interfaces exist, a number of maintenance activities and time are spent in tightening interfaces on the oil tank. Therefore, tightening interface and repair tool are the two most influential factors for maintenance time. The oil tank is regarded as a line replaceable unit, most maintenance operations are disassembly, installation and adjustment. Consequently, among qualitative MDFs, disassembly time and installation and adjustment time are the two most important factors.

2) Importance degree of relationship between qualitative MDFs and FCDFs at the unit level

For relationships of qualitative MDFs and FCDFs at the unit level, the evaluation results can be found in *Fig. 9*. As shown in the figure, for qualitative MDFs, input interface and output interface are the two most important FCDFs; the importance degrees are both 0.528. For FCDFs, ergonomics is the most important qualitative MDF, and the importance degree is 0.532.

From engineering experience, input and output interfaces are important parts of regular preventive maintenance work and require frequent routine maintenance. If input and output interfaces are leaking or clogged, the lubrication system will not work normally. In the design phase, designers should focus on input and output interfaces. Ergonomics reflects the interaction between people and product, which is one of the most important factors. At the beginning of the product functional construction design, the designer should take maintenance personnel into account, providing convenient maintenance conditions, such as comfortable posture and appropriate loads for maintenance

Table 6. Unit importance of the relationship between quantitative MDFs and FCDFs

FCDFs \ Maintainability quantitative factors			Preparation time	Detection and isolation time	Disassembly time	Replacement time	Installation and adjustment time	Test and recovery time
Oil tank	Attribute class	Size	3	3	5	2	5	2
		Weight	2	3	4	3	4	3
		Source of risk	2	3	4	2	4	2
		Maintenance frequency	3	2	3	2	3	3
	Interface class	Tightening interface	4	4	8	3	8	3
		Operating interface	3	2	6	2	4	3
		Warning interface	3	2	4	2	2	4
		Grip interface	2	3	3	3	3	5
		Input interface	2	7	2	1	3	2
		Output interface	2	7	2	1	3	2
	Constraint class	Repair tool	3	3	8	2	8	3
		Spatial constraint	3	2	7	2	6	2
		External hazard feature	4	2	2	3	4	1
		Space and physical environment	5	1	3	3	4	1

Note: 1 indicates little correlation; 3 indicates a certain correlation; 5 indicates a strong correlation; 7 indicates stronger correlation; 9 indicates the strongest correlation; 2, 4, 6, 8 are the scaling values corresponding to the intermediate states between the two adjacent numerical judgements.

Table 7. Unit importance of the relationship between qualitative MDFs and FCDFs

FCDFs \ Maintainability qualitative factors			Accessibility	Ergonomics	Simplified design	Standardization and interchangeability	Errors prevention	Maintenance safety	Diagnostic test	Reparability
Oil tank	Attribute class	Size	7	8	2	2	2	2	1	2
		Weight	2	9	3	2	2	2	2	2
		Source of risk	3	3	3	3	2	8	3	3
		Maintenance frequency	4	2	2	2	1	3	2	9
	Interface class	Tightening interface	4	1	1	4	2	2	3	4
		Operating interface	2	8	1	4	3	2	2	3
		Warning interface	2	5	1	4	4	1	1	2
		Grip interface	3	4	2	3	5	2	1	4
		Input interface	2	3	4	8	7	2	8	4
		Output interface	2	3	4	8	7	2	8	4
	Constraint class	Repair tool	8	6	2	4	4	3	2	5
		Spatial constraint	6	8	4	4	3	1	3	5
		External hazard feature	2	3	1	3	3	7	2	3
		Space and physical environment	2	4	1	2	3	2	1	3

Note: 1 indicates little correlation; 3 indicates a certain correlation; 5 indicates a strong correlation; 7 indicates stronger correlation; 9 indicates the strongest correlation; 2, 4, 6, 8 are the scaling values corresponding to the intermediate states between the two adjacent numerical judgements.

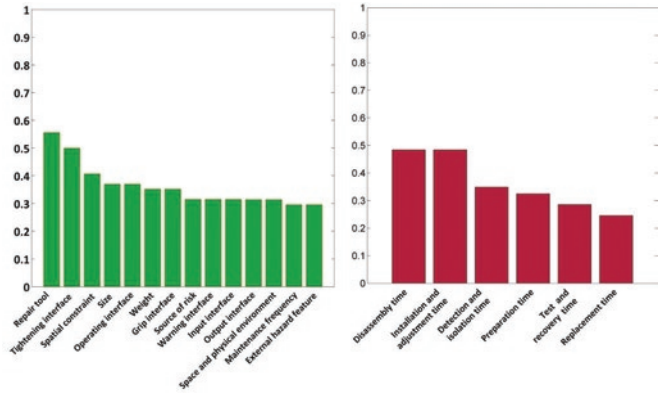

Fig. 8. Importance degree of relationship between quantitative

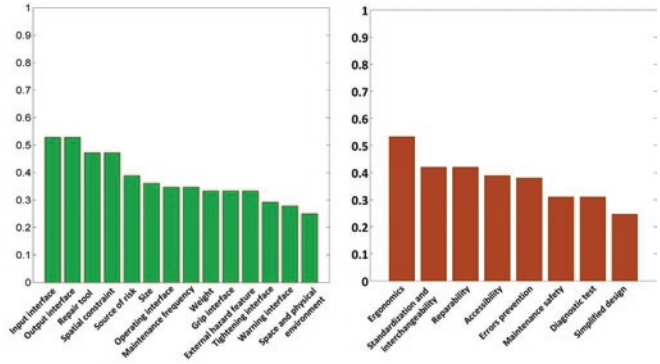

Fig. 9. Importance degree of relationships between qualitative MDFs and FCDFs at the unit level

personal. Design considerations should focus on ergonomics when designing functional structures of products at the unit level.

3) Importance degree of relationship between MDFs and FCDFs at the system level

For relationships of MDFs and FCDFs at the system level, the evaluation results are shown in *Fig. 10*. For MDFs, the importance degrees of layout, unit structure, maintenance channel, and pipe line direction are 0.704, 0.593, 0.5 and 0.426. For FCDFs, the most important MDF is average pipe fold degree where the importance degree is 0.722. Therefore, when designing products at the system level, layout and average pipe fold degree are the most important FCDF and MDF.

From engineering experience and collected data, because there are various units in the lubrication system, the layout of units impacts the maintenance space, accessibility, detectable rate and specific maintenance process. For systems, efficient layout can reduce maintenance cost. Therefore, layout is the most important FCDF considering product maintainability. Because of different types of pipes and lines in the system, the average pipe fold degree is vulnerable to product design

Table 8. System importance of the relationship between MDFs and FCDFs

FCDFs		System level MDFs					
		Once reachable rate	Once reachable degree	Once detectable rate	Weight comfortable rate	No debugging rate	Average pipe fold degree
Lubrication system	Layout	8	7	7	4	4	8
	Pipeline direction	2	3	3	3	3	9
	Unit structure	7	2	8	3	7	5
	Maintenance channel	5	3	3	7	5	4

Note: 1 indicates little correlation; 3 indicates a certain correlation; 5 indicates a strong correlation; 7 indicates stronger correlation; 9 indicates the strongest correlation; 2, 4, 6, 8 are the scaling values corresponding to the intermediate states between the two adjacent numerical judgements.

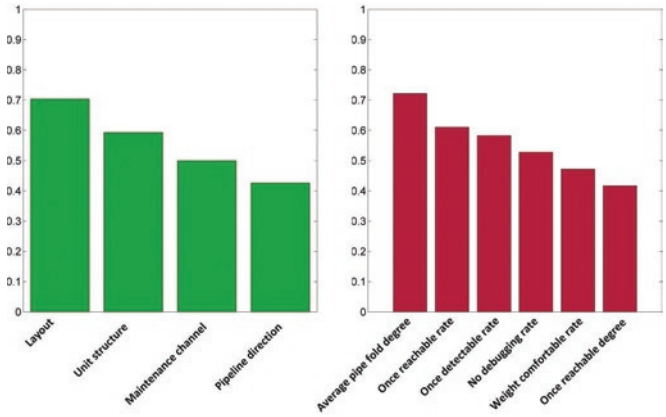

Fig. 10. Importance degree of relationship between MDFs and FCDFs at the system level

of function and construction. Practically, the factor of average pipe fold degree affects most functional construction design of products.

The results obtained by the proposed method are consistent with engineering practice, which validates the effectiveness and feasibility of the proposed method. Through this design approach, maintenance design guidance can be provided for designers early in the design stage.

4. Conclusions

To improve product quality level, maintainability should be designed and related with function and construction at the design stage. To achieve this purpose, the paper proposes a design approach based on correlative relationships between maintainability and functional construction. The primary innovations of this paper are the following: (1) design requirements and characteristics of maintainability and functional construction are defined and classified into MDFs and FCDFs at the system and unit level; (2) a relationship model of maintainability and functional construction is proposed by combining the MDFs and FCDFs based on topography theory; (3) to provide quantitative suggestions on design, an importance evaluation is developed based on a QM and the relationship model.

An engineering application is studied by applying the approach to the design of the lubrication system of an armoured vehicle. Compared with engineering experience and practical data, the results obtained by the proposed approach are useful and effective and can be useful quantitative guides for design of product maintainability and functional construction. The proposed approach overcomes the lagging problem of maintainability design and enriches the integrated design of product maintainability and functional construction.

Although integrated design of maintainability and functional construction is important, there is little peer-reviewed literature or work conducted on this issue. Therefore, the proposed approach cannot be validated by comparison to other methods. In addition, due to confidentiality of the data, details on the product in the case cannot be provided. Future efforts will be on approach improvements and extension of applications.

References

1. Ali A, Chen X, Yang Z, Lee J, and Ni J. Optimized maintenance design for manufacturing performance improvement using simulation. Winter Simulation Conference 2008; 1811-1819, https://doi.org/10.1109/WSC.2008.4736270.
2. Baidya R, Dey P K, Ghosh S K, and Petridis K. Strategic maintenance technique selection using combined quality function deployment, the analytic hierarchy process and the benefit of doubt approach. International Journal of Advanced Manufacturing Technology 2016: 1-14, https://doi.org/10.1007/s00170-016-9540-1.
3. Barabadi A, Garmabaki A H S, Yuan F, and Lu J. Maintainability analysis of equipment using point process models. in IEEE International Conference on Industrial Engineering and Engineering Management 2016: 797-801.
4. Bohlin M, Forsgren M, Holst A, Levin B, Aronsson M, and Steinert R. Reducing vehicle maintenance using condition monitoring and dynamic planning. in Iet International Conference on Railway Condition Monitoring 2008: 1-6, https://doi.org/10.1049/ic:20080329.
5. Chang L, Du E X, Zhang C L, and Tang X X. Reliability and maintainability analysis of vehicle anti-tank missile. in International Conference on Quality, Reliability, Risk, Maintenance, and Safety Engineering 2012: 1400-1402, https://doi.org/10.1109/ICQR2MSE.2012.6246483.
6. Coulibaly A, Houssin R, and Mutel B. Maintainability and safety indicators at design stage for mechanical products. Computers in Industry 2008; 59(5): 438-449, https://doi.org/10.1016/j.compind.2007.12.006.
7. Da X U, Chuang L I, Jiao Q, and Yang L I. Research on the comprehensive evaluation of equipment maintainability qualitative index based on VIKOR. Manufacturing Technology & Machine Tool 2014: 9.
8. Deloux E, Castanier B, and Berenguer C. Maintenance policy for a non-stationary deteriorating system. Annual Reliability & Maintainability Symposium 2008: 496-501, https://doi.org/10.1109/RAMS.2008.4925846.
9. Dohi T, Kaio N, and Osaki S. A new graphical method to estimate the optimal repair-time limit with incomplete repair and discounting . Computers & Mathematics with Applications 2003; 46(46): 999–1007, https://doi.org/10.1016/S0898-1221(03)90114-3.
10. Ertas, M W, Smith, Tate, W D , Lawson, T B, Baturalp. Complexity of system maintainability analysis based on the interpretive structural modeling methodology: transdisciplinary approach 2016; 25(2): 254-268.
11. Guo L. The research of equipment maintainability forecasts methods based on support vector machine. in Chinese Automation Congress 2016: 486-488.
12. Jardine A K S and Tsang A H C. Maintenance, replacement, and reliability : theory and applications. CRC Press, Taylor & Francis 2013.
13. Jia Q S. Engine maintenance policy optimization with succinct value function representation. in Asian Control Conference, 2009. Ascc 2009: 1548-1553.
14. Khandelwal D, Sharma J, and Ray L. Optimal periodic maintenance of a machine. IEEE Transactions on Automatic Control 1979; 24(3): 513-513, https://doi.org/10.1109/TAC.1979.1102068.
15. Li Q, Huang D, Wang F, Zheng Y, Li J, and Yan D. Analysis of the equipment maintainability qualitative evaluation index based on interpretive structure modeling. in International Conference on Fuzzy Systems and Knowledge Discovery 2016; 649-653.

16. Liu W and Shui-Jun Y U. Study on Decision Support System for Electronic Armament's Maintenance Structure. Computer Simulation 2006; 23(1): 5-3.
17. Lu Z, Zhou J, and Li N. Maintainability fuzzy evaluation based on maintenance task virtual simulation for aircraft system 2015; 17(4): 504-512.
18. Luo X, Yang Y, Ge Z, Wen X, and Guan F. Fuzzy grey relational analysis of design factors influencing on maintainability indices. Archive Proceedings of the Institution of Mechanical Engineers Part E Journal of Process Mechanical Engineering. Part E: Journal of Process Mechanical Engineering 2015; 229(1): 78-84, https://doi.org/10.1177/0954408914522616.
19. Mazurkiewicz D. Computer-aided maintenance and reliability management systems for conveyor belts. Eksploatacja i Niezawodnosc - Maintenance and Reliability 2014; 16(3): 377-382.
20. Nakagawa T. Maintenance Theory of Reliability. Springer London. 2005.
21. Peng W, Huang H Z, Zhang X, Liu Y, and Li Y. Reliability based optimal preventive maintenance policy of series-parallel systems. Eksploatacja i Niezawodnosc - Maintenance and Reliability 2009; 42(2): 4-7.
22. Saxena A, Wu B, and Vachtsevanos G. A hybrid reasoning architecture for fleet vehicle maintenance. Instrumentation & Measurement Magazine IEEE 2006; 9(4): 29-36, https://doi.org/10.1109/MIM.2006.1664039.
23. Senivongse T and Puapolthep A. A Maintainability Assessment Model for Service-Oriented Systems. Proceedings of the World Congress on Engineering and Computer Science 2015: 1.
24. Stjepandić J, Wognum N and Verhagen W J C. Concurrent Engineering in the 21st century. Foundations, developments and challenges. Cham [Switzerland]: Springer, 2015.
25. Yang Y. Maintainability-based facility layout optimum design of ship cabin. International Journal of Production Research 2015; 53(3): 677-694, https://doi.org/10.1080/00207543.2014.919416.
26. Yau S S and Collofello J S. Some stability measures for software maintenance. in Computer Software and Applications Conference, 1979. Proceedings. COMPSAC 79. The IEEE Computer Society's Third International 2002; 6: 545-552.
27. Yin Y, Wu W H, Cheng T C E, and Wu C C. Due-date assignment and single-machine scheduling with generalised position-dependent deteriorating jobs and deteriorating multi-maintenance activities. International Journal of Production Research 2014; 52(8): 2311-2326, https://doi.org/10.1080/00207543.2013.855833.
28. Zhen F, Univ X, and An X. Maintenance Design for Product Level Reuse Based on House of Quality. Computer Integrated Manufacturing Systems 2004; 10(4): 476-480.
29. Zhou D, Jia X, Lv C, and Li Y. Maintainability allocation method based on time characteristics for complex equipment. Eksploatacja i Niezawodnosc - Maintenance and Reliability 2013; 15(4): 441-448.
30. Zhou D, Wang M H, Guo Z Q, and Lv C. Maintenance Simulation and Maintainability Design Based on Virtual Reality. Key Engineering Materials 2011; 467: 457-461, https://doi.org/10.4028/www.scientific.net/KEM.467-469.457.
31. Zhou H, Gan M Z, Liu A Q, and Liu J M. Maintainability design of product based on concurrent engineering. Journal of Machine Design 2003; 20(9): 3-5.

Chunhui GUO
Chuan LYU
Jiayu CHEN
Dong ZHOU
School of Reliability and Systems Engineering, Beihang University
State Key Laboratory of Virtual Reality Technology and Systems, Beihang University
Science and Technology on Reliability and Environmental Engineering Laboratory, Beihang University
No. 37 Xueyuan Road, Haidian District, Beijing, China, 100191

E-mails: guochunhui@buaa.edu.cn, lc@buaa.edu.cn, chenjiayu@buaa.edu.cn, zhoudong@buaa.edu.cn

Article citation info:
KNOPIK L, MIGAWA K. Multi-state model of maintenance policy. Eksploatacja i Niezawodnosc – Maintenance and Reliability 2018; 20 (1): 125–130, http://dx.doi.org/10.17531/ein.2018.1.16.

Leszek KNOPIK
Klaudiusz MIGAWA

MULTI-STATE MODEL OF MAINTENANCE POLICY

WIELOSTANOWY MODEL DECYZJI EKSPLOATACYJNYCH*

Preventive replacement is applied to improve the device availability or increase the profit per unit time of the maintenance system. In this paper, we study age-replacement model of technical object for n-state system model. The criteria function applied in this paper describe profit per unit time or coefficient of availability. The probability distribution of a unit's failure time is assumed to be known, and preventive replacement strategy will be used over very long period of time. We investigate the problem of maximization of profit per unit time and coefficient availability for increasing the failure rate function of the lifetime and for a wider class of lifetime. The purpose of this paper is to obtain conditions under which the profit per unit time approaches a maximum. In this paper we shows that the criteria function (profit per unit time or coefficient availability) can be expressed using the matrix calculation method. Finally, a numerical example to evaluate an optimal replacement age is presented.

Keywords: maintenance, preventive replacement, profit per unit time, availability, lifetime distribution, failure rate function, IFR class, MTFR class.

Wymiany prewencyjne stosuje się w celu podnoszenia gotowości systemów eksploatacji maszyn i wzrostu dochodu na jednostkę czasu systemu eksploatacji. W pracy analizuje się model wymian obiektów technicznych według wieku dla n-stanowego systemu. Funkcja kryterialna stosowana w pracy wyraża zysk przypadający na jednostkę czasu lub współczynnik gotowości. Zakłada się, że rozkład prawdopodobieństwa czasu do uszkodzenia obiektu technicznego jest znany i strategia wymian prewencyjnych będzie stosowana na długim przedziale czasowym. Bada się problem maksymalizacji zysku na jednostkę czasu i współczynnika gotowości dla rosnącej funkcji intensywności uszkodzeń lub funkcji intensywności z szerszej klasy. Celem tej pracy jest sformułowanie warunków, przy których zysk na jednostkę czasu osiąga maksimum. W pracy pokazano, że badaną funkcję kryterialną (zysk na jednostkę czasu lub współczynnik gotowości) można wyrazić za pomocą metod rachunku macierzowego. Na końcu pracy przedstawiono przykład numeryczny oceny optymalnego wieku wymiany dla rzeczywistego procesu eksploatacji.

***Słowa kluczowe**: utrzymanie, wymiana prewencyjna, zysk na jednostkę czasu, gotowość, rozkład czasu życia, funkcja intensywności uszkodzeń, klasa IFR, klasa MTFR.*

1. Introduction

Industrial system management requires implementation of various operational activities. The crucial tasks in which the role of economic optimization will increase include maintaining the operation system as well as the replacement of technical objects. Maintenance and replacement are not only technical issues but also an economic problem. Maintenance strategy is focused mostly on preventive maintenance mainly in the area of operational research and management studies. Age replacement strategy for technical objects implies preventive replacement of the object when it reaches age T or corrective (failure) replacement before it reaches age T. Preventive replacements are less expansive and cheaper than the corrective ones. It is known that the time of preventive replacement is usually shorter than the time of corrective replacement. Fundamental facts for age replacements are included in papers [2, 3]. A review of results connected with preventive replacements is to be found in papers [5, 21, 24]. Certain generalizations of the question of preventive replacements were arrived at in papers [12, 13]. Much later, methods of preventive replacements for multistate systems were analyzed. Testing multistate systems was introduced in [14-19, 25-26]. The article [7] uses fuzzy variables (fuzzy sets), while paper [22] examines multistate systems with components requiring minimal repair. Using simulation methods for testing preventive renewals was presented in paper [20]. This paper examines operation systems in which the technical object may at a given moment appear in one of the n states. For such systems optimal preventive replacements basing on the criteria function expressing the profit per time unit or availability coefficient. The structure of criteria function is based on the values of semi-Markov process [6, 9], as opposed to the classic approach based on the theory of renewal. The most quoted work in defining the criteria function based on the elements of renewal theory is paper [23]. The paper includes an analysis of sufficient conditions for existing of maximum profit per time unit and maximum asymptotic coefficient of availability of n-state operation system. Values of criteria function depend on the lifetime distribution, the mean value of preventive replacement time, mean repair time value, mean values of remaining at other states, profits per time unit, transition probability matrixes embedded in the semi-Markov process of Markov chain.

In Chapter 2, the basic markings and assumptions used in the paper were presented. In Chapter 3 a model of technical object operation was prepared and the criteria function defining the profit per time unit at infinite time horizon was created. The crucial goal of this chapter is to introduce into the research criteria function in matrix form. In Chapter 4 sufficient conditions for occurrence of maximum profit per unit are analyzed, as well as asymptotic availability factor. Conditions for occurrence of extreme criteria function were formulated for the class of distributions with increasing failure rate function (IFR) as well as for a wider class introduced by one of the authors of the class (MTFR). Numerical example of the optimization of the maintenance system was analyzed in Chapter 5. In the example it was asserted that

(*) Tekst artykułu w polskiej wersji językowej dostępny w elektronicznym wydaniu kwartalnika na stronie ***www.ein.org.pl***

the lifetime of technological object has Weibull distribution. Data for this example were obtained from an existing municipal bus operation process.

2. Markings and assumptions included in the paper

The paper will examine semi-Markov model of preventive age replacement. An n-state semi-Markov process X(t) is considered with the space of states S = {1, 2, …, n}. If X(t) = i, then the considered technical object at moment t is at state i. It is asserted that 1 is the state of failure-free functioning, 2 is the state of repair, n is the state of preventive replacement, while remaining states i, where $2 \le i \le n-1$ are other states of system maintenance.

By z_i, i = 1, 2, …, n, profit per unit is marked per state i. The paper assumes that $z_1 > 0$, $z_i \le 0$ for $2 \le i \le n$. If the technical object is in state 1, it brings profit, while if technical object is in state i, where $2 \le i \le n$, then technological object generates loss.

It is assumed that $\tau_0 < \tau_1 < \tau_2 < ... < \tau_k < ...$ are leap moments and $v_k < \tau_k - \tau_{k-1}$ for $k \ge 1$, $v_0 = 0$ are times of remaining at states of process X(t). The semi-Markov process is fully defined if the initial distribution is known:

$$P\{X(0)=i\}=p_i^{(0)},\ \ i=1,2,...,n$$

and its semi-Markov kernel defined by matrix:

$$Q(t)=\left[Q_{ij}(t)\right],\ \ i,j=1,2,...,n,$$

where:

$$Q_{ij}(t)=P\left\{X(\tau_{k+1})=j,\tau_{k+1}-\tau_k<t\middle|X(\tau_k)=i\right\},\ i,j=1,2,...,n$$

Sequence $X(\tau_k),\ k \in N$ of random variables is Markov chain with transition probability matrix:

$$P=\left[p_{ij}\right]=\left[Q_{ij}(\infty)\right]\ \ for\ \ i,j=1,2,...,n$$

is called embedded Markov chain. Random variables T_i, i = 1, 2, …, n stand for times of remaining in the state and have distribution functions in the form of:

$$F_i(t)=P\{T_i<t\}=P\left\{\tau_{k+1}-\tau_k<t\middle|X(\tau_k)=j\right\}$$

or otherwise:

$$F_i(t)=\sum_{j=1}^{n}Q_{ij}(t),\ \ i=1,2,...,n\,. \tag{1}$$

Distribution function of remaining at state i, before moving to state j, is defined as follows:

$$F_{ij}(t)=P\left\{\tau_{k+1}-\tau_k<t\middle|X(\tau_{k+1})=j,\ \ X(\tau_k)=i\right\},\ \ for\ i,j=1,2,...,n,k\in N. \tag{2}$$

For distribution function $F_{1i}(x)$ defined by formula (2) it is assumed that $F_{1i}(x)=F_1(x)$ exists for i = 2, 3, 4, …, n. While constructing criteria function, the limit theorem is used for finite semi-Markov processes [6, 8]. It is assumed that mean values ET_i, i = 1, 2, …, n are finite, positive and Markov chain $X(\tau_k),\ k=0,1,2,...$, has one ergodic class. These assumptions allow one to formulate limit theorem of the form:

$$P_j=\lim_{t\to\infty}P\{X(t)=j\}=\lim_{t\to\infty}P\{X(t)=j\mid X(0)=i\}\ \ for\ \ i=1,2,...,n,$$

where:

$$P_j=\frac{p_j^*ET_j}{\sum_{k=1}^{n}p_k^*ET_k}, \tag{3}$$

where $p_j^*,\ j=0,1,2,...,n$ is a limit distribution of embedded Markov chain $X(\tau_k)$, where $k \in N$ with transition probability matrix $P=\left[p_{ij}\right]$, where $p_{ij}=Q_{ij}(\infty),\ i,j=0,1,2,...,n$. Limit probabilities $p_j^*,\ j=0,1,2,...,n$ are a solution for a system of linear equations:

$\sum_{i=1}^{n}p_i^*p_{ij}=p_j^*$ with condition $\sum_{i=1}^{n}p_i^*=1$, where i, j = 1, 2, …, n.

3. Criteria function

Let X(t) be semi-Markov process with continuous kernel Q(t). The counting process is defined:

$$K_j(t)=\int_0^t I\{X(u)=j\}du\ ,$$

Where I is an indicator determined as follows:

$$I\{X(u)=j\}=\begin{cases}1 & for\ \ X(u)=j,\\ 0 & for\ \ X(u)\ne j.\end{cases}$$

It is total time of remaining of process X(t) at state i as well as in interval [0, t]. The value:

$$L(t)=\sum_{i=1}^{n}z_iEK_i(t)$$

is the expected profit per time unit in interval [0, t]. The limit:

$$L=\lim_{t\to\infty}\frac{L(t)}{t}$$

is the expected profit per time unit for infinite time interval. The limit

is the basis for building criteria function. From the definition of the process $K_j(t)$, j = 1, 2, …, n, it is:

$$\lim_{t\to\infty}\frac{EK_j(t)}{t}=P_j,\ \text{j=1, 2, …, n,}$$

thus:

$$L=\sum_{i=1}^{n}z_iP_i.$$

According to (3) the following is true:

$$L=\frac{\sum_{i=1}^{n}z_ip_i^*ET_i}{\sum_{i=1}^{n}p_i^*ET_i}. \tag{4}$$

The unit is replacement at age T or when it failed, whichever comes first. $T_1(x)$ defines the time of replacement or failure. Variable $T_1(x)$ may be written as:

$$T_1(x)=\begin{cases}T_1, & if \quad T_1<x,\\ x, & if \quad T_1\geq x.\end{cases} \tag{5}$$

Using formula (5), a semi-Markov process is obtained with transition probability matrix P(x) of embedded Markov chain. Elements of the first verse of matrix P(x) depend on x. For $p_{1n}(x)$ is:

$$p_{1n}(x) = P\{X(\tau_{k+1}) = n \mid X(\tau_k) = 1\} =$$
$$P\{X(\tau_{k+1}) = n \mid X(\tau_k) = 1, T_1< x\}\ P\{T_1 < x \mid X(\tau_k) = 1\} +$$
$$P\{X(\tau_{k+1}) = n \mid X(\tau_k) = 1, T_1 \geq x\}\ P\{T_1 \geq x \mid X(\tau_k) = 1\}.$$

For (5), the following is true:

$$P\ \{X(\tau_{k+1}) = n \mid X(\tau_k) = 1, T_1 \geq x\} = 1.$$

Using qualities of conditional probability, the following is obtained:

$$P\{X(\tau_{k+1}) = n \mid X(\tau_k) = 1, T_1< x\}$$

$$P\{X(\tau_{k+1}) = n, T_1< x \mid X(\tau_k) = 1\}/ P\{T_1 < x \mid X(\tau_k) = 1\} = Q_{1n}(x) / F_1(x),$$

thus:

$$p_{1n}(x) = Q_{1n}(x) + R_1(x)\ \text{, where } R_1(x) = 1 - F_1(x).$$

For (2), the following is true:

$$p_{1n}(x) = p_{1n}F_{1n}(x) + R_1(x).$$

Similarly, for probability $p_{1i}(x)$ where $2 \leq i \leq n - 1$, the following is true:

$$p_{1i}(x) = P\{X(\tau_{k+1}) = i \mid X(\tau_k) = 1\} =$$
$$P\{X(\tau_{k+1}) = i \mid X(\tau_k) = 1, T_1< x\}\ P\{T_1 < x \mid X(\tau_k) = 1\} +$$
$$P\{X(\tau_{k+1}) = i \mid X(\tau_k) = 1, T_1 \geq x\}\ P\{T_1 \geq x \mid X(\tau_k) = 1\}.$$

Definition (5) concludes in:

$$P\{X(\tau_{k+1}) = i \mid X(\tau_k) = 1, T_1 \geq x\} = 0,$$

which results in:

$$P\{X(\tau_{k+1}) = i \mid X(\tau_k) = 1, T_1< x\} = Q_{1i}(x) / F_1(x)$$

as well as:

$$p_{1i}(x) = Q_{1i}(x) = p_{1i}F_{1i}(x) \text{ for } i = 2, 3, \ldots, n-1.$$

Now, the matrix P(x) of transition probabilities is as follows:

$$P(x)=\begin{bmatrix}0 & p_{12}F_{12}(x) & p_{13}F_{13}(x) & \ldots & p_{1n}F_{1n}(x)+R_1(x)\\ p_{21} & 0 & p_{23} & \ldots & p_{2n}\\ p_{31} & p_{32} & 0 & \ldots & p_{3n}\\ \ldots & \ldots & \ldots & \ldots & \ldots\\ p_{n1} & p_{n2} & p_{n3} & \ldots & 0\end{bmatrix}.$$

On the basis of (4), criteria function may be written in the form:

$$g(x)=\frac{ET_1(x)z_1p_1^*(x)+\sum_{i=2}^{n}ET_iz_ip_i^*(x)}{ET_1(x)p_1^*(x)+\sum_{i=2}^{n}ET_ip_i^*(x)}, \tag{6}$$

where $p_i^*(x)$, i = 1, 2, …, n are limit probabilities of Markov chain with transition matrix P(x), while $ET_1(x)$ is the value of mean random variable $T_1(x)$. Mean value $ET_1(x)$ is calculated from the formula:

$$ET_1(x)=\int_0^x dF_1(t)+xP\{T_1\geq x\}.$$

Integration by parts results in:

$$ET_1(x)=\int_0^x R_1(t)dt. \tag{7}$$

Limit probabilities $p_i^*(x)$, i = 1, 2, …, n meet the following system of linear equations:

$$\begin{bmatrix}-1 & p_{21} & p_{31} & \ldots & p_{n1}\\ p_{12}F_{12}(x) & -1 & p_{32} & \ldots & p_{n2}\\ p_{13}F_{13}(x) & p_{23} & -1 & \ldots & p_{n3}\\ \ldots & \ldots & \ldots & \ldots & \ldots\\ p_{1n}F_{1n}(x)+R(x) & p_{2n} & p_{3n} & \ldots & -1\end{bmatrix}\begin{bmatrix}p_1^*(x)\\ p_2^*(x)\\ p_3^*(x)\\ \ldots\\ p_n^*(x)\end{bmatrix}=\begin{bmatrix}0\\0\\0\\ \ldots\\0\end{bmatrix}. \tag{8}$$

The system of equations is homogenous and has infinite number of solutions. Replacing the last equation of system (8) with normalization condition of the form:

$$\sum_{i=1}^{n}p_i^*(x)=1, \tag{9}$$

the system of linear equations has the form:

$$\begin{bmatrix} -1 & p_{21} & p_{31} & \dots & p_{n1} \\ p_{12}F_{12}(x) & -1 & p_{32} & \dots & p_{n2} \\ p_{13}F_{13}(x) & p_{31} & -1 & \dots & p_{n3} \\ \dots & \dots & \dots & \dots & \dots \\ 1 & 1 & 1 & \dots & 1 \end{bmatrix} \begin{bmatrix} p_1^*(x) \\ p_2^*(x) \\ p_3^*(x) \\ \dots \\ p_n^*(x) \end{bmatrix} = \begin{bmatrix} 0 \\ 0 \\ 0 \\ \dots \\ 1 \end{bmatrix}. \quad (10)$$

The $u_i(x)$ marks algebraic completion of i-th one in n-th verse of the matrix of the equation system (10). Taking into consideration the right side of the system (10), the solution of the system has the form $p_i^*(x) = u_i(x) / W(x)$ where W(x) is the determinant of the system (10). Embedding $u_i(x)$ in formula (6) instead of $p_i^*(x)$, the criteria function (6) does not change its value. From determinant value, the numerator of criteria function (6) may be written as:

$$L(x; z_1, z_2, \dots, z_n) = \begin{vmatrix} -1 & p_{21} & p_{31} & \dots & p_{n1} \\ p_{12}(x) & -1 & p_{32} & \dots & p_{n2} \\ p_{13}(x) & p_{23} & -1 & \dots & p_{n3} \\ \dots & \dots & \dots & \dots & \dots \\ z_1ET_1(x) & z_2ET_2 & z_3ET_3 & \dots & z_nET_n \end{vmatrix}. \quad (11)$$

Denominator M(x) of criteria function (6) is expressed as: M(x) = L(x; 1, 1, …, 1). For the formula (11), the following is true that the criteria function (6) may now be written as coefficient of determinants

$$g(x) = L(x; z_1, z_2, \dots, z_n) / L(x; 1, 1, \dots, 1). \quad (12)$$

The latter equation is an important result of the work. Representation of criteria function g(x) in the form of (12) makes it possible to calculate the value of function without determining limit probabilities $p_i^*(x)$. In paper [9] the criteria function g(x) is expressed in the form (6). The A_1 means algebraic completion of element $z_1ET_1(x)$. It is known that A_1 does not depend on x, z_2, z_3, …, z_n. $D_i(x)$ denotes the algebraic completion of i-th one in matrix of equation system (10). Limit probability $p_i^*(x)$ is expressed by the formula:

$$p_i^*(x) = D_i(x) / W(x), \quad i = 1, 2, \dots, n, \quad (13)$$

where W(x) is the indicator of the matrix of equation system (10). The matrix obtained from the matrix of the system (10) by crossing out the n-th verse and the n-th column has the dominant diagonal. In this case it means that the sum of the elements of each column, bypassing the element on the diagonal, is lower than 1. On the basis of the qualities of matrix [4] the sing of completion of element z_nET_n may be written in the form of $(-1)^{n-1}$. On the basis of (13) it is concluded that the sign of the determinant W(x) is also equal to $(-1)^{n-1}$. The determinant of completion $D_1(x)$ is the determinant from independent matrix from x, z_1, z_2, …, z_n and the sign of this determinant equals $(-1)^{n-1}$. The numerator and the denominator of the criteria function g(x) given by the formula (13) is multiplied by W(x) $(-1)^{n-1}$. Asserting that the above markings of the criteria function g(x) given in the formula (6) may be written in the form:

$$g(x) = \frac{Az_1ET_1(x) + \sum_{i=2}^{n} z_iET_iE_i(x)}{AET_1(x) + \sum_{i=2}^{n} ET_iE_i(x)}, \quad (14)$$

where $E_i(x) = D_i(x)\,(-1)^{n-1}$, $A = A_1(-1)^{n-1}$. It is now known that for each $x \geq 0$ is $E_i(x) \geq 0$ and $A \geq 0$. From the form of the matrix of equation system (10) it is concluded that $E_i(x)$ is a linear function of the distribution function $F_1(x)$. There exist a continuous G_i i H_i so that $E_i(x) = G_iF_1(x) + H_i$. Embedding x = 0, it is concluded that $H_i \geq 0$.

Assuming that:

$$B_1 = \sum_{i=2}^{n} z_iET_iG_i,\ C_1 = \sum_{i=2}^{n} z_iET_iH_i,\ B = \sum_{i=2}^{n} ET_iG_i,\ C = \sum_{i=2}^{n} ET_iH_i \quad (15)$$

the criteria function (14) may be written as:

$$g(x) = \frac{Az_1ET_1(x) + B_1F_1(x) + C_1}{AET_1(x) + BF_1(x) + C}. \quad (16)$$

It is easy to notice that $g(0) = C_1 / C \leq 0$ as well as $g(\infty) = (A\,z_1ET_1 + B_1 + C_1) / (A\,ET_1 + B + C)$.

4. Sufficient conditions for existing of maximum criteria function

In this subsection of the paper the sufficient conditions are formulated for the occurrence of maximum criteria function assuming that the time to failure T_1 is a random variable of the function of increasing failure rate $\lambda_1(t)$. This fact is written as follows: $T_1 \in$ IFR (Increasing Failure Rate). The second discussed distribution class is the class with unimodal failure rate included in MTFR (Mean Time to Failure or Repair) class. The qualities of MTFR class were examined in detail in papers [1, 10, 11]. Derivative g'(x) of criteria function is expressed by the formula:

$$g'(x) = \{A[B_1 - Bz_1][ET_1(x)f_1(x) - F_1(x)R_1(x)] + R_1(x)A(Cz_1 - C_1) + f_1(x)(B_1C - BC_1)\}/M^2(x),$$

where M(x) is the denominator in formula (16). In conclusion, the derivative g'(x) may be written as:

$$g'(x) = \frac{1}{M^2(x)}(A\alpha r_1(x) + \beta R_1(x) + f_1(x)\gamma), \quad (17)$$

where:

$$\begin{aligned} \alpha &= A(B_1 - Bz_1), \\ \beta &= A(Cz_1 - C_1), \\ \gamma &= B_1C - BC_1, \\ r_1(x) &= ET_1(x)f_1(x) - F_1(x)R_1(x). \end{aligned} \quad (18)$$

At the beginning of Chapter 2 it was asserted that $z_1 > 0$, $z_i \leq 0$ for $2 \leq i \leq n$. This assertion as well as formulas (15), (16), (17) and (18) allow one to formulate conclusions 1 and 2.

Conclusion 1. If $z_1 > 0$, $z_i \leq 0$, $F_{1i}(x) = F_1(x)$ for i = 2, 3, 4, …, n, then inequality $\beta > 0$ is true.

Conclusion 2. If $z_i = z_j$ for $2 \leq i \leq n$, $2 \leq j \leq n$, then $\gamma = 0$.

The theses of conclusions 1 and 2 are very useful while formulating criteria for occurrence of maximum availability rate (conclusions

7 and 8). Below it is assumed that the function of failure rate $\lambda_1(x)$ is continuous for $t \geq 0$.

Conclusion 3. If $T_1 \in$ IFR, $\beta + \gamma f(0^+) > 0$, $\alpha < 0$, $\gamma < 0$, $A\alpha(ET_1 \lambda_1(\infty) - 1) + \beta + \gamma\lambda_1(\infty) < 0$, then the criteria function g(x) reaches exactly one maximum.

Proof. It is assumed that $\lambda_1(\infty)$ is the border of the function $\lambda_1(t)$ with $t \to \infty$ or upper limit of function $\lambda_1(t)$ with $t \to \infty$. Let $s(x) = \alpha r(x) + \beta + \gamma\lambda_1(x)$, where $r(x) = \lambda_1(t)\, ET_1(x) - F(x)$. Formula (17) results in the mark of derivative g'(x) is the same as the mark of function s(x). The assumptions $\alpha < 0$, i $\gamma < 0$ result in the function s(x) is continuous and decreasing from $s(0) = \beta + \gamma f_1(0^+)$ to $s(\infty) = A\alpha(ET_1 \lambda_1(\infty) - 1) + \beta + \gamma\lambda_1(\infty)$. If $s(0) > 0$ and $s(\infty) < 0$, there exists exactly one x_0 so that $s(x_0) = 0$ and $g'(x_0) = 0$. Thus g(x) reaches one maximum.

Conclusion 4. If $T_1 \in$ IFR, $\alpha < 0$, $\beta + \gamma f_1(0^+) < 0$, $\lambda_1(\infty) = \infty$, then the criteria function g(x) reaches exactly one maximum.

Proof. If $\lambda_1(\infty) = \infty$, then $s(\infty) < 0$. Conclusion 3 results in the fact that criteria function g(x) reaches exactly one maximum.

Conclusion 4 results in the following conclusion:

Conclusion 5. If $T_1 \in$ IFR, $\alpha < 0$, $f_1(0^+) = 0$, $\lambda_1(\infty) = \infty$, then the criteria function g(x) reaches exactly one maximum.

Conclusions 3, 4 and 5 include sufficient conditions for occurrence of maximum function g(x) for distributions of times to failure from IFR class. Below, conditions for existing of maximum for MTFR class are formulated.

Definition. Random variable $T_1 \in$ MTFR, if $r_1(x) \geq 0$ for every $x \geq 0$.

MTFR class includes certain random variables with unimodal failure rate functions.

Conclusion 6. Let the time to failure T_1 have a distribution with unimodal failure rate function $\lambda_1(t)$. The equality $T_1 \in$ MTFR is true only when $ET_1 \lambda_1(\infty) \geq 1$.

Replacing $z_1 = 1$, $z_2 = 0$, $z_3 = 0$,…, $z_n = 0$, the criteria function g(x) expresses asymptotic availability coefficient. For the availability coefficient $g(0) = 0$ as well as $g(\infty) = A\, ET_1 / (A\, ET_1 + B + C)$.

Conclusion 7. If $T_1 \in$ IFR, $\alpha < 0$, $\lambda_1(\infty) > (1 - \alpha/\beta) / ET_1$, then the availability coefficient reaches maximum value.

Proof. It is known on the basis of conclusion 2 that for availability coefficient $\gamma = 0$. It results from the fact that function $s(x) = \alpha\, r(x) + \beta$ decreases from $s(0) = \beta > 0$ to $s(\infty) = \alpha\, (ET_1 \lambda_1(\infty) - 1) + \beta < 0$. Function s(x) changes the mark from „+" to „–" exactly once.

Conclusion 8. If $T_1 \in$ MTFR, $\alpha < 0$, $\lambda(t)$ is unimodal, $\lambda_1(\infty) > (1 - \alpha/\beta) / ET_1$, then availability coefficient g(x) reaches maximum value.

Proof. Derivative of function s(t) equals $s'(t) = \lambda'_1(x)\, [\alpha\, ET_1(x) + \gamma]$. If it results from the fact that function $\lambda_1(t)$ is unimodal, then the function s(t) is also unimodal. Paper [9] shows that unimodal nature of function s(x) may be proven without asserting differentiability of function $\lambda_1(t)$. In order for function s(t) to have precisely single zero position it is enough for the following inequalities to be true $s(0) = \beta > 0$ and $s(\infty) < 0$. Condition $s(\infty) < 0$ is equivalent to condition $\lambda_1(\infty) > (1 - \alpha/\beta) / ET_1$.

5. Numeric example

In this chapter, numeric example illustrating results obtained in chapters 3 and 4 are analyzed. An 8-state process of municipal buses operation process is discussed. The following states have been singled out:

S_1 – completion of transport task,
S_2 – repair after failure,
S_3 – preventive replacement (repair),
S_4 – condition control after repair,
S_5 – fuel delivery,
S_6 – service on working day,
S_7 – periodic technical service,
S_8 – stoppage at depot parking space.

It is asserted that time to failure has Weibull distribution with reliability function: $R_1(t) = \exp(-(t/a)^c)$ for a, c > 0, $t \geq 0$. Rate function for this distribution has the form: $\lambda_1(t) = (c/a)\, (x/a)^{c-1}$, $t \geq 0$. Based on the statistic analysis of the data from operation for mean values of remaining at states, the following ratings were obtained: $ET_1 = 8.852$, $ET_2 = 3.619$, $ET_3 = 1.501$, $ET_4 = 0.164$, $ET_5 = 0.096$, $ET_6 = 0.122$, $ET_7 = 3.885$, $ET_8 = 5.659$. Unit profits resulting from working at states of the system were rated as: $z_1 = 4$, $z_2 = -2$, $z_3 = -0.2$, $z_4 = -0.2$, $z_5 = -0.2$, $z_6 = -0.2$, $z_7 = -0.2$, $z_8 = -1$. The rating of transition probability matrix for Markov chain embedded in the process is the following:

$$P = \begin{bmatrix} 0 & 0.239 & 0.104 & 0 & 0.657 & 0 & 0 & 0 \\ 0 & 0 & 0 & 1 & 0 & 0 & 0 & 0 \\ 0 & 0 & 0 & 1 & 0 & 0 & 0 & 0 \\ 0.277 & 0 & 0 & 0 & 0.723 & 0 & 0 & 0 \\ 0 & 0 & 0 & 0 & 0 & 0.982 & 0.178 & 0 \\ 0 & 0 & 0 & 0 & 0 & 0 & 0 & 1 \\ 0.234 & 0 & 0 & 0 & 0 & 0 & 0 & 0.766 \\ 1 & 0 & 0 & 0 & 0 & 0 & 0 & 0 \end{bmatrix}$$

Values of factors A, B, B_1, C and C_1 were calculated using the unmarked factor method. For the values of parameters given above it was calculated: $\alpha = -5.778$, $\beta = 2.400$, $\gamma = -4.133$. For every $c \in \{2, 2.5, 3, 3.5\}$ the value of parameter b was calculated so that $ET_1 = 8.852$. Figure 1 presents charts of profit function per time unit depending on the moment of preventive replacement (repair). Each of the four completions of criteria function reach maximum value.

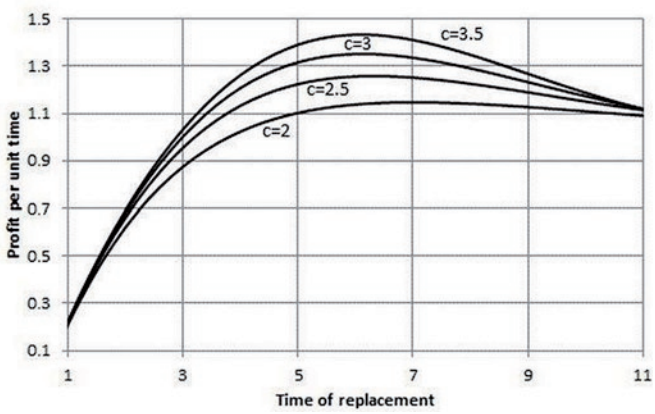

Fig. 1. Graphs of the criteria function g(x) for c {2, 2.5, 3, 3.5}

6. Conclusions

The paper discusses the issue of age replacement of technical objects for multi-state operation systems. The criteria function examined in this paper is the profit per time unit and availability coefficient. The first of the objectives of the article was the matrix representation of the criteria function (formula (12)), while the second was to show

how, with certain general assumptions, it was possible to formulate sufficient conditions for occurrence of the maximum of the criteria function.

References

1. Asha G, Unnikrishanan N N. Reliability properties of means time to failure in age replacement models. International Journal of Reliability, Quality and Safety Engineering 2010; 17(1): 15-26, https://doi.org/10.1142/S0218539310003640.
2. Barlow R E, Hunter L. Optimum preventive maintenance policies. Operations Research 1960; 8: 90-100, https://doi.org/10.1287/opre.8.1.90.
3. Barlow R E, Proschan F. Mathematical theory of reliability. John Wiley & Sons, 1965.
4. Bellman R. Introduction to matrix analysis. New York: McGraw-Hill, 1971.
5. Feldman R M, Valdez-Flores C. Applied probability and stochastic processes. Springer, 2010, https://doi.org/10.1007/978-3-642-05158-6.
6. Grabski F. Semi-markowskie modele niezawodności i eksploatacji [Semi-Markov models of reliability and maintenance]. Warszawa: IBS PAN, 2002.
7. He Q, Zha Y, Zhang R, Sun Q, Liu T. Reliability analysis for multi-state system based on triangular fuzzy variety subset Bayesian networks. Eksploatacja i Niezawodnosc - Maintenance and Reliability 2017; 19(2): 152-165, https://doi.org/10.17531/ein.2017.2.2.
8. Howard O. Dynamic probabilistic system. Vol. 2. Semi-Markov and decision processes. John Wiley, 1971.
9. Knopik L. Metoda wyboru efektywnej strategii eksploatacji obiektów technicznych [Method of selection of strategy of maintenance of technical objects]. Wydawnictwo Uniwersytetu Technologiczno-Przyrodniczego im. Jana i Jędrzeja Śniadeckich w Bydgoszczy, Rozprawy nr 145, 2010.
10. Knopik L. Some results on ageing class. Control and Cybernetics 2005; 34(4): 1175-1180.
11. Knopik L. Characterization of a class of lifetime distributions. Control and Cybernetics 2006; 35(2): 1175-1180.
12. Knopik L, Migawa K. Optimal age-replacement policy for non-repairable technical objects with warranty. Eksploatacja i Niezawodnosc - Maintenance and Reliability 2017; 19(2): 172-178, https://doi.org/10.17531/ein.2017.2.4.
13. Knopik L, Migawa K, Peszyński K, Wawrzyniak S. Some remarks on preventive replacement model. Engineering Mechanics, Institute of Thermomechanics Academy of Sciences of the Czech Republic 2017; 470-473.
14. Lesnianski A, Levitin G. Multi-state system reliability: Assessment, optimization and application. Series on Quality, Reliability and Engineering Statistics Vol. 6, Word Science Publishing, 2003, https://doi.org/10.1142/5221.
15. Levitin G, Lesnianski A. Optimal replacement scheduling in multi-state series-parallel system (short communication). Quality Reliability Engineering International 2000; 16: 157-162, https://doi.org/10.1002/(SICI)1099-1638(200003/04)16:2<157::AID-QRE311>3.0.C O;2-J.
16. Levitin G, Lesnianski A. Structure optimization of multi-state system with two failure mode. Reliability Engineering System Safety 2001; 72: 75-89, https://doi.org/10.1016/S0951-8320(00)00105-8.
17. Liu Y, Huang H Z. Optimal replacement policy for multi-state system under imperfect maintenance. IEEE Transactions on Reliability 2010: 483-495, https://doi.org/10.1109/TR.2010.2051242.
18. Liu Y W, Kapur K C. Reliability measures for dynamic multi-state systems and their applications for system and design and evaluation. IIE Trans. 2006; 38: 511-520, https://doi.org/10.1080/07408170500341288.
19. Liu Y W, Kapur K C. Customer's cumulative experience measures for reliability of non-repairable aging multi-state systems. Quality Technology Quantitative Management 2007; 4: 255-234, https://doi.org/10.1080/16843703.2007.11673147.
20. Masaro MF, Cavalcante CAV. Random preventive maintenance policy based on inspection for multicomponent system using simulation. Eksploatacja i Niezawodnosc - Maintenance and Reliability 2017; 19(4): 552-559, https://doi.org/10.17531/ein.2017.4.8.
21. Nakagawa T. Maintenance theory of reliability. Springer, 2005.
22. Quin J, Niu Y, Li Z. A combined method for reliability analysis multi-state system of minor-repairable components. Eksploatacja i Niezawodnosc - Maintenance and Reliability 2016; 18(1): 80-88, https://doi.org/10.17531/ein.2016.1.11.
23. Ross S M. Introduction to probability models. 9th eds. Elsevier, 2007.
24. Tadj L, Ouali M S, Yacouunt S, Kadi D A. Replacement models with minimal repair. Springer, 2010.
25. Yu L. Optimal replacement policy for multi-state system under imperfect maintenance. IEEE Transactions on Reliability 2010; 59(3): 483-495, https://doi.org/10.1109/TR.2010.2051242
26. Zhang Y L, Yam R C M, Zuo M J. Optimal replacement policy for multistate repairable system. Journal of Operational Research Society 2002; 53: 336-341, https://doi.org/10.1057/palgrave.jors.2601277.

Leszek KNOPIK
Faculty of Management
UTP University of Science and Technology
ul. Fordońska 430, 85-890 Bydgoszcz, Poland

Klaudiusz MIGAWA
Faculty of Mechanical Engineering
UTP University of Science and Technology
al. prof. S. Kaliskiego 7, 85-796 Bydgoszcz, Poland

E-mails: knopikl@utp.edu.pl, klaudiusz.migawa@utp.edu.pl

Article citation info:
STANIK W, JAKÓBIEC J, MAZANEK A. Engine tests for coking and contamination of modern multi-injection injectors of high-pressure fuel supplies compression-ignition engine. Eksploatacja i Niezawodnosc – Maintenance and Reliability 2018; 20 (1): 131–136, http://dx.doi.org/10.17531/ein.2018.1.17.

Winicjusz STANIK
Janusz JAKÓBIEC
Aleksander MAZANEK

ENGINE TESTS FOR COKING AND CONTAMINATION OF MODERN MULTI-INJECTION INJECTORS OF HIGH-PRESSURE FUEL SUPPLIES COMPRESSION-IGNITION ENGINE

BADANIA SILNIKOWE DOTYCZĄCE KOKSOWANIA I ZANIECZYSZCZENIA NOWOCZESNYCH WIELOOTWOROWYCH WTRYSKIWACZY WYSOKOCIŚNIENIOWEGO UKŁADU ZASILANIA PALIWEM SILNIKÓW ZS*

The paper presents the results of engine tests for contamination and coking of modern multi-injection injectors of high-pressure fuel supplies compression-ignition engines. The subject of research is base diesel fuel with 7% (v / v) FAME, and effectiveness of the detergent-dispersant additives plays a key role. The engine tests were performed according to the CEC procedure F-98-08 PSA DW-10, it was essential for the coking and contamination of modern multi-injection injectors of high-pressure fuel supplies compression-ignition engines and for the conclusions.

***Keywords**: engine, injector, fuel, detergent-dispersant additive.*

W pracy przedstawiono wyniki badań silnikowych dotyczących zanieczyszczenia i koksowania nowoczesnych wielootworowych wtryskiwaczy wysokociśnieniowego układu zasilania paliwem silników o zapłonie samoczynnym (ZS). W zapobieganiu tym zjawiskom wiodącą rolę odgrywa skuteczność działania dodatków detergentowo-dyspergujących o odpowiednim poziomie dozowania. Przedmiotem badań jest bazowy olej napędowy z udziałem 7%(v/v) FAME. W celu sprawdzenia skuteczności działania badanych dodatków wykonano testy silnikowe zgodne z procedurą CEC F-98-08 PSA DW-10 pod kątem koksowania i zanieczyszczenia nowoczesnych wielootworowych wtryskiwaczy wysokociśnieniowego układu zasilania silników o ZS oraz sformułowano wnioski.

***Słowa kluczowe**: silnik, wtryskiwacz, paliwo, dodatek detergentowo-dyspergujący.*

1. Introduction

The development of motorisation features intensive research in the field of engine fuels improvement, including packages of improvers. Fuels for compression-ignition engines (D), satisfying high requirements of modern drives, equipped with high pressure common rail systems (HPCRS) and catalytic multifunctional exhaust gas cleaning systems, must feature appropriate physicochemical and practical properties.

The optimisation of the charge combustion process in a compression-ignition engine at a multi-stage injection of hydrocarbon fuel and of biocomponents-containing fuel in the Common Rail system determines the main directions of research work in the field of technology and thermooxidising stability of biofuels and of engine design development, including the fuel feed system.

The course of blend combustion in the working space of the engine decides about its practical efficiency and about a positive ecological effect – reduction of harmful compounds emission to the air.

2. Factors shaping the process of nozzles fouling in high-pressure fuel injection HPCRS

The introduction to the automotive market of modern compression-ignition engines equipped with direct fuel injection systems named 'High Pressure Common Rail System' (HPCRS) increased the tendency of multi-nozzle high-pressure injectors to coke.

In this case a small diameter of nozzles – less than 150 µm – is the main problem as well as a high temperature of the injector tip situated in the combustion chamber [2]. The design of the aforementioned fuel injection systems and extreme working conditions (high temperature of injector tips, exceeding 300°C, high working pressure of up to 250 MPa for injectors with hydraulic amplification, small diameter of fuel nozzle orifices) cause the formation of hydrocarbon deposits (coke) originating at the outlet of injector nozzles [3, 5].

According to [1] the following factors have a significant impact on injector tips coking:

- physicochemical properties of the fuel, component composition, heat and oxidation resistance;
- temperature of injector tip and resistance to the thermal degradation of fuel;
- design of injector tip, the inner diameter and geometrical shape of the nozzle as well as wettability of internal surfaces of the injector by the fuel.

Temperature has a significant influence on the process of nozzles coking [18], Leperhoff has shown that temperatures higher than 300°C cause a quick deposition of coke on injector tips, resulting from the diesel fuel cracking and from the kinetics of thermal condensation reaction of cracking products [6]. To ensure cleanness and efficiency of HPCRS injection systems the diesel fuel should meet not only minimum requirements related to its quality acc. to PN-EN 590:2013-12 standard, but also guidelines of injection systems

(*) Tekst artykułu w polskiej wersji językowej dostępny w elektronicznym wydaniu kwartalnika na stronie ***www.ein.org.pl***

manufacturers, presented in the form of a common position declaration 'Fuel Requirements for Diesel Injection System – Diesel Fuel Injection Equipment Manufacturers – Common Position Statement 2012'. Also the guidelines of the Worldwide Fuel Charter for category 4 diesel fuel – edition 5 from September 2013 – are a necessary condition.

Some properties of the fuel, such as high viscosity, low volatility, content of olefins, aromatic compounds, content of biocomponents (FAME) facilitate formation of carbon deposits and coke on the injector tips. The progress in the field of detergent-dispersant improvers technology and the levels of their dosing allow to resolve many design issues of injectors themselves and also to influence positively the kinetics of fuel combustion kinetic reactions in a compression-ignition engine.

3. Engine tests in the field of fouling assessment of modern multi-nozzle injectors

In the modern compression-ignition engines, manufactured now, their complicated system of operation control and also a precise dose of injected fuel depend more and more on the presence of deposits in the fuel, and also on the deposits formed during the process of fuel combustion in the engine [12].

In March 2008 the European Standardisation Committee (CEC) formalised and implemented a new engine testing procedure CEC F-98-08 'Direct Injection Common Rail Diesel Engine Nozzle Coking Test' related to coking and fouling modern multi-nozzle injectors as a standard test for the assessment of the fuel quality and of effectiveness of detergent additives action.

A Peugeot DW-10 compression-ignition engine with direct injection was chosen, meeting requirements of Euro 4 exhaust gas emission standard, widely used on the European market in Peugeot 407 2.0 HDi 16V cars, equipped with injectors meeting requirements of Euro 5 exhaust gas emission standard.

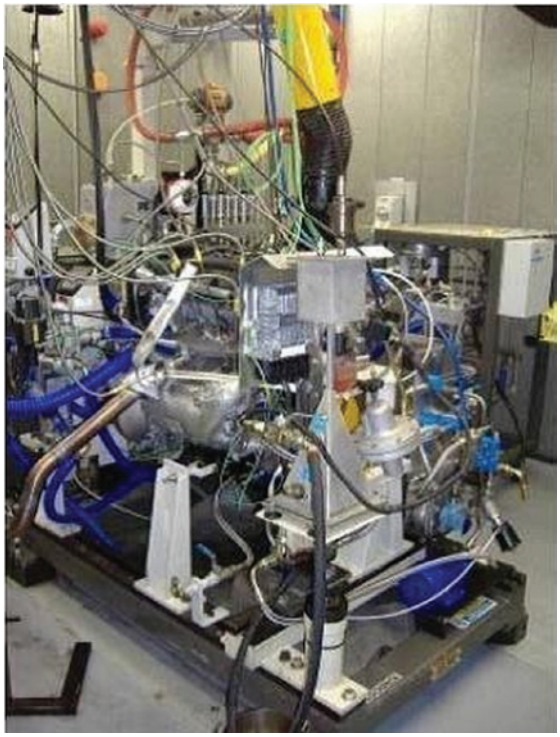

Fig. 1. PSA DW-10 engine test bed Experimental tests in the field of injectors fouling were carried out based on the CEC F-98-08 procedure, on a PSA DW-10 engine, which featured:

An engine test bed designed to carry out tests based on the CEC F-98-08 procedure was chosen, using a turbocharged four-stroke PSA DW-10 compression-ignition engine with direct injection. (Fig. 1.)

- direct injection;
- four valves per cylinder;
- capacity of 1998 cm^3;
- turbocharging with exhaust gas recirculation (EGR) and a particulate filter;
- rated power of 100 kW at 4000 rpm;
- maximum torque of 320 Nm at 2000 rpm;
- Siemens VDO, Euro 5 injectors;
- 'Common Rail' type injection system of 160 MPa pressure;
- piezoelectrically controlled 6-nozzle injectors with spray nozzles 110 µm in diameter.

The Worldwide Fuel Charter (WWFC 2013) introduced the procedure CEC F-98-08 to the assessment of cleanness of both pintle injectors and to the assessment of cleanness of high-pressure multi-nozzle injectors for category 4 and 5 diesel fuels acc. to the Worldwide Fuel Charter, apart from the procedure CEC F-23-01. Fig. 2 presents relative spray nozzle diameters for injectors used to assess the fuel tendency to foul the injectors. [17]

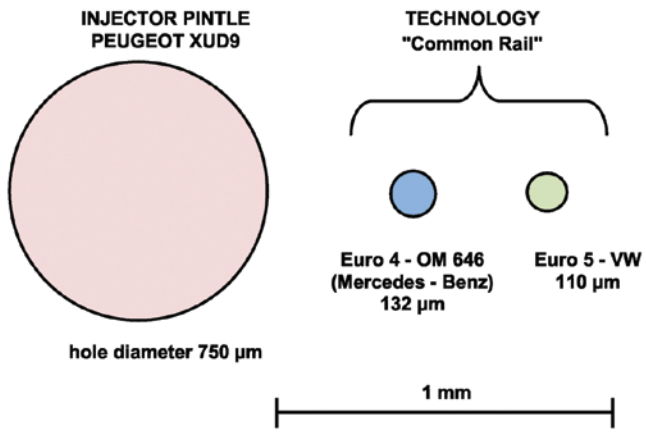

Fig. 2. Relative diameters of various injectors spray nozzles

According to the Worldwide Fuel Charter (WWFC 2013) for category 4 and 5 of diesel oils maximum 2% of engine power loss is allowed after testing acc. to the procedure CEC F-98-08. The PSA DW-10 engine test simulates the conditions of driving on a road. The engine tests were carried out at defined engine rotational speeds and loads, including 60-minute cycles consisting of 12 phases. Table 1 presents parameters of individual phases, while Fig. 3 presents a load-rotation profile of the course of one 60-minute test cycle.

For each performed test a new set of injectors is installed, which are checked in a 16-hour test on a reference fuel not fouling them. The observed power is checked, as well as the amount of engine gases blowthrough to the crankcase versus the engine torque and the fuel consumption in comparison with known values. Also the lubricating oil consumption is monitored before tests start and end. The test procedure comprises alternating four 8-hour sequences of the engine operation acc. to the load-rotation profile presented in Fig. 3 and three sequences of 4-hour engine standstill. So the total test time is 16 + 32 + 12 = 60 hours.

Table 1. Parameters of 12 phase test cycle on a PSA DW-10 engine

Phase	Time [min]	Engine rotations [rpm] ± 20 rpm	Load [%]	Torque [Nm] ± 5 Nm
1	2	1750	(20)	62
2	7	3000	(60)	173
3	2	1750	(20)	62
4	7	3000	(80)	212
5	2	1750	(20)	62
6	10	4000	100	*
7	2	1250	(10)	25
8	7	3000	100	*
9	2	1250	(10)	25
10	10	2000	100	*
11	2	1250	(10)	25
12	7	4000	100	*
	Σ = 60			

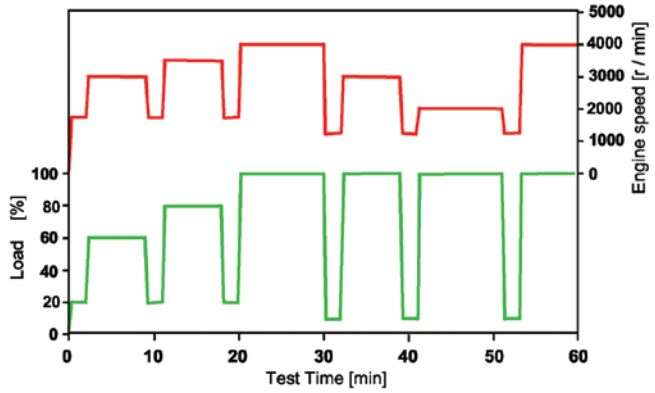

Fig. 3. Load-rotation profile of one testing cycle on a PSA DW-10 engine

4. CEC F-98-08 PSA DW-10 procedure for testing the detergent-dispersant additives action effectiveness

The CEC F-98-08 PSA DW-10 procedure enables also testing the effectiveness of detergent-dispersant additives action in the field of their properties related to removing the fouling from injectors after approx. 16-hour dirtying in the 'dirt-up' test. The engine 'dirt-up' test is carried out using a reference diesel fuel CEC RF 06-03 without any FAME as a certified fuel for legislation testing of engines meeting requirements of Euro 4 and Euro 5 exhaust gas emission standards. To accelerate the injectors fouling in the 'dirt-up' procedure 1 mg/kg of zinc in the form of zinc neodecanoate is added to the fuel. Table 2 presents properties of the reference fuel CEC RF 06-03

After an engine test comprising a 'dirt-up' cycle a 32-hour 'clean-up' test is performed using a fuel containing effectively acting detergent-dispersant additives with admixture of 1 mg/kg Zn in the form of zinc neodecanoate. The engine tests of 'Power Diesel' diesel fuel

Table 2. Properties of the reference fuel CEC RF 06-03

Properties	Unit	Results of test	
		minimum	maximum
Cetane number		52.0	54.0
Density at 15°C	kg/m^3	833.0	837.0
Fractional composition: - to 245°C distilled - to 350°C distilled - distillation end temperature	 % (V/V) % (V/V) °C	 50.0 95.0 -	 - - 370
Ignition temperature	°C	55.0	-
Cold filter plugging point	°C	-	-5
Kinematic viscosity at 40°C	mm^2/s	2.3	3.3
Sulphur content	mg/kg	-	10.0
Content of polynuclear aromatic hydrocarbons	% (m/m)	3.0	6.0
Resistance to oxidation, total insoluble deposits	g/m^3	-	25.0
Fatty acids methyl esters (FAME) content	% (V/V)	none	none
Lubricity, corrected trace diameter	µm	-	400
Acid number of strong acids	mg KOH/g	-	0.02
Water content	mg/kg	-	200

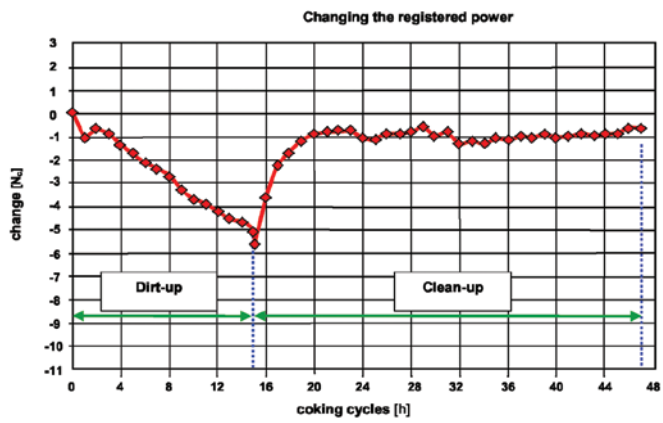

Fig. 4. The course of engine power variability in the 'dirt-up' cycle and in the 'clean-up' cycle

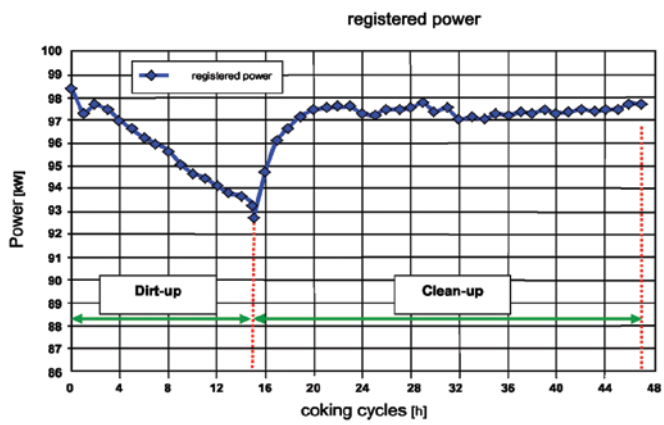

Fig. 5. The course of engine power variability in percent after the 'dirt-up' cycle and 'clean-up' cycle

containing 500 mg/kg of Petropak® and 1200 mg/kg of Energocet® were carried out according to the CEC F-98-08 PSA DW-10 'dirt-up' and 'clean-up' procedure and performed in the Engine Laboratory of the SGS Drive Technology Centre in Austria.

Fig. 4 presents the course of engine power loss in percent after 16-hour cycle of 'dirt-up' test, while Fig. 5 is related to the power recovery after a 32-hour 'clean-up' test cycle. The power loss after the 'clean-up' test was below one percent.

5. Compatibility of multi-function detergent-dispersant and cetane-detergent additives with engine oils

The compatibility with engine oils, lubricating radial and axial piston fuel pumps, used in delivery vans and lorries, is an important issue for multi-function detergent-dispersant and cetane-detergent additives. Such tests are carried out based on the German Society Petroleum and Coal Science and Technology DGMK 531-1 'Test for engine oil compatibility' procedure. They consist in mixing the SAE 15W/40 'Super High Performance Diesel Oil' SHPDO engine oil with a package of diesel oil additives in the proportion of 50:50, storage at 90ºC during 72 hours, then cooling the sample down to 20ºC during 1 hour, and a visual assessment of deposits, gels, turbidities formed in it. In the field of sample homogeneity the visual assessment was expanded with turbidimetric analyses. The sample was diluted, supplementing to 500 ml with the basis diesel oil, mixed, and the solution appearance was assessed. After 2 hours the solution was mixed again and filtered at a pressure of 800 hPa, through a filter with pores 0.8 micrometer in average diameter, and the filtration time of 500 ml of the solution was measured. The filtration time should not exceed 900 s, and the final solution should be clear and without any deposits. Table 3 presents the results of tests of engine oil compatibility with packages of Petropak® and Energocet® additives to the diesel oil.

Table 3 Results of tests of packages of Petropak® and Energocet® additives compatibility with the SHPDO SAE 15W/40 engine oil acc. to the DGMK 531-1 procedure

Tested package	Filtration time [s]	Solution appearance
Petropak®	106	clear no deposit
Energocet®	187	clear no deposit

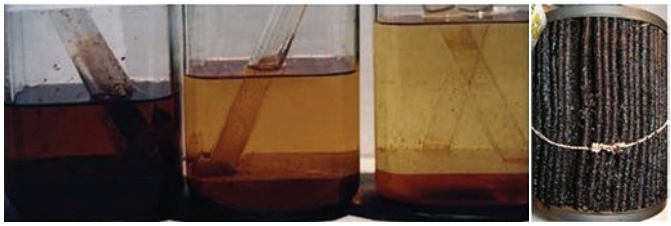

Fig. 6. Microbiological infection of diesel fuel and a fouled fuel filter a) microbiologically infected diesel fuel b) fuel filter fouled with a deposit after microbiological degradation of fuel

The experimental tests were related also to the assessment of the fuel propensity to the development of microbiological contamination. The application of diesel fuel with ultra-low sulphur content (below 10 mg/kg) with 7 % (V/V) FAME content resulted in increased fuel propensity to microbiological contamination. Fatty acids methyl esters as a renewable component of the diesel oil with hygroscopic properties easily biodegrade, being an excellent nutrient medium for the development of microbiological life. Fatty acids methyl esters biologically degrade four times faster than a conventional diesel fuel originating from oil [10]. Moreover, in the temperature range from 4ºC to 35CºC fatty acids methyl esters absorb 15 to 25 times more water than the conventional diesel fuel. These factors are favourable to the development of microbiological life during such fuel storage and distribution. A microbiological infection of the fuel results in turbidity, colour change, increased pollution in the form of deposits and slurries, increase in viscosity and deterioration of the fuel filterability.

Fig. 6 presents pictures of microbiologically infected diesel fuel and a fuel filter fouled with a deposit after fuel microbiological degradation.

Biocidal additives play a crucial role in preventing and eliminating problems related to micro-organisms presence in the diesel fuel. In the presented paper a multi-function detergent-dispersant additive Petropak® contained biocides compatible with the applied polyisobutylene succinic imides described in detail in inventions PL 217137 and PL 218043 [8, 9]. The effectiveness of their biocidal action was determined in a preventing test acc. to the ASTM E-1259:10

Table 4. Results of testing the biocides action effectiveness in the field of microbiological protection in a preventing test acc. to the ASTM E-1259:10 method

No	Test duration (weeks)	Tested fuel	Examined material	Microbes content in the fuel (cell/l) and water (cell/l) phase		
				aerobic bacteria	yeast	mould fungi
1	1	Summer diesel fuel, grade B +7%(V/V) FAME 'Premium' (500 mg/kg Petropak®	fuel	< 200	< 200	< 200
			water	< 200	< 20	< 20
2	2	Summer diesel fuel, grade B +7%(V/V) FAME 'Premium' (500 mg/kg Petropak®	fuel	< 200	< 200	< 200
			water	< 200	< 20	< 20
3	3	Summer diesel fuel, grade B +7%(V/V) FAME 'Premium' (500 mg/kg Petropak®	fuel	< 200	< 200	< 200
			water	< 200	< 20	< 20
4	4	Summer diesel fuel, grade B +7%(V/V) FAME 'Premium' (500 mg/kg Petropak®	fuel	< 200	< 200	< 200
			water	< 200	< 20	< 20

* *At the amount of less than 200 cells per litre of fuel it is considered free of microbiological life*

** *At the amount of less than 200 cells/ml in water for aerobic bacteria and below 20 for yeast and mould fungi, the water is considered not infected by microbes*

Table 5. Results of tests of a multi-function detergent-dispersant package and detergent-cetane package in diesel fuels

Basis diesel fuel summer grade B +7 %(V/V) FAME			Packages	
			Petropak®	Energocet®
Dosing mg/kg			500	1200
Lubricity, acc. to PN-EN ISO 12156-1, µm	max. 460		399	427
Compatibility acc. to DGMK 531-1 filtration time, s	max. 300		106	87
Cetane number	min. 51/55		52	59.8
Nozzles patency reduction index, % acc. to CEC F-23-01	max. 60		31	-
Nozzles patency reduction index, % acc. to CEC F-23-01 (500 mg/kg Petropak® + 1200 mg/kg Energocet®)	max. 30		-	11
Power loss after 'dirt-up / clean-up' testing acc. to CEC F-98-08, %	max. 2		-	< 1
Resistance to oxidation (Rancimat), h	min. 40		60.0	56.7
Corrosion acc. to ASTM D665A	max. B^{++}		A	-
Foaming acc. to NF M07-075 - foam volume, cm^3 - foam decay time, s	 max 100 max 15		 30 4.8	 - -
Interaction with water acc. to ASTM D 1095 - change of water layer volume - interface appearance - degree of phase separation	 ± 3.0 max 1b max 2		 1.0 1b 2	 1.0 1b 2
Microbes content in the fuel (cell/l) and water (cell/l) phase after four-time fuel contacts with the contaminated water phase:				
- aerobic bacteria	fuel	< 200	< 200	-
	water	< 200	< 200	-
- yeast	fuel	< 200	< 200	-
	water	< 20	< 20	-
- mould fungi	fuel	< 200	< 200	-
	water	< 20	< 20	-

'Evaluation of Antimicrobials in Liquid Fuels Boiling Below 390ºC' method, determining the microbes content in the fuel phase by the IP385 'Determination of viable aerobic microbial content of fuel components boiling below 390ºC' method. The applied methodology reflects a four-time pumping of the fuel in the distribution chain with a contaminated water phase at the ratio of fuel to water phase of 400: 1. The test lasts four weeks. Table 4 presents the results of testing the biocides action effectiveness in the field of microbiological protection in a preventing test [13].

Table 5 presents selected test results of practical assessment of multi-function detergent-dispersant package and detergent-cetane package in 'Premium' diesel fuel containing 500 mg/kg of Petropak® and 'Power Diesel' diesel fuel containing 500 mg/kg of Petropak® and 1200 mg/kg of Energocet®.

6. Summary

In the modern compression-ignition engines, manufactured now, their complicated system of operation control, and a precise dose of injected fuel depend more and more on the presence of deposits related to the course of many occurring chemical reactions of the fuel and hydrocarbons decomposition products existing in the injector nozzle and on the outside nozzle surface [7].

The knowledge related to deposits formation mechanisms in IDID (Internal Diesel Injector Deposits) injectors, and also to their chemical composition is still insufficient. The number and complexity of factors initiating the formation and build-up of internal IDIDs in HPCR systems injectors in compression-ignition engines still require carrying out research determining their importance and the interaction mechanisms [8,9,15,16].

The explanation of IDID deposits formation mechanisms and also of coke formation on the nozzles is difficult due to the lack of appropriate testing tools simulating very difficult conditions existing inside the combustion chamber and inside high-pressure injectors.

In this field a significant testing tool consists of engine tests carried out according to procedures suggested and agreed by injection systems and compression-ignition engines manufacturers. They are presented in the Worldwide Fuel Charter (WWFC 2013) according to CEC F-98-08 for compression-ignition engines with direct fuel injection to the combustion chamber for category 4 of diesel fuel, edition five, September 2013 [19].

Progressing design and technological development of piston combustion engines and fuel injection systems applied in them, and also the changing fuel technologies will require developing and applying more and more effective detergent-dispersant additives of multidirectional action.

The IDID type deposits produced in simulation engine tests resulted in characteristic, occurring during real vehicles operation, dysfunctions of HPCR type fuel injection systems, frequently making their operation impossible.

The conclusions formulated by the Authors based on experimental tests during engine tests comprising a 'dirt-up' and 'clean-up' operation cycle prove the importance of improvers action effectiveness and their compatibility, which is confirmed by other authors [4,7,9,14,16,17].

A biocidal action preventing and removing microbes fouling the fuel is an important element of practical assessment of a multi-function additive.

References

1. Birgel A, Ladommatos N, et al. Deposit Formation in the Holes of Diesel Injector Nozzles: A Critical Review. SAE Paper 2008-01-2383, https://doi.org/10.4271/2008-01-2383.
2. Caprotti R, Bhatti N, et al. Deposit Control in Modern Diesel Fuel Injection Systems. SAE Paper 2010-01-2250, https://doi.org/10.4271/2010-01-2250.
3. Caprotti R, Breakspear A. Injector Deposit Test For Modern Diesel Engines. 5th International Colloquium Fuels TAE Esslingen 2005.
4. Fuel Requirements for Diesel Fuel Injection Systems Diesel Fuel Injection Equipment Manufacturers Common Position Statement 2012.
5. Leedham A, Caprotti R, et al. Impact of Fuel Additives on Diesel Injector Deposits. SAE Paper 2004-01-2935, https://doi.org/10.4271/931032.
6. Lepperhoff G, and Houben M. Mechanisms of Deposit Formation in Internal Combustion Engines and Heat Exchangers. SAE Paper 931032, https://doi.org/10.4271/2009-01-0848.
7. Matzke M, Litzow U, et al. Diesel Lubricity Requirements of Future Fuel Injection Equipment. SAE Paper 2009-01-0848.
8. Mazanek A. Ocena parametrów użytkowych wtryskiwaczy piezoelektrycznych na podstawie badań wizualizacyjnych procesu rozpylania paliwa. Nafta - Gaz 2016; 4: 279-284, https://doi.org/10.18668/NG.2016.04.07.
9. Oleksiak S, Łukasik Z. Nowoczesne układy wtrysku paliwa w silnikach Diesla i ich wpływ na jakość paliw i dodatków detergentowo - dyspergujących. Nafta - Gaz 2009; 1: 58-64.
10. Patent PL 217137 "Uniwersalny pakiet do bioestrów", 2014, 30.06.2014.
11. Patent PL 218043 "Wielofunkcyjny pakiet dodatków biobójczo-stabilizujących", 2014, 30.09.2014.
12. Sorensen G, Dennis V, et.el Microbial growth studies in biodiesel blends. Bioresource Technology 2011; 103: 5259-5264, https://doi.org/10.1016/j.biortech.2011.02.017.
13. Stanik W, Jakóbiec J, Wądrzyk M. Design factors affecting the formation of the air-fuel mixture and the process of combustion in compression ignition engines. Combustion Engines 2013; 52(3): 40-50.
14. Stanik W. Badania poliizobutylenobursztynoimidów w zakresie oceny użytkowej dodatków detergentowo - dyspergujących do paliw silnikowych",Monografia - Praca Naukowa Instytutu Nafty i Gazu - Państwowego Instytutu Badawczego 2015; 26, https://doi.org/10.18668/PN2015.206.
15. Stępień Z. Przyczyny i skutki tworzenia wewnętrznych osadów we wtryskiwaczach silnikowych układów wysokociśnieniowego wtrysku paliwa. Nafta - Gaz 2013; 3: 256-262.
16. Stępień Z. A study of factors influencing the formation of harmful deposits in the diesel engine injectors. Eksploatacja i Niezawodnosc - Maintenance and Reliability 2017; 19 (3): 331-337, https://doi.org/10.17531/ein.2017.3.3.
17. Velaers A, and de Goede S. The Properties and Injector Nozzle Fouling Performance of Neat GTL and GTL/EN590 Diesel Blends in Various Diesel Engines. SAE Paper 2012-01-1692, https://doi.org/10.4271/2012-01-1692.
18. Watkinson A P, Wilson D I. Chemical reaction fouling: A review. Experimental Thermal and Fluid Science 1997; 4: 315-469, https://doi.org/10.1016/S0894-1777(96)00138-0.
19. Worldwide Fuel Charter, Fifth Edition, 2013, September 2013.

Winicjusz STANIK
Oil and Gas Institute – National Research Institute – Krakow
ul. Lubicz 25A, 31-503 Kraków, Poland

Janusz JAKÓBIEC
AGH - University of Science and Technology - Krakow
al. Mickiewicza 30, 30-059 Kraków - Poland

Aleksander MAZANEK
Oil and Gas Institute - National Research Institute - Krakow
ul. Lubicz 25A, 31-503 Kraków, Poland

E-mails: stanik@inig.pl, jjakobie@agh.edu.pl, mazaneka@inig.pl

Article citation info:
BUCHACZ A, BAIER A, HERBUŚ K, OCIEPKA P, GRABOWSKI Ł, SOBEK M. Compression studies of multi-layered composite materials for the purpose of verifying composite panels model used in the renovation process of the freight wagon's hull. Eksploatacja i Niezawodnosc – Maintenance and Reliability 2018; 20 (1): 137–146, http://dx.doi.org/10.17531/ein.2018.1.18.

Andrzej BUCHACZ
Andrzej BAIER
Krzysztof HERBUŚ
Piotr OCIEPKA
Łukasz GRABOWSKI
Michał SOBEK

COMPRESSION STUDIES OF MULTI-LAYERED COMPOSITE MATERIALS FOR THE PURPOSE OF VERIFYING COMPOSITE PANELS MODEL USED IN THE RENOVATION PROCESS OF THE FREIGHT WAGON'S HULL

BADANIA PORÓWNAWCZE WIELOWARSTWOWYCH MATERIAŁÓW KOMPOZYTOWYCH NA POTRZEBY WERYFIKACJI MODELU PANELI KOMPOZYTOWYCH STOSOWANYCH DO RENOWACJI POSZYCIA WAGONÓW TOWAROWYCH*

The paper presents the procedure sequence for modelling multilayer composite materials using PLM Siemens NX software. Virtual studies were referring to three-point and four-point flexural test of composite material samples. Composite materials containing fiber reinforced epoxy resin composites were considered. Within the carried out research, a virtual experiment to test composite samples composed of 5, 7 and 10 layers was conducted. Then the virtual model was matched to the results obtained during the stationary tests. As a result of matching the composite material model to the real model, correct results of the virtual bending experiment of composite samples were obtained. The presented procedure sequence for modelling composite material was used to analyse the MES of the scaled side of the freight wagon. The modification consisted in the use of composite panels as reinforcing elements of the wagon's hull from inside to extend its life. The presented modelling approach enabled the initial strength verification of the modified side of the freight wagon's hull.

***Keywords**: composite materials, FEM method, modelling, flexural test.*

W pracy przedstawiono sposób postępowania przy modelowaniu wielowarstwowych materiałów kompozytowych z zastosowaniem oprogramowania PLM Siemens NX. Badania wirtualne odnosiły się do próby trójpunktowego i czteropunktowego zginania próbek kompozytowych. Rozważano materiały kompozytowe będące kompozycją żywicy epoksydowej ze wzmocnieniem włóknistym. W ramach prowadzonych badań przeprowadzono wirtualny eksperyment badania próbek kompozytowych będących kompozycją złożoną z 5, 7 i 10 warstw. Następnie dopasowano wirtualny model do wyników otrzymanych na drodze badań stanowiskowych. W wyniku dopasowania modelu materiału kompozytowego uzyskano poprawne wyniki wirtualnego eksperymentu zginania próbek kompozytowych. Zaprezentowany tok postępowania odnośnie modelowania materiału kompozytowego zastosowano do analizy MES pomniejszonego fragmentu zmodyfikowanej burty bocznej wagonu. Modyfikacja polegała na zastosowaniu paneli kompozytowych jako elementów wzmacniających poszycie wewnętrzne wagonu mających na celu wydłużenie jego czasu eksploatacji. Przedstawiony sposób modelowania umożliwił wstępną weryfikację wytrzymałościową zmodyfikowanego fragmentu burty bocznej wagonu towarowego.

***Słowa kluczowe**: materiały kompozytowe, metoda MES, modelowanie, próba zginania.*

1. Introduction

The inevitability of using composite materials as construction materials forces engineers to use numerical models describing their structure and properties. Microscale non-homogeneous materials, such as composites, may also be considered on a macro scale as the homogeneous material. To determine the properties of the resultant material a mixture based rule is usually applied, which takes into consideration the volume of components in total volume. It is also possible to use methods based on the approximation of heterogeneous bodies or on the basis of virtual work [1, 2, 14, 15, 17, 26].

In models based on the classical composite materials theory (lamination theory), it is assumed that the laminate consists of layers bonded together in an unbreakable way and the joints have an infinitesimal thickness (they have a thickness close to 0) and do not allow shear between layers. This means that the deformations in thickness of the composite are continuous and no layer can move relative to another. A composite as an integrity forms macroscopically one layer with values of properties that are the resultant of values of the layers forming it. In order to determine the durability of a laminate composite, it is necessary to know the stresses in each individual layer. For this purpose, Hooke's law is used, taking into consideration the determined

(*) Tekst artykułu w polskiej wersji językowej dostępny w elektronicznym wydaniu kwartalnika na stronie ***www.ein.org.pl***

deformation values. The criteria for the destruction of composite materials are also commonly used [3, 11, 12, 17, 29].

Composite properties and accuracy of the models used can be verified during the experiments. These experiments can be carried out using destructive methods as well as nondestructive methods. During the destructive tests in the structure of the composite material, undesirable and irreversible changes may occur. This aspect often disqualifies a particular method in the research process. In case of nondestructive testing, the examined object will not be damaged so that key information will not be lost and can be obtained. In the research process of composite materials, the key values are displacement and stress [3, 11, 12, 17, 27].

Both destructive and nondestructive methods are used to verify the results of numerical tests. In that process methods based on resistance and optical strain, bending and impact methods are used. In addition, non-destructive methods are used to analyze the occurrence of defects in the composite structure. More sophisticated methods include thermal imaging, ultrasonic, radiological and visual methods can be defined. [11, 13, 26, 27, 29].

Modelling and verification of components made of fibrous composite materials can be supported by numerical analysis using the finite element method. There are two basic approaches during the process of modelling laminate with MES. In the first case, the internal structure of the examined object the number of layers is taken into consideration. We also consider the type and weave of the reinforcement and the degree of resin impregnation. The properties of the various components of the laminate, that is the properties of the matrix and the individual strands of the fabric, are also taken into consideration. Applying this method leads to building models with a large number of variables and a large number of degrees of freedom. Due to the complexity of the problem and limited computing power, this method is used in the analysis of relatively small elements characterized by uncomplicated geometric form. Regarding larger elements of greater complexity, the calculation is based on the analysis of the properties of the composite slice. At this stage, attributes of the replacement material are determined, which is then applied to the entire model. In this case, the model is created using solid elements with properties of the composite material. As a result, the solids are given with special replacement properties, which are characteristic to the previously studied section, without penetrating the internal structure of the composite material. [2, 10, 12, 16, 20, 23, 25, 26].

Two methods are used to describe the structure of a composite material using a finite element mesh. In the first of them, the 2D surface elements mechanical parameters and a virtual thickness parameter are given. In the second method, 3D spatial elements are used for which the thickness is known. Then it is divided into the number of layers for which the properties of the laminate are applied. Both methods take into consideration the volume constituents of the components and the number of layers and their orientation relative to each other. Material constants are determined by experiment or supplied by the manufacturer of the material [2, 10, 12, 16, 19, 20, 23, 25, 26, 28].

The main objective of the conducted research was the verification of numerical strength calculations regarding the analysis of composite panels used to renovate the hull of freight wagons. In the first step, the simplest MES models were tested to verify the convergence of numerical and experimental results. Experimental tests performed on a strength machine were used to compare and verify the results. These were strength tests conducted to composite samples subjected to three-point and four-point bending tests. Experimental FEM models were then developed. Verification of the results allowed for fitting (modification) of FEM numerical models to obtain convergent results. At the next stage, a strength verification was carried out on panels mounted on the side of the freight wagon's hull. It was planned that the numerical results would be verified on a test bench constructed to study the behaviour of the composite panels on the freight wagon's hull. For this purpose, a FEM numerical analysis was carried out which allowed us to initially estimate the expected stresses and displacements, and to identify where the sensors for the experimental analysis would be fixed. In the next step, a strength analysis on a specially built test bench using resistance strain gauges and displacement sensors was carried out. Based on the experience gained during the numerical modelling and with respect to simple strength tests, the FEM models of the freight wagon hull's sidewall was fitted to produce convergent results to those obtained in test bench tests. Matched models are the basis for further research carried out within the framework of the project.

2. The results of experiments of samples made of a composite material

The experiments of composite samples consisted of two types of bending strength tests:

- four-point bending strength test of carbon fiber reinforced by epoxy resin,
- strength test of carbon fiber reinforced by epoxy resin samples performed in triple point bending test.

Experimental research was carried out by the Technical-Humanistic Academy in Bielsko-Biała as part of a research project, the authors of this paper carried out numerical analyzes using the finite element method.

Figure 1 shows the load and support scheme of the tested samples for four-point bending tests. Whereas Figure 2 shows the load and support scheme of the examined samples for the three-point bending tests.

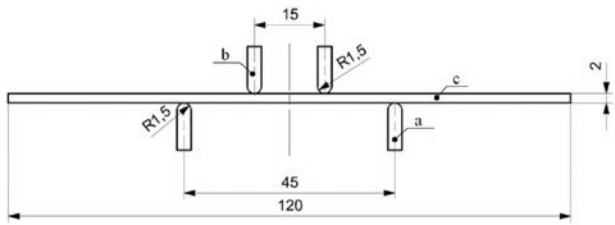

Fig. 1. Scheme of load and support of samples used in four-point bending tests: a – support, b – punch, c – test sample

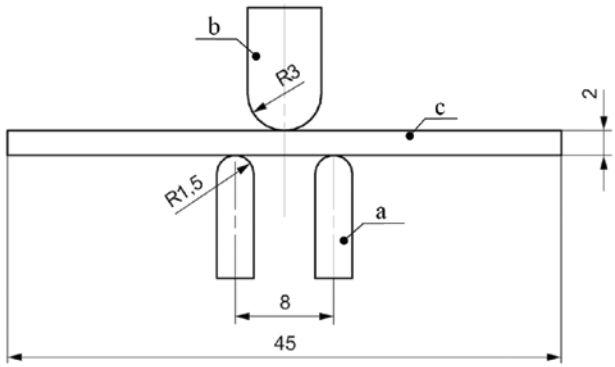

Fig. 2. Scheme of load and support of samples used in three-point bending tests: a – support, b – punch, c – test sample

The strength tests of laminates subjected to a four-point bending test were performed for samples of dimensions of 120 mm x 20 mm x 2 mm. The strength tests of laminates subjected to the three-point bending test concerned samples of dimensions of 45 mm x 4 mm x 2 mm. The thickness of the samples was in the range of 2 to 2.25 mm and the width was in the range of 20 to 20.15 mm. The experi-

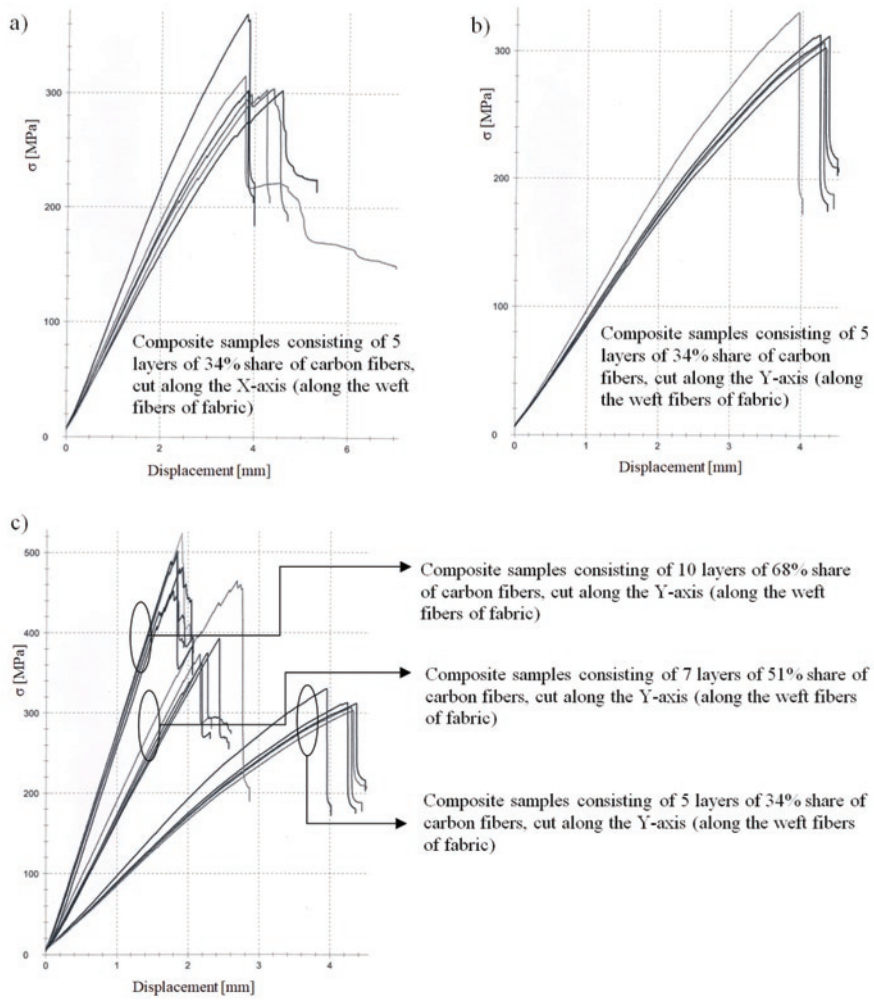

Fig. 3. Examples of results of experimental testes of composite samples in relation to the four-point bending method

mental tests on the testing machine in both cases were performed for samples cut from composite panels made of epoxy resin and fabric with the plain type of weave. Composite panels have been made in the serial production process by infusion method, which guarantees the assumed reinforcement-matrix ratio. Three panels of carbon fiber volume (34%, 51% and 68%) were chosen for the study. The coefficient of a volume of warp fibers to weft fibers was equal to 0.5. Samples were cut in three directions: in the direction of alignment of the warp fibers of the carbon fabric, in the direction of the direction of the weft of the carbon fiber weft and at an angle of 45 ° to the carbon fiber warp yarns. The analyzes also concerned samples of composite panels consisting of a composite of epoxy resin and carbon fibers arranged in one direction, made in 3 variants of carbon fiber volumetric share percentage (38%, 51% and 68%). In this case, the samples were cut in the direction of fiber orientation and at an angle of 90 ° with respect to the orientation of the fibers in the layer. All layers, within the structure of the composite material of the sample, had the same orientation. These bending tests were carried out in accordance with test standard ASTM D 6272-02 at a load velocity (punch velocity) of 2 mm / min.

Fig. 3 illustrates the experimental results of composite samples of the four-point bending test. Figs. 3a and 3b show bending results of composite samples composed of 5 layers, where each layer is a combination of epoxy resin and carbon fiber with plain weave, assuming a 34% carbon fiber content in the composite structure. Figure 3a shows the results of the tests of samples cut along the axis aligned to the carbon fabric weft direction, in Figure 3b the results of the tests are presented of the samples cut along the axis in accordance with the axis of alignment of the carbon fiber matrix. In Fig. 3c, the results of the tests were compiled for composite samples composed of 5, 7 and 10 layers, where each layer was a combination of epoxy resin and carbon fiber with a plain weave, assuming respectively for a number of layers of 34%, 51% and 68% of carbon fiber in the composite structure. By analyzing the presented results, in the case of samples cut along the weft fabric, the stress values were approximately 10% higher than those of the identical composite material cut along the fiber matrix, of the composite at the same displacement of the punches, could be seen. On the other hand, with reference to the results of the studies of 5, 7 and 10 layers of composite samples with respectively 34%, 51% and 68% of volume of carbon fiber, with the increase in the number of layers and the percentage of fibers in the composite structure, the value of archived stresses in the sample increases, for the same displacement value of the stamps could be seen. In Fig. 3c, three separate areas of strength characteristics can be observed depending on the number of layers and percentage infill of fibers.

3. Virtual modelling of three-point and four-point bending tests using finite element method

For representing the three-point and four-point bend test, the models of test benches with the test samples were developed in the PLM Siemens NX10 system. The created solid models were subjected to a discretization process by applying a finite element mesh to individual parts. In the next step, boundary conditions were defined in such a way, that virtual tests were as much comparable as the research on the real test stand.

In the models prepared for FEM analysis, the following boundary conditions were defined (Figures 4 and 5): fixing of the supports, surface to surface contact between the test sample and the supports and

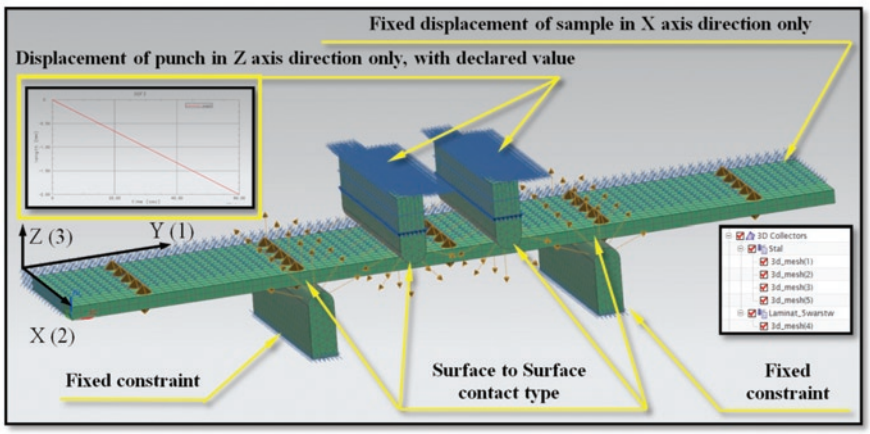

Fig. 4. FEM model with defined boundary conditions and loads for four-point bending strength tests

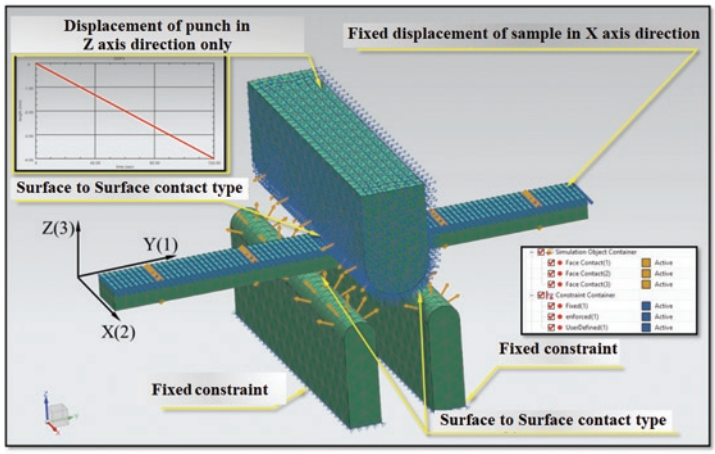

Fig. 5. FEM model with defined boundary conditions and loads for three-point bending strength tests

stamps, fixing of one degree of freedom of the sample for removing the possibility of moving along the X axis, forcing the displacement of punches only along the Z axis. The type of contact used enables the displacement of the discretized samples, supports and punches relative to each other - which is a necessary condition in order to correctly characterize the displacement of the testing sample. In the virtual experiment, the load was defined as the displacement of the stamps in the direction of the Z axis at a speed of 2 mm / min. The applied displacement represents the movement of the actual punches of the testing machine.

The next stage of the research was to map material form of samples made of composite materials subjected to strength tests on the endurance machine. Virtual studies included strength analyzes using finite element method, epoxy resin and carbon fiber composite samples, straight weave and epoxy resin and unidirectional carbon fiber composites. The composite material consisting of 5, 7 and 10 layers were considered.

To define the composite material in PLM Siemens NX 10 software the first layer is described first. Based on the manufacturer's data in relation to used warp and fiber types the following basic layers of laminate composite material were defined: 34_Woven_2W_90, 38_Woven_1W, 51_Woven_2W_90, 51_Woven_1W, 68_Woven_2W_90, 68_Woven_1W.

In the assumed designations values of 34, 38, 51 and 68 determine the volume ratio of carbon fiber to epoxy resin. Mean percentage of carbon fiber in one layer of composite material is respectively 34%, 38%, 51% and 68%. Woven_2W_90 denotes the use of a fabric with a plain weave in which the weft and warp yarns are woven in two directions at an angle of 90 °. The name Woven_1W means the use of carbon fiber weft in one direction. Table 1 summarizes the basic parameters for single components, and Table 2 shows the basic parameters for individual layers of composite material.

The next step in the modelling of the composite material is the reproduction of the composition of the composite material of the tested samples. The following compositions (composite material structures) are defined: SL-0_90-34-5layers, SL-45_45-34-5layers, SL-0_1W(Y)-38-5layers, SL-90_1W(X)-38-5layers, SL-0_90-51-7layers, SL-45_45-51-7layers, SL-0_1W(Y)-51-7layers, SL-90_1W(X)-51-7layers, SL-0_90-68-10layers, SL-45_45-68-10layers, SL-0_1W(Y)-68-10layers, SL-90_1W(X)-68-10layers. A total amount of 12 composite material compositions were defined.

Table 1. Summary of basic parameters of components of a single layer of composite material

Epoxy resin	Carbon Fiber HTA40
Density – 1300 kg/m^3	Density – 1770 kg/m^3
Younge modulus – 3000 MPa	Younge modulus – 240000 MPa
Poission's ratio – 0,37	Poission's ratio – 0,22

Table 2. Summary of basic parameters with respect to exemplary single layers of composite material

34_Woven_2W_90 layer	38_Woven_1W layer
Matrix material – epoxy resin	Matrix material – epoxy resin
Volumetric share of matrix material – 0,66	Volumetric share of matrix material – 0,62
Matrix warp yarn material – carbon fiber	Matrix warp yarn material – carbon fiber
Weft fiber material – carbon fiber	Volumetric share of fiber – 0,38
Volumetric share of fiber – 0,34	Younge modulus E_1 – 93060 MPa
The coefficient of volume of warp fibers to weft fibers – 0,5	Younge modulus E_2 – 4802 MPa
The angle of alignment of the fibers relative to each other – 90°	Younge modulus E_3 – 4802 MPa
Younge modulus E_1 – 44240 MPa	Poission's ratio ν_{12} – 0,313
Younge modulus E_2 – 44240 MPa	Poission's ratio ν_{13} – 0,313
Younge modulus E_3 – 3000 MPa	Poission's ratio ν_{23} – 0,37
Poission's ratio ν_{12} – 0,032	Shear modulus G_{12} – 1754 MPa
Poission's ratio ν_{13} – 0,345	Shear modulus G_{13} – 1754 MPa
Poission's ratio ν_{23} – 0,345	Shear modulus G_{23} – 1095 MPa
Shear modulus G_{12} – 1649 MPa	Density – 1479 kg/m^3
Shear modulus G_{13} – 1047 MPa	
Shear modulus G_{23} – 879 MPa	
Density – 1460 kg/m^3	

The general way of describing composite material structures using Woven_2W_90 layers can be written as follows: SL-A_B-C-D. In the used method of writing, the SL symbol means that a given structure is formed as a solid laminate structure, A symbol denotes a measure of the angle of laying of the matrix fibers of the layer relative to the main direction of fiber orientation, B denotes the value of the angle of position of the weft yarn relative to the main direction of the yarn (angle between the fibers the warp and the warp in the layer always equals 90 °), C denotes the percentage of fibers in the layer, D denotes the number of layers in the structure. In this case, of Woven_1W composite structure, the following name can be written as SL-E_F (G) -HI, where E denotes the angle of unidirectional yarns in the layer relative to the main fiber orientation, F denotes the use of unidirectional fibers, G denotes the reference method of placing the fibers in the layer to the absolute coordinate system of the model, H denotes the percentage of fibers in the layer, I denotes the number of layers of the laminate composition.

Virtual strength tests of composite samples using the finite element method were performed to match the virtual model to the real object. This adjustment is necessary to implement the correct model's

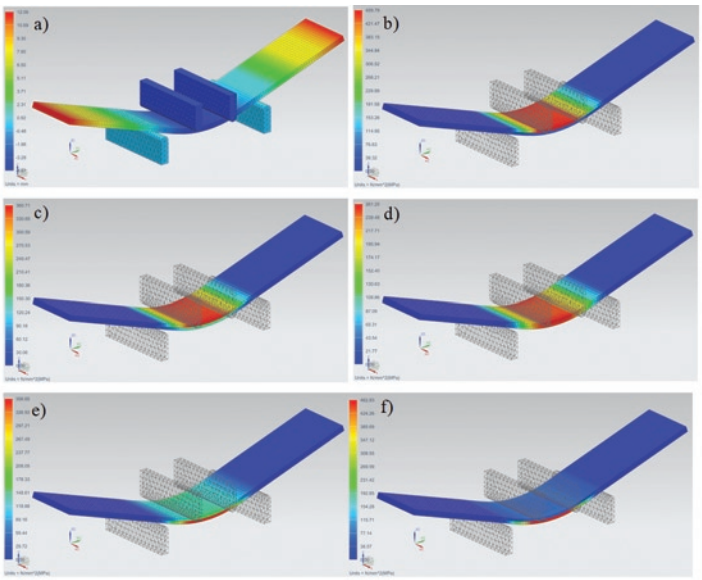

Fig. 6. Exemplary results of a virtual experiment (four-point bending test) using finite element method for SL-0_90-34-5 composite material: a) map of displacement, b) map of reduced stress in first layer, c) map of reduced stress map in second layer, d) map of reduced stress in the third layer, e) map of reduced stress in the fourth layer, f) map of reduced stress in the fifth layer

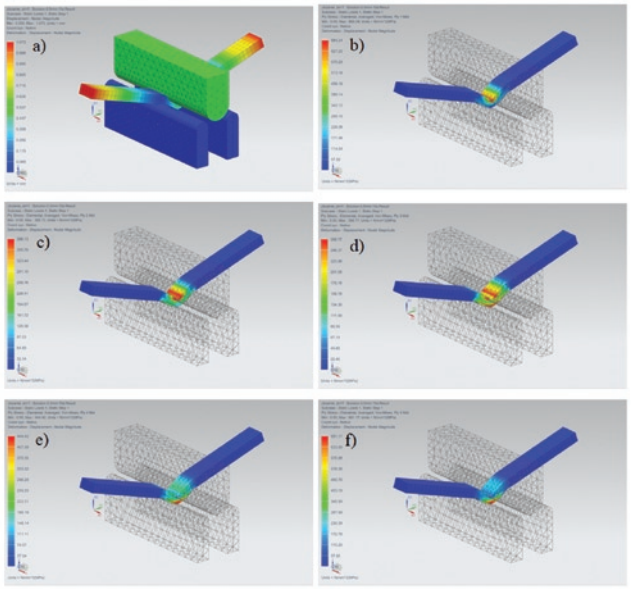

Fig. 7. Exemplary results of a virtual experiment (three-point bending test) using finite element method for SL-0_90-34-5layers composite material: a) map of displacement, b) map of reduced stress in first layer, c) map of reduced stress map in second layer, d) map of reduced stress in the third layer, e) map of reduced stress in the fourth layer, f) map of reduced stress in the fifth layer

Table 3. Examples of the results of virtual experiment on analyzed samples (four-point bending test)

Material symbol	Displ. of the sample [mm]	Layer nr 1 (σ [MPa])			Middle layer nr 3, 4 or 5 (σ [MPa])			Last layer nr 5, 7 or 10 (σ [MPa])		
	z_{max}; z_{min}	σ_{red}	σ_{11max}	σ_{11min}	σ_{red}	σ_{11max}	σ_{11min}	σ_{red}	σ_{11max}	σ_{11min}
SL-1, t_1	12,1; -4,6	460	48,9	-482,7	261	254,4	-261	463	472	-55,3
SL-2, t_2	7,2; -2,9	420	30,7	-442,8	225	221,8	-224,9	419	424,5	-33,7
SL-3, t_3	5,6; -2,3	455	22	-480	257	207,5	-257,2	450	454,2	-26,4

Table 4. Comparison of the FEM analysis results and the four-point bend test of the composite material SL-0_90-34-5 (volumetric share of the fabric 34%)

Punch displacement [mm]	Time [s]	The maximum value of stress (FEM analysis)	Stress values (bending test)		Relative error
			Range	Mean	
		[MPa]	[MPa]		
0,5	15	55	40 – 50	45	18%
1,0	30	112	80 – 100	90	19%
1,5	45	169	125 – 142	133,5	21%
2,0	60	228	165 – 195	180	21%
2,5	75	287	205 – 238	221,5	23%
3,0	90	347	218 – 270	244	29%

Table 5. Comparison of the results of the FEM analysis and four-point bending test for the composite material SL-0_90-51-7layers (volumetric share of the fabric 51%)

Punch displacement [mm]	Time [s]	The maximum value of stress (FEM analysis)	Stress values (bending test)		Relative error
			Range	Mean	
		[MPa]	[MPa]		
0,5	15	83	80 – 95	87,5	5%
1,0	30	167	165 – 190	177,5	6%
1,5	45	252	245 – 290	267,5	6%
2,0	60	339	320 – 380	350	3%

properties on other models made of composite materials used in specific constructional solutions. The virtual model was matched to the real object by changing parameters, such as finite element size, finite element mesh fit to the geometry of model of the sample and Young modulus.

The boundary conditions and the form of loads were defined in the created model. That enabled the achievement of correct deformities of the test sample according to the actual deformation distribution of the real sample during the four-point bending test (Figure 6) and the three-point bend (Figure 7). Based on the virtual bending of samples made of the composite material experiment, the values of displacement, deformation and stresses were calculated for each layer.

Figures 6 and 7 show the results of the analysis using the finite element method of the adjusted composite material, which was a composition of five layers, labelled as SL-0_90-34-5. The Figures illustrate the maps of displacement of the sample (a), the maps of reduced stress, presented in layers 1 (b), 2 (c), 3 (d), 4 (e) 5 (f).

Table 6. Comparison of the results of the FEM analysis and four-point bending test for the composite material SL-0_90-68-10layers (volumetric share of the fabric 68%)

Punch displacement [mm]	Time [s]	The maximum value of stress (FEM analysis)	Stress values (bending test)		Relative error
			Range	Mean	
		[MPa]	[MPa]		
0,5	15	113	120 – 140	130	15%
1,0	30	227	260 – 270	265	17%
1,5	45	343	390 – 420	405	18%

The results of the virtual experiment were also maps of the values of all the stress components (11 (YY), 22 (XX), 33 (ZZ), 12 (YX), 13 (YZ), 23 (XZ) - according to the global coordinate system showed on Figure 4), and deformation, which allows to precisely determine the influence of used load and boundary conditions on the applied composite material of the test sample.

Tables 4 - 6 summarizes the comparison results based on the FEM analysis and four-point bending test. The match was achieved for the composite material SL-0_90-51-7layers (the volumetric share of the fabric 51%). In this case, the maximum relative error was 6%. In case of composite material SL-0_90-68-10 layers (68% volumetric share of the fabric) the maximum relative error was 18%. Compared to the composite material SL-0_90-34-5 (volumetric share of the fabric 34%), a maximum error of 29% was obtained. However, it should be noticed that the material SL-0_90-34-5 was characterized by a large non-linearity of the stress characteristic in the sample as a function of the displacement of the punch in the range of displacements larger than 2 mm. In all the analyzed cases the FEM model includes the same match degree of mesh to the geometrical form of the sample and the other elements of the model, the same size of the finite element, and the same material properties.

4. Application of the composite material model for the strength analysis of the scaled freight wagon hull's sidewall

As part of the research [4 – 9, 18, 21, 22, 24] conducted by the research team in the scope of the project aimed at extending the life of freight wagons, the use of internal lining of the wagon hull in the form of the fiber reinforced composite panels was considered. The life of the wagon depends on the condition of its hull, which is made of metal sheet. Damages of the sidewall of the wagon can be caused by: the mechanical impact of the load carried on the wagon, the mechanical impact of the actuators of the loading and unloading machines and the chemical impact of the aggressive substances contained in the transported cargo. As a result of the mentioned effects, plastic deformation and local defects can occur in the sheet of metal. These hazards regarding the operation of freight wagons were the basis for the selection of fiber reinforced composites. Epoxy resin was used as the matrix, while glass fiber and carbon fiber were considered as reinforcing material.

Due to the need of carrying out a test of a modified version of the wagon's hull plating, the sidewall of the 418V dumper wagon (Fig. 8) was isolated. The method of isolation was selected to ensure the possibility of building a physical of test bench (Fig. 9 and Fig. 11) and to improve conducting of the numerical strength analysis and their validation.

For the purposes of the research, a test stand was designed and built, of which the basic elements are shown in Figure 9. The test stand consists of a support frame 1 to which the side sidewall 2 has been attached. A hydraulic cylinder 3 was attached to the lower part of the frame, which interacts with force on the analyzed part of the sidewall. A changeable pressure element is mounted to the actuator's piston rod 4 and presses against the side plating. Changing the length and width of this element allows for different types of load to be considered (point, surface). A control system has also been developed which allows for a smooth adjustment of the force in the range of 0 to 30 kN. In addition, the actuator can be moved smoothly in the XZ plane, which allows the load to be generated in different areas of the considered sidewall.

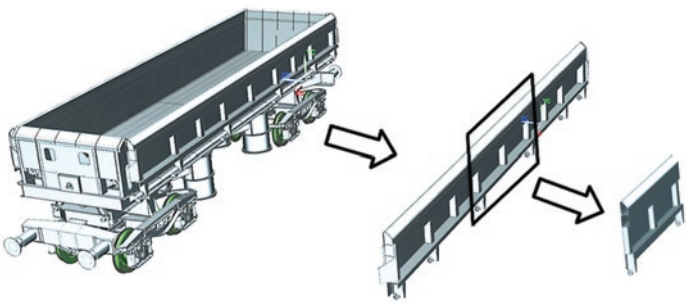

Fig. 8. Selected part of analyzed freight wagon's hull [6]

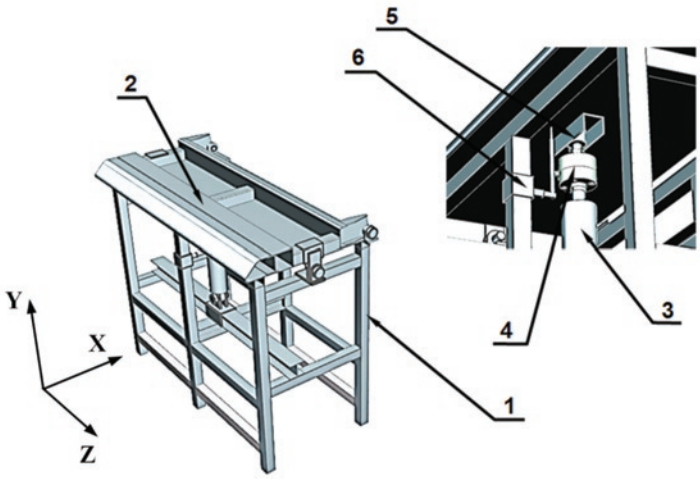

Fig. 9. CAD model of test bench [6]

The developed research bench was equipped with a system of sensors necessary to carry out the planned test cycle. It was assumed that the state of stresses and displacements on the sidewall before and after mounting the composite panels would be analyzed. For measuring the deformations a resistance strain gauges with a resistance of 120 Ω were used. For force measurement, a force transducer (HB2 U2B) was used, which was mounted on the piston rod of the hydraulic cylinder. A displacement transducer (HBM WA-T) was used to measure the displacement of the sidewall by which the displacement of the test area of the sidewall during the test was measured.

For the data acquisition and visualization of the results, a measuring circuit was developed and constructed (Figure 10). Signals from strain gauges were sent via the CANHED multi-channel amplifier to the computer on which the CATMAN data acquisition software was installed. This application is used to visualize and acquire measurement data. The obtained data packets were saved in a format com-

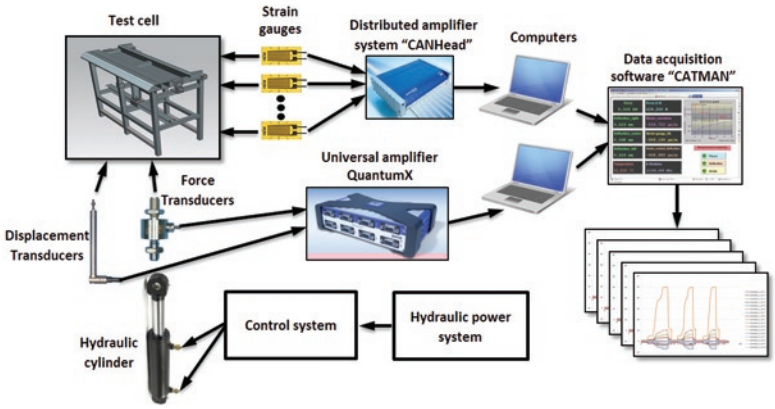

Fig. 10. Measuring circuit of a developed test bench[6]

patible with MS Excel software, and graphs were then generated for the analyzed quantities. Analogously, force and displacement values were measured and analyzed. Signals from the displacement transducer and force transducer were transmitted through the QuantumX multichannel amplifier to a computer and saved with a CATMAN software.

Firstly, the MES analysis of the scaled sidewall of the wagon's hull was performed to determine the places where significant stress values should be expected regarding the actual object.

Then, strain gauges were placed on the test bench (Fig. 12) and the wagon sidewall model was adjusted to the actual object [6].

The adjustment process of the wagon's sidewall FEM model consisted in the applying of such modifications in the model so that the results were consistent with the results obtained by experimental studies (strain gauges). The conformed numerical model of the hull's sidewall of the wagon became the basis for numerical analysis using the FEM method of the upgraded part of the freight wagon. In this case, composite panels (Fig. 13) were added to the FEM model and the stresses and displacements were calculated for the whole set of objects of the scaled sidewall. Numerical tests were performed in PLM Siemens NX software. In the first step, a mesh of finite elements was generated regarding the steel parts of the sidewall of the wagon. In this case, CTETRA finite elements (10 nodes tetragonal finite elements) were used. A finite element mesh was then defined for composite panels. In this case, finite elements of the CHEXA type (8 hexagonal finite elements) were used. All the finite elements of the wagon's plating mesh were assigned a steel type material. On the other hand, in the case of mounted composite panels, the previously described method of modelling multilayer composite materials was used. Two composite materials have been included in the numerical study. The first composite material was defined as an epoxy resin and carbon fiber fabric, while the other was an epoxy resin and glass fiber fabric composite. Regarding to both composite materials a composition consisting of four layers was used. The basic properties of both compositions are shown in Table 7.

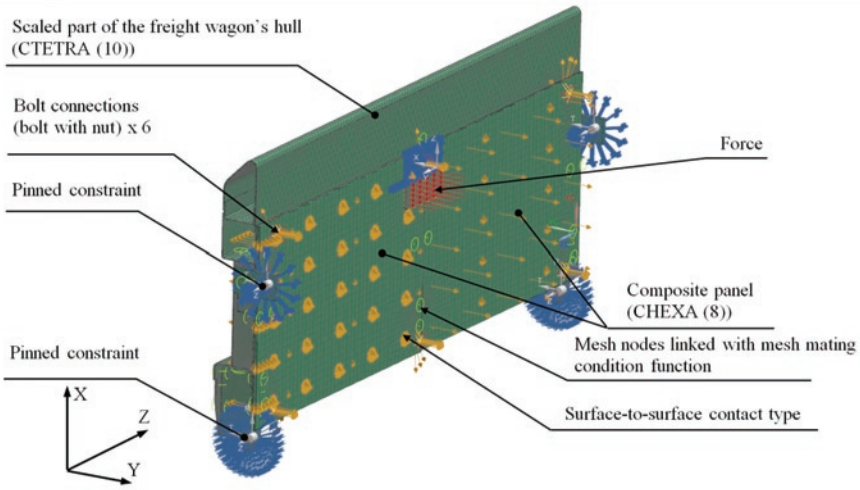

Fig. 13. Sidewall model of the wagon with mounted composite panels prepared for FEM analysis

Fig. 11. CAD model and actual layout of test bench

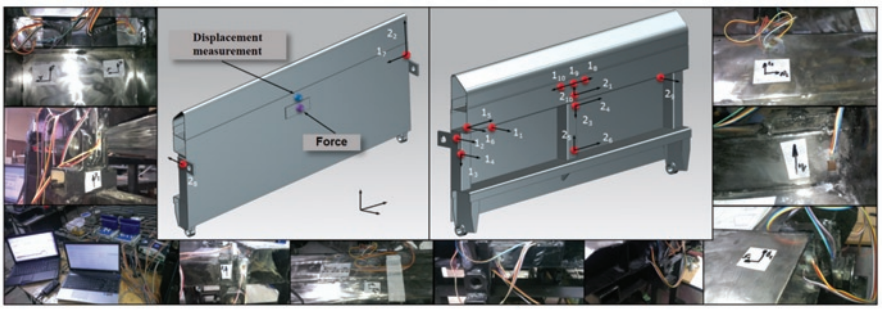

Fig. 12. Measurement points on the analyzed sidewall

Regarding the composition, the following parameters are defined: the main direction of fiber orientation according to the Z axis of the global coordinate system, the direction of layering according to the Y axis, the thickness of the single layer equal to 1 [mm] and the angle of laying of the layer within the defined composition equal to 0 °.

In order to represent the problem, the following boundary conditions were defined:

- „pinned constraint" – this type of constraint was used to imitate the method of fixing the sidewall,
- „mesh mating condition" linking mesh nodes function – by which the elements of the wagon's hull are connected to each other permanently,
- „surface-to-surface" contact type – by which the nature of the interactions between the elements that come into contact by load existing in the system (between the wagon's hull plates and the composite panels) was defined,
- „bolt connections" – by which the method of fixing composite panels to the wagon's hull plates was imitated.

Table 7. Summary of basic properties of the composite material layer consisting of epoxy resin and carbon fiber and fiberglass

Carbon fiber layer	Glassfiber layer
composite matrix material - epoxy resin	composite matrix material - epoxy resin
volume ratio of composite matrix material - 0.47	volume ratio of composite matrix material - 0.45
fabric matrix material - carbon fiber	fabric matrix material - glassfiber
fabric weft material - carbon fiber	fabric weft material - glassfiber
volume ratio of fiber - 0.53	volume ratio of fiber - 0.55
weight of warp and weft fibers – 0,5	weight of warp and weft fibers – 0,53
alignment angle between fibers – 90°	alignment angle between fibers – 90°
Young's modulus E_1 - 67220 MPa	Young's modulus E_1 - 24250 MPa
Young's modulus E_2 - 67220 MPa	Young's modulus E_2 - 22230 MPa
Young's modulus E_3 - 3000 MPa	Young's modulus E_3 - 3000 MPa
Poission's ratio ν_{12} – 0,027	Poission's ratio ν_{12} – 0,079
Poission's ratio ν_{13} – 0,33	Poission's ratio ν_{13} – 0,32
Poission's ratio ν_{23} – 0,33	Poission's ratio ν_{23} – 0,326
hear modulus G_{12} – 2283 MPa	shear modulus G_{12} – 2329 MPa
shear modulus G_{13} – 1110 MPa	shear modulus G_{13} – 1118 MPa
shear modulus G_{23} – 1189 MPa	shear modulus G_{23} – 1443 MPa
density – 1547 kg/m^3	density – 1982 kg/m^3

Based on such prepared model, a series of strength tests was performed using the finite element method. Table 8 summarizes the results of FEM analysis regarding the scaled side wall of the wagon with mounted composite panels. Based on the results obtained, it can be assumed that composite material panels made of epoxy resin and glass or carbon fiber will not be destroyed as a result of the load coming from the cargo carried by the freight wagon.

For economic reasons, a scaled part of the sidewall of the wagon with mounted panels made of composite material consisting of epoxy resin and glass fibers was subjected to experimental verification. Due to the highest stress values in this area, Fig. 15 shows the stress distribution, regarding the matched model, on the outer side of the freight wagon's hull. In contrast, Fig. 16 shows the results of measurements using strain gauges, where the strain gauge number 21 was highlighted, which recorded the highest values of stresses in the analyzed system with the applied force of 15 kN. It can be noticed that the application of reinforcement on the inner surface of the wagon's hull in the form of composite panels caused the reduction of the component stresses on the sidewall of the wagon in the Z-Z direction from about 76 MPa to about 60 MPa. Adjustment of the FEM model to the stationary test results was made by modification of the finite element size, the method of matching the finite elements mesh to the geometric form of the model, and the value of the Young modulus.

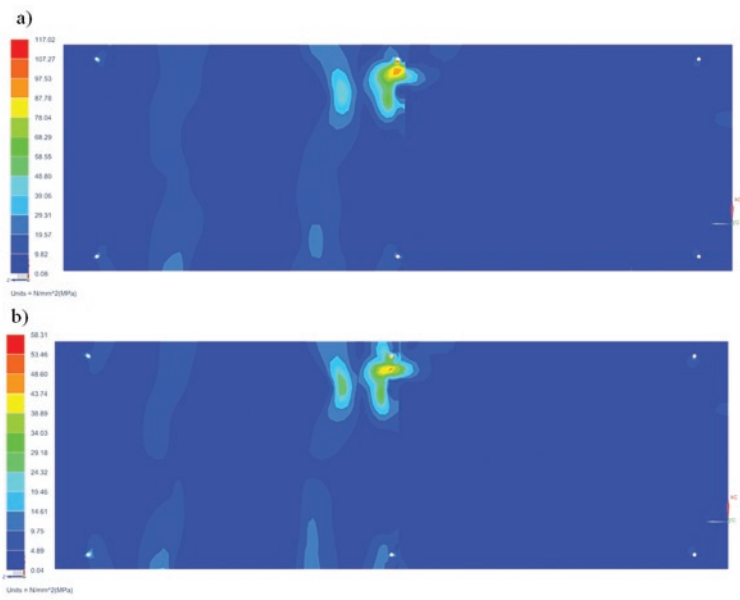

Fig. 14. Stress distribution occurring in panels made of composite material (layer 1), which is a composition of epoxy resin and carbon fibers (a) and glass fibers (b)

Table 8. Comparison of the FEM analysis results regarding the model of scaled sidewall of the wagon with mounted composite panels for the load of 15 kN of force applied

Layer number	Maximum values of reduced stresses in composite panels (carbon fiber) [MPa]	Maximum values of reduced stresses in composite panels (glass fiber) [MPa]
1	117,02	58,31
2	53,94	28,64
3	49,48	47,05
4	109,16	87,99

5. Conclusions

The developed model based on the acoustic method (ATH) is suitable for use in non-destructive testing of composite panels used in freight wagons.

The best match of the virtual model to the results of analysis carried out on the actual samples was achieved for seven-layered composite material with 51% of fabric content.

The tests carried out at the test bench shown in Figure 9 correlate sufficiently with the tests carried out on the actual object which was the sidewall of the wagon.

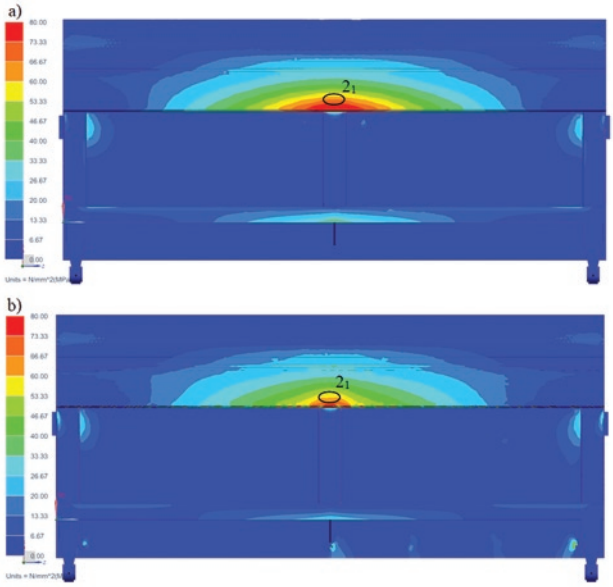

Fig. 15. Stress distribution in Z-Z direction on the sidewall of the scaled freight wagon's hull: without reinforcement (a), reinforced in the form of fiberglass composite panels (b)

The diagrams in Fig. 16 show that the placement of the reinforcement on the sidewall of the freight wagon's hull in the form of a 4mm composite panel will reduce the stresses on the by about 20%.

The computer-assisted modelling technique for modelling the three-point and four-point bending of composite samples, presented in this paper, allows to prepare, perform and obtain correct results of the virtual bending experiment of multilayer composite samples.

The suggested way of describing the composite material allows it to be modeled in the form of a composition of any number of layers. Particular attention should be paid to the possibility of creating and testing samples made of a composite material whose individual layers may be composed of different fabrics and resin types. In addition, each of the layers in the composite material composition may have a different angular position relative to the global coordinate system, which implies obtaining various strength properties of the sample in different directions.

The main purpose of using the inner lining of a freight wagon's hull in the form of composite panels was to protect it from mechanical and chemical damage. However, the protective "coating" applied in form of the proper composite material composition and the number of composite layers may also act as a reinforcement to the wagon's hull. This is very important from the point of view of servicing of already damaged wagons(reduced sheet thickness due to corrosion). This would allow a dramatic reduction in the number of operations involved in cutting damaged sheet metal from the wagon's hull and inserting a new one.

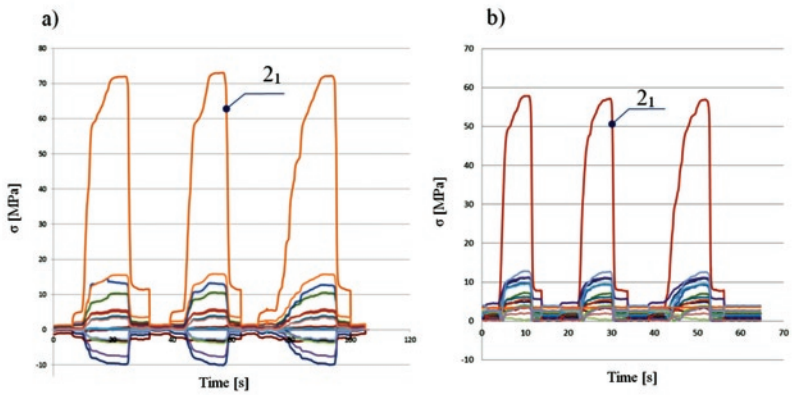

Fig. 16. Results of test bench measurements of the scaled sidewall of the freight wagon: without reinforcement (a), with reinforcement in the form of fiberglass composite panels with a thickness of 4 mm (b)

References

1. Beluch W. Metody inteligencji obliczeniowej w zagadnieniach optymalizacji identyfikacji parametrów włóknistych kompozytów warstwowych. Monografia, Wydawnictwo Politechniki Śląskiej, 2013.
2. Bienias J, Dębski H, Surowska B, Sadowski T. Analysis of microstructure damage in carbon/epoxy composites using FEM. Computational Materials Science 2012; 64: 168–172, https://doi.org/10.1016/j.commatsci.2012.03.033.
3. Boisse P, Borr M, Buet K, Cherouat A. Finite element simulations of textile composite forming including biaxial fabric behavior. Composites Part B: Enginnering Journal 28B 1997; 453-464, https://doi.org/10.1016/S1359-8368(96)00067-4.
4. Buchacz A, Baier A, Herbuś K, Majzner M, Ociepka P. Examination of a cargo space of a freight wagon modified with composite panels. Applied Mechanics and Materials 2015; 809-810: 944-949, https://doi.org/10.4028/www.scientific.net/AMM.809-810.944.
5. Buchacz A, Baier A, Herbuś K, Majzner M, Ociepka P. Application of programs of the CAD/CAE class for creating the virtual laboratory stand. Applied Mechanics and Materials 2015; 809-810: 841-846, https://doi.org/10.4028/www.scientific.net/AMM.809-810.841.
6. Buchacz A, Baier A, Herbuś K, Majzner M, Ociepka P. Investigations of Composite Panels Mounted in the Cargo Space of a Freight Wagon. Springer Proceedings in Mathematics & Statistics, Dynamical Systems: Modelling 2016; 181: 97-105.
7. Buchacz A, Baier A, Herbuś K, Ociepka P. An investigation of the influence of a fiber arrangement of a laminate on the values of stresses in the composite panel of a modified freight wagon using the FEM method. MATEC Web of Conferences 2017; 112: 04015, https://doi.org/10.1051/matecconf/201711204015.
8. Buchacz A, Baier A, Płaczek M, Herbuś K, Ociepka P, Majzner M. A concept of technology for non-destructive testing of modernized freight cars based on analysis of their vibration. Vibroengineering Procedia 2016; 10: 333-338.
9. Buchacz A, Baier A, Świder J, Płaczek M, Wróbel A, Herbuś K, Ociepka P, Banaś W, Sobek M, Grabowski Ł, Majzner M. Analytical and experimental tests and determination of Characteristics of components working as assemblies of innovative structures of repaired freight cars. Monografia, Wydawnictwo Politechniki Śląskiej, Gliwice 2016.

10. Cecot W, Oleksy M. High order FEM for multigrid homogenization. Computers and Mathematics with Applications 2015; 70: 1391–1400, https://doi.org/10.1016/j.camwa.2015.06.024.
11. Chen J, Lussier D S, Cao J, Peng X Q. Materials characterization methods and material models for stamping of plain woven composites. International Journal of Forming Processes 2001; 4: 269 – 283.
12. Dąbrowski H. Wytrzymałość polimerowych kompozytów włóknistych. Oficyna Wydawnicza Politechniki Wrocławskiej, Wrocław 2002.
13. Dębski H. Eksperymentalno-numeryczne badania pokrytycznych zachowań kompozytowych kolumn o przekroju omegowym, Eksploatacja i Niezawodność 2013; 15; 106-110.
14. Dobrzański L A. Podstawy nauki o materiałach i metaloznawstwo. Wydawnictwo Naukowo Techniczne, Warszawa 2002.
15. Fangueiro R. Fibrous and composite materials for civil engineering applications. Woodhead Publishing Limited, Cambridge 2011, https://doi.org/10.1533/9780857095583
16. Folega P. Study of dynamic properties of composite and steel-composite flexsplines of harmonic drives. Journal Of Vibroengineering 2015; 17: 155-163.
17. German J. Podstawy mechaniki kompozytów włóknistych. Wydawnictwo Politechniki Krakowskiej, Kraków 2001.
18. Herbuś K, Ociepka P. A study of an influence of a fiber arrangement of a laminate ply on the distribution and values of stresses in the multi-layered composite material. MATEC Web of Conferences 2017; 112: 04022, https://doi.org/10.1051/matecconf/201711204022.
19. Jaśkowiec J, Pluciński P, Stankiewicz A, Cichoń Cz. Three-dimensional modelling of laminated glass bending on two-dimensional in-plane mesh. Composites Part B: Engineering Journal 2017; 120: 63-82, https://doi.org/10.1016/j.compositesb.2017.03.008.
20. Martinsa R, Reisa L, Marat-Mendesa R. Finite element prediction of stress-strain fields on sandwich composites. Procedia Structural Integrity 1, 2016; 066–073.
21. Ociepka P, Herbuś K. Strength analysis of parallel robot components in PLM Siemens NX 8.5 program. IOP Conf. Series: Materials Science and Engineering 2015; 95: 012101, https://doi.org/10.1088/1757-899X/95/1/012101.
22. Płaczek M, Wróbel A, Baier A. Computer-aided strength analysis of the modernized freight wagon. IOP Conf. Series: Materials Science and Engineering 2015; 95: 012042.
23. Polit O, Gallimard L, Vidal P, D'Ottavio M, Giunta G, Belouettar S. An analysis of composite beams by means of hierarchical finite elements and a variables separation method. Computers and Structures 2015; 158: 15–29, https://doi.org/10.1016/j.compstruc.2015.05.033.
24. Sobek M, Baier A, Buchacz A, Grabowski Ł, Majzner M. Carbon fiber based composites stress analysis. Experimental and computer comparative studies. IOP Conf. Series: Materials Science and Engineering 2015; 95: 012011.
25. Song W, Zhong Y, Xiang J. Mechanical parameters identification for laminated composites based on the impulse excitation technique. Composite Structures 2017; 162: 255–260, https://doi.org/10.1016/j.compstruct.2016.12.005.
26. Stadnicki J, Tokarz Z. Model obliczeniowy kompozytu warstwowego — kalibracja z wykorzystaniem optymalizacji. Biuletyn WAT, Warszawa 2007; LVI: 207-216.
27. Stadnicki J, Tokarz Z. Mesoscale finite element model for calculating deformations of laminate composite constructions. Advances in Mechanical Engineering 2016; 8: 1–9, https://doi.org/10.1177/1687814016633604.
28. Śledziewski K. Experimental and numerical studies of continuous composite beams taking into consideration slab cracking. Eksploatacja i Niezawodnosc – Maintenance and Reliability 2016; 18: 578–589, https://doi.org/10.17531/ein.2016.4.13.
29. Venkatesan S, Kalyanasundaram S. Finite element analysis and optimization of process parameters during stamp forming of composite materials. IOP Conf. Series: Materials Science and Engineering 2010; 10: 012138, https://doi.org/10.1088/1757-899X/10/1/012138.

Andrzej BUCHACZ
Andrzej BAIER
Krzysztof HERBUŚ
Piotr OCIEPKA
Łukasz GRABOWSKI
Michał SOBEK
Institute of Engineering Processes Automation
and Integrated Manufacturing Systems
Faculty of Mechanical Engineering
Silesian University of Technology
ul. Konarskiego 18A, 44-100 Gliwice, Poland

E-mails: andrzej.buchacz@polsl.pl, andrzej.baier@polsl.pl, krzysztof.herbus@polsl.pl, piotr.ociepka@polsl.pl, lukasz.grabowski@polsl.pl, michal.sobek@polsl.pl

Article citation info:
TABASZEWSKI M, FIRLIK B. Assessment of the track condition using the Gray Relational Analysis method. Eksploatacja i Niezawodnosc – Maintenance and Reliability 2018; 20 (1): 147–152, http://dx.doi.org/10.17531/ein.2018.1.19.

Maciej TABASZEWSKI
Bartosz FIRLIK

ASSESSMENT OF THE TRACK CONDITION USING THE GRAY RELATIONAL ANALYSIS METHOD

OCENA STANU TOROWISKA Z WYKORZYSTANIEM METODY GREY RELATIONAL ANALYSIS*

The article concerns the developed methodology for assessing the technical condition of a tramway track. Thanks to the data collected from multiple tram journeys equipped with an on-board vibration recording system, it was possible to create profiles of crossings through track sections in different technical condition. In order to identify the track condition, an algorithm based on the gray-scale modeling was proposed, and a similarity comparison between the obtained track profiles. A new measure of similarity has been proposed that has not been used so far in gray-scale modeling. The obtained results confirm the applicability of the proposed methodology.

***Keywords**: track, maintenance, monitoring, tramway, GRA.*

Praca dotyczy opracowanej metodyki do oceny stanu technicznego toru tramwajowego. Dzięki zgromadzonym danym z wielokrotnych przejazdów tramwaju wyposażonego w pokładowy system rejestracji drgań, udało się stworzyć profile przejazdów przez odcinki torów w różnym stanie technicznym. W celu identyfikacji stanu toru zaproponowano algorytm oparty na metodzie modelowania szarych systemów oraz badanie podobieństwa pomiędzy uzyskanymi profilami przejazdów. Zaproponowano także nową miarę podobieństwa nie stosowaną do tej pory w zagadnieniach modelowania szarych systemów. Uzyskane wyniki potwierdzają aplikacyjność zaproponowanej metodyki.

***Słowa kluczowe**: track, maintenance, monitoring, tramway, GRA.*

1. Introduction

The execution of current research on recording the acceleration caused by tram vibrations in operating conditions, using on-board diagnostics systems and wireless data transmission, enables the track condition assessment based on the vehicle dynamic response analysis [5 ÷ 7]. This issue is very important from the infrastructure maintenance point of view, as it allows for an ongoing assessment of its technical condition in normal operating conditions. Such systems are particularly suitable for rail networks where driving conditions are constant, reproducible and without significant interference or changes in driving behavior [e.g. 1; 3; 12]. In urban conditions, this is not a trivial task, as it results from the substantial spread of data received even from the same vehicle type and the same measuring section. This is due to the fact that the vehicle is moving at different speeds within the same track, variable load (number of passengers), driving behavior of the motorists (rapid or gentle acceleration and deceleration), weather conditions, traffic at different hours and days, technical condition of the vehicle, etc. The measurement uncertainty of the monitoring system itself should also be taken into account. All of these factors make it difficult to estimate the track condition for light rail vehicles using the acceleration level measured in the vehicle.

In order to eliminate some of the above mentioned factors and to propose a methodology for evaluating the track condition, it was decided to, at the first stage, select the data from different track sections (in different parts of the city) of one type, i.e. with 60R2 tram rail, excluding areas using a classic railway track (mainly 49E1). In addition, it was decided to include the tram speed recordings for a given track, forming a certain profile characteristic for a particular track condition (the relation between the effective acceleration values and the tram speed). For each passing, the maximum speed was taken into account, assuming that the information about the technical condition of the track will be most visible for such driving speed. Another factor, whose impact was eliminated, was the technical condition of the vehicle itself. The data considered were from a new vehicle, but this does not limit the application of the proposed methodology. In practice, it is always possible to eliminate this factor by installing a vibration measurement system on a new or renovated vehicle.

The presented analysis used data collected from more than two months of operation of a modern low-floor tram in normal passenger traffic. The information on the vibration acceleration value determined from a 1 second time window in the range of 0 to 100 Hz, recorded on the vehicle body located above the first bogie. Thus this is in a way a measure of travel comfort (there are currently no official legal acts in this field dedicated to light rail vehicles such as a tram). The effective value of vibration acceleration was selected after a comparative analysis of various statistical measures [7].

Evaluation of the track sections actual technical condition was determined on the basis of independent information obtained from maintenance services, assisted by independent measurements of track geometry. Finally, the data presented in Table 1 and presented in Figure 1 were taken into account. The proposed grading scale of the track technical condition assessment is deliberately coincidental with that adopted in MPK Poznan (local tramway operator).

(*) Tekst artykułu w polskiej wersji językowej dostępny w elektronicznym wydaniu kwartalnika na stronie ***www.ein.org.pl***

Table 1. Main data included in the analysis

Technical condition	Number of track sections	Total number of dynamic response measurements of the vehicle
Good	8	1086
Satisfactory	2	278
Poor	3	103
Critical	2	240

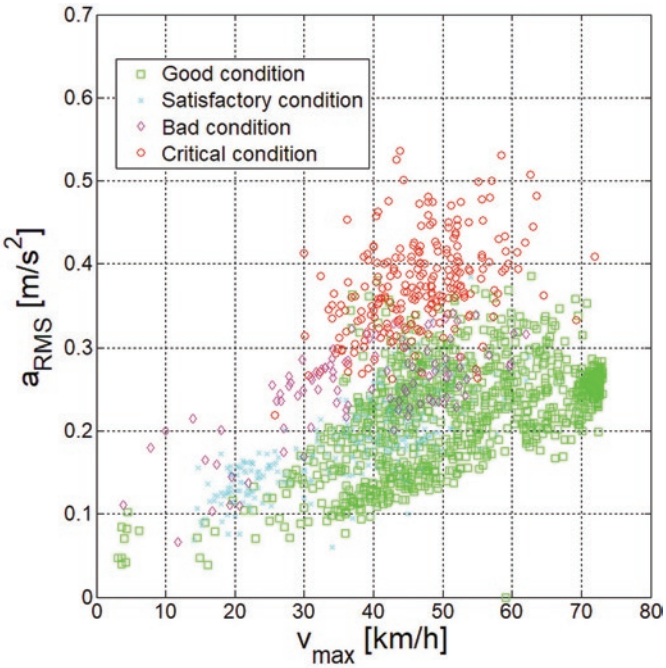

Fig. 1. Speed and acceleration profiles on track sections with different technical condition

As shown in Figure 1, data on various track technical conditions strongly intertwine and are strongly dependent on the maximum vehicle travel speed. In addition, the available speed range for certain data may vary due to the fact that sections of different technical conditions are located in a different "urban environment". These can be i.e. sections where the tram travels without stopping and sometimes it may be necessary to brake and accelerate. Hence, the range of maximum speed values should also be considered. Available data also differ in their number (different number of passes through a particular track section), which needs to be taken into account in the proposed methodology.

While it is easy to determine good and critical track conditions based on average or maximum effective vibration acceleration, the remaining intermediate states are no longer easily distinguishable due to large scattering (see Table 2, columns 1 and 2). Another simple solution would be to create a linear regression model of the passage profile for each of the track conditions and to evaluate the y-intercept or the slope of the line accordingly. Unfortunately, the slope does not carry information about the track condition, and the information contained in the y-intercept does not distinguish between good and satisfactory. The relevant data is given in Table 2.

Since the use of the aforementioned simple methods is not effective in unequivocally determining the track condition, it was decided to resort to methods based on the similarity of specific data to the reference values. The reference will be based on the passage profile for the track section in good condition. The idea of the method will be to compare the obtained passage profile with the previously constructed model. In actual operating conditions, it will take only a few days to collect certain data from a particular controlled track section, because of the repeated passes on the same route by the same vehicle. This is a relatively short measurement time.

Due to the fact that the data can be very scattered, it was decided to use gray-scale modeling tools that can be used not only when there is little data available, but also when the data is uncertain. This is where the gray GM models can be used to model a particular profile. It is also necessary to define the similarity measure of the individual driving profiles. This can also be performed using methods for modeling gray systems (GRAs).

2. Track technical condition determination methodology

The main part of the research activities will be based on the gray systems modeling methods, so it is worthwhile to present some of the foundations of this theory. Theory of gray systems was proposed by prof. J-L. Deng, and has many different research areas and uses [4]. One of them is the study of similarity between data sequences (GRAs) [10]. Studying the similarity of data in different collections is of great importance in this methodology as it allows for a comparison of a given drive profile with the reference for a good track condition. The specified measure of similarity in the conditions of maximum travel speed can then be easily parameterized giving a single number indicating the degree of compliance with the model, and thus the technical condition of the track.

For this purpose, the travel profiles similarity measures should be defined. There are a number of measures in the GRA literature that define the relation between the data. An example is a generalized GRA model, which is used to analyze relationships between sequences and measures based on distance and similarity. A detailed overview of the methods can be found in [10]. Certain other measures have been proposed in [13].

An important role in this approach is played by the gray GM systems modeling in relation to the data set. As a result of certain operations, it can be treated as a series which allows it to be modeled with a gray model, such as GM(1,1) [4; 8; 11; 14; 16; 17]. This provides an opportunity for a model representation of primary data that is characterized by high uncertainty and dispersion. One feature of this model is the smoothing of local fluctuations (series) by the use of AGO (Accumulated Generating Operation), which allows for the replacement of the original data with model data, which are largely smoothed out.

Figure 2 shows a flowchart illustrating an algorithm for modeling passage profiles, determining similarity measures, and determining the technical condition of a track.

Assuming that further realizations of passages for a given track

Table 2. Simple statistical parameters describing the collected data

Track technical condition	RMS vibration acceleration value [m/s^2]	Maximum RMS vibration acceleration value [m/s^2]	Regression line slope describing the travel profile	Regression line y-intercept describing the travel profile
Good	0.224	0.386	0.0024	0.0918
Satisfactory	0.184	0.385	0.0034	0.0632
Poor	0.250	0.341	0.0029	0.1408
Critical	0.375	0.537	0.0030	0.2330

section are available. Let $X_i(k)$, $X_j(k)$, $i=1,2, ..n, j = 1,2,...,m$ denote vectors whose elements are the measure of the value of travel comfort for the passage through travel profiles i and j. Original data obtained using GM(1,1) models must be removed in cases where exactly the same speed values correspond to different values of effective vibration acceleration. This is necessary due to the fact that the GM(1,1) models describe a series. Although the speed values are determined to the nearest 0,01 km/h, the situation for which different acceleration readings are obtained for the exact same speed is quite common and should be taken into account.

In the next step of the algorithm, the original data is replaced by the results of linear interpolation. This is due to the fact that the basic GM(1,1) model requires a constant interval between the data, and that the compared vectors Xi and Xj must have the same number of elements. This is a condition for calculating the similarity measure of both profiles. For this purpose, it may also be necessary to cut out some data so that the compared sets cover the same maximum speed range in both comparable passage profiles – the tested one and the reference.

In order to model the resulting series, it is necessary to use the AGO, which according to [8] can be represented for the Xi vector as:

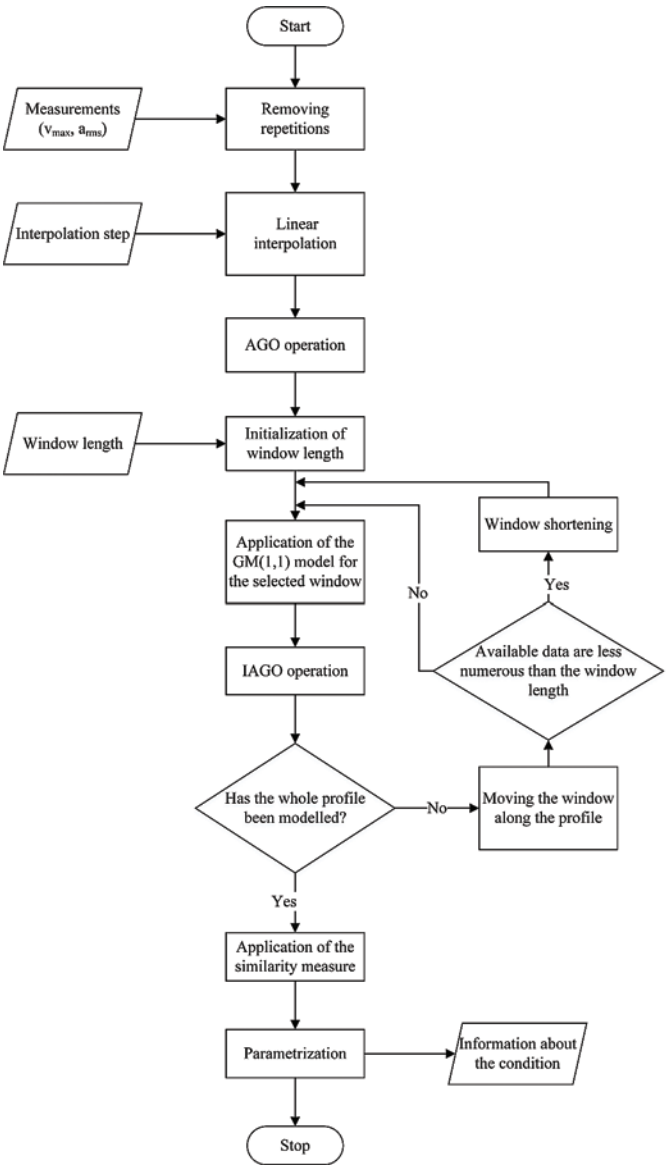

Fig. 2. Algorithm for the determination of the technical condition of the track on the basis of the similarity study of the profile of crossings: recognized and referenced

$$X^{(1)}{}_i(k) = \sum_{r=1}^{k} x_i(r)\,. \tag{1}$$

The previously mentioned GM(1,1) model is derived from the general description of the gray system in the form of a differential equation (2). In general for the case where the equation of the p order with excitation of m order GM(p,m) as described in [2] the following equation will be obtained:

$$\sum_{l=0}^{p} a_l \frac{d^{p-l} X_i^{(1)}}{dt^{p-l}} = \sum_{i=1}^{m-1} b_i X_{i+1}^{(1)}\,, \tag{2}$$

where: X_1 is a vector of original observations x_1(r), $X_1^{(1)}$ is a system state variable vector derived from the original observation vector after the AGO operation according to (1) , X_{i+1} is the input vector, a_l , b_h are constant coefficients.

Model GM(1,1) for a given data set X can be expressed as:

$$\frac{dX^{(1)}(t)}{dt} + aX^{(1)}(t) = b \tag{3}$$

The solution of equation (3) with unit step k can be represented [8] as:

$$\hat{x}^{(1)}(k+1) = \left[x^{(0)}(1) - b/a\right]\exp(-ak) + b/a \tag{4}$$

where $\hat{x}^{(1)}$ is the predicted value of the cumulative series element. Using finite differences and expressing equation (3) as a series of equations for discrete values, according to [8] the following approximation is obtained:

$$x^{(1)}(k+1) - x^{(1)}(k) = -\frac{a}{2}\left[x^{(1)}(k) + x^{(1)}(k+1)\right] + b \tag{5}$$

Model parameters are calculated based on the equation (5) using the least squares method [16]:

$$\begin{bmatrix} \hat{a} \\ \hat{b} \end{bmatrix} = \left(\mathbf{Z}^T\mathbf{Z}\right)^{-1}\mathbf{Z}^T\mathbf{Y} \tag{6}$$

where:

$$z(k) = -\frac{1}{2}\left(x^{(1)}(k+1) + x^{(1)}(k)\right),$$

$$\mathbf{Y} = \begin{bmatrix} x^{(0)}(2) \\ x^{(0)}(3) \\ .... \\ x^{(0)}(n) \end{bmatrix}, \quad \mathbf{Z} = \begin{bmatrix} z(1) & 1 \\ z(2) & 1 \\ ... & ... \\ z(n-1) & 1 \end{bmatrix}$$

The parameters of the GM(1,1) model can be estimated using all available rolling window methods [15]. Estimating parameters based on all data can cause the model to excessively smooth the values and

as a result not capture certain changes in their trend. Using a narrow window causes the model to adapt to the trend and reflect it. The model can be used when there is little data, so using narrow windows is feasible. A window with a length of 80 measurements was arbitrarily chosen as a compromise between good data averaging and the ability to adapt the model to the data at an interpolation step for the track passage profile made up of 360 measurement points. At each step of the model construction, the window was shifted one measurement and the smoothed modeled values were estimated. In cases where the number of data points available for the model parameters evaluation was less than the window length, the window was shortened respectively. Theoretically, the window can only be shortened to four measurements that are necessary for the estimation of the GM(1,1) model parameters. The last four model values are derived from forecasts using the model and the last parameters estimated.

The next step is to calculate the similarity of modeled passage profiles. With constant interpolation k, it is possible to define a matrix of mutual change own similarity [13]:

$$\pounds_k = \begin{bmatrix} \sigma_{11}(k) & \dots & \sigma_{1m}(k) \\ \dots & \dots & \dots \\ & \sigma_{jj}(k) & \sigma_{jm}(k) \\ \dots & \dots & \dots \\ & & \sigma_{mm}(k) \end{bmatrix} \tag{7}$$

where: $\sigma_{ij}(k)$ is a measure of similarity for passage profiles i and j for a given step k, corresponding to a given maximum speed. Here the most interesting are the relative measures: $\sigma_{21}(k)$, $\sigma_{31}(k)$, $\sigma_{41}(k)$, that relate to the travel profiles associated with particular technical conditions of the track (satisfactory, poor and critical) and the reference (labeled as good track conditions).

The proposed definition of similarity measure of profiles may be expressed as:

$$\sigma_{ij} = \frac{\alpha A_{ij} + \beta B_{ij} + \gamma C_{ij}}{\alpha + \beta + \gamma} \tag{8}$$

where:

$$A_{ij} = \begin{cases} \dfrac{\hat{x}_i^{(0)} \hat{x}_j^{(0)}}{\max(\hat{x}_i^{(0)}) \cdot \max(\hat{x}_j^{(0)})} & \text{for } \hat{x}_i^{(0)} \neq \hat{x}_j^{(0)} \\ 1 & \text{for } \hat{x}_i^{(0)} = \hat{x}_j^{(0)} \end{cases},$$

$$B_{ij} = \begin{cases} \dfrac{\max(\Delta_{ij}) - \Delta_{1ij}}{\max(\Delta_{ij}) - \min(\Delta_{ij})} & \text{for } \max(\Delta_{ij}) \neq \min(\Delta_{ij}) \\ 1 & \text{for } \max(\Delta_{ij}) = \min(\Delta_{ij}) \end{cases},$$

$$C_{ij} = \begin{cases} \dfrac{\max(\Delta_{ij}) - \Delta_{ij}}{\max(\Delta_{ij}) - \min(\Delta_{ij})} & \text{for } \max(\Delta_{ij}) \neq \min(\Delta_{ij}) \\ 1 & \text{for } \max(\Delta_{ij}) = \min(\Delta_{ij}) \end{cases},$$

$$\Delta_{1ij} = \left| \hat{x}_{1i}^{(0)} - \hat{x}_{1j}^{(0)} \right|, \ \Delta_{ij} = \left| \hat{x}_i^{(0)} - \hat{x}_j^{(0)} \right|$$

$\hat{x}^{(0)}$ – series values vector after smoothing with the model GM(1,1), $\hat{x}_1^{(0)}$ – first series value, A – a component characterizing the similarity of "shapes" of the compared passages, B – a component taking into account different profile values for the smallest travel speed, C – a component characterizing the differences in values, α, β, γ – individual components influence coefficients (the weight of individual characteristics taken into account).

The sum of all components in formula (8) does not exceed 1.0 and they represent partial similarities in terms of individual characteristics. By adjusting the influence coefficients, different characteristics can be given a different level of significance. Part C is used in the GRA literature as a measure of similarity, for example [9], while B is an adaptation of this measure for the first value of the series.

The use of the GM(1,1) adaptive model in the proposed methodology is important in that it allows to capture the similarity features associated with the „local" changes in the compared travel profiles values. In the case of linear regression modeling of these profiles, the information would be lost. It should be noted that the proposed measure of similarity is universal and can be used to compare different sets of data concerning aspects other than the discussed problem.

Ultimately, the obtained similarity values can easily be parameterized by calculating the average or maximum value and on this basis, operational decisions or decisions on additional checks on a particular track section can be made.

3. Results

The described method was applied to the collected data presented in Figure 1. Interpolated and smoothed passage profiles with the GM(1.1) model with a measuring window of 80 points are shown in Figure 3. Different change rates of the vibration effective acceleration value as a function of the vehicle driving speed can be seen. The resulting smoothed profiles represented the input for the similarity calculation procedure $\sigma_{21}(k)$, $\sigma_{31}(k)$, $\sigma_{41}(k)$, where index 1 refers to the track profile for the good track condition. The mean values of the similarity calculation for the various weight values are shown in Table 2.

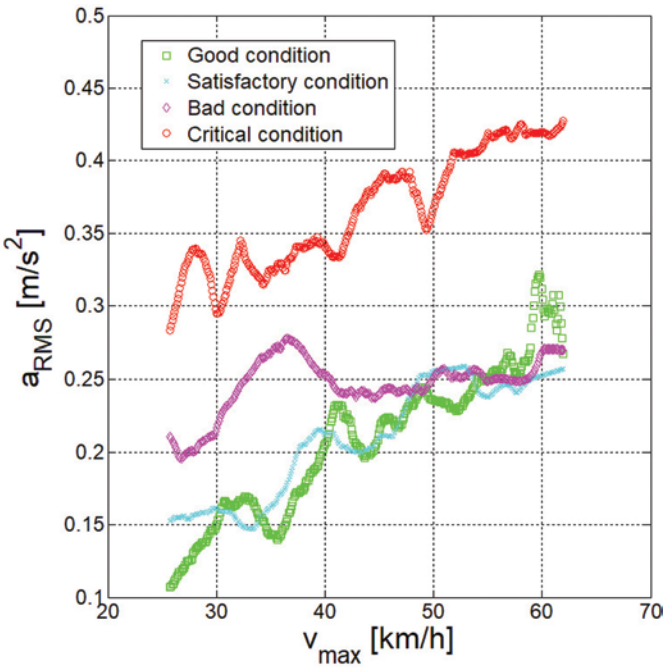

Fig.3. Result of GM model (1,1) with sliding window

Table 3. Sample results of the mean similarity measure for the data in Figure 1 and different weights

Similarity	α=1, β=1, γ=1	α=2, β=1, γ=1	α=1, β=2, γ=1	α=1, β=1, γ=2	α=0, β=0, γ=1
Satisfactory – good condition	0.538	0.539	0.489	0.586	0.731
Poor – good condition	0.483	0.507	0.471	0.526	0.654
Critical – good condition	0.448	0.478	0.413	0.453	0.469

The data in Table 3 indicates that in all cases the track technical condition becomes distinctive (as in Table 1). A smaller number means less similarity of a given profile to the profile corresponding to good track condition. The profiles that were obtained from passages in satisfactory track condition were most similar to the pattern defined for the track sections as good technical condition. A lower similarity can be seen between the data of passages through tracks in poor technical condition, and the smallest, for those in critical condition.

If greater significance is assigned to the distance of these profile values from the reference profile values, the distinction becomes particularly pronounced, hence this feature becomes the most important in the obtained profiles. According to the analyzes, this feature (and thus the commonly used GRA measure) is sufficient to clearly distinguish between the track conditions and, in this case, to better distinction of these states, it seems however, that a more flexible definition may have wider applications also to other data.

Thanks to the methodology used it is possible to clearly distinguish between the technical conditions of the tracks when measuring their exploitation in real operating conditions, which is very important from the practical point of view.

3. Conclusions

The problem of evaluating the technical condition of the track in real operating conditions is not trivial due to a number of factors influencing the measurement results, which are difficult to directly account for in the models. The idea of recording the vibration acceleration by the on-board system mounted on the tram (provided from the vehicle in good technical condition) and the creation of passage profiles on a given tested track section enables the classification of the technical track condition. However, this can be difficult due to the large spread of measurement data values. This classification can be performed through modeling of such a profile and then calculating the similarity of the measured profile and the reference profile. The gray systems theory provides a good foundation for this type of modeling, as in principle, it allows the modeling of uncertain data, and thus also data sets with large scattering. Using the GRA methodology in this case gives unambiguous results and allows to distinguish between the technical conditions of the track by simple parameterization of the mutual similarities between the modeled passage profiles. The proposed methodology allows for a relatively quick track condition diagnosis. Due to the multiple passages of a given vehicle on a given track, gathering the necessary data and creating a profile is not a difficult task. This underlines the practicality of the proposed methodology.

The similarity measure proposed in the article is very flexible and can be applied to a variety of problems. It embraces various aspects of the similarity between series. In the case of the data used, the obtained results are very good, although in this case the simpler GRA method also fulfills the task.

Acknowledgement

All presented research work is realized within the framework of a research Project - „Monitoring of Technical State of Construction and Evaluation of its Lifespan" within the Innovative Economy Operational Programme, Measure 1.1 Support for scientific research for establishment of a knowledge – based economy, Sub-measure 1.1.2 Strategic programmes of scientific research and development works.

References

1 Barbera A N, Corradi R, Barilaro P, Li Z, Wacrenier P L. A Track Quality Monitoring System Designed to be Installed on Vehicles in Normal Operation. Proceedings of the First International Conference on Railway Technology: Research, Development and Maintenance 2012; Paper 43.
2. Chen H W, Chang Ni-Bin. Prediction analysis of solid waste generation based on grey fuzzy dynamic modelling. Resources, Conservation and Recycling 2000; 29: 1-18, https://doi.org/10.1016/S0921-3449(99)00052-X.
3. Chen J, Roberts C, Weston P. Fault detection and diagnosis for railway track circuits using neuro-fuzzy systems. Control Engineering Practice 2008; 16(5): 585-596, https://doi.org/10.1016/j.conengprac.2007.06.007.
4. Deng J L. Introduction to grey system theory. The Journal of Grey System 1989; 1(1): 1-24.
5. Firlik B, Czechyra B, Chudzikiewicz A. Condition Monitoring System for Light Rail Vehicle and Track. Key Engineering Materials 2012; 518: 66-75, https://doi.org/10.4028/www.scientific.net/KEM.518.66.
6. Firlik B, Tabaszewski M. Dynamical Problems in Condition Monitoring of a Light Rail Vehicle. Proceedings of 13th Mini Conference on Vehicle System Dynamics, Identification and Anomalies – VSDIA 2012; 293-301.
7. Firlik B, Tabaszewski M, Sowiński B. Vibration-based symptoms in condition monitoring of a light rail vehicle. Key Engineering Materials 2012; 518: 409-417, https://doi.org/10.4028/www.scientific.net/KEM.518.409.
8. Kayacan E, Ulutas B, Kaynak O. Grey system theory-based models in time series Prediction. Expert Systems with Applications 2010; 37: 1784-1789, https://doi.org/10.1016/j.eswa.2009.07.064.
9. Lin S L, Wu S J. Is grey relational analysis superior to the conventional techniques in predicting financial crisis? Expert Systems with Applications 2011; 38: 5119-5124, https://doi.org/10.1016/j.eswa.2010.09.139.
10. Liu S F, Yang Y Y, Xie N M. A summary on the research of GRA models. Grey Systems: Theory and Application 2013; 3(1): 7-15, https://doi.org/10.1108/20439371311293651.
11. Luo M, Kuhnell B T. Forecasting machine condition using grey-system theory. Bulletin of MCCM, Monash Univ. Australia 1990; 2(1).
12. Parkinson H, Iwincki S. An Intelligent Track Monitoring System. AIC conference on Infrastructure Management, London, February 1999.
13. Tabaszewski M, Cempel C. Similarity measures for diagnostic symptom evolution. Grey Systems: Theory and Application 2016; 6: 51-63, https://doi.org/10.1108/GS-10-2015-0072.
14. Wang T C, Liou M C, Hung H H. Application of grey theory on forecasting the exchange rate between TWD and USD. International Conference on Business and Information, Academy of Taiwan Information System Research and Hong Kong Baptist University, July 2005.

15. Yao A W L, Chi S C. Analysis and design of a Taguchi-Grey based electricity demand predictor for energy management systems. Energy Conversion and Management 2004; 45: 1205–1217, https://doi.org/10.1016/j.enconman.2003.08.008.
16. Zhang H, Li Z, Chen Z. Application of grey modelling method to fitting and forecasting wear trend of marine diesel engines. Tribology International 2003; 36: 753-756, https://doi.org/10.1016/S0301-679X(03)00056-2.
17. Zhang L, Wang Z, Zhao S. Short-term fault prediction of mechanical rotating parts on the basis of fuzzy-grey optimizing method. Mechanical Systems and Signal Processing 2007; 21: 856-865, https://doi.org/10.1016/j.ymssp.2005.09.013.

Maciej TABASZEWSKI
Institute of Applied Mechanics
Poznan University of Technology
ul. Jana Pawła II 24, 60-965 Poznań, Poland

Bartosz FIRLIK
Department of Rail Vehicles
Poznan University of Technology
ul. Piotrowo 3, 60-965 Poznań, Poland

E-mails: maciej.tabaszewski@put.poznan.pl, bartosz.firlik@put.poznan.pl

Article citation info:
ŁUKASZEWSKI K. Adaptive reliability structures of heat exchange surface in turbine condenser. Eksploatacja i Niezawodnosc – Maintenance and Reliability 2018; 20 (1): 153–159, http://dx.doi.org/10.17531/ein.2018.1.20.

Krzysztof ŁUKASZEWSKI

ADAPTIVE RELIABILITY STRUCTURES OF HEAT EXCHANGE SURFACE IN TURBINE CONDENSER

ADAPTACYJNE STRUKTURY NIEZAWODNOŚCIOWE POWIERZCHNI WYMIANY CIEPŁA SKRAPLACZA TURBINY PAROWEJ*

In this paper adaptive reliability structures of heat exchange surface in turbine condenser was proved from the angle of effective heat exchange in variable conditions of its exploitation. Then, determinant factors for design and exploitation in assessment of reliability of pipe subsystem in turbine condenser were suggested. The influence of change of scheme of the pipes, constituting the surface of heat exchange, which stems from the matter of regulating the surface in an attempt to both condense the given amount of steam and maintain the given pressure in the condenser in variable conditions of its exploitation on the reliability of the pipe subsystem was determined. The surface of heat exchange is regulated by enabling and disabling the flow of cooling water through given amount of pipes, in a given way, that is by enabling or disabling possible combination of given pipes in given exploitation conditions. An algorithm to assess the reliability of the pipe subsystem in the condenser in given exploitation conditions, means of regulating the surface and up-to-date technical condition was put forward. The reliability of pipe subsystem has a significant influence either on reliability of the condenser while exploited or in the further course, indirectly on sustaining the requested reliability in the power system therein. Effective operation of the condenser in technical power system is performed by sustaining the given pressure of steam condensation, which is vital in maintaining the required energy efficiency of technical power system in variable exploitation conditions. The exemplification of the aspects put forward in the paper pertains to steam turbine condensers.

Keywords: *adaptive reliability structure, reliability, turbine condenser, designing of heat exchangers, exploitation of heat exchangers.*

W artykule wykazano adaptację struktur niezawodnościowych powierzchni wymiany ciepła skraplacza turbiny parowej z punktu widzenia efektywnej wymiany ciepła w zmiennych warunkach jego eksploatacji. Następnie, wskazano istotne uwarunkowania projektowo-eksploatacyjne oszacowania niezawodności podsystemu rur skraplacza turbiny parowej. Wykazano wpływ zmian układów rur stanowiących powierzchnię wymiany ciepła, które wynikają ze sposobu regulacji tej powierzchni w celu skroplenia zadanej ilości pary wodnej i utrzymywania zadanej wartości ciśnienia w skraplaczu w zmiennych warunkach jego eksploatacji, na niezawodność podsystemu rur. Powierzchnię wymiany ciepła reguluje się poprzez włączanie i wyłączanie przepływu wody chłodzącej przez zadaną liczbę rur, w określony sposób tzn. poprzez włączanie albo wyłączanie możliwych kombinacji określonych układów rur w zadanych warunkach eksploatacyjnych. Przedstawiono algorytm oszacowania niezawodności podsystemu rur skraplacza względem określonych warunków eksploatacyjnych, sposobu regulacji tej powierzchni i aktualnego stanu technicznego. Niezawodność podsystemu rur ma istotny wpływ na niezawodność skraplacza turbiny parowej w czasie jego eksploatacji, a dalej pośrednio na utrzymywanie wymaganej niezawodności systemu energetycznego, w którym występuje. Efektywne funkcjonowanie skraplacza w technicznym systemie energetycznym jest realizowane poprzez utrzymywanie zadanego stałego ciśnienia skraplania pary wodnej, co jest istotne z punktu widzenia utrzymywania wymaganej sprawności energetycznej technicznego systemu energetycznego w różnych warunkach eksploatacyjnych. Egzemplifikacja zawartych w pracy zagadnień odnosi się do rurowych skraplaczy turbin parowych.

Słowa kluczowe: *adaptacyjna struktura niezawodnościowa, niezawodność, skraplacz turbiny parowej, projektowanie wymienników ciepła, eksploatacja wymienników ciepła.*

1. Introduction

The aim of the paper is to prove adaptive reliability structures of heat exchange surface, which stems from the matter of regulating the surface in order to maintain effective process of heat exchange by sustaining the requested pressure of steam condensation in variable exploitation conditions, which determines changes in the pipe system of the condenser and involves assessment of reliability of its surface of heat exchange.

Adaptive reliability structures of surface of heat exchange (pipe subsystem) are the reliability structures, which are altered in the course of adjusting the pipe system to the actual exploitation conditions of the condenser in the power system.

Having delved into the current state of the art with IT data bases (Science Direct, Knovel, Nauka Polska, BazTech, google) it was concluded that there has been no algorithm for assessing reliability of surface of heat exchange of steam turbine condenser which would include regulation of the surface in order to exchange the heat effectively and sustain the requested pressure of steam condensation in variable exploitation conditions, which has a significant influence on the quality of the technical power system exploitation, in which the condenser is a part.

Publication [10] shows that sustaining given pressure of steam condensation in the condenser in variable conditions is vital for maintaining requested power efficiency of the technical power system. The aforementioned publication puts forward a particular technical solu-

(*) Tekst artykułu w polskiej wersji językowej dostępny w elektronicznym wydaniu kwartalnika na stronie ***www.ein.org.pl***

tion, which comes to proper division of the heat exchange surface of the condenser at the stage of its design (a particular number of non-adjustable parts of surface and one part of regulated surface of heat exchange), as well as the setup of the part while being exploited. Such technical solution while the condenser is exploited in the steam power system enables effective regulation of the flow of the water cooling the condenser. The regulation then not only allows for a particular heat exchange between the fluids, but also considers relations among the velocity of the cooling water flow, the erosion and deposition of pollutants on the surface of heat exchange as well as the costs of pumping the cooling water.

In publications [2, 8] the influence of exploitation conditions of turbine steam condensers on power plant efficiency was proved.

The method of designing technical heat exchangers in power systems with regard to requested reliability of them was included in [12, 13]. In methods of designing heat exchangers, including steam turbine condensers described in publications [3-5,7,9,12,13,16-18], the surface of heat exchange is treated as a one, non-adjustable composition (element).

Publication [11] includes the problems of assessing the reliability of the exchanger and heat exchangers. It is possible to determine the models of reliability heat exchangers structures on the basis of the models of basic reliability structures of technical objects, included i.a [6,14].

Sources lack the presence of adaptive structures of reliable surfaces of heat exchange in steam turbine condensers, which may be caused by the means of regulating these surfaces to maintain the given pressures of condensation of the steam in variable exploitation conditions due to exploitation of technical power systems, of which they are a part.

As concerns the aim of the paper and the research into the current state of art the following problem recurs: how to sustain the requested reliability of the steam turbine condenser while it is exploited to a given time?

2. Designing process of reliability structures of heat exchange in the condenser

At the stage of designing of the steam turbine condenser, its reliability model is created $R_{wc}(t)$, taking into consideration applications in technical power system, possible kinds of damages to it as well as the construction of the condenser in accordance with the method included in publication [12]. That is, $R_{wc}(t)$ reliability model for the condenser depicted in figure 1 may be referred to as a serial structure of reliability of subsystems of given elements, i.e. each of tube sheets $R_{1,i}(t)$, each of covers $R_{2,i}(t)$, the shell $R_3(t)$, each of the ith of nth number of pipes $R_{4,i}(t)$, each of the seals $R_{5,i}(t)$, each ith of mth number of connecting screws $R_{6,i}(t)$, system of regulation of the surface of heat exchange $R_{7,i}(t)$ (system of adjusting the valves shutting off the flow of cooling water through given pipes of the condenser).

The reliability model $R_{ps,r}(t)$ of pipe subsystem, which refers to the algorithm in figure 1, is determined with serial reliability structure of nth number of pipes:

$$R_{ps,r}(t) = [R_{4,i}(t)]^n . \tag{1}$$

Model (1) is defined within given exploitation conditions: maximal value of the heat stream $\dot{Q}_{1,\max}$ of condensation of the steam in the condenser, minimal value of the overall heat transfer coefficient $k_{i,\min}$ (through the surface of heat exchange with depositions), maximal value of temperature $T'_{2,\max}$ of cooling water on the input of the condenser. In these conditions while the condenser is being exploited, the flow of cooling water through all the pipes is enabled.

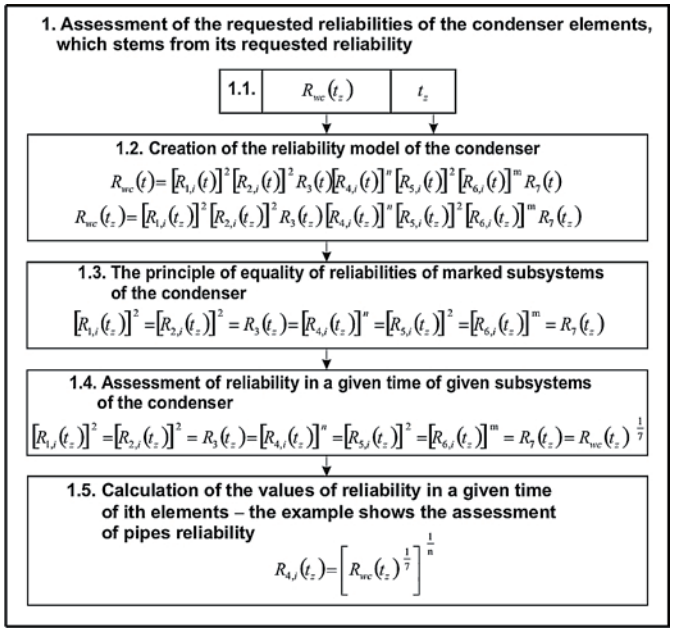

Fig. 1. The algorithm of assessing expected reliabilities of elements of the condenser due to assumed reliability of the condenser (the formula in blocks 1.4 and 1.5 is due to transformation of reliability of the condenser into desirable pipes reliabilities - publication [12] involves the description).

The next significant stage of condenser design is the division of heat exchange surface with regard to anticipated, typical exploitation conditions as present in paper [10]. Both insights allow to assume the following reliability model of pipe subsystem $R_{ps,r}(t)$:

$$R_{ps,r}(t) = R_R(t) R_{NR}(t) , \tag{2}$$

in which $R_R(t)$ stands for the reliability model of pipes subsystem of an adjustable number of pipes, and $R_{NR}(t)$ stands for the model of reliability of pipe subsystem, consisting of a number of mth pipe systems with a particular number of enabled and disabled pipes in these systems.

In the first row, it is considered how to divide the surface of heat exchange of the condenser in terms of typical, anticipated states of exploitation of the condenser due to maximize heat exchange efficiency. Thus, in this way a particular way of regulating the heat exchange surface is implicated, that is for given exploitation conditions, the flow of cooling water (with optimal value of flow velocity) is enabled through minimal number of pipes so as to sustain requested and constant pressure of steam condensation. The next implication revolves around creating particular reliability structures of pipe subsystem and implementing them into the $R_{ps,r}(t)$ model. As a result, $R_R(t)$ model is determined with a serial-parallel structure and hence is a part of n_R number of pipe subsystem.

The subsystem is a proper combination of the structure as for the grading of enabling and disabling a given nth number of pipes out of n_R number in given systems in given exploitation conditions, in which $p=n_R-n$:

$$R_R(t) = \prod_{i=1}^{n} R_{R,1,i}(t)\{1 - \prod_{j=1}^{p}[1 - R_{R,1,j}(t)]\}\ , \quad (3)$$

while n= $n_{R,1}$ then:

$$R_R(t) = \prod_{i=1}^{n} R_{R,1,i}(t)\ , \quad (4)$$

and, while p= $n_{R,1}$:

$$R_R(t) = \{1 - \prod_{j=1}^{p}[1 - R_{R,1,j}(t)]\}\ , \quad (5)$$

in case the pipe subsystem is adjusted by enabling single pipes, then function $R_{R,1,i}(t) = R_{R,1,j}(t) = R_{4,i}(t)$.

The $R_{NR}(t)$ model may also be determined with the serial-parallel structure and it makes the pipe subsystem of n_{NR} number of pipes. Consequently, the subsystem makes a proper combination of the structure as for grading of enabling and disabling given mth pipe systems, where $k=m_{NR}-m$ in given exploitation conditions:

$$R_{NR}(t) = \prod_{i=1}^{m} R_{NR,1,i}(t)\{1 - \prod_{j=1}^{k}[1 - R_{NR,1,j}(t)]\}\ , \quad (6)$$

while $m= m_{NR,1}$

$$R_{NR}(t) = \prod_{i=1}^{m} R_{NR,i}(t)\ , \quad (7)$$

or, while $k=m_{NR}$:

$$R_{NR}(t) = \{1 - \prod_{j=1}^{k}[1 - R_{NR,1,j}(t)]\}\ , \quad (8)$$

in case if mth systems of n-numbered pipes are adjusted than functions $R_{NR,1,i}(t) = R_{NR,1,j}(t) = [R_{4,i}(t)]^n$.

The next step is to consider the division of the surface of heat exchange with regard to typical, assumed exploitation states of the condenser due to maximum reliability $R_{ps,r}(t)$ of pipe subsystem in random configuration of enabling and disabling particular pipe systems while sustaining the requested pressure in the condenser. In such approach, the models $R_R(t)$ and $R_{NR}(t)$ are defined with a threshold reliability structure of *k-out-of-n* type since there is no need to retain the grading to enable and disable particular pipe systems (assuming identical reliability functions of elements of the structure):

$$R_R(t) = \sum_{n=1}^{n_{R,1}} \binom{n_{R,1}}{n} \left[R_{R,i}(t)\right]^n \left[1 - R_{R,i}(t)\right]^{n_{R,1}-n}\ , \quad (9)$$

and:

$$R_{NR}(t) = \sum_{m=1}^{m_{NR}} \binom{m_{NR}}{m} \left[R_{NR,i}(t)\right]^m \left[1 - R_{NR,i}(t)\right]^{m_{NR}-m}\ . \quad (10)$$

3. The reliability structures of heat exchange surface in exploitation

Figure 2 below presents the algorithm to assess reliability $R_{ps,r}(t_i)$ of pipe subsystem in a given time t_i of exploitation of the condenser, which includes the following change of values in given time spans $[t_{i,\min}, t_{i,\max}]$: stream of heat $\dot{Q}_i$ transferred in the condenser, temperature of $T'_{2,i}$ cooling water on the input of the condenser, the number of pipes or change of the number of enabled pipes $\sum_{i=1}^{m} n_{NR,i} + n_{R,i}$ (with the cooling water flow), which has an influence on heat transfer efficiency, the number of disabled pipes $n_{e,p,i} = \sum_{i=1}^{m}(n_{NR,i} - n_{NR,u,i}) + (n_{R,i} - n_{R,u,i})$ (u index) from the exploitation ("jammed"), the pollution of pipe surface as well as the possible air mass content in condensation of steam by calculating the value of overall heat transfer coefficient $k_{e,p,i}$ in given time (problems of ridding of the air in the condenser are not discussed in the paper and hence treated as background problems).

This allows for assumed regulation of the heat surface with regard to a given effective transfer heat $\dot{Q}_i$ in given time spans t_i considering the assessment of pipe subsystem reliability $R_{ps,r,e,i}(t_i) \in [R_{ps,r,e,0}(t_{i,\min}), R_{ps,r,i}(t_{i,\max})]$ in these time spans basing on actual reliability nth pipes $R_i(t_i)$, which stems from function $R_i(t) = f(t_i)_{\{CI_{e,i}, W_{e,i}, W_{ru,e,i}\}}$. The values of quantities from the sets $CI_{e,i}, W_{e,i}, W_{ru,e,i}$ defines respectively the identification features of ith elements of the condenser, conditions of exploitation of these elements and kinds of their damages (publication [12] describes $CI_{e,i}, W_{e,i}, W_{ru,e,i}$ in detail).

The algorithm afterwards may either be treated as an operational tool to verify the function of reliability of pipes $R_i(t) = f(t_i)_{\{CI_{e,i}, W_{e,i}, W_{ru,e,i}\}}$, implemented at the stage of design, or provide opportunity to alter (update) the reliability function at the stage of the condenser exploitation.

While the condenser is being exploited in technical power system, the following values are monitored: pressure p_1 of steam condensation in the condenser and average velocity w_2 of the flow of cooling water through the condenser pipes, which indicate the efficiency of heat transfer with regard to both assumptions as for the steam turbine operation and economic reasons (the cost of pumping the cooling water). This gives ground, according to the algorithm from figure 2., to assess the exploitation surface $A_{e,i}$ of heat transfer and mass cooling water flow volume $\dot{m}_{2,i}$ through particular system of pipes. Subsequently, the electrical conductivity of the condensate Γ is being constantly monitored. In case the value of the conductivity is below the admissible value, reliability structure of pipe subsystem $R_{ps,r}(t_i)$. needs to be redefined.

Otherwise, if Γ value is higher than admissible, it may cause damage to the pipe (a burst). In such circumstances, different system of pipes needs to be implemented urgently: $n_{e,p,i} = \sum_{i=1}^{m}(n_{NR,i} - n_{NR,u,i}) + (n_{R,i} - n_{R,u,i})$. Newly designated value of the surface of heat exchange $A_{e,i}$ is then examined whether it provides effective heat transfer in given exploitation conditions. It must be stressed that only systems with given number of pipes do have an influence on the process of heat transfer. The velocity of the cooling

water flow through the pipes may be increased from above the optimal value to the maximum admissible value $w_{2,i} + \Delta w_{2,i} \le w_{2,\max}$ and is performed in case bigger number of pipes needs to be enabled than this would result from sustaining optimal cooling water flow after damage in a particular number of pipes. This aims to sustain requested pressure in the condenser p_1 ($R_i(t) = f(t_i)_{\{CI_{e,i}, W_{e,i}, W_{ru,e,i}\}}$ function is estimated for a given maximal interval of value of cooling water velocity $w_{2,i} \in < w_{2,opt}, w_{2,\max} >$ [m/s]).

Increasing the value of the pressure of condensation in the condenser $p_{1,p,i}$ to maximal admissible value $p_{1,p,i} + \Delta p_{1,i} \le p_{1,\max}$, which is the result of the decrease in the heat stream transferred in the condenser $\dot{Q}_{1,\min}$ and the decrease of effective power Ne,p,i in the steam turbine, results from the assumed condition of the seal flow of the cooling water through particular pipe system. Ultimately, the condenser should be excluded from exploitation and either include another one or shut down the power system and thus cease to exploit it. The enumerated actions are determined by functioning of a power system in given time of the condenser operation.

It is assumed that experimental researches of ith pipes have been conducted in order to estimate the reliability function $R_i(t) = f(t_i)_{\{CI_{e,i}, W_{e,i}, W_{ru,e,i}\}}$ in given ith time intervals $0 \le t_i \le t_{i,\max}$ by the pipe producers. The researches include the $CI_{e,i}$ characteristics, identifying ith pipes of the condenser, exploitation conditions of the pipes $W_{e,i}$ and the damages thereof $W_{ru,e,i}$ (the scope and value of damage is determined and hence the pipe is considered damaged if the determined values are exceeded).

Values of reliability of pipes $R_i(t_z)_{\{CI_{e,i}, W_{e,i}, W_{ru,e,i}\}}$ in given time t_z are read with the use of reliability function $R_i(t) = f(t_i)_{\{CI_{e,i}, W_{e,i}, W_{ru,e,i}\}}$ of ith pipes. This allows to introduce and implement the values of reliability to models of particular reliability systems of pipe subsystem and calculate reliability of the subsystem in given time and given exploitation conditions.

In case that ith number of pipes have been damaged, they are replaced with ones of the same kind. In case the difference among their real value of reliabilities and the values obtained from the implemented functions $R_i(t) = f(t_i)_{\{CI_{e,i}, W_{e,i}, W_{ru,e,i}\}}$ exceeds the admissible value, new (updated) reliability functions $R_i(t) = f(t_i)_{\{CI_{e,i}, W_{e,i}, W_{ru,e,i}\}}$ are to be estimated on the basis of monitoring the durability of the pipes (Fig. 2, block 2.7.1) while the condenser is being exploited. Each enabling and disabling the cooling water flaw through given pipes $\sum_{i=1}^{m} n_{NR,i} + n_{R,i}$, out of the group (interval) of a given reliability structures $R_{ps,r}(t_i)$, results in a feedback, while estimating the exploitation of heat exchange surface $A_{e,i}$ as for current monitoring purpose and, having reconsidered the condition suggesting that the reliability value $R_{ps,r}(t_i)$ calculated when the condenser is exploited is equal or higher than assumed admissible reliability $R_{ps,r,dop}(t_i)$ in a given time interval t_i. Subsequently it results also in monitoring current exploitation conditions and forecasting these conditions in further time intervals t_i.

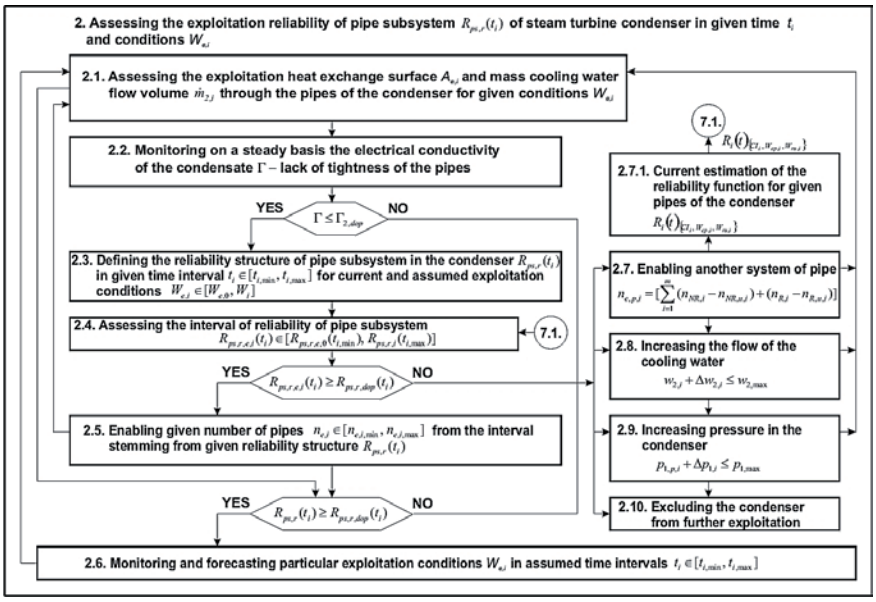

Fig. 2. The algorithm of assessing exploitation reliability of pipe subsystem of steam turbine condenser in given time and conditions

4. Exemplification of the adaptive characteristic of the heat exchange surface in the steam turbine condenser

The calculation example pertains to empirical studies of the damage to the condenser pipes, included in publication [1,15], on the basis of which, normal distribution has been assumed. The parameters of the distribution m=15,7, and σ=6,2 as for 100 pieces of condenser pipes were included into the calculation on the basis of studies of damages to condenser pipes of power units 225MW (publication [15]). According to paper [10] the overall number of pipes (12000) was assumed. Calculations and diagrams were generated with the use of BlockSim software by HBM Prenscia (BlockSim - integrated software allowing for analysis of RBD reliability structures). The example illustrates the calculations of reliability of pipe subsystem with regard to the contents of the paper, in case they include reliability function of pipes made out on the basis of empirical studies of power units condensers. The abridged method for designing heat exchangers of technical power systems with regard to their requested reliability is included in papers [12,13], where means of increasing the reliability of heat exchangers, if necessary, were highlighted.

The pipe subsystem of the steam turbine condenser of 12000 pipes consists of the following pipe systems: $n_{R,i}$=2000, means 20 pipe system 100 pipes each, where the function of reliability of a system may be determined as $R_{R,1,i}(t) = [R_{4,i}(t)]^{100}$ and n_{NR}=10000, where m=5 pipe systems, 2000 each, where consequently the function of reliability of a system may be determined as $R_{NR,1,i}(t) = [R_{4,i}(t)]^{2000}$. There is lack of damaged pipes („jammed"), $n_{NR,u,i}$=0, $n_{R,u,i}$=0.

The first example of calculation (Fig.3) pertains to the application of formulas (11-15) in given exploitation conditions $W_{e,i}$. The latter examples, defined by the number of pipes as follows 6100, 6000, 4100, 4000, 2100, with the flow of cooling water through each, are analogous to the presented formulas (11-15).

The function of reliability $R_{ps,r}(t)$ of pipe subsystem may be defined with the formula (11) if the current exploitation conditions $W_{e,i}$ determine enabling the cooling water flow through 12000 pipes:

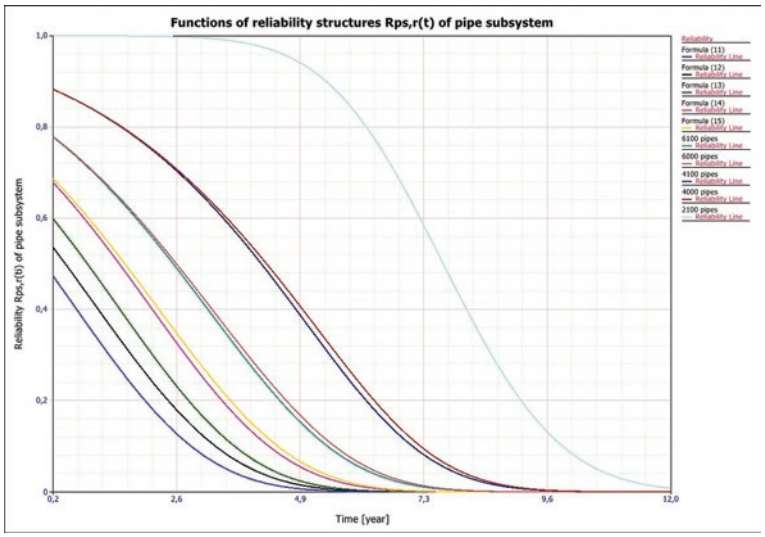

Fig. 3. Functions of reliability structures $R_{ps,r}(t)$ of pipe subsystem

$$R_{ps,r}(t) = \prod_{i=1}^{20} R_{R,1,i}(t) \prod_{i=1}^{5} R_{NR,1,i}(t) \ . \qquad (11)$$

The reliability function $R_{ps,r}(t)$ may be defined with formula (12) if current exploitation conditions $W_{e,i}$ determine enabling the cooling water flaw through 10100 pipes, and 900 pipes are a backup to streams of transferred fluid heat:

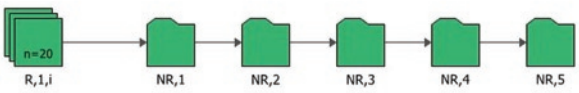

Fig. 4. Flowchart of reliability structure of pipe subsystem – formula (11), where box R,1,i means 20 systems ($R_{R,1,i}(t) = [R_{4,i}(t)]^{100}$) of pipes in serial structure, and sub diagrams NR,1-NR,5 pipe systems ($R_{NR,1,i}(t) = [R_{4,i}(t)]^{2000}$) in serial structure

$$R_{ps,r}(t) = \{1 - \prod_{j=1}^{20} [1 - R_{R,1,j}(t)]\} \prod_{i=1}^{5} R_{NR,1,i}(t) . \qquad (12)$$

Fig. 5. Flowchart of reliability structure of pipe subsystem - formula (12), where box R,1,i means 20 systems ($R_{R,1,i}(t) = [R_{4,i}(t)]^{100}$) of pipes in parallel structure, and sub diagrams NR,1-NR,5 pipe systems ($R_{NR,1,i}(t) = [R_{4,i}(t)]^{2000}$) in serial structure

The function of reliability may be defined $R_{ps,r}(t)$ with the formula (13) if the current exploitation conditions $W_{e,i}$ determine enabling the cooling water flow through 10000 pipes and 2000 pipes are a backup to streams of transferred fluid heat:

$$R_{ps,r}(t) = \prod_{i=1}^{20} R_{R,1,i}(t) \prod_{i=1}^{3} R_{NR,1,i}(t) \{1 - \prod_{j=1}^{2} [1 - R_{NR,1,j}(t)]\} \ . (13)$$

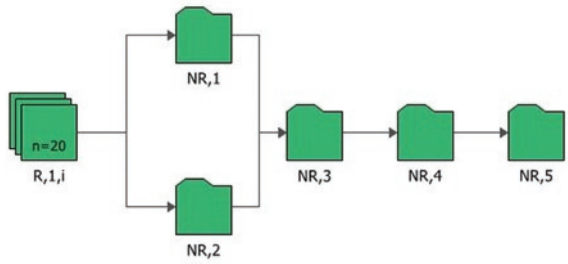

Fig. 6. Flowchart of reliability structure of pipe subsystem – formula (13), where box R,1,i means 20 systems ($R_{R,1,i}(t) = [R_{4,i}(t)]^{100}$) of pipes in serial structure, and sub diagrams NR,1-NR,2 pipe systems ($R_{NR,1,i}(t) = [R_{4,i}(t)]^{2000}$) in parallel structure, and the latter in serial structure

The function of reliability may be defined $R_{ps,r}(t)$ with the formula (14) if the current exploitation conditions $W_{e,i}$ determine enabling the cooling water flow through 8100 pipes and 3900 pipes are a backup to streams of transferred fluid heat:

$$R_{ps,r}(t) = \{1 - \prod_{j=1}^{20} [1 - R_{R,1,j}(t)]\} \prod_{i=1}^{3} R_{NR,1,i}(t) \{1 - \prod_{j=1}^{2} [1 - R_{NR,1,j}(t)]\}. \quad (14)$$

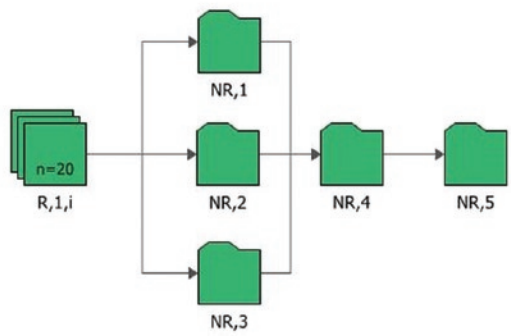

Fig. 7. Flowchart of reliability structure of pipe subsystem – formula (14), where box R,1,i means 20 systems ($R_{R,1,i}(t) = [R_{4,i}(t)]^{100}$) of pipes in parallel structure, and sub diagrams NR,1-NR,2 pipe systems ($R_{NR,1,i}(t) = [R_{4,i}(t)]^{2000}$) in parallel structure, and the latter in serial structure

The function of reliability may be defined $R_{ps,r}(t)$ with the formula (15) if the current exploitation conditions $W_{e,i}$ determine enabling the cooling water flow through 8000 pipes and 4000 pipes are a backup to streams of transferred fluid heat:

$$R_{ps,r}(t) = \prod_{i=1}^{20} R_{R,1,i}(t) \prod_{i=1}^{2} R_{NR,1,i}(t) \{1 - \prod_{j=1}^{3} [1 - R_{NR,1,j}(t)]\} \ . (15)$$

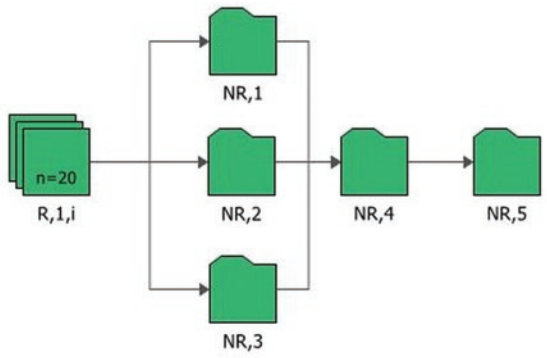

Fig. 8. Flowchart of reliability structure of pipe subsystem - formula (15), where box R,1,i means 20 systems ($R_{R,1,i}(t)=[R_{4,i}(t)]^{100}$) of pipes in serial structure, and sub diagrams NR,1-NR,2 pipe systems ($R_{NR,1,i}(t)=[R_{4,i}(t)]^{2000}$) in parallel structure, and the latter in serial structure

The example illustrated with Figure 3. shows that the reliability $R_{ps,r,e,i}(2)$ of the steam turbine condenser in the second year of exploitation for assumed, considering the ground for effective heat transfer, regulation of the heat exchange surface depending on given exploitation conditions $W_{e,i}$ is the following in respect to Fig.3:

$R_{ps,r}$(t=2)=0,194214; $R_{ps,r}$(t=2)=0,255212; $R_{ps,r}$(t=2)=0,31621; $R_{ps,r}$(t=2)=0,415523; $R_{ps,r}$(t=2)=0,434681; $R_{ps,r}$(t=2)=0,571202; $R_{ps,r}$(t=2)=0,577219; $R_{ps,r}$(t=2)=0,758509; $R_{ps,r}$(t=2)=0,760399; $R_{ps,r}$(t=2)=0,99922.

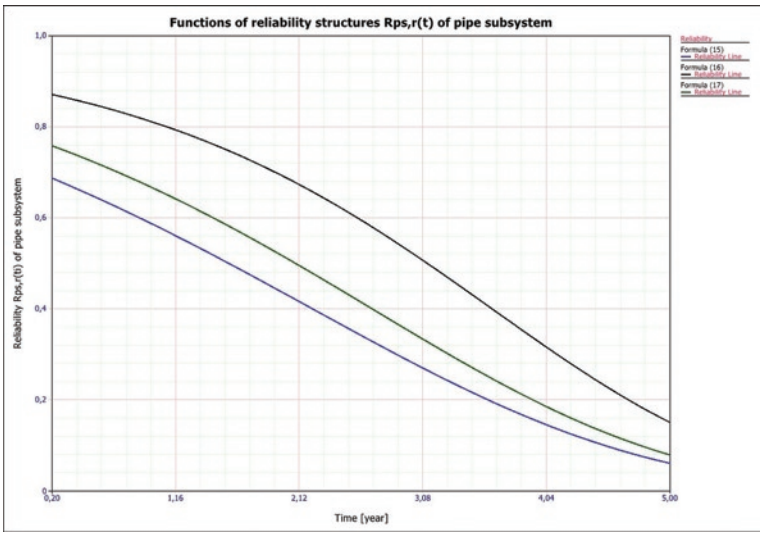

Fig. 9. Functions of reliability structures $R_{ps,r}(t)$ of pipe subsystem

The next example of calculations, illustrated with Fig.9., concerns with application of formulas (15), (16), (17) and given exploitation conditions $W_{e,i}$, which determine enabling the cooling water flow through 8000 pipes of 12000 total.

$$R_{ps,r}(t)=\prod_{i=1}^{20}R_{R,i}(t)\left\{\sum_{m=3}^{5}\binom{5}{m}\left[R_{NR,i}(t)\right]^{m}\left[1-R_{NR,i}(t)\right]^{5-m}\right\}. \quad (16)$$

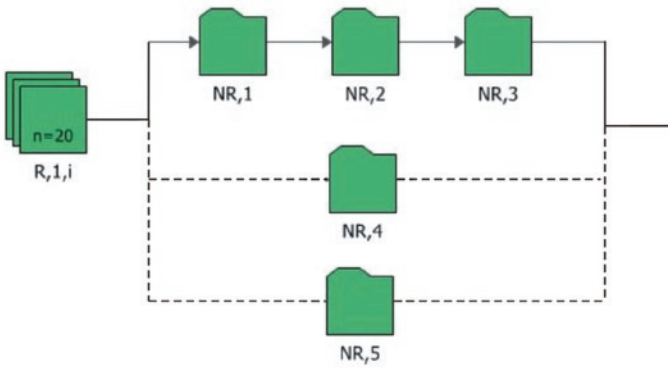

Fig. 10. Flowchart of reliability structure of pipe subsystem - formula (16), where box R,1,i means 20 systems ($R_{R,1,i}(t)=[R_{4,i}(t)]^{100}$) of pipes in serial structure, and sub diagrams NR,1-NR,5 pipe systems ($R_{NR,1,i}(t)=[R_{4,i}(t)]^{2000}$) in structure k-out-of-n

$$R_{ps,r}(t)=\prod_{i=1}^{20}R_{R,i}(t)R_{NR,1,i}(t)\{1-\prod_{j=1}^{2}[1-R_{NR,1,j}(t)]\}\{1-\prod_{j=1}^{2}[1-R_{NR,1,j}(t)]\}. \quad (17)$$

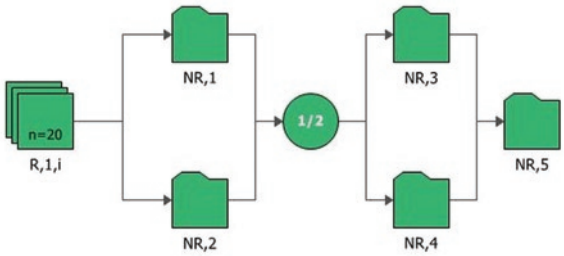

Fig. 11. Flowchart of reliability structure of pipe subsystem - formula (17), where box R,1,i means 20 systems ($R_{R,1,i}(t)=[R_{4,i}(t)]^{100}$) of pipes in serial structure, and sub diagrams NR,1-NR,5 pipe systems ($R_{NR,1,i}(t)=[R_{4,i}(t)]^{2000}$) in serial-parallel structure

The example illustrated with Figure 9. shows that in the second year of exploitation of the steam turbine condenser the reliabilities $R_{ps,r}(t_i)$ of pipe subsystem, defined with formulas (15), (16), (17) equal respectively: $R_{ps,r}$ (t=2) = 0,434681; $R_{ps,r}$ (t=2) = 0,69078; $R_{ps,r}$ (t=2) = 0,514836 in given exploitation conditions.

The calculations allow for the conclusion that the means of regulation of the pipe systems has a significant influence on reliability $R_{ps,r}(t_i)$ of pipe subsystem.

4. Conclusions

It has been proved essential to take into consideration the adaptive property of reliability structure of heat exchange surface both in the process of designing the steam turbine condenser and in the process of its exploitation. The significance of the property is reflected in sustaining the requested value of reliability of the system exploitation and sustaining requested energy efficiency of the technical power system.

By monitoring and forecasting the reliability of the pipe subsystem during exploitation of the steam turbine condenser, the accuracy of estimating the reliability of the condenser is increased.

The algorithm put forward in the paper allows for assumed regulation of the heat exchange surface in respect to effective operating of the condenser in technical power system, considering its current (up-to-date) reliability.

A new approach to estimating the condenser needs to be suggested, involving consideration of regulation of the heat exchange surface, current wear and tear of the pipe system as well as changeable exploitation conditions.

References

1. Aronson K.E. Estimation of the residual life of steam turbine condensers based on statistical models. Thermal Engineering, 2015, 62, 11: 785-789, https://doi.org/10.1134/S0040601515110051.
2. Attia S. I., The influence of condenser cooling water temperature on thermal efficiency of a nuclear power plant. Annals of Nuclear Energy, 2015, 80: 371-378, https://doi.org/10.1016/j.anucene.2015.02.023.
3. Christian J.L, Hermes Ch. J. L. Thermodynamic design of condensers and evaporators: Formulation and applications. International Journal of Refrigeration, 2013, 36: 633-640, https://doi.org/10.1016/j.ijrefrig.2012.10.032.
4. Edwards E. J. Design and rating shell and tube heat exchangers. Retrieved 10th January 2012, from, http://www.chemstations.net/documents/shell.pdf.
5. Fraas P. A, Ozisik N. M. Heat Exchange Design. John Wiley & Sons, Inc, 1965.
6. Gertsbakh I. Reliability Theory. With Applications to Preventive Maintenance. Springer, 2000.
7. Hesselgreaves, John E., Richard Law, and David Reay. Compact heat exchangers: selection, design and operation. Butterworth-Heinemann, 2016.
8. Ibrahim M. A. and Badawy R., A parametric study of the impact of the cooling water site specific conditions on the efficiency of a pressurized water reactor nuclear power plant. International Journal of Nuclear Energy, 2014, 2014:1-6.
9. Kakac S, Liu H. Heat exchangers selection, rating and thermal design. CRC Press LLC, Florida 1998.
10. Łukaszewski K. Efektywność funkcjonowania skraplacza turbiny parowej – zagadnienia projektowo-eksploatacyjne. Energetyka 2016; 4: 240-246.
11. Łukaszewski K., Eksploatacyjne badania niezawodności wymienników ciepła wspomagane komputerowo. Materiały XII Szkoły Komputerowego Wspomagania Projektowania, Wytwarzania i Eksploatacji, Wojskowa Akademia Techniczna, Warszawa 2008, Jurata 2008: 225-230.
12. Łukaszewski K. Metoda projektowania wymienników ciepła technicznych systemów energetycznych ze względu na wymaganą niezawodność tych systemów – część 1. Zeszyty Naukowe Akademii Morskiej w Gdyni 2014; 83: 149-173.
13. Łukaszewski K., Metoda projektowania wymienników ciepła technicznych systemów energetycznych ze względu na wymaganą niezawodność tych systemów – część 2. Zeszyty Naukowe Akademii Morskiej w Gdyni 2014; 83: 174-193.
14. Rausand M. System Reliability Theory. Models, Statistical Methods, and Applications. John Wiley & Sons, 2004.
15. Salij A, Stępień J. C. Praca skraplaczy turbinowych w układach cieplnych bloków energetycznych. Lublin: KAPRINT, 2013.
16. Shah, Ramesh K., and Dusan P. Sekulic. Fundamentals of heat exchanger design. John Wiley & Sons, 2003, https://doi.org/10.1002/9780470172605.
17. Smith E. M. Thermal design of heat exchangers. John Wiley & Sons, Inc, 1997.
18. Zhu K, Chen X, Dai B, Wang Y, Li X, Li L. Eksperimental study on the thermal performance improvement of a new designed condenser with liquid separator. Energy Procedia, 2016, 104: 269-274, https://doi.org/10.1016/j.egypro.2016.12.046.

Krzysztof ŁUKASZEWSKI
Faculty of Marine Engineering
Gdynia Maritime University
ul. Morska 81-87, 81-225 Gdynia, Poland

E-mail: klukasz@am.gdynia.pl

INFORMATION FOR AUTHORS

Eksploatacja i Niezawodnosc – Maintenance and Reliability – the journal of the Polish Maintenance Society, under the scientific supervision of the Polish Academy of Sciences (Branch in Lublin), published four times a year.

The scope of the Quarterly

The quarterly *Eksploatacja i Niezawodnosc – Maintenance and Reliability* publishes articles containing original results of experimental research on the durability and reliability of technical objects. We also accept papers presenting theoretical analyses supported by physical interpretation of causes or ones that have been verified empirically. *Eksploatacja i Niezawodność – Maintenance and Reliability* also publishes articles on innovative modeling approaches and research methods regarding the durability and reliability of objects.

The following research areas are particularly relevant to the journal:

1. degradation processes of mechanical and biomechanical systems,
2. diagnosis and prognosis of operational malfunctions and failures.
3. analysis of failure risk/wear,
4. reliability-and-environmental-safety engineering in the design, manufacturing and maintenance of objects,
5. management and rationalization of object maintenance,
6. risk management in the processes of operation and maintenance,
7. the human factor and human reliability in operation and maintenance systems.

Terms and Conditions of Publication

The quarterly *Eksploatacja i Niezawodnosc – Maintenance and Reliability* publishes only original papers written in English or in Polish with an English translation. Translation into English is done by the Authors after they have received information from the Editorial Office about the outcome of the review process and have introduced the necessary modifications in accordance with the suggestions of the referees! Acceptance of papers for publication is based on two independent reviews commissioned by the Editor.

The quarterly *Eksploatacja i Niezawodnosc – Maintenance and Reliability* proceeds entirely online at submission.ein.org.pl

Technical requirements

- After receiving positive reviews and after acceptance of the paper for publication, the text must be submitted in a Microsoft Word document format.
- Drawings and photos should be additionally submitted in the form of high resolution separate graphical files in the TIFF, SVG, AI or JPG formats.
- A manuscript should include: names of authors, title, abstract, and key words that should complement the title and abstract (in Polish and in English), the text in Polish and in English with a clear division into sections (please, do not divide words in the text); tables, drawings, graphs, and photos included in the text should have descriptive two-language captions, if this can be avoided, no formulae and symbols should be inserted into text paragraphs by means of a formula editor; references (written in accordance with the required reference format); author data – first names and surnames along with scientific titles, affiliation, address, phone number, fax, and e-mail address.

The Editor reserves the right to abridge and adjust the manuscripts. All submissions should be accompanied by a submission form.

Detailed instructions to Authors, including evaluation criteria can be found on the journal's website: www.ein.org.pl

Editor contact info

Editorial Office of „Eksploatacja i Niezawodnosc - Maintenance and Reliability"
Nadbystrzycka 36, 20-618 Lublin, Poland
e-mail: office@ein.org.pl

INFORMATION FOR SUBSCRIBERS

Fees

Yearly subscription fee (four issues) is 100 zloty and includes delivery costs. Subscribers receive any additional special issues published during their year of subscription free of charge.

Orders

Subscription orders along with authorization to issue a VAT invoice without receiver's signature should be sent to the Editor's address.

Note

In accordance with the requirements of citation databases, proper citation of publications appearing in our Quarterly should include the full name of the journal in Polish and English without Polish diacritical marks, i.e.,

Eksploatacja i Niezawodnosc – Maintenance and Reliability.

Wydawca:
Polskie Naukowo Techniczne
Towarzystwo Eksploatacyjne
Warszawa

Publisher:
Polish Maintenance Society
Warsaw

Członek:
Europejskiej Federacji
Narodowych Towarzystw
Eksploatacyjnych

Member of:
European Federation of National
Maintenance Societies

Patronat naukowy:
Polska Akademia Nauk
Oddział Lublin

Scientific Supervision:
Polish Academy of Sciences
Branch in Lublin